

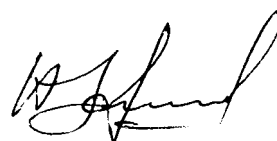
REPORT DOCUMENTATION PAGE				Form Approved OMB No. 0704-0188	
Public reporting burden for this collection of information is estimated to average 1 hour per response, including the time for reviewing instructions, searching existing data sources, gathering and maintaining the data needed, and completing and reviewing the collection of information. Send comments regarding this burden estimate or any other aspect of this collection of information, including suggestions for reducing the burden, to Department of Defense, Washington Headquarters Services, Directorate for Information Operations and Reports (0704-0188), 1215 Jefferson Davis Highway, Suite 1204, Arlington, VA 22202-4302. Respondents should be aware that notwithstanding any other provision of law, no person shall be subject to any penalty for failing to comply with a collection of information if it does not display a currently valid OMB control number. PLEASE DO NOT RETURN YOUR FORM TO THE ABOVE ADDRESS.					
1. REPORT DATE (DD-MM-YYYY) 29-03-2004		2. REPORT TYPE Final Report		3. DATES COVERED (From – To) 01-Apr-02 - 01-Jan-04	
4. TITLE AND SUBTITLE Studying of atomic and molecular interaction processes in rarefied hypervelocity expanding flows by methods of emissive spectroscopy				5a. CONTRACT NUMBER ISTC Registration No: 2234	
				5b. GRANT NUMBER	
				5c. PROGRAM ELEMENT NUMBER	
6. AUTHOR(S) Dr. George Karabadzhak				5d. PROJECT NUMBER	
				5d. TASK NUMBER	
				5e. WORK UNIT NUMBER	
7. PERFORMING ORGANIZATION NAME(S) AND ADDRESS(ES) TSNIIMASH Pionerskaya street 4 Korolev 141070 Russia				8. PERFORMING ORGANIZATION REPORT NUMBER N/A	
9. SPONSORING/MONITORING AGENCY NAME(S) AND ADDRESS(ES) EOARD PSC 802 BOX 14 FPO 09499-0014				10. SPONSOR/MONITOR'S ACRONYM(S)	
				11. SPONSOR/MONITOR'S REPORT NUMBER(S) ISTC 00-7046	
12. DISTRIBUTION/AVAILABILITY STATEMENT Approved for public release; distribution is unlimited.					
13. SUPPLEMENTARY NOTES					
14. ABSTRACT The Project includes three relatively independent tasks joined by a common idea to elucidate complex phenomena occurring in hypervelocity rarified flows of electric propulsion (EP) and liquid propulsion (LP) motor exhausts. Processing and interpretation of experimental data obtained on board of Russian space station "Mir" during experiment on April 26, 2000. In that experiment a large-scale UV-glow was observed in the LP motors exhaust flow of the Russian space vehicle (SV) "Progress". Problems associated with the "Progress" plume glow radiation modeling were addressed, as the glow radiation is directly related to parameters of hypervelocity collisions between plume and atmospheric species. Modern approaches to simulation of the rarified non-equilibrium reacting flows exploit ideas of total elastic and inelastic molecular collision cross-sections. Finally, Hall-effect thrusters (HETs) and their plasma plumes were studied. Plasma probes were developed, calibrated and applied to the plume. The xenon emission was measured and interpreted via a collisional-radiative model. A cluster of 3 HETs was developed and its operation tested and the plume studied.					
15. SUBJECT TERMS EOARD, Propulsion, Engines and Fuels, Electric & Ion Propulsion					
16. SECURITY CLASSIFICATION OF:			17. LIMITATION OF ABSTRACT UL	18. NUMBER OF PAGES 202	19a. NAME OF RESPONSIBLE PERSON INGRID J. WYSONG
a. REPORT UNCLAS	b. ABSTRACT UNCLAS	c. THIS PAGE UNCLAS			19b. TELEPHONE NUMBER (Include area code) +44 (0)20 7514 4285

CENTRAL RESEARCH INSTITUTE FOR MACHINE-BUILDING
(TSNIIMASH)

**Studying of Atomic and Molecular Interaction Processes in Rarified
Hypervelocity Expanding Flows by Methods of Emissive
Spectroscopy**

Final Technical Report for ISTC Partner Project #2234p

General Director of TSNIIMASH



N.A. Anfimov

Project Manager and Principal Investigator



G.F. Karabadzhak

Korolev, Moscow region, February 2004.

CONTENT

List of abbreviations.....	5
1. Introduction.....	6
2. Processing and interpretation of the data obtained in 26 April 2000 experiment.....	9
2.1. Ballistic scheme and observation conditions	9
2.2. Motor set and atmospheric parameters.....	10
2.2.1. Motor set parameters.....	10
2.2.2. Modeling of the atmospheric parameters	11
2.3. Description of the experimental apparatus.....	12
2.3.1. Ultraviolet imager	12
2.3.2. UV-NIR spectrometer	13
2.4. Data processing.....	13
2.4.1. Processing of the imager data.....	14
2.4.2. Processing of the spectrometer data	16
2.5. Calibration of the instruments.....	16
2.5.1. Calibration of the imager.....	16
2.5.1.1. Imager FOV, single pixel FOV and spatial resolution.....	16
2.5.1.2. Point source response	17
2.5.1.3. Uniformity of the imager response over the FOV	19
2.5.1.4. Relative spectral and absolute response.....	19
2.5.1.5. Temporal resolution.....	22
2.5.2. Spectrometer calibration	22
2.5.2.1. Effective FOV.....	22
2.5.2.2. Spectral response	23
2.5.2.3. Wavelength calibration	24
2.5.3. Spatial affixment and temporal synchronization of the imager and spectrometer output signals ..	25
2.5.3.1. Spatial affixment.....	25
2.5.3.2. Time histories of the instrument signal and time synchronization.....	25
2.6. Analysis and interpretation of the April 26, 2000 experiment data.....	26
2.6.1. The glow images	26
2.6.2. Spectral composition of the plume glow and analysis of the spectra	27
2.6.3. Time histories of in-band radiation intensities	29
2.6.4. Filter measurements	31
2.6.5. Absolute radiation intensity of the glow measured by the imager	32
2.6.6. Plume glow induction and decay.....	33
2.7. Concluding remarks to the data processing and analysis	33
3. Improvement of the TAL plasma optical diagnostic technique	35
3.1. General remarks to the current status of the HET plasma optical diagnostics	35
3.2. Phenomenological collisional-radiative model for the HET plasma.....	37
3.2.1. Modeling of the HET plasma radiation intensity	37
3.2.2. Emission excitation cross-sections and rate coefficients.....	41
3.2.2.1. Atomic emissions	41
3.2.2.2. Ionic emissions	45
3.3. Practical application of the suggested CRM for HET plasma diagnostics.....	48
3.3.1. Applicability of the developed CRM in the HET plasma.....	48
3.3.2. Utilization of the XeI emissions for measurements of the HET plume parameters	49
3.3.3. Problems of the XeI emissions utilization for measurements of the TAL discharge parameters ..	54
3.3.4. Potential utilization of ionic emissions for a HET plasma diagnostics	55
3.4. Concluding remarks to Chapter 3	57
4. Development and preparation of triple TAL cluster.	59
4.1. Development and manufacturing of the cluster assembly, its verification and study of integral characteristics.....	60
4.2. Description of the cluster design.....	60
4.2.1. Cluster	60
4.2.2. Power Supply and Measurement System	61
4.3. Experimental investigation of the cluster.....	64
4.3.1. Study of Integral Parameters of Diverse Cluster Architectures.....	64
4.3.2. Cluster Thrust Measurements.....	64
4.3.3. Influence of cathode position on thruster and cluster performance.....	66
4.3.4. Research of oscillations of discharge current in cluster circuits.....	69
4.4. Conclusion to Chapter 4.....	71
5. Development of the plume diagnostic system and testing on a single thruster plume	72

5.1.	Description of the developed / used diagnostic tools	72
5.1.1.	2D near field zone positioning system.	72
5.1.2.	3D far field zone positioning system.	73
5.1.3.	Systems for control and measurement.	74
5.2.	Selection, improvement and verification of probe designs and sizes. Improvement of the measurement procedure.	76
5.2.1.	Selection of the probe size and geometry.	77
5.2.2.	Comparison of flat probes of different sizes.	82
5.3.	Experimental results of investigation of a single thruster plume	86
5.3.1.	Results of the probe measurements	86
5.3.1.1.	Probe measurements of a thruster plume.	86
5.3.1.2.	Measurements of ion energy spectrums.	90
5.3.2.	Influence of thruster operating mode on characteristics of flow	93
5.3.3.	Influence of test conditions on the flow characteristics.	95
5.3.3.1.	Influence of electrical circuit.	95
5.3.3.2.	Influence of pressure.	96
5.4.	Conclusion to Chapter 5	97
6.	Initial characterization of the triple TAL cluster plume flow.	99
6.1.	Ion current distribution in the cluster plume.	99
6.2.	Plasma potential and electron temperature in the cluster plume	104
6.3.	Cluster plume ion energy spectrum study.	108
6.4.	Conclusion to Chapter 6	110
7.	Modeling of the Hall effect thruster plume flow parameters and comparison with experimental data	112
7.1.	Mathematical model of EP plume.	112
7.1.1.	Characteristics of the primary plasma flow.	114
7.1.2.	Characteristics of secondary plasma.	115
7.2.	Comparison of theoretical models with experimental data.	117
7.2.1.	Choice of the coordinate system.	117
7.2.2.	Comparison of modeling results with SPT and TAL plume parameters measured in vacuum chambers.	119
7.3.	Comparison of the SSM-model plasma plume with Express flight data	122
7.4.	Verification of SSM-model on measurements of D-55 plume parameters obtained on TSNIIMASH test facility	124
7.5.	Conclusions for Chapter 7	130
8.	Modeling of the high altitude plume glow intensity and verification of the molecular collision cross-section models through comparison with space experiment data	132
8.1.	General description of the glow model and basic assumptions	132
8.2.	Comparison of different computing models of the glow	133
8.2.1.	General formulation and possible simplifications	133
8.2.1.1.	Spatial scales for principal processes in the plume	133
8.2.1.2.	Simplification of the plume flow kinetic model	134
8.2.2.	Computation of the gasdynamic parameters of the PME plume flow in Zone I	135
8.2.3.	Algorithms for simulation of radiation intensity in Zone II	139
8.2.3.1.	TPMC method for glow radiation modeling	139
8.2.3.2.	FNSAF method	140
8.2.3.3.	1-D analytical solution	140
8.3.	Modeling of the molecular collisions at hypervelocity condition	141
8.3.1.	Elastic collisions	141
8.3.2.	Reaction cross-section	144
8.3.3.	Influence of the elastic collision cross-section choice onto results of the glow intensity computation by TPMC method	146
8.4.	Computation of the PME glow radiation	150
8.4.1.	Influence of the dimensions of the computational domain	150
8.4.2.	Comparison between TPMC and full DSMC computation	151
8.4.3.	Comparison between TPMC and FNSAF methods	152
8.5.	Comparison of the PME glow modeling results with experiment and determination of the elastic and reaction cross-sections.	153
8.6.	ACS motor cluster plume flowfield modeling	157
8.6.1.	Flow parameters at the nozzle exit	157
8.6.2.	Modeling of a single ACS motor plume flow parameters	158
8.6.3.	Modeling of the 8xACS motor cluster plume flow parameters	160
8.7.	Modeling of the 8xACS motor plume glow radiation	165

8.8.	Comparison of 8xACS motor plume flow radiation modeling results with 26 April 2000 experimental data	169
9.	Extension of the glow radiation model	171
9.1.	Improvement of the computational methods.....	171
9.2.	Consideration of other reactions producing excited OH(A) molecules	175
9.2.1.	Reaction between hydrogen and oxygen.....	175
9.2.2.	Water luminescence under VUV radiation.....	175
9.2.3.	Reaction of the vibrationally-rotationally excited water molecules with atmospheric oxygen ...	175
9.2.4.	Reaction of water with metastable oxygen.....	176
9.3.	Consideration of other molecular band emissions	177
9.3.1.	Reactions producing NH(A) radiation.....	177
9.3.2.	Reaction between carbon dioxide and atmospheric oxygen.....	178
9.4.	Attenuation of the radiation in the plume flow	179
9.4.1.	Resonant scattering of the OH(A→X) radiation in the plume flow	179
9.4.2.	Evaluation of the effect of the unburned fuel droplets onto redistribution of the OH(A→X) radiation in the 8xACS plume flow.....	184
9.4.2.1.	Water condensation on unburned propellant droplets.....	184
9.4.2.2.	Attenuation of the radiation by the droplets	186
9.5.	Comparison of the improved glow radiation model predictions with results of 26 April 2000 experiment.....	188
9.6.	Concluding remarks on the glow radiation modeling	190
	Appendix.....	192
	References.....	196

List of abbreviations

ACS - Attitude Control System
ADC - Analog to Digit Converter
AFRL - Air Force Research Laboratory,
CEX - Charge Exchange
CFD - Computational Fluid Dynamics
CMC - Combined Monte-Carlo
cpp - counts per pixel
CRM - Collisional-Radiative Model
DSMC - Direct Simulation Monte-Carlo
EEDF - Electron Energy Distribution Function
EP - Electric Propulsion
FFT - Fast Fourier Transform
FNSAF - Fast Numerical Solution of Analytical Formulation (method of computation)
FOV - Field-of-View
GEO - Geostationary Earth Orbit
HET – Hall Effect Thruster
IR - infrared
LEO - Low Earth Orbit
LIF - Laser Induced Fluorescence
LP - Liquid Propulsion
LTE – Local Thermal Equilibrium
NARJ - Numerical Analysis of Real Jets (CFD code)
PME - "Progress" Main Engine
PNS - Parabolized Navier-Stokes
“Progress” – Russian automatic cargo space vehicle serving manned space stations
SC - Single Collision
“Soyuz” – Russian manned transportation spacecraft serving space stations
SPT - Stationary Plasma Thruster
SSM – Self-Similar Model
SV – Space Vehicle
TAL - Thruster with Anode Layer (Anode Layer Thruster)
TCE – Total Collision Energy
TD - Trajectory Dynamics
TPMC - Test Particle Monte-Carlo
UV - Ultraviolet
VAC - Volt-Ampere Characteristic
VHS - Variable Hard Sphere
VUV – Vacuum Ultraviolet

Executive Summary

The attached Report documents the technical activities and results obtained within the frame of ISTC/EOARD/TSNIIMASH Partner Project #2234p. The Project includes three relatively independent Tasks A, B and C joined by a common idea to elucidate complex phenomena occurring in hypervelocity rarefied flows of electric propulsion (EP) and liquid propulsion (LP) motor exhausts. The Project started on April 1, 2002 and lasted 21 months.

Task A: Processing and Interpretation of data obtained during 26 April, 2000 on Mir Station.

The purpose of Task A, detailed in Chapter 2, was to process and interpret experimental data obtained on board the Russian space station “Mir” during an experiment on April 26, 2000. In that experiment a large-scale ultraviolet (UV)-glow was observed in the liquid rocket engine exhaust flow of the Russian space vehicle (SV) “Progress”. The source of that glow was assumed to be effluent plume molecules colliding with oxygen atoms in the Earth atmosphere. Measurements of *absolute intensity* and spatial distribution of the resulting molecular band radiation provide valuable data for study of the collision characteristics. In addition, plume spectra were obtained on April 26, 2000 during the “Progress” de-orbiting. Analysis of the experimental data elucidated the glow spectral composition problem and increased previous imager data value significantly. Some earlier glow images and auxiliary data obtained in a 28 February 1999 experiment have also been processed. Analysis of these data provided additional arguments supporting the glow radiation model. The OH(A>X) (all bands in 300-320 nm region) and NH(A>X) (all bands in 325-345 region) radiation intensities along the plume flow centerline have been determined at 155 sec after the motors burn started: $W_{OH}=1.85\pm0.3\cdot10^{-5}$ W/m²sr, $W_{NH}=3.9\pm0.6\cdot10^{-5}$ W/m²sr. In addition to the molecular bands, atomic oxygen emissions related to metastable states O(¹D) and O(¹S) have been identified in the plume glow. Also, an unexpected growth of the NH(A>X) in-band radiation intensity was observed during the final minute of the motor set operation. Two hypotheses have been put forward to explain this growth. Detailed discussion of the experimental data processing is presented in Chapter 2.

Task C: Understanding the physical mechanism that produces the UV “Progress” plume glow radiation.

An emphasis was to deduce the values of the physical collision and reaction cross sections between atomic oxygen and plume molecules at high energies. Typical values for these available in the literature are limited to a temperature range of several thousands degrees, or $kT \sim 0.5$ eV. The spatial distribution of the glow radiation was demonstrated to be sensitive to the value elastic collision cross-section and the imagery data provides a unique means by which to measure its value in the collision energy range ~ 5 eV, which is of great interest for gas simulations under orbital conditions. Also, measurements of plume glow absolute radiation provide a direct way to validate cross-sections for the production reaction. The primary source of the OH(A>X) radiation in the plume glow is hypothesized to be a single-step endoergic reaction between oxygen and water which results in electronically excited products. Reactions of this kind have seldom been studied. Therefore, any data about probability of these reactions would be valuable. An effective reaction cross-section for the single-step reaction between oxygen and water has been evaluated in this work and the radiation modeling and collisional cross-section verification are addressed in Chapter 8.

Direct simulation Monte Carlo and simplified single-collision models of OH(A) production in the plume are presented in Chapters 8 and 9. The glow observation experiments render an opportunity for verification of the cross section values. An effective elastic cross-sections $\sigma_{e,eff} = 9.0\pm1.5 \cdot 10^{-16}$ cm² is inferred. Any reaction model must result in the effective reaction cross-section $\sigma_{r,eff} = 0.6\pm0.2 \cdot 10^{-18}$ cm² in the condition of February 28, 1999 experiment and $\sigma_{r,eff} = 0.5\pm0.17 \cdot 10^{-18}$ cm² in the condition of April 26, 2000 experiment. Different values of the effective cross-sections do not imply any inconsistency between the two experimental data sets. The difference is caused by different experimental conditions, which result in different effective cross-section values due to differences in mean free path. The inability to set a lower limit for the reaction cross-section results from an uncertainty of the spectral composition of the glow radiation measured by the imager in February 28, 1999 experiment and uncertainty of the share of the multi-step reactions in production of the OH(A>X) radiation.

In the end of Chapter 8 and further in Section 9.1 the predicted glow radiation intensity is compared with 26 April 2000 experimental data and a factor of 2-3 discrepancy between the model prediction and

experiment has been found. The most probable reason for this discrepancy is that experimental conditions on 26 April 2000 permit secondary processes to contribute to the glow radiation in addition to the single-step reaction between atmospheric oxygen and water and they more significant in this data set than in previous ones. In this regard, efforts have been undertaken to study additional processes, which might influence the glow radiation during the 26 April 2000 experiment. In particular, the importance of multi-step reactions between water molecules and oxygen atoms has been estimated. The multi-step processes might produce OH(A>X) radiation having a wider spatial distribution in comparison with the primary single-step reaction. Along with the study of additional processes, results of an earlier 28 February 1999 experiment are critically re-considered in Chapter 9.

Task B: Hall-effect Thruster (HET) studies

The efficiency of HETs for on-orbit propulsion give them the potential for reducing costs and enabling more agile and responsive satellite missions. A need for increased thrust and reduced spacecraft contamination require further studies into the plasma physics of the device and the thruster plumes. Analysis of emission spectra is well known as a powerful and non-intrusive diagnostic method, which might advance our knowledge about the HET plasma properties, but the spectra are impossible to interpret without a reasonable collisional-radiative model (CRM). A partial CRM based on the latest cross section data is developed and presented. Although development of a universal CRM for xenon emissions is not possible at this moment, due to lack of the cross-section data for excitation from metastable states and excitation of ions, a selective choice of the diagnostic HET plasma emissions, which may be described by a simplified CRM, is presented; it allows for measurement of electron temperature in D-55 TAL plume. It is also concluded that analysis of XeI visible emissions may help to determine the xenon ion content in the plume region where electron temperature doesn't exceed 2-3 eV. Basics of the CRM in the HET xenon plasma and application of new experimental data for the plasma diagnostics are discussed in Chapter 3 of the Report. Illustrations of the application of the HET optical diagnostic method and recommendations on how it can be improved finalize Chapter 3 -- the improved optical diagnostic technique may successfully complement traditional probe diagnostics, especially in the very near field region.

A proposed solution to the need for higher thrust HET devices is to cluster several together. These clusters form a complex plasma flow caused by interaction of individual HET plumes. Physical mechanisms of interaction between discharges and plasma flows in a HET cluster have not been studied in detail. In this regard, Task B of the Project included several dedicated sub-tasks. In particular, development, assembling and experimental testing of a triple Hall plasma source module has been accomplished. TSNIMSH Hall thrusters with anode layer (TAL) D-55 were utilized for this purpose, with thorough examination of the operation mode, power system and test condition effects. Details of the HET assembly used, measurement results, and analysis are discussed in Chapter 4. The conclusions are: 1) the resulting thrust value of the cluster in all studied regimes is equal to the sum of individual thrust values in all tested schemes; 2) the influence of the "cathode to cluster" distance on cluster operation showed no influence on the thruster performances or on start-up voltages for the distance variation up to 0.5 m; 3) discharge current oscillations of each thruster and oscillations of the summarized current of three thrusters operating from one common power supply were independent in each thruster discharge circuit; 4) measured amplitude of common current oscillations is of the same order as for one in individual thruster circuits.

Investigations of the plasma plume parameters both for the single HET and the cluster have been made. A specialized probe diagnostic system has been designed and assembled which renders extended capabilities for measurements of the cluster plume parameters. Prior to measurement of the cluster plume characteristics the diagnostic system was thoroughly tested, validated and calibrated on a well-characterized single D-55 TAL plume. Issues related to the probe diagnostic system development and testing are discussed in Chapter 5 including: 1) there is significant influence of the probe design and size on measured value of ion flow density; 2) variation of residual pressure in the vacuum chamber causes significant changes in the value and distribution of electron temperature and plasma potential; 3) the measured value of electron temperature is a function of two "quantities": both the operational mode of thruster and test conditions; 4) the energy spectrum of ions has shown that rather fast secondary ions, which are not generated in the discharge inside the thruster, are generated in the plume. All results of the single D-55 plume flow parameters are presented in Chapter 5.

Chapter 6 presents the initial measurements of the cluster plume properties. The cluster plume has an irregular complex structure caused by interaction of three individual hypervelocity ionic beams and cannot be described as a simple linear combination of the individual plumes. The first measurements of the triple-thruster plume characteristics clearly demonstrate this feature. Measured values of electron temperatures and plasma potential in the cluster plume are of the same order as those measured for a single thruster. General trends in ion energy spectrums obtained in the cluster plume are similar to those for a single thruster. However, in part of the cluster tests some instability has been observed. This instability results in the appearance of different energy distributions of ions accelerated perpendicular to the cluster axis.

Insight into the microscopic HET plasma properties undertaken within the scope of Task B of the Project has facilitated further improvement of an analytical Self-Similar Model (SSM). This model has been devised in TSNIIMASH for prediction of the hypervelocity EP plume flow properties. The development and results of the SSM model are discussed in Chapter 7, including: 1) the model describes adequately the distribution of HET plasma plume parameters both for thrusters operating in ground-based vacuum chambers and in space conditions, allowing for such factors as background pressure and conductivity of the vacuum chamber walls; 2) an analysis of thermal processes right behind the crossover zone of HET thruster plume and distribution of the plasma parameters indicate the development of intensive collective processes, which reduce the effective collision mean free path of electrons by orders of magnitude and control electrostatic field intensity and dynamics of the flow expansion further downstream; 3) results of space experiments prove the dominating effect of both the internal electrical self-consistent field and external magnetic field on the dynamics of the plume; 4) based on the SSM-model, a number of fast-running software codes have been developed and successfully applied for evaluation of interaction between plasma plumes and on-board spacecraft systems. Model predictions are compared in Chapter 7 with predictions of other contemporary models and with result of experiments.

List of abbreviations

ACS - Attitude Control System
ADC - Analog to Digit Converter
AFRL - Air Force Research Laboratory
CEX - Charge Exchange
CFD - Computational Fluid Dynamics
cpp - counts per pixel
CRM - Collisional-Radiative Model
CMC - Combined Monte-Carlo
DSMC - Direct Simulation Monte-Carlo
EEDF - Electron Energy Distribution Function
EP - Electric Propulsion
FFT - Fast Fourier Transform
FNSAF - Fast Numerical Solution of Analytical Formulation (method of computation)
FOV - Field-of-View
GEO - Geostationary Earth Orbit
IR - infrared
LEO - Low Earth Orbit
LIF - Laser Induced Fluorescence
LP - Liquid Propulsion
LTE – Local Thermal Equilibrium
TD - Trajectory Dynamics
NARJ - Numerical Analysis of Real Jets (CFD code)
PME - "Progress" Main Engine
PNS - Parabolized Navier-Stokes
SC - Spacecraft
S-C - Single Collision
SPT - Stationary Plasma Thruster
SSM – Self-Similar Model
TAL - Thruster with Anode Layer (Anode Layer Thruster)
TPMC - Test Particle Monte-Carlo
UDMH - Unsymmetrical DiMethylHydrazine
UV - ultraviolet
VAC - Volt-Ampere Curve
VHS - Variable Hard Sphere
VUV – Vacuum Ultraviolet

1. Introduction

This Report documents technical activity and output result obtained within the frame of ISTC/EOARD/TSNIIMASH Partner Project #2234p. The Project includes three relatively independent Tasks A, B and C joined by a common idea to elucidate complex phenomena occurring in hypervelocity rarified flows of electric propulsion (EP) and liquid propulsion (LP) motor exhausts. The Project started on April 1, 2002 and supposed to be finished on June 30, 2003. However, at the final stage of the Project new important aspects of the research became evident and it was extended to December 31, 2003 upon mutual agreement of the Project parties.

Purpose of **Task A** of the Project was to process and interpret experimental data obtained on board of Russian space station “Mir” during experiment on April 26, 2000. In that experiment a large-scale UV-glow was observed in the LP motors exhaust flow of the Russian space vehicle (SV) “Progress”. Source of that glow was assumed to be effluent plume molecules colliding with oxygen atoms in the Earth atmosphere. Some of these collisions might lead in production of particular molecular band radiation. Measurements of absolute intensity and spatial distribution of this radiation provide valuable data for studying of the collision characteristics. It should be noted that such kind of glow was observed yet earlier both from the US Shuttles¹ and Russian “Mir” space station². Essential difference between the glow observations from the Shuttles and “Mir” was that Shuttle instruments looked at the plumes of the LP motors installed on the Shuttle itself, whereas “Mir” instruments observed the plumes of Russian space vehicles “Soyuz” and “Progress” located at a distance of 10 to 60 kilometers away from the station. The latter observation scheme is more favorable for studying of the large-scale spatial distribution of the glow emissions. Also, studying of the Shuttle UV-glow has been limited by the NH(A→X) emission, whereas “Mir” experiments were aimed mainly to understanding of the nature and specific features of the OH(A→X) emission¹. Analysis of the plume images obtained on board of the “Mir” station since 1993 resulted in an idea that OH(A→X) emissions must be one of the main contributor to the UV-glow radiation intensity measured by the imager^{2,3,4,5}. Strong NH(A→X) radiation observed in the Shuttle plume¹ was supposed to be filtered off by the imager. However, some degree of uncertainty remained about the final conclusion on how big were shares of the OH(A→X) and NH(A→X) radiation in the broadband filtered imager’s signal. This uncertainty impeded exact interpretation of the UV-imager measurements and, generally, understated value of the experimental data. To resolve this uncertainty several attempts were undertaken to measure the glow spectra^{6,7}. Most successful one happened on April 26, 2000 during the “Progress” de-orbiting. Both the UV-imager and UV/visible spectrometer installed on board of the “Mir” station acquired the data in that experiment. Analysis of the experimental data elucidated the glow spectral composition problem and raised previous imager data value significantly. In addition, this analysis facilitated discovery of a new features of the glow not clearly accentuated in previous experiments. Interpretation of these features required additional efforts, which have been undertaken within the frame of the Project extension. In particular, some earlier glow images and auxiliary data obtained in 28 February 1999 experiment have been processed. Analysis of these data provided additional arguments supporting the glow radiation model. Detailed discussion of the experimental data processing is presented in Chapter 2.

Task B of the study was necessitated by growing interest to space application of the xenon operating Hall effect type thrusters (HET). In this regard, understanding of elementary processes in the HET plasma outflow has become another important problem. None of the contemporary models can claim to be a complete one in accurately predicting the HET discharge and plume properties in the variety of its operating modes. This is explained by complexity of the phenomena occurring in the non-equilibrium rarified beam-plasma environment of the HET outflow. Therefore, experimental measurements of the plasma parameters and simplified phenomenological models are very demanded nowadays.

Analysis of emission spectra is well known as a powerful and non-intrusive diagnostic method, which might advance our knowledge about the HET plasma properties^{8,9,10,11}. General problem of any optical diagnostic technique is to set up a connection between the plasma characteristics, excited particles number density and emitted radiation. This has used to be done within a conventional collisional-radiative model. Collisional-radiative model of the HET plasma relates the plasma species number densities and energy distributions with radiation through the emission excitation cross-sections. Right choice of the collisional-radiative model and exact knowledge of the cross-sections for collisionally induced excitations entirely control efficiency and accuracy of the optical diagnostic technique. Measurements of collisionally induced emissions in xenon have been conducted recently in AFRL^{11,12,13}. These measurements provided valuable material for both elaboration of the collisional-radiative model of the HET plasma and determination of the emission cross-section values. In addition to the electron impact excitation cross-sections reported by other authors the AFRL experiments suggested valuable data for the XeI and XeII emission excitation in both electron-atomic collisions and collisions between xenon ions and atoms. The latter turned out to be able playing important role in the xenon emission

¹ At the moment of the Project completion a paper was released devoted to the OH(A→X) glow in the Shuttle PRCS motor plume³⁶.

excitation process¹¹. Basics of the collisional radiative model in the HET xenon plasma and application of new experimental data for the plasma diagnostics are discussed in Chapter 3 of the Report. The discussion brings along recommendations on how the HET optical diagnostic technique can be improved. Illustrations of the advanced HET optical diagnostic method practical application finalize Chapter 3.

Along with the study of a single plasma source conducted by different groups of scientists all over a world, particular interest is growing nowadays in study of several interfering HET plasma sources, which form complex plasma flow caused by interaction of individual HET plumes. Studying of these interactions is of fundamental interest stimulated by variety of projects where high power plasma systems are utilized for orbital insertion and interplanetary missions^{14,15,16}. Consideration of different options for development of perspective electric propulsion systems leads to necessity of use of several simultaneously operating thrusters. In scientific literature simultaneously operating thrusters assembly has been conventionally called as cluster.

Physical mechanisms of interaction between discharges and plasma flows in a HET cluster have not been studied in details. Moreover, phenomenological description of possible interaction effects and their dependence on the multi-source flow features and test conditions have had fragmentary character. Very limited data about systems including a number of simultaneously operating HETs has been available prior to the Project beginning. Previous experimental tests of the HET assembly operation have been performed with use of two well-known modifications: anode layer thrusters (TAL) and stationary plasma thrusters (SPT). At the same time, there are no data about plumes of the cluster assemblies, whereas specific phenomena may occur in a composed multi-source plume flow in addition to those occurring in a single-source plume. Influence of test conditions and cluster operating regimes onto the plasma flow characteristics has not been studied at all. Thus, available data could not satisfy the need of analysis and understanding of the physical nature of complex phenomena occurring in the HET cluster plasma plume. In this regard, Task B of the Project included several dedicated sub-tasks. In particular, development, assembling and experimental testing of a triple Hall plasma source module has been accomplished. TSNIIMSH Hall thrusters with anode layer D-55 were utilized for this purpose. This module has been supposed to serve for examination of simultaneously operating several Hall plasma sources, in particular for thorough examination of the operation mode, power system and test condition effects. The module facilitates fundamental investigation of the phenomena occurring in the multi-source plasma plume. The HET assembly, which was used in the Project, measurement results and operation parameters analysis of such modules as well as questions connected with measurements of its plume parameters are discussed in Chapter 4.

Investigation of the plasma plume parameters both for the single HET and the cluster has been made. Specialized probe diagnostic system has been designed and assembled within the frame of the Project. This system renders extended capabilities for measurements of the cluster plume parameters. Prior to measurement of the cluster plume characteristics the diagnostic system was thoroughly tested on a single D-55 TAL plume, which characteristics are fairly well known. Issues related to the probe diagnostic system development and testing are discussed in Chapter 5. Also, results of measurements of D-55 plume flow parameters are presented in this Chapter.

Chapter 6 addresses to initial measurements of the cluster plume properties, which have been carried out within the Project extension. The cluster plume has irregular complex structure caused by interaction of three individual hypervelocity ionic beams. The cluster plume flow can not be described as a simple linear combination of the individual plumes. First measurements of the triple-thruster plume characteristics clearly demonstrated this feature.

Insight into the microscopic HET plasma properties undertaken within the scope of Task B of the Project has facilitated further improvement of the Self-Similar Model (SSM). This model has been devised in TSNIIMASH for prediction of the hypervelocity EP plume flow properties. In particular, the model was successfully used for computation of the real HET plume parameters both in laboratory and space conditions. The SSM model is discussed in Chapter 7. Results of the model predictions are compared in this Chapter with predictions of other contemporary models and with result of experiments.

Problems associated with the “Progress” plume glow radiation modeling have been addressed in **Task_C** of the Project. The glow radiation is directly related to parameters of hypervelocity collisions between plume and atmospheric species. Modern approaches to simulation of the rarified non-equilibrium reacting flows exploit ideas of total elastic and inelastic molecular collision cross-sections¹⁷. A number of phenomenological models for the cross-section simulation are now available^{17,18,19}. Application of the phenomenological models into practical computation is justified by the absence of direct data and complexity of more realistic collisional models. All phenomenological models have adjustable parameters that may be tuned up to fit the model predictions to experiment. Some transport properties of real flows appeared to be very sensitive to the cross-section values, rendering a way for verification of the collisional models. Typically the modeled flow parameters (viscosity and diffusion coefficients, reaction rates) are compared with experimental data obtained in a temperature range limited from upper side by several thousands degrees, that is at $kT \leq 0.5$ eV. From the other side there are big variety of the molecular flows in space (including orbital vehicle motor exhaust flow), which involve species with hyperthermal velocities corresponding to energies $E \sim 1-10$ eV. Contemporary collisional models have not been tested at these collisional energies, so application of these models for hypervelocity conditions doesn't guarantee true results. Task_C activity was particularly addressed to testing of commonly used collisional models at abovementioned energies of colliding partners. These tests seem to be well-timed,

because all earlier simulations of the plume glow had one or another cross-section model involved^{1,4,20,21,22,23}. Spatial distribution of the glow radiation was demonstrated to be sensitive to elastic collision cross-section choice. So, comparison of modeled glow radiation distribution with experimental one suggests a method for verification of elastic cross-section models at hypervelocity condition.

Also, measurements of plume glow absolute radiation provide direct way to validate cross-sections for reactions, producing the glow radiation. Primary source of the OH(A→X) radiation in the plume glow was supposed to be single-step reaction between oxygen and water. Distinctive feature of this single-step reaction is that it results in electronically excited products upon the first hypervelocity collision. Reactions of this kind have not been studied so far. Therefore, any data about probability of these reactions would be valuable. Effective reaction cross-section for the single-step reaction between oxygen and water has been evaluated in this work. Any reactive cross-section model can be verified now through comparison of the model prediction with suggested cross-section value. Issues related to the plume glow radiation modeling and collisional cross-section model verification are addressed in Chapter 8. In the end of this Chapter and further in Section 9.1 predicted glow radiation intensity is compared with 26 April 2000 experimental data. Factor of 2-3 discrepancy between the model prediction and experiment has been found. Most probable reason for this discrepancy was that due to specific experimental conditions on 26 April 2000, other processes contributed to the glow radiation in addition to the single-step reaction between atmospheric oxygen and water. Indeed, the same processes occurred in other experiments as well. However, they couldn't affect the observed radiation distribution that much as in 26 April 2000 experiment. In this regard, efforts have been undertaken within the Project extension to study additional processes, which might influence the glow radiation in condition of 26 April 2000 experiment. In particular, importance of multi-step reactions between water molecule and oxygen atoms has been stated. The multi-step processes might produce the OH(A→X) radiation, having wider spatial distribution in comparison with the primary single-step reaction. Analysis of potential effect of this and some others processes onto the glow radiation is presented in Chapter 9 of the Report. Along with the study of additional processes, results of earlier 28 February 1999 experiment are critically re-considered in this Chapter and primary reaction cross-section is corrected. Inclusion of additional processes and corrected primary reaction cross-section into the glow radiation model substantially improves agreement between the model predictions and results of the April 26, 2000 experiment. This is illustrated in Section 9.5 of Chapter 9.

General edition of the document has been accomplished by G.F.Karabadzha. Chapters 1-3, 8 and 9 were edited by G.F.Karabadzha, Chapters 4-6 – by A.V.Semenkin and Chapter 7 – by E.M.Tverdokhlebova.

2. Processing and interpretation of the data obtained in 26 April 2000 experiment

The 26 April 2000 experiment was devised to synchronously acquire UV-images and spectra from the large-scale glow induced by the exhaust flow of Russian service cargo space vehicle “Progress”. This experiment was highly demanded because none of the earlier attempts to acquire the glow spectra was fully successful. All issues related to this experiment and data processing are described in this Chapter.

2.1. Ballistic scheme and observation conditions

The “Progress” plume glow was observed on 26 April 2000 from the “Mir” space station on the night part of the orbit from the windward side (tail view). The glow was induced by the de-orbiting retro-impulse produced by the space vehicle. The observation started some minutes before motors ignition and finished some minutes after shutdown. So, entire period of the burn for more than 10 minutes was utilized for the data acquisition. Observation scheme is shown in Figure 1. The figure also explains principal geometric definitions:

H – the “Progress” altitude,

L – distance between “Mir” and “Progress”,

θ - pitch angle (angle between the “Progress” main axis and velocity vector),

β - aspect angle (angle at which the “Progress” axis is viewed from “Mir”).

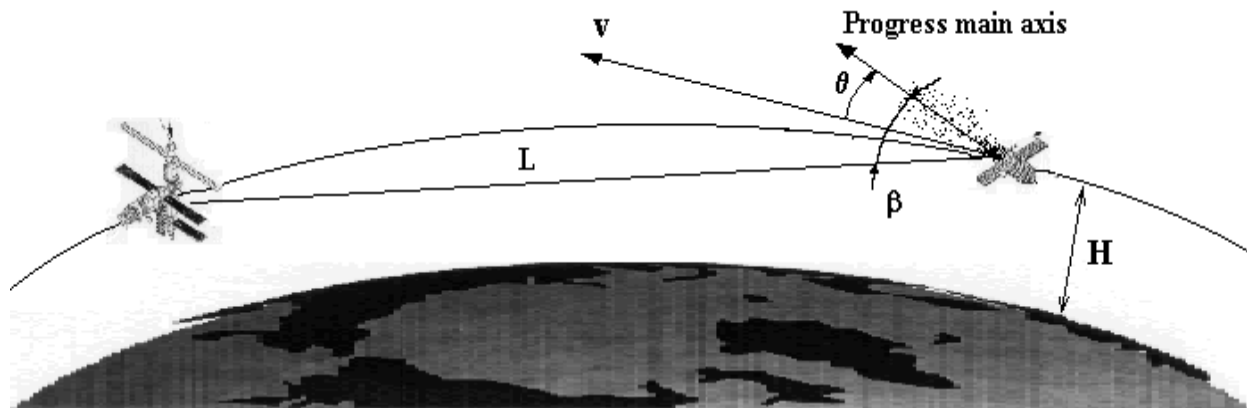


Figure 1. Progress plume glow observation scheme and principal geometric definitions.

Both the space station and the space vehicle flew with orbital velocity $v=7416$ m/sec prior the retro-impulse. At the end of the impulse “Progress” decelerated down to $v=7326$ m/sec. Due to the relative motion of the space vehicle and the station all geometrical parameters of the observation scheme continuously changed during the experiment. Some principal parameters are plotted in Figure 2.

Also, cosmonauts on the “Mir” station controlled manually the instrument line-of-sight direction moving it around the “Progress” location. So, the data were acquired from various parts of the plume.

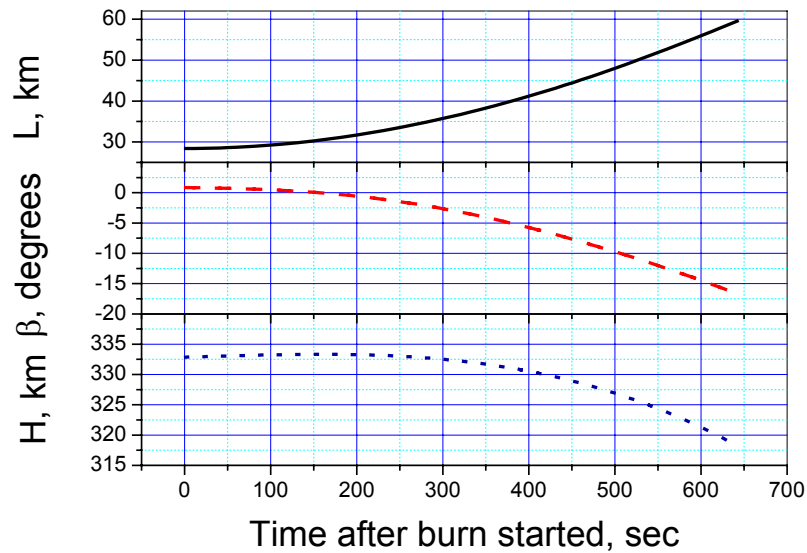


Figure 2. “Mir” and “Progress” trajectory parameters in the April 26, 2000 experiment: altitude H, aspect angle β and distance L.

2.2. Motor set and atmospheric parameters

2.2.1. Motor set parameters

During the experiment eight identical Attitude Control System (ACS) motors operated simultaneously in almost continuous mode providing the de-orbiting impulse. Motor locations on the space vehicle body are depicted schematically in Figure 3. Each pair of the motors was tilted at 20° toward the space vehicle main axis.

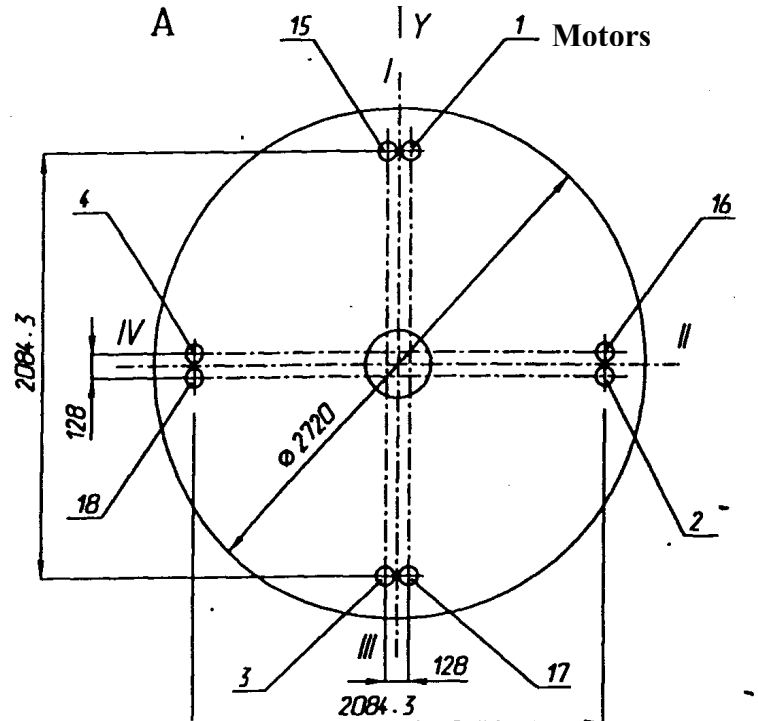


Figure 3. ACS motor set layout (tail view).

The “Progress” position and firing parameters were monitored during the experiment and recovered afterward from telemetry data. The space vehicle was positioned with its main axis parallel to the velocity vector ($\theta \approx 0$) all along the experiment. Generally, deviations of the main axis from this direction not exceeded 1 degree.

The motors operated in nominal mode for about 9 minutes from the start-up, having the flow rate 0.046 kg/sec through each of the eight motor nozzles. However, after the nine minutes of nominal operation pressure in the oxidizer line dropped down and all motors worked for about 50 seconds in essentially fuel rich condition. After that pressure in the fuel line also dropped to the level of nominal fuel to oxidizer ratio and the last minute of the firing motors worked at a decreased level of thrust. In addition, sometimes four motors (1, 2, 15, 16 in Figure 3) stopped firing for a very short period of time, whereas some motors from another ASC motor set (not shown in Figure 3) might burst forth controlling the space vehicle position. As follows from the telemetry data analysis, such kind of transient interruptions of the motor cluster operation could not essentially disturb general motor set characteristics. The major outflow parameters may be considered as being steady for the nine minutes burning period, allowing for a seldom short-timescale oscillations, however. From the other side, the motor shutdowns (even transient) could essentially influence the content of some minor plume components. For instance, relative content of the unburned fuel is much higher in the transient operation regimes of the ACS type motors²⁴.

The outflow parameters at the nozzle exit of each ASC motor may be predicted in a 1-D approximation basing on following nominal motor characteristics:

- ❑ Fuel and oxidizer – UDMH+NTO ($(\text{CH}_3)_2\text{N}_2\text{H}_2 + \text{N}_2\text{O}_4$)
- ❑ Mixture ratio (O/F) – 1.84
- ❑ Combustion chamber pressure, $P - 6.2 \cdot 10^5$ Pa
- ❑ Combustion chamber temperature, $T - 2680$ K
- ❑ Nozzle throat radius, $R_{th} - 0.0061$ m
- ❑ Nozzle exit radius, $R_{ex} - 0.04375$ m

For more accurate 2-D modeling the motor nozzle shape is required. A conventional Laval nozzle contour may serve as a good prototype for the real motor's one. Analysis of the Laval nozzle fitting parameters has been performed and the nozzle contour presented in Figure 4 has been suggested for accurate 2-D modeling of the flow parameters at the nozzle exit.

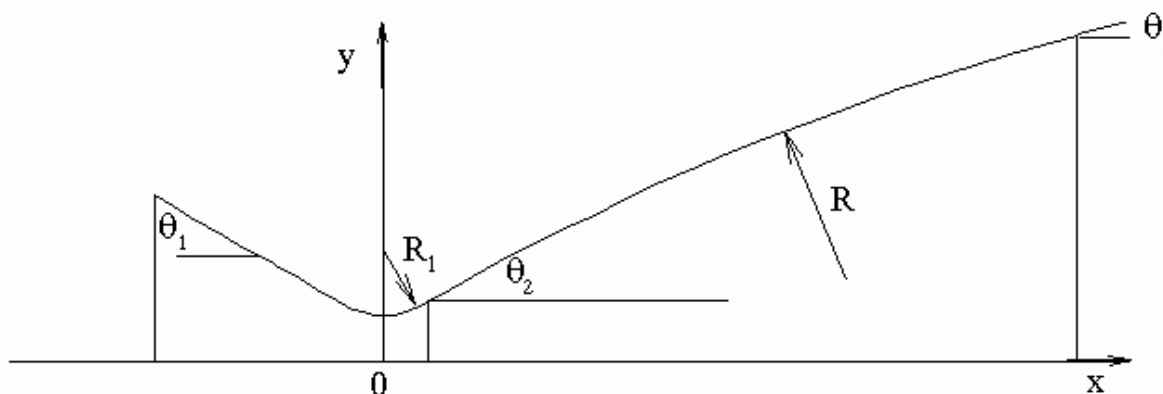


Figure 4. ASC nozzle contour approximation: $\theta_1=30^\circ$, $\theta_2=30^\circ$, $\theta_3=15^\circ$, $R_1=1.6R_{th}$

2.2.2. *Modeling of the atmospheric parameters*

The Earth atmospheric parameters were simulated with the use of MSIS-90 model²⁵. This model is a follow-on realization of the MSIS-86 thermosphere model²⁶ extended to the middle and low atmospheric altitudes. The model extrapolates numerous satellite and ground facility measurements of the atmospheric parameters. The atmospheric parameters are modeled as the functions of altitude, latitude, longitude, local time, solar and geomagnetic activity. Accuracy of the modeling has been checked through comparison of the model outputs with experimental data^{25,26}. For instance, at altitudes 300-400 km atmospheric temperatures are reproduced with accuracy ~3-4%, whereas atomic oxygen number density is modeled with accuracy 15-17%. Parameters of the atmosphere at four particular moments of observation during 26 April 2000 experiment are listed in Table 1.

Table 1. Atmospheric parameters at some moments of 26 April 2000 experiment.

INPUTS				
TAMS	15	155	446	574
DAY	117	117	117	117
UT	69973.	70113.	70409.	70537.
ALT	333.	333.	329.	323.
LAT	31.	37.	48.	50.
LONG	43.	50.	72.	82.
LST	22.	23.	0.	1.
F107A	186.	186.	186.	186.
F107	205.	205.	205.	205.

OUTPUTS				
TINF	1115.68	1093.90	1097.27	1091.95
TG	1110.86	1090.59	1093.82	1087.70
HE	4.224E+06	4.423E+06	4.284E+06	4.441E+06
O	5.653E+08	5.547E+08	5.504E+08	5.561E+08
N2	8.463E+07	8.350E+07	9.516E+07	1.064E+08
O2	2.562E+06	2.378E+06	2.553E+06	2.881E+06
AR	1.422E+04	1.294E+04	1.557E+04	1.751E+04
H	5.510E+04	5.609E+04	5.131E+04	5.179E+04
N	1.426E+07	1.304E+07	1.030E+07	7.498E+06
RHO	1.945E-14	1.907E-14	1.945E-14	2.007E-14

Meanings of the abbreviations in this table are as follows.

Inputs:

TAMS – time after motor start, sec

DAY – sequent number of the day in the year

ALT – altitude, km

LAT – geodesic latitude, degrees

LONG – geodesic longitude, degrees

LST – local solar time, hours

F107A – solar activity index $\langle F_{10.7} \rangle$ (averaged over 90 days)

F107 – current index of solar activity $F_{10.7}$.

Outputs:

TINF – temperature of exosphere, K

TG – temperature of atmosphere, K

HE, O, N2, O2, AR, H, N – number densities of He, O, N₂, O₂, Ar, H and N particles, cm⁻³

RHO – atmospheric density, g/cm⁻³

2.3. Description of the experimental apparatus

In most of experiments, including the one of 26 April 2000, two principal instruments were used on-board of the “Mir” station for the plume glow observations: ultraviolet imager and miniature UV-NIR spectrometer. Some description of the instruments and their characteristics may be found in Ref.^{2,3,7,27}. During the years of operation the instruments were modified and somewhat improved. A brief description of the instruments that were used for the April 26, 2000 plume glow observation is given below.

2.3.1. Ultraviolet imager

The UV-imager was an ICCD based device that included F/1 aperture telescope followed by image intensifier with solar-blind Cs₂Te photocathode. A relay lens transferred image from the output screen of the image intensifier onto a conventional CCD camera. Imagery data were recorded in customary magnetic tapes by a commercial Sony 8 mm camcorder, SONY CCD -TR502E, utilizing PAL format. The tapes were delivered back to the ground with each cosmonaut shift. Despite that the imager’s photocathode was almost insensitive to the visible radiation, a wideband color-glass UV-filter was permanently installed on the imager. This filter provided even better blocking of the off-band visible and near UV radiation. Three narrowband interference filters (20 nm FWHM) were available for proper waveband selection within the imager sensitivity region as well. In the April 26, 2000 experiment the imager had 9.8 angular degrees circular field of view, and spatial resolution of about 4.7 angular minutes (FWHM of a point source response). The imager was an indoor instrument. During observation it was installed on one of the UV transparent quartz windows of the “Mir” station. Some characteristics of the UV-imager are presented in Table 2. Picture of the UV-imager is shown in Figure 5.

Table 2. The UV-imager characteristics.

Operating wavelength region, nm	200 - 360
Wide band color UV filter, nm	240 - 360
Waveband centers of the interference filters, nm	260, 284, 315
Telescope effective diameter, mm	55
Telescope focal length, mm	78
Maximal field of view, degrees	11
Typical angular resolution, angular minutes	4.5-5
Temporal resolution, sec	0.04
Sensitivity at max of the response curve, W/cm ² per count	$\sim 2\text{-}2.5 \cdot 10^{-17}$

2.3.2. *UV-NIR spectrometer*

Commercially available OceanOptics S2000 spectrometer was utilized in the experiments. Technically the spectrometer was an integral part of the instrumental set, capable of independent operation, however. Its line of sight was co-aligned with the imager's one, so that looking at the plume image one can definitely say what part of the plume was observed by the spectrometer. This feature was insured by rigid attachment of the input lens of the spectrometer on the spectrometer's mount frame. Radiation from the lens transferred to the entrance slit of the spectrometer through an optical fiber cable. Some characteristics of the spectrometer are given in Table 3. Picture of the spectrometer is shown in Figure 5. The instrument set-up assembly is also shown in Figure 6.

Table 3. Characteristics of the spectrometer.

Wavelength region, nm	200-800
Effective field of view, degrees	2.6
Number of wavelength channels	2048
Spectral resolution, nm	8-10
Acquisition time, sec	0.02-10
Digitization, bits	12
Dynamic range (single sample)	about 500



Figure 5. UV-imager (left) and UV-NIR spectrometer (right).

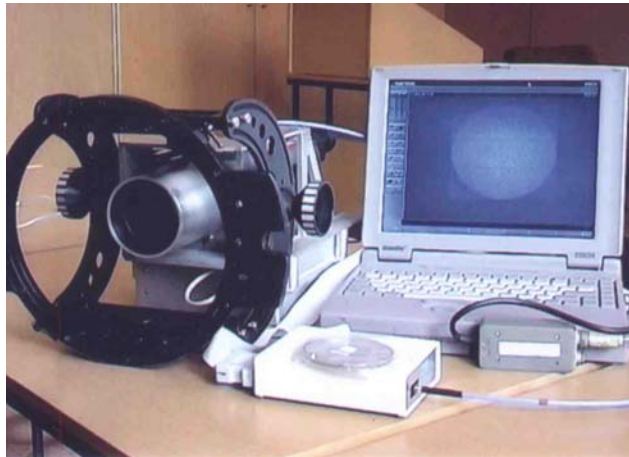


Figure 6. Instrument set-up assembly.

2.4. *Data processing*

Raw data obtained in the April 26, 2000 experiment represented tape-recorded glow images in a conventional TV format and the glow spectra recorded in the form of digital data arrays. Because of essential difference between the data sets, different data processing procedures were applied for the imager and spectrometer data.

2.4.1. *Processing of the imager data*

Analog video signal containing imagery data stream was digitized and set of more than $2 \cdot 10^4$ digital files was generated. The files represent 768×576 pixels 8-bit (256 counts) gray scale images taken with the time step of 0.04 sec. Stability and linearity of the digitization channel was carefully studied before the data processing. A simple set-up was assembled for these tests (see Figure 7).

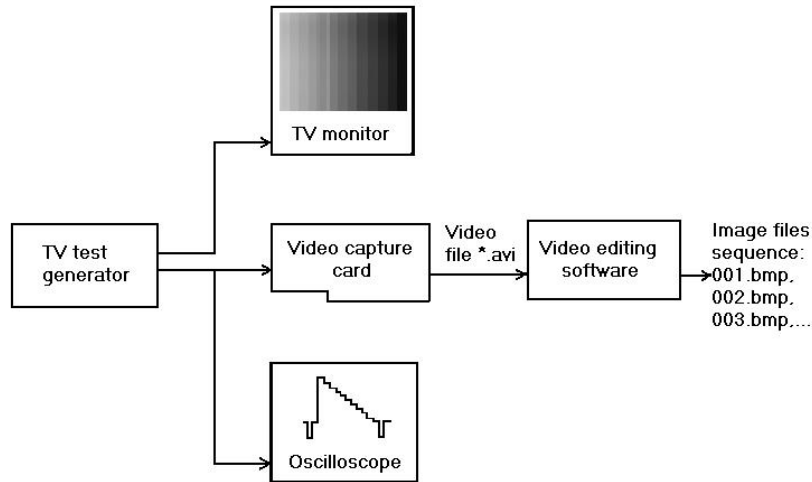


Figure 7. Schematic view of the digitization channel test set-up.

In these tests, controlled TV-coded stepwise signal from a specially developed generator fed the digitization channel input for a relatively long period of time. The digitization board time-by-time randomly sampled video sequences of 20 seconds duration. Corresponding digitization levels in ADC (analog-to-digit converter) counts were compared with the signal levels in volts. The result of this comparison is plotted in Figure 8. Apparent linear fit is also shown in the figure. The measurement points fall very accurately onto the line. Standard deviation of the linear fit is about 1.4 counts, which reasonably corresponds to the accuracy of the digitization and analog signal measurements. Upper level of the signal found among all experimental data since 1997 was about 230 counts per pixel (cpp), whereas typical single frame noise level was about 5-7 cpp, for reference. Evidently, the digitization channel response may be considered linear, at least in the range where the experimental data signals are located. The conclusion could eventually be made that any non-linearity in the imager response found in the experimental data should be addressed to the imager itself, not to the processing hardware or method. Also, it should be noted, that some signal offset is present in the digitization channel. This offset depends on the particular features of the digitization hardware and method and remains constant as far as the hardware and method are not changed.

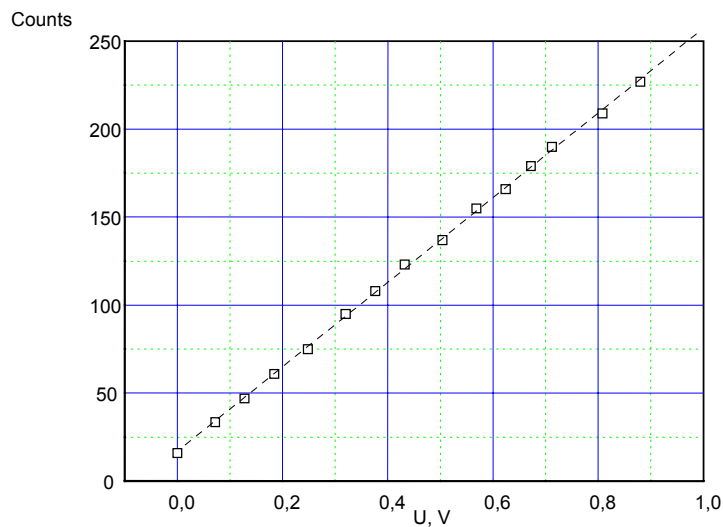


Figure 8. Digitization channel linearity curve.

Stability of the output signal from the digitization channel was tested by measuring time histories of the signal. For this purpose, the digitized signal was integrated over all pixels inside a pre-selected box in each image of the video sequence. The box itself was located within the borders of an arbitrary, but a single strip in the step-wise pattern of the image (see Figure 7). Selected time histories of the integral counts in the boxes are shown in Figure 9 for different boxes and different levels of the input signal. The signal behavior in the figure looks quite typical and varies only slightly from sample to sample. Constant level of the output signal indicates the digitization channel stability.

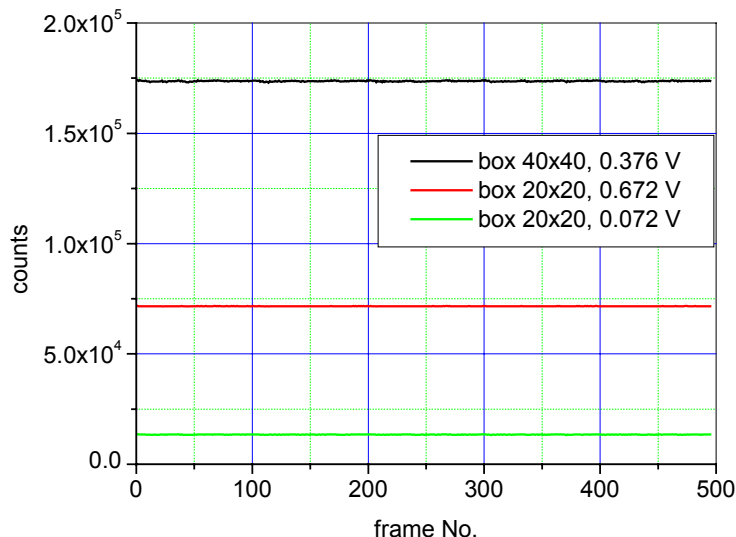


Figure 9. Selected time histories of the test signal.

Typical glow signals in the April 26, 2000 experiment were 5-10 cpp, that is slightly above the noise level. To enhance the signal to noise ratio procedures of spatial and time averaging were applied. Because of the random character of the imagery noise, its level could be essentially reduced due to the averaging procedures. Figure 10 exemplifies this assertion. As evident from the figure, the noise distribution in the 50 frames averaged image is about 7 times narrower than in a single frame image, that is in accordance with the statistical law for the random distribution. Note, that constant offset level was subtracted from the images.

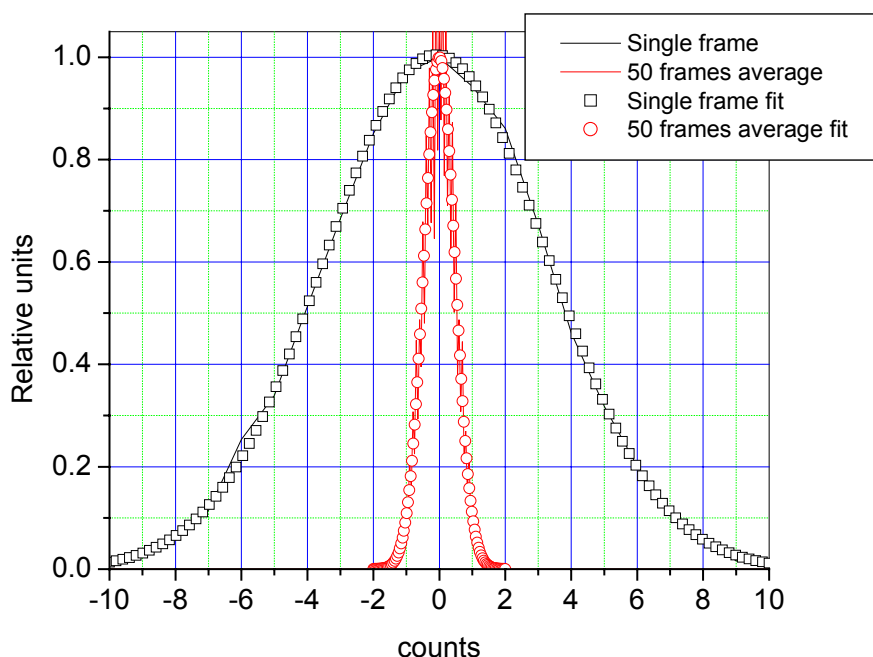


Figure 10. Single frame and 50 frames average noise distributions.

Examples of the 50 frames averaged glow images taken in February 28, 1999 and April 26, 2000 experiments are presented in Figure 11. Interpretation of the images features and representation of the images in the form of 2-D radiation maps will be given in Section 2.6.1 after discussion of the imager calibration issues.

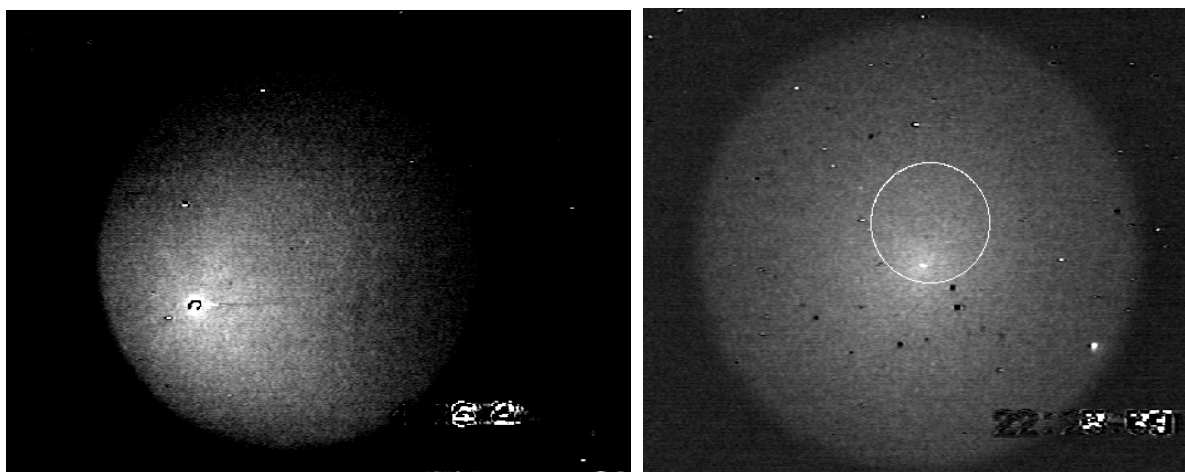


Figure 11. Examples of the 50 frames averaged glow images taken in February 28, 1999 (left) and April 26, 2000 (right) experiments.

2.4.2. Processing of the spectrometer data

In contrast to the imager, in the April 26, 2000 experiment spectrometer acquired data with about 2.6 sec time steps. In a whole, 330 samples were consecutively recorded by the spectrometer including more than 250 samples with the glow spectra. Processing of the spectrometer raw data is more simple procedure than the video data processing. The spectra were recorded in a simple text format and could be easily manipulated with any data processor. In spite of the relatively long integration time, spectrometer signal appeared to be very weak, so that practically impossible was to recover any signal from a single spectrum sample. Therefore, spectrometer data were averaged over multiple samples and within a relatively wide waveband (about 10-12 nm). Indeed, this approach didn't allow analysis of fast processes and understanding the molecular band fine structure. From the other hand, spectrometer resolution was more than 8 nm and the molecular band structure could not be resolved anyway. Also, the plume glow observation condition didn't change much within 30-40 sec intervals in the experiment (see Figure 2). So, the time averaging procedure did make a sense. And finally, noise background subtraction and FFT-smoothing procedures were applied for further improvement of the signal to noise ratio.

2.5. Calibration of the instruments

All principal characteristics of the instruments were routinely measured in the laboratory prior to the delivery on board. However, after mounting of the instruments on the "Mir" station window, the window became an integral part of the optical scheme. During exploitation the instrument throughput and other characteristics (the window transparency in particular) might change. In addition, some of the instrument parameters allowed manual tuning. Therefore in-flight calibrations were also performed to track possible variation of the instrument characteristics.

2.5.1. Calibration of the imager

2.5.1.1. Imager FOV, single pixel FOV and spatial resolution

Dimension of the imager's FOV was controlled in daytime nadir observations. The daytime atmospheric glow illuminated entire FOV of the imager (see Figure 12), so the FOV diameter could be readily measured in pixels. In the April 26, 2000 experiment the FOV diameter was 9.8 degrees. In other experiments it might be different. For example, in February 28, 1999 experiment⁵ it was 9.55 degrees. Maximal FOV was about 11.5 degrees.

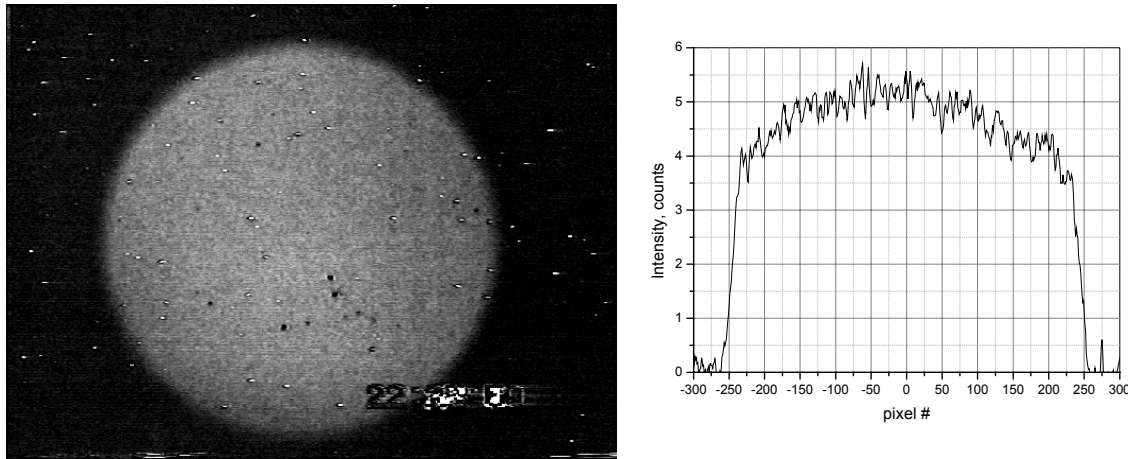


Figure 12. FOV measurement: image of the daytime Earth glow and its horizontal signal scan.

FOV of a single pixel (the pixel angular dimension in the image) was determined from analysis of stellar images. Angular distances between stars may be found in stellar catalogues²⁸. Measurement of the distances between the star images and comparison with actual angular distances provided the pixel cost. In the April 26, 2000 the pixel FOV was $1.96 \cdot 10^{-2}$ degrees, whereas in February 28, 1999 one it was $1.98 \cdot 10^{-2}$ degrees. It should be noted that almost the same single pixel FOV was determined both in the center of the image and in the edge, indicating absence of any noticeable aberration.

2.5.1.2. Point source response

Apparently the single pixel FOV dimension doesn't reflect capability of the imager to resolve fine features of an object. In other words, the pixel angular dimension is not equivalent to the imager angular resolution. It simply represents the minimal picture element fixed at the digitization of the video signal. The imager angular resolution was determined from analysis of the images of different stars. Any star image may obviously be considered as the image from a point source located in the infinity. Analysis of the point source response provides both the imager instrument function and angular resolution.

The imager response to the point source radiation was studied through analysis of numerous star images. Orion constellation image clip (100-frames averaged) is shown in Figure 13, for instance. Orion offers a variety of stars with different intensities for the analysis. Signal profiles taken in the horizontal direction from the images of selected stars from the Orion constellation are shown in Figure 14 together with their error function fits. The profiles are pulled apart and stacked in the plot for better representation. In fact, the profiles represent the imager point source response at different intensity levels.



Figure 13. Enlarged clip of the part of Orion constellation.

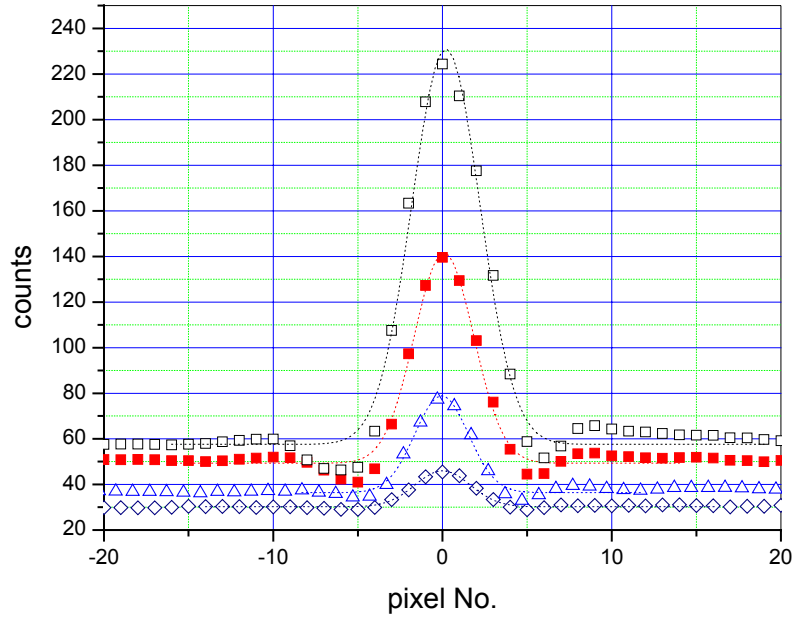


Figure 14. Measured horizontal profiles of some selected stars of different magnitude from the Orion constellation. Apparent Gaussian fits are shown by the dotted lines for each profile. The profiles are pulled apart and stacked.

Width of the profiles were analyzed and found to be dependent on height. This is clearly seen from Figure 15. In this figure the error function widths of the horizontal profiles of the various stars are plotted versus their heights.

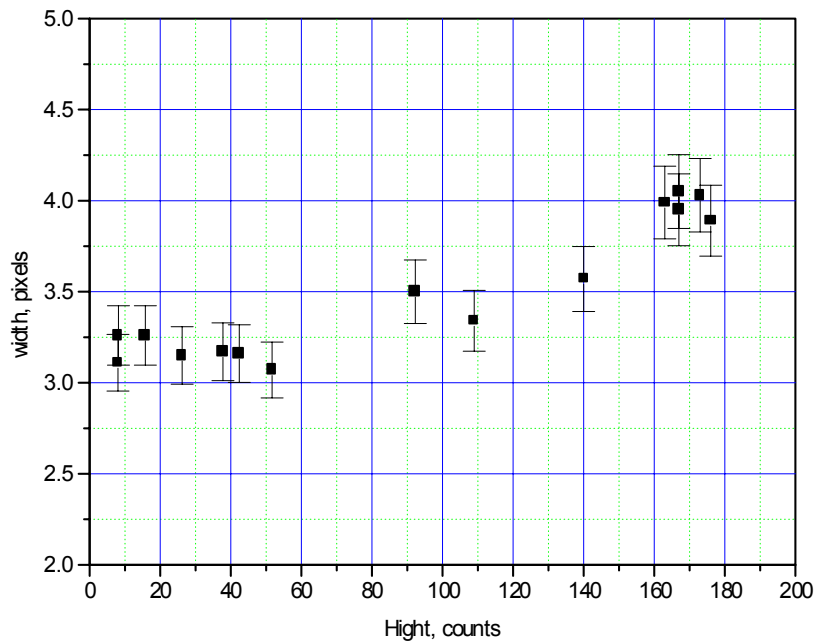


Figure 15. Dependence of the point source image width on the peak intensity.

Distinct growth of the point source width is noticeable in the plot starting from the signal heights of approximately 90 counts. This growth reflects non-linearity of the UV-imager response. This non-linearity develops in the image intensifier, which saturates at high levels of the input radiation²⁹.

In the April 26, 2000 experiment the imager's angular resolution was about 0.08 degrees FWHM of a non-saturated point source response.

2.5.1.3. Uniformity of the imager response over the FOV

Uniformity of the imager response across the FOV was measured in the laboratory. No non-uniformity was discovered over almost entire FOV. Only at the very edge of the FOV the imager response fell down. This was not an unexpected result. The imager design assumed spatial uniformity of its response. Nevertheless, spatial uniformity of the imager's response was also measured in some in-flight tests. In those measurements cosmonauts were instructed to take images of a selected star moving the imager's FOV centerline around it. As the result, image of the star appeared in different places of the video picture. Relative intensity of the star image measured in different locations reflected spatial variation of the imager's response over its FOV. Similar to the laboratory measurements decrease of the response appeared only near the edge of the FOV. Example of the FOV uniformity measurement is shown in Figure 16. Black spots on the plot represent relative intensity of stars located at different distances from the FOV center. The data were retrieved in the April 26, 2000 experiment.

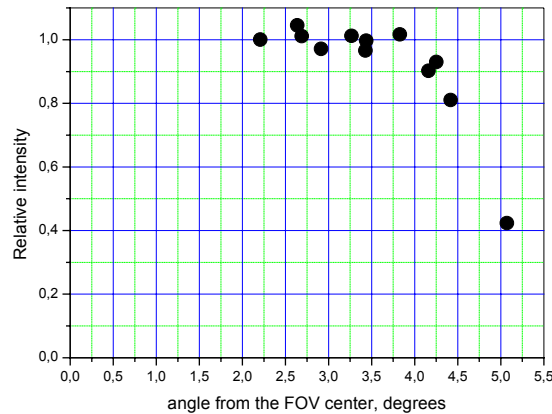


Figure 16. Illustration of the imager response degradation at the edge of the FOV.

2.5.1.4. Relative spectral and absolute response

Spectral response of the imager was measured in the laboratory prior the instrument delivery. However, as mentioned above the "Mir" window transparency could affect the total throughput of the channel. Due to the attenuation of the radiation passing through the window both relative spectral sensitivity and absolute sensitivity in the maximum of the spectral curve might change. Measurements of the Moon and Jupiter spectra (see Paragraph 2.5.2.2) showed that relative spectral transparency of the window didn't change in the region of the imager sensitivity in the course of the "Mir" station mission. On the contrary, absolute transparency of the window did changed. So, the relative spectral response curve of the imager together with window might be corrected by a simple multiplication of the imager's response on the window transparency. The product curve is presented in Figure 17. Also in the figure presented are spectral transparency curves of the interference filters, which were put on the imager's telescope for short time periods during 26 April 2000 experiment.

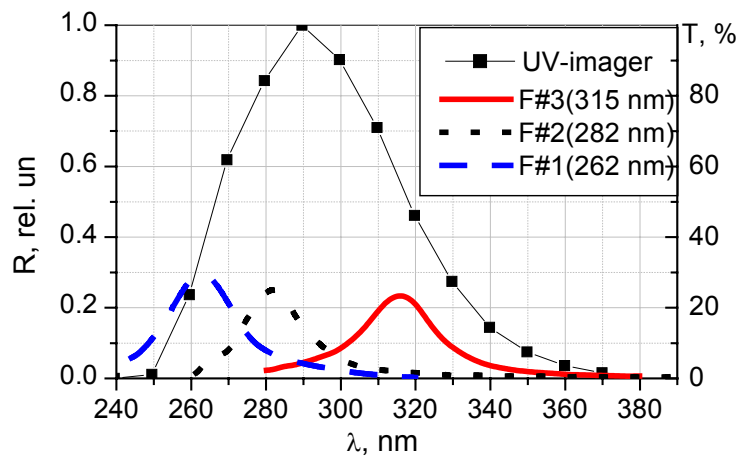


Figure 17. Imager's relative spectral response and transparency of interference filters.

The imager absolute response (in ADC counts per W/cm²) at the maximum of the spectral response curve was also determined, that made possible radiometric measurements with the imager. Procedure of the absolute response calibration was as follows.

Consider a star radiation flux of intensity I_λ at the outer surface of the “Mir” station window. This flux will generate a point source image with N integral ADC counts. Relation between N and I_λ may be expressed as:

$$N = T_{wm} R_{imm} \int_{\lambda} I_{\lambda} R_{\lambda} T_f d\lambda = R_m W$$

$$R_m = T_{wm} R_{imm}$$

$$W = \int_{\lambda} I_{\lambda} R_{\lambda} T_f d\lambda$$
(2.1)

where R_λ is relative spectral response (Figure 17), R_{imm} – absolute response of the imager without window, T_{wm} – window transparency at the maximum of the imager’s response curve, T_f – spectral transparency of the interference filter ($T_f \equiv 1$ if no filter was installed), R_m – absolute response of the imager in the maximum including the window, W – integral star flux converted with the imager relative spectral response curve.

Values of the I_λ for numerous stars have been measured and tabulated in stellar catalogues²⁸. So integrals W can be readily calculated. Total number of counts can also be determined directly from the star images. As soon as the R_m value doesn’t depend on what particular star is being observed, it may be determined from the slope of the $N(W)$ linear dependence. This dependence is plotted in Figure 18. Stellar images obtained exclusively during the April 26, 2000 glow observation were processed for this figure. The HD catalog numbers of the stars are as follows: HD68980, HD69081, HD70060, HD70556, HD71801 and HD74575. The absolute response value $R_m = 4.8 \cdot 10^{16}$ counts per W/cm² was derived from the plot. Thus, imager’s absolute response curve (Figure 18) was reconstructed.

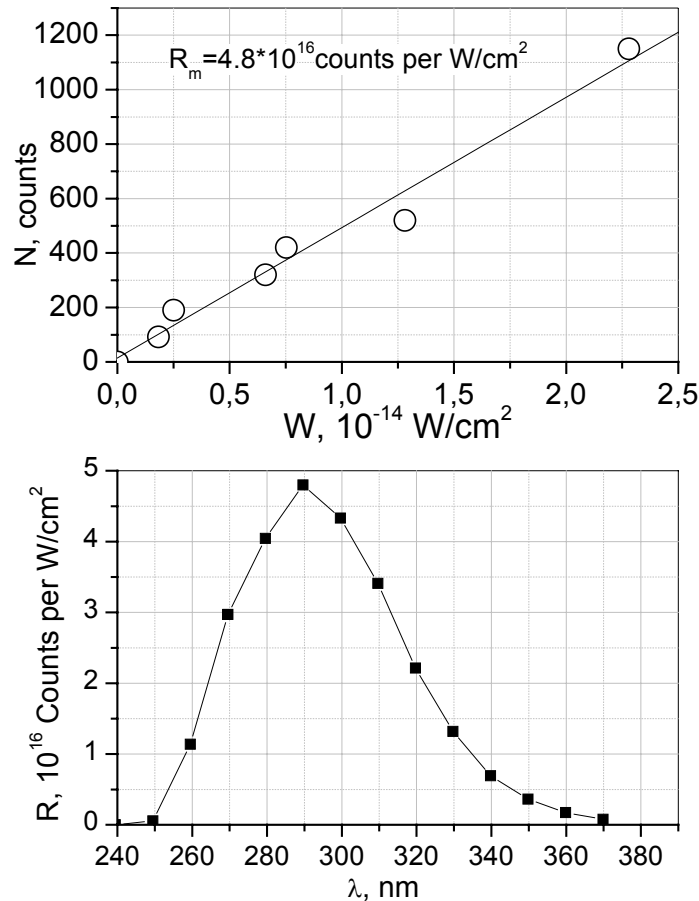


Figure 18. Imager’s response in maximum (top) of the spectral curve and absolute spectral response (bottom) measured in the 26 April 2000 experiment.

The calibration technique described above provides true value of the absolute response if the window transparency doesn’t change during the data acquisition. In the meantime, the window transparency might change

from one data acquisition event to another. Also, some observations were made through another quartz window located in different module of the “Mir” station. The slope of the $N(W)$ dependence in Figure 18 should reflect accurately only the April 26, 2000 absolute response value. Dependence of $N(W)$ for other star images is given in Figure 19. These measurements of the absolute response were performed at different times through different windows, having different transparency. Apparently, the data in Figure 19 have some scatter. This scatter was attributed to the window transparency variation at the maximum of the imager’s response curve. Data obtained in a single experiment over relatively short time period (see Taurus stars from 20.07.99 or Orion stars from 12.01.99) fit better to a particular linear dependence. Averaged over the long observation period response value, which may be derived from Figure 19 equals $R_m = 4.2 \pm 0.7 \cdot 10^{16}$ counts per W/cm^2 . Also, in contrast to Figure 18, where only weak stars were observed, general non-linearity related to saturation of the image intensifier is clearly seen in Figure 19 at high levels of intensity.

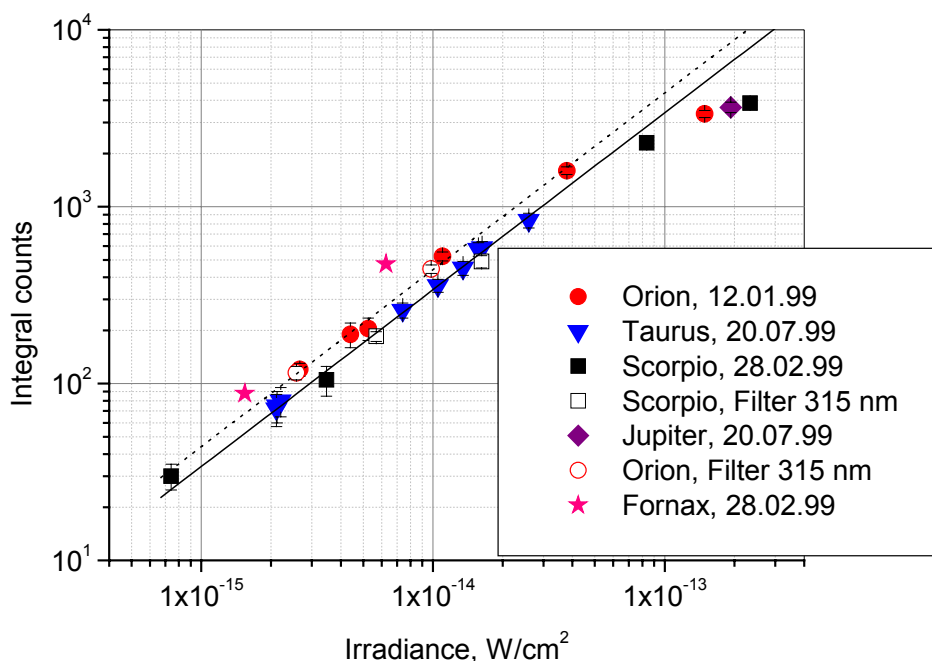


Figure 19. Measurement of the imager’s absolute response versus irradiance from various stars observed in earlier experiments. Stars from different constellations are marked by different symbols.

It's interesting to not, that on February 28, 1999 two sets of the calibration experiments were made. The first one was the dedicated calibration of the imager two hours prior the observation of the space vehicle plume glow. This calibration was accomplished versus Scorpio constellation stars and provided the response value around $R_m = 3.7 \pm 0.4 \cdot 10^{16}$ counts per W/cm^2 . Another calibration was performed against two stars, which were occasionally captured right at the plume glow observation. This calibration resulted in the $R_m = 6.5 \pm 1.0 \cdot 10^{16}$ responseⁱ. Therefore, for February 28, 1999 glow observation experiment data interpretation some averaged value $R_m = 4.4 \cdot 10^{16}$ counts per W/cm^2 has used to be applied. In the meantime, the two different response values don't look like a random scatter. More probably, they reflect variation of the window transparency in time. The window transparency may decrease due to sputtering by ACS motor exhausts and other contaminants emanating from the space station. From the other side window cleaning effect may take place when the window surface is exposed by intensive flux of the atomic oxygen. This effect has been noticed on the "Mir" station and also studied in laboratory³⁰. Analysis of the station attitude on February 28, 1999 showed, that right before the first calibration the space station was re-oriented to have the Scorpio constellation visible through the quartz window, where the imager was mounted. Adjacent to the window ACS motors provided the re-orientation impulse. After completion of the calibration, the station changed its position again, so that quartz window became looking to the ram. At this attitude the window experienced very effective bombardment by the atomic oxygen. This might cause the window cleaning. In part this idea may be supported by analysis of the v-For star (Fornax constellation) intensity variation during the plume glow observation. Of course, the star radiation intensity was assumed to be constant during the experiment. Time history of the v-For radiation intensity is shown in Figure 20.

ⁱ Statistical scatter was bigger at the second calibration, of cause.

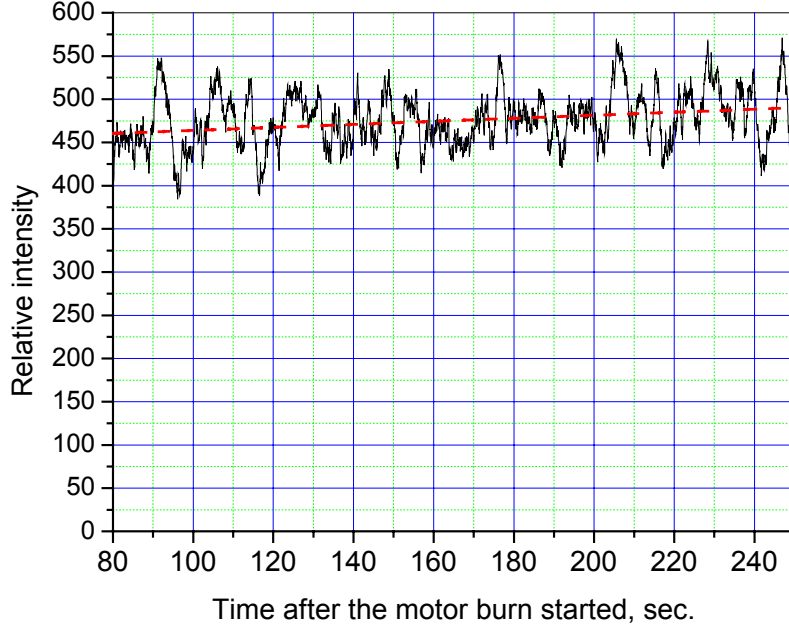


Figure 20. Variation of relative intensity of the v-For UV-radiation measured in 28 February 1999 experiment. Oscillations represent a noise. Apparent linear fit is shown by the dashed line.

Evidently, the star was observed on the plume glow background. This background was subtracted during the star image processing, so that star intensity in Figure 20 is not affected by the plume glow intensity variation. Disregarding oscillations in the curve (which are actually instrumental and data processing noise), one could conclude that window transparency grew at about 7% for the 170 sec. In this respect, different response values obtained at different times on February 28, 1999 do not look surprising.

Approximate estimates of the glow radiation intensity may probably be based on an average value of the absolute response. Precise measurements of the plume glow intensity in February 28, 1999 experiment would require more accurate consideration of the windows transparency variation.

2.5.1.5. Temporal resolution

Temporal resolution of the imager was limited by the camcorder frame rate, which was 25 frames per second. Apparently, this rate results in the temporal resolution of 0.04 sec. This resolution might be further limited by any internal inertial characteristics of the image intensifier. However, numerous tests showed that both imager's signal rise and fall induced by stepwise intensity jumps occurred almost immediately within the 0.04 sec and without any noticeable delay.

2.5.2. Spectrometer calibration

2.5.2.1. Effective FOV

Figure 21 illustrates response of the spectrometer R_α to a parallel radiation flux depended on the off-axis angle α . This response was determined through measurement of the output signal of the spectrometer illuminated by a diffusive radiation source with variable angular dimensions. The spectrometer's response is almost flat at the small off-axis angles. At some critical angle it falls down abruptly. This angle is controlled by the optical cable aperture and by the focal distance of the spectrometer lens. The angular response eventually determines spectrometer effective solid angle Ω_{eff} , which should be used for the spectrometer data processing:

$$\Omega_{eff} = 2\pi \int_0^\pi R_\alpha \sin \alpha d\alpha \quad (2.2)$$

This angle equals $1.6 \cdot 10^{-3}$ steradians. Corresponding plane angle (2α) is about 2.6 degrees.

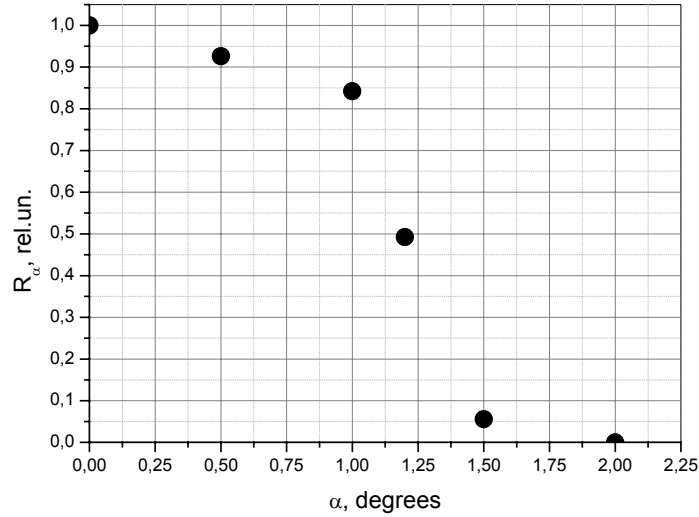


Figure 21. Angular response of the spectrometer.

2.5.2.2. Spectral response

Similarly to the imager the spectrometer's spectral response was routinely measured in the laboratory. State certified tungsten strip lamp and deuterium lamp were used for the spectral response measurements. However, in-flight calibration of the spectrometer was also carried out to take the "Mir" window transparency into account. The Moon was used as the radiation source in most in-flight calibrations. One time in July of 1999 the spectrometer was calibrated versus Jupiter radiation. Generally, all in-flight measurements provided almost the same relative spectral response curve as measured in laboratory. However, some deviations (within 15%) were found in the region $\lambda=680-800$ nm. The response curve corrected through the in-flight calibration is presented in Figure 22.

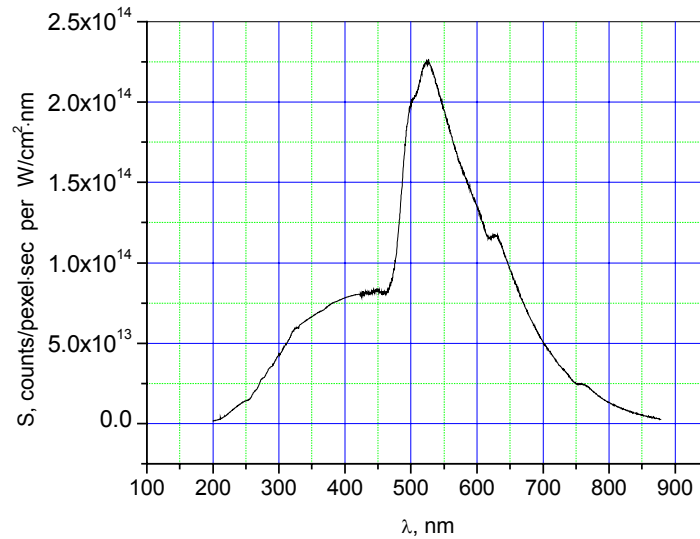


Figure 22. Spectral response of the spectrometer measured in laboratory and corrected in the course of in-flight calibrations.

Figure 23 illustrates quality of the spectrometer response calibration. In this figure measured Moon spectrum is compared with two modeled spectra. The modeled spectra were computed through convolution of the solar spectrum with the Moon albedo. Accurate procedure for the Moon spectrum modeling is described in Ref.³¹. The modeling was based on semi-empirical law for the Moon radiation intensity, which takes into account Moon phase and conditions of the Moon illumination by the Sun for the day of measurement. Different published solar spectrum data were implied for the Moon spectrum computation^{31,32,33}. The Moon albedo was borrowed from Ref.³⁴. In fact, the computation results were almost identical.

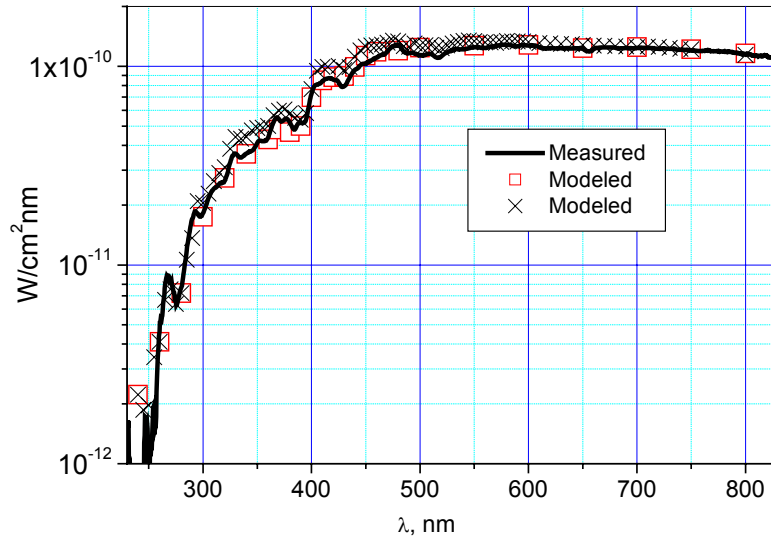


Figure 23. Moon spectrum measured on June 12, 2000 (solid) in comparison with modeled curves basing on two different Sun spectra – from Ref.³¹ (squares) and Ref.^{32,33} (crosses).

Excellent agreement between measured and modeled spectra is evident almost over all spectral region. In the meanwhile some deviation of the measured spectrum from the modeled one is seen at the edge of the window transparency region ($\lambda \approx 250$ nm). This discrepancy once again indicates that window transparency has to be taken into account at the edge regions.

2.5.2.3. Wavelength calibration

The wavelength calibration was accomplished through a standard procedure. Spectrum of a mercury-argon lamp was measured and spectrometer channels at the centers of the emission lines were correlated with the corresponding wavelengths. Dependence of the wavelength on the channel number was approximated by a second order polynomial. This method ensured accuracy of the wavelength specification better than 1 Å°, that is much less than spectral resolution of the spectrometer. Figure 24 illustrates correlation between measured spectrum and tabulated mercury-argon lamp emission data. Shape of each individual line represents the spectrometer response to the monochromatic radiation.

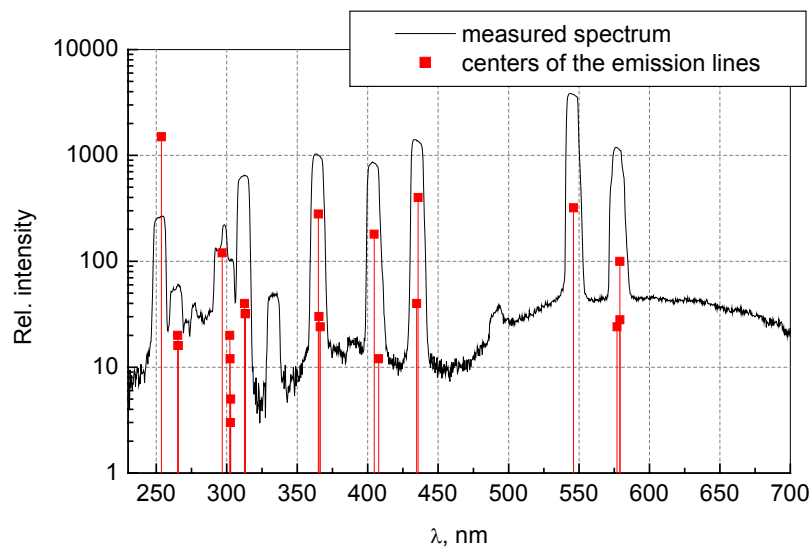


Figure 24. Correlation of the measured mercury-argon lamp spectrum with tabulated emission data.

2.5.3. Spatial affixment and temporal synchronization of the imager and spectrometer output signals

2.5.3.1. Spatial affixment

Once the spectrometer had been integrated into the instrument set-up onboard the “Mir” station, its line of sight became rigidly bound to the imager’s one (see Section 2.3.2). Design of the spectrometer assumed that both lines of sight must be parallel. However, the spectrometer was developed and delivered onboard while the imager had already been operating. So, colinearity of the spectrometer and imager lines of sight was checked in dedicated tests.

In these tests both instruments simultaneously acquired imagery and spectra of the Moon while cosmonaut moved the imager’s line of sight. At the moments when the spectrometer signal reached its maximum the coordinates of the Moon image apparently indicated direction of the spectrometer FOV centerline within the imager FOV. These coordinates correspond to the center of the small white circle in the right image in Figure 11. The circle diameter represents effective field of view of the spectrometer computed through formula (2.2).

2.5.3.2. Time histories of the instrument signal and time synchronization

During experiments both spectrometer and imager were switched on a while before the space vehicle engine startup and stopped the data acquisition some time after its shutdown. The rise and drop of the signal are clearly seen on the spectrometer’s and imager’s time history curves (Figure 25). The imager’s signal time dependence was built in the way explained in Section 2.4.1. Spectrometer’s signal time history was obtained by a similar way. In each sequential sample of spectrum spectrometer’s signal was integrated in a particular wavelength region providing dependence of the signal intensity on the sample number. In particular, the curve in Figure 25 represents integral signal in OH(A→X) NH(A→X) and O¹D bands. Then the sample number was converted into the time scale. The conversion factor was carefully measured in the ground prior to the instrument delivery. It should be noted, that both imager’s and spectrometer’s signals began rising almost exactly at the preset time of the motor startup. This fact indicates to excellent synchronization of the instruments in the experiment. Fine adjustment of the synchronization was accomplished by a small shift (less than one second) of the spectrometer’s time reference relative to the imager’s one along the time axis. This shift resulted in a full coincidence of the imager’s and spectrometer’s signal initial rise and final drop related to the motor operation (see Figure 25).

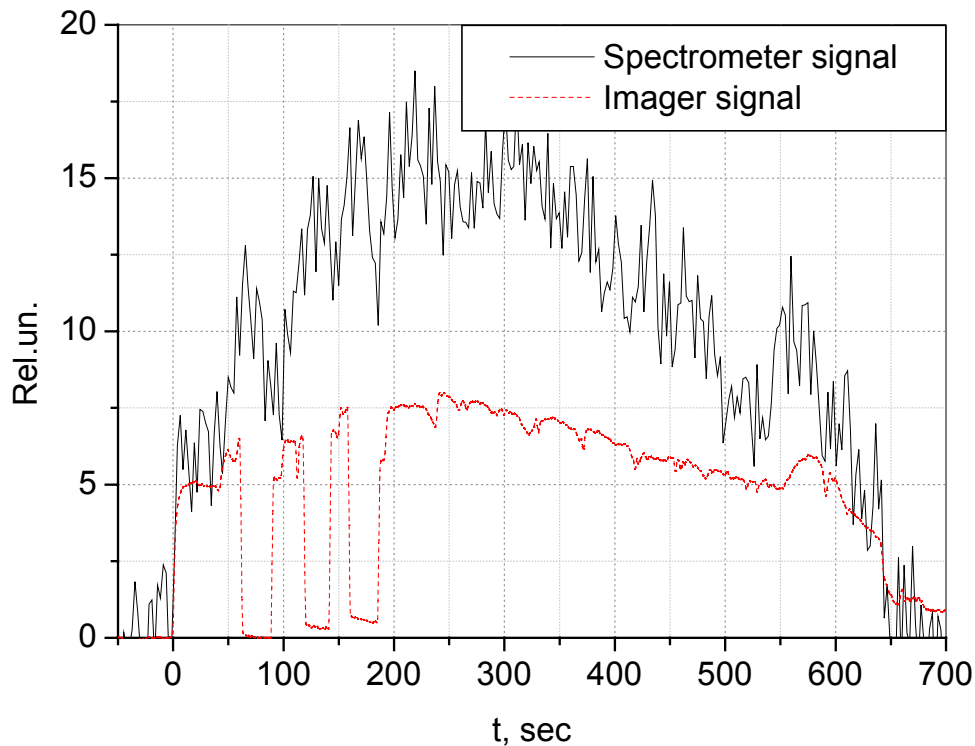


Figure 25. Time synchronization of the spectrometer and imager signals.

2.6. Analysis and interpretation of the April 26, 2000 experiment data

2.6.1. The glow images

Selected processed images of the plume glow taken in April 26, 2000 experiment are presented in Figure 26.

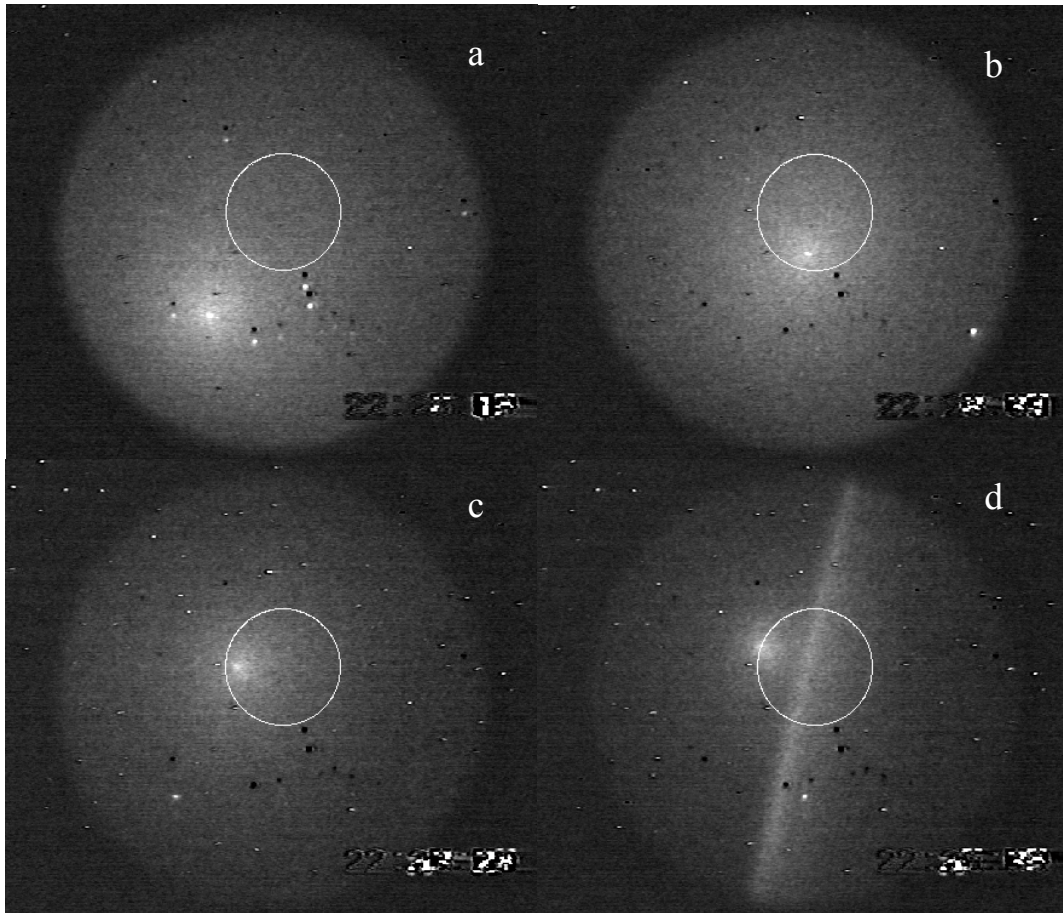


Figure 26. Glow images taken on 26 April 2000 at: a) 14 sec, b) 155 sec, c) 446 sec and d) 574 sec after the motor set burn started. Circles in the images represent field of view of the spectrometer.

Bright spot at the center of the glow in these images is located along direction toward the space vehicle. Apparently, radiation in the bright spot represents not only the far field plume glow, but may include a near field plume radiation of a different from the far field plume glow origin. This fact has to be taken into account at a modeling effort of the glow. Other bright spots in the images represent some stars, occasionally appeared in the FOV during the plume glow observation. Some “hot” pixels are also seen in the images. These pixels look like small dots in comparison with the star images that extend over several pixels.

The glow intensity smoothly decreases in radial direction from the center toward the edge of the imager’s FOV. Apparently, the intensity doesn’t come to zero level within the FOV. So, the total FOV is clearly seen in the images in the form of a diffuse circular disc. Smaller white circles in the center of the images represent effective FOV of the spectrometer.

Spatial distribution of the radiation may be characterized through the radiation intensity profile, that is angular dependence of the glow radiation in any radial direction outward the “Progress” location in the glow image. Modeling of the intensity spatial distribution showed its high sensitivity to the choice of elastic collision cross-sections^{20,21,23}. So, comparison between measured and modeled intensity profiles may be effectively used for the elastic collision model verification at the collision energies of several eV. Figure 27 provides the plume glow profiles derived from the images in Figure 26.

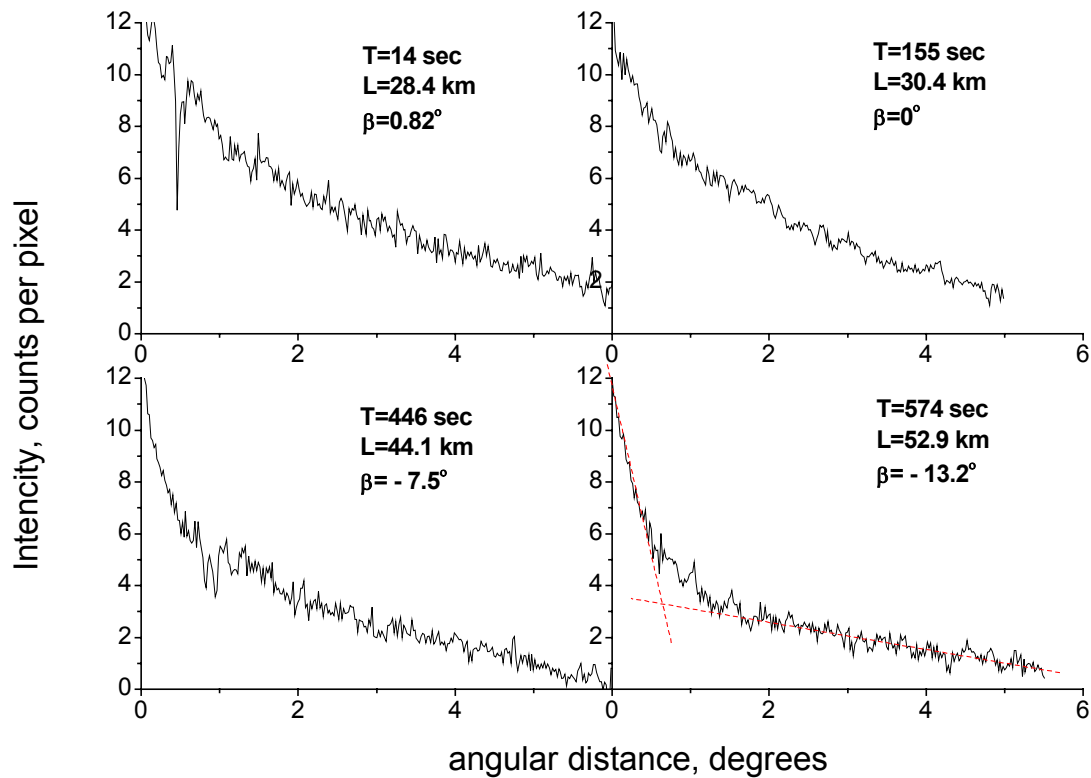


Figure 27. Glow intensity profiles measured in horizontal direction from the space vehicle. Times of measurements T, distances L and aspect angles β are shown in the picture. Dashed lines outline a bend in the last profile.

Distinctive feature of the new profiles in comparison with those taken before from the “Progress” main engine⁵ is that ACS plume profiles look wider in peripheral regions. Also, a small bend persists in every profile about one degree away from the plume center. The bend becomes more evident at longer distances and steeper aspect angles. Change of the slope in the intensity profile curves may indicate either a complex pattern of the multi-source flow or change of mechanism responsible for the plume glow generation.

2.6.2. Spectral composition of the plume glow and analysis of the spectra

Figure 28 shows composite spectrum of the glow averaged through the entire observation period. This composite spectrum allowed identification of most important emissions associated with the plume glow. Identified in the spectrum were emissions related to $\text{OH}(A^2\Sigma^+ \rightarrow X^2\Pi, \lambda=309-315 \text{ nm})$, $\text{NH}(A^3\Pi \rightarrow X^3\Sigma, \lambda=335-336 \text{ nm})$, $\text{O}(^1D_2 \rightarrow ^3P_{1,2}, \lambda=630-636 \text{ nm})$ and $\text{O}(^1S_0 \rightarrow ^1D_2, 557,7 \text{ nm})$ transitions. There were some other emissions of secondary interest identified in the spectrum. The most intensive one, the atmospheric oxygen band $\text{O}_2(b^1\Sigma_g^+ \rightarrow X^3\Sigma_g^-)$, is also seen in the figure at the wavelength about 762 nm. As will be proved below, this emission originates not from the plume, but from the natural atmospheric glow.

Most of the emissions in the spectrum were identified, but some were not. Persistent rise of the spectrum from 400 nm to shorter wavelengths hints at possible presence of some molecular band radiation in this region. Unfortunately, low spectral resolution of the spectrometer and extremely weak signal in these bands made impossible identification of these emissions.

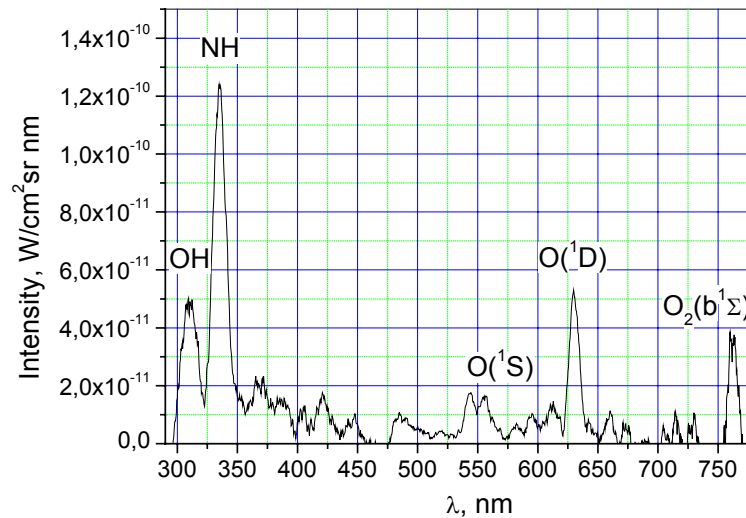


Figure 28. Processed spectra of the “Progress” plume glow taken in 26 April 2000 experiment.

Intensities of the emissions in Figure 28 are given in absolute values. For absolute calibration the response curve measured in laboratory and improved in dedicated calibration experiments (see Figure 22) was applied.

The glow emission intensity did not stay constant throughout the observation. Instead, it changed in time mirroring up its dependence on continuously changing conditions of the experiment, such as geometry of observation, motor operating parameters and like. General appearance of temporal variation of the glow spectrum is illustrated in Figure 29. In this figure depicted are the spectra taken around the same time as the images in Figure 26. The spectra were averaged over time intervals 1-2 min to obtain optimal signal to noise ratio. As becomes evident from Figure 29, only NH(A→X) radiation persists in the spectrum all over the motor set burning. Atomic oxygen lines O(¹S→¹D) and O(¹D→³P) may be found in all four spectra too, with essentially different intensities however. OH(A→X) radiation is well seen in the first three spectra, falling down to the noise level in the last one. The molecular band radiation around 300-400 nm presents only in earlier spectra, while the O₂(b¹Σ) band appears only in the latest one.

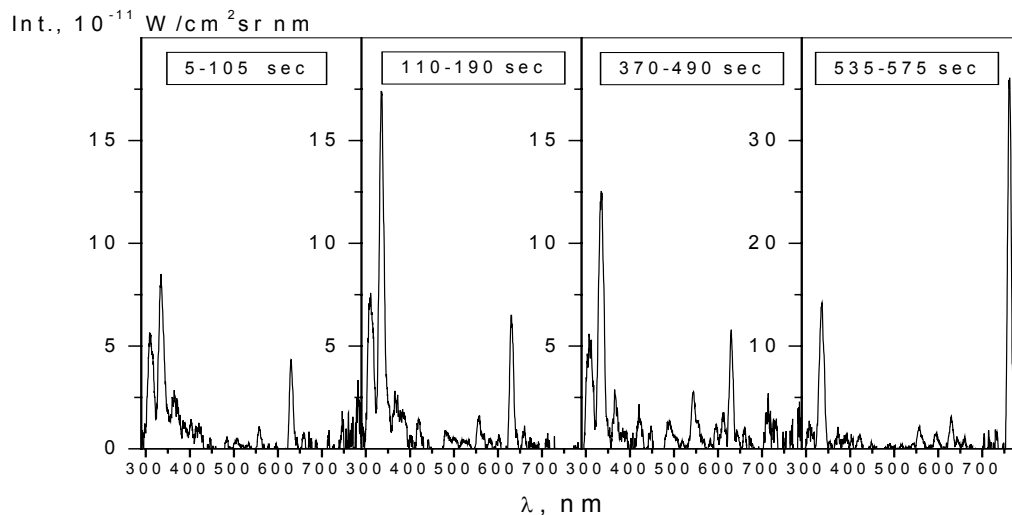


Figure 29. Plume glow radiation spectra averaged within indicated time intervals. Note the different intensity scale at the last graph.

Despite that difference between the four spectra is evident in Figure 29 it doesn't reflect particularities of the plume glow emission temporal behavior. Understanding of this behavior may be gained through consideration of the in-band radiation intensity time histories.

2.6.3. Time histories of in-band radiation intensities

Figure 30 shows time histories of some in-band radiation intensities measured by the spectrometer. These plots were obtained through integration of the spectrometer signals in each sample of the glow spectrum around respective band centers: $\lambda=310$ (OH), 336 (NH), 558 (O^1S), 630 (O^1D) and 762 (O_2) nm. In the bottom right window of Figure 30 signal measured by the UV-imager in the box $2.3^\circ \times 2.3^\circ$ is shown. The box center coincided with the center of the spectrometer's FOV. Box dimensions were also chosen to make its area equal to the area of the spectrometer FOV. Also in this window shown is angular distance between the spectrometer FOV center and the space vehicle position. All curves in the figure were smoothed to suppress random noise and sharp oscillations.

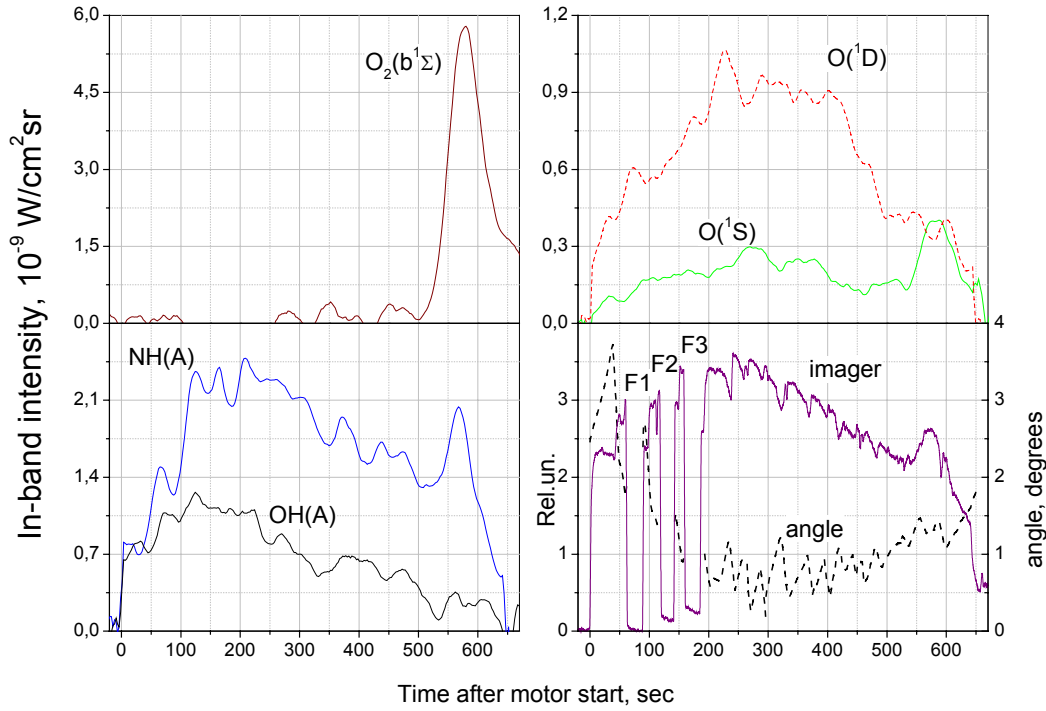


Figure 30. Time histories of some in-band radiation intensities measured by the spectrometer and imager. Angle between the spectrometer line of sight and direction toward the space vehicle is also shown.

Evidently, time history curves in Figure 30 are correlated in general. Signal rise in the first 200 seconds of firing occurred due to re-location of the spectrometer line of sight closer to the direction toward the space vehicle. Note the diminution of the angular distance in the figure at this time. After about 300-400 seconds the angular distance began rising again resulting in general decrease of measured glow intensities. Sharp drops of the imager signal around 75th, 130th and 175th seconds are associated with installation of the narrow band filters onto the imager's telescope. Of course, this could not affect the spectrometer operation by any way.

In the meanwhile some differences in the time histories are also apparent in the figure. For example, NH(A \rightarrow X) emission intensity gained more than factor of 3 from the beginning to the middle of the firing, whereas OH(A \rightarrow X) emission intensity increased on just about 50 percents. This difference in signal behavior may be explained by different radial distribution of the emitting plume components. In this case one should conclude that OH(A) concentration in peripheral plume zone declines gentler than the NH(A).

Also, a pronounced peak appears in the NH(A \rightarrow X), $O(^1S \rightarrow ^1D)$ and imager's signal time history curves around 560th second of the motor set burn. This peak by no way can be associated with the instrument line of sight relocation. Instead, it is well correlated with appearance of the molecular oxygen $O_2(b^1\Sigma_g^+ \rightarrow X^3\Sigma_g^-)$ emission in the spectrum. This emission is characteristic to a nightglow occurring in the Earth atmosphere at altitudes $H=80-110$ km³⁵. At the moment of the signal rise the instrument line-of-sight crossed the atmosphere exactly at these tangential altitudes and the atmospheric glowing layer was captured by the imager (see Figure 26d). Similar peak is much smoother on the $O(^1D \rightarrow ^3P)$ time history curve and it almost vanishes on the OH(A \rightarrow X) one. The atmospheric glow emits $O(^1S \rightarrow ^1D)$ and some UV radiation, presumably in the

$O_2(A^3\Sigma_u^+ - X^3\Sigma_g^-)$ Herzberg molecular band³⁵. So, the $O(^1S \rightarrow ^1D)$ and imager's peaks may look not surprising from this standpoint. With a great reserve atmospheric glow emissions could account for the $O(^1D \rightarrow ^3P)$ signal rise, because, typically, this emission has a maximum at much higher tangential altitudes $H=250-300$ km³⁵. Big surprise is the peak in the $NH(A \rightarrow X)$ intensity time history curve. This emission has not been reported so far as an atmospheric glow component. By some way it should be related with the space vehicle motor operation. One hypothetical explanation is that space vehicle effluents penetrating into lower atmospheric altitudes react with metastable atomic and molecular oxygen abundant in Earth atmosphere at the lower altitudes. And the instruments observed a kind of global afterburning of the unburned fuel in the atmosphere at altitudes 80-100 km. It should be mentioned, however, that about the same time when the signal rise started, pressure in the oxidizer feed pipeline became dropping down. This is schematically illustrated in Figure 31. The oxidizer to fuel ratio progressively changed and the motors were operating in essentially fuel rich condition. Consequently, one should expect a change of the outflow parameters and related emissions as well. This variation in the motor operation almost coincided with instrument line of sight scanning the atmospheric layer both in time and duration. So, the signal rise might potentially be explained by this variation as well. The only reason against this hypothesis is that the oxidizer to fuel ratio variation started a bit later than the $NH(A \rightarrow X)$ intensity growth began.

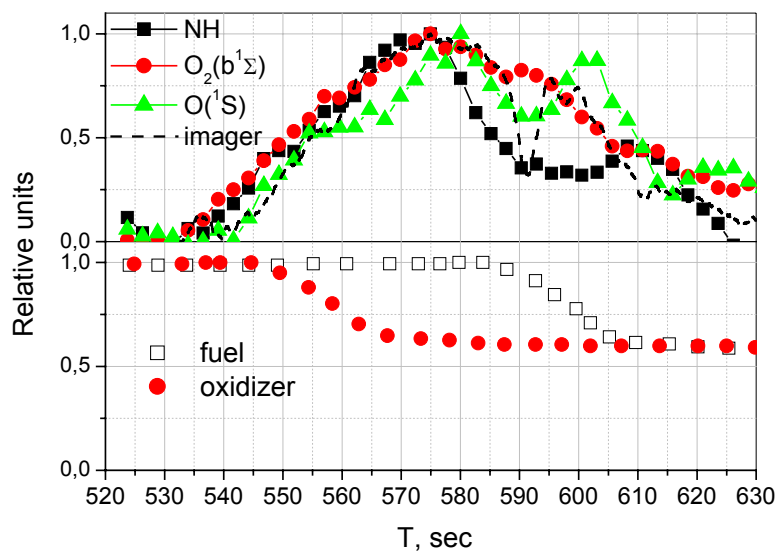


Figure 31. In-band signal variation occurred when the instrument line of sight crossed atmospheric layer (top) and variation of fuel and oxidizer pressures in the combustion chamber feed pipelines (bottom).

Radiation intensity time histories provide the answer on how the signal measured by the imager was shared between $OH(A \rightarrow X)$ and $NH(A \rightarrow X)$ emissions. The shares of these two emissions may be readily obtained by multiplication of the in-band signals on corresponding responses of the imager. The result is shown in Figure 32 for the first 400 seconds of burn. Later the $OH(A \rightarrow X)$ signal becomes too weak for meaningful estimate of the shares. Two pares of curves are shown in this figure. Solid lines represent shares of the $OH(A \rightarrow X)$ and $NH(A \rightarrow X)$ emissions obtained with the assumptions that no other than $OH(A \rightarrow X) (v'=0, v''=0)$ vibrational band radiation contributes to the spectrum. In the meantime recent analysis of the similar Shuttle glow radiation spectra showed presence of other vibrational-rotational bands, characterized $\Delta v=1$ in particular³⁶. Intensity of each band is smaller than (0-0) band intensity, so they could not be detected in 26 April 2000 experiment over the spectrometer noise. However, integral intensity over all $\Delta v=1$ bands is comparable with the primary (0-0) band intensity, whereas their spectral location is even closer to maximum of the wavelength of the maximum in the imager sensitivity curve. Assuming contribution of the $\Delta v=1$ bands at about the same level as the (0-0) band, shares of the $OH(A \rightarrow X)$ and $NH(A \rightarrow X)$ radiation into the imager signal may be re-estimated. These new shares are presented in Figure 32 by dashed lines. At the bottom part of Figure 32 angular distance between the spectrometer center and space vehicle location is plotted once again. It's worth to note evident correlation between the angular distance and the molecular band shares: with increase of the angle share of OH band grows, while share of the NH lowers. This is clearly seen from general behavior of the curves in relatively long time period, as well as from behavior of the curves at particular moments, especially in the beginning of the motor burn when signals were relatively big. Note, that share variations in the figure look smother than angle drops and raises, because the $OH(A \rightarrow X)$ and $NH(A \rightarrow X)$ in-band intensity signals were smoothed.

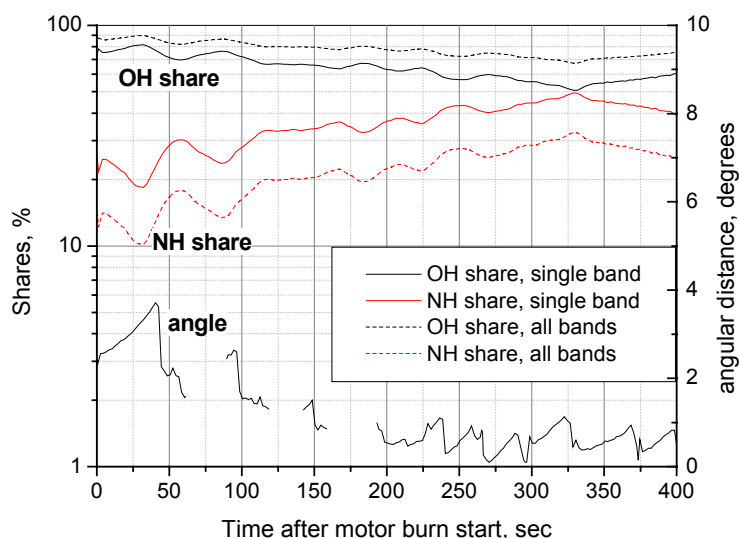


Figure 32. Shares of OH(A→X) and NH(A→X) band emissions in total signal measured by the imager: solid lines - only (0-0) OH(A→X) band included; dashed lines - all other OH(A→X) bands included. Angular distance between spectrometer line-of-sight and direction toward the “Progress” is shown at the right axis.

Despite that NH(A→X) band absolute radiation intensity was higher all over the observation, the imager signal yielded more from OH(A→X) emission due to the deference of the imager’s spectral response at 310 and 335 nm. Evidently, that images taken at the beginning of the experiment suit better for verification of the OH(A→X) glow models. The OH(A→X) radiation share was around 80-90% there. The images taken later contain smaller share of the OH(A→X) emission. One should keep this fact in mind comparing the experimental images with modeled glow radiation maps.

2.6.4. *Filter measurements*

As it has already been mentioned, the interference filters were installed on the imager for a while during the plume glow observation in 26 April experiment. At the moments of filter installation imager signal abruptly decreased (see Figure 25 and Figure 30). Evidently, the filtered measurements help in more precise determination of the glow radiation source in the UV region. Filter #3 was installed at about 160th sec after motor startup and stayed for about 30 seconds. When the filter was installed it effectively blocked the NH(A→X) radiation, so that contribution of the NH(A→X) radiation to the imager signal became yet smaller. If shares of non-filtered OH(A→X) and NH(A→X) signals were 70/30 at the moment of the filter #3 installation (see Figure 32), these shares became 90/10 after the filter was put on. Assuming that only OH and NH molecules contributed to the imager’s signal, one can conclude that in filtered image of the glow at around 180 second after motor start the OH(A→X) radiation strongly dominated. Figure 33 compares radiation intensity profiles taken from of the filtered and non-filtered images. The filtered signal was much weaker than non-filtered one. So, signal to noise ratio is much lower in the filtered curve. For better representation FFT smoothed curve is also depicted in the figure. Figure 33 demonstrates that spatial distribution of the imager signal induced by the OH(A→X) radiation was identical to the total signal distribution within the measurement accuracy limits. It should be noted, however, that NH(A→X) radiation intensity distribution may differ from the OH(A→X) one. This was indirectly proved above in Section 2.6.3 and supported by numerical modeling^{20,21,22}. Nevertheless, coincidence of the radiation profiles in Figure 33 is not surprising, given substantially different response of the imager to the NH(A→X) and OH(A→X) UV radiation. In other words, in the first part of the April 26, 2000 experiment the imager detected mainly the OH(A→X) emission, that is in compliance with Figure 32. The small share of the signal induced by the NH(A→X) emission didn’t disturb the OH(A→X) radiation profile much. So, for modeling purpose relatively accurate approximation would be accounting for the NH(A→X) radiation affecting the total radiation level in accord with its share, having the spatial distribution undisturbed. Note, that at later moments share of the NH(A→X) may be bigger, so that radiation profile may be somewhat affected by the NH(A→X) contribution.

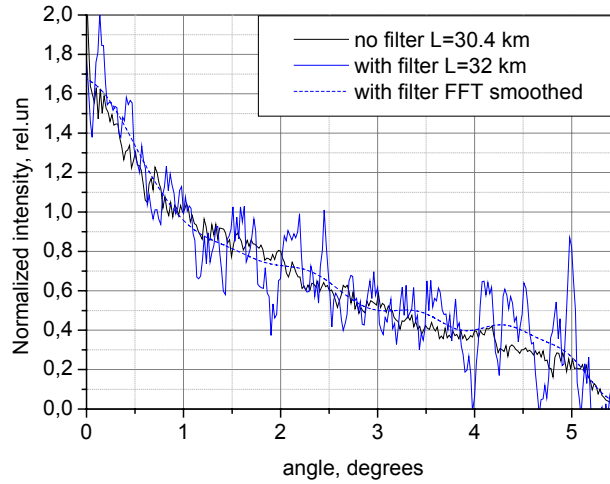


Figure 33. Comparison of the glow radiation intensity profiles obtained with Filter #3 (180 second, L=32 km) and without it (155th second L=30.4 km).

2.6.5. *Absolute radiation intensity of the glow measured by the imager*

It should be kept in mind that total in-band radiation intensity measured by the spectrometer was very weak in the April 26, 2000 experiment. Spectrometer's signal to noise ratio was low. So, quantitative measurements might have relatively big degree of uncertainty – up to 50% at low. Absolute radiation measurements performed by the imager were much more reliable in this regard. For instance signal level from the non-filtered radiation in Figure 27 and Figure 33 is more than 10 times higher than random noise. For derivation of the count per pixel cost in terms of radiation intensity ($\text{W}/\text{cm}^2\text{sr}$) following relation may be used:

$$I_{OH}R_{OH} + I_{NH}R_{NH} = X_{OH} + X_{NH} = \frac{1 \text{ cpp}}{\Omega_{pix}} \quad (2.3)$$

where I_{OH} and I_{NH} are in-band radiation intensities yielding corresponding shares X_{OH} and X_{NH} into each count measured by the imager, $R_{OH,NH}$ – imager's response at the respective band wavelengths 310 and 335 nm (see Figure 18), Ω_{pix} – pixel solid angle. For each particular moment relative spectral composition of the imager signal may be determined from spectral measurements. Relative composition may be measured more precisely than absolute radiation values. For example, at 155th second ratio $\frac{I_{OH}}{I_{NH}} = 0.5$ was derived from the

glow radiation spectrum (only 0-0 OH(A→X) band was considered). Given the $\Omega_{pix} = 1.17 \cdot 10^{-7} \text{ sr}$, equation (2.3) may be resolved, yielding $I_{OH} = 1.7 \cdot 10^{-10} \text{ W}/\text{cm}^2\text{sr}$. So, the OH(A→X) absolute radiation intensity at 155th second after the motor start may be determined by multiplication of measured signal (in cpp) onto the normalization factor $I_{OH} = 1.7 \cdot 10^{-10} \text{ W}/\text{cm}^2\text{sr}$. A pseudo-color 2-D map of the OH(A→X) radiation intensity is shown in Figure 34 for illustration. By similar way the engineering values may be assigned to the radiation levels in Figure 27, where the radiation intensity profiles are presented in terms of cpp versus angle.

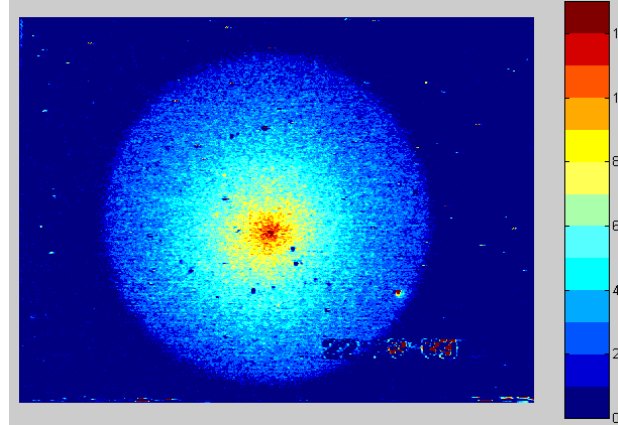


Figure 34. Map of the OH(A→X) absolute radiation intensity measured in the plume glow at 155 second after the burn started. Each level corresponds to $1.7 \cdot 10^{-10} \text{ W}/\text{cm}^2\text{sr}$. Imager's FOV – 9.8°.

2.6.6. *Plume glow induction and decay*

Another useful characteristic, which can be utilized for verification of the high altitude plume flow models, is the glow induction and decay time history. The glow signal induction and decay time histories may be measured in different parts of the glow, providing a mean for verification of the models for non-stationary rarified expanding flows²¹. The glow intensity time histories measured at the initial stage along different lines of sight in the April 26, 2000 experiment are presented in Figure 35. In fact, integral signals in $0.4^\circ \times 0.4^\circ$ boxes centered at 0, 1, 2 and 4 degrees away from the direction toward the "Progress" are plotted versus time in the figure. The signals are normalized to their maximums. Time is measured from the firing start-up moment.

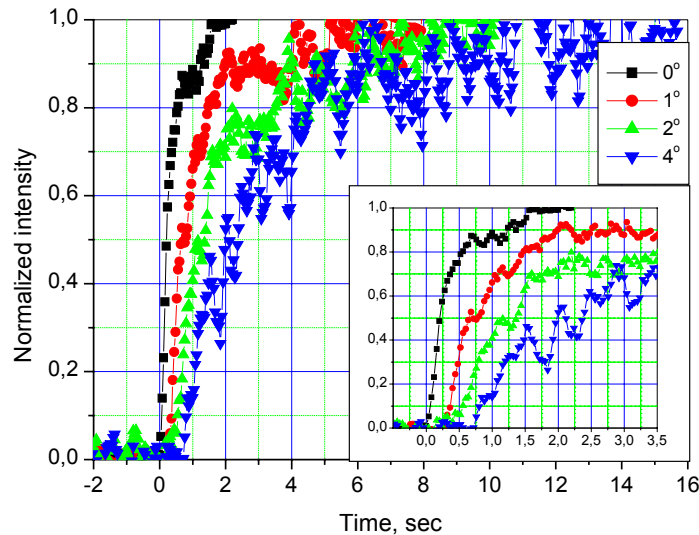


Figure 35. Normalized glow intensity signal induction measured along different lines of sight with regard to the space vehicle position.

Small lags of the glow signal front are clearly seen in the non-zero angle curves. Apparently, these delays and longer induction times should be addressed to physical propagation of the outflow over peripheral regions at the motor set burning start-up.

2.7. *Concluding remarks to the data processing and analysis*

Processing of the 26 April 2000 experimental data has brought along the high quality radiometric glow images and qualitative low resolution glow spectra. The data analysis allowed determination of absolute glow radiation intensity of some molecular bands located in the spectral region of the imager's sensitivity. The OH(A→X) (all bands in 300-320 nm region) and NH(A→X) (all bands in 325-345 nm region) radiation intensities along the plume flow centerline have been determined at 155 sec after the motors burn started: $W_{OH} = 1.85 \pm 0.3 \cdot 10^{-5} \text{ W/m}^2\text{sr}$, $W_{NH} = 3.9 \pm 0.6 \cdot 10^{-5} \text{ W/m}^2\text{sr}$. The accuracy margins result from uncertainty of the imager calibration factor, which in turn depends on the "Mir" station window transparency at the moment of experiment, and uncertainty of the in-band spectral structure of respective molecular bands. Fortunately, a number of bright stars were captured during the 26 April 2000 experiment, so both the window transparency and calibration factor could be monitored during the data acquisition and related uncertainty could be reduced to minimum. Relative variation of the radiation in time and in space has been measured with much better accuracy 6-8%. This accuracy is consequence of slightly non-uniform respond of the imager over its FOV and the data processing noise. So, high quality radiation intensity time histories and spatial profiles may be suggested for further scientific analysis. Time resolved imagery made possible examination of the glow radiation induction and decay processes at the motor set ignition and shut down moments. Variation of the glow intensity within parts of a second time period may be readily reduced from the imager data stream.

Spectrometer data can apparently be utilized for qualitative analysis of the glow emissions. In addition to abovementioned NH(A→X) and OH(A→X) molecular bands, atomic oxygen emissions related to metastable states O(¹D) and O(¹S) have been identified in the 8xACS plume glow. Absolute intensities of these emissions and their relative variations in time have been reduced from the spectra, but with poorer accuracy in comparison with imager. Spectra taken at earlier moments of the 26 April 2000 experiment allude to presence of some other radiation source in the UV region. Because of the weak radiation intensity of this source and low spectral resolution of the spectrometer, this radiation could not be reliably associated with any molecular band. Some emissions not related to the plume glow have been also identified in the spectra. These emissions were attributed to the natural Earth nightglow.

Generally, the 26 April 2000 data are self-consistent and correlate with earlier glow measurements. Absolute radiation intensity is around expected level. Signal variation exactly correlates with re-location of the instrument line-of-sight. Internal instrument timer was perfectly correlated with on-board clock.

In the meanwhile, some new features have been found in the experimental data. In particular, spatial distribution of the glow emissions appeared to be wider than expected. The glow profiles have distinctive bend indicating to a composite character of the 8xACS motor plume glow radiation. Also, unexpected growth of the NH(A→X) in-band radiation intensity was observed during final minute of the motor set operation. Two hypotheses have been put forward to explain this growth. Further experiments and data analysis is needed for elaboration of these hypotheses.

3. Improvement of the TAL plasma optical diagnostic technique

3.1. *General remarks to the current status of the HET plasma optical diagnostics*

Optical diagnostic methods have been often applied for measurements of the xenon operating HET plasma parameters. Generally, the HET optical diagnostic methods may be subdivided on active and passive methods. By active methods HET plasma species number densities and velocities are derived from measurements of fluorescent emissions induced in these species by a probing laser radiation. Passive methods are based on analysis of the HET plasma emission intensity, which in turn must be related with the species number density and temperature through appropriate collisional-radiative model (CRM). At the face of it the active methods (Laser Induced Fluorescence – LIF, in particular) look more attractive, as they seemingly do not need the CRM. However, due to the big energy gap between ground and excited states in xenon atom and ion and limitations in generation of probing radiation frequencies, only excited particles number density may be measured by the LIF method. Relation between the excited species number density and other plasma characteristics, such as ground state species and electron number density and energy distributions, has to be modeled anyway. Therefore, CRM should be essential part of any optical diagnostic method, excluding the LIF velocimetry, perhaps.

Extended and relatively complete CRMs have been suggested for different systems other than xenon operating HET. Analysis of those CRM is far beyond the scope of current study. However, it would be worth mentioning here Ref.^{37,38}, devoted to elaboration of a collisional-radiative model for argon discharges. This work gives an impression on how sophisticated should be the complete CRM in noble gases. It has to consider some tens of effective levels for each gas specie involved into production of radiation and handle hundreds of collisional and radiative parameters, such as collisional excitation cross-sections and transition probabilities. From the other hand the CRM developed for argon (or other noble gas) can't be readily applied for description of the xenon system. In spite of similarity inherent to the noble gases atomic level systems, the CRM parameters may differ substantially between the elements. In the meantime, only two works^{39,40} have been found so far, where general CRM for a HET xenon plasma is addressed. Big variety of processes involved into the CRM and absence of an extended database for the excitation/de-excitation cross-sections are the main problems of those and similar CRMs. Under these circumstances the CRM developers have to model theoretically the cross-sections and other parameters involved.

There are a number of approaches to modeling of the electron collision excitation cross-sections. Extended discussion of this topic is given in Ref.⁴¹, for example. Close Coupling States (CCS) method and R-matrix method are more accurate and in general provide better agreement with experiment. However, these methods are very complex and require extensive time-consuming computations. Basically, they are inappropriate for engineering applications. Well-known Born approximation is often utilized for more simple computations. Actually, this approximation works well when velocity of colliding electron is markedly more than orbital velocities of the bound electrons. At the threshold and in the region of the cross-section maximum accuracy of the Born approximation is worse. Nevertheless, Born approximation provided a basis for a number of analytical expressions for the cross-section energy dependence. Among these expressions Bethe's, Drawin's and Van Regemorter's formulas have to be mentioned in the first turn. These formulas are very convenient for practical applications, but a priori they can't guaranty acceptable accuracy of the cross-section modeling even in comparison with a computation in classical Born approximation. Also, these formulas can be applied only in case of optically coupled dipole transitions. In the meantime, some improvements of the Born approximation have been made. In particular, effect of the atomic field on the colliding electron, exchange interaction and correct normalization of the cross-section values have been taken into account. This approximation was named "generalized Born approximation" in Ref.⁴¹. Generalized Born approximation is applicable for wider range of transitions, than the classical Born approximation, having about the same accuracy.

Scatter of the results obtained by different computational methods may rich substantial value. Authors of Ref.³⁹ modeled excitation cross-sections for Xe 5p⁵6s levels out from the ground state by different methods and obtained scatter of the results factor of 2 for optically allowed transitions and factor of 3-4 for forbidden transitions. For transitions between excited states the scatter may be even more. Basically, a priori modeling of the excitation cross-sections in xenon results in only qualitative agreement between different methods and experiment (where available). Quantitative agreement remains very poor. This fact makes almost impossible developing of the complete and accurate CRM for xenon operating HET. Elaboration of such kind of CRM represents a separate problem, which is much wider than particular task addressed in this study.

Alternative to the extended CRM model could be a Local Thermal Equilibrium (LTE) model^{42,43}. The LTE model doesn't include excitation cross-section and even doesn't specify particular collisional processes responsible for the excitation. Instead, it employs statistical laws relating the plasma parameters. Primary assumption, which forms a basis of the LTE model, is equality of direct excitation and reverse de-excitation

processes. The LTE model assumes Maxwellian electron energy distribution and Boltzmann distribution over the excited states. The LTE model was applied in Ref.⁸ for determination of plasma parameters at the exit of SPT-100 thruster. Analysis of the results in Ref.⁸ unambiguously demonstrated that xenon HET plasma spectra couldn't be explained basing on these distributions. Obviously, assumption about equality of direct and reverse excitation/de-excitation processes is not valid for most of the noticeable xenon emissions in the HET plasma. In the meantime, some high levels of the xenon atomic (ionic) system located nearby the ionization threshold may probably have Boltzmann energy distribution. However, radiation from these levels is extremely weak, impeding its use for diagnostic purpose.

Irrelevance of the Boltzmann statistics for modeling of the excited state distribution in a HET was stated in Ref.⁹ as well. In this work suggested was to utilize so called corona model^{42,43} for relation between the plasma parameters and radiation. Actually, the corona model is utmost limit of the complete CRM for rarified plasmas like the solar coronal one. In terms of the corona model excitation of atomic levels results from collisions between electrons and ground state atoms. Any level may be excited either directly or through radiative cascade transitions from upper levels. General postulate of the corona model is that collisional excitation originates only from the ground state, being balanced by radiative decay exclusivelyⁱ. This assumption holds perfect for strong emissions stemming from short-leaving states in rarified plasmas. When the rate of cascade transitions is negligibly small in comparison with the rate of direct level excitation, the corona model comes to its simplest limit. In this limit the only parameter required by the model for relation of any particular emission intensity with the plasma parameters is the emission excitation cross-section. There is quite a number of works dedicated to measurements and computations of the xenon emission excitation cross-sections out of ground state (see Subsection 3.2.2 for further details). So, implementation of the corona model in its simplest form for HET plasma diagnostics looks very attractive. Unfortunately, this form of the corona model is unacceptable for diagnostics of a xenon operating HET. Energy gap between the ground state and resonant levels in xenon atomic and ionic level systems is much bigger than energy gap between the excited states. Therefore, if energy of electrons in plasma is big enough for excitation of any level, the neighbor upper level should be excited too and radiative cascade transitions have to be taken into account anyway.

Generally the corona model works well in plasmas with electron number density $N_e \sim 10^8 - 10^{10} \text{ cm}^{-3}$. But even in these conditions the corona model may not obligatorily describe radiation from highly excited long-leaving levels. The bigger is electron number density the lesser is number of emissions that obey to the corona model requirements. Electron number density in the HET plasma may vary in the range $N_e \sim 10^{10} - 10^{13} \text{ cm}^{-3}$, having a chance to come beyond upper limit of the corona model applicability. Moreover, utilization of the corona model for description of the xenon emissions even more complicated by presence of metastable states in xenon atomic and ionic level systems. In earlier diagnostic efforts the corona model was utilized for estimation of a HET VUV radiation intensity⁴⁴, for measurements of effective electron temperature⁴⁵, electron energy distribution function⁴⁶, atomic xenon number density and excitation rates for xenon species⁴⁷ in SPT channel region. Plasma properties of an SPT operating in transient mode were studied in Ref.⁴⁸ through analysis of temporal behavior of some XeI and XeII emissions. The corona model approximation was utilized there too to relate the plasma emissions with electron energy distribution and species number densities. Corona model has been assumed by default in the studies of HET plasma oscillations^{49,50,51} and measurements of thruster erosion rate¹⁰ as well. Among above listed works Ref.⁴⁵ is a sole exclusion where authors provided some reasoning to prove the corona model application in their particular case. In all other works the corona model was applied without any direct estimate of its validity. Typical argumentation is that HET plasma is rarified enough making radiative decay to be dominant mechanism of the excited states depopulation.

In the meanwhile, authors of Ref.⁴⁸ indirectly evidenced that metastable levels of XeI and XeII should play essential role in the xenon species excitation in SPT channel, limiting the corona model utilization in the SPT discharge plasma. Importance of the metastable atoms for xenon excitation in the TAL plasma has also been mentioned earlier in Ref.¹¹. Authors of Ref.⁴⁷ have also found that corona model failed to describe intensity of some plasma emissions in the ionization region of the SPT channel. They introduced a more complex CRM, which included stepwise excitation, and obtained better agreement with experiment.

Generally, analysis of previous works results in the conclusion that application of the corona model for description of any particular xenon emission in a HET must be thoroughly verified to avoid incorrect results. In case when validity of the corona approximation is questionable a more complex CRM has to be developed. At this moment no universal receipt exists on how to work it out. It's hard to imagine that unified comprehensive CRM, which is capable to address all cases of interest, could be developed now for the HET plasma description. More fruitful idea seems to be developing of a simplified case-sensitive CRM, which could be modified for one or another particular application. Because of substantial difficulties and poor accuracy in simulation of the excitation cross-sections and transition probabilities for xenon and its ions, the model should be rather simple and phenomenological as far as possible. That means experimentally measured parameters for the model must be favored.

ⁱ Within the corona model some authors allow the level excitation not only from the ground state, but from the excited states too, emphasizing the balance between collisional excitation and radiative decay as the distinctive feature of the model. We will not refer to this kind of model as the corona one, considering it as a particular form of a general CRM.

Along with the questionable choice of the CRM one of the most essential shortcomings of previous HET optical diagnostic efforts was that only excitation of xenon species by electrons were considered in the CRM. Neglected were such important processes as excitation induced by heavy particle collisions and resonant scattering of radiation coupled with the ground state. Perhaps, one could argue that collisions between heavy particles in the HET plasma should be adiabatic, because the heavy particle velocity at the collision energy 300-600 eV is much smaller in comparison with the orbital velocity of the electrons in xenon atom (Massey criterion⁵²). However, noble gas atomic systems may not follow this rule. High values of the excitation cross-sections in relatively slow collisions between noble gas heavy particles were reported in Ref.^{12,53,54,55}, for instance. The cross-sections were high even at collision energies 50-200 eV, where the Massey criterion predicts almost negligible values of the respective cross-sections. Plausible reason for this phenomenon is thought to be formation of the noble gaseous dimers, which decay immediately after collision, producing excited species. From this perspective high values of the xenon atomic and ionic collisional excitation cross-sections measured in the AFRL¹² doesn't look surprising. At some circumstances the heavy particle collisions are able to compete seriously with electronic collisions in excitation of xenon species in the HET plasma¹¹.

Non-linear pressure dependence of the xenon emissions intensity induced by the electron collisions in the range of $p=0.1-2$ mTorr was reported in Ref.⁵⁶. Authors explained this non-linearity by re-absorption of the emission lines coupled with the ground state. Despite that neither xenon emission in UV through IR wavelength region is associated with a transition to the ground state (only VUV emissions are), the re-absorption may indirectly affect the long wavelength emissions too. In Ref.⁵⁶ intensities of XeI IR lines related to $5p^56p \rightarrow 5p^56s$ and $5p^56p' \rightarrow 5p^56s'$ transitions were measured in electron beam experiments. Beam of electrons with fixed energy was directed through xenon gaseous cell. Variation of the xenon pressure in the cell resulted in variation of the beam induced emissions. Dependence of the emission intensity on pressure appeared to be nonlinear and, as the result, the emission excitation cross-section turned out to be markedly dependent on pressure. In contrast to the case of resonant radiation re-absorption effect, apparent cross-section in Ref.⁵⁶ increased with the pressure growth. Authors of Ref.⁵⁶ proved that excitation of the $5p^56p(p')$ levels in xenon goes through two routes of comparable effectiveness: direct excitation from the ground state and cascade transitions from upper $5p^5ns(s')$ and $5p^5nd(d')$ levels. Because some of the $5p^5ns(s')$ and $5p^5nd(d')$ levels are strongly coupled with the ground state, radiation stemming from these levels to the ground state may be effectively reabsorbed and re-emitted all over the entire cell volume. Apparently, excitation of the $5p^56p(p')$ levels through the cascades may be affected by this re-absorbed/re-emitted radiation resulting in pressure dependence of the apparent emission excitation cross-section. Of course, direct excitation cross-section of the $5p^6 \rightarrow 5p^56p(p')$ transition, which doesn't include cascade transitions, showed no pressure dependence in Ref.⁵⁶.

Non-linear pressure dependence of the electron beam induced XeI emissions has also been found in AFRL experiments¹³. Basically, this dependence is to be not just on pressure, but on the product of the pressure and spatial scale representing effective absorption optical path. Pressure in the HET test vacuum chambers is often ranges from 0.01 to 0.3 mTorr, whereas optical path may be much longer than one reported in Ref.^{13,56}. Therefore, effect of the non-linear pressure dependence of measured emission intensity may occur in the HET test chambers even at low pressures. Therefore, prior to any particular measurement of a xenon emission, preliminary study has to be undertaken to answer the question whether this emission is affected by resonant radiation trapping or not. Otherwise, the resonant radiation trapping effect has to be somehow included in the CRM.

The optical diagnostic method discussed in this section has three distinctive features in comparison with earlier efforts:

- ❑ Thorough choice of the CRM is implemented for each particular emission involved. The CRM and the method itself reduce utilization of the ambiguous collisional and radiative parameters to minimum.
- ❑ Heavy particle collision induced excitation is taken into account.
- ❑ Excitation cross-section pressure dependence effect is carefully studied and reduced values of the cross-sections are utilized.

3.2. Phenomenological collisional-radiative model for the HET plasma

3.2.1. Modeling of the HET plasma radiation intensity

Xenon operating HET plasma emission spectrum is very rich. Almost full set of tabulated XeI and XeII lines may be found there. Evidently, the emissions result from collisions between plasma particles. Additionally to the xenon first ion, second, third and even fourth ions may be found in the HET plume⁵⁷. At typical operating voltages $U=150-700$ V, the third and fourth ion content in the HET plasma is relatively small^{8,57,58,59}. Therefore, present consideration doesn't include collisions involving third and higher charge ions. Furthermore, we will be attempting to pick up from the HET emission spectrum those lines, which may be described by a simplest CRM. So, among big variety of different processes resulting in formation of the excited species in xenon plasma, only

those are discussed below, which will be anyway included in the simplest CRM developed in the course of this study.

□ Electron impact excitation out of the ground state

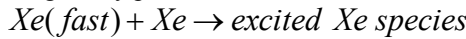


These processes should play important role almost everywhere in the HET plasma and have to be presented in any CRM. Along with cascade radiative transitions they are basic excitation processes in the corona limit approximation.

□ Heavy particle collision excitation

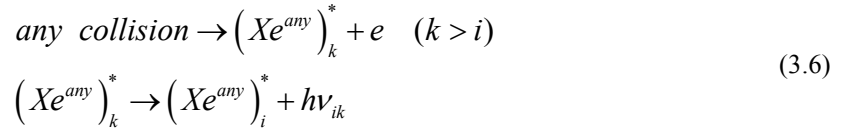


The heavy particle collision excitation may compete with the electron impact excitation in the HET plasma, especially in the plume flow, where electron temperature is small and the ion flux is intensive. At some conditions, the heavy particle collision excitation may even dominate over the electron one. Other processes involving heavy particles like



are not considered in this study because of their secondary importance and lack of knowledge about respective cross-sections.

□ Cascade transitions



where Xe^{any} represents a xenon specie in any ionization state (neutrals, first and second ions).

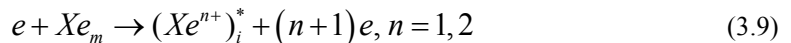
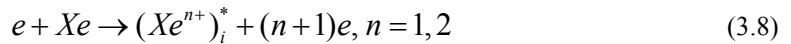
Cascade transitions have to be presented in any xenon CRM including the simplest corona limit approximation, where they play primary role together with reactions (3.1)-(3.3).

□ Stepwise excitation



This process becomes important when radiative lifetime of the excited Xe_m^* atoms increases. Basically, upper levels of xenon atomic and ionic systems have longer radiative lifetimes and stepwise excitation may play important role in their population. Inclusion of process (3.7) into a CRM would make it substantially more complex and lessen its practical value. So, attractive would be to avoid working with the emissions related to the levels affected by the stepwise excitation. This is probably easy to do in case of many principal XeII emissions. However, it turns out to be impossible to exclude the stepwise excitation of xenon atom in many cases of practical interest, because among four lowest $5p^56s(s')$ levels of the xenon atomic system two are metastable. Therefore process (3.7) has been included into general consideration, assuming the m subscript to be attribute of a metastable state.

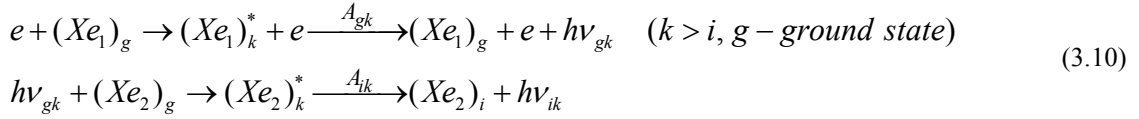
□ Excitation of ionic emissions out from atomic states



Reactions (3.8) and (3.9) are alternative routes to the ordinary excitation of the ionic lines (processes (3.2), (3.3)). Because excitation of the ionic lines in reactions (3.8) and (3.9) results from the collisions of electrons with xenon atoms, threshold of these reactions exceeds the one for reactions (3.2) and (3.3) on corresponding ionization energy. Obviously, processes (3.8) and (3.9) should be important in plasma with small ionization degree in presence of relatively hot electrons. Hot electrons are potentially available in the HET discharge plasma, whereas the ionization degree may vary in a wide range, depending on place and operating

mode. In some very specific cases reactions (3.8) and (3.9) may contribute to the excitation of xenon ionic emissions in HET plume plasma, therefore they have been included into general consideration.

- Effect of absorption and re-emission of the radiation coupled to the ground state



Here Xe_1 and Xe_2 are two identical but different atoms located in different places, A_{gk} and A_{ik} are transition probabilities from k to g and from k to i state respectively. Note that in contrast to all other processes, excitation of the xenon atom through set of processes (3.10) may happen even outside the HET plasma flow, everywhere in the test chamber. In these conditions modeling of the radiation intensity measured by a spectrometer represents a complex problem comparable with developing of the full collisional-radiation model of the HET plasma. One should not expect satisfactory accuracy from that complex problem solution. Need of modeling processes (3.10) would make the diagnostic method unjustifiably sophisticated, not reliable and not attractive for practical applications. From the other side, effectiveness of the excitation through absorption/re-emission of the ground state coupled radiation strongly depends on the experimental conditions (operating pressure, propellant mass flow rate, observation geometry etc), hence, any data can't be readily borrowed from one measurement and applied to another. Therefore, in this particular study suggested was to use for the HET plasma diagnostics only those emissions, which are not affected by the radiation re-absorption. Appropriateness of one or another emission line to the formulated requirement should be thoroughly tested beforehand.

We haven't found any publication where similar effect is reported for xenon ionic emissions. Nevertheless, should it happen, same reasoning as for the atomic emissions must be applied.

- Photo-recombination



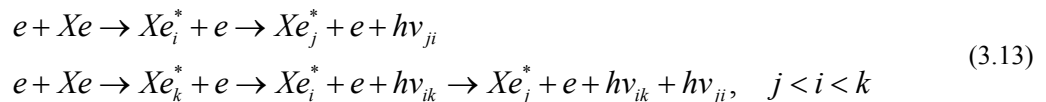
Recombination is typically being excluded from the list of excitation processes, because in stationary operation condition probability of the recombination induced excitation is negligibly small in comparison with other excitation channels. This conclusion has been proved by direct estimate of the recombination cross-section through Kramers's formula⁶⁰. Also, this has been indirectly proved by absence of any reports about observation of the recombination continuum in the HET radiation spectrum.

In view of the above consideration specific (per unit volume) radiation power J_ν of any emission line with frequency ν in the HET plasma may be expressed as a sum of contributions from different processes:

$$J_\nu = e_\nu + H_\nu + C_\nu + M_\nu$$
(3.12)

where e – electron impact excitation, H – heavy particle impact excitation, C – cascades from the collisionally excited upper levels and M – stepwise excitation from a metastable level.

Right side terms in (3.12) are related with plasma parameters through atomic constants and collision excitation cross-sections. General idea of the suggested diagnostics method is to make this relation as simple as possible, utilizing excitation cross-sections that may be measured experimentally with satisfactory accuracy. In most beam experiments, where collisional excitation cross-sections have been measured, apparent emission line excitation cross-sections can be readily reduced from the beam induced radiation spectra. These cross-sections include both collisional excitation directly from the ground state and all possible cascade transitions. For example, $i \rightarrow j$ emission induced by electron collision with a neutral xenon atom may result from both processes (3.1) and (3.6):



Here k represents all upper levels where cascade transitions may originate. Evidently, total radiation power for both processes in (3.13) may be described by a single parameter – emission excitation cross-section $\sigma_{ve0}^*(E_e)$, which depends on the electron energy E_e and characterizes particular emission line with frequency ν :

$$J_{\nu e0} = e_{\nu 0} + C_{\nu e0} = \frac{h\nu_{ji}}{4\pi} N_e N_0 \int_0^\infty f_e(E_e) \cdot \sigma_{ve0}^*(E_e) \cdot u_e dE_e$$
(3.14)

where $J_{\nu e0}$ is share of the radiation power induced by the electron impact with a ground state atom including all related cascades $C_{\nu e0}$, $f_e(E_e)$ is electron energy distribution function (EEDF) normalized to unity, u_e – electron velocity, N_e and N_0 – number densities of the electrons and neutral xenon atoms in the ground state.

Evidently, relation (3.14) is also good for modeling of the radiation produced in reaction (3.8). Furthermore, it may be extended to electron collisions with ions and metastable atoms (reactions (3.2), (3.3), (3.7) and (3.9)). In this case parameters corresponding to electron-atom collision (neutral xenon number density and electron-atom collision excitation cross-section) must be replaced by their values corresponding to the respective processes:

$$J_{vep} = e_{vp} + C_{vep} = \frac{h\nu_{ji}}{4\pi} N_e N_p \int_0^\infty f_e(E_e) \cdot \sigma_{vep}^*(E_e) \cdot u_e dE_e \quad (3.15)$$

where subscript p indicates attribute of the respective parameter to one or another particular process. Apparently, total power of the radiation caused by electron collisions with plasma particles is the sum over all processes: $J_{ve} = \sum_p J_{vep}$.

Similar approach may be suggested for the emissions induced by heavy particle collisions (reactions (3.4) and (3.5)):

$$J_{vHq} = H_{vq} + C_{vHq} = \frac{h\nu_{ji}}{4\pi} N_0 N_q \int_0^\infty f_q(E_q) \cdot \sigma_{vq}^*(E_q) \cdot u_q dE_q \quad (3.16)$$

Here subscript q indicates affiliation of the respective values to the first ($q=1$) and second ($q=2$) xenon ions. Similarly to the electron collision induced radiation, total radiation power in the case of heavy particle collision may be expressed as the sum of the first and second ion shares: $J_{vH} = J_{v1} + J_{v2}$.

Introduction of the J_{ve} and J_{vH} into expression (3.12) will give the total radiation power per unit volume:

$$J_v = \frac{h\nu_{ji}}{4\pi} N_0 N_e \left(\sum_p \frac{N_p}{N_0} \int_0^\infty f_e(E_e) \sigma_{vep}^*(E_e) u_e dE_e + \sum_q \frac{N_q}{N_e} \int_0^\infty f_q(E_q) \sigma_{vq}^*(E_q) u_q dE_q \right) \quad (3.17)$$

Integrals in relation (3.17) represent the emission excitation rate coefficients. In terms of the excitation rates this relation may be expressed as:

$$J_v = \frac{h\nu_{ji}}{4\pi} N_0 N_e \left(\sum_p \frac{N_p}{N_0} R_{vep} + \frac{N_1}{N_e} R_{v1} + \frac{N_2}{N_e} R_{v2} \right) \quad (3.18)$$

where R_{vep} is emission excitation rate coefficient for electron collision with p -th plasma particle, R_{v1} is emission excitation rate coefficient for collision of the first ion with neutral xenon atom and R_{v2} is emission excitation rate coefficient for collision of the second xenon ion with neutral atom:

$$R_{vep} = \int_0^\infty f_e(E_e) \cdot \sigma_{vep}^*(E_e) \cdot u_e dE_e \quad (3.19)$$

$$R_{v1} = \int_0^\infty f_1(E_1) \cdot \sigma_{v1}^*(E_1) \cdot u_1 dE_1 \quad (3.20)$$

$$R_{v2} = \int_0^\infty f_2(E_2) \cdot \sigma_{v2}^*(E_2) \cdot u_2 dE_2 \quad (3.21)$$

Such form of representation is useful when contribution from different processes needs to be evaluated.

Relations (3.19)-(3.21) may be further specified if electron and ion energy distribution functions are known. In the HET plasma Maxwellian EEDF is often assumed:

$$f_e(E_e) = 2 \sqrt{\frac{E_e}{\pi (kT_e)^3}} \exp\left(-\frac{E_e}{kT_e}\right) \quad (3.22)$$

Ion energy distribution in the HET plume was measured in Ref.^{57,58,59}. It is featured by several peaks of different heights and widths (see also Paragraph 5.3.1.2). Each peak represents a group of ions of different charge. Typically, most intensive is the first ion peak centered at the energy some tens below of $e \cdot V$, where e is electron charge and V - thruster anode voltage. The second ion peak is noticeably smaller and located at about twice of

the distance to the first peak in the energy scale. Width of the peaks is about several tens of volts. From the other side, it has been found out that ion collision excitation cross-sections $\sigma_{v1}^*(E_1)$ and $\sigma_{v2}^*(E_2)$ vary smoothly in the range 100-800 eV^{11,12}. Therefore, in the baseline approximation the ionic cross-sections may be considered as constants within the energy interval corresponding to the ion beam energy distribution in the HET plume.

Given the distribution functions explicitly expressed, excitation rate coefficients may be represented through electron temperature and ion beam energy in the following way:

$$R_{vep} = \int_0^\infty 2E_e \sqrt{\frac{2}{\pi (kT_e)^3 m_e}} \exp\left(-\frac{E_e}{kT_e}\right) \sigma_{vep}^*(E_e) dE_e \quad (3.23)$$

$$R_{v1} \approx \sigma_{v1}^*(eV) \cdot \sqrt{\frac{2eV}{M}} \quad (3.24)$$

$$R_{v2} \approx \sigma_{v2}^*(2eV) \cdot \sqrt{\frac{4eV}{M}} \quad (3.25)$$

where m_e - mass of the electron, M - mass of the xenon ion, e - electron charge and V - HET operating voltage.

Introduction of the electron temperature substantially simplifies equations (3.17) and (3.18). However it is not always justified. Substantial deviations from Maxwellian EEDF may occur in the HET plasma, especially in the discharge region. Ion energy distribution may also broaden in the plume far field and peripheral regions. Under these conditions relations (3.19)-(3.21) have to be applied for computation of the excitation rate coefficients. And finally, number of parameters in equations (3.17) and (3.18) may be reduced if condition of plasma quasineutrality is taken into account. $N_e = N_1 + 2N_2$. In this situation equation (3.17) takes a form:

$$J_v = \frac{h\nu_{ji}}{4\pi} N_0 N_e \left(\sum_p \frac{N_p}{N_0} R_{vep} + \alpha \cdot R_{v1} + \frac{1-\alpha}{2} R_{v2} \right) \quad (3.26)$$

where $\alpha = \frac{N_1}{N_e}$ - ratio of the first ion number density to the electron number density.

3.2.2. Emission excitation cross-sections and rate coefficients

Equations (3.17) and (3.26) may be used for determination of plasma species number densities, EEDF and electron temperature (where appropriate) from measurements of radiation power of different emissions, provided that energy dependence is known for the emission excitation cross-sections and rate coefficients involved. As mentioned above, uncertainty of the direct electron collision excitation cross-sections is often factor of two and more. Obviously, the line emission cross-sections, which include cascade transition probabilities, may be modeled with even worse accuracy. Heavy particle collision induced emission cross-sections have not been modeled yet at low collision energy. Therefore, if possible, utilization of the reliably measured cross-sections would be highly desirable. Detailed analysis of the emission excitation cross-section data in xenon represents a separate complex task, which extends far beyond the current project framework. Most of the cross-section data utilized in this study have been taken from recent AFRL beam experiments^{12,13}. Only when the AFRL data were insufficient for modeling the HET plasma emissions, other literature sources have been addressed. Excitation cross-sections and corresponding rate coefficients are considered below separately for xenon atoms and ions.

3.2.2.1. **Atomic emissions**

Electron impact excitation of atomic xenon out from the ground state has been studied most intensively. Not pretending to a completeness of the list, Ref.^{13,41,56,61,62,63,64,65,66,67,68} may be suggested as a source of spacious material about both level and emission excitation cross-sections by electron impact. In addition to the AFRL data other experimental data^{56,61} also look appropriate for the HET diagnostics purposes. In Ref.⁵⁶ cross-sections of both level and emission excitation induced by electron impact in xenon are scrupulously measured in dedicated electron beam experiments. Essential feature of the work is that pressure dependence of the level excitation cross-sections has also been discussed and presented in a form of the cross-section versus pressure plots. Consideration of the cross-section energy and pressure dependence is limited by $5p^56p(p') \rightarrow 5p^56s(s')$ transitions in Ref.⁵⁶. Indeed, these transitions are most intensive and very appropriate for the diagnostic purpose, however no tabulated data have been presented for any of these transitions.

Energy dependence of the emission excitation cross-sections for a number of intensive XeI lines is tabulated in Ref.¹³ in the energy range from 10 through 70 eV. This may be insufficiently wide interval for diagnostics of

the HET discharge plasma having electron temperature of several tens of eV. Energy dependence of the line emission excitation cross-sections in the extended energy interval (up to 400 eV) has been studied in Ref.⁶¹. Authors found some similarity in the energy dependence curves. For practical utilization, all these curves were subdivided onto four groups, representing different types of the cross-section energy dependence. The data presented in Ref.^{56,61} are in a good agreement both with AFRL results¹³ and with theoretical modeling of the direct level excitation cross-section⁶⁵. Therefore, in this particular study the XeI line emission cross-sections were compiled basing on the results of the abovementioned references. Cross-sections for several XeI emission lines are presented in Figure 36 depending on energy. Because, the cross-sections exhibited marked pressure dependence, they were reduced to the minimal pressure ($p=0.1$ mTorr) where data are available in Ref.⁵⁶. Level specification is given in Paschen notation. Corresponding emission excitation rate coefficients are presented in Figure 37.

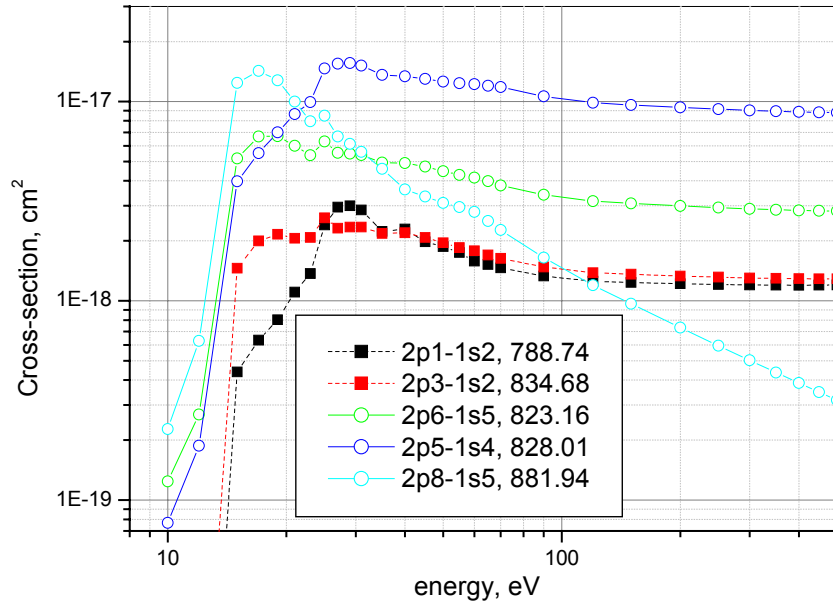


Figure 36. Atomic emission excitation cross-sections for selected XeI lines.

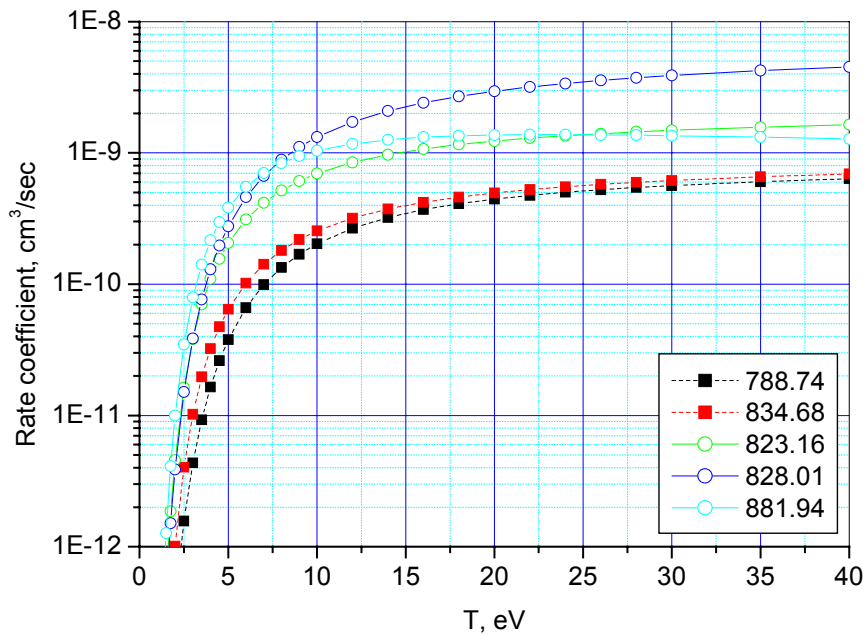


Figure 37. Atomic emission excitation rate coefficients.

Atomic and ionic emissions induced by collisions between xenon atoms and ions were measured in guided beam experiments in AFRL^{12,13}. Excitation cross-sections for selected XeI lines induced by the heavy particle collisions are presented in Table 4. The cross-sections were suggested by AFRL scientists¹³ basing on the analysis of luminescent spectra obtained in the ion beam experiments at $E_H/q = 300$ V ion energy. Energy dependence of the ion-induced emission cross-sections has not been reported so far. However, in the relatively narrow range of ion energy around $E_H/q = 300$ V it may be considered as constant in the baseline approximation. Therefore relation (3.25) is applicable for calculation of corresponding rate coefficients. The excitation rate coefficients for the same XeI emissions are presented in Table 5.

Table 4. Ion collision induced excitation cross-sections for selected XeI lines, 10^{-18} cm².

XeI emission wavelength, nm / Reaction	$Xe^+ + Xe$	$Xe^{2+} + Xe$
462.43	1.91	0
467.12	3.59	0.83
473.31	0.39	0.49
480.7	0.6	0.012
788.74	4.6	1.73
823.16	242	21.1
828.01	31.8	3.25
834.68	27.4	7.35
881.94	640	45.1
895.22	104	8
904.54	173	11.5
916.27	200	18.4
979.97	430	16.6

Table 5. Ion collision induced excitation rate coefficients for selected XeI lines, 10^{-11} cm³/s.

XeI emission wavelength, nm / Reaction	$Xe^+ + Xe$	$Xe^{2+} + Xe$
462.43	0.38	0
467.12	0.72	0.24
473.31	0.078	0.14
480.7	0.12	0.0034
788.74	0.92	0.495
823.16	48.4	6.04
828.01	6.36	0.93
834.68	5.48	2.10
881.94	128	12.90
895.22	20.8	2.29
904.54	34.6	3.29
916.27	40	5.26
979.97	86	4.75

Pressure dependence of the heavy particle collision induced emissions has not been that thoroughly studied as for the electrons. However, assuming the cross-section versus pressure dependence mechanism suggested in Ref.⁵⁶, one could make a conclusion about not very important role of this mechanism for the $5p^56p(p') \rightarrow 5p^56s(s')$ XeI transition lines induced by heavy particle collisions. According to the mechanism, the cross-section pressure dependence occurs when cascades to the $5p^56p(p')$ levels from $5p^5ns(s')$ and $nd(d')$ levels bring a marked contribution to the emission excitation. Ion collision induced radiation spectra of xenon obtained in AFRL have been analyzed and compared with the similar electron collision induced radiation spectra. The comparisons showed that $5p^5ns(s') \rightarrow 5p^56p(p')$ emission intensities in the ion collision induced spectra are factor of 3-5 smaller than the same intensities in the electron collision luminescence spectra. Emissions related to the $5p^5nd(d') \rightarrow 5p^56p(p')$ transitions are about order of magnitude weaker in the ion-induced spectra. In the meanwhile contribution of the cascade transitions to the electron induced $5p^56p(p') \rightarrow 5p^56s(s')$ emissions is order of tens percents. Hence, one may suppose that contribution of the cascades to the same ion induced emissions should be order of percents or 10-15% maximum. This reasoning allows ignoring the cross-section pressure dependence for the ion-induced emissions in the baseline model approximation.

Excitation of metastable xenon atoms by electron impact (reaction (3.9)) is less explored. Handbook⁶⁸ gives only one reference⁶⁹ where these cross-sections were modeled in Born approximation and another one⁷⁰ where the cross-sections were measured experimentally with a poor accuracy. Under these circumstances computation of the cross-sections seemed to be useful for crosschecking of the data reliability. Theoretical computation of the electron collision induced $5p^56s \rightarrow 5p^56p$ transition cross-sections was accomplished within the frame of current

study in generalized Born approximation⁴¹. Typically the cross-sections for optically allowed transitions are between 10^{-15} and 10^{-14} cm². For optically forbidden transitions the cross-sections are more than one order of magnitude less. This is illustrated in Figure 38. Calculated cross-section for transition between optically non-coupled levels is presented in top window. Cross-sections for transitions between optically coupled levels are exemplified in the bottom window of the figure.

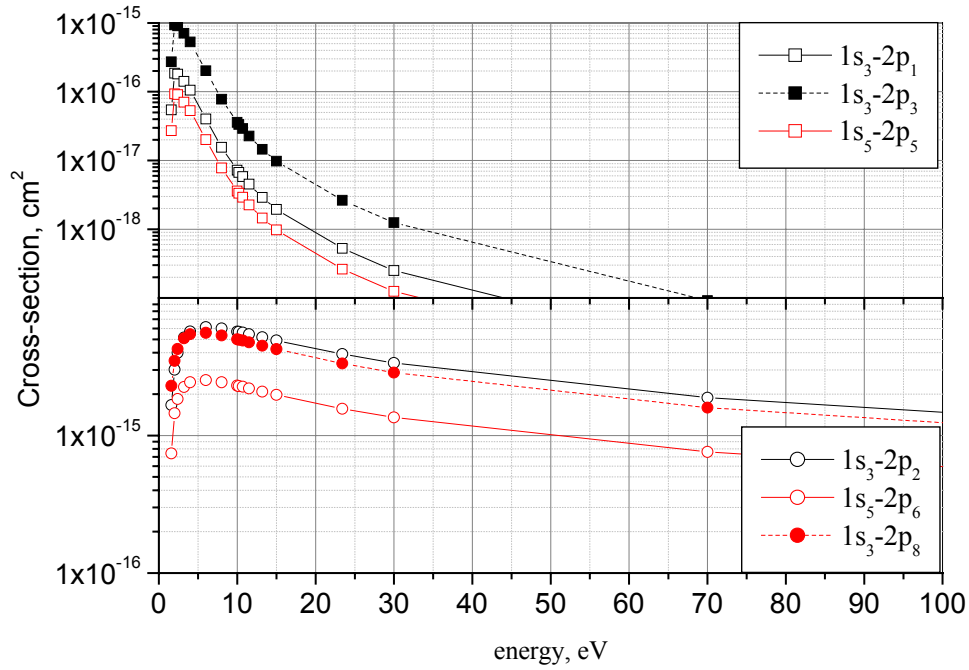


Figure 38. Energy dependence of the electron impact excitation cross-sections out from xenon metastable states.

To double check the computation, estimates of the cross-section energy dependences $\sigma_{kn}(E)$ for some allowed transitions between levels k and n have also been made through the well-known Drawin approximation^{60,71}:

$$\sigma_{kn}(E_e) = 4\pi a_0^2 \left[\frac{Ry}{E_{th}} \right]^2 f_{kn} \sigma_o(E_e) \quad (3.27)$$

$$\sigma_o(E_e) = \begin{cases} 0 & \text{for } u < 0 \\ \frac{u}{(u+1)^2} \ln[1.25(u+1)] + \frac{X}{u+1} & \text{for } u \geq 0 \end{cases}$$

where a_0 - Bohr radius, $Ry=13.6$ eV, $E_{th}=E_n-E_k$ - the excitation threshold energy, f_{kn} - oscillator strength for transition between k and n levels, $u = \frac{E_e - E_{th}}{E_{th}}$ and X is the model parameter⁷¹, which is set to $X=0.3$ for excitation from the ground state to the first excited, $X=0.2$ for excitation to higher levels and $X=0.1$ for collisional transitions between excited levels.

For particular case of two transitions presented in Figure 38 the following parameters were used:

Transition	$1s_5 \rightarrow 2p_8$	$1s_5 \rightarrow 2p_6$
$\lambda, \text{ nm}$	881.9	823.2
f_{kn}	0.49	0.29
$E_{th}, \text{ eV}$	1.41	1.51
X	0.1	0.1

The oscillator strengths were borrowed from Ref.⁷² and X -values from Ref.⁷¹ Energy dependence of the Drawin approximation based cross-sections appeared to be almost the same as in Figure 38, while absolute values came out higher on factor of 3.5-4.

It would be also useful to estimate the rate coefficients (formula (3.23)) for transitions out from the excited levels. These coefficients are presented in Figure 39 in dependence on electron temperature for the same transitions as in previous figure.

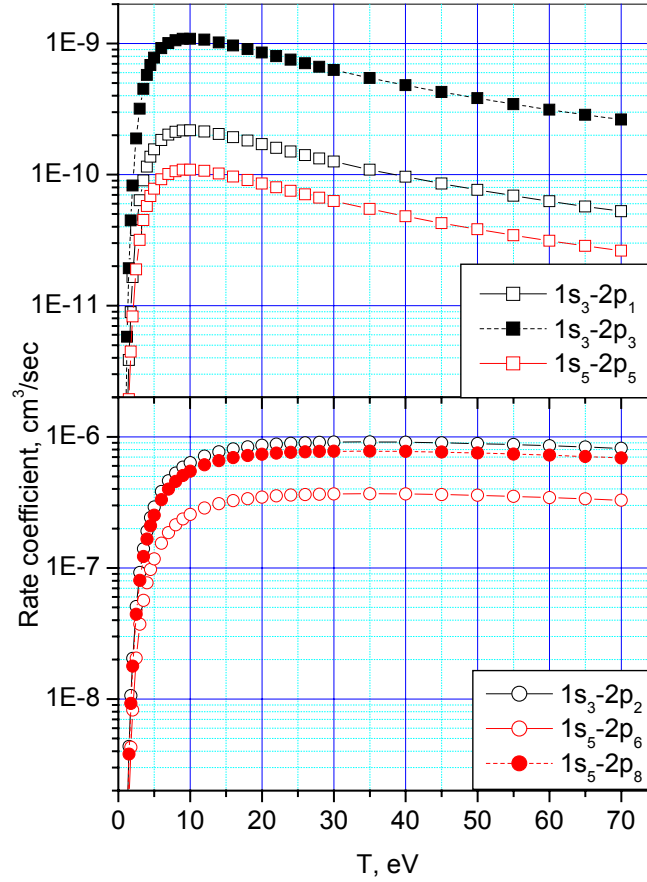


Figure 39. Excitation rate coefficients out from excited states for some transitions in atomic xenon.

Given the qualitative character of the electron impact excitation cross-sections out from the metastable states the data from Figure 38 and Figure 39 may be used only for rough estimates.

3.2.2.2. Ionic emissions

We are not aware about experiments where XeII and XeIII emission excitation cross-sections were studied in reactions (3.2) and (3.3). The only way to evaluate these cross-sections is modeling. The electron-ion collision are used to model similarly to the electron-atom excitation cross-section (see page 35). The only difference is that electron scattering is now considered in the Coulomb field. In these conditions the simplified Born approximation is modified to the Coulomb-Born one, which provides a basis for different semi-empirical formulas and engineering approximations. Extended analysis of different methods for modeling of ion excitation by electron collision and comparison with available experimental data is presented in Ref.⁷³. Among these approximations so called g -formula gave better agreement with experiment, so it has been utilized here for evaluation of the electron-ion collision excitation cross-sections¹:

$$\sigma_{kn} = \frac{8\pi}{\sqrt{3}} \cdot \frac{f_{kn}}{E_e} \cdot \frac{\bar{g}}{E_{th}} \cdot \pi a_0^2 \quad (3.28)$$

where a_0 - Bohr radius, $E_{th}=E_n-E_k$ - the excitation threshold energy in Ry ($Ry=13.6$ eV), f_{kn} - oscillator strength for transition between k and n levels and \bar{g} is effective Gaunt factor, which is to be set to 0.2 for a first ion. Electron collision energy must also be expressed in Ry terms in this formula.

¹ Note, that choice of the engineering computation method is rather subjective. Perhaps somebody may find Drawin's formula or other approach more convenient.

Most intensive XeII emissions are associated with transitions between $5p^46p(p') \rightarrow 5p^46s(s')$ electronic configurations. Upper levels of these transitions are not optically coupled to the ground state. In this case, similarly to the xenon atomic system, cascades from adjacent levels, which have strong coupling with the ground state, should be effective pathway for excitation of these levels in a HET plasma. Electron impact excitation cross-sections have been evaluated for several intensive XeII emissions assuming cascade transitions as primary mechanism to the emission excitation. The emissions and corresponding cascades are listed in Table 6 along with the data necessary for computation of the cross-section energy dependence. The cross-sections were computed through g -formula (3.28). Results are presented in Figure 40. Corresponding rate coefficients are given in Figure 41.

Table 6. Direct and cascade transition specification for some intensive XeII lines.

Emission			Cascade			
λ , nm	Transition	E_2 , eV	λ , nm	Transition	E_2 , eV	f_{12}
529.2	$6s^4P_{5/2} - 6p^4P^o_{5/2}$	13.89	486.2	$6p^4P^o_{5/2} - 7s^4P_{3/2, 5/2}$	16.47	0.2
541.9	$6s^4P_{3/2} - 6p^4D^o_{5/2}$	14.07	508.1	$6p^4D^o_{5/2} - 7s^4P_{3/2, 5/2}$	16.47	0.2
460.3	$6s^4P_{3/2} - 6p^4D^o_{3/2}$	14.48	525.9			
			609.4	$6p^4D^o_{3/2} - 7s^4P_{1/2, 3/2}$	16.62	0.22
			546.9			
504.5	$6s^4D_{3/2} - 6p^4P^o_{1/2}$	16.46	448.09	$6p^4D^o_{3/2} - 6d^4F_{5/2}$	17.24	0.39
			461.9	$6p^4P^o_{1/2} - 6d^4P_{1/2}$	19.14	0.16
			457.2	$6p^4P^o_{1/2} - 6d^4D_{3/2}$	19.17	0.10
			479.6	$6p^4P^o_{1/2} - 6d^4P_{3/2}$	19.04	0.18

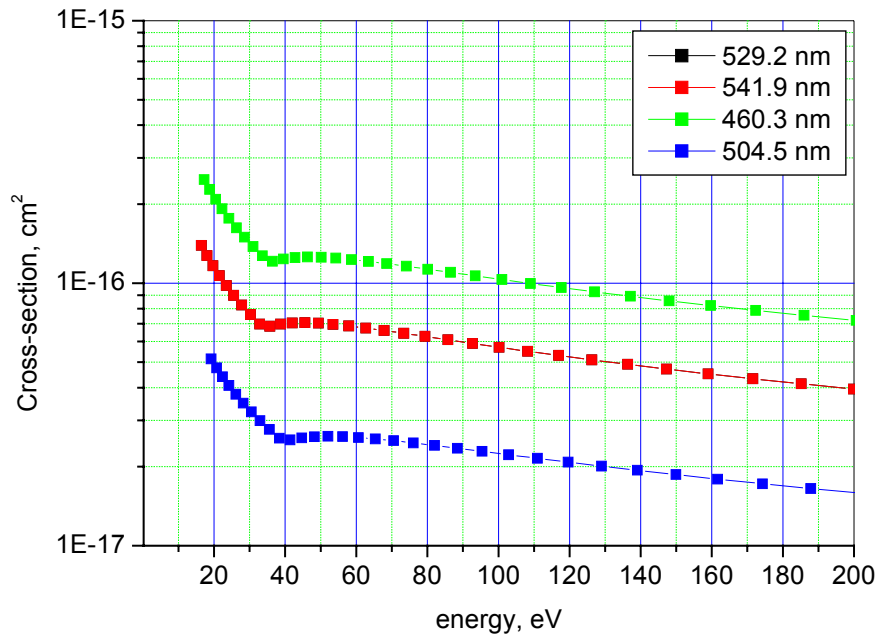


Figure 40. Electron collision excitation cross-sections for selected XeII lines.

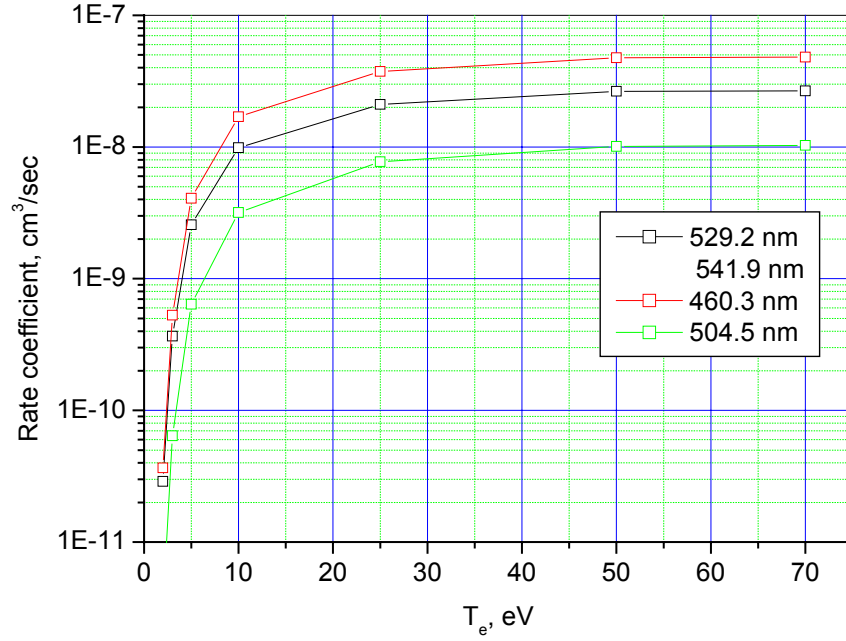


Figure 41. Electron collision excitation rate coefficients for selected XeII lines.

The $6s^4P_{5/2} - 6p^4P_{5/2}^o$ and $6s^4P_{3/2} - 6p^4D_{5/2}^o$ transition curves are identical in these figures, because input data coincide for them.

It should be kept in mind that ion emission data has rather qualitative character and may be used for estimates only.

Measurements of XeII and XeIII emission cross-section induced by the collisions of electrons with xenon atoms in the ground state (reaction (3.8)) were reported in Ref.^{13,61,74}. Generally, the cross-section values for excitation XeII emissions turned out to be relatively small - order of 10^{-18} in maximum. As expected, excitation thresholds have been located in the energy range 25-30 eV, which is 15-20 eV higher than thresholds characteristic for electron-ion collisions. As the result, excitation rates are much less in comparison with the electron-ion collision case. For illustration, excitation rate coefficient of the XeII 529.2 nm line in reaction (3.8) is presented in Figure 42. The rate coefficient was computed basing on AFRL cross-section measurements¹³.

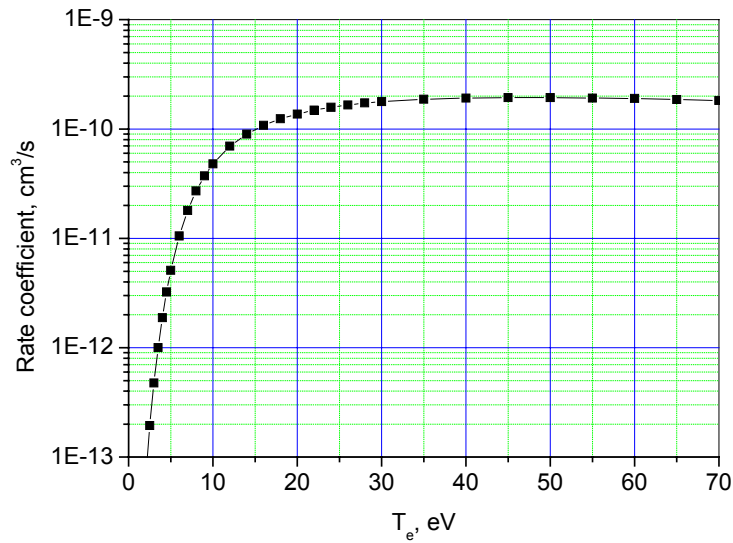


Figure 42. Excitation rate for XeII 529.2 nm emission line in the process of collision between electron and xenon atom in the ground state.

Cross-sections for excitation of XeII emissions in collisions between heavy particles are presented in Table 7, corresponding excitation rate coefficients are presented in Table 8. The cross-sections were measured in AFRL¹³. Note, that cross-sections and excitation rates for the second ion collisions are noticeably higher.

Table 7. Heavy particle collision induced excitation cross-sections for some XeII lines, 10^{-18} cm^2 .

XeII emission wavelength, nm / Reaction	$Xe^+ + Xe$	$Xe^{2+} + Xe$
406.3	0.27	3.01
504.5	0.4	1.32
529.2	2.02	15.74
541.9	1.78	14.19

Table 8. Rate coefficients for ionic emission lines induced by heavy particle collision, $10^{-11} \text{ cm}^3/\text{sec}$.

XeII emission wavelength, nm / Reaction	$Xe^+ + Xe$	$Xe^{2+} + Xe$
406.3	0.054	0.85
504.5	0.08	0.37
529.2	0.404	4.45
541.9	0.356	4.01

3.3. Practical application of the suggested CRM for HET plasma diagnostics

3.3.1. Applicability of the developed CRM in the HET plasma

Equations (3.17) and (3.26) may be directly used for determination of the HET plasma parameters, such as electron temperature, EEDF and particle number densities, provided that emission excitation cross-sections are known. As discussed above, these equations were derived basing on the assumption that excitation processes are balanced solely by radiative decay. This assumption may be expressed algebraically as:

$$\tau_{rad,i} \nu_{dex,i} \ll 1 \quad \text{or} \quad A_i = \sum_k A_{ik} \gg \nu_{dex,i}, \quad k < i \quad (3.29)$$

where $\tau_{rad,i}$ is radiative lifetime of the upper i -th level, ν_{dex} is frequency of the excited i -th level quenching by a collision with a plasma particle, A_{ik} - Einstein coefficients for transition $i \rightarrow k$. Potentially, depopulation of the excited states in xenon may be forced by a collision with any plasma particle. However, in the condition of the HET plasma electron collisions must have much higher frequency in comparison with heavy particle collisions, due to the HET plasma low density and substantially higher electron velocity. Then relation (3.29) may be re-written as:

$$A_i \gg N_e \int_0^\infty f_e(E_e) \cdot \sigma_{de}(E_e) \cdot u_e dE_e,$$

and in terms of the excitation rate as:

$$A_i \gg N_e R_{de}$$

where $\sigma_{de}(E_e)$ is electron collision de-excitation cross-section for i -th level and R_{de} - corresponding de-excitation rate coefficient. The de-excitation rate coefficients in xenon may reach very high values characteristic for collisional transitions between adjacent states coupled by a dipole transition. Estimates of the cross-sections and rate coefficients made on the basis of generalized Born approximation⁴¹ for most intensive $5p^5 6p_j \rightarrow 5p^5 5d_j, 7s_j$ transitions resulted in the rate coefficients comparable with those, depicted in Figure 39 (bottom window) and even higher. Plots from that figure may be borrowed for estimates of the de-excitation rate coefficient value in a HET plasma. For instance, at typical for the D-55 TAL plume electron temperature $T_e \leq 5 \text{ eV}$ and number density $N_e \leq 10^{11} \text{ cm}^{-3}$ (see Ref.^{75,76}) requirement (3.29) turns into:

$$A_i \gg 2 \cdot 10^4 \text{ s}^{-1} \quad (3.30)$$

In the very near field of the plume and in the discharge region electron number density grows up to $N_e \geq 10^{12} \text{ cm}^{-3}$ and bulk of electrons have energies $E_e \geq 10 \text{ eV}$ there. In these conditions requirement (3.29) becomes much stricter:

$$A_i \gg 3 \cdot 10^6 \text{ s}^{-1} \quad (3.31)$$

Transition probabilities and excited state lifetimes in xenon were reported in quite a few of publications (see for example Ref.^{72,77,78,79,80,81} and bibliography therein). Extended material has been also collected in Ref.⁸ and

Ref.⁸². Generally, data from different sources exhibit substantial scatter. Difference between the data often reaches factor of 2-3 and even more. So, utilization of the data for quantitative computations is rather problematic. Nevertheless, qualitative conclusion can be made that upper levels of all noticeable XeI and XeII emissions in the HET plasma meet the requirement (3.30) and, therefore, may be used for plume plasma diagnostics in the frame of the suggested CRM. Also, most of the XeII emissions stem from the levels complying requirement (3.31). So, they could be used for both HET plume and discharge plasma diagnostics. The list of XeI lines appropriate for discharge and very near field HET plume diagnostics within the simplified CRM is fairly limited. Among big variety of the UV, visible and near IR emissions only transitions from $5p^56p(p')$ levels are probably compatible with requirement (3.31), allowing the intensive near IR and some visible XeI lines to be employed for the diagnostic purposes. Utilization of other transitions in the suggested simplified CRM has to be considered individually for each particular experimental condition. Note, that two resonant XeI $5p^56s[J=1]$ and $5p^56s'[J=1]$ states have very short radiative lifetimes and decay through the radiation with a great reserve.

Due to substantial difference between requirements (3.30) and (3.31) practical application of the relations (3.17) and (3.26) for HET plasma diagnostics has to be considered separately in the plume and discharge regions. Furthermore, absence of reliable cross-section data on excitation of ions by electron impact implies separate consideration of neutral and ionic xenon emission capabilities for diagnostic purposes.

3.3.2. *Utilization of the XeI emissions for measurements of the HET plume parameters*

Usually integral radiation I_v along the spectral device line-of-sight is measured experimentally:

$$I_v = \int J_v ds \quad (3.32)$$

In axisymmetric systems the Abel conversion technique⁴² allows to extract specific radiation power J_v from these measurements. Single HET plume flow may be safely considered as axisymmetric in most test facilities. Therefore, the Abel conversion technique has been utilized in this study for the plume flow diagnostics.

Entire radiation spectrum was measured along spans in a selected section of the plume flow by a multichannel spectrometer. The spectrometer acquired radiation through an optical cable equipped by lens at its detecting end. The lens was relocated in vertical direction by a precise step-wise motor mechanism, taking the radiation along horizontal lines-of-sight (see Figure 43). Integral (span-ward) radiation along could be easily extracted from these measurements for any spectral line of interest.

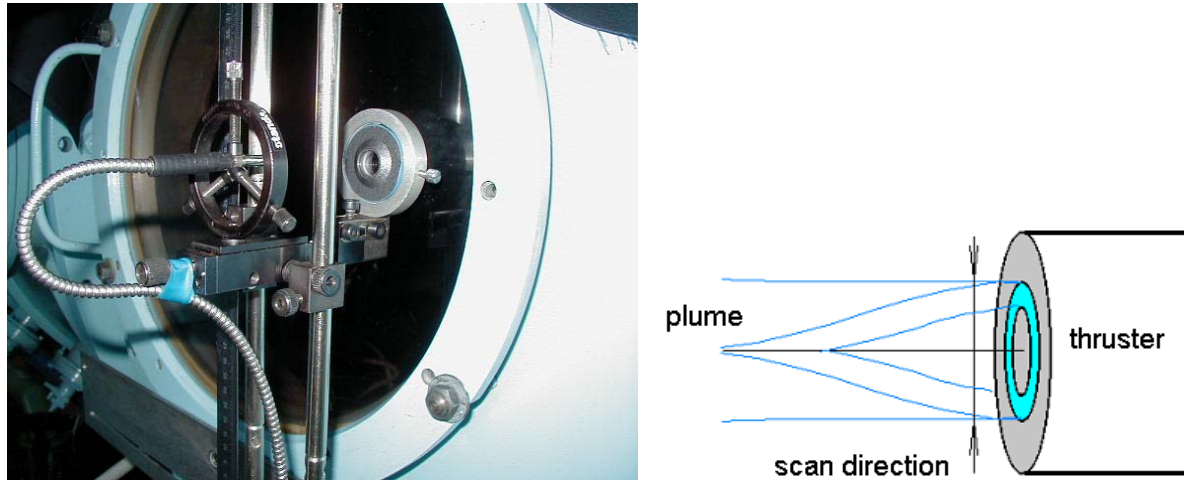


Figure 43. Photo of scanning assembly (left) and the plume scanning scheme (right).

After that radial dependence of spectral line intensity was reconstructed from the span-ward profiles with the use of Abel de-convolution procedure. According to the Abel conversion formula the I_v and J_v value are related as follows:

$$I_v(H) = 2 \int_0^\infty J_v(R) dx = 2 \int_H^\infty J_v(R) \frac{RdR}{\sqrt{R^2 - H^2}}$$

$$J_v(R) = -\frac{1}{\pi} \int_R^\infty \frac{dI_v(H)}{dH} \frac{dH}{\sqrt{H^2 - R^2}}$$

where H - is vertical coordinate for the detector head relocation, R - radial coordinate. Figure 44 exemplifies how the reconstructed radiation profiles differ from the measured span-ward distribution.

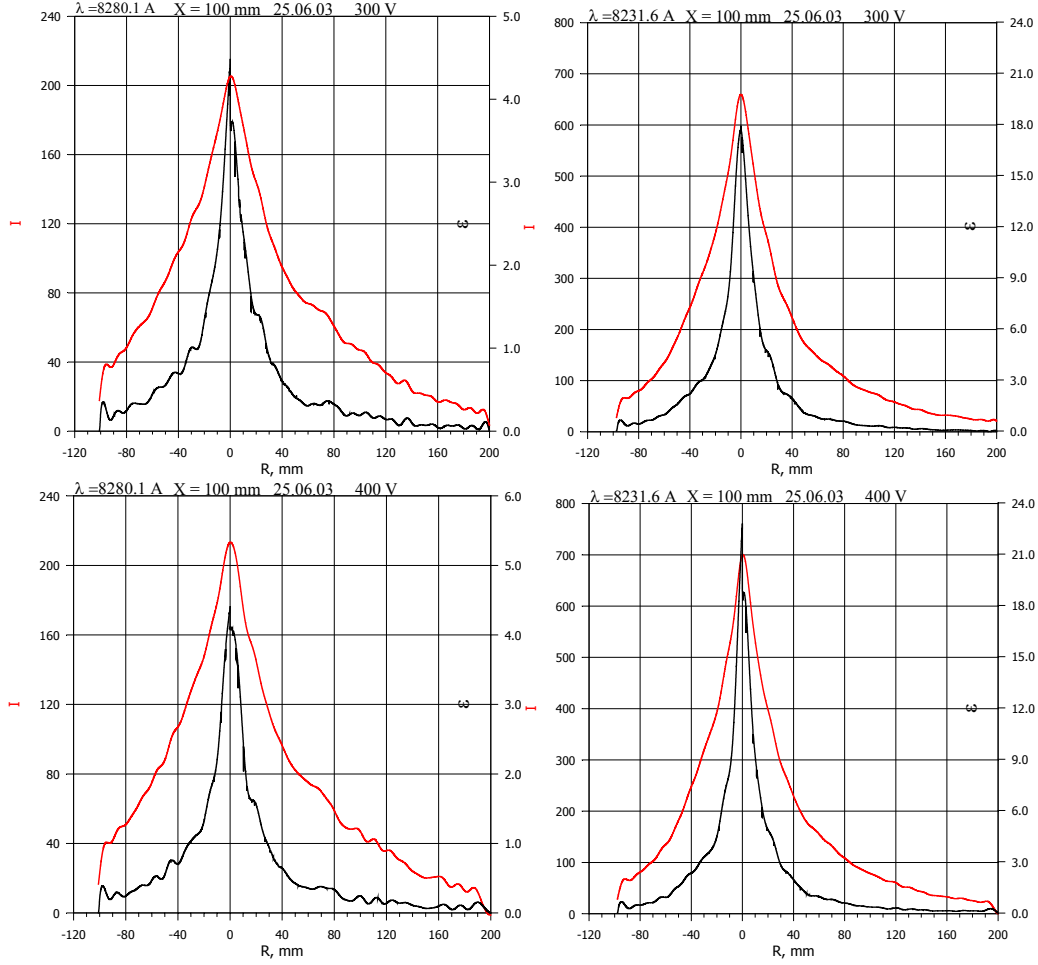


Figure 44. Examples of measured radiation profiles (wider distribution) and reconstructed through Abel de-convolution technique(narrower one) for XeI 828.01 nm and 823.16 nm. Measurement on D-55 thruster at X=100 mm section of the plume flow at operating voltage 300 and 400 V.

Measurements have been conducted in the near field of the D-55 plume flow down to 200 mm from the thruster, where application of the probes causes a lot of problems and difficulties. In fact sensitivity of instruments allowed moving further downstream, however, measurements there were limited by proximity of the window edge.

All XeI emission lines, which are utilized in this study for demonstration of capabilities of the improved diagnostics method, have been examined from the standpoint of non-linear pressure dependence of their intensities. For this purpose radiation spectra from the discharge and near field of a TAL were recorded depending on the background pressure. The background pressure in the tank changed by shutting the evacuation pumps one by one. No any pressure effect similar to the aforecited one⁵⁶ (see Section 3.1) has been found up to pressure $p=0.1$ mTorr. At higher pressures small non-linear effect was observed. But typically the background pressure never exceeded the critical level. So the non-linear pressure effect onto XeI emission intensity may be ruled out in this particular study.

Not all processes listed in Subsection 3.2.1 may lead in generation of XeI emissions. Therefore, with regard to the atomic emissions relation (3.26) may be specified as:

$$J_v = \frac{h\nu_{ij}}{4\pi} N_0 N_e \left(R_{ve0} + \frac{N_m}{N_0} R_{vem} + \alpha \cdot R_{v1} + \frac{1-\alpha}{2} R_{v2} \right) \quad (3.33)$$

where each kind of collision is represented by respective excitation rate coefficient: R_{ve0} - electrons and ground state atoms; R_{vem} - electrons and metastable atoms; R_{v1} - first ion and atom; R_{v2} - second ion and atom.

Margins for variation of the first ion relative content α in a HET plume may be estimated from numerous measurements of the ion energy distribution (see Ref.^{8,57,58} for instance). Typically α varies within 0.7-0.95 range, depending on the thruster type and operating mode. Relative content of the metastable atoms in HET has not been measured yet. Estimates of the metastable state content result in 0.1-1% values in most HETs at

reasonable operating conditionsⁱ. Despite that accurate evaluation of the metastable atom content represent a complex problem, even its rough evaluation allows substantial simplification of equation (3.33), provided that diagnostic emission lines are chosen properly. For some XeI emissions in the HET plasma second term in the right side of that equation may be disregarded. This would be really useful simplification because this term is fairly uncertain. Example of such emissions is XeI 788.74 nm, 828.01 nm and 834.68 nm lines, corresponding to the transitions $2p_1 \rightarrow 1s_2$, $2p_5 \rightarrow 1s_4$ and $2p_3 \rightarrow 1s_2$ (Paschen notation). Upper levels of these transitions are not optically coupled with metastable levels. So, rate coefficients for excitation of these states out from the metastables are much smaller in comparison with allowed transitions (see top window of Figure 39 for reference). Taking the excitation rates R_{ve} , R_{v1} and R_{v2} from Figure 37 and Table 5 and assuming metastable atoms content less than 1%, simple estimate may be done, which reveals negligibly small values of the emission excitation rate coefficients corresponding to the transitions from $2p_1$, $2p_3$ and $2p_5$ levels in comparison with others. Omitting the metastable state term in equation (3.33) results in:

$$J_v = \frac{h\nu_{ij}}{4\pi} N_0 N_e \left(R_{ve0} + \alpha \cdot R_{v1} + \frac{1-\alpha}{2} R_{v2} \right) \quad (3.34)$$

As far as the excitation rate coefficients R_{v1} and R_{v2} are known (see Table 5) Equation (3.34) can be readily utilized for determination of the HET plasma parameters. For example, ratio of the emission intensities of two different emissions depends only on the electron temperature (through R_{ve0} rate coefficient) and relative number density of the first ion α :

$$\frac{J_{v_i}}{J_{v_k}} = \psi(T_e, \alpha) = \frac{\lambda_k}{\lambda_i} \cdot \frac{R_{v_i e0} + \alpha \cdot R_{v_i 1} + \frac{1-\alpha}{2} R_{v_i 2}}{R_{v_k e0} + \alpha \cdot R_{v_k 1} + \frac{1-\alpha}{2} R_{v_k 2}} \quad (3.35)$$

Ratio of the intensities $\psi(T_e, \alpha)$ of XeI 834.68 nm to XeI 828.01 nm emission is plotted in Figure 45 versus electron temperature for different values of α .

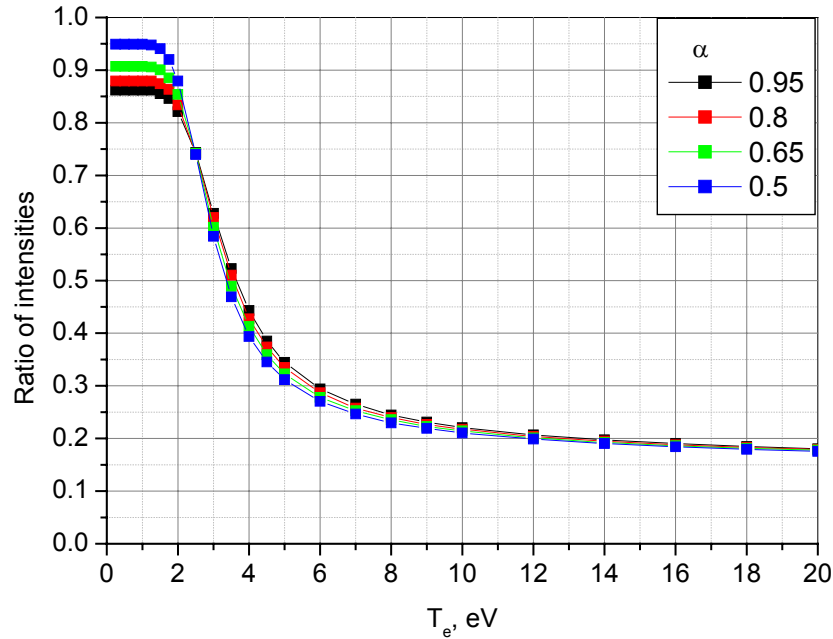


Figure 45. Ratio of XeI 834.68 nm to 828.01 line intensities for different meanings of α .

Of course, utilization of the XeI 834.68 nm and XeI 828.01 nm lines for measurement of the electron temperature in a HET plasma potentially ensures better accuracy, because excitation through metastable states is not very important here in contrast to other emissions. However, at low and moderate temperatures these lines (XeI 834.68 nm especially) are not very intensive in the HET plasma spectrum. Sometimes intensity of XeI 834.68 nm line is too weak for reliable measurements of the intensity ratio. In this case utilization of stronger

ⁱ The metastable atom content in a HET plasma is discussed in Appendix.

lines for diagnostic purpose is highly desirable. Thus, XeI 823.16 nm line instead of the XeI 834.68 nm one was used for TAL electron temperature measurement in Ref.¹¹. However, contribution of the metastable atoms to the XeI 823.16 nm line excitation was not taken into account then, that might cause inaccuracy in the electron temperature determination. This contribution may be taken into account by introduction into relation (3.34) of a slowly varying function $K(T_e, \alpha)$ (see Appendix), so that XeI 823.16 nm to XeI 828.01 nm emission intensity ratio will be expressed as:

$$\psi(T_e, \alpha) = \frac{J^{823}}{J^{828}} = \frac{828.01}{823.16} \cdot \frac{R_{e0}^{823} + \alpha \cdot R_1^{823} + \frac{1-\alpha}{2} R_2^{823}}{R_{e0}^{828} + \alpha \cdot R_1^{828} + \frac{1-\alpha}{2} R_2^{828}} \cdot \left(1 + \frac{k(T_e, \alpha)}{8.36} \right) \quad (3.36)$$

This ratio is plotted in Figure 46 as a function of electron temperature T_e for different values of α .

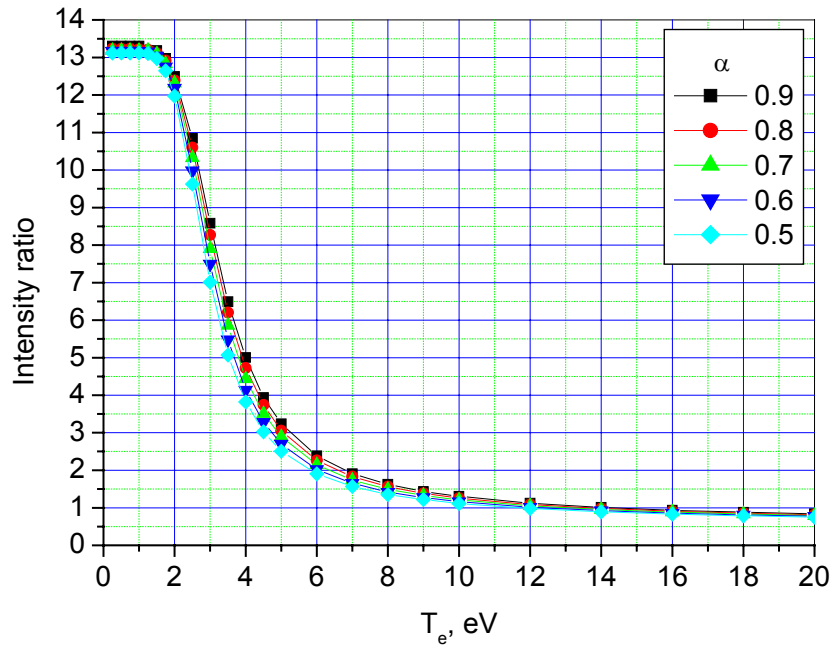


Figure 46. Ratio of XeI 823.16 nm to 828.01 line intensities for different meanings of α .

Apparently, best accuracy of the electron temperature determination from the intensity ratio in Figure 45 and Figure 46 will be achieved in $T_e \approx 2-8$ eV range. Beyond this interval the ratio doesn't exhibit marked dependence on temperature. Also, variation of α in relatively wide interval doesn't noticeably affect the intensity ratio. Obviously, this must be a positive factor when electron temperature is being measured, because uncertainty of the first ion relative content can't cause any significant error in the temperature determination. And finally, selection of neighbor lines in the emission spectrum minimizes instrument calibration errors, because optical throughput response, window transparency and detector sensitivity are almost identical at closely located wavelengths.

The improved method has been applied for measurement of electron temperature in the near field of the D-55 TAL along its plume centerline. Specific radiation intensity of three XeI emissions 823.16 nm, 828.01 nm and 834.68 nm were determined at the thruster axis from the span-ward measurements through Abel conversion procedure. Temperatures reduced from the ratios of two different pares appeared to be almost identical, indicating to the method reliability (Figure 47). Small discrepancy is evident at 200 mm point. Signal to noise ratio for 834/828 line ratio is not that big as closer to the thruster. Data obtained with 823/828 ratio is more reliable from this standpoint. The optical diagnostic results were compared with probe measurements and modeling results (Section 7.4, Figure 142). Good agreement have been obtained there as well.

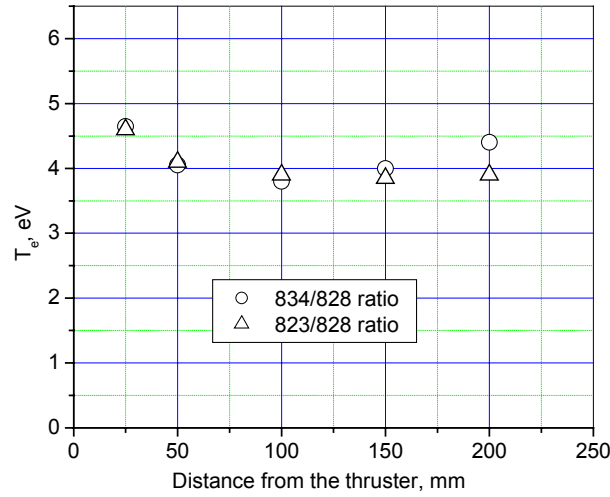


Figure 47. Electron temperature along a D-55 thruster axis reduced from measurements of XeI radiation intensity ratios. $U=300$ V, $I=3.2$ A.

It should be noted, that disregarding of ionic collision contribution to excitation of the XeI emissions results in absolutely different temperature values, which are not compatible with other measurements and modeling results. Importance of the ion collisions contribution is illustrated in Figure 48, where relative contributions of different processes to excitation of some XeI emission lines are compared. Shares of electron, first and second ion impact excitations have been computed at different temperatures basing on respective excitation rates from Figure 37 and Table 5. The shares are normalized to the sum of these three contributions, $\alpha=0.8$ was applied at this modeling. General behavior of the curves is typical for other examined XeI emissions too.

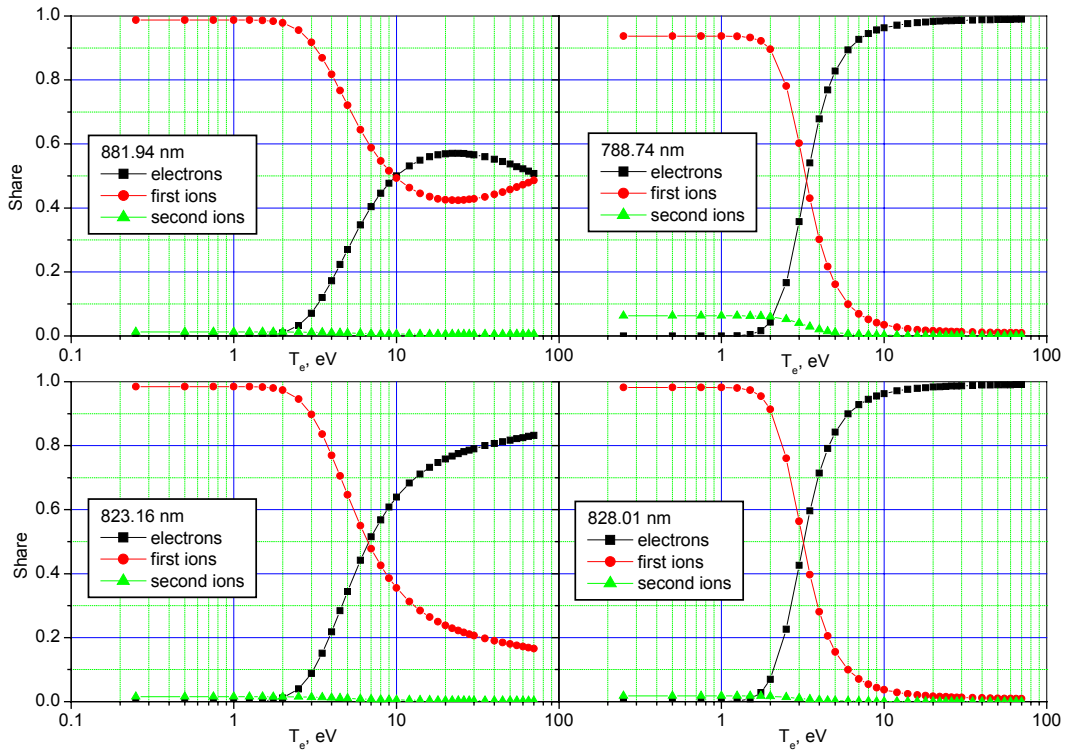


Figure 48. Relative contribution of different processes into excitation of XeI emission lines in TAL plasma.

Apparently, role of the ionic collisions for some emissions stays important even at high electron temperatures. In the meantime, at temperatures below 2-2.5 eV intense XeI emissions are almost entirely induced by the ion-neutral collisions, which are not affected by the electron temperature. Energy of electrons at these temperatures is too low for excitation of xenon atoms. This is also seen in Figure 45 and Figure 46, where the line intensity ratio comes to a constant at low temperatures. In this region the XeI emissions may be utilized for accurate determination of the α coefficient and first to second ion content ratio. Omitting electron collision terms in expression (3.35), ratio for the ion induced emission may be offered in the form of:

$$\frac{J_{v_i}}{J_{v_k}} = \frac{\lambda_k}{\lambda_i} \cdot \frac{\alpha \cdot R_{v_i1} + \frac{1-\alpha}{2} R_{v_i2}}{\alpha \cdot R_{v_k1} + \frac{1-\alpha}{2} R_{v_k2}} \quad (3.37)$$

Dependence of the XeI IR emissions induced by ionic collisions upon relative content of the ions appeared to be rather weak. So, utilization of the IR emissions for the ion charge ratio measurements doesn't make much sense. Fortunately, visible emissions may be utilized for this purpose. In contrast to the IR emissions, where contribution of the first ion collisions dominates over the second one, some XeI emissions in visible spectral region may be excited by both first and second ions with comparable probabilities (see Table 5). So, pairs of lines may be found, which intensity ratio is very sensitive to the relative content of different ions. Good candidates for the ion charge content probing through measurement of the intensity ratio are XeI 467.12 and 473.31 nm emissions. Ratio of their emission intensities, modeled through relation (3.37) with variable α value, is plotted in Figure 49.

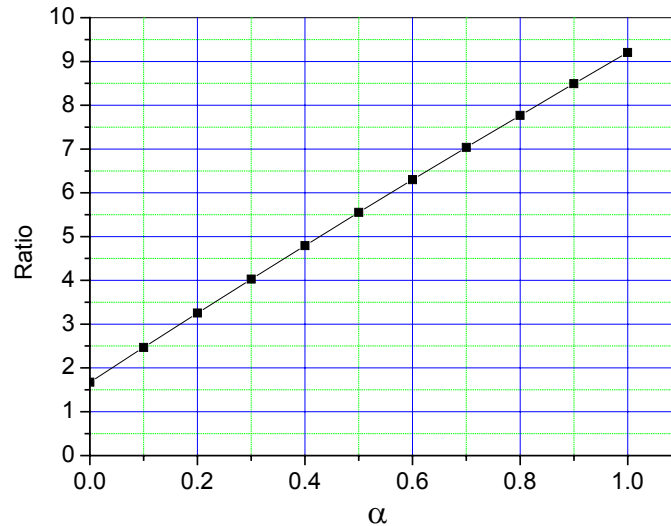


Figure 49. Ratio of the XeI 467.12 to 473.31 nm emission intensities modeled through relation (3.37) for different values of α .

Low temperature $T_e < 2$ eV is characteristic feature of the plume flow in the far field - 0.5 -1 m downstream from the thruster. Due to the limitations of the observation geometry, measurements in these plume regions were impossible within the frame of this study. So, approbation of the method was left for future experiments.

3.3.3. Problems of the XeI emissions utilization for measurements of the TAL discharge parameters

Generally, methods for measurement of the HET discharge characteristics should be the same as for the plume. From one side, intensity of the discharge radiation is much higher, so that more emission lines have signal to noise ratios acceptable for the analysis. From another side, the HET discharge plasma is characterized by higher gradients of all critical plasma parameters such as specie number densities and temperatures. This in turn results in high gradients of the specific radiation power emitted by the HET plasma. In this situation, very fine spatial resolution is required to resolve the higher gradients of the parameters. This is especially true for TALs, which have much narrower discharge region in comparison with SPTs. Furthermore, most probably that EEDF in the HET discharge is non Maxwellian. So, that measurement of "effective electron temperature" made by different methods may result in substantially different values of the temperature. Under these circumstances determination of the EEDF becomes extremely important problem.

Optical diagnostic method for measurements of the EEDF has been discussed earlier¹¹. It is based on the solution of an equation system, which relates intensity of numerous emission lines with plasma species number density and EEDF. The more is the number of independent (non coupled by collisional, radiative and level mixing processes) emissions in the system the better is accuracy of the EEDF measurements. To resolve this system excitation cross-section energy dependence is required for all emissions involved. As mentioned above choice of independent XeI emissions, which may be described by a simplified CRM, is not big. Also, despite the relatively high temperature, ion collision contribution to the emissions excitation is still important in the discharge (see Figure 48). From the other hand ions in the discharge region have noticeably lower energy than in the plume and, therefore, emission excitation cross-sections may differ from the listed in Table 4. All these limitations hamper application of the optical diagnostics methods (utilizing XeI emissions in particular) in the discharge region¹. Nevertheless, analysis of the TAL discharge spectra results in some qualitative conclusions, which are in a good agreement with general conceptions about the TAL discharge plasma properties. As an illustration, profile of "effective electron temperature" across the discharge region is presented in Figure 50. The profile has been measured through intensity ratio of XeI 823.16 and 828.01 nm emission lines with spatial resolution of about 3-5 mm. Closer to the axis and beyond 40 mm in radial direction signal to noise ratio was too low for meaningful representation of the intensity ratio.

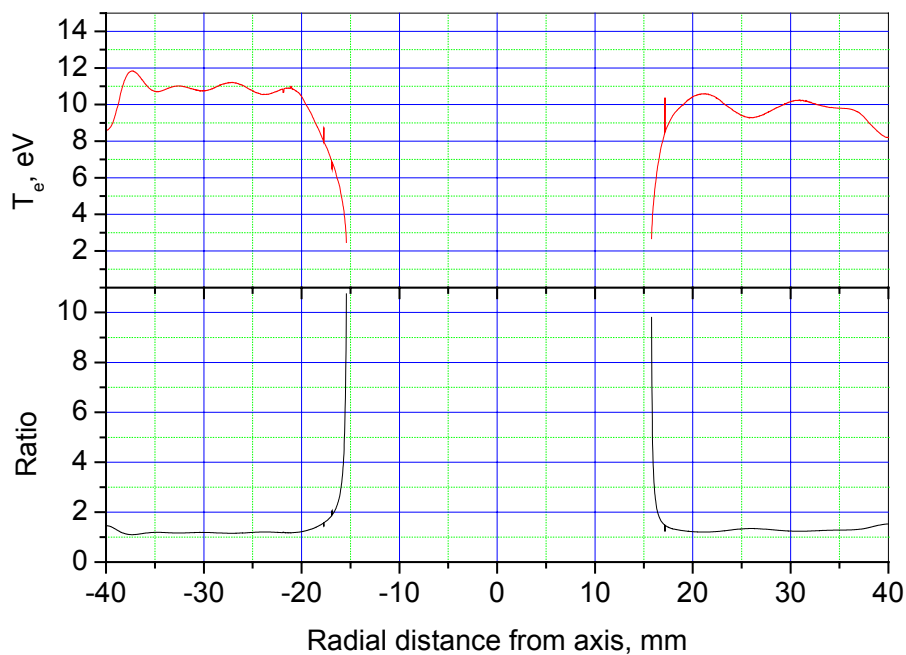


Figure 50. Ratio of XeI 823.16 to 828.01 nm line intensities across the D-55 TAL discharge operating at $U=300$ V, $I=3$ A (bottom plot) and "effective electron temperature" reduced from the ratio measurements (top plot).

In general, the effective temperature profile has an expected form. Temperature stays constant along the annular shaped discharge region, where electric and magnetic fields are maximal and falls down abruptly outside this region. Note, that absolute value of the electron temperature may not reproduce the real one, because it is averaged at least over a several mm region. In a TAL type HET substantial gradients of the electric field may occur in the discharge along this short scale. Utilization of a more powerful optics or, perhaps, LIF technique would warrant better spatial resolution, not eliminating generic problems of the TAL discharge plasma diagnostics, however. Additional efforts are required to leverage the TAL discharge diagnostic technique on a qualitatively new level.

3.3.4. Potential utilization of ionic emissions for a HET plasma diagnostics

Potentially, utilization of the ionic emissions for diagnostics of HET plasma parameters reveals much promise. This is particularly true for the first xenon ion, which transitions are more intensive and well represented in the HET plasma radiation spectrum. Generally, strong XeII emissions are characterized by higher

¹ Note, that alternative methods also encounter serious problems at diagnostics of the TAL discharge.

transition probabilities (Einstein coefficients) than XeI emissions. That means radiative lifetimes of the excited XeII states are shorter. Also, metastable states in the XeII system can't play that remarkable role in the excitation kinetics as in the XeI system. These two distinctions of the XeII system allow wider selection of the emissions, which may be accurately described by a simplified CRM even in the corona limit approximation. Principal disadvantage of the ionic lines is that no data have been found so far for energy dependence of the electron collision excitation cross-section for xenon ions (reactions (3.2) and (3.3)). So, only rough estimates of the emission excitation rates may be done that are not acceptable for more or less accurate measurements of the HET plasma parameters. One may suggest that perhaps in some regions of the HET plasma flow processes of ion excitation by electron collision might be too weak in comparison with other excitation mechanisms. Table 9 gives a comparison of the excitation rate coefficients estimated in different places of the HET plasma flow basing on the data from Paragraph 3.2.2.2. The HET plasma ionization degree margins characteristic for the facilities with xenon background pressure $p \leq 10^{-4}$ Torr are also given in the table.

Table 9. Comparison of the XeII emission excitation rate coefficients for different processes.

Process/Plume zone	$e + Xe^+$	$e + Xe$	$Xe^+ + Xe$	$Xe^{2+} + Xe$	$\frac{N_e}{N_0}$
Discharge and very near field: $L=1-10$ cm $N_e \sim 10^{12} \text{ cm}^{-3}$, $T_e \sim 5-20$ eV	$3 \cdot 10^{-8}$	10^{-11}	10^{-12}	10^{-11}	0.1-0.3
Near field: $L=20-50$ cm $N_e \sim 10^{10}-10^{11} \text{ cm}^{-3}$, $T_e \sim 2-4$ eV	10^{-9}	10^{-12}	10^{-12}	10^{-11}	0.01-0.1
Far field: $L=50-100$ cm $N_e = 10^9-10^{10} \text{ cm}^{-3}$, $T_e \sim 1.5-2$ eV	10^{-11}	$< 10^{-13}$	10^{-12}	10^{-11}	$10^{-2}-10^{-3}$

Recalling that emission excitation frequency is a product of the rate coefficient and number densities of the particles involved into the reaction, important conclusions may be inferred from the estimates presented in Table 9:

- ❑ In the discharge and very near field region the XeII emissions are almost entirely produced by electron-ionic collisions. Uncertainty of respective cross-sections prevents utilization of the ionic emissions for efficient diagnostics of the HET plasma parameters in this region.
- ❑ In the near field plume region the electron-ion collisions still play very important role. Meanwhile, the heavy particle collisions cannot be *a priori* neglected here. Each emission should be considered individually from the standpoint whether the heavy particle collisions contribute to the radiation intensity or not. Again, uncertainty of the excitation cross-sections for the electron-ion collision processes makes impossible any accurate diagnostics of the plasma parameters through analysis of the ionic emissions.
- ❑ In the far field region where electron temperature is too low for excitation of the ionic emissions, the heavy particle collisions become more important. In ground test facilities with the background pressure at the level of $10^{-5}-10^{-6}$ Torr these two processes provide comparable contributions in the XeII emissions intensity. Perhaps in a not very clean test facility the heavy particle collisions become dominating mechanism, but it should be kept in mind, that due to the CEX reactions at higher background pressures energy spectrum of the ion beam in the plume far field may substantially differ from the one in the near field. Actually, in this case the far field plume almost completely represents secondary plasma induced by the ion flow in the conditions of high background pressure.

One of the parameter that can be measured in the very near field is plasma charge density distribution. Electron-ion collisions absolutely dominate over others XeII emission production mechanisms here. From the other hand, as spectral measurements show, relative distribution of the ionic emission intensities in the plasma spectrum in this region doesn't exhibit considerable variations. Small variation 10-20% appears only in the regions right against the anode layer in its nearest proximity. This fact implies that emission excitation rate coefficients either vary similarly to each other or (more probable) don't vary at all in this region. In any case, according to relation (3.26), intensity of the XeII emissions must be proportional to the product of the electron and first ion number densities. Hence, the plasma charge density must be proportional to the square root from the radiation intensity. Normalized distributions of the plasma charge density, re-created from the XeII emission intensity profiles, are presented in Figure 51. As usually, radiation intensity profiles have been obtained from the span-ward measurements followed by Abel de-convolution procedure.

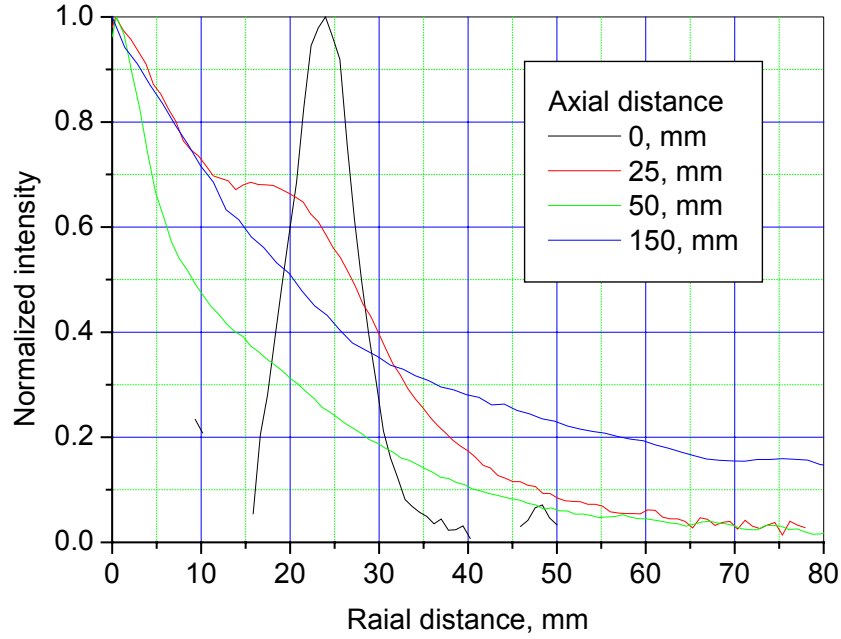


Figure 51. Radial distribution of the ion flux density in the plume sections at different axial locations. TAL D-55 $U=300$ V, $I=3.15$ A.

It should be noted, that in absence of the CEX reactions plasma charge density profiles in the near field must coincide with distribution of the primary xenon ions in the accelerated ion beam. Maximum of the charge distribution in the discharge plane is located as expected against the annular hole within the thruster anode layer. In the next examined section 25 mm away from the motor considerable amount of the plasma relocates closer the thruster axis. However, local maximum still may be found in front of the anode layer. Further downstream at 50 mm most of the charge is located nearby the axis. At this place needle-like plasma region forms along the thruster axis. It's easily observable by a naked eye. And finally, 150 mm downstream from the thruster the plume flow starts its gradual expansion.

3.4. Concluding remarks to Chapter 3

Analysis presented in this Chapter has clearly demonstrated importance of the CRM, which is used for interpretation of the HET plasma radiation measurements. Correct CRM has to include heavy particle induced excitation and step-wise excitation processes. Perhaps in some particular cases the CRM must take into account effect of the radiation re-absorption. Development of universal, practically useful CRM for xenon emissions is not possible at this moment. Instead, selective choice of the diagnostic HET plasma emissions, which may be described by a simplified CRM would be more reasonable. Consideration of the emission excitation processes in the HET plasma allowed introducing such simplified CRM for a number of XeI lines. Utilization of the IR XeI 823.16 nm, 828.01 nm and 834.68 nm emission lines for measurement of electron temperature in D-55 TAL plume brought self-consistent results, which are in general agreement with results of other measurements. Conclusion has also been made that analysis of XeI visible emissions may help to determine the xenon ion content in the plume region where electron temperature doesn't exceed 2-3 eV. In general, the improved optical diagnostic technique may successfully complement traditional probe diagnostics, especially in the very near field region.

Potentially, exploitation of ionic emissions for the HET plasma diagnostics reveals more promise. However, absence of reliable emission excitation cross-section data for electron-ion collisions seriously hampers utilization of the ionic emissions for diagnostic purposes. Only relative measurements of the charge distribution in the very confined near-field plume region may be realized at this moment through analysis of the ionic emission radiation profiles.

Accuracy and reliability of the plasma characteristics derived from radiation measurements entirely depend on the basic CRM parameters, such as excitation cross-sections. Lack of the cross-section data, such as energy dependence for heavy particle collision excitations, excitation from metastable states and excitation of ions, imply limitations on wider application of the optical diagnostic technique. As soon as new more accurate cross-section data will be arriving accuracy of the optical diagnostic technique will be growing.

Radiation from the triple TAL cluster set plume has also been measured in the frame of the Project extension. Similarly to the single TAL the triple TAL plume radiation has been measured in different planes along the lines-of-sight perpendicular to the cluster set axis. Most distant plane, where the measurements were carried out, was located at 200 mm downstream from the cluster. In all planes radiation intensity distribution was found to be asymmetric. Pronounced non-uniformity of the distribution caused by individual plumes has been observed. In this situation application of the Abel de-convolution technique is impossible. At this moment there is no way to extract the specific (per unit volume) radiation power from integral intensity measured along the span-ward lines-of-sight. So, no reliable data on the plume parameters can be reduced from passive optical measurements. LIF and other measurement methods, which are capable to extract local plume characteristics, have to be addressed for the non-symmetric cluster plume characterization.

4. Development and preparation of triple TAL cluster.

At present phase of development and application, electric propulsion (EP) is characterized both with increasing number of implementations solving ordinary needs of long-life spacecraft (e.g., orbit correction), and also with expansion of the range of needs to be resolved with EP.

Projects aimed at EP use for final insertion of spacecraft into high operating orbits (including GEO), and for needs of cruise flight during deep space missions to distant planets are under consideration. Power-to-weight ratio of modern spacecraft grows: for advanced telecommunication systems the level of on-board electrical power reaches 20...40 kW¹⁵. This tendency results in a need for higher-powered EP systems.

There are two possible ways for creation of higher-powered EP systems:

- ❑ development and use of higher- and higher-powered thrusters;
- ❑ use of bunches of several, simultaneously working thrusters, i.e. thruster clusters.

A number of activities have been dedicated to investigate capabilities of the two different ways as well as a rational combination of the both^{15,16,83}.

It follows from the available data that the cluster approach can be deemed as essentially important for advance propulsion systems. Using a narrow range of tried engines of a relatively small power, one can overcome difficulties with ground development tests and improvement of a high-power EP system, because it will be enough to develop the components, which it contains. So, a cluster (once developed and improved) enables designing of propulsion systems, which have diverse power. It is achievable via mere scaling, just by adding available propulsion modules (clusters), and allows saving time and money necessary for improvement of a system.

In spite of visual simplicity, implementation of EP on the basis of several electric thrusters, aggregated in a system and working at a time, needs investigation of some basic aspects:

- ❑ Summarization of the thrusts of engines in a cluster (additivity of thrust).
- ❑ Interaction of exhaust plumes of engines in a cluster (to ensure correct estimation of their effect on surfaces of a spacecraft).
- ❑ Interference (cross effect) of cluster engines.
- ❑ Effects due to electromagnetic noise generated by engines of a cluster.
- ❑ Stability of a cluster in case of parameter deviations or even failure of one of the thrusters.

The architecture (functional scheme) of modern EP systems on ion or Hall-effect thrusters is, as a rule, based on a linear principle - every engine has its individual cathode-neutralizer, propellant supply system, power supply and control system.

A cluster - an integrated system, consisting of several, at-a-time operating engines, aimed at executing a common flight task - enables application of new schemes of EP systems in which, e.g., functions of feeding and control for every thruster can be integrated in one device for all, and one cathode-neutralizer can serve for operation of several thrusters etc^{15,16,84}.

Thus, being a good solution for the main challenge - creation of a high-power EP system having any specified power, under conditions of a poor range of tried engines - the cluster technology provides new capabilities: it enables achieving of maximum flexibility and reliability of an EP system with reducing its weight as compared to the design when several, actually independent propulsion systems are just put together¹⁶.

To make these capabilities real, a number of special engineering solutions inherent to the clusters, which were not investigated earlier, need an intensive research. In particular, the following problems should be investigated:

- ❑ Possibility for operation of several engines from a common power supply and a common, working fluid (propellant) feed system.
- ❑ Possibility for a cluster operation from a common cathode-neutralizer, probable limitations on the sizes of a cluster in case of the possibility.
- ❑ Optimization of the number of thrusters in a cluster.
- ❑ Probable interaction of cluster thrusters, both through plasma and through internal electric circuits.
- ❑ Stability of a cluster operation under deviations of parameters of some thrusters in a cluster.

According to the current Project technical specifications (Statement of Work) and the refinements elaborated during the interim presentation of the work at AFRL workshop, efforts under this activity were concentrated in two main directions:

- ❑ Development and manufacturing of a cluster, its verification and study of integral performances
- ❑ Development and verification of the diagnostic equipment for investigation of multi-thruster system plumes.

It was also deemed that execution of the work plan should create a technologic basis for the next phase of research dedicated to a detail investigation of plasma plumes of the operating cluster.

4.1. Development and manufacturing of the cluster assembly, its verification and study of integral characteristics

Development of a cluster of three D-55 thrusters with anode layer (TAL), which are similar to that used in flight experiment aboard STEX spacecraft in RHETT II program⁸⁵, was one of the Project tasks. Design of these TALs is the best studied one. There is an extensive base of experimental data collected from tests of these thrusters both in Russia and USA. Therefore, analysis of the thruster operation parameters can easily be made in case of need through comparison with earlier results.

The whole program of work on a triple D-55 thruster cluster development contained several phases:

- ❑ Verification of characteristics for every engine during individual tests.
- ❑ Designing and manufacturing of a cluster assembly, systems for power supply and measurements.
- ❑ Verification of parameters for every engine after mounting in cluster assembly.
- ❑ Elaboration of a program of tests and experimental investigation of cluster performances.

Verification phases pursued the goal of obtaining the basic characteristics of thrusters under the same conditions and on the same test equipment, which then was used during tests of the whole cluster. The work was carried out in compliance with measurement procedure established in TSNIMASH. As a result of the step-by-step verification it was obtained that in all testing modes all the three thrusters (tested under the same conditions) showed identical characteristics for thrust, specific impulse, discharge ignition voltage. A database on experimental characteristics of tested thrusters has been collected. For further investigations of the cluster, the mode with xenon flow rate of 3,5 mg/s into the anode of a thruster and varied discharge voltage (200, 300 and 400 V) was chosen as a baseline one. The flow of 3,5 mg/s was chosen to ensure a thruster operation stability and keeping the residual pressure in vacuum chamber at the level not worse than 0.2 mTorr during operation of the triple-thruster cluster.

Mounting of the thrusters in a cluster assembly – which demanded (as it is shown below) changes in the relative position of a thruster and a cathode in comparison with the flight configuration of D-55⁸⁵ - resulted in no changes of integral parameters of the thrusters.

4.2. Description of the cluster design

The main requirement to designing of a cluster and its power supply systems was ensuring of the feasibility of diverse functional diagrams, simulation of cluster design features and operational modes. In particular:

- ❑ Series actuation of one, two and three thrusters in the cluster.
- ❑ Simultaneous operation of the three engines, each being fed from an individual power supply.
- ❑ Operation of all the three thrusters from a common source of discharge voltage.
- ❑ Operation of the thrusters with individual cathode-neutralizers.
- ❑ Operation of some thrusters with one cathode.
- ❑ Operation of each of the thrusters in the cluster in a floating scheme and in a grounded scheme (cathode-neutralizer and vacuum chamber walls are galvanically coupled).

It is worth clearing up that the last was used to simulate operating conditions for a thruster with various cathodes, because discharge voltage and floating potential can essentially vary: i) during a cathode service and; ii) on change from one cathode to another one. Use of the grounded and floating schemes enables simulation of influence of the cathode parameters on both the thruster parameters and measurement results of plume parameters.

The measuring equipment provided measurements of the following values:

- ❑ electrical parameters in all circuits of a thruster;
- ❑ xenon flow rate into each thruster and cathode-neutralizer;
- ❑ thrust;
- ❑ oscillations of discharge current in the circuit of each thruster;
- ❑ pressure in the vacuum chamber.

Below, the developed cluster design and test-bench systems are described in detail.

4.2.1. Cluster

The scheme of a cluster assembly based on three D-55 thrusters with anode layer⁸⁵ was chosen as a base-line configuration for the investigations. In (Figure 52) a general view of the assembly with a common cathode mounted in the center is shown. The assembly configuration enabled also installation of several cathodes (that is described below in detail). On the basis of the results of development testing represented in the next sections of this Report, the scheme with a common central cathode was chosen to be the basic one. TSNIMASH's laboratory cathode ensuring electron current up to 10 A was used in the bench tests. Cases of the thrusters and cathodes were electrically isolated from each other and from the subplate. All necessary galvanic

couplings were provided via commutation in the feed and control circuit outside the vacuum chamber. It enabled realization of various operation modes of the cluster without opening the vacuum chamber during the tests.



Figure 52. Overall configuration of the cluster system.

The cluster was mounted on a pendulum-type, thrust measuring device in a vacuum chamber of 10 m³ volume (1.7 m diameter, 4 m length) with five diffusion vacuum aggregates (**Figure 53**).



Figure 53. TSNIMash facility external view.

4.2.2. Power Supply and Measurement System

To test the cluster assembly, multipurpose systems for power supply and propellant feeding were developed and integrated. The power supply system (**Figure 54**) enabled testing of the cluster both with a common power supply and with individual ones.



Figure 54. Overall configuration of the control system.

The power supply system included:

- ❑ 3 power supplies for each thruster (power up to 1.5kW, voltage up to 500V, current up to 5 A);
- ❑ 1 power supply for the 3-thruster assembly (power up to 4.5kW, voltage up to 500V, current up to 15A);
- ❑ 3 magnet power supplies (power up to 30W);
- ❑ 3 cathode power supplies (power up to 70 W (keeping), ignition voltage up to 1000 V)

The power supply system enabled testing of thrusters both individually, and at a time.

The propellant feed system (Figure 55) included:

- ❑ 3 channels for each thruster (*up to 5 mg/s*);
- ❑ 1 channel for the 3-thruster assembly with tripled mass flow rate (*up to 15 mg/s*);
- ❑ 3 channels for 3 cathodes (*up to 5 mg/s*).

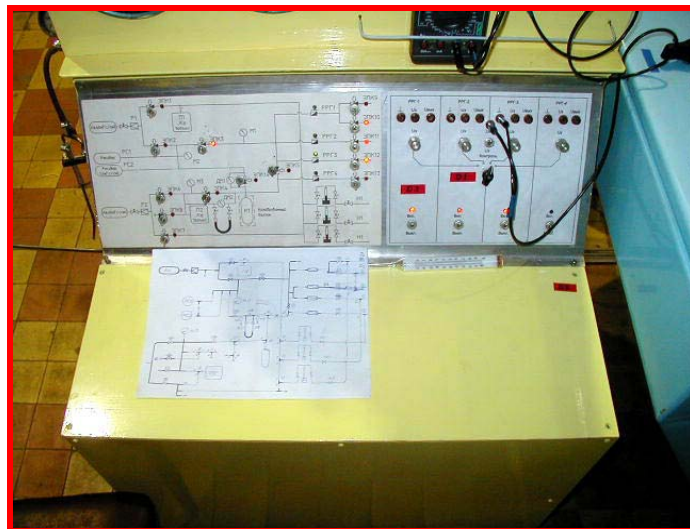


Figure 55. System for propellant feed control.

The applied systems for power supply and propulsive gas feed enabled testing of the cluster in various electrical circuits. The measuring instruments, measured quantities, range of measurements and accuracy of the measuring equipment are shown in **Table 10**. Electrical quantities were measured according to schemes in **Figure 56** and **Figure 57**.

Table 10.

Measured quantity	Measuring device	Function	Measurement range	Accuracy	Resolution
m_a , mg/s	Metex M-3860D	Direct voltage	400 mV – 4 V	$\pm 0.3\% + 1$	1 mV
V_d , V	Fluke 73	Direct voltage	0...400 V	$\pm 0.5\% + 1$	0.1 V
I_d , A	Fluke 73	Direct current	0...10 A	$\pm 1\% + 1$	0.01 A
F, gf	Thrust Meter ET-5	Thrust and Calibration	5...20 gf	$\pm 1.5\%$	—
	Computer	Direct voltage		$\pm 0.5\%$	—

The thrust was measured according to a standard technique. The calibration of the thrust-meter was made at each measurement of thrust by means of a built-in system of calibrated weights.

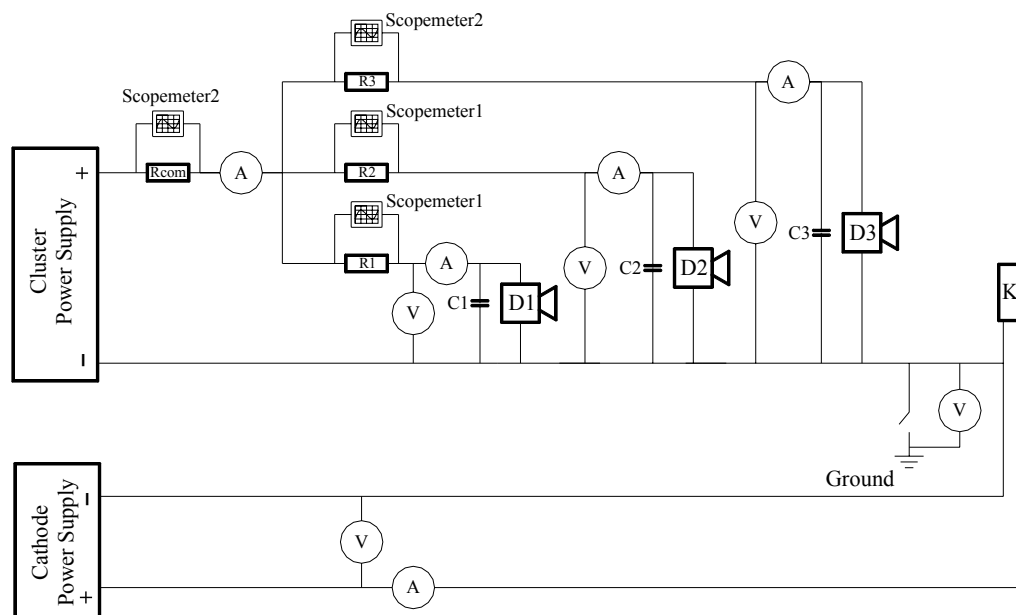


Figure 56. Electric circuit: common power supply.

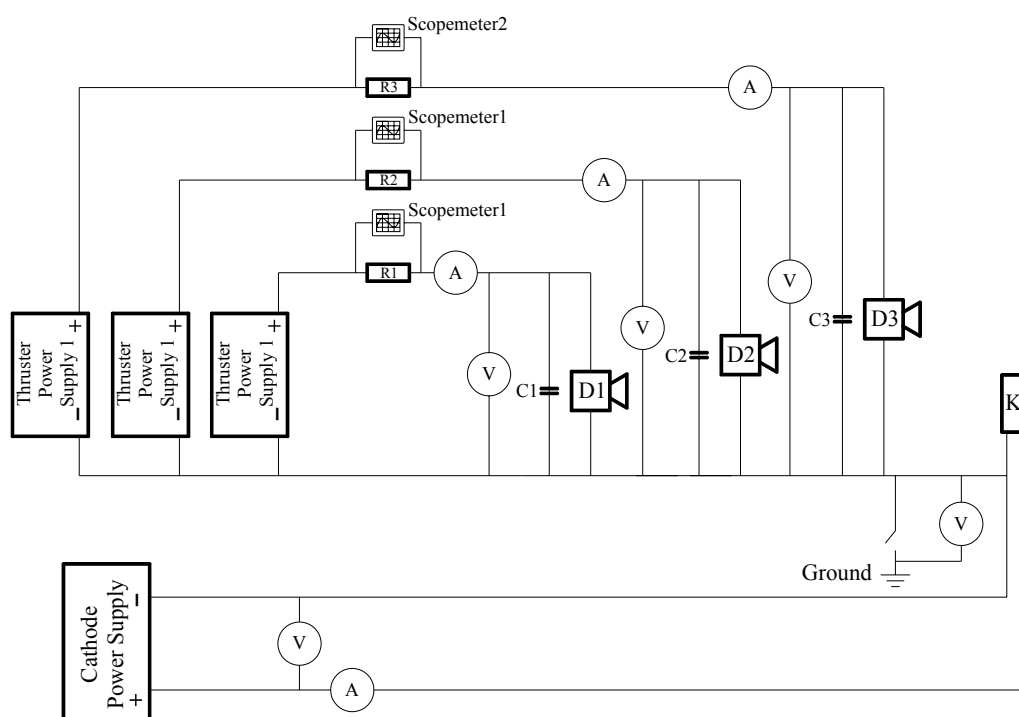


Figure 57. Electric circuit: individual power supplies.

4.3. Experimental investigation of the cluster

4.3.1. Study of Integral Parameters of Diverse Cluster Architectures

Main questions investigated during the cluster tests were additivity of the thrust and zero distortion of the performance parameters of thrusters as compared to the case of individual operation of each thruster. The last was used as a criterion for verification of the workability of diverse cluster configurations. The following cluster architectures were tested:

- ❑ Operation of three thrusters from a common power supply and one cathode.
- ❑ Operation of three thrusters from individual power supplies and one cathode.
- ❑ Operation of three thrusters and one cathode at varying parameters of one of the thrusters (flow rate and discharge voltage).

To investigate the possible influence of the amount of cathodes in a cluster and position of the cathode-neutralizer on integral performances of a cluster assembly, tests were carried out for the following cases:

- ❑ Operation of three thrusters and one cathode spaced at the distances of 300 and 500 mm.
- ❑ Operation of three thrusters with two cathodes.

In the last two cases, in addition to the integral performances, radial distribution of the parameters of the plasma flow generated by a thruster was measured.

Test modes (for each thruster):

- ⇒ flow rate in the anode - 3,5 mg/s;
- ⇒ discharge voltage - 200, 300, 400 V;
- ⇒ discharge current - 3 A.

Maximum flow rate in the anode of each thruster was limited by the capacity of the vacuum bench.

Measurements of the thruster/cluster parameters were taken under two schemes of electrical circuit. In the first scheme the cathode negative was connected to the negative of thrusters and was connected to the ground. In the second case there was no connection to the ground (switch “Ground” **Figure 56, Figure 57**).

4.3.2. Cluster Thrust Measurements

Goal of this series of tests was revealing of a relationship between the thrust of a single engine and a total thrust of three simultaneously operating engines. Before integration of the thrusters in a cluster, each thruster passed verification with its thrust measurement. The difference between the thrust values did not exceed 2% in all test modes. After the integration of the thrusters into the cluster, each engine was also verified as a part of the cluster. Measurements of thrust were taken both under the grounded scheme and floating scheme, which were then used during development of the procedure of local parameters measurements and studies of the plasma flow of a thruster. No changes in integral parameters of the thrusters after mounting in a cluster were discovered.

Table 11 contains the measured thrust values for each thruster as a part of cluster in case of the grounded scheme.

Table 11.

$V_f = 0$	Thruster D1		Thruster D2		Thruster D3	
Discharge voltage, V	Discharge current, A	Thrust, mN	Discharge current, A	Thrust, mN	Discharge current, A	Thrust, mN
200	3.04	43.7	3.02	43.5	3.09	44.6
300	3.03	57.2	3.03	56.1	3.06	57.0
400	2.98	65.2	2.98	64.9	3.02	65.3

From **Table 11** one can see that thrust differences do not exceed the accuracy of thrust measuring device and, therefore, the thrusters can be regarded as identical in all test modes.

Since the residual pressure in the vacuum chamber during a cluster operation is higher than that during individual tests of thrusters, influence of the pressure on the integral performances of thrusters was investigated. The upper residual pressure being tested corresponds to the conditions of operation of a three-thruster cluster with the xenon flow rate of 3.5 mg/s in each thruster. The test results are shown on the diagram in **Figure 58**. In the tested range of the residual pressure variation, the thrust variation of the engine at both constant xenon flow and discharge voltage did not exceed 3%, and the discharge current increase with increase of the residual pressure made up to 5%.

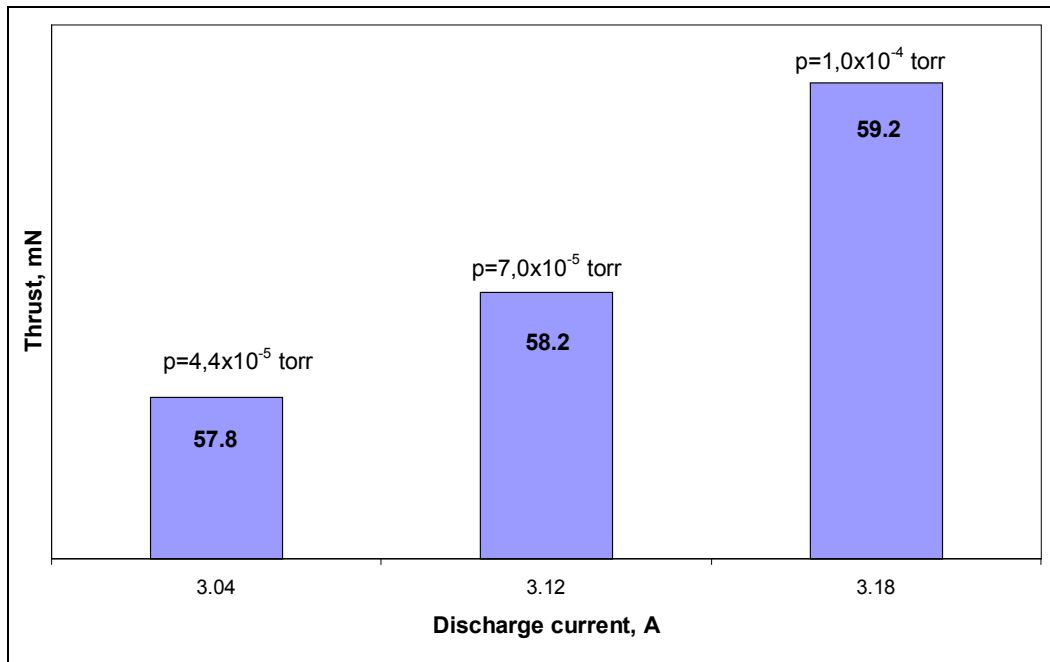


Figure 58. Influence of the pressure on the integral performances.

After verification of individual thrusters, thrust measurements of the three engines operating simultaneously were taken for two schemes of power supply:

- ❑ from one common source and one cathode K1 (Figure 56).
- ❑ with use of individual supply sources for each thruster (**Figure 57**).

Results of measurements taken during a cluster operation from a common power supply are collected in **Table 12**.

Table 12.

Discharge voltage, V	Thruster D1		D1+D2+D3				
	Discharge current, A	Estimated triple thrust, mN	Floating potential, B	Discharge current D1, A	Discharge current D2, A	Discharge current D3, A	Measured total thrust, mN
200	3.04	131.2	0	3.12	3.17	3.21	135.8
			15.4	3.15	1.18	3.22	136.2
300	3.03	171.5	0	3.16	3.15	3.16	176.7
			20.1	3.18	3.13	3.18	175,5
400	2.98	195.6	0	3.08	3.10	3.12	201.5
			18.5	3.10	3.12	3.17	204.1

As one can see from **Table 12** the resultant thrust of three thrusters is a sum of individual engine thrusts in all investigated modes. Comparison of the data on the thrust values of a cluster in the cases of a common power supply and supply of each thruster from an individual power source is shown in **Table 13**.

Table 13.

Discharge voltage, V	Common Power Supply		Individual Power Supplies	
	Floating potential, V	Measured total thrust, mN	Measured total thrust, mN	Floating potential, V
200	0	135.81	138.85	0
	15.4	136.21	136.50	19.3
300	0	176.67	175.82	0
	20.1	175,53	175.04	20.2
400	0	201.48	204.55	0
	18.5	204.06	204.55	19.6

Data in **Table 13** demonstrate that whatever the scheme of power supply is, there are no essential differences between the thrust magnitudes of a cluster in all investigated modes, and (within the accuracy of measurements) the resultant thrust is merely equal to the sum of thrusts of the three engines.

In addition to the measurements taken when the operational mode of all the three thrusters in a cluster was identical, operation of the cluster was also investigated when the operational mode of one of the three thrusters deviating from the two others. Such case is interesting from the point of view of simulation of probable emergencies onboard a spacecraft and deviations of parameters of one of the thrusters. Besides, verification of the capability for variation (control) of parameters of one of the thrusters enables control of both direction and magnitude of the thrust vector of such system. **Table 14** and **Table 15** represent measured thrusts for the cases of variation of discharge voltage of one thruster and flow rate (discharge current) respectively. The results are given both for the case of a common power supply, and for the case of individual sources. In case of a common power supply the magnitude of discharge voltage on one of the thrusters was varied by means of a variable resistor built into the thruster discharge circuit.

Table 14.

Thruster	Discharge voltage, V	Common Power Supply			Individual Power Supplies		
		Floating potential, V	Discharge current, A	Measured total thrust, mN	Measured total thrust, mN	Discharge current, A	Floating potential, V
D1	200	20.5	3.23	162.0	160.3	3.18	19.6
D2	300		3.17			3.14	
D3	300		3.22			3.17	

Table 15.

Thruster	Discharge voltage, V	Common Power Supply			Individual Power Supplies		
		Floating potential, V	Discharge current, A	Measured total thrust, mN	Measured total thrust, mN	Discharge current, A	Floating potential, V
D1	300	20.5	4.15	195.8	195.7	3.18	20.5
D2			3.17			3.16	
D3			3.19			4.18	

As one can see from **Table 14** and **Table 15**, in case of parameter changes of one of the thrusters there is no essential difference between thrust magnitudes of the three thrusters - when using both a common power supply and individual ones. The total thrust of a cluster is coincident to the sum of thrusts of individual engines in respective modes.

On the basis of obtained results, it is possible to make a conclusion that in all tested cluster architectures, within the investigated range of the discharge voltage 200 to 400 V and variation of the xenon flow rate 3 to 4 mg/s, the operational mode of each thruster as a part of a cluster coincided to the thruster operational mode at its individual tests, and the thrust magnitude of a cluster was the sum of those of the three thrusters.

Thus, the test results confirmed the basic property of thrust additivity for a cluster based on TALs as well as capability for application of a new architecture of EP in which several thrusters, working in parallel, are supplied from one power source and with one common cathode-neutralizer.

4.3.3. Influence of cathode position on thruster and cluster performance

At present, all Hall Effect Thrusters (HET) are equipped with individual cathodes (one or two) mounted in close proximity from the thruster exit. Potential size of a cluster, running from one common cathode, depends on the ability of a thruster in a cluster to operate with the cathode, which is not mounted in close proximity, but at a distance from the exit of this thruster. So, this spacing can affect the possible number of engines in a cluster available round a common cathode.

To study the influence of the cathode position on the performance of a thruster, LaB₆-based laboratory-grade cathodes were placed at the spacing $R = 0, 300$ and 500 mm from the cluster axis (**Figure 59**). Also, the central cathode ($R = 0$) was at the distance of 90 mm from the axis of thruster D1. As it was shown during verification tests, at such placement of the cathode the performances of D-55 are completely identical to those of a flight configuration of the thruster⁸⁵.

During the tests the changes of D1 parameters were investigated when the thruster operating with each of the three mounted cathodes, in turn.

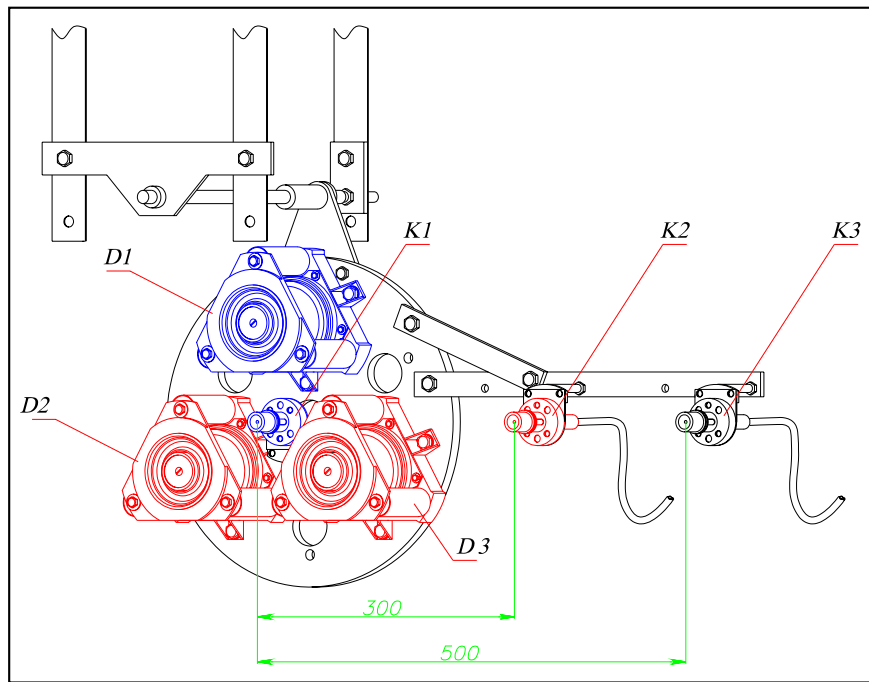


Figure 59. Scheme of the cathodes.

To estimate the influence of the cathode position, in all the three cases the characteristics were determined as follows:

- ❑ discharge ignition voltage in thruster D1;
- ❑ thrust performance of thruster D1 when operating with each cathode;
- ❑ distribution of the electrical field across the plume of thruster D1 when operating with each cathode.

The distributions of electrical field were obtained with use of an emission probe mounted on the movement drive of a “near-zone” diagnostic system. Instrumentation and technique of probe measurements are described in detail in section below. During testing the following procedure was used. The cathode was ignited and kept heated by auxiliary discharge (15...20 V, 3 A). By that time the xenon flow rate in the anode of thruster had been provided, and the coils of thruster had been powered from independent supply sources. Then the voltage was supplied to the thruster and then stepped slowly up until discharge ignition in the thruster. After ignition in the thruster, the voltage was boosted up to the rated value of 300 V. On completion of taking measurements of the performances, the thruster and cathode were shut down, and the next cathode was ignited then. The procedure was repeated then.

The rated operating mode was as follows:

- ❑ discharge voltage – 300 V,
- ❑ discharge current – 3 A,
- ❑ chamber pressure – 4.4×10^{-5} mm Hg.

The discharge ignition voltage in a thruster in all the tested configurations was 150...170V, and no definite relation of this voltage with the cathode-thrusters spacing was revealed. In all the cases of the cathode placement, the measured thrust was 57 ± 1 mN (**Table 16**). The deviation of the thrust magnitude did not exceed the accuracy of keeping the thruster operation parameters as well as accuracy of thrust measurements.

Table 16.

Cathode	Discharge voltage, V	Discharge current, A	Thrust, mN	Floating potential, V
K1	300,4	3,07	57,5	0
	300,2	3,07	58,0	16,8
K2	300,6	3,08	57,8	0
	300,4	3,06	56,8	17,2
K3	300,2	3,06	58,3	0
	300,0	3,05	56,3	18,7

In all the three cases of the cathode placement, distributions of electrical field in a cross section of plume were obtained with the emission probe (**Figure 60**).

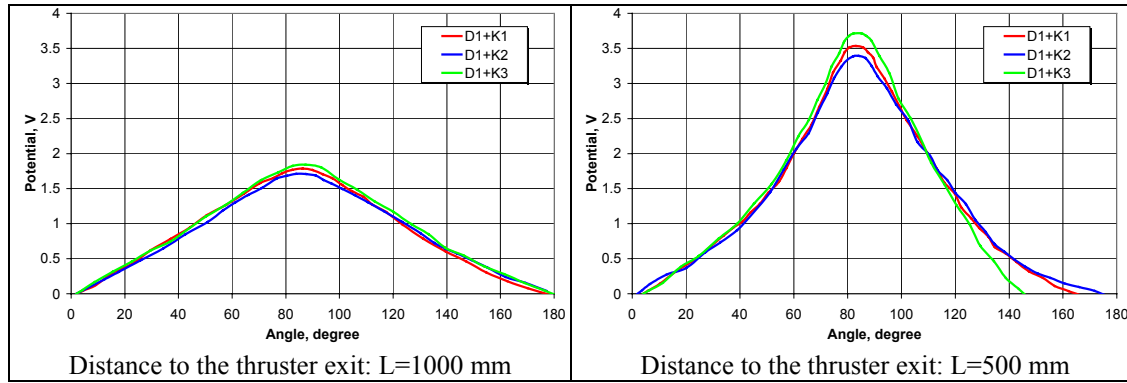


Figure 60. Normalized distribution of plasma potential in the plume cross-section.

The left part of the curves in

Figure 60 corresponds to the location of cathodes K2 and K3, and the top of the curves corresponds to the center of the plasma plume. As one can see from

Figure 60, the curves keep the symmetry and practically coincide with each other irrespective of the cathode position. On the diagrams the magnitude of potential is in relative units. In the plume peripheral zones the value of potential was assumed to be zero for all measurements.

As follows from the obtained data, no essential influence of the cathode-to-thruster spacing on the discharge voltage, thrust and electrical field distributions in a plume can be found. Such result confirms possibility for use of an integrated multi-thruster module with one cathode-neutralizer. The maximum cathode-to-thruster distance equals to 500 mm in the tests was limited by the vacuum chamber size. It can not be deemed as boundary for the effective work of thruster. Greater spacing should be investigated as it is of a particular importance w.r.t. additional capabilities for thrusters arrangement on a spacecraft. It is necessary to note that the obtained result is true under these test circumstances and demands its verification, first of all under conditions of higher vacuum.

To confirm the results obtained during investigation of the influence of the cathode position on a thruster performances, a cluster consisting of three thrusters with cathodes also placed at the distances of 300 and 500 mm was tested (**Figure 59**). The cluster was powered from a common source of discharge voltage (**Figure 56**). Results of measurement of the thrust of the three HETs operating with cathodes at different distances are represented in **Table 17**.

Table 17.

Floating potential, V			Thruster	Discharge voltage, V	Discharge current, A	Thrust, mN		
K1	K2	K3				K1	K2	K3
0	0	0	D1	300,1	3,16	177,1	176,4	177,8
			D2	304,2	3,12			
			D3	306,9	3,13			
20,1	14,2	14,4	D1	298,8	3,18	175,5	176,6	172,0
			D2	303,5	3,13			
			D3	305,5	3,18			

As one can see from **Table 17**, the thrust of three engines operating from one cathode does not depend (under these test circumstances) on the cathode position, and spread of thrust values does not exceed the accuracy of measurement.

On the final phase of investigation of various cluster designs, the ability of a cluster for operation with two cathode-neutralizers, functioning at a time, was tested. The thrusters were powered from individual supplies. Thruster D1 was integrated into an electrical circuit with cathode K1, and thrusters D2 and D3 with cathode K2 (**Figure 59**). Data on the thrust measurements of three HETs operating from two cathodes are shown in **Table 18**. The scheme D1+K1 was grounded, and scheme D2+D3+K2 was “floating” (not grounded) in order to

simulate the maximum possible difference between the floating potentials of the engines working with different cathodes.

Table 18.

Floating potential, V	Thruster	Discharge voltage, V	Discharge current, A	Measured total thrust, mN
0	D1	200	3.14	139.2
11	D2		3.15	
	D3		3.19	
0	D1	300	3.13	176.1
12	D2		3.13	
	D3		3.14	

As one can see from **Table 18**, despite that intentional increase of the asymmetry in the cluster operation, the total thrust of the triple-thruster assembly with two cathodes coincides with the thrust of the cluster with one cathode obtained in the same modes (**Table 13**), and is equal to the sum of individual engine thrusts. No any additional effect and unsteadiness due to differences brought into operational mode of engines were found. So, when using various electrical circuits, various positions and quantities of cathodes, and also when varying the parameters of cluster engines, the thrust of the tested cluster had property of additivity.

4.3.4. *Research of oscillations of discharge current in cluster circuits*

Knowledge of the kind and pattern of oscillations in circuits of a cluster as well as measured thrust is important for understanding the processes arising in such multi-engine propulsion systems when using different schemes and operational modes. Change of amplitude, synchronization and amplification of discharge current oscillations in the cluster engines is one of the criteria of the mutual influence of engines at their parallel operation. Possibility for such amplification and synchronization of oscillations in the thrusters integrated in a cluster was demonstrated in Ref.⁸⁶. This is of fundamental importance for further examination of the cluster electromagnetic compatibility via taking measurements of an individual thruster performances. To study this factor, an investigation of the oscillations of discharge current in the circuits of a cluster was started.

On the first phase of tests, a layout with a common power supply was used (**Figure 56**). This scheme, on the one hand, is the most interesting if speaking of simplification of the cluster architecture, and on the other hand, is the most risky w.r.t. phased oscillations generation in the thrusters, working in parallel. The oscillation of discharge current were measured from the calibrated shunts (bypasses) placed in the circuits of each engine as well as in the common circuit. The oscillations were registered by means of Industrial Scopemeter Fluke 123.

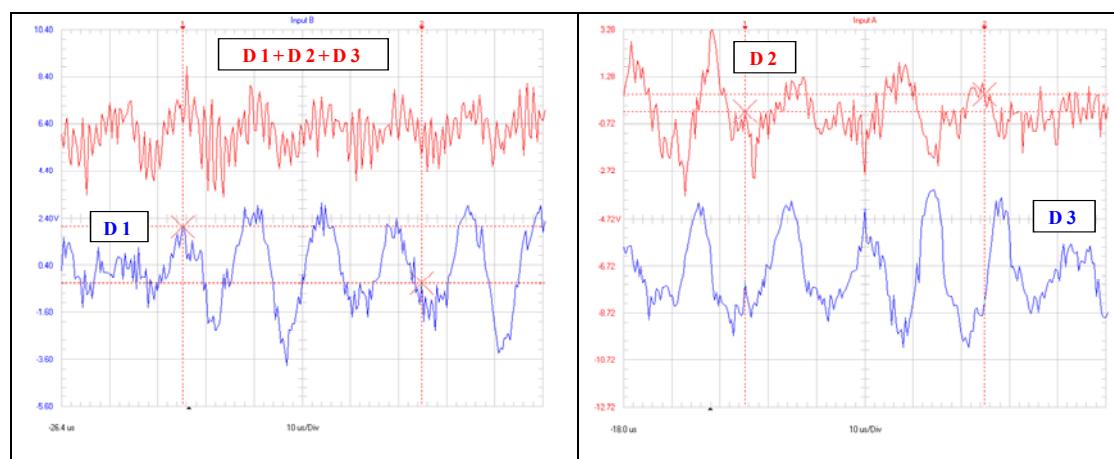


Figure 61. Oscillations of discharge currents in the circuits of cluster engines (D1, D2, D3) and in the common circuit (D1+D2+D3)

An illustration of the discharge current oscillations in circuits of thrusters D1, D2, D3 for a mode of 200 V, 3 A as well as in the common circuit D1+D2+D3 is depicted in Figure 61. One can see that although the frequencies of oscillations in all the three engines are close, the phases of oscillations are different and vary arbitrarily in each thruster. The oscillations of two of the three tested engines are close to antiphase, and the amplitude measured in the common circuit is of the same order with the one in the circuit of one engine. This result is confirmed statistically by numerous repeated measurements, including after the cutoff and re-ignition of the cluster. The pattern of oscillations in discharge circuits for an engine in a cluster was similar to the one

observed at individual tests of the engine. Obtained result demonstrates that synchronization of the discharge current oscillations in the engines of a cluster is not a mandatory requirement to the simultaneous operation of several thrusters even in the layout with a common source of discharge voltage, which is the most "vulnerable" from this point of view.

This result was obtained when all the engines operating in identical modes and the amplitude and typical frequencies of the discharge current oscillations in all engines were close to each other. However, one can suppose that the oscillations in one of the engines (upon achieving some level) can have an impact on the oscillations in two other engines as well as on the common discharge current of the three engines. To study this effect the cluster was tested when one of the engines (D2) was purposely (by an intentional change of the magnetic field in its discharge) shifted into so-called 'abnormal' mode when a drastic increase in the amplitude of the discharge current oscillations typically develops. The oscillograms of the discharge current oscillations in circuits of each engine and in the common circuit of a cluster powered from a common source of discharge voltage are depicted in **Figure 62**.

As one can see from **Figure 62**, the oscillations of discharge current in D2 influenced the currents in the other two engines and also the total signal from the cluster. The oscillograms demonstrate that all patterns of oscillations are similar to that of unsteady working D2. So, one can see that impact of engine D2 can spread to the whole system. Such impact can take place both via internal discharge circuits and through plasma.

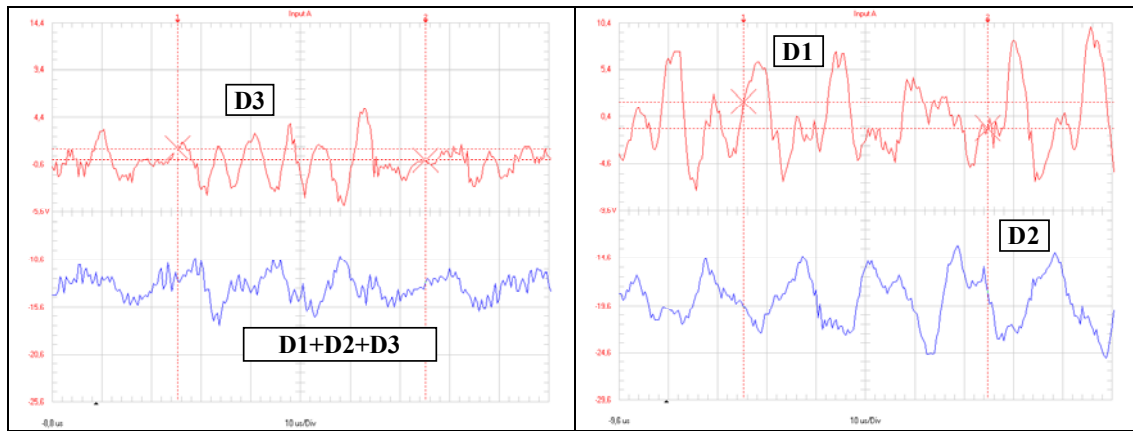


Figure 62. Discharge current oscillations when one engine (D2) is shifted into abnormal mode

Trying to resolve such dual-impact problem, a test was carried out when each engine in the cluster was powered from an independent, individual source (**Figure 57**). Such electric circuit can actually eliminate the interference of engines in a cluster via internal discharge circuits.

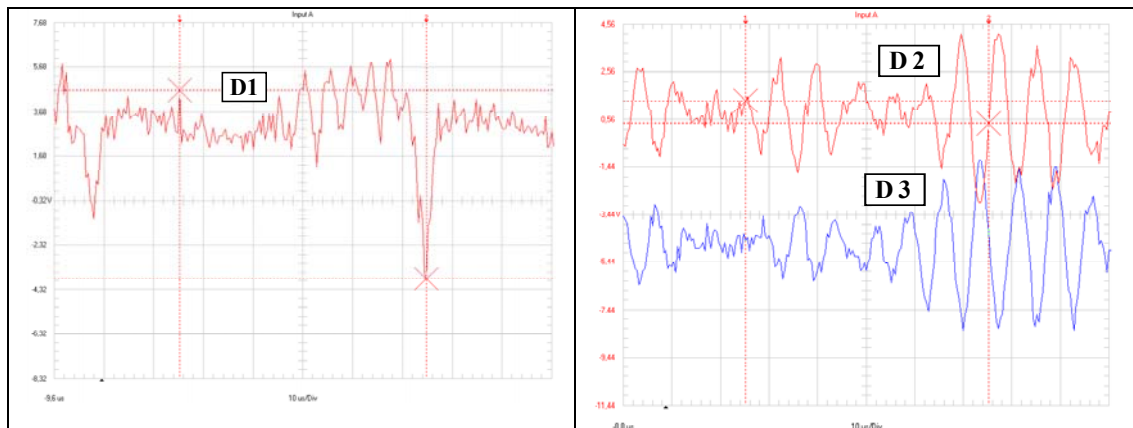


Figure 63. Discharge current oscillations when one engine (D1) is shifted into abnormal mode in case of individual power supplies

Oscillograms of the discharge currents in three engines in case of use of individual power supplies for each cluster engine are depicted in **Figure 63**. Engine D1 is in the anomalous mode. As one can see from the patterns, the remaining thrusters (D2, D3) did not change the patterns of oscillations, and there is actually no effect of engine D1. From this result one can make a conclusion that oscillations in such systems are mainly impacted via internal circuits, and not through plasma. Obviously, obtained results are rather preliminary, and require further systematic studies of oscillation processes and electromagnetic noise in the cluster, stability of a cluster operation at variations in the mode of the integrated engines.

Taking into account further plans in regard to the cluster plume diagnostic, it should be mentioned, that information obtained within the scope of current Project allows to conclude that for future cluster plume diagnostic functional scheme of the cluster is not essential and further study can be made with existing triple-thruster cluster, power supply and xenon feed system.

4.4. Conclusion to Chapter 4.

- ❑ Three D-55 thrusters have been integrated into the cluster and tested individually and simultaneously. Resulted thrust value of the cluster in all studied regimes is summa of individual thrust values in all tested schemes.
- ❑ Influence of the "cathode to cluster" distance on cluster operation has been studied. No influence on the thruster performances and start up voltages were observed for the distance variation up to 0.5 m.
- ❑ Discharge current oscillations of each thruster and oscillations of the summarized current of three thrusters operating from one common power supply were studied. Observed oscillations were independent in each thruster discharge circuit despite on operation from common power supply. Measured amplitude of common current oscillations is of the same order as for one in individual thruster circuits.

5. Development of the plume diagnostic system and testing on a single thruster plume

Generally, description of a EP thruster exhaust plume assumes specification of following plume parameters:

- ❑ structure of plume: the number densities of neutral particles, singly and multiply charged ions;
- ❑ directional velocity: the value and direction for every group of heavy particles;
- ❑ temperature (chaotic velocity) of each component of heavy particles;
- ❑ temperature of electrons;
- ❑ velocity (value and direction) of the directional motion of electrons;
- ❑ electric potential of space (domain of plasma spread) .

It is important to measure *local* parameters, and this requirement predetermines the choice of electrical probes mounted on coordinate devices as the basic diagnostic method. The method of probes is the most informative and also enables determination of most of the parameters listed above as well as their spatial distributions. The missing information can be filled up with other methods: energy and mass analysis, LIF measurements, spectrometry etc. Although application of probes for investigations of plasma has a long history, a lot of particularities of measurements in electric thruster plumes are studied insufficiently. The measurements procedure and design of probes demands improvement and verification with regard to specified test conditions. Therefore, when creating a diagnostic system dedicated to investigation of the plumes of a three D-55 thruster cluster, an experimental check and verification of probes of diverse designs were executed first.

It was important about the tests to be executed, that in case of a plume of a *cluster* the model of a plasma source as a point one (used in most research of the plume of a *thruster*) was not acceptable. So, it resulted in necessity of change to a cylindrical coordinate system when selecting the kinematical scheme of a device for probe movements, in contrast to most of known investigations of EP⁸⁷, when measurements were made in a polar coordinate system, the center of which coincided with the center of exit cross-section of the engine.

5.1. Description of the developed / used diagnostic tools

The area of plume to be diagnosed by probes can be divided into two zones: 'near field' and 'far field'. Higher concentration and density of the current are typical to the first zone while the second has lower energy level and a low gradient of parameter variations. In the first zone due to high intensity of particle fluxes from out of plasma, an essential heating and destruction of probes as well as gears designed for their movement can occur. It entails necessity of taking measurements during a time interval shorter than the time of heating of a probe, and moving the probes rather fast in this zone. In the second zone these are not important. In view of the differences in the measurement conditions, there is a necessity of creation of two different diagnostic systems, individually, for the "near field" and "far field" zones. On the basis of earlier activities, with regard to thruster D-55 the "near field" zone is defined as the interval from 0 up to 500 mm from the exit of the source of ions, and the "far field" zone - as beyond 500 mm from the source exit. For each zone a dedicated coordinate device was designed.

5.1.1. 2D near field zone positioning system.

To study the plasma flows generated by an electrical thruster in the zone close to its exit, a dedicated device for moving probes in the planes perpendicular to the direction of flow was developed. Schematic diagram of the driving device is shown in Figure 64. The overall configuration of the device is shown in Figure 65.

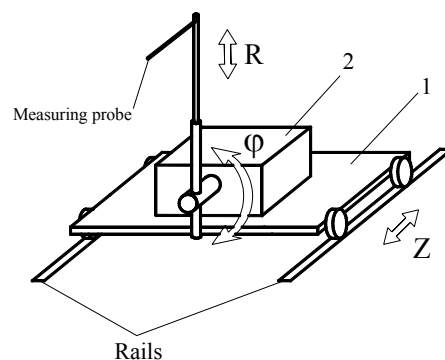


Figure 64. Schematic diagram of the "near"-zone probe driving device.

1 - the carriage (Z), 2 - the probe driver for angular movement (φ).

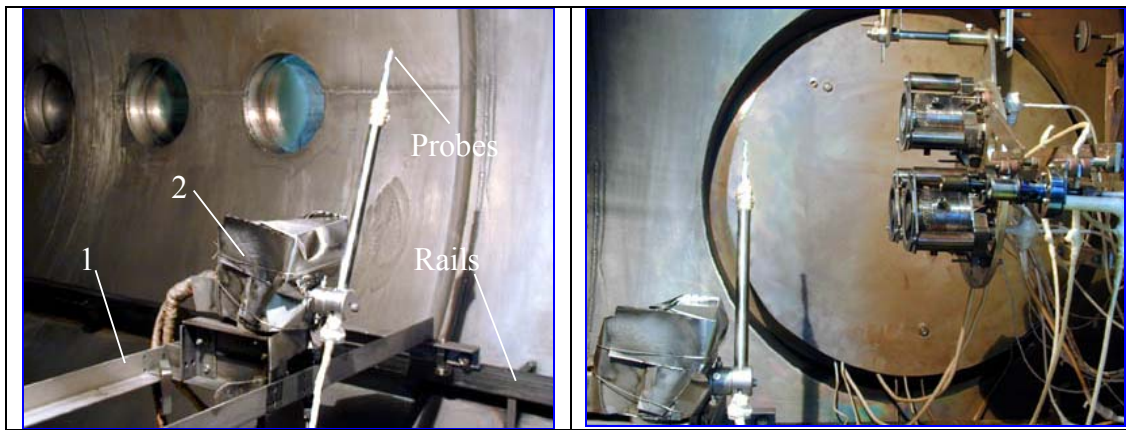


Figure 65. Exterior of the "near field" zone probe driving device.

1 - the carriage (Z), 2 - the probe driver for angular movement (φ).

Driver 2 is a gear providing an angular movement (coordinate φ). The output shaft of the driver is connected with a boom on which probes are mounted (Figure 64, Figure 65). Angular movement driver 2 is fixed on carriage 1 which is capable to move on rails along the axis of chamber. The basic performances of the system are shown in Table 19.

Table 19.

Coordinate	Parameter Range	Velocity	Accuracy of Positioning
Z	0...2000 mm	2 mm/s	± 1 mm
φ	$\pm 100^\circ$	90 degree/s	$\pm 0.1^\circ$

5.1.2. 3D far field zone positioning system.

To obtain the data about spatial parameter distributions of plasma flows, movement of probes (or other primary sensors) to any specified point of tested area should be ensured. Therefore, within the framework of this Project, development of a 3D positioning system has been carried out. The system is dedicated to place the probes, analyzers etc. into any point of investigated plasma - by means of PC (under a special software) or manually, by means of an electronic control block. Schematic diagram of the 3D driving system is depicted in Figure 66. The overall view on the system is shown in Figure 67.

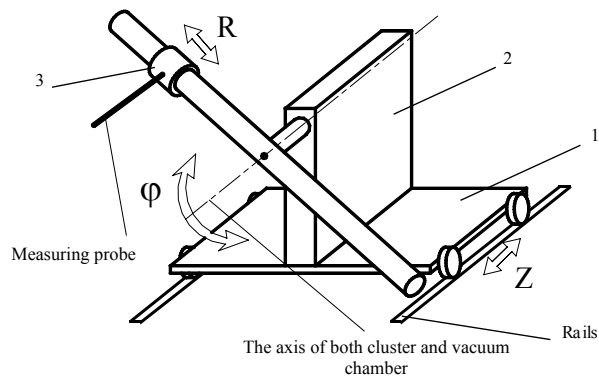


Figure 66. Schematic diagram of the "far filed" zone probes driving system.

1 - the carriage (Z), 2 – the probe driver for angular movement (φ), 3 - the probe (sensor) driver for movement along the radius of the carriage (R).

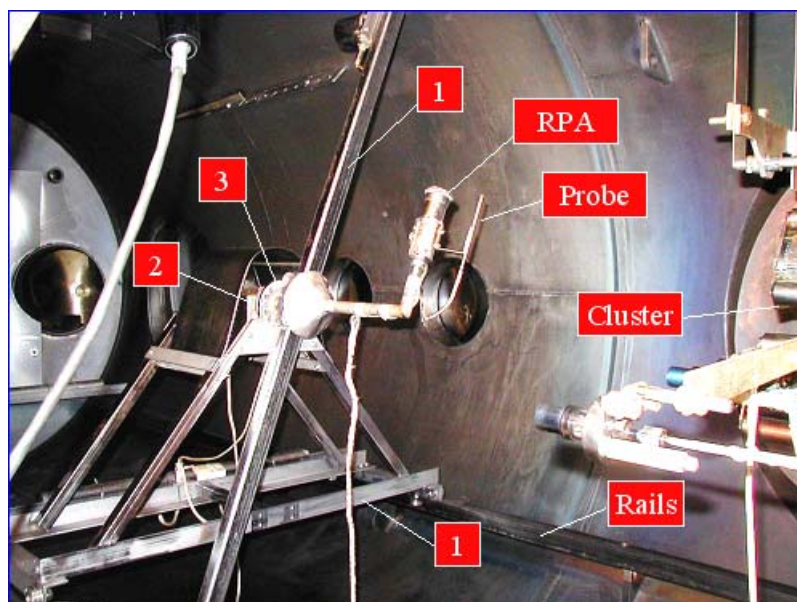


Figure 67. Exterior of the "far field" zone probes driving system.

1 - the carriage (*Z*), *2* - the probe driver for angular movement (ϕ), *3* - the probe (sensor) driver for movement along the radius of the carriage (*R*).

The system consists of three interconnected units. Along the chamber, there are rails for movement of carriage *1* (coordinate *Z*). Carriage *1* with installed probe drivers for angular (coordinate ϕ) and radius (coordinate *R*) movements are driven by an electric motor with the reduction gearbox (Figure 66, Figure 67).

Accuracy of positioning of primary sensors (probes) at a specified point depends on the actuating devices as well as the electronic circuit of positioning. Main performances of the system are represented in Table 20.

Table 20.

Coordinate	Parameter Range	Velocity	Accuracy of Positioning
<i>Z</i>	0...2000 mm	2 mm/s	±1 mm
ϕ	±100°	3 degree/s	±0.5°
<i>R</i>	±600 mm	40 mm/s	±0.5 mm

5.1.3. *Systems for control and measurement.*

To control the coordinate systems for positioning and automated registration of probe characteristics, a dedicated instrumentation (Figure 68) which ensures placement of probes in predetermined points of space with a capability of dynamical taking of measurements (manually or with a PC under a specialized software) was used.



Figure 68. Automated system for control and measurement of probe characteristics.

The schematic diagram of the control and measurement system is shown in Figure 69.

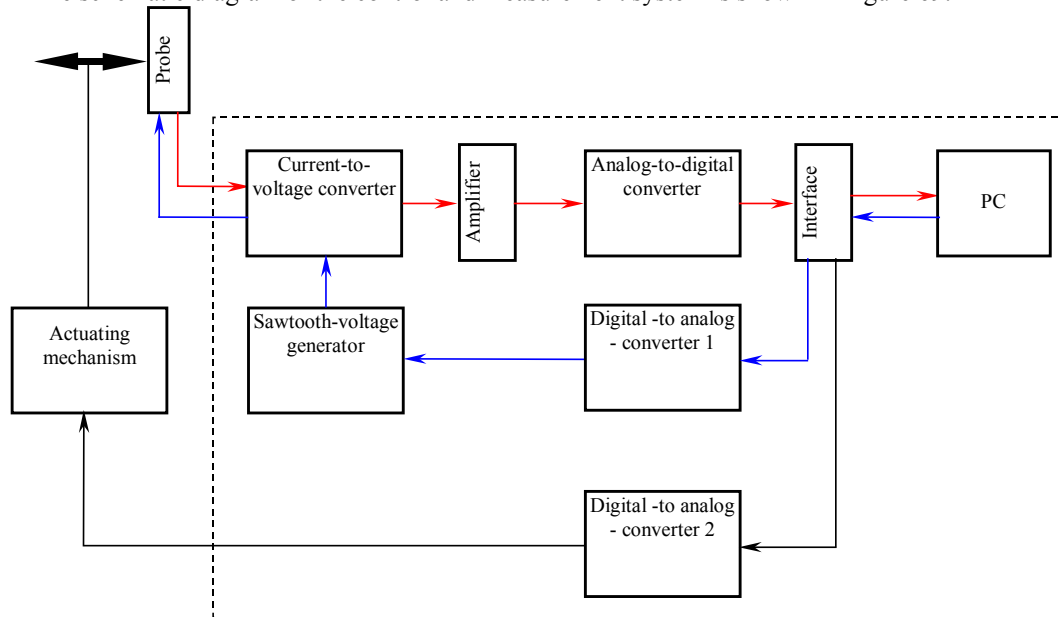


Figure 69. The schematic diagram of the control and measurement system.

The system enables registration of probing characteristics in an automatic mode, under a predetermined computer program which ensures preset of the algorithms for drivers simultaneously with the performances registration (on a computer). There are three independent channels available for probe (or an analyzer) performances measurement, that ensures parallel (simultaneous) registration of signals from three probes. Each channel has its individual set-up that enables use of probes of diverse types at a time, and analyzers too. The system has three measuring ranges of the current coming on the probe of a channel: 15 mA, 50 mA and 150 mA. This enables selection of optimum parameters for measurement at diverse points in plasma. Generator of saw-toothed voltage provides a probe with the bias voltage in the range from -25 V up to +50 V that enables obtaining of a complete probing performance.

This instrumentation supports registration of probing characteristics in two ways. The first one consists of a direct measurement of volt-ampere (current-voltage) characteristic of a probe or an analyzer. The second way differs by that probing characteristics are obtained via averaging of several measurements. This reduces the probability of random failure and noise during the measurement. Also, a unit for manual control of the drivers with the appearance shown in

Figure 70 was designed. This device enables positioning of probes in a vacuum chamber without use of a computer.



Figure 70. Manual control unit.

5.2. Selection, improvement and verification of probe designs and sizes. Improvement of the measurement procedure.

Since the final goal of the developed system is measurement of complex plumes of a cluster while the trajectory of the ions coming to a tested point is unknown, getting complete characteristic of the plume in every point requires determination of three components of a flow in three mutually perpendicular directions. It is a complex engineering problem, which has not been solved earlier, demanding a dedicated research. Nevertheless, for the first estimate, a system consisting of three probes pointed in three mutually perpendicular directions can be used.

For hardware realization of such a diagnostic instrument a probe designs improvement program was carried out within the framework of current Project. It included the following phases:

- ☐ improvement of the design (with a guard ring and without it) and sizes of flat probes;
- ☐ verification of measurement results via comparison of the data obtained from diverse probe types and independent measurements.

The basic criteria for selection of the probe designs were:

- ☐ minimal size - to obtain as higher resolution as possible and the lowest disturbance of the tested flow;
- ☐ simplicity of manufacturing and reproducibility of the design;
- ☐ agreement of the measurement results with the data obtained by other independent methods.

To verify the measurement results, a heated emitting probe and a cylindrical probe were used, because these are the most investigated and extensively described in literature⁴³.

The probes are shown in

Figure 71.

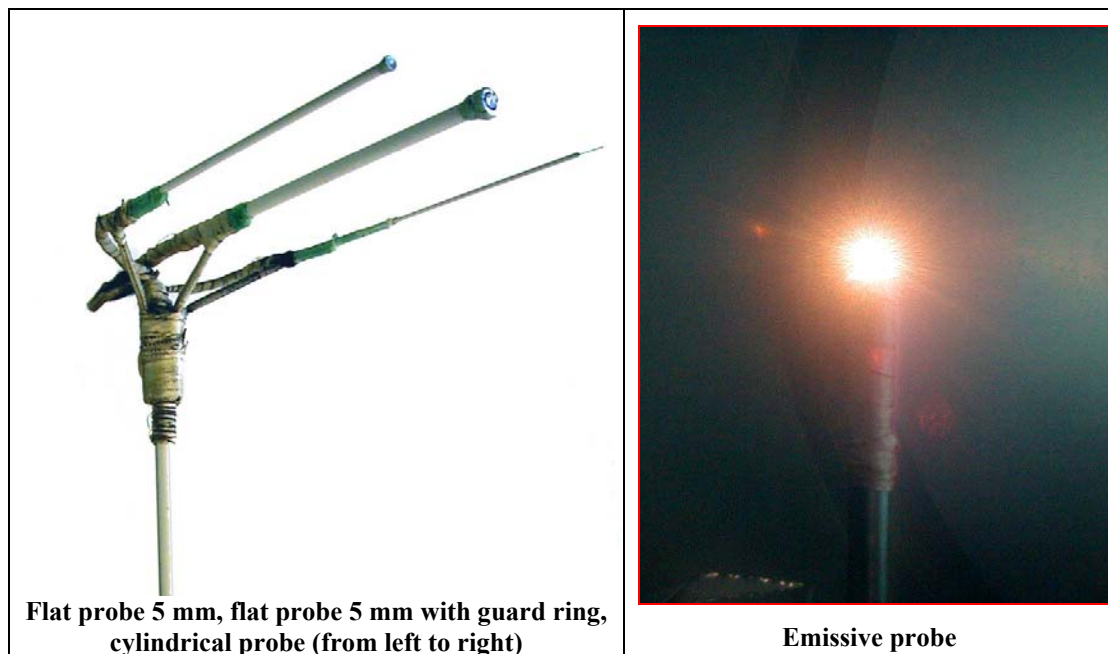


Figure 71. External view of the probes.

Current-voltage probe characteristics were measured according to a standard scheme when biasing the probe in the range of $-25\text{ V} \dots +50\text{ V}$. Volt-amps curves (VAC) were recorded on a computer controlled by a routine software To eliminate accidental errors and electromagnetic noise effect in a registered signal, recording of a VAC curve was made in two ways:

- ☐ at a single change of the bias;
- ☐ via averaging of 10...25 measurements at each point.

All the results represented below were obtained under coincidence of measurements in both ways of registration.

The emitting probe was a 4-mm loop/spiral made of W-Re alloy. The spiral was heated up by energizing from an independent power supply. When using an emitting probe, the VAC were measured for the probe while cold and heated (similar to case of Langmuir probes). The point where coincidence of these curves ceased was assumed as the plasma potential⁴³.

Plasma parameters were estimated with the following relations.

Ion current density:

$$j_i = \frac{I_i}{S_p},$$

where I_i – saturation ion current, S_p – geometrical area of a collecting probe surface.

Electron temperature:

$$T_e = \frac{e}{k \cdot \left(\frac{d \ln(I_e - I_i)}{dV_p} \right)},$$

where I_i – saturation ion current, I_e – electron current, V_p – probe potential.

5.2.1. *Selection of the probe size and geometry*

Among the problems solved on the phase of improvement of probe designs was a well-grounded selection of the size of a flat probe. As a rule, the size of Langmuir probe is determined from the following relation:

$$d_p \gg \lambda_D, \quad (5.1)$$

where d_p – the characteristic size of a probe; λ_D – Debye radius.

$$\lambda_D = \sqrt{\frac{\epsilon_0 \cdot k \cdot T_e}{2 \cdot N_e \cdot e^2}} = 17,6 \cdot \sqrt{\frac{T_e}{N_e}}, \quad (5.2)$$

where T_e and N_e – electron temperature and number density.

The bigger is the probe size, the less is the measurements error caused by the change of the effective collecting surface of a probe (due to formation of boundary layer of the order of λ_D). On the other hand, the bigger is the probe, the greater are disturbances in the tested plasma and deformations of plasma initial parameters. So, selection of the probe size assumes a compromise to be found between the mutually opposite requirements.

Typical parameters of the accelerated flow of D-55 thruster at the distance of about 0.5 m are: $T_e = 2$ eV; $n_e = 3 \cdot 10^9 \text{ cm}^{-3}$. So, the Debye radius is: $\lambda_D \sim 0,5 \text{ mm}$.

On the basis of condition (5.1), the size of a flat probe was initially chosen equal to 5 mm. This size coincides with the sizes of similar probes used in earlier and passed through the cross tests in several laboratories⁸⁸.

Probes of two types were manufactured:

- ❑ a Ø5-mm flat probe;
- ❑ a Ø5-mm flat probe with a guard ring.

Although the second design is more complicated, it ensures more reliable measurements.

The material for probes is molybdenum.

Also, to get an extended database for comparison of the plasma flow parameters obtained with probes of a diverse design, cylindrical probes of Ø0.5x10 mm were made and tested. These probes also satisfy condition (5.1).

In Figure 72 and Figure 73 there is an example of the plasma potential obtained with three types of probes at the distances of 300 mm and 500 mm from the D-55 thruster exit along the plume flow direction. In Figure 74 and Figure 75 the density of ion current obtained with a flat probe and a probe with a guard ring at the same distances from the thruster exit are depicted. The curves are plotted depending on the radial distance from the geometrical axis of thruster. Electron temperature distributions obtained with the same types of probes at 300-mm and 500-mm distances from the thruster exit are shown in Figure 76 and Figure 77. Thruster D1 operating in the base mode of 300 V, 3 A was used in all these cases.

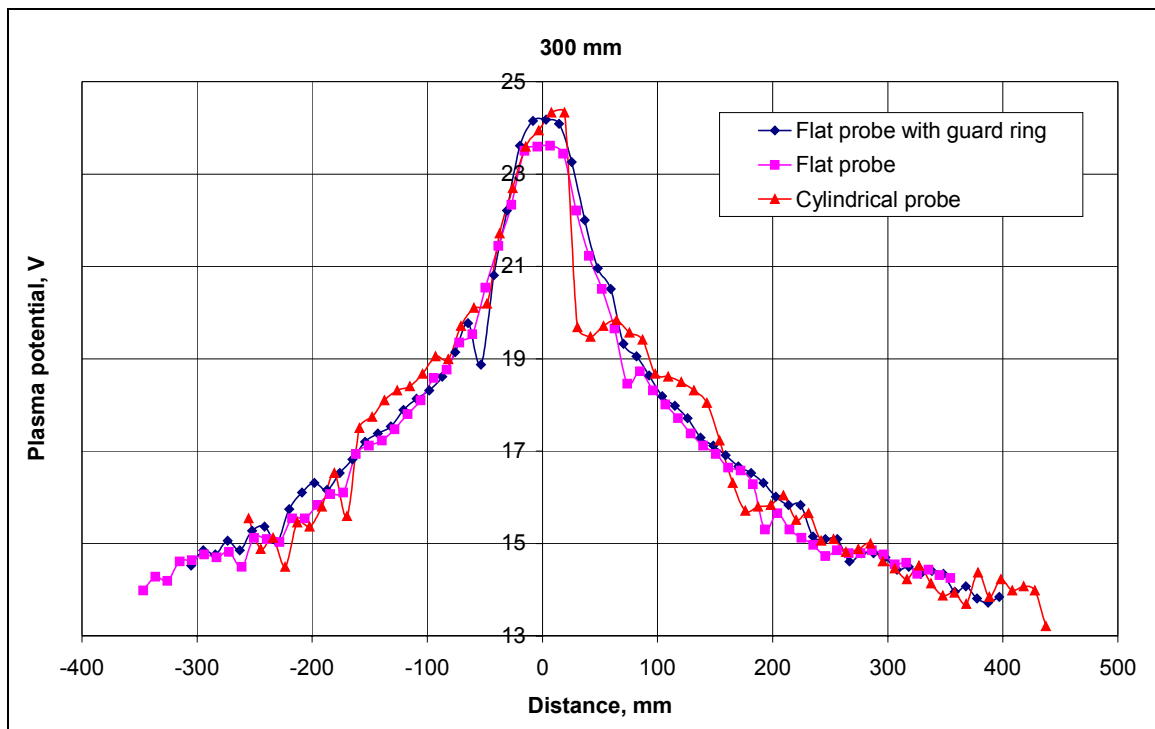


Figure 72. Plasma potential measured with probes of diverse types, 300 mm.

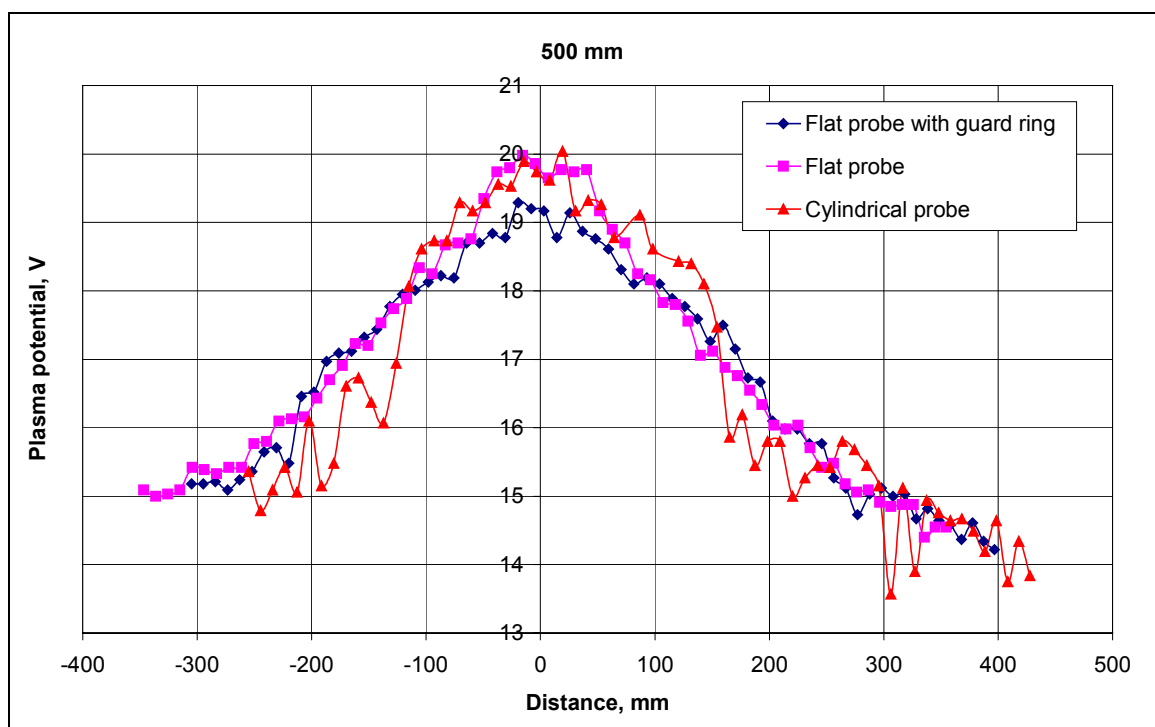


Figure 73. Plasma potential measured with probes of diverse types, 500 mm.

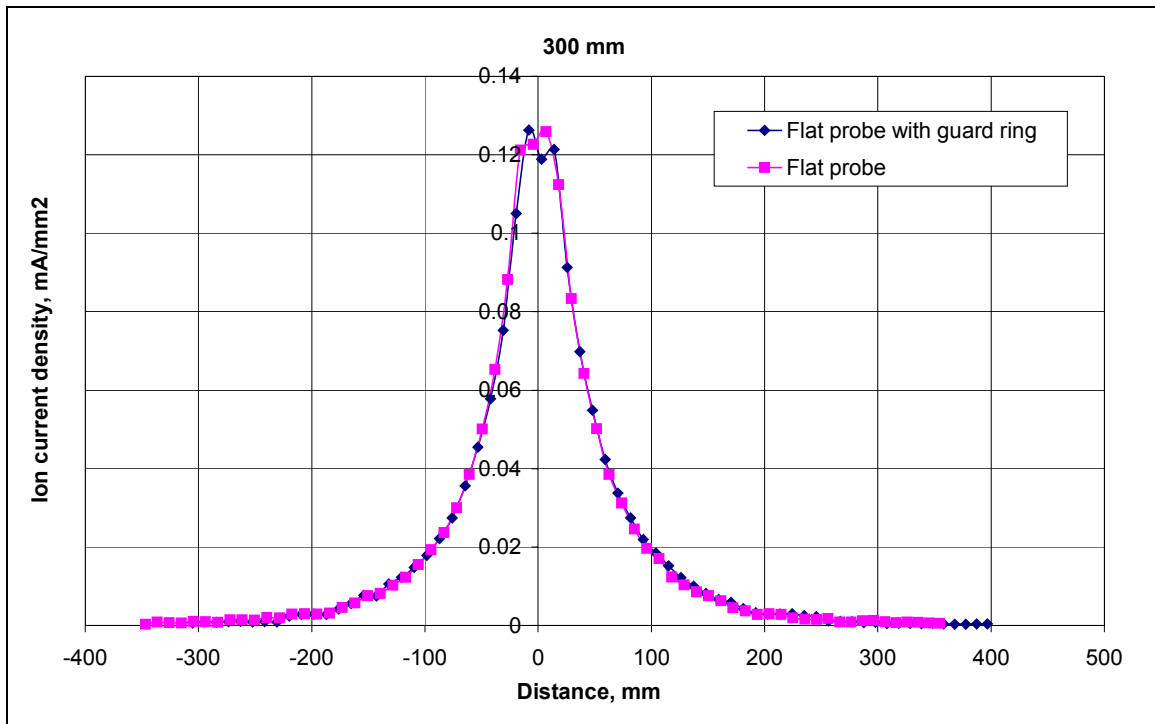


Figure 74. Density of ion current measured with a flat probe and flat probe with a guard ring, 300 mm.

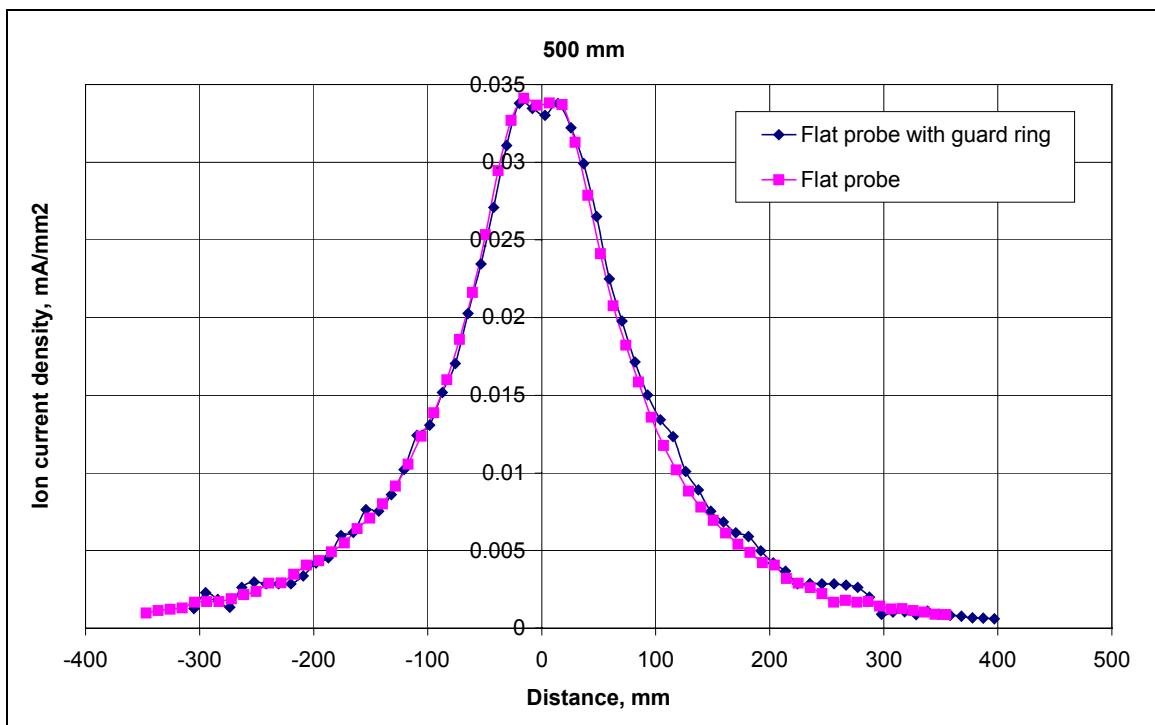


Figure 75. Density of ion current measured with a flat probe and flat probe with a guard ring, 500 mm.

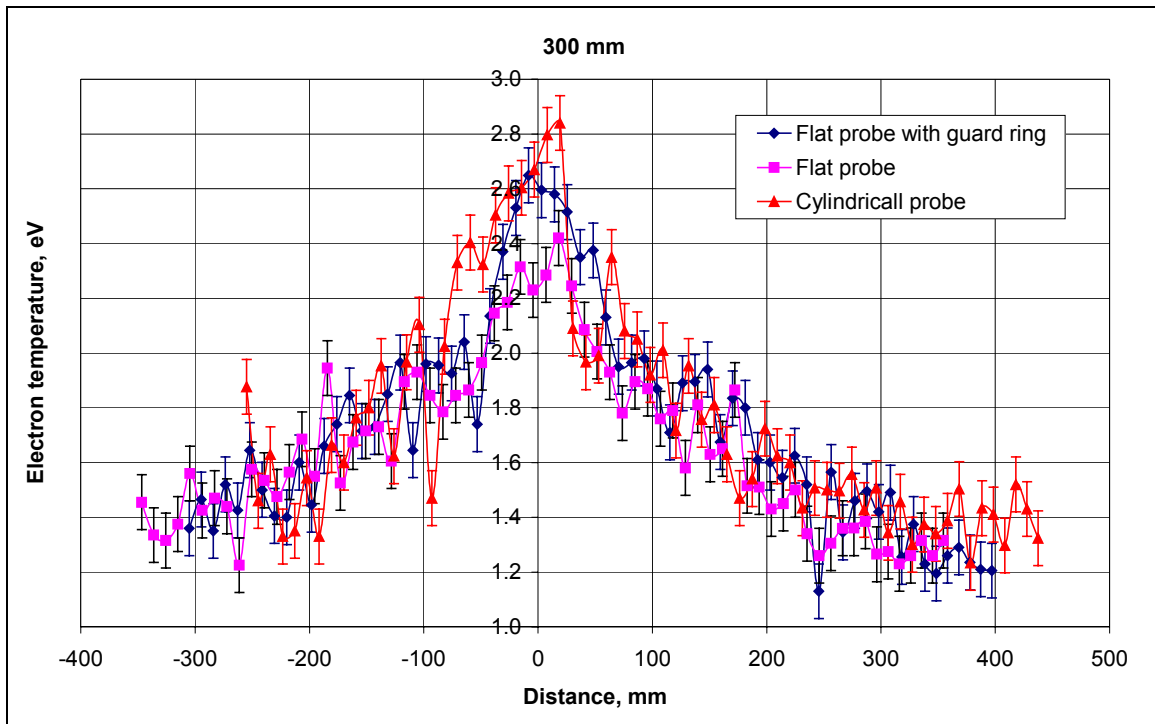


Figure 76. Temperature of electrons, measured with probes of diverse types, 300 mm.

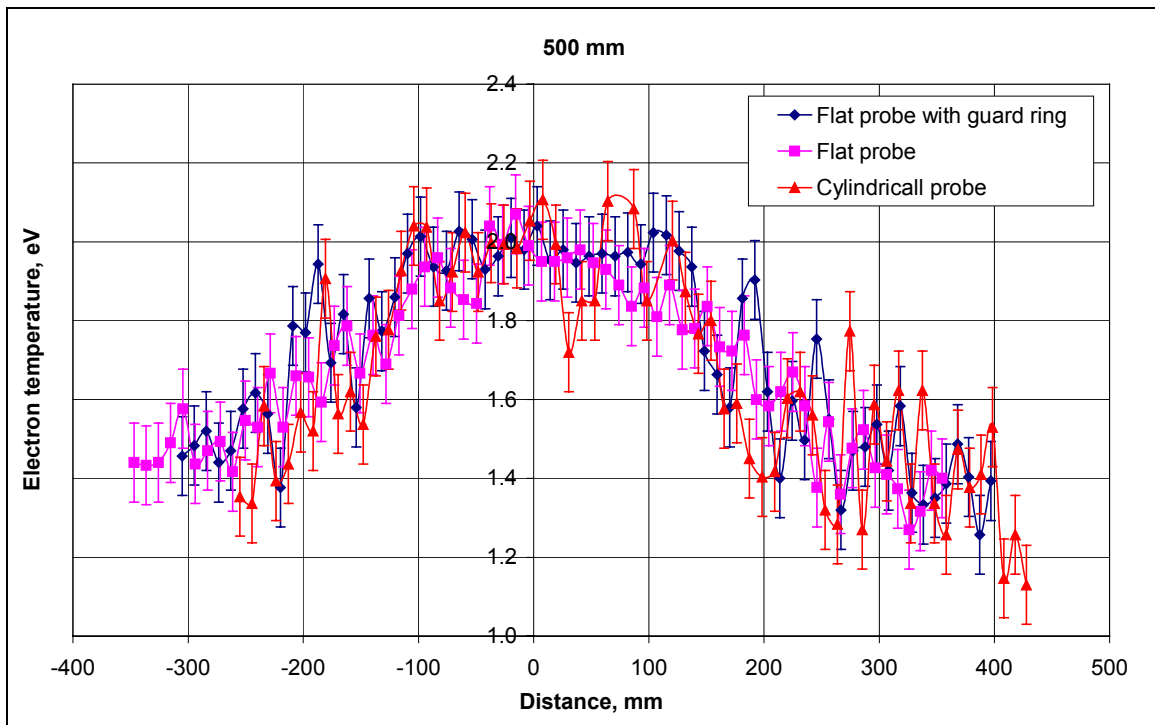


Figure 77. Temperature of electrons, measured with probes of diverse types, 500 mm.

As one can see from Figure 72, Figure 73, Figure 76, Figure 77, there are no essential differences between the plasma potentials or between electron temperatures, measured with cylindrical and flat probes. Also, as follows from Figure 74, Figure 75, densities of the ion current obtained with the flat probe and the flat probe with a guard ring have a good-accuracy coincidence (the density of ion current of the cylindrical probe is not submitted here in view of the uncertainty of the collecting surface size for such a probe under conditions of accelerated plasma flow). These results were true in all the investigated volume of a plume at the distances of 300...1000 mm from the thruster exit.

The obtained quantities are in a good agreement with the data obtained earlier⁸⁷, that proves the executed measurements.

Since no essential difference between parameters of plasma measured with the tested probes has been found, the flat probe with no guard ring (which design is more simple and reliable) can be used under these test conditions. The obtained characteristics of plasma potential are verified by the measurements with an emitting probe as an independent method of measurement. The results of measurement with the emitting probe are represented in **Figure 78**. One can see, that the plasma potentials measured in two ways coincide rather well that, in its turn, confirms correctness of the measurements.

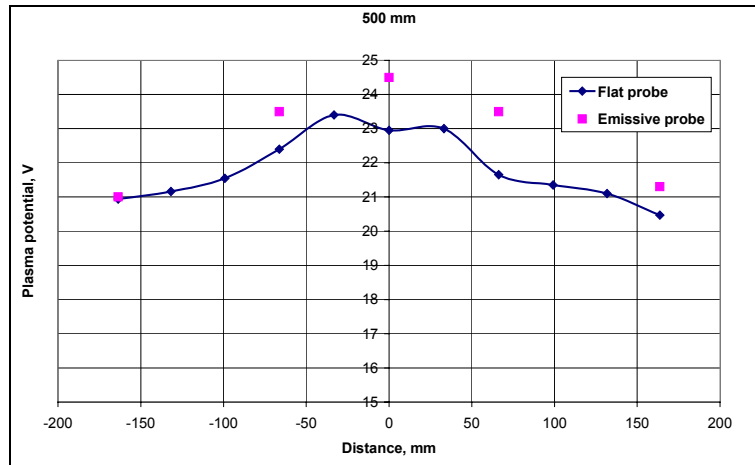


Figure 78. Plasma potential measured with a flat probe and emitting probe.

As one can see from the data above, results of measurements with single flat probe of 5-mm diameter and with a similar probe having a guard ring are completely coincident. No differences between the VAC of probes and the results of plasma parameters estimations are revealed. It is an evidence of that actually the size of the 5-mm probe is essentially greater than Debye radius and there is a capability of reduction of the probe size. There are two reasons for desirability of such reduction:

- probes of the smaller size enables a higher spatial resolution;
- reduction of the probe size decreases the disturbance contributed by it into tested plasma.

An exotic view of the probe volt-amps diagram when measured at a distance of 500 mm and closer (for some operating modes of a thruster) indicates a possibility of an essential impact of a probe on plasma parameters (see **Figure 79**). One can see that a segment with a negative inclination appears in the electronic part of relation. It can be supposed that it is connected to some disturbance of plasma during measurements and also to the change of potential of space at a contact with a probe, because the electronic current, collected on it, came closer to 0.5 A (that is a tangible part of a whole flow).

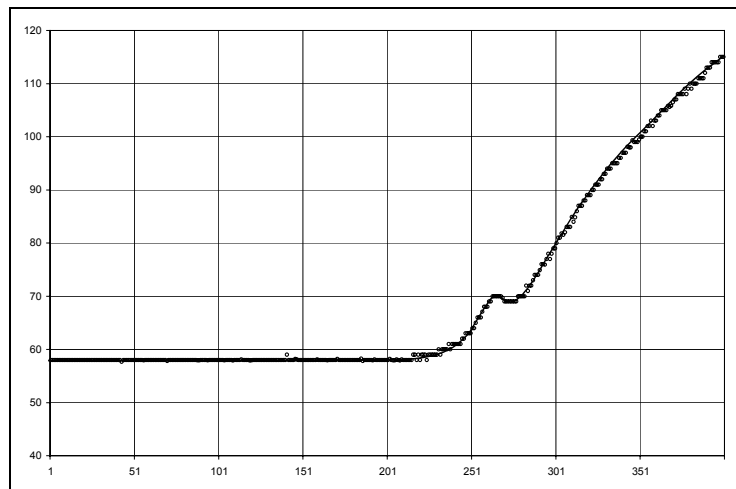


Figure 79. Abnormal probe characteristic.

However, the minimal size of a probe has a limitation described by expression (5.1). The values of Debye radius calculated after handling of characteristics of a Ø5-mm flat probe at D1 plume measurements are depicted in Figure 80. The values of Debye radius are plotted depending on the distance between the thruster

center and position of the probe in a direction perpendicular to the axis of the flow. The values are shown for three distances from the engine exit along the axis of a flow: 300, 500 and 1000 mm. The D1 operation mode was 300 V, 3 A.

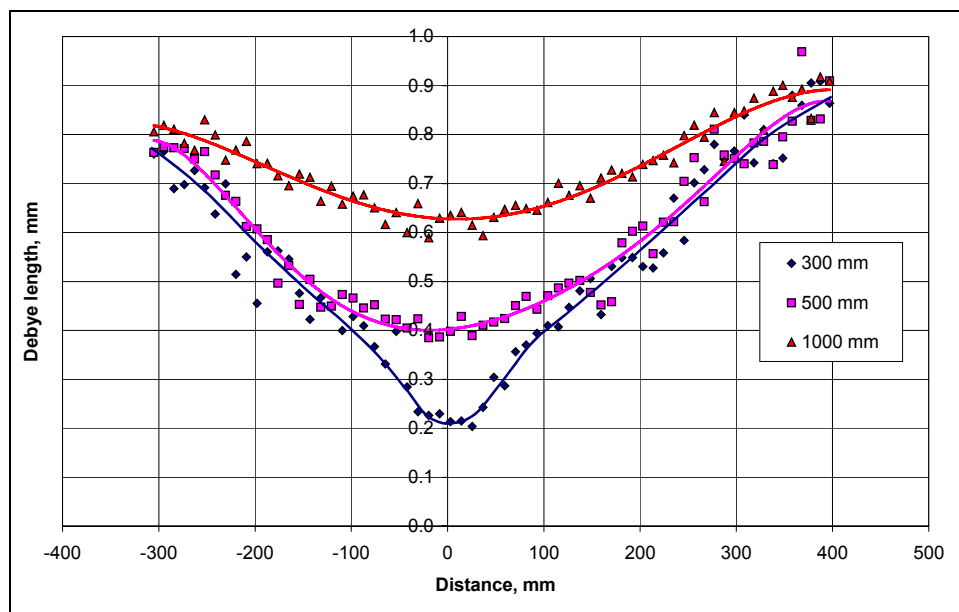


Figure 80. Debye radius.

From the presented data one can see that, if the size of probe is less than 5 mm, relation (5.1) is not true for a significant part of a plume and an experimental check of the possibility for its use is required.

5.2.2. Comparison of flat probes of different sizes.

Since application of smaller probes is important for creation of an assembly of several directed probes, special efforts were aimed at investigation of possibility of using of the probes for which condition (5.1) is not true. Operation of flat probes of a 2-mm diameter was studied. Similar to the previous case, two possible designs were tested:

- a flat probe with a guard ring;
- a flat probe.

The 2-mm size was chosen, on the one hand, to reduce essentially the probe size comparatively to the design described above, and on the other hand, to avoid technological difficulty while manufacturing details from molybdenum. At the 2-mm diameter of the probe the technological tolerance on this size is (± 0.1 mm) that is quite acceptable for measurement of the ion flow density.

For a functional check of small probes, plasma parameters measured with the 2-mm diameter probes of two types and with a 5-mm probe (which was used as a reference one) were compared. The measurements were taken at a base operational mode of a thruster: 300 V, 3 A. The VACs of a single, Ø2-mm flat probe and Ø2-mm flat probe with a guard ring are depicted in Figure 81. In spite of some discrepancy in the electronic part of the curves, in the ionic part the values of current for these probes coincide, i.e. use of a guard ring is not important for measurements of ion component of the probe current.

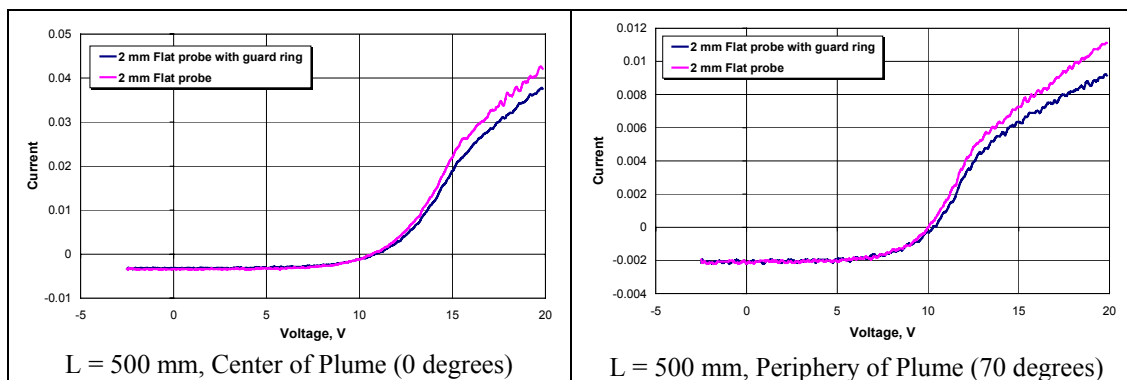


Figure 81. Characteristics of Ø2-mm flat probe and Ø2-mm flat probe with a guard ring.

To define the influence of the design of a probe upon measured electronic temperature and potential of plasma, measurements were taken with both probes. The characteristics of a plume obtained at the distances of 500 and 1000 mm from the thruster exit with the flat probe and the flat probe with a guard ring are shown in **Table 21**.

Table 21

L	Probe position	Ø2-mm flat probe		Ø2-mm flat probe with guard ring	
		Plasma potential, V	Electron temperature, eV	Plasma potential, V	Electron temperature, eV
500 mm	Center of plume	14,56	1,86	14,68	1,89
	Periphery of plume	12,33	1,74	12,6	1,81
1000 mm	Center of plume	12,11	1,62	12,31	1,72
	Periphery of plume	11,62	1,61	11,90	1,72

One can see from **Table 21** that the difference in values of plume parameters does not exceed 6 % for electron temperature and 2,5 % for plasma potential, that is significantly less than typical accuracy of measurement by probe methods. So, obviously, the use of a more complex design with a guard ring does not give a tangible result while determining ion current density, plasma potential and electron temperature.

The distribution of plasma potential, measured with a flat probe of 2 and 5 mm, which can be considered as a standard is shown in Figure 82. The values of plasma potential obtained with both probes (as can be seen from Figure 82) differ from each other in a value exceeding not more than 1 V. It is close to the threshold of sensitivity in our measurements, which is about 0.5 V.

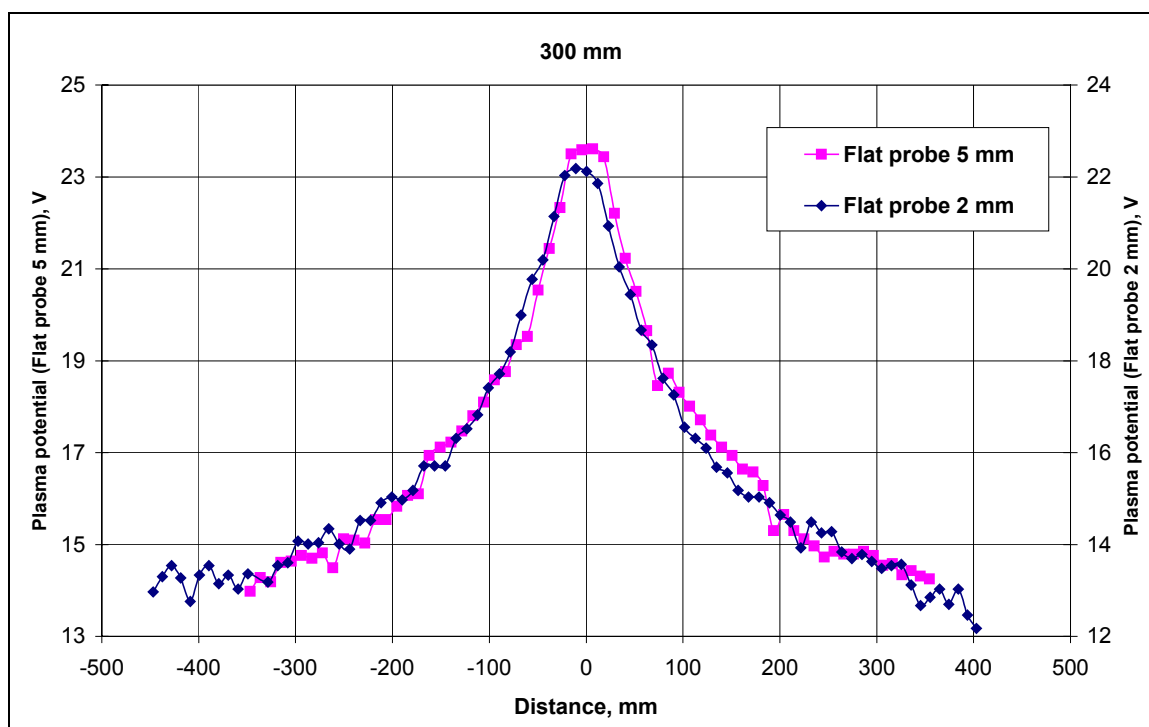


Figure 82. Plasma potential measured with a flat probes of 2 and 5 mm.

Taking the classical probe theories as a basis, it is possible to expect the greatest difference between the parameters, measured with the probe, sized close to Debye radius, and the results of measurements with a rather large probe for which the condition (5.1) is true, at a great distance from the ion engine (where the plasma particle number density drops and Debye radius increases). However, direct comparison of the results for the density of ion flow measurement with probes of 2-mm and 5-mm diameters at the distance of 1 m actually demonstrates their coincidence. The difference between the indications of probes increases with approaching to the exit of thruster (Figure 83) that contradicts the results, which could be expected basing on a classical probe theory.

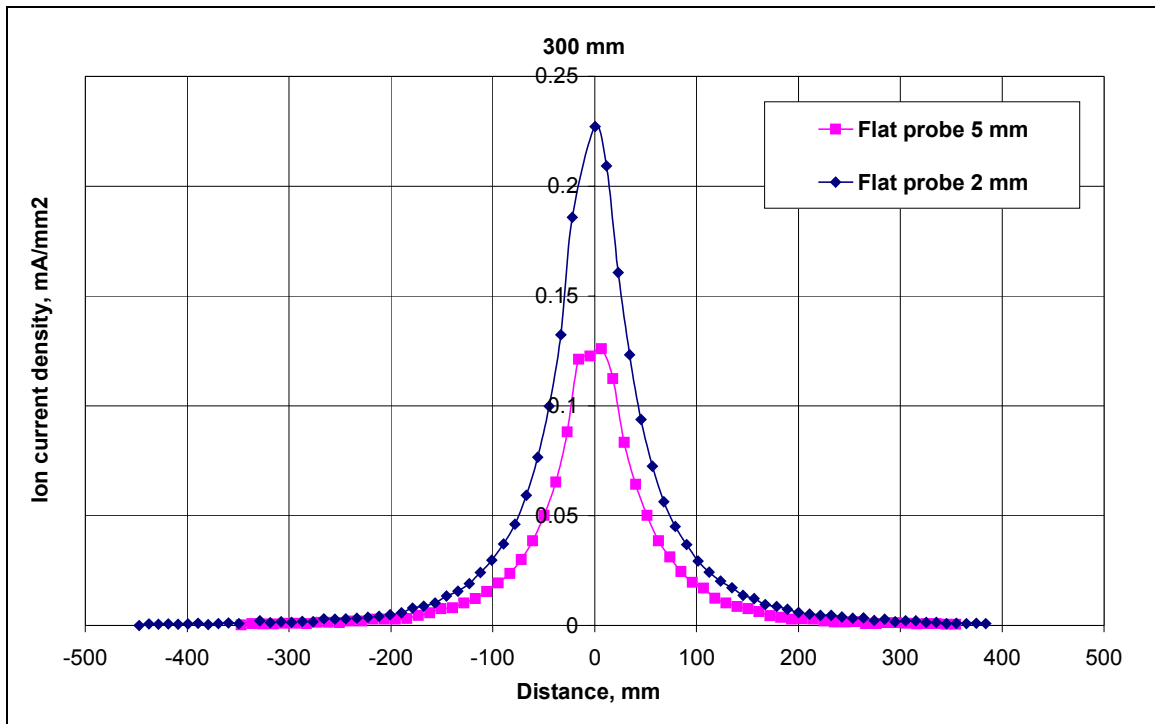


Figure 83. Densities of ion current, measured with flat probes of 2 mm and 5 mm.

Figure 84 illustrates a characteristic change in the density of ion flowing the center of a plume measured with 2-mm and 5-mm probes depending on the distance from the thruster exit.

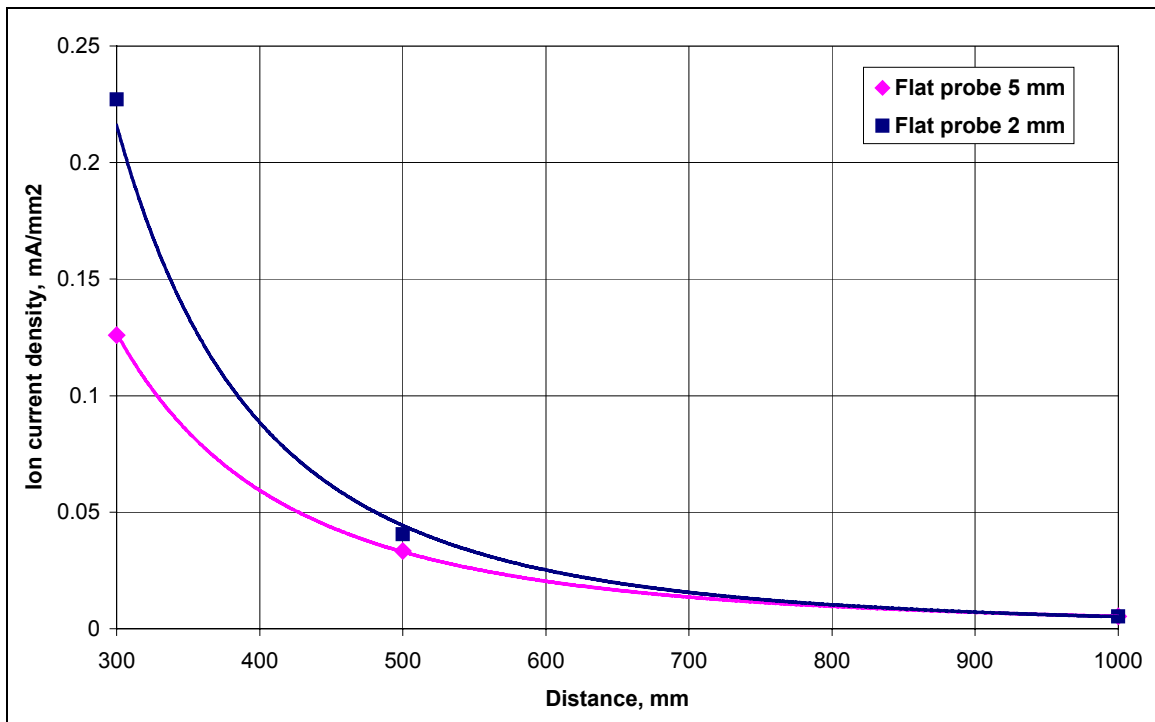


Figure 84. Density of ion current of 2-mm and 5-mm flat probes .

A future investigation is demanded to understand the noticed divergence.

It should be mentioned that owing to the design features and different heat sink from the collecting surface, a small probe was essentially heated up at a distance closer than 500 mm to a thruster. At the distance of 300 mm it was visible to the naked eye that the probe was heated up to the temperature of red heat (Figure 85). A possibility of an abnormally high electronic emission from a hot metal surface located in dense plasma is denoted in paper⁸⁹. However, it is only one of possible hypotheses explaining the difference between the results of measurements of ion current. The problem demands its further study, including a more detail investigation of

the capability of measurements with a "shooting probe", having the residence time in a flow much less than the time of its surface heating.



Figure 85. Heating of probes.

With regard to the task of a future cluster investigation, it can be noted that the system for ion currents measurement enables registration of ion current density relative changes. However, an additional calibration of the system is necessary for more precise quantitative measurements. The discrepancy of the density of ion current measured with different probes renders a comparison of the ion current magnitudes impossible. Nevertheless, it is of the essence that the results of measurement of plasma potential as well as of electronic temperature completely coincided. It allows to talk about, at least of a possible limited application of small probes (the linear sizes are comparable with Debye radius) to measurement of local parameters of plasma.

As an illustration for the said, a distribution of Electron temperature across a plume, obtained with 2-mm and 5-mm flat probes, is depicted in Figure 86. As one can see from Figure 86 the electron temperatures are rather close to each other.

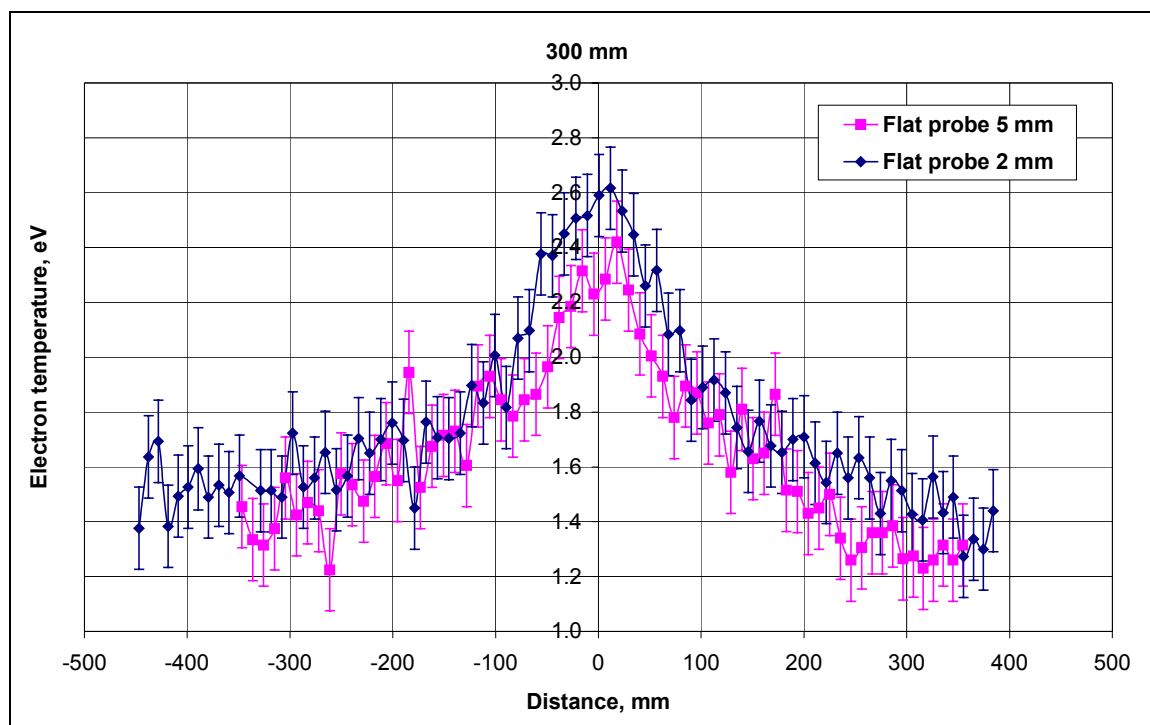


Figure 86. Electron temperatures, measured with flat probes of 2 and 5 mm.

So, the represented data denote the applicability of 2-mm probes in our conditions in spite of the fact that the size of the probe is comparable to the Debye radius for some part of a plume. Thus, for further investigation of plumes, flat directed probes enabling more definite registration of the direction of flow in comparison with cylindrical probes and also having smaller sizes and design simplicity in comparison with flat probes with a guard ring were chosen.

In **Figure 87** the scheme of directed flat probes of 2-mm diameter chosen for future studies is shown.

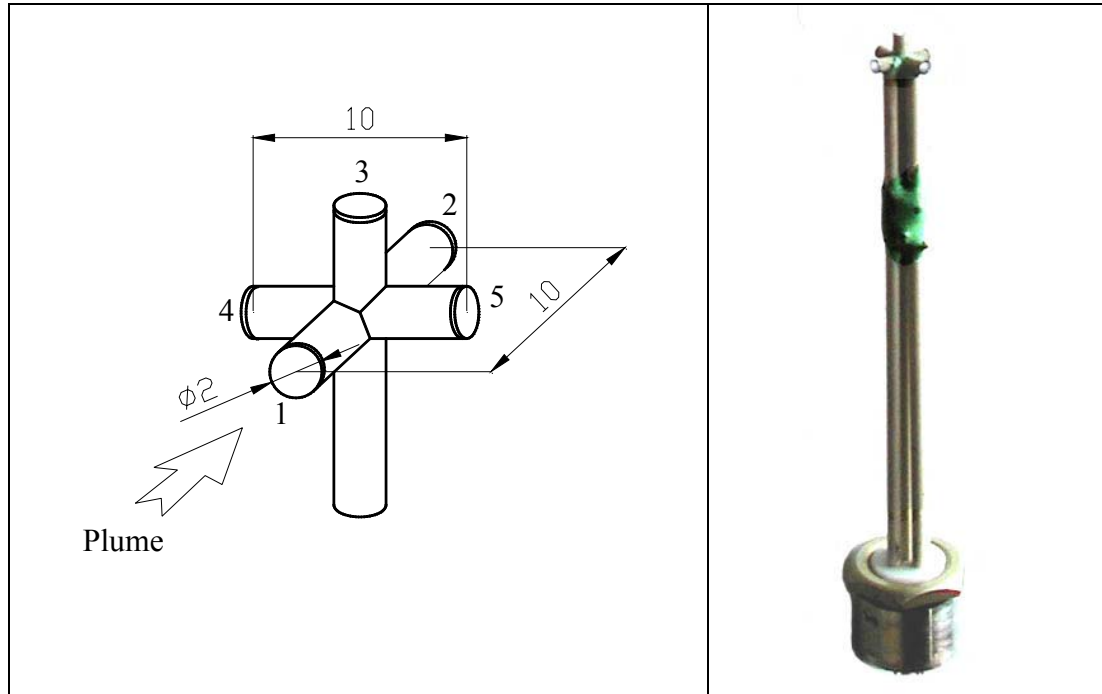


Figure 87. Oriented flat probes.

5.3. Experimental results of investigation of a single thruster plume

Study of a plume of a single thruster was aimed at generation of a database for next comparison with the measurement results obtained for the plume of a cluster. The measurements were taken with thruster D1 mounted as a part of an three-thruster assembly with central cathode as shown above (see **Figure 59**). With directed probes installed on a coordinate device, spatial distributions of electron temperature, potential of plasma and ion flow the thruster plume were investigated. By means of an analyzer of the energy spectrum of ions, ion flows have been studied in two directions:

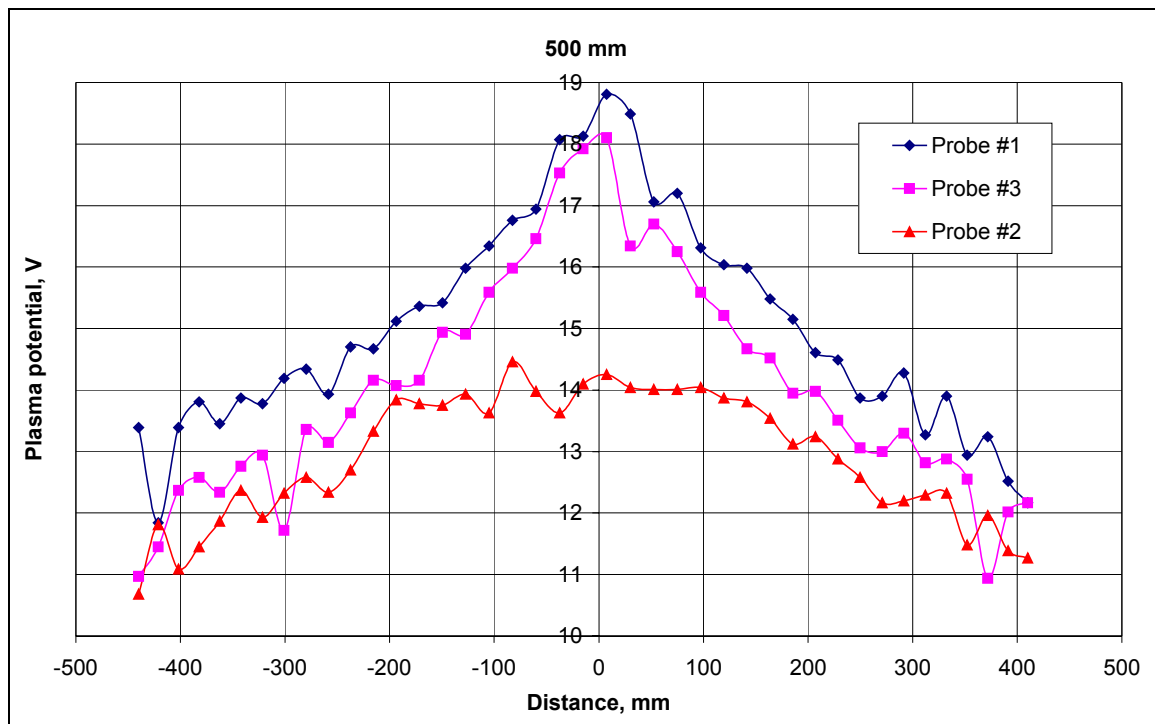
- ❑ along the axis of thruster. For that, the analyzer was directed along the plume and moved (on a 3D coordinate device) along the flow and along its radius.
- ❑ across the axis of thruster. The analyzer was fixed perpendicular to the main ion flow, and moved then along the plume at the distance of 460 mm from its geometrical axis.

5.3.1. Results of the probe measurements

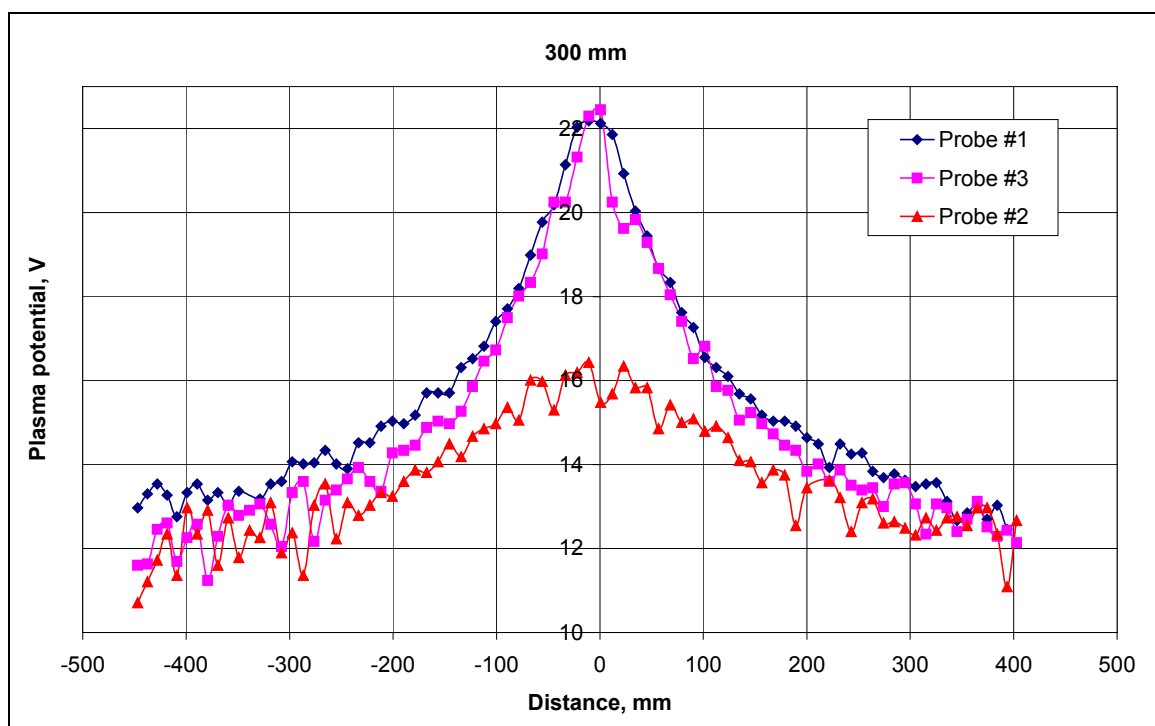
5.3.1.1. Probe measurements of a thruster plume.

Distributions of plasma potential, measured across the D1 plume at the distances of 300 mm and 500 mm from the D1 thruster exit with directed probes **1**, **2** and **3** (**Figure 87**) are shown in Figure 88. Probe **1** was placed across the incident plume, probe **2** - at the rear, in the "shadow" of the incident flow, and the face of probe **3** was directed in parallel to the engine axis.

Distributions of ion current density and electron temperature (measured with probes **1**, **2** and **3** across the plume at the same distances from the thruster exit) are depicted in Figure 89 and Figure 90.

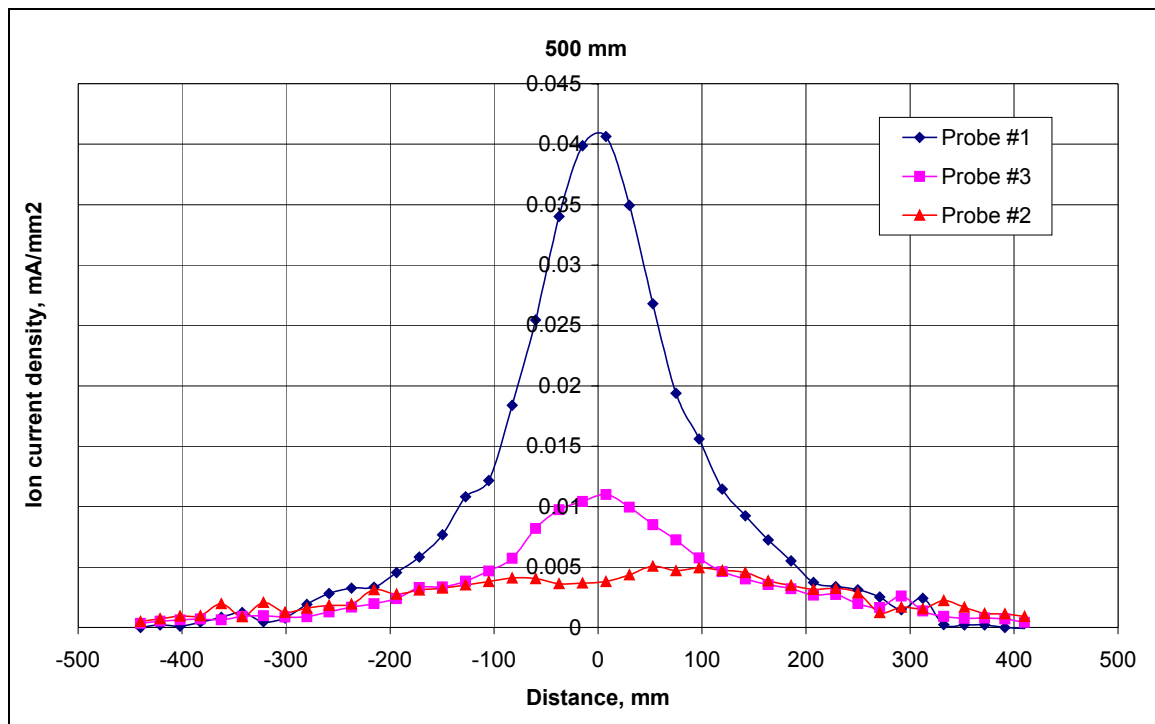


a)

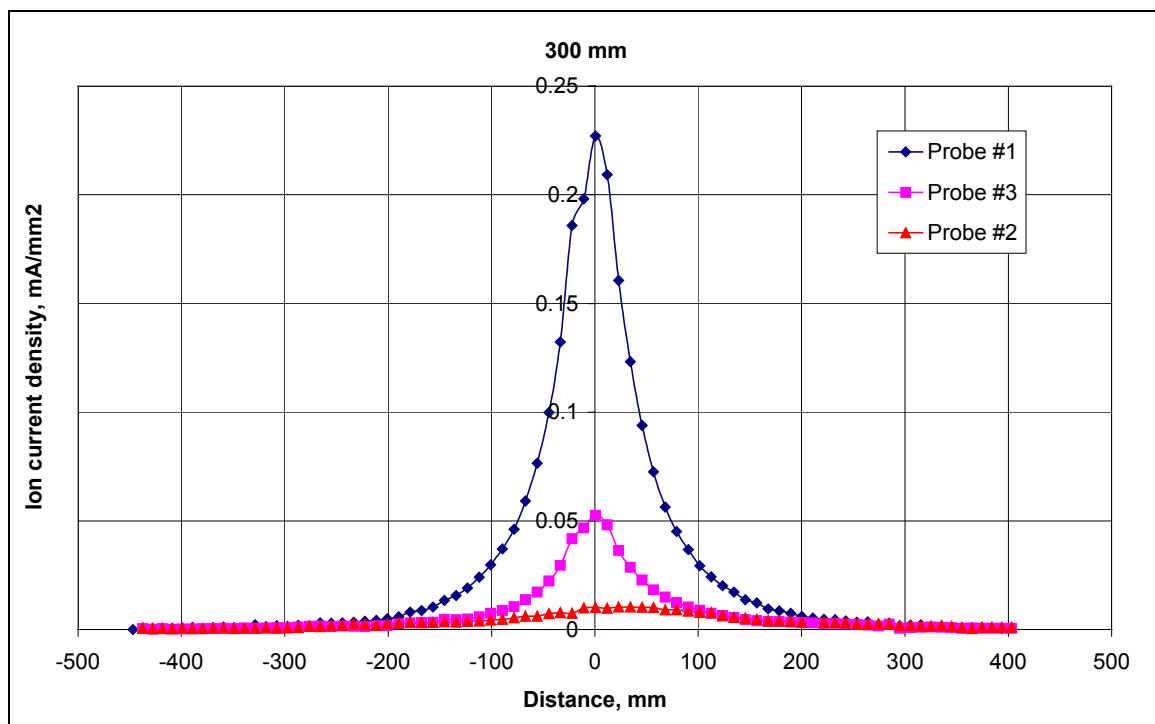


b)

Figure 88. Plasma potential: a) $Z = 500$ mm, b) $Z = 300$ mm.

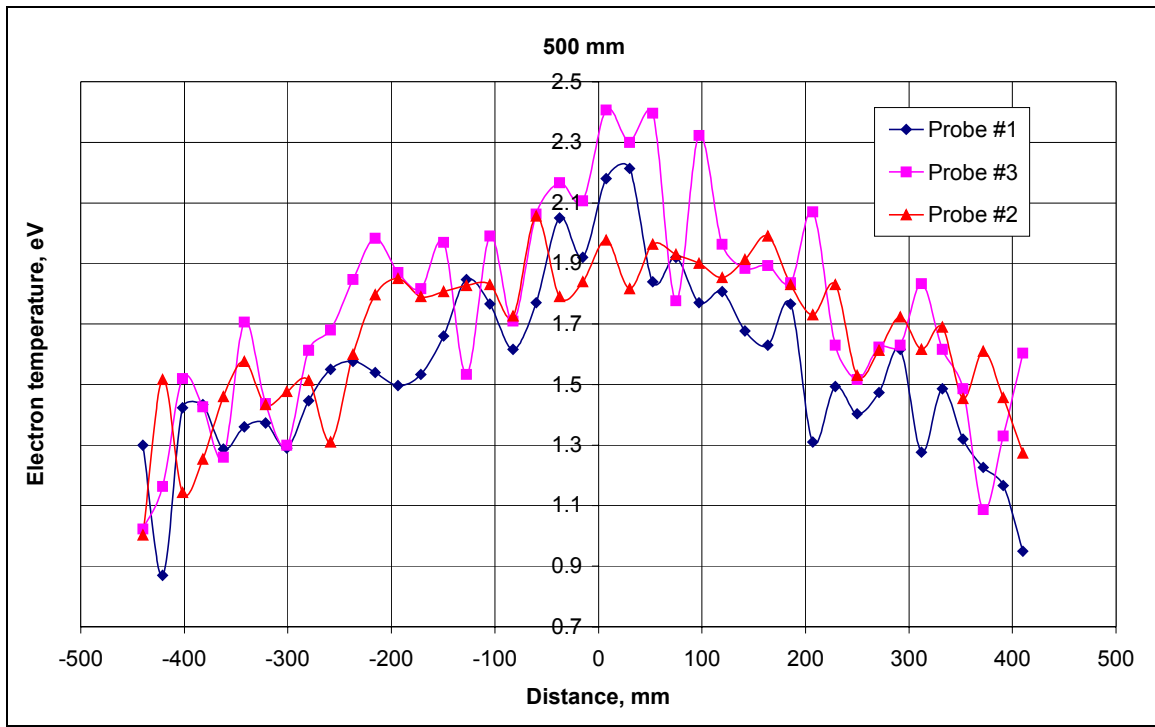


a)

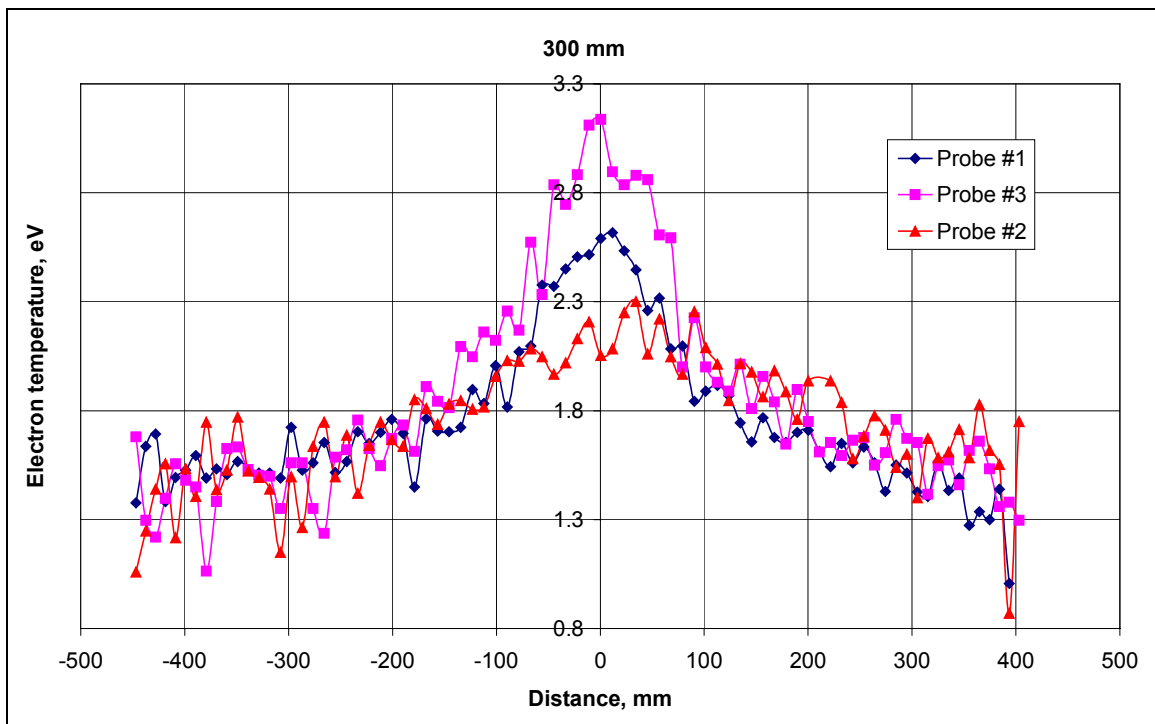


b)

Figure 89. Density of ion current: a) $Z = 500$ mm, b) $Z = 300$ mm.



a)



b)

Figure 90. Electron temperature: a) $Z = 500$ mm, b) $Z = 300$ mm.

The difference of the ion current collected on probe 1 and that on probe 3 is approximately proportional to the ratio of directional and chaotic velocity of the ion component⁹⁰. With moving away from the center of a plume, the directional speed drops, and at some distance it is compared to the chaotic speed of secondary plasma. The later may be considered as a criterion to determine boundary of accelerated plume. In cross-section $X = 300$ mm: the directional flow practically disappears in the radius of 200 mm; for $X = 500$ mm - in the radius of not

more than 300 mm. It corresponds to the divergence of an accelerated plume within the angle of approx. ± 30 degrees.

The electron temperature measurements of three directed probes are practically coincident in periphery of a flow and at great distances from the thruster exit where concentration of the secondary plasma is comparable to concentration of an accelerated flow. In the near zone $X = 300$ mm, in the central part of a plume there is a difference in the values of temperature measured with probes of diverse orientation. It can be assumed that such difference is connected to the directional motion of tested plasma, but this question demands the further study.

When approaching the thruster discharge (thruster exit) the temperature of electrons grows and (see Ref.⁷⁵) reaches 10...15 eV at the distance of 10...15 mm from the thruster exit. The obtained change of temperature along the radius of a plume is similar to data of work⁸⁷.

As one can see from Figure 88, the plasma potentials measured with probes **1** and **3** are close to each other. However, the potential of plasma obtained with probe **2** differs essentially from the first two. Presence of this probe in the "shadow" created by the very assembly of directed probes can be a reason of such difference. A similar phenomenon is well-known in plasma and space engineering. Nevertheless, in the periphery of the plume where both velocity and density of a flow are not so high, the values of plasma potential for all the three probes are rather close to each other.

In general, it can be stated that the tested measuring instrumentation under an appropriate technique enables measurement of electron temperature with the resolution of 0.1...0.2 eV, and the plasma potential - not worse than 0.2 V. It can support investigation of a rather fine structure of a flow and potential effects, which may accompany an interaction of several plasma plumes during a cluster operation. The magnitudes of the measured quantities obtained by means of independent methods, are practically coincident to the experimental and thus verify the results of this study.

5.3.1.2. Measurements of ion energy spectrums.

The analyzer (**Figure 91**) used in this work has a scheme with plane-parallel geometry of grids (meshes) and collector which is described in detail in the Ref.^{91,92}. Analyzing electrode is a twin grid (mesh) on which the analyzing voltage is swept. As a result an integral energy spectrum of ions is recorded. The analyzer enables registration the energy of the incident flow particles in the range 0...1300 eV. The energy resolution (at a full sweep of analyzing voltage) is less than 1 eV. The current sensitivity is not worse than 10^{-12} A. The angle of view of the analyzer is $\pm 15^\circ$, and is determined by a built-in system of collimators.

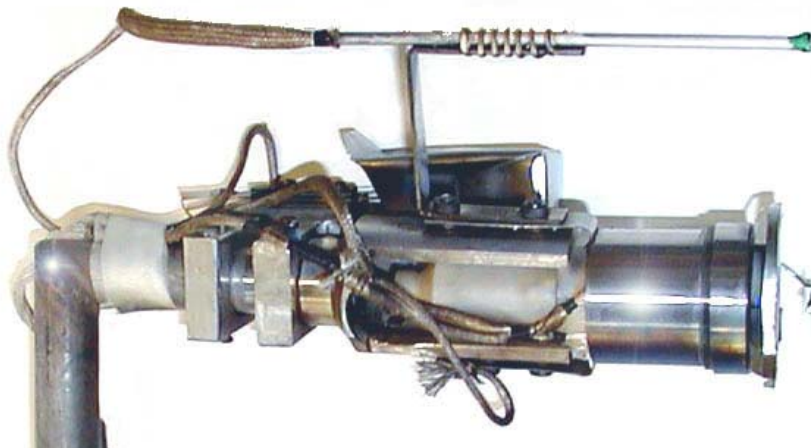


Figure 91. Ion energy spectra analyzer.

The analyzer was located at various distances from thruster exit (Z) and at different radial distances from thruster axis. The measurements were made for two analyzer orientation: along and perpendicular to the plume axis.

In general, the spectra measured along the axis of a thruster plume correspond to the data obtained earlier⁹¹. The sensitivity of the used instrumentation is enough to detect the groups of ions with energy of 3/2 and 2 of discharge voltage value due to presence of a noticeable quantity of double- and triple-charged ions in a plume (**Figure 92**).

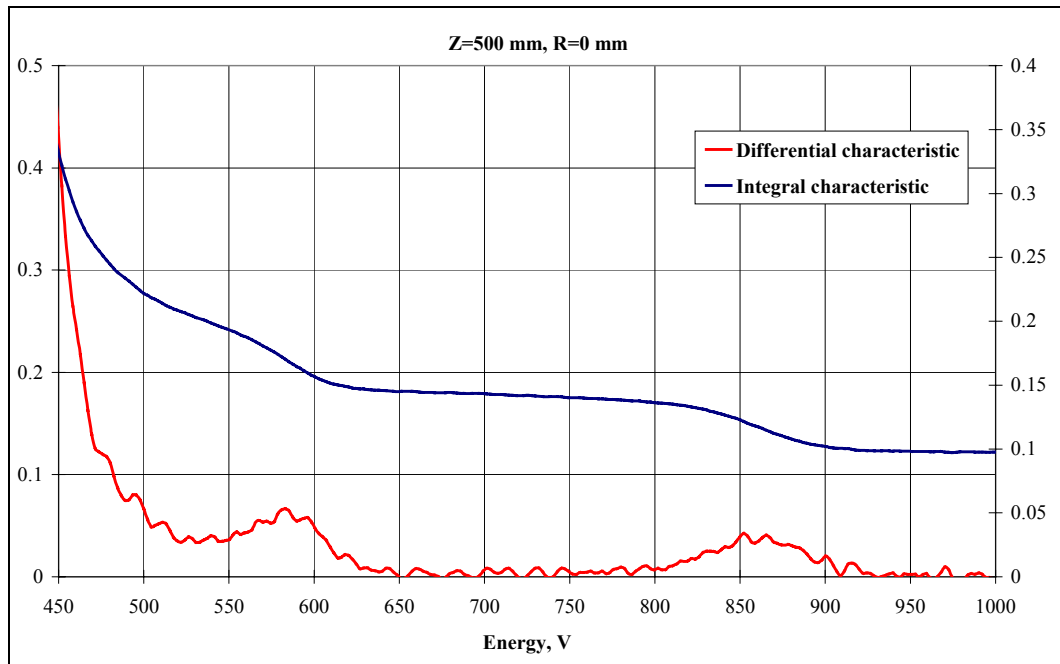


Figure 92. High-energy groups of ions.

When the analyzer is moving along the radius of a plume, decrease of the energy of ions in the main peak (**Figure 93**) can be noticed. This change approximately corresponds to the estimated change of the x -th component of the energy of a flow within the angle of ± 15 degrees from the plume axis, and is well described by the ratio: $E_x = E_0 \cos(a)$, where the angle "a" is counted off the axis of a plume in a polar coordinate system the center of which is coincident with the center of thruster exit.

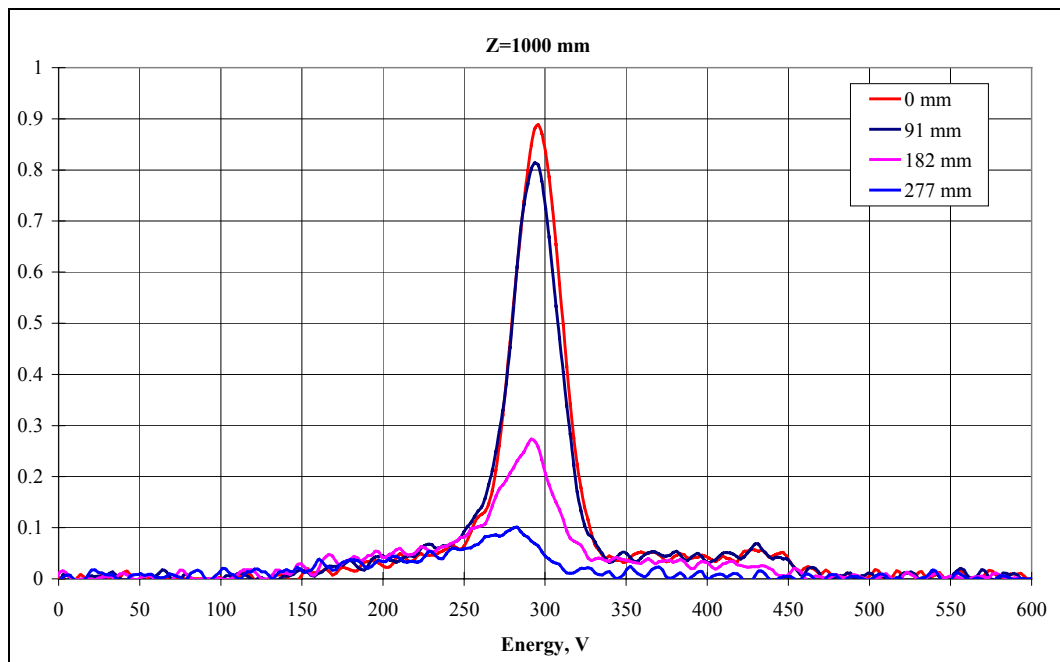


Figure 93. Distribution of the energy of ions along the radius of plume at 1000-mm distance from the thruster exit.

Out of the angle of ± 15 degrees the analyzer stops recording of the accelerated component, because the exit of the thruster discharge channel is out of the angle of view of the device (which is limited by a system of collimators).

Measurements of the energy of ions in a transverse direction reveal the main group of ions with the energy approximately corresponding to the value of plasma potential in the vicinity of the plume center (**Figure 94**). Obviously, they are the ions of secondary plasma generated as a result of the charge exchange with the accelerated ion flow.

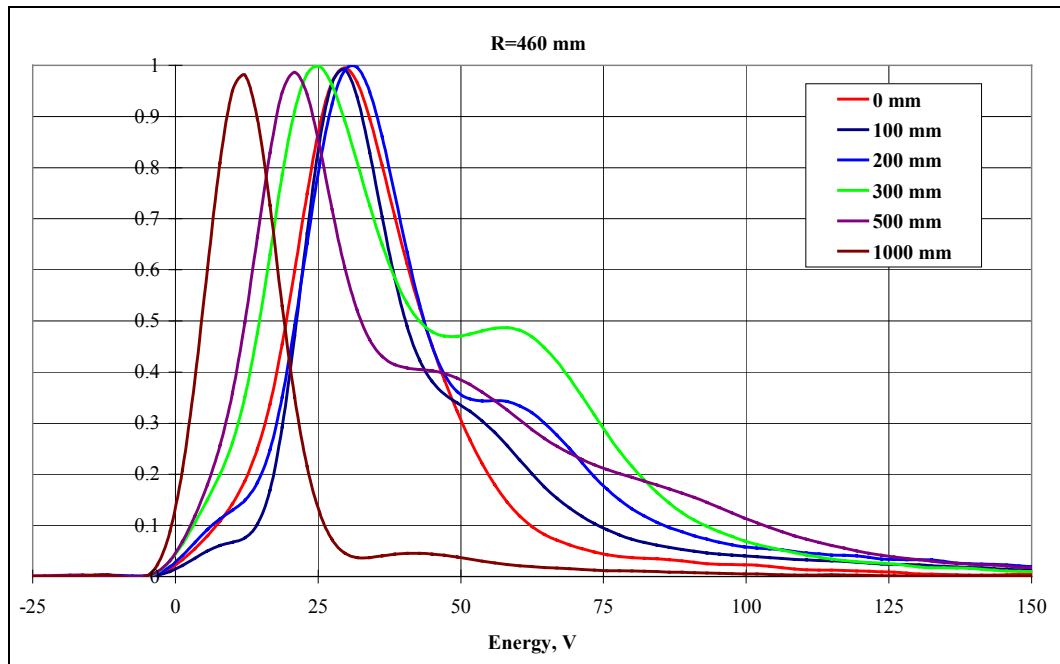


Figure 94. Distribution of ion energy measured perpendicular to the plume axis.

During the measurements the zone of thruster discharge remained visible for the analyzer in the range $L=0\ldots100$ mm. It is important that in this part there is no noticeable quantity of high-energy ions in spite of the fact that the engine works under the scheme with “external anode layer”, and the zone is moved out of the thruster channel at 6...8 mm. The specific features of spectrum can be observed at the characteristic distances of 200...300 mm from the thruster exit (**Figure 94**). There, the second group of ions with the energies much more higher than the characteristic energy of the ions of secondary plasma, measured along the whole plume, is visible. Also, in this spatial interval, the radial ion current reaches its maximum (**Figure 95**). The distance of 200...300 mm corresponds to the zone of intensive charge exchange of accelerated ions on the atoms of residual gas, as a result, an area -a source of secondary ions- is formed. Appearance of a group of secondary ions with the energy of 50...60 eV (**Figure 94**) can be connected to the oscillatory processes arising in plasma. However, it is only one of probable hypotheses, and the physics of this phenomenon should be a subject of further studying.

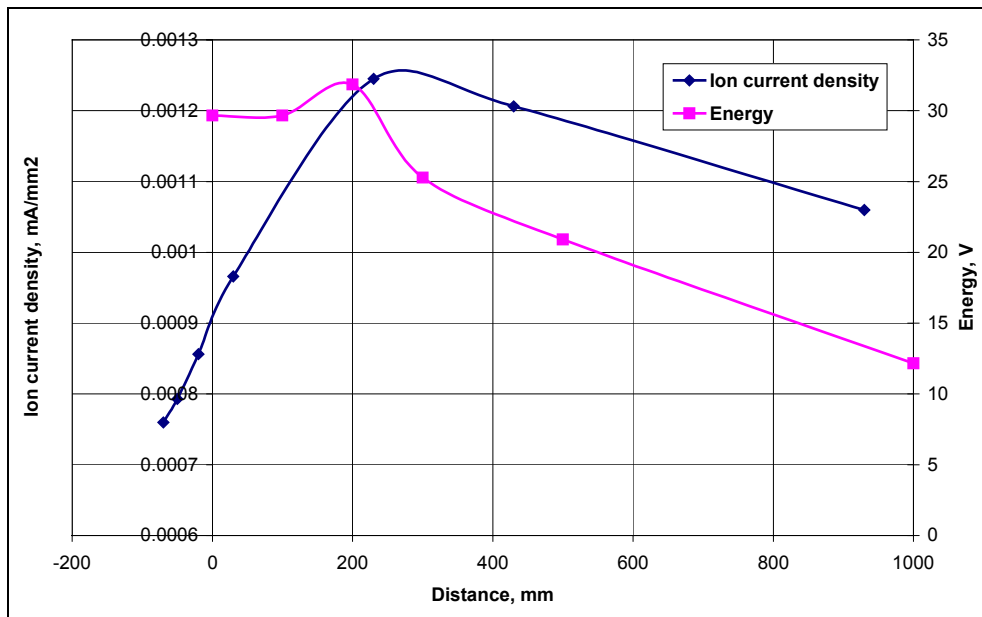


Figure 95. Distribution of ion current and energy of main peak measured perpendicular to the plume axis.

From the point of view of studying complex flows of a cluster, it is important that in an exhausted plume (under certain conditions due to interactions of plasma flows) non-linear phenomena may arise resulting

in a noticeable distortion of the pattern of plume from several thrusters relatively the case of a simple superposition of flows. Obviously, occurrence of these non-linear effects can be connected with a certain interval of concentration and relative velocity of flows that should be a subject of studying on the next project phases. Nevertheless, it is important, that even in case of a plume of a single thruster, owing to investigation of the spectrum of ions in a plume cross-section, an area of a plume with essential peculiarities can be detected. These peculiar properties result in appearance of rather fast secondary ions, which are *not* generated in the discharge of thruster, but in the plume.

5.3.2. *Influence of thruster operating mode on characteristics of flow*

To study the influence of an operating mode of a thruster on characteristics of its plume, probe testing of the plume of D1 engine was executed at the modes of 200, 300 and 400 V, 3 A. The distributions of plasma potential and Electron temperature across the plume are depicted in **Figure 96**, **Figure 97** respectively. Flat probe #1 of 2-mm diameter (**Figure 87**) was used at the distance of 300 mm from the thruster exit and discharge voltages 200 and 300 V.

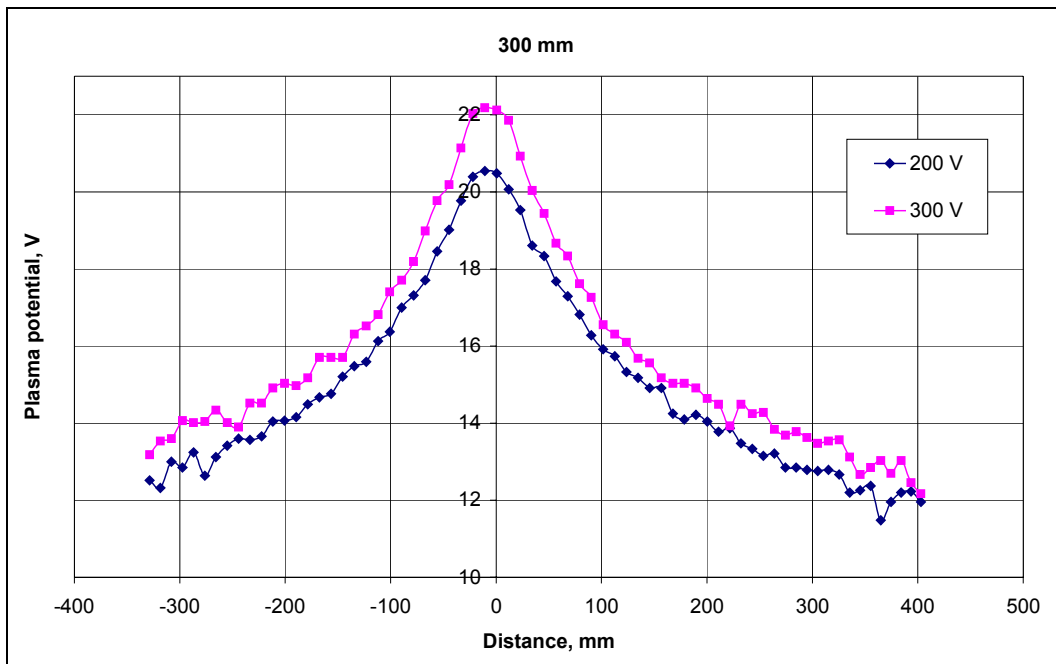


Figure 96. Plasma potential at discharge voltage of 200 V and 300 V.

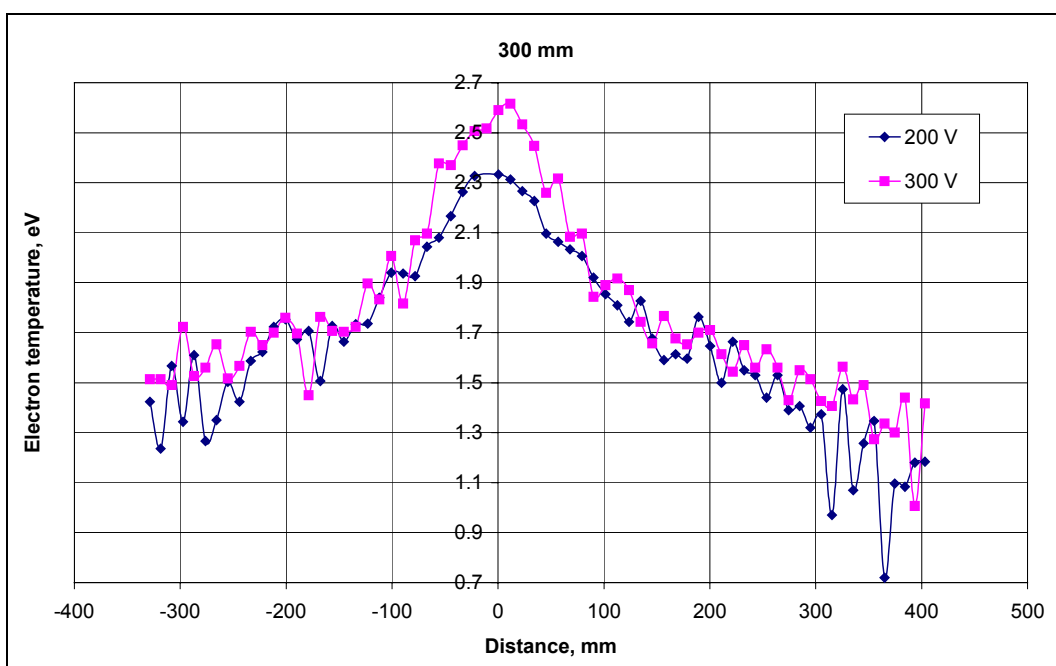


Figure 97. Electron temperature at discharge voltage of the thruster 200 V and 300 V.

The density distributions of the ion current, obtained with the same probe at discharge voltages of 200 V and 300 V are shown in **Figure 98**. As one can see from **Figure 98**, an increase of discharge voltage results in growth of the density of ion current and better focusing of the plume that was already shown earlier.

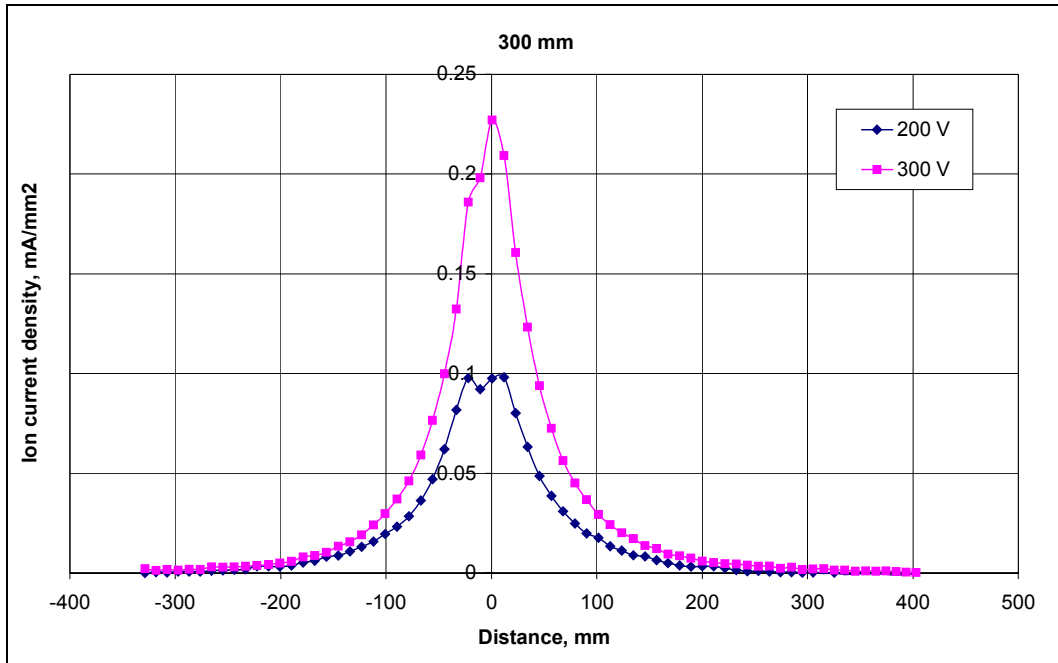


Figure 98. Distribution of ion current density at different discharge voltage of thruster: 200 V and 300 V.

An example of variation of the ion current distribution at the distance of 500 mm and voltage 300...400 V is represented in **Figure 99** (obtained by the flat probe of 5-mm diameter).

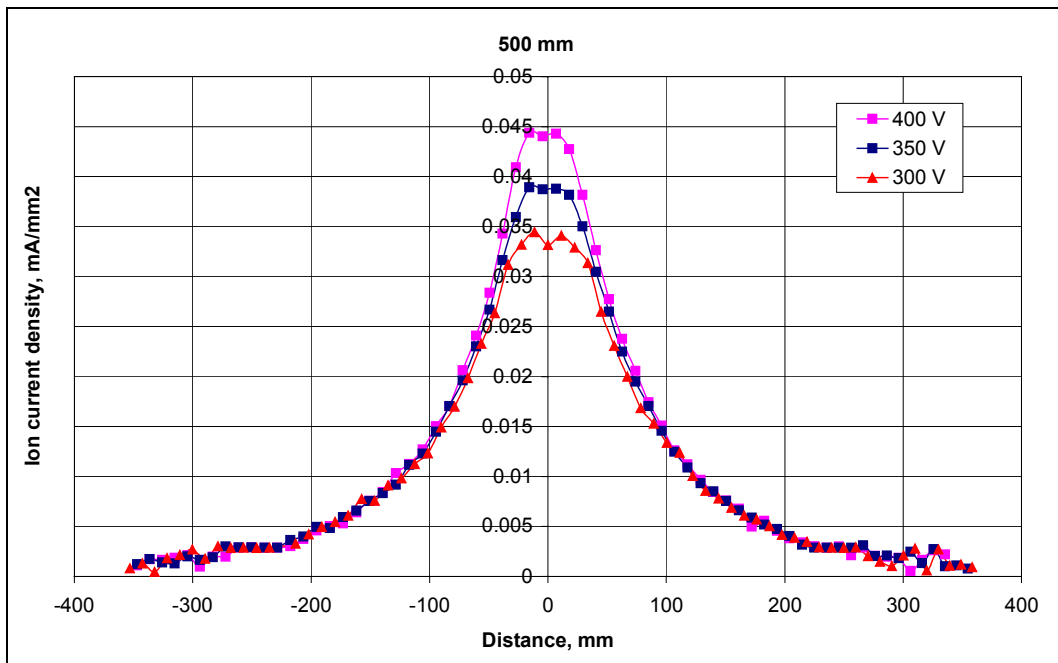


Figure 99. Distribution of ion current density at different discharge voltage of thruster: 300, 350, 400 V.

As one can see from the presented data, variation of discharge voltage results in an essential difference of the distribution of ion flow. At the same time, the differences between the values of plasma potential as well as electron temperatures are not so essential. The variations of both electron temperature and potential are much weaker in comparison with the change of discharge voltage causing it. Therefore, it can be stated that a relatively little variations in the operational mode of one of the cluster engines will not cause a noticeable asymmetry in

plumes parameters – electron temperature and plasma potential of these engines. It is important for the follow-up analysis of plumes from several thrusters, which operational modes in a cluster may not coincide.

5.3.3. Influence of test conditions on the flow characteristics

5.3.3.1. Influence of electrical circuit.

The influence of electrical circuit on characteristics of a thruster plume was tested on the basis of comparison of two electric circuits - grounded and floating. Owing to the change of circuit, a change of floating potential of a thruster when changing cathode-neutralizer characteristics is simulated.

It should be noticed that at the same time the capability of the electron component of plasma to interact with the vacuum chamber wall also varies. In the floating (not grounded) circuit the cathode potential is lower than the vacuum chamber walls one. In the grounded circuit the cathode potential is equal to the walls potential, and emitted electrons are capable to leave the cathode for the vacuum chamber wall.

In Figure 100, Figure 101, Figure 102 distributions of space potential, density of ion current and electron temperature obtained with a 5-mm flat probe at the distance of 500 mm from the thruster exit at diverse electrical circuits are shown. The thruster operated in its basic mode of 300 V, 3 A.

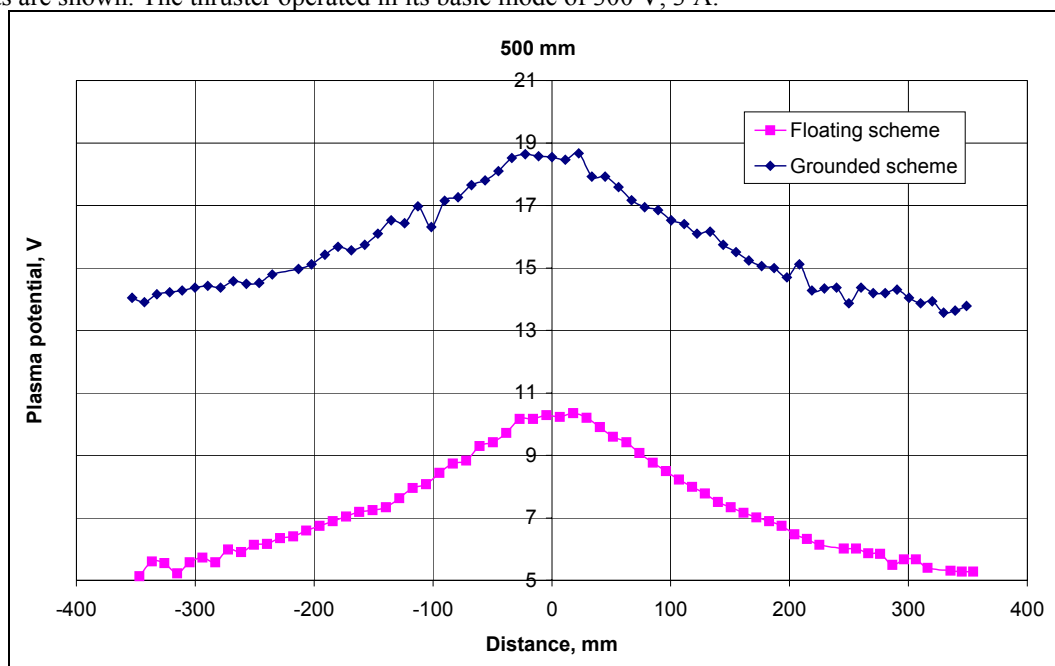


Figure 100. Plasma potential at diverse electric circuits.

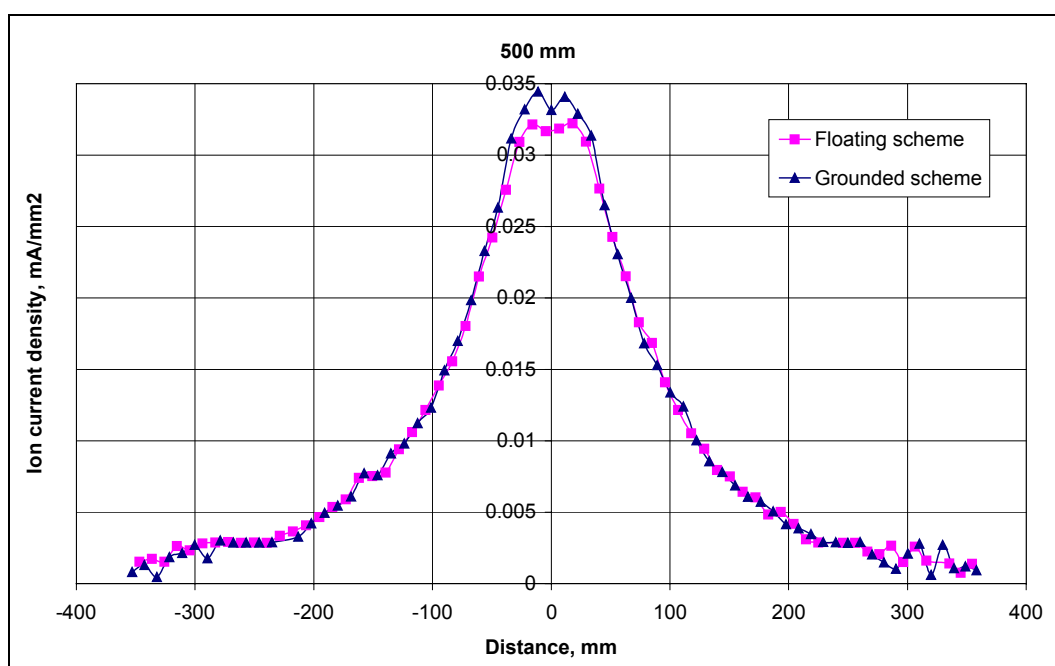


Figure 101. Density of ion current at diverse electric circuits.

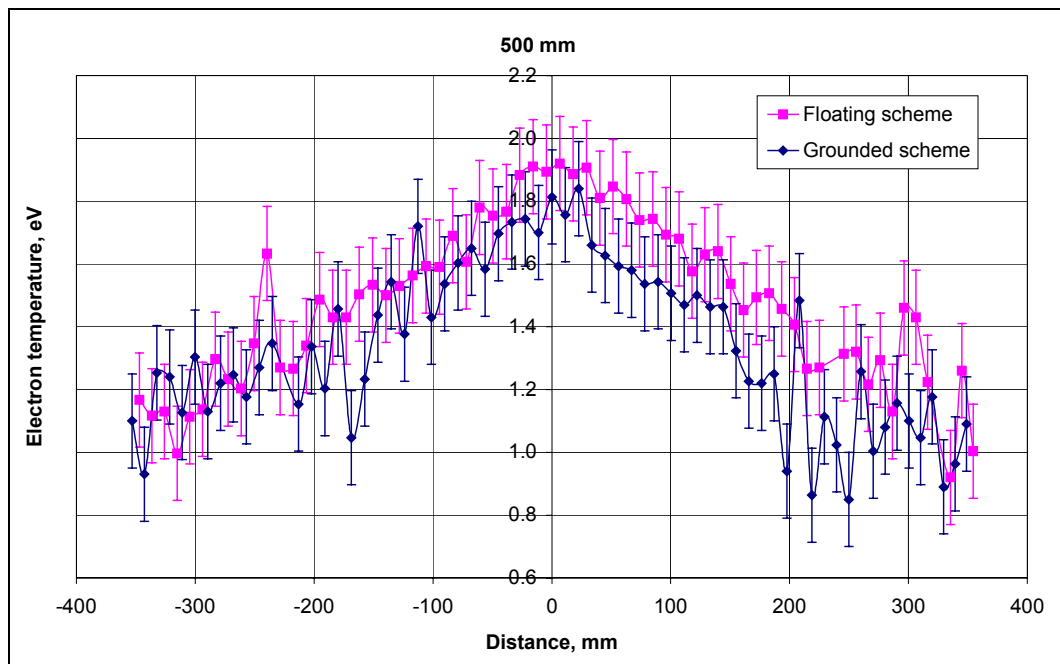


Figure 102. Electron temperature of at diverse electric circuits.

On the basis of analysis of presented data, it can be concluded that when changing the electric circuit:

- ☐ the electron temperature value and distribution remain practically the same;
- ☐ distribution of ion current varies, but the changes make some percent only;
- ☐ plasma potential varies essentially, but practically in the whole tested range the gradient of potential remains along the radius of plume. It can be stated that in the central part the potential has changed on a constant.

Even in case of floating circuit (when the cathode-neutralizer potential is lower than the one on the vacuum chamber walls) such a distribution of potential appears in the plume when the plasma potential is higher than that of vacuum chamber walls, and so, good conditions for keeping the electrons in the central part of a plume are created. It can be concluded from the above stated that the electron temperatures, gradient of potential in the central part of a plume are determined by the conditions of generation and maintenance of the secondary plasma in the domain of plasma flow spread.

In case of the grounded circuit, emission from the cathode-neutralizer makes 10...20 % from the electron current emitted in case of the floating circuit. In the latter case the cathode neutralizes both the current and the spatial charge of ion flow, and in case of the grounded circuit - only the spatial charge. In spite of this, both electron temperature and ion current density distribution in a plume are practically identical, that can be interpreted as a weak influence of operating conditions of the cathode on the said parameters.

5.3.3.2. Influence of pressure.

As it was already noticed earlier, during a cluster operation the residual pressure in the vacuum chamber is higher than that during individual thruster testing. Therefore, the influence of pressure on characteristics of a thruster plume was investigated. The upper tested value of residual pressure corresponds to the conditions of operation of a three-engine cluster with the xenon flow rate of 3.5 mg/sec in each engine. The bottom tested residual pressure corresponds to operation of one engine. The thruster worked in the reference mode of 300 V, 3 A.

Variation of residual pressure in the vacuum chamber causes significant changes in the value and distribution of electronic temperature and plasma potential (**Figure 103**, **Figure 104**). With increase of the pressure the electron temperature drops abruptly (**Figure 104**). It could be possibly accounted for cooling of electrons during interaction with atoms of residual gas. This fact is important, since the quantity of electron temperature is crucial for computer simulation of propagation of a plasma flow and its interaction with surfaces of a space vehicle. As it follows from the obtained data, the measured value of electron temperature is a function of two "quantities": both the operational mode of thruster and test conditions. Therefore, in future it is important to define the test conditions, which would enable obtaining of electron temperature values appropriate to the conditions of EP flight operation, or to develop methods of data recalculation of ground tests to the conditions of flight operation.

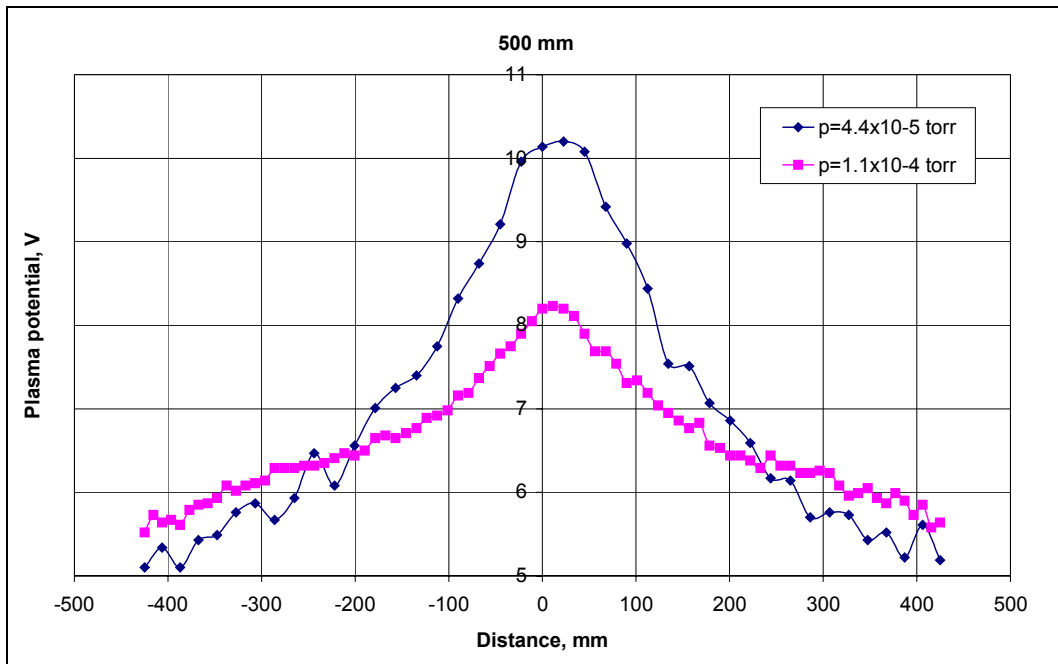


Figure 103. Plasma potential at various pressure.

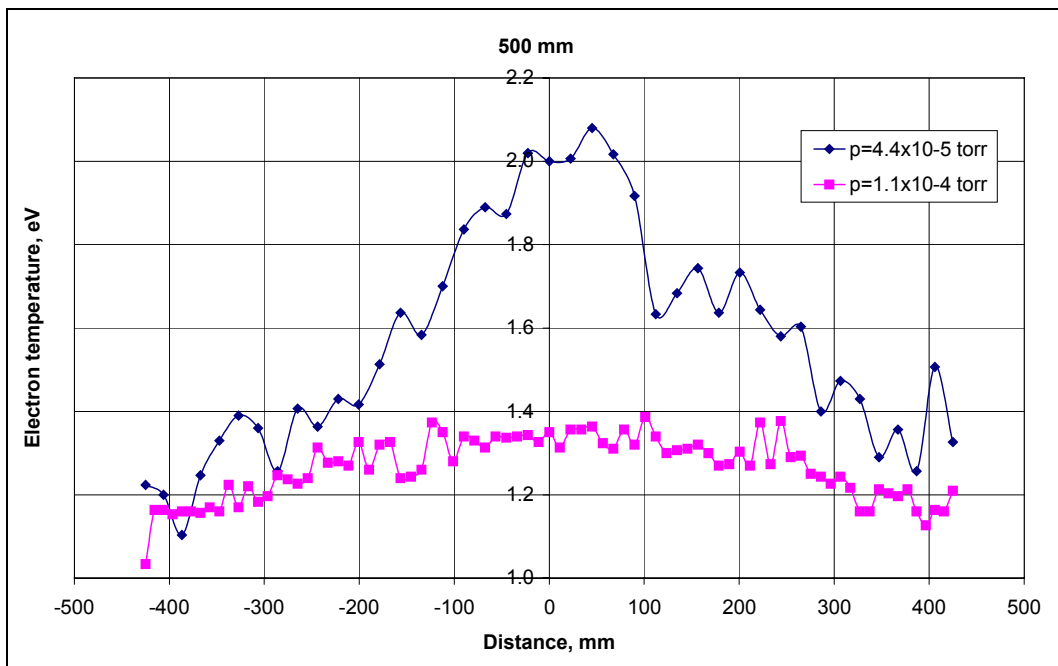


Figure 104. Electron temperature at various pressure.

5.4. Conclusion to Chapter 5.

- Measurement equipment utilizing different types of probes for plasma diagnostics have been designed, assembled and tested. Design of the oriented flat small probes has been selected as most simple one and allowed to perform fine measurements with good space resolution. In general, it can be stated that the tested measuring instrumentation under an appropriate technique enables measurement of electron temperature with the resolution of 0.1...0.2 eV, and the plasma potential - not worse than 0.2 V.
- The measured plasma parameters have been proven by independent methods and are in a good compliance with data obtained earlier. Conditions of applicability of small flat probes for electron temperature and plasma potential measurements have been identified. Significant

influence of the probe design and size on measured value of ion flow density has been determined.

- ❑ Electron temperature, plasma potential, ion energy and flow density data base of single thruster plume has been collected for different operation modes of the thruster and variable test conditions.
- ❑ Variation of residual pressure in the vacuum chamber causes significant changes in the value and distribution of electronic temperature and plasma potential. With increase of the pressure the electron temperature drops abruptly. This fact is important, since the quantity of electron temperature is crucial for computer simulation of propagation of a plasma flow and its interaction with surfaces of a space vehicle. The measured value of electron temperature is a function of two “quantities”: both the operational mode of thruster and test conditions. Therefore, in future it is important to define the test conditions, which would enable obtaining of electron temperature values appropriate to the conditions of EP flight operation, or to develop methods of data recalculation of ground tests to the conditions of flight operation.
- ❑ Study of the energy spectrum of ions in a plume cross-section has showed that there is an area of a plume with essential peculiarities. These peculiar properties result in appearance of rather fast secondary ions, which are not generated in the discharge of thruster, but in the plume. Physical nature of this phenomenon not clear and further study is required.

6. Initial characterization of the triple TAL cluster plume flow.

After the study of the single thruster plume diagnostic of the cluster plume has been initiated with a goal to get initial information about the cluster plume and to identify specifics of the composed cluster plume in comparison with the plume of single thruster. This portion of work has been performed in a frame of extension of the ISTC grant.

Cluster plume characterization was realized in two steps:

- Plume probe measurements in different cluster cross-sections. Refined in Chapter 5 probes (Figure 87) and measurement procedure were used.
- Ion energy spectrum measurements. Measurements were carried out by energy spectra analyzer. Analyzer was oriented perpendicular to the cluster symmetry axis and located at a radial distance 370 mm from the axis. As it was demonstrated in Chapter 5, such lay out provides the information about periphery of ion flux, which is the most critical from spacecraft/plume interaction point of view. Refined in Chapter 5 RPA and measurement procedure were used.

In accordance with approved experiment program the only base operation mode was chosen for characterization of the composed cluster plume. All thruster was operated at one and the same regime with the discharge voltage equal to 300 V and discharge current equal to 3 A. Electric scheme was grounded (Figure 57), and cathode-neutralizer K1 (Figure 59) at the center of the cluster. Residual tank pressure was equal to 1×10^{-4} torr.

The diagnostic equipment and test procedures for the cluster study were identical to ones used for single thruster plume study and described above.

Plume parameters measurements were carried out in three cross-sections, marked as 1, 2 and 3 on Figure 105, at the distances 300...1000 mm from the cluster exit plane.

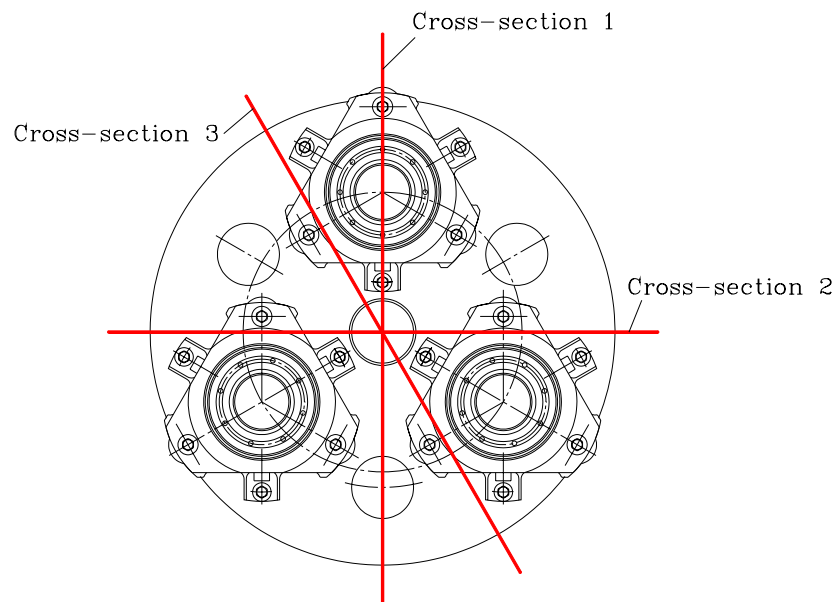


Figure 105. Cross-section map.

6.1. Ion current distribution in the cluster plume.

Typical radial ion current density distributions measured in the three cross-section of the cluster plume are given in Figure 106, distance between probe and cluster exit plane was equal to 500 mm.

Ion current peak corresponding to the plume of the thruster D1 (located at 90 mm from the cluster center – 0 mm) can be seen in the cross-section 1. Ion current density distributions measured in geometrically equal cross-sections 2 and 3 are in close agreement, and it is an indication of symmetry of the plume. Distribution of ion current density at the plume periphery is one and the same in all azimuth cross-sections.

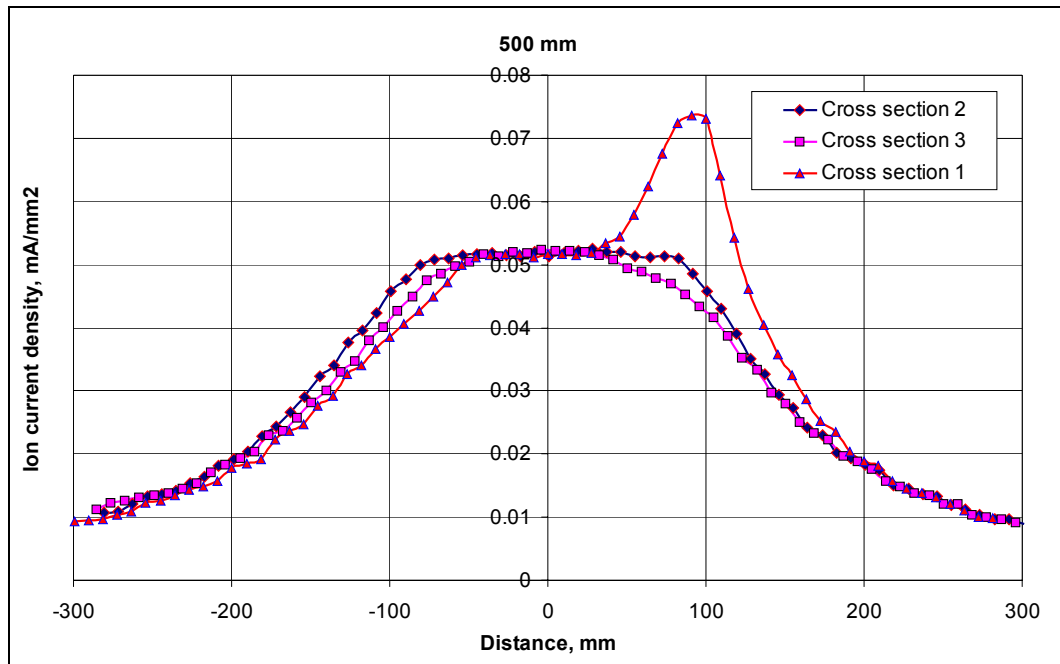


Figure 106. Distribution of the cluster ion current density.

Cluster ion current density space distributions measured at the distances 300, 500 and 1000 mm are given in Figure 107, Figure 108 and Figure 109 correspondingly.

As one can see, at the distances 300 (Figure 107) and 500 (Figure 108) mm three peaks corresponding to the plumes of three thrusters are well distinguished. With the distance increasing cluster plume transforms. At the distance equal to 1000 (Figure 109) mm plume areas corresponding to each thruster are almost disappeared. Thus, at long distances plume generated by three thrusters becomes similar to a plume generated by some single thruster located at the center of the cluster.

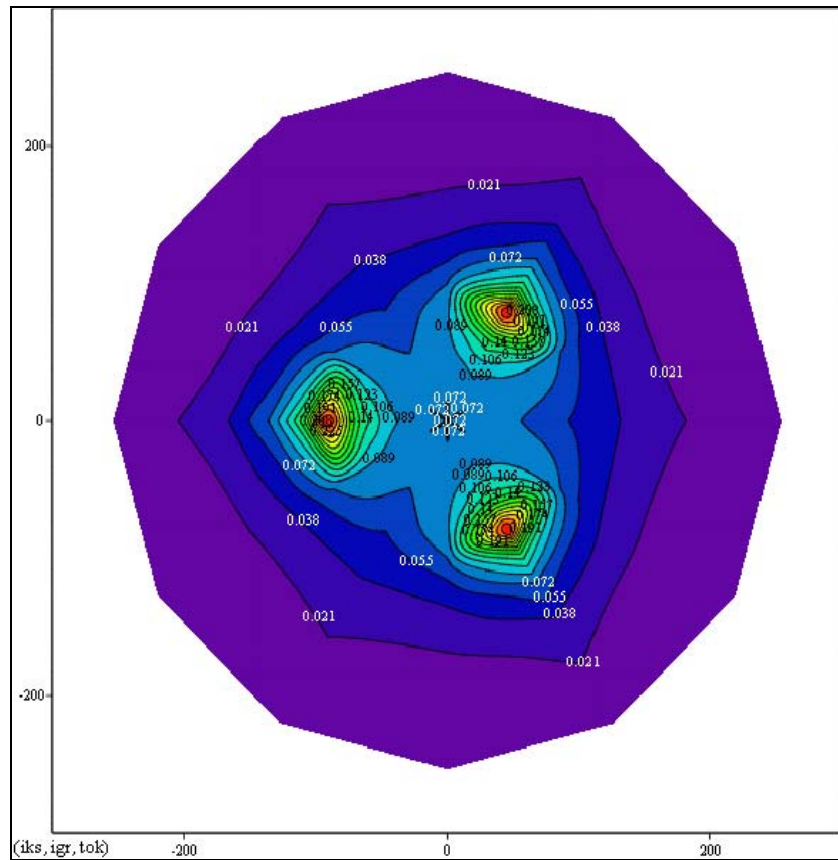
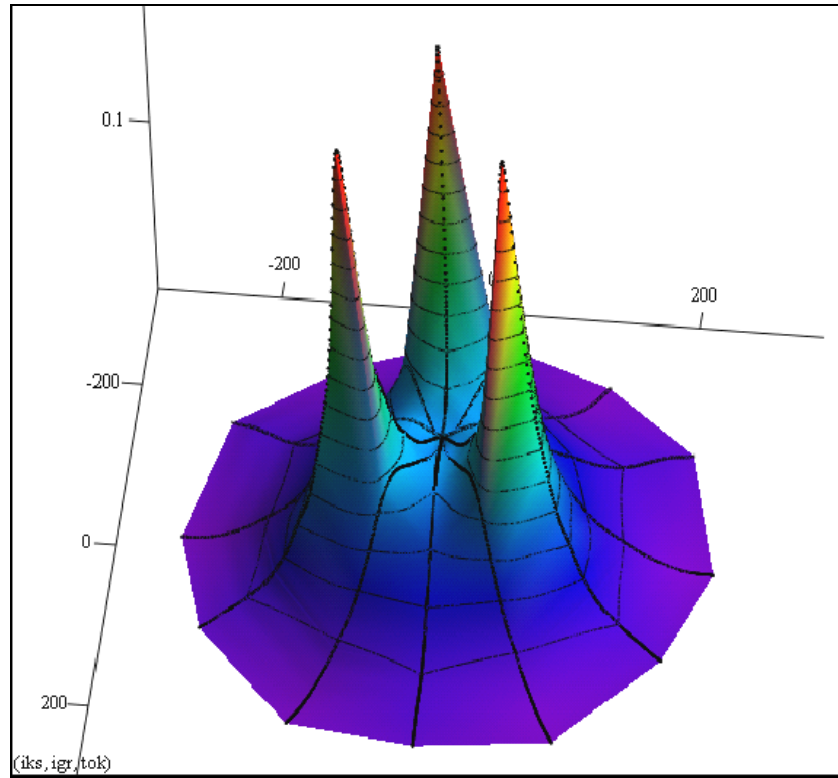


Figure 107. Cluster ion current density distribution. 300mm.

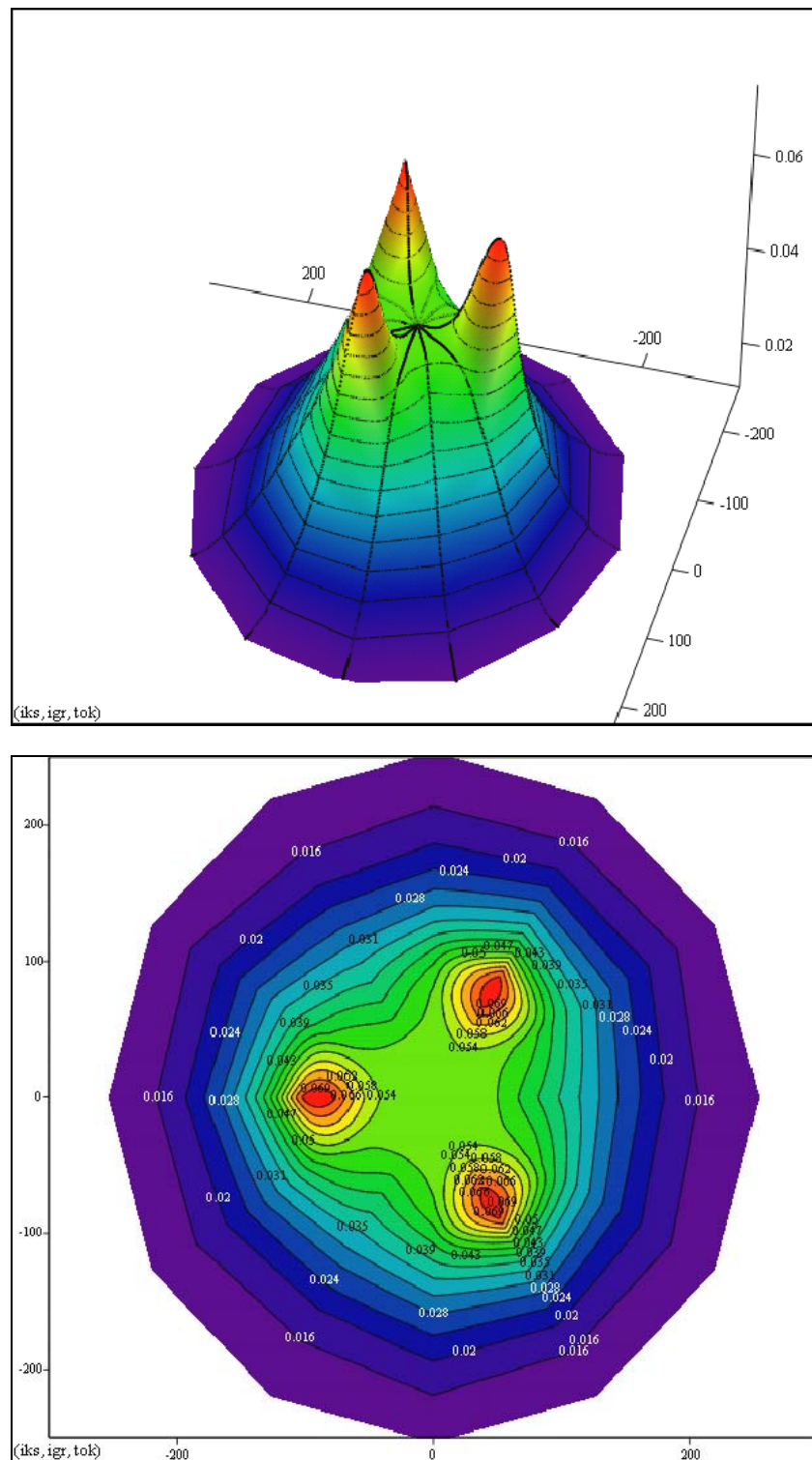


Figure 108. Cluster ion current density distribution. 500mm.

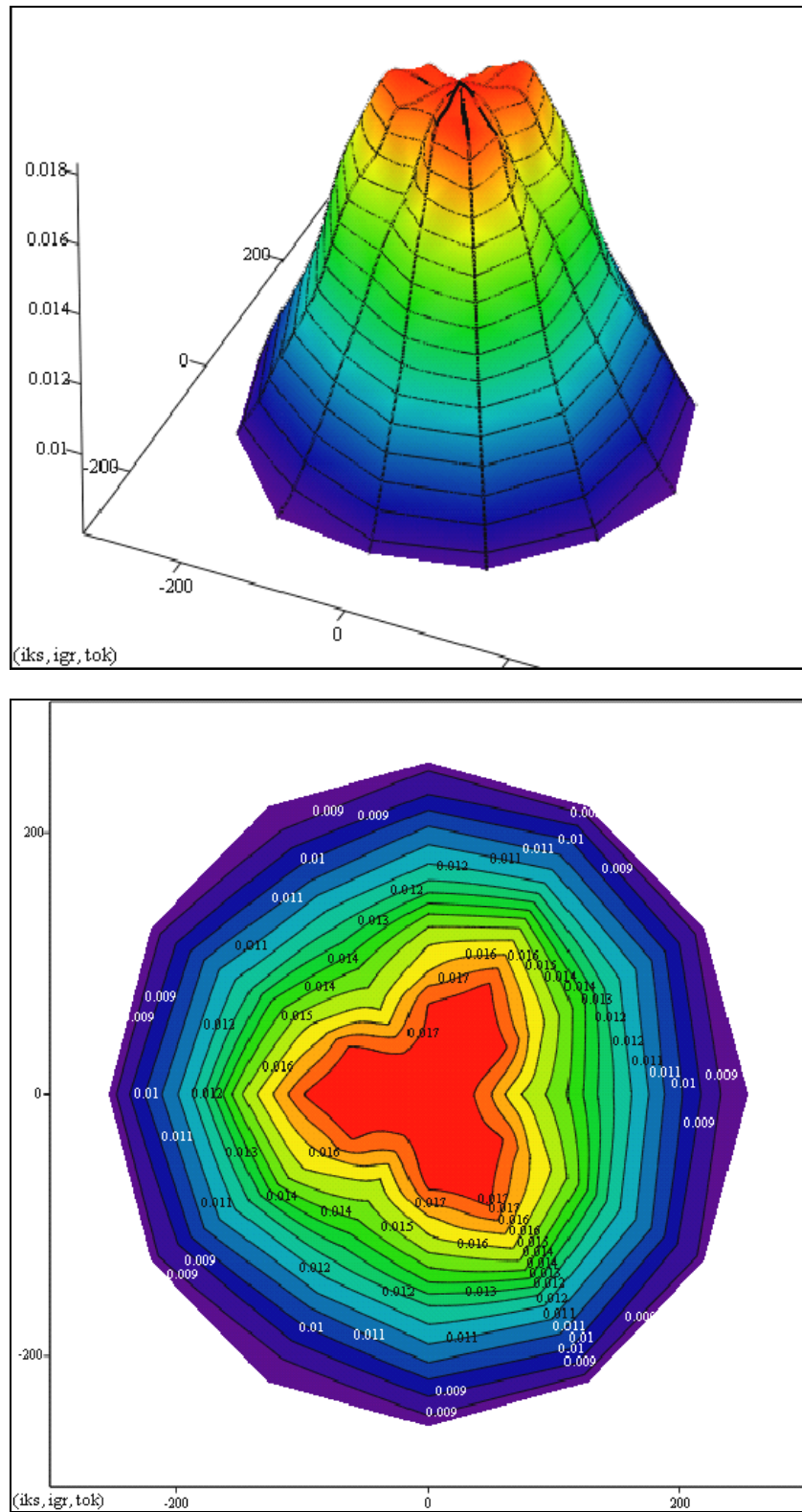


Figure 109. Cluster ion current distribution. 1000mm.

Comparison of measured cluster plume profile with calculated summa of the individual thruster plumes was made to verify additivity of the plumes. Corresponding data are shown in Figure 110. Measured single thruster D1 (red curve) and cluster (blue curve) plume profiles are given in this figure. Black curve in Figure 110 corresponds to the calculated cluster plume profile, obtained by mathematical adding of three single thruster ion current distributions. One can see, that mathematically obtained curve differs from the measured one in the high density area, which corresponds to the thruster D1 axis, but in remaining (periphery) areas both curves coincide. This difference exists in the central high density zone of the plume at all tested distances (300, 500 and 1000 mm) from the cluster, and radial dimension of this zone increases with the distance increase.

Obtained data allow to conclude, that the cluster plume distribution is not simple sum of distributions obtained for single thrusters operation.

As far as in all studied modes (as it was shown above) the cluster thrust is the sum of the thrust values of individual thrusters, one can assume, that the ion flux generated by each operated thruster in cluster corresponds to the ion flux generated by thruster operated individually. Therefore, the most probable reason causing the difference between measured and mathematically obtained cluster plume profile, is difference of the charge exchange conditions for the cluster plume as compared with plume of the thruster operated individually. Should be noted, that measured tank pressure in all compared cases was one and the same, so average density of the neutrals was one and the same also, but local variations of the neutral atom density could be the reason of observed phenomenon.

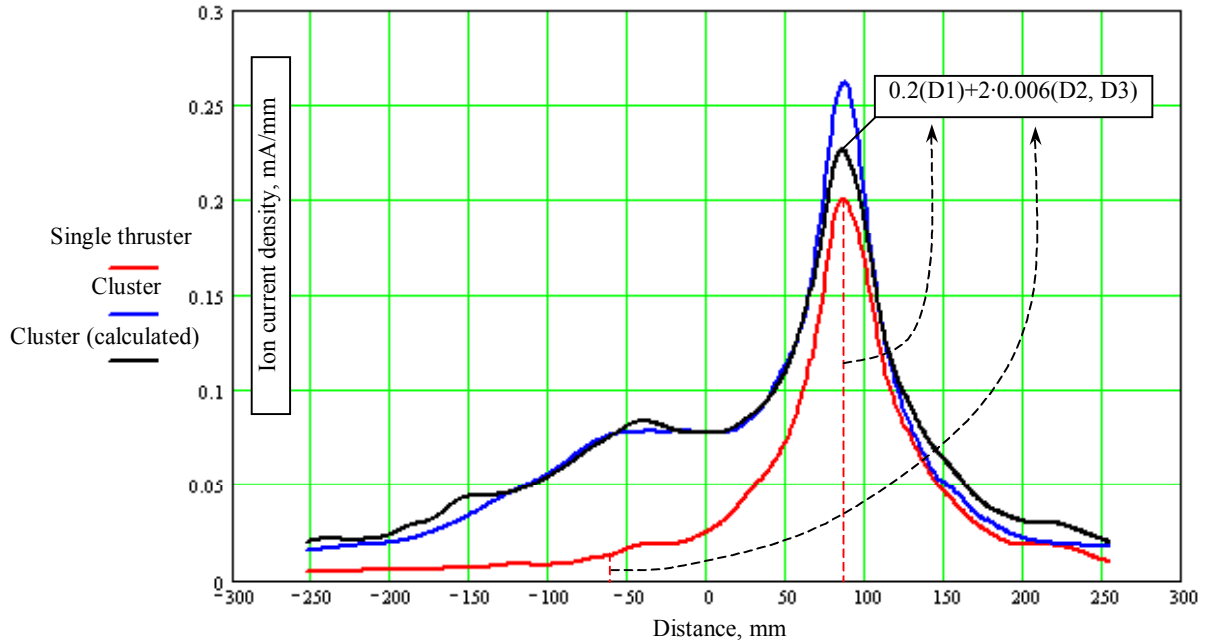


Figure 110. Ion current density distribution of the cluster compared with a single thruster.

6.2. Plasma potential and electron temperature in the cluster plume

Measurements of the plasma parameters were conducted in cross-sections 1,2,3 (Figure 105) of a plume at the distances 300, 500 and 1000 mm from the cluster exit plan..

For example, plasma potential distributions at the cross-section 1 for both the cluster and single thruster D1 measured at the distance 500mm from the exit plane are represented in Figure 111. Corresponding distribution of the ion current density in this cross-section is given in Figure 106. As is obvious, plasma potential distribution of the cluster has symmetrical view, in spite of nonsymmetrical distribution of ion current density in this cross-section. And expected peak of the potential associated with center of D1 thruster plume did not appear. Besides that smoothing of the plasma potential distribution in radial direction takes place. In case of the cluster total drop of plasma potential from the center to periphery is 2 V, while for single thruster – 3.5 V.

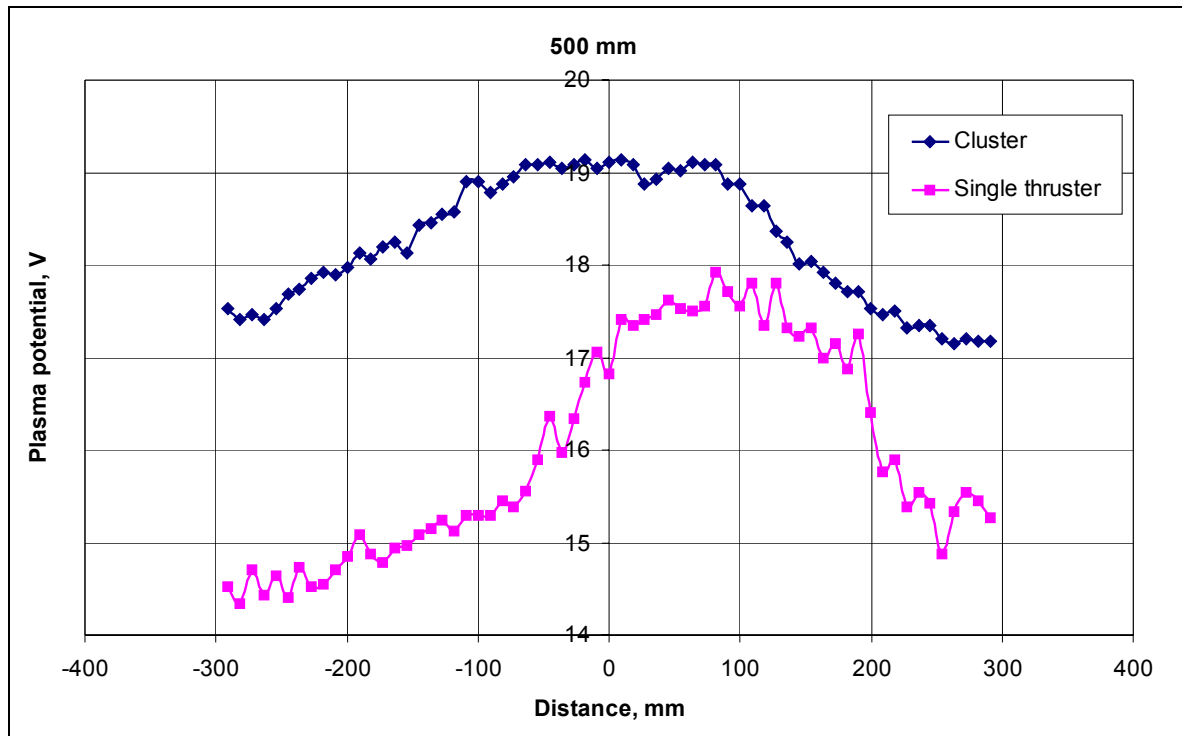


Figure 111. Both cluster and single thruster plasma potential distribution.

Electron temperature distributions in the cross-section 1 of the cluster and single thruster D1 plumes, measured at the distance 500 mm from cluster assembly exit, are shown in Figure 112.

Electron temperature distributions in the different cross-sections 1,2 and 3 of the cluster plume, measured at the distance 500 mm from the cluster exit plane, are represented in Figure 113.

As it can be observed from Figure 112, electron temperature distribution in the cluster plume has more uniform view as compared with single thruster distribution. Data Figure 113 show that electron temperature does not essentially change in radial and azimuth directions in the observed area of the cluster plume.

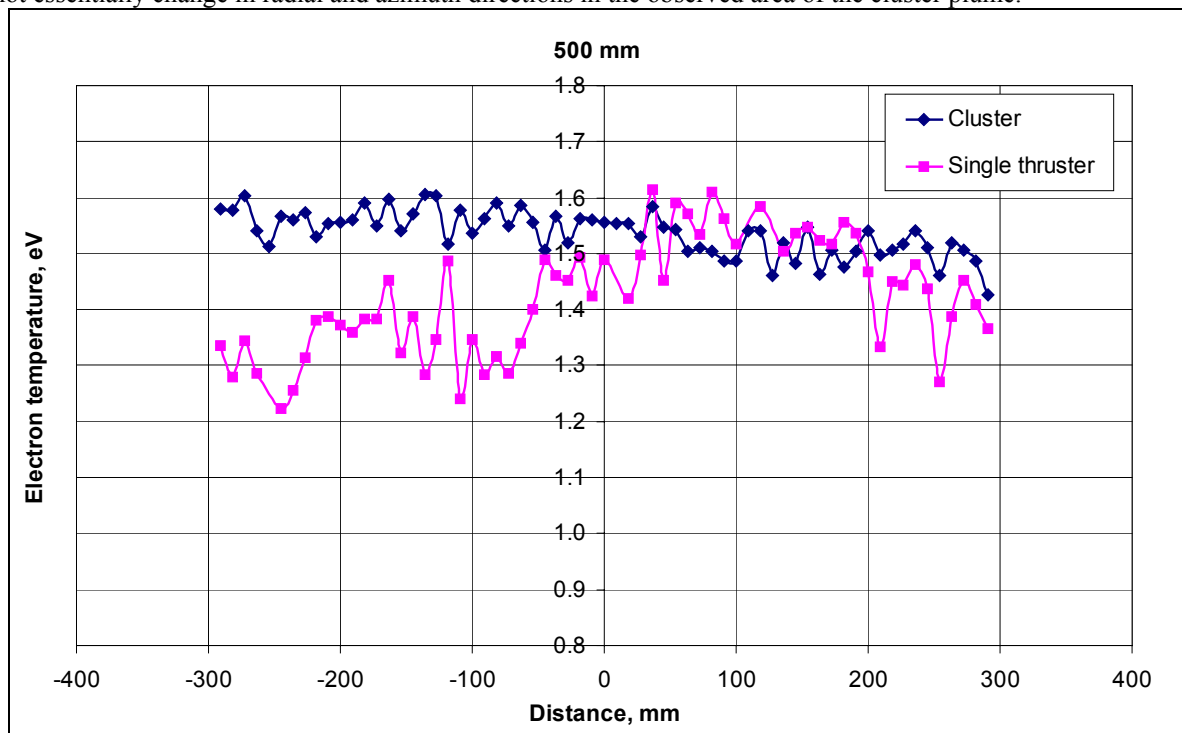


Figure 112. Electron temperature distribution for the cluster and single thruster plumes.

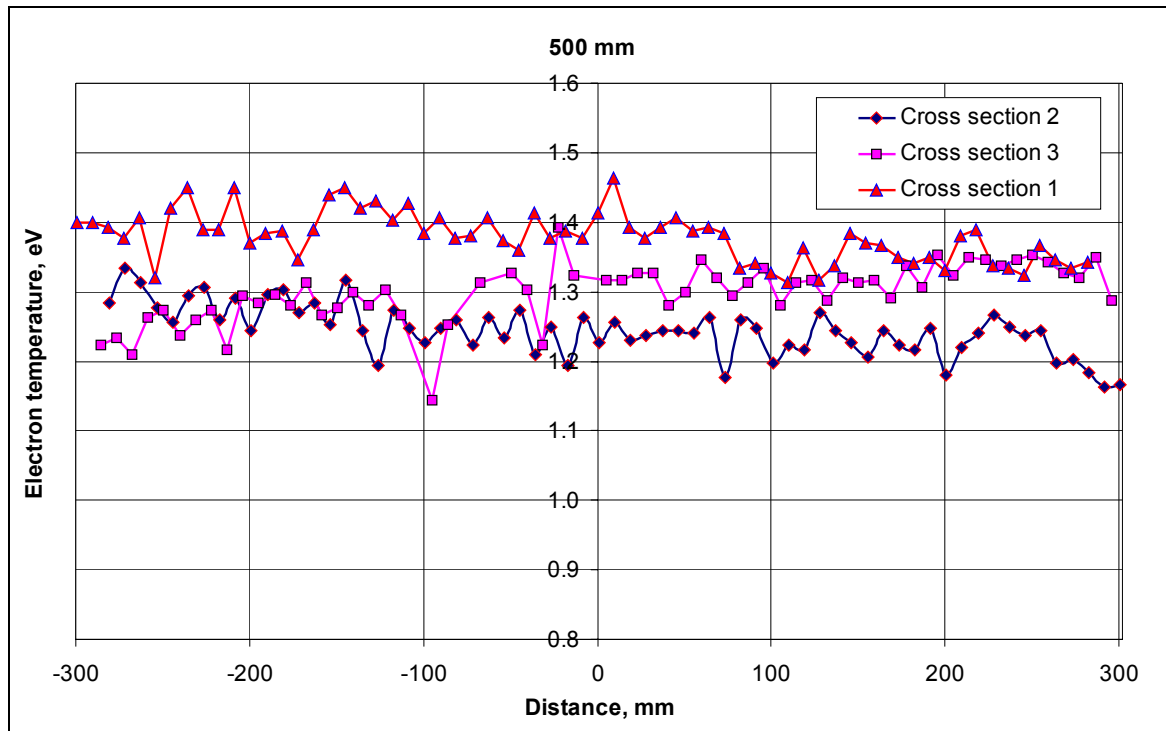


Figure 113. Electron temperature distribution in different cross-sections of the cluster plume.

During series of experiments, which were conducted to collect statistic, instability of the cluster plume plasma potential was detected. As an example, plasma potential distributions, measured in cross-section 1 and 2 during different experimental days are shown in Figure 114. According to Figure 114, the plasma potential distributions measured in one and the same cross-sections and at one and the same cluster operation mode may differ from each other in both absolute value and distribution curve view. In spite of plasma potential distributions difference, ion current density and electron temperature distributions were invariable. Since controllable cluster parameters such as discharge currents and voltages, magnetic system currents, cathode and anode mass flow rates, residual pressure in vacuum chamber were retained at the constant level during all experiments, then their influence on measured plasma potential can be excluded. Observed instability can be caused by some uncontrolled process influencing ion flux neutralization, that in one's turn depends on both cathode operation condition and secondary electron emission from the vacuum chamber walls.

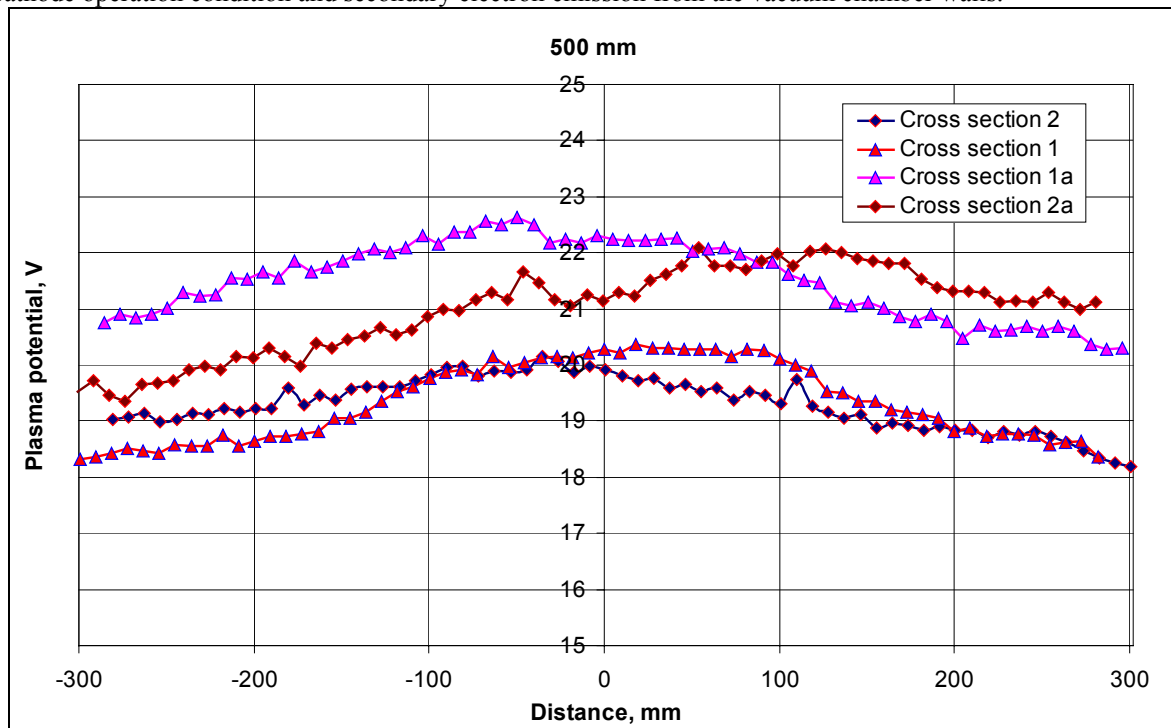


Figure 114. Plasma potential variation.

Detected instability necessitated to perform special experiment with single thruster D1 with a goal to identify influence of neutralization effects on the plume characteristics. In the context of the experiment three electric schemes of connection thruster D1 and cathode K1 were tested. In these schemes neutralization processes of the plume varies, and it allows to identify correlation between this variation and measured plasma plume parameters.

The first scheme – called "grounded" (Figure 57), was basic one for all performed measurements of the cluster plume. Thruster body and cathode emitter are connected to the vacuum chamber ("ground"). The necessary electron current from the cathode to neutralize space charge of the plume in this scheme is about 10% of the thruster ion current. As it was determined earlier, in this scheme influence of the cathode parameters on the studied plume is minimal.

The second scheme is "ungrounded" one (Figure 57). Thruster body and cathode emitter are disconnected from the "ground" and are floating in respect to vacuum chamber. Unlike to the first scheme, electron current from the cathode has to be equal to the thruster ion current.

The third scheme is "grounded" and similar to the first one, but the thruster body was connected to the another cathode electrode - "keeper", and both are connected to the vacuum chamber. This case is called "inverse cathode scheme". In this scheme influence of the cathode on the plume is also minimal. But in addition, potential influence of the voltage, applied between emitter and keeper to keep auxiliary discharge in the cathode, on the plasma plume potential is excluded. The plasma plume contacts only with grounded surfaces.

Thruster D1 operated at operation point 300V, 3A was used. Residual pressure in vacuum chamber was 4.4×10^{-5} torr.

Plasma potential distributions in the D1 plume, measured at the distance 500mm from thruster exit are shown in Figure 115. Curves corresponding to scheme 1 and 2 have similar view but different absolute values, it has been already demonstrated in Chapter 5 (Figure 100). However, in the case of scheme 3, which is grounded like scheme 1, curve of the plasma potential coincides with one, measured under the scheme 2 conditions.

Despite the difference in plasma potential values, electron temperature (Figure 116) and ion current (Figure 117) distributions in the case of all three schemes are in close fit.

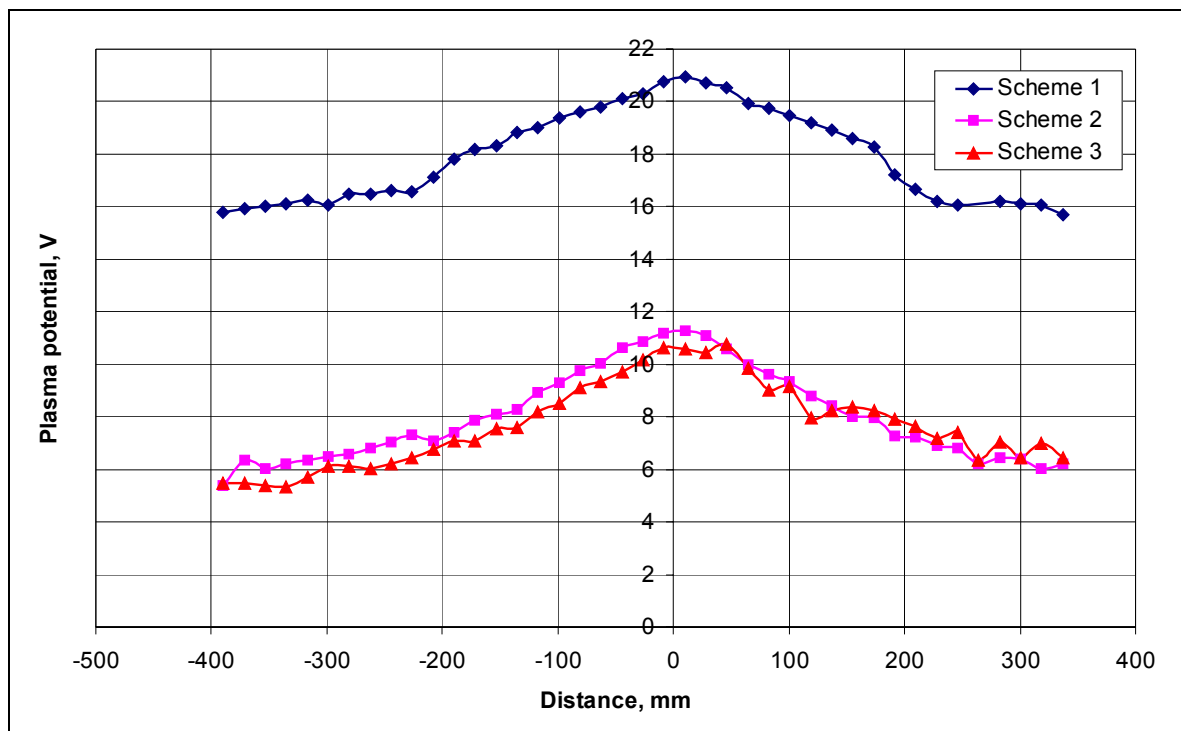


Figure 115. Plasma potential distribution in the plume of D1 thruster operated in different schemes.

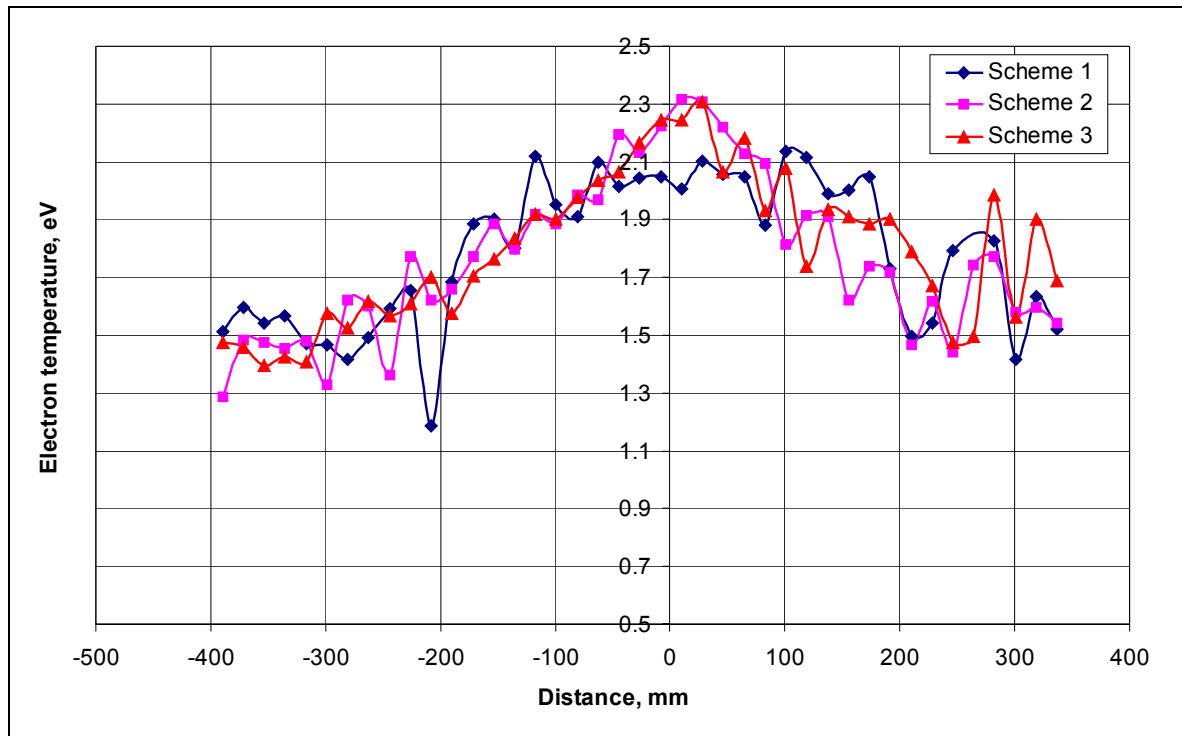


Figure 116. Electron temperature distribution in the plume of D1 thruster operated in different schemes.

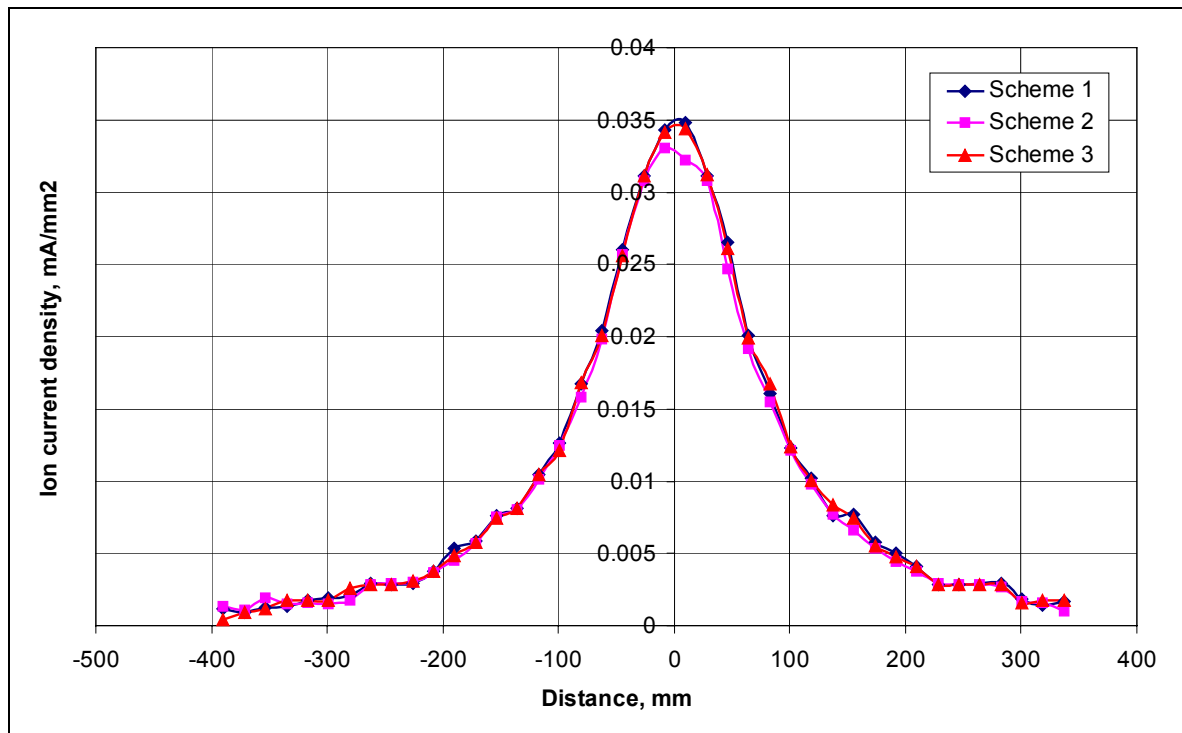


Figure 117. Ion current density distribution in the plume of D1 thruster operated in different schemes.

Thus, experiment conditions and specific of the plume neutralization have essential influence on plasma potential measurements. Probably in the case of the cluster operation some conditions, which lead to spontaneous variation of plasma potential, can arise in plasma volume.

It can be assumed, that similar spontaneous variations always exist, but for single thruster plume the effect is small and it is almost undetectable by used diagnostics, while in the complex cluster plume such effects are significantly amplified.

6.3. Cluster plume ion energy spectrum study.

As it was shown in Chapter 5 and described above, along the plume there is an area with intensive ion fluxes directed perpendicular to the thruster axis. These fluxes can cause essential influence on spacecraft

elements, but there is no existing mathematical models of the plume describing this phenomenon. So that, primary interest for cluster plume energy spectrum diagnostics was to identify and to study similar effects in the composed plume.

While measuring energy spectra, analyzer was oriented perpendicular to the cluster symmetry axis and located at a radial distance 370 mm from the axis.

Measured cluster plume ion energy spectra distributions obtained at different locations of the RPA along the cluster plume are given in Figure 118. The typical distributions have pronounced low voltage peak and some diffuse high energy ions area, which are similar to ones obtained for single thruster (Chapter 5, Figure 94). In addition the new kind of energy spectrums were observed (see Figure 119).

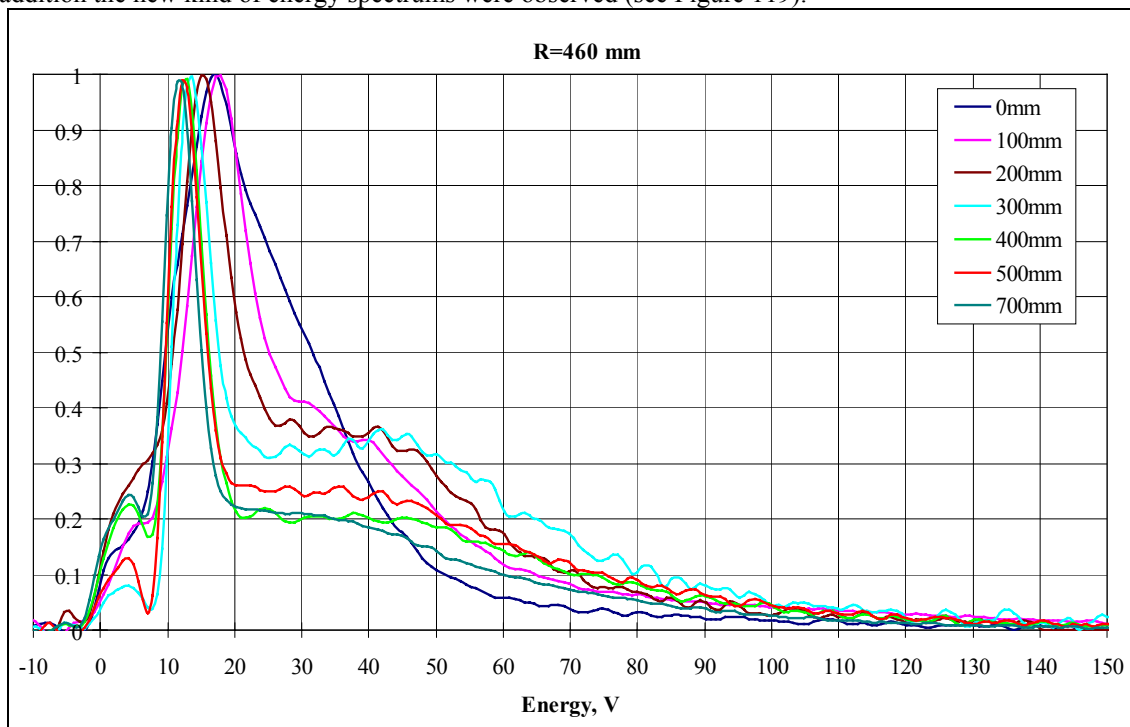


Figure 118. Ion energy spectrum.

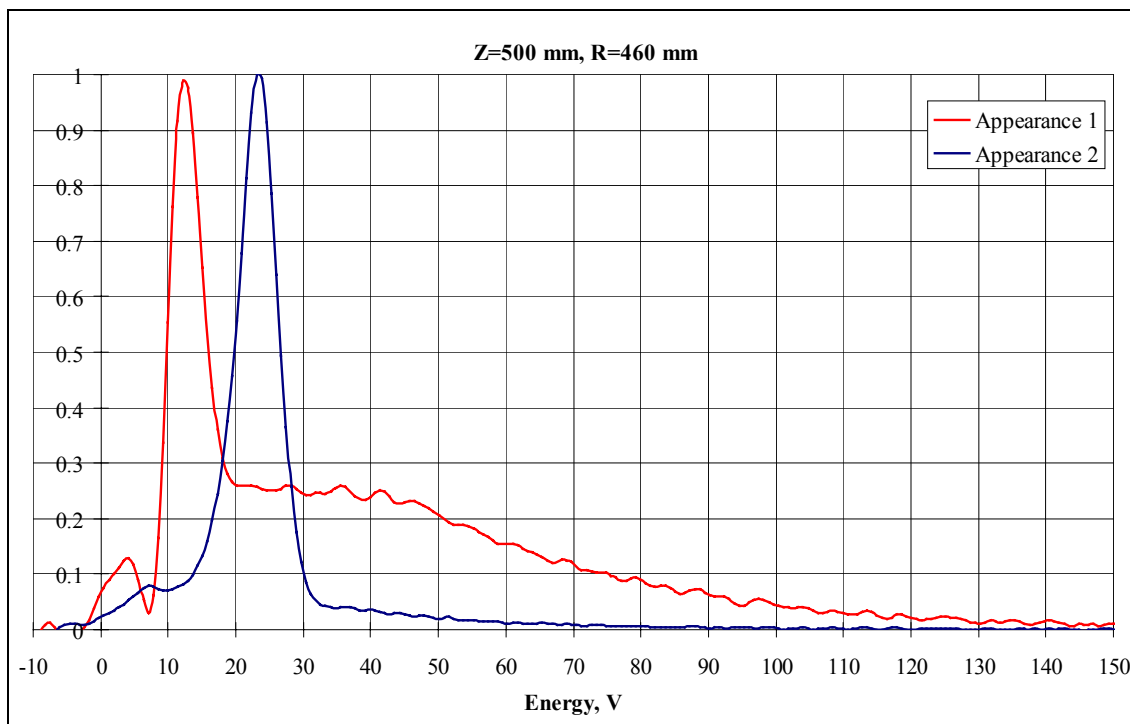


Figure 119. Ion energy difference.

Presumably such difference can be explained by influence of the cluster plume plasma potential variation (see above for detail). To prove or to disprove the assumption ion energy distribution measurements were conducted on the cluster and single thruster in different electrical schemes used during plasma potential study (see previous issue).

Cluster plume ion energy distributions obtained at 500 mm from the cluster exit plane in grounded, ungrounded and grounded with inverse cathode schemes are given in Figure 120. One can see that energy spectrum varies with variation of the scheme. Nevertheless, character of all spectrums, obtained at that day (Figure 120) differ from ones in previous tests (Figure 118). Tests of the single thruster at that day in different schemes allowed to identify the only conditions when measured ion energy distribution turned back to the character shown in Figure 118. It was the "fourth" scheme: "ungrounded" with inverse cathode connection. The corresponding energy spectrum is given in Fig. 16. Unfortunately, due to safety reasons it was impossible to test the cluster in this "fourth" scheme also.

The data show, that measured energy spectrums significantly depend on test condition. Shift of low voltage peak location and transformation of the diffuse high energy portion of the ion flux can be seen for different schemes.

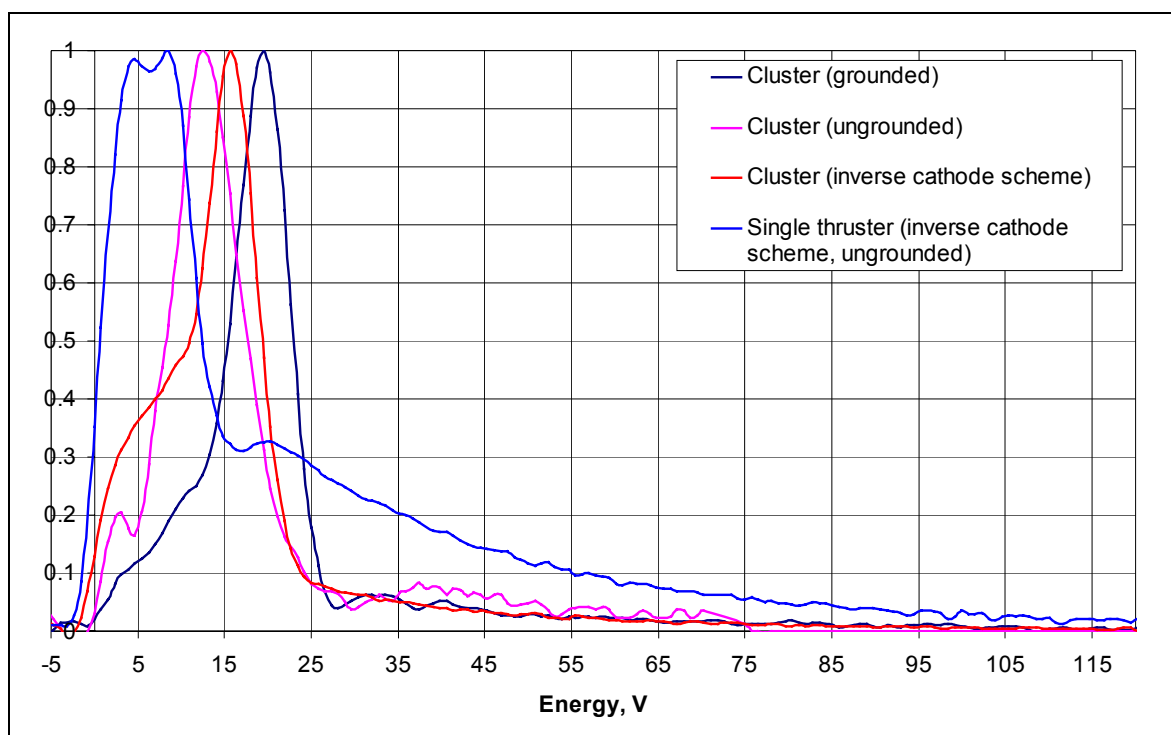


Figure 120. Ion energy spectrums measured in different electric schemes of the cluster.

Thus ion energy spectra measurements, as well as plasma potential probe measurements, depend on plume neutralization specific and experiment conditions. Spontaneous process appearing in the composed cluster plume can be the reason of observed variation of energy spectrums. To reveal the cause of such process appearing further research is needed.

6.4. Conclusion to Chapter 6.

The cluster plume study provided initial experimental database for the complex cluster plume and allowed to identify specific features of the cluster plume in comparison with a one of single thruster.

Analysis of the ion current density measurements showed that in the central zone of the cluster plume the ion current is not a simple sum of the currents measured for a single thruster, while the peripheral regions the cluster plume can be considered as summa of the plumes of individual thrusters. Measured values of electron temperatures and plasma potential in the cluster plume are of the same order as those measured for a single thruster. General trends in ion energy spectrums obtained in the cluster plume are similar to those for a single thruster. However, in part of the cluster tests some instability has been observed. This instability resulted in appearance of different energy distributions of ions accelerated perpendicular to the cluster axis. To clarify the instability nature further study is necessary.

Complex character of the triple-thruster plume transforms in the far-field plume regions. Ion current density peaks associated with individual plumes disappear and the ion current density distribution becomes similar to the distribution in a single thruster plume, as if it would be placed at the center of the cluster set.

7. Modeling of the Hall effect thruster plume flow parameters and comparison with experimental data

7.1. Mathematical model of EP plume.

In conditions of space flight EP thruster plasma plume flows out in an environment characterized with a low density of neutral atoms in the space vehicle environment ($n_n \leq 10^9 \div 10^8 \text{ cm}^{-3}$). In this case expansion of plasma can be considered as free, if the plasma doesn't have electrical contact with the space vehicle body or this contact is faint. Unlike in space conditions, during EP operation in vacuum tank the electrical contact of plasma with conductive walls of the tank is very tight. It results in distorting distribution of both electric potential and currents in the plume, i.e. distorting of dynamic characteristics of the plasma jet. This must especially be true at the periphery of the jet. In this region secondary plasma is effectively produced by interaction between primary plasma flow and background gas. The secondary plasma in laboratory is three-four orders of magnitude denser than in space conditions. It affects directly on both the expansion of primary jet and a distribution of electric potentials inside it and, finally, on dynamic characteristics of the plasma flow.

During investigations of plasma plume characteristics it was discovered that their dynamics is influenced by intrinsic electric and magnetic fields^{93,94}. During those investigations the processes, which allow controlling plasma dynamic were studied. It is possible to accelerate and slow down the flow⁹⁵ for the purpose either of focusing or expanding⁹⁶ and even diverting it from the initial trajectory by means of controlling the intrinsic fields and currents^{96,97}.

Main goal of the present development of the EP plasma plume model was to describe correctly the distribution of electric fields and currents inside the jet taking into account abovementioned electro-physical properties of the plasma plumes.

In the plasma plumes of modern EP thrusters the plasma is almost completely ionized. In particular in Hall-effect thrusters (HET) and ion engines 95% and more of propellant is ionized. And it becomes higher with modernization of the propulsion systems. That is why influence of neutrals on the characteristics of the main plume in space conditions is low. On the contrary, in a laboratory facilities influence of neutrals onto the flow properties may be noticeable^{98,99}.

The values of plasma parameters in the jet make the effective frequency of collisions rather important^{96,100}. Besides, in acceleration channel and in initial area of the plume, where ions leave the fields of accelerator and ion beam interacts with plasma of cathode-neutralizer, different instabilities¹⁰¹ occur and intensive fluctuations are generated^{102,103,104}. Many types of these beam-plasma fluctuations may be considered as scattering centers¹⁰⁵ for both electrons and ions. Due to this phenomenon "effective interaction" mean free path of electrons becomes substantially smaller than characteristic gradient of the plasma parameters and utilization of continual approaches for description of the rarefied flow such as EP plume becomes quite justified. The kinetic method, which takes into account the field oscillations, should give more precise solutions, indeed. However, the large laboriousness of the kinetic task makes simplification of the problem solutions highly desirable. Modern kinetic models of a plume are realized with the use of approximate description of stationary electric field distribution in the plume^{106,107} and without taking of pulsing fields into consideration. Actually, both approaches (continual and kinetic) are approximate: their accuracy can be examined only by comparison with experimental results.

To describe the dynamic characteristics of a jet we have used a set of the Braginskiy equations for two-component plasma¹⁰⁸. These equations take into account the effect of electrical and magnetic fields as well as the effect of electric currents on the dynamic of the jet. Particularly, the equation takes into account thermoelectronic and thermomagnetic effects. Many terms of these equations of both momentum and energy variation are bonded with the Onzager relations. These relations, in turn, assume existence of self-similar solutions for many problems. The feature of a self-similarity is prevailing in nature. It was proved many times that real distribution, which is not self-similar at the beginning, afterwards transforms into a self-similar one¹⁰⁹. This feature is valid for the EP plumes also: results of experimental tests and numerical calculations demonstrate that plasma flow, which is hollow-like at the initial section, then transforms into a self-similar one.

Solution of the Braginskiy system for two-dimensional and three-dimensional plumes has been obtained in the self-consistent form^{110,111}. A plasma plume exhibits the 3D- shape under effect of magnetic field, when the velocity of the plasma flow is directed at the angle of a vector of geomagnetic field.

Criteria may be introduced, which allow determining the plume flow regime. The criteria and involved parameters are as follows:

$$M = \left(\frac{m_i u^2}{\gamma T} \right)^{1/2} - \text{Mach number}$$

$S = \frac{\sigma u^2 B^2 \pi a^3}{2 \dot{N} T}$ - parameter of magnetic interaction (Ampere parameter) characterizes the influence of magnetic field on a plasma flow¹¹¹. When $S < 1$ – magnetic field does not influence on plasma dynamics. When $S > 1$ - magnetic field influences essentially on plasma dynamics

$\Pi = \frac{a T_e \sigma}{\dot{N} e^2}$ - this parameter characterizes a comparative role of transfer processes in plasma, particularly its

heat conductivity¹¹⁰. When $\Pi < 1$ – a flow expands adiabatically, and when $\Pi > 1$ – it is isothermal.

β - pitch angle between a vector of magnetic induction and flow velocity.

$Kn_e = \frac{\lambda_{CEX} a'}{a}$ - Knudsen number for ions.

Here: σ - plasma conductivity, T – temperature, u - velocity, $a = a(x)$ – transverse size of a jet; \dot{N} - ion flow rate in a jet; B – induction of magnetic field, m_i – ion mass, e - ion charge; γ - adiabatic exponent, λ_{CEX} – ion mean free path for charge-exchange processes.

For the purpose of simplification of the initial system we used two small parameters, which are practically always realized in a HET plume:

$\frac{1}{M^2} \ll 1$ - the flow is hypersonic ,

$a' = \frac{da}{dx} \ll 1$ - the beam is narrow and expands weakly.

Smallness of these parameters means that longitudinal gradients of basic characteristics of a plume are markedly less than transverse gradients.

In presented work we compare our mathematical model with experimental data of HET plumes. For these plumes the following values of the criterions are realized: $S \ll 1$, $M^2 \gg 1$, $\Pi \geq 1$, $Kn \sim 1$. Therefore the Braginskiy system of equations can be written as follows:

$$\nabla(n\vec{u}) = 0,$$

$$\nabla j = 0,$$

$$m n \vec{v} \cdot \nabla \vec{v} + \nabla(nT) - \vec{j} \times \vec{B} = F_i + F_e, \quad T = T_e + T_i,$$

$$-\nabla \varphi + \vec{v} \times \vec{B} + \frac{1}{en} \nabla(nT_e) - \frac{1}{en} \vec{j} \times \vec{B} = \frac{\vec{j}_{\parallel}}{\sigma_{\parallel}} + \frac{\vec{j}_{\perp}}{\sigma_{\perp}} + \frac{1}{en} \vec{R}_T,$$

$$\frac{3}{2} n \vec{v} \cdot \nabla T + n T \nabla \vec{v} = \frac{j_{\parallel}^2}{\sigma_{\parallel}} + \frac{j_{\perp}^2}{\sigma_{\perp}} + \frac{\vec{j}}{en} (\vec{R}_T - \nabla p_e) - \nabla \vec{q} + Q_e + Q_i, \quad \vec{q} = \vec{q}_e + \vec{q}_i - \frac{5}{2} \frac{\vec{j}}{e} \nabla T_e$$

$$\frac{3}{2} n \vec{v} \cdot \nabla T_i + n T_i \nabla \vec{v} = -\nabla q_i + Q_i + Q_{\Delta},$$

Here:

$n_i = n_e = n$ – concentration of the plasma components;

\vec{v} – ion flow velocity;

m, e – mass and charge of an ion;

B – induction of the magnetic field;

$\vec{j}_{\parallel}, \vec{j}_{\perp}$ – current density along and across \vec{B} ;

$\sigma_{\parallel}, \sigma_{\perp}$ – conductivity along and across \vec{B} ;

T_e, T_i – temperature of electrons and ions;

p_e, p_i – pressure of electrons and ions;

φ – electric potential;

\vec{R}_T – thermal force;

F_e, F_i – forces of viscosity;

\vec{q}_e, \vec{q}_i – heat fluxes;

Q_i, Q_e – heat flux caused by viscosity;

Q_{Δ} – heat exchange flux between electrons and ions.

These equations accurately describe the effect of electrical and magnetic fields and also effect of electrical currents on the plasma flow dynamics. They also take into account thermoelectronic and

thermomagnetic effects. Velocity gradients and energy exchange are small in the plasma flows released in vacuum by all modern electrical thrusters. Therefore, we can neglect all terms that describe viscosity effects ($F_{e,l}$, $Q_{e,i}$) and energy exchange between electrons and ions (Q_A).

Special software codes for description of expansion of hypersonic flow of fully ionized plasma have been designed in TsNIIMASH. Self-similar models (SSM) of primary ion flows are developed for the following cases:

1. $S \ll 1$, $II \ll 1$. The flow adiabatically expands in vacuum; the influence of magnetic field is insignificant. This mode is realized in the proximal zone of the dense low-temperature plume of arcjet-type thrusters.
2. $S \ll 1$, $II \gg 1$. The flow isothermally expands in vacuum without the influence of the magnetic field, but under the influence of its own electrostatic field. This mode is realized at a geostationary orbit in the rarefied plasma jets emitting from Hall thrusters and ion engines.
3. $S \ll 1$, $II > 1$ or $I -$ the flow of plasma with a finite thermal conductivity.
4. $S > 1$ or I , $II > 1$, $\beta = 0$. The flow expands along magnetic lines. When $S < 1$ (in the proximal zone), the flow is isothermal. When $S > 1$ (distal zone), expansion of the flow decreases to the velocity of transverse diffusion in the magnetic field. The plume has a “needle” shape.
5. $S > 1$, $II \geq 1$, $0 < \beta \leq \pi/2$. The flow expands across magnetic field lines. The plume has a “petal” shape elongated in the plane of \mathbf{B} and \mathbf{U} vectors.

For each of the five cases the Braginskiy system of equations can be substantially simplified. For an axially symmetrical two-dimensional jet (cases 1-4), the solution of a set of plasma dynamic equations in cylindrical coordinates (x, r) is as follows:

$$u = u_c(x) \cdot y(\eta); \quad w = u \cdot da / dx \cdot \eta; \quad \eta = \frac{r}{a};$$

$$T = T_c(x) \tau(\eta); \quad nu = \dot{N}v / \pi a^2 \cdot \zeta(\eta)$$

Where

u and w – components of velocity along coordinates x and r respectively;

η – self-similar variable;

7.1.1. Characteristics of the primary plasma flow.

Results of the calculations are distributions of the following values in cylindrical system of coordinates (x, r) :

- ☐ concentrations of primary ions in the plume $n_i(x, r)$.
- ☐ densities of currents of ions, $j_i(x, r)$
- ☐ electron temperature, T_e
- ☐ electric potential $\varphi(x, r)$.

Initial data for these calculations are:

N^* – ion flow rate at the exit from discharge region [sec^{-1}].

u – flow velocity at the exit from the thruster [m/sec].

a_0 – specific size of the flow in the initial cross-section.

a'_0 – divergence of the flow in the initial cross-section.

T_{eo} , T_{io} – temperature of flow component in the initial cross-section.

T_{ek} – electron temperature at distant zone of a plume.

Experimental measurements of SPT-100 and D-55 thrusters give the next values of these parameters^{112,113,114,115}:

$N^* = 2 \cdot 10^{19} [\text{s}^{-1}]$; $u = 1.7 \cdot 10^4 [\text{m/s}]$; $k = (a'_0)^{-2} = 26$;

$T_{eo} = 10 \text{ eV}$; $T_{ek} = 1 \div 2 \text{ eV}$;

Calculation results of TAL D-55 plume parameters distribution at the mode 300V, 4.5A are illustrated on **Figure 121** and **Figure 122**.

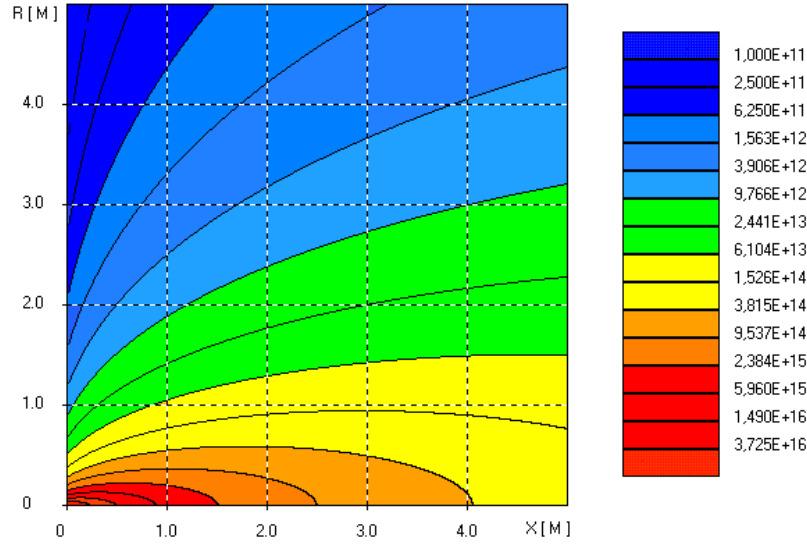


Figure 121 Distribution of primary ion density, n_l [m^{-3}]

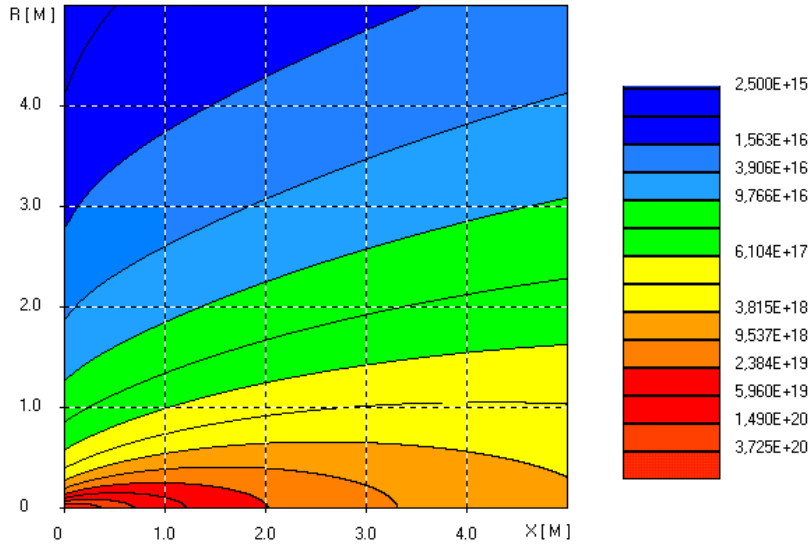


Figure 122. Distribution of density of primary ion flow, $n_l u_l$ [$\text{m}^{-2} \text{sec}^{-1}$]

7.1.2. *Characteristics of secondary plasma.*

Secondary plasma occurs in processes of charge exchange and ionization of neutral atoms and molecules in the plume of a HET. At calculation of secondary ion generation rate, $q(x, r) [\text{m}^{-3} \text{sec}^{-1}]$, the following mechanisms of formation of secondary plasma have been taken into account:

- charge exchange between the accelerated ions Xe^+ and Xe^{++} and slow neutrals of $\text{Xe}^{12,116}$,
- ionization of neutrals by high energy electrons¹¹⁷.

Secondary plasma creates a slow expanding cloud near the thruster; the density of generated ions in the secondary plasma is not big. But as the velocity of neutrals is much less than the velocity of primary beam ions, so the neutral density in the zone of the secondary plasma generation has the same order of magnitude as the density of the primary beam.

Under the influence of electrostatic field these slow secondary ions move predominantly across the axis of the primary beam and partially backwards, forming backflows of ions to a space vehicle. At the same time, in this electric field they get the energy $E_i \sim 10 \div 30$ eV. The estimation of the energy magnitude coincides with the

experimental data (see paragraph 5.3.1.2 and Ref.^{118, 119}). If the density of secondary plasma is comparable with the density of primary ions, the secondary plasma distorts the distribution of electric potential of primary beam.

To calculate the secondary plasma parameters the **SPlaF** and **CFSP**¹²⁰, software has been developed using the free-molecular and continual approaches correspondingly. Results of calculation of the secondary plasma flow obtained by use of the continual equations coincide almost with the results obtained by use of model of collisionless acceleration of newly born ions. An advantage of continual model (in comparison with collisionless one) consists in a possibility to readily take into account that the secondary ions, newly-born in points with different value of a potential, influence on a distribution of potentials of electrostatic field of primary beam. It finally tells about the spread in values of energy of secondary ions.

Figure 123 - Figure 126 illustrate results of the **CFSP** calculations of the main characteristics of the secondary plasma arising in the plume of 1.35 kW HET operating at the background concentration Xe neutrals $n_n = 2 \cdot 10^{12} cm^{-3}$.

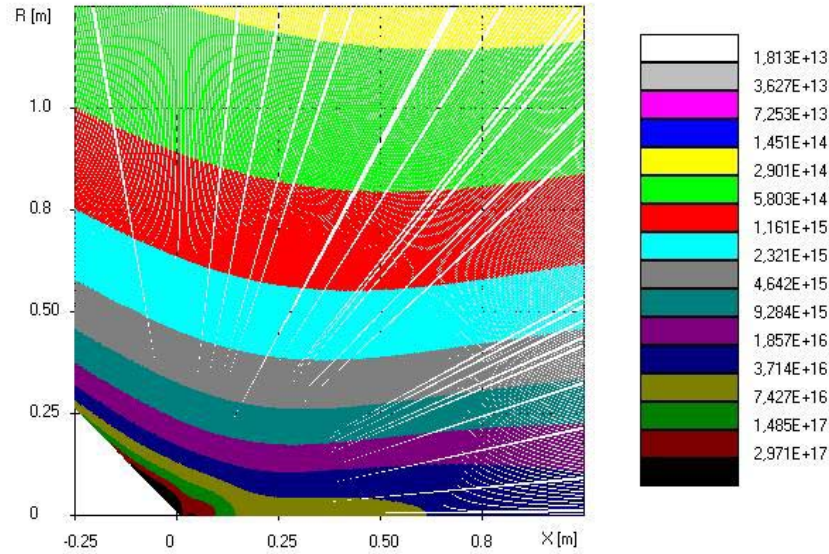


Figure 123. Distribution of the secondary plasma density, $n_2[m^{-3}]$

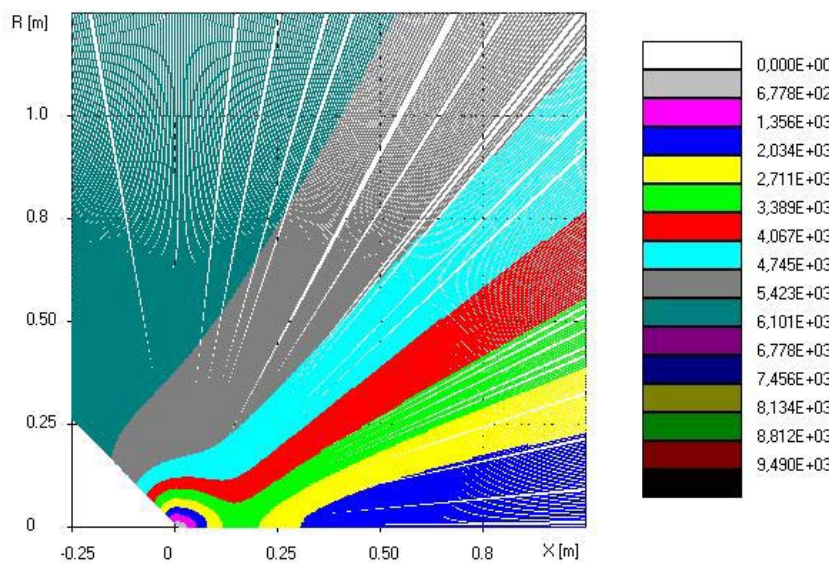


Figure 124. Distribution of velocity of secondary ions, u_2 [m/sec]

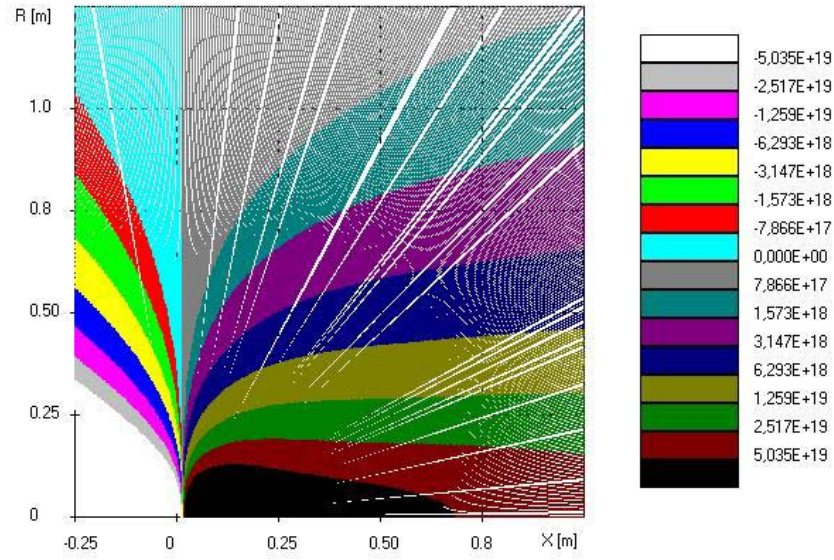


Figure 125. Distribution of axial flow density of secondary plasma, $n_2 u_{2x} [\text{m}^{-2} \text{sec}^{-1}]$

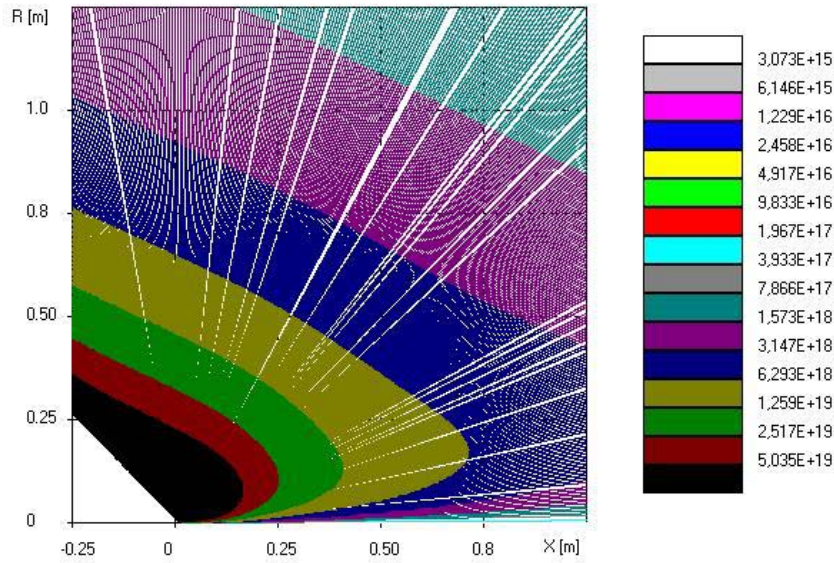


Figure 126 Distribution of radial flow density of secondary plasma, $n_2 u_{2r} [\text{m}^{-2} \text{sec}^{-1}]$

7.2. Comparison of theoretical models with experimental data.

7.2.1. Choice of the coordinate system.

In most modern theoretical and experimental works spherical coordinate system has been used. It would be justified choice in case of a conical flow. Many authors assume this type of flow either directly or indirectly. However, analysis shows that conical flow is not the case of EP plumes. Only small initial areas of the jet can be approximately described as conical. Our estimate shows that in axially symmetric jets either additional jet expansion takes place ($a' > 0$, $a'' > 0$) with weak effect of magnetic field or expansion is restricted ($a' > 0$, $a'' < 0$) when the longitudinal magnetic field B is noticeable. This is illustrated in Figure 127.

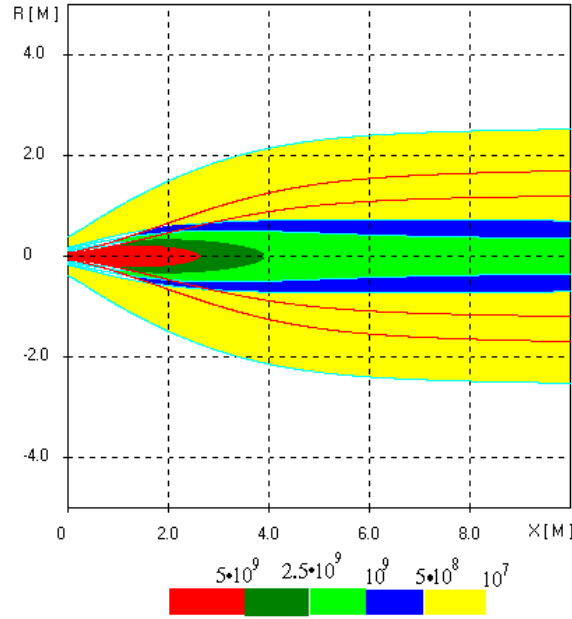


Figure 127 Distribution of density , n/cm^{-3} , and lines-of-current (red curves) of SPT-100 magnetized plasma plume on a geostationary orbit

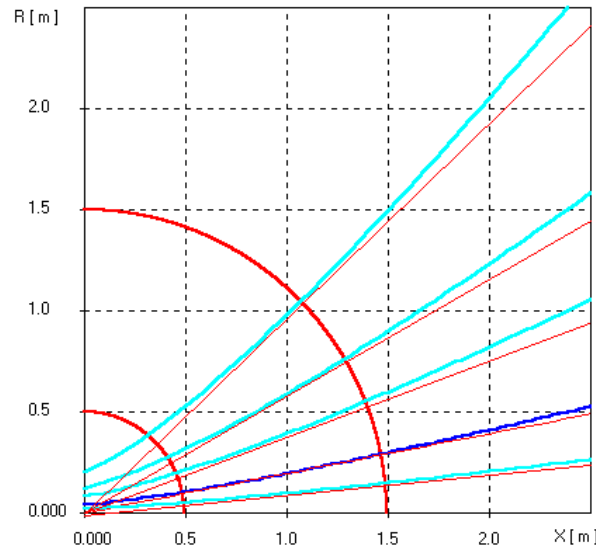


Figure 128 Comparison of flow lines between conical and real flow in plasma jet.

Real lines of current (blue curves) in D-55 plasma plume are illustrated in Figure 128 together with conical expansion lines of current. We can see that lines of current divert and only a region $0.5m < \rho < 1.5m$ can be imagined as conical with polar $x_0=0$. Most experimental measurements of D-55 and SPT-100 plume parameters were conducted at distances $0.6 \div 1.2m$. At that the sensors of ion flow density were positioned to obtain the angular distributions of radial flows in plasma. In other words, the experimental distributions are presented in most works in polar coordinates. For given below comparison of our model with experimental data obtained in test facilities we described this area of the plume with almost conical flow, where $a' = const$, $a'' = 0$, using simplified SSM-model in polar coordinates.

$$j = \frac{\dot{N}k\nu}{\pi\rho^2} \frac{(1 + tg^2\theta)^{3/2}}{(1 + k \cdot tg^2\theta)^{p+1/2}}, \quad \nu = p - 1/2$$

with pole in the center of the exit cross-section of the thruster. Here ρ and θ – polar coordinates,

$$p = \frac{\gamma M^2}{\gamma M^2 - 1} \cong 1, \quad k = \frac{1}{a^2} - \text{divergence characteristic of the plume. This description is true for the moderate}$$

distances ($0.7 < \rho < 1.5m$) from a HET of 1.35kW. Outside of this range jet expansion differs noticeably from conical. Figure 128 shows real lines of current (blue curves) and lines of current in conical expansion approximation (red lines) for distant areas. We can see that at a distance more than 2m the flow differs from conical. It is true for very the plume near field as well.

Cylindrical system of coordinates was used in Michigan¹²¹ at experimental measurements of plume parameters in very near zone. Non-conical character of flow was discovered then. In Figure 129 experimental data from Ref.¹²¹ are shown in the left window and dependence of transverse beam size versus longitudinal coordinate, $a(x)$ derived from these data is shown in the right window. Presented dependence $a(x)$ demonstrates that the beam converges first (the value a_{min} corresponds to the crossover), and diverges then. In other words the angle of divergence changes along the beam.

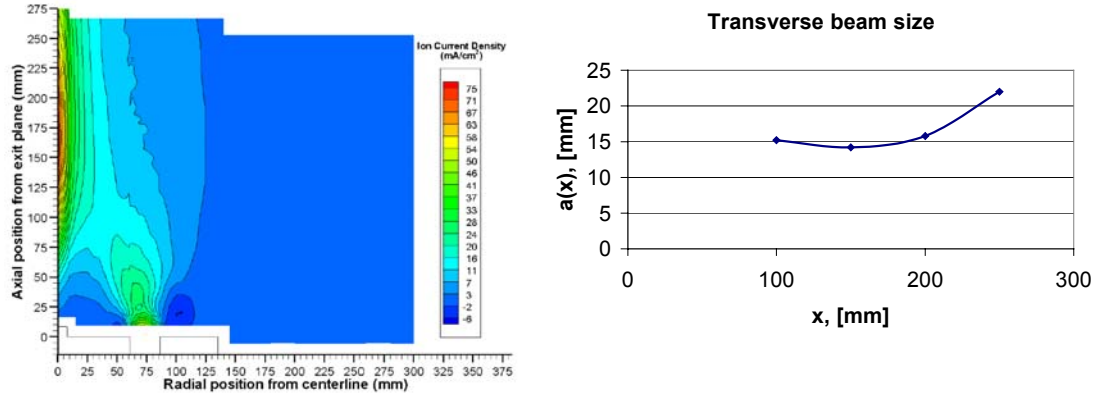


Figure 129. Transverse beam size constructed with use of the experimental data from Ref.¹²¹.

Borders of flow area, which can be considered as conical, change with variation of initial parameters, especially ion flow rate \dot{N} and power W . Center of the polar coordinate system shifts along the axis of the flow. Thus, a conclusion can be made that selection of the polar system of coordinates for experimental measurements of parameters distribution of 1kW-class SPT and TAL is not reasonably justified. In general case cylindrical system of coordinates is more natural for this kind of flows. Cartesian system of coordinates should be natural for a three-dimensional plume.

7.2.2. Comparison of modeling results with SPT and TAL plume parameters measured in vacuum chambers.

Analytical models and approximations have been used till recently to describe dependency of plasma concentration on coordinates. Assignment of distribution in analytical view has advantages in practical use of models, for example, for estimation of radio physical characteristics of the jet. In Ref.¹¹⁸ we compared experimental data of the plasma density distribution, $n(r, \theta)$, and results of calculations by different analytical models: Carney's approximation¹²² developed in NASA for arcjet plumes; Roberts's approximation¹²³, widely used for determination of a hypersonic flow density ($M^2 \gg 1$); Narasimha's model of free molecular beam¹²⁴, exponential approximation¹²⁵, developed in University of Michigan for calculation of radio waves propagation through SPT plume. It was shown in Ref.¹¹⁸ that these models describe correctly the central part of the flow, and within the angle $< 40^\circ$ calculations coincide with experimental results. But they are not suitable for description of the plume far field at the angles more than 40° . Beside the Hall-effect thrusters with closed electron drift the comparison of experimental data of other types of thrusters, namely: ion engine, end-Hall thruster and arcjet, was conducted in that work (see Ref.¹¹⁸). It was shown that SSM-model can be used for description of jet expansion of any EP thruster.

With the improvement of computer hardware it has become possible to use models based on kinetic equations solution. In the same work¹¹⁸ we compared results of SSM-model solutions with the results of calculations of current density distribution, $j(r, \theta)$, in SPT plume by Bishaev's and Kalashnikov's model¹²⁶ and by Hastings's and Oh's PIC model¹²⁷. Both these models and above mentioned analytic solutions had the same disadvantage. It means that they describe the central part of the flow satisfactorily but they are not suitable to describe far field of the thruster plume.

Nowadays in many organizations as in USA and Europe models for description of parameters in plasma jet based on the PIC method are being developed. Among them we can see the version of Boyd's model which takes into account existence of the dense secondary plasma⁹⁹ and agrees with experimental data to maximum

extent. Four theoretical dependencies, which describe density distribution of ions flow in polar coordinates, are compared on Figure 130. We illustrated these dependencies in specially defined terms $f(tg^2 \theta)$. Purpose of such selection was to show differences in current density distribution in far field of the jet at large off-axis angles. This zone is important from the standpoint of characterization of the plume effect onto the space vehicle elements. In these coordinates self-consistent dependence for isothermal flow ($IP \gg I$) is performed as line

$$f = 1 + k \cdot tg^2 \theta, \text{ where } k - \text{divergence of the flow defined above, and } f = \left(\frac{j_c}{j \cdot \cos^3 \theta} \right)^{2/3}. \text{ We can see}$$

that at large angles θ self-similar dependency and Boyd's solution give denser flows in the far field of the jet than Oh's model and Bishaev's model.

Figure 131 and Figure 132 show comparison between two theoretical angular dependencies of flow density and experimental data obtained for D-55 TAL and SPT-100 in different vacuum benches. For example, Figure 131 shows comparison in absolute values between SSM-model theoretical distribution and experimental data obtained in Michigan University¹²⁸. Author of Ref. [99] provides comparison with the same experimental data and verifies his own calculation results in the range 0.5m and 1m from the thruster. We presented all these dependencies in special coordinates in Figure 132. Red line relates to SSM-model, lower blue line relates to Boyd's solution for 1 m distance, upper blue line relates to 0.5m distance. We can see that all experimental data converted into non-dimensional form are in self-similar dependency while Boyd's solutions are different for every set of experimental data.

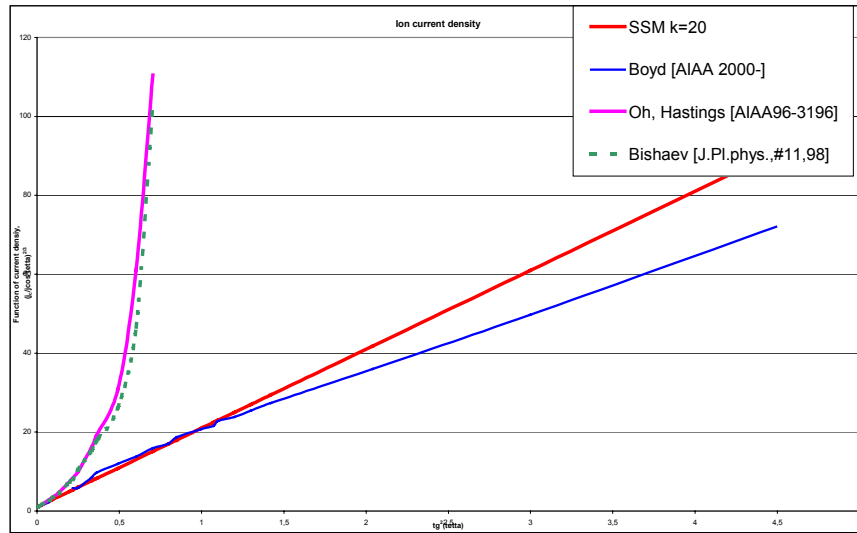


Figure 130 Comparison of theoretical models of Hall thruster's plume.

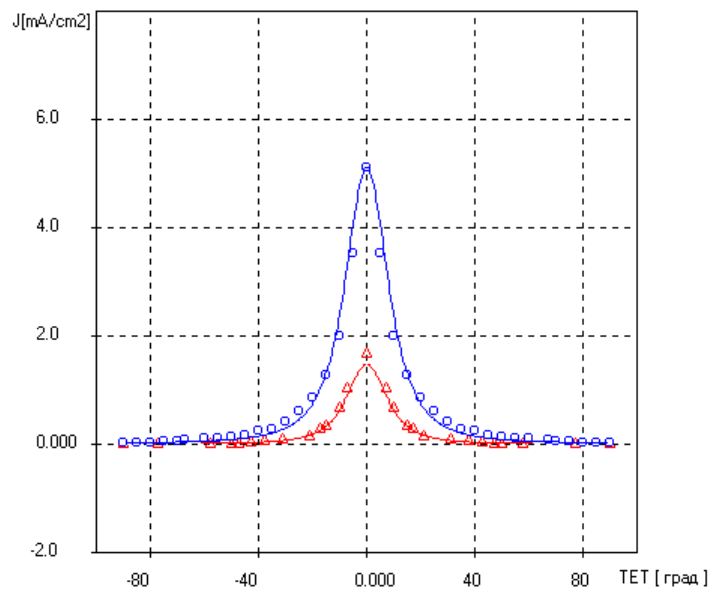


Figure 131 Comparison of SSM- model with experimental data from ¹²⁸.

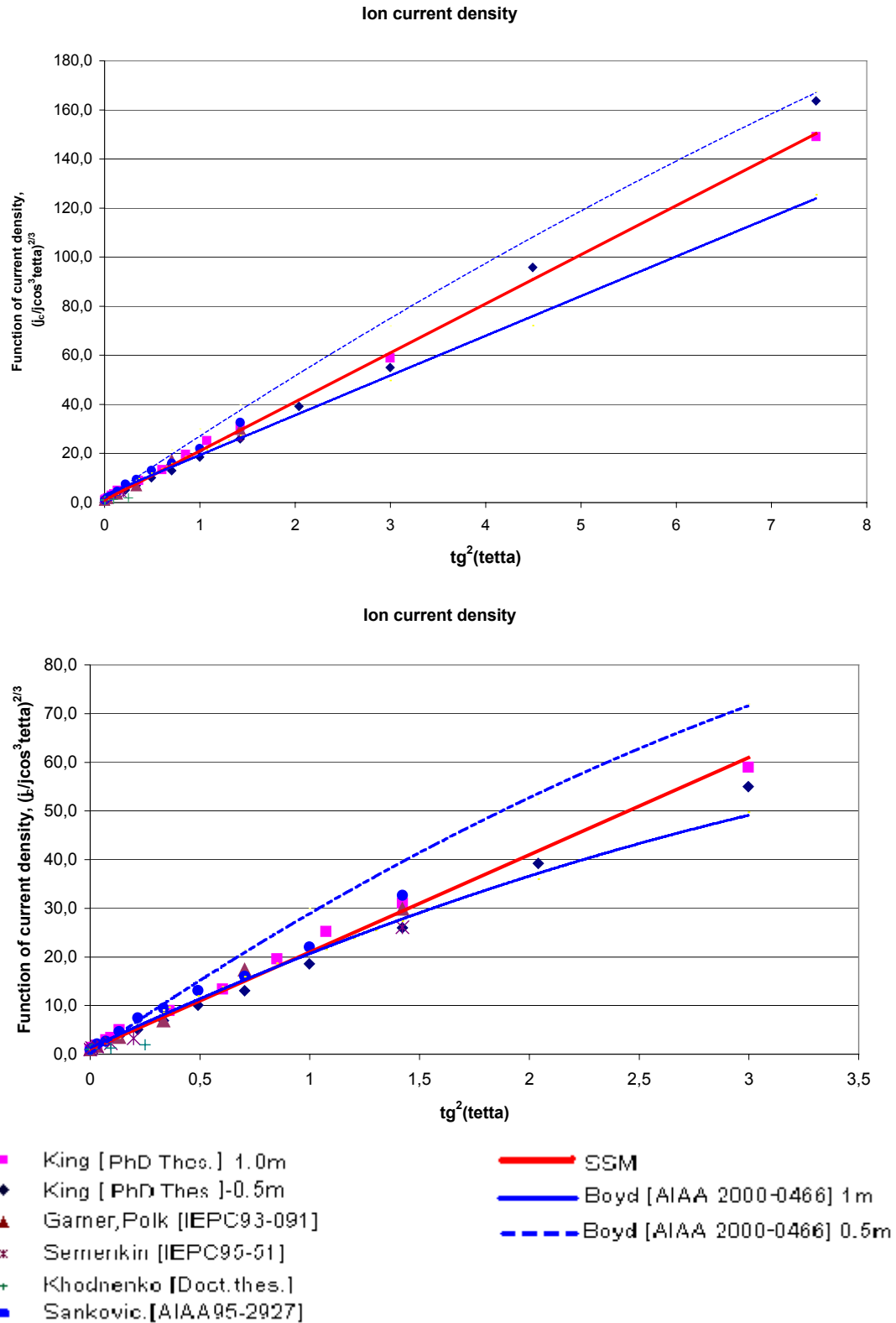


Figure 132 Comparison of SSM-model and Boyd's model with experimental data of ion current density $j(\theta)$. Upper window – big range of angles (a periphery of a flow is included) , lower window – small range of angles (flow core)

We have lesser experimental data about electron density distribution than about ion current density. Data in Ref.^{98,129} relate to direct measurements. Figure 133 shows distributions for isothermal conical flow in special

coordinates – $f(\text{tg}^2 \theta)$, where $f = \frac{n_c}{n \cdot \cos^2 \theta}$, which gives us more visual picture of the far field of the jet.

Besides, we can see experimental and theoretical values obtained by SSM-model and by the Boyd's model version, which takes into account variation of the electron temperature. The analysis of provided comparisons

shows that only models, which are able to describe dense far field of the plasma jet, agree with experimental data.

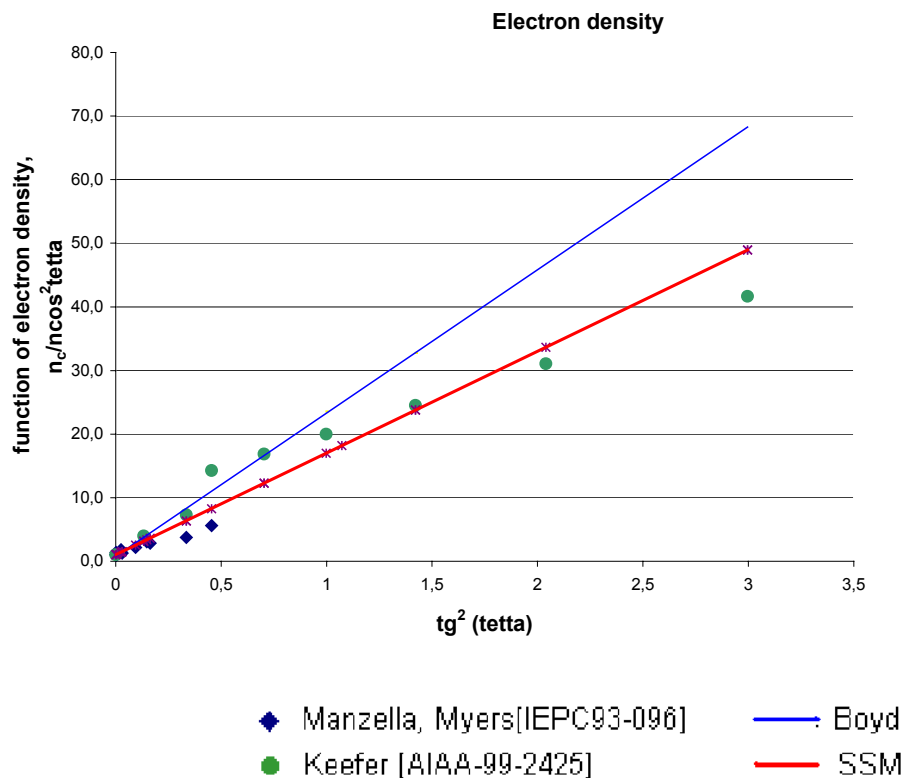


Figure 133 Comparison of SSM-model and Boyd's model with experimental data of electron density $n(\theta)$

7.3. Comparison of the SSM-model plasma plume with Express flight data

Comparison of calculation results obtained with use of SSM-model with flight data was conducted in Ref.¹³⁰. The data of *Meteor* and *Cosmos* LEO satellite and *Express* GEO satellite were used. *Express* data are of particular interest due to a number of reasons: first, this is the latest data, second, they were obtained with the modern thruster SPT-100, third, the measurements are not random, but systematic.

The GEO satellite *Express* carried on board probes for measurements of both ion current density and ion energy distribution. The probes were mounted at distances of $x_1 = 1\text{m}$, $x_2 = 3.8\text{m}$, $x_3 = 8.8\text{m}$ from the thruster. According to calculations in Ref.¹³¹ for SPT-100 operated in GEO conditions the influence of Earth magnetic field upon plasma plume expansion becomes sufficient at distance of $x_b \approx 40\text{m}$ from the thruster. That is why at calculation of plume parameters in case of *Express* satellite influence of the geomagnetic field can be neglected.

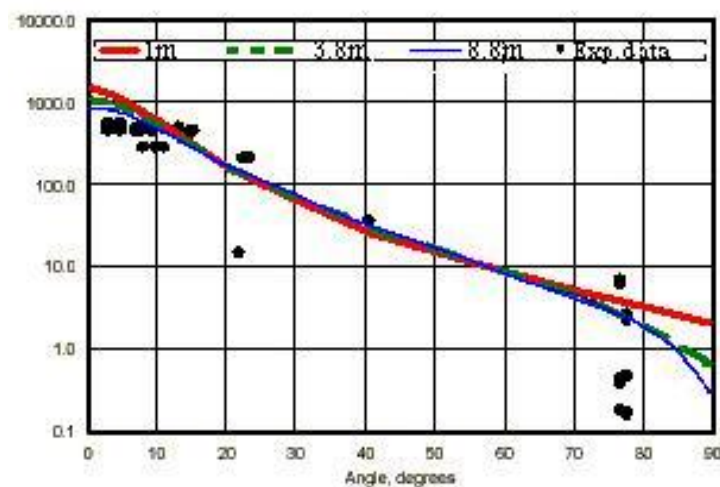


Figure 134 Comparison of Express experimental data and SSM-distribution of axial current density, j_x , for different distances .

Distributions of axial component of ion currents densities for different distances from SPT are plotted in Figure 134 in polar coordinate system. All of experimental data depicted in Figure 134 and theoretical distribution of current density at different distances also are normalized for distance $1m$ from the thruster. Normalized flight data are taken from Ref.^{132,133}.

Theoretical curves $j(\theta)$ basing on self-similar distributions for axis-symmetrical plume expanding on GEO coincide good enough with the flight data. Note, that all these curves were obtained as an outcome of a single run for all three distances both in the near and far field zone of expansion.

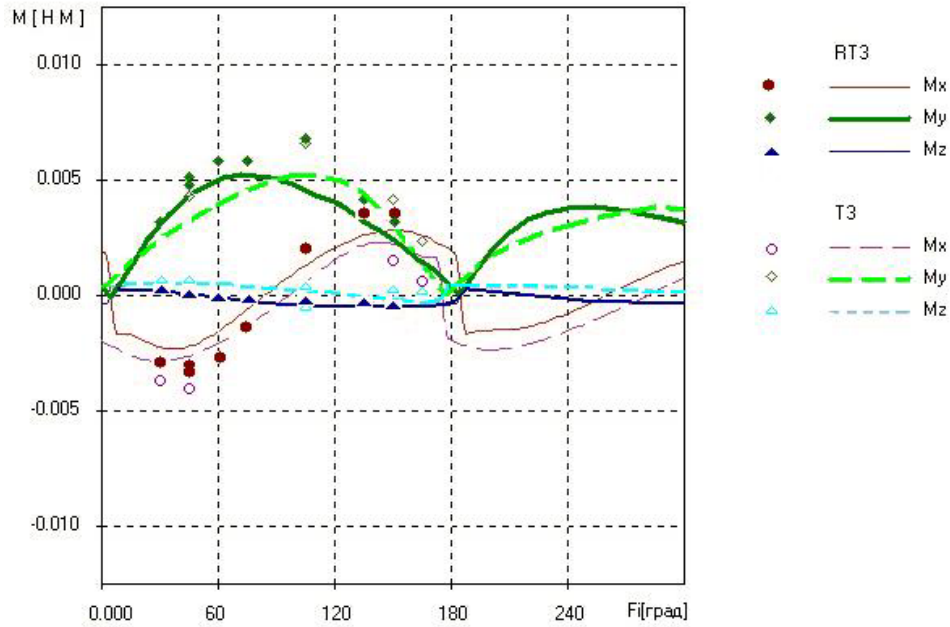


Figure 135 Comparison of calculated torque with Express data for T3, RT3¹³².

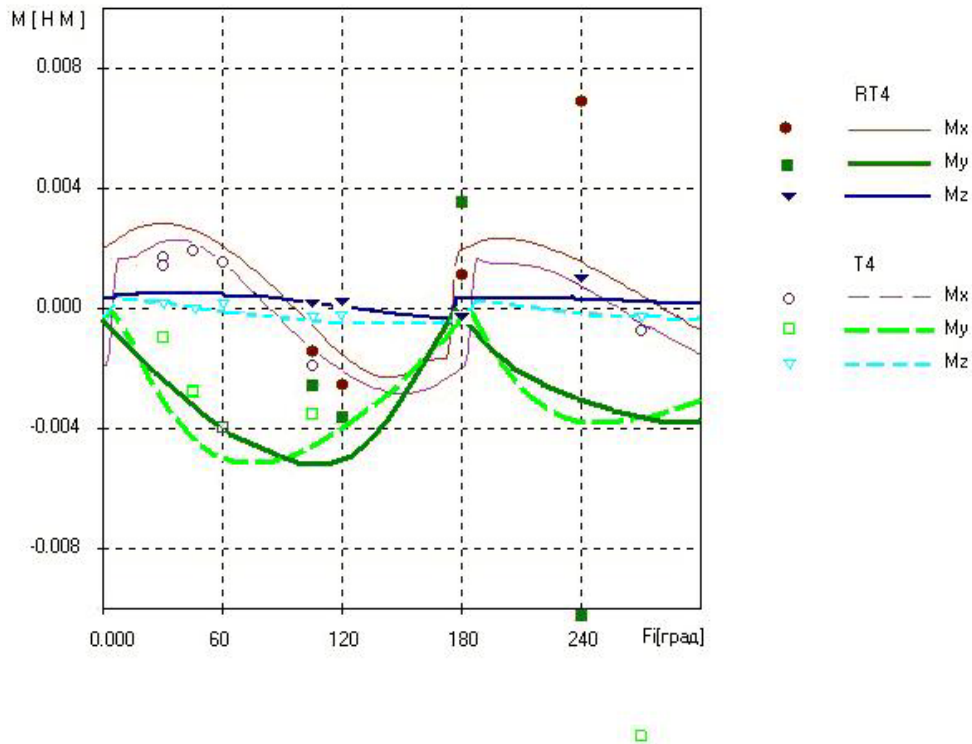


Figure 136 Comparison calculated torque with Express data for T4, RT4¹³².

Figure 135 and Figure 136 show the calculated results of all three torque components Mx , My , Mz , which appear on *Express* satellite when the SPT operates. In the figures hollow dots correspond to experimental values of torque of working thrusters (T3 and T4). Filled dots correspond to reserve thrusters (RT3 and RT4).

The angular distributions of three torque components are sufficient for definition of several plume parameters. In particular, on the assumption of smallness of the relations $\frac{M_z}{M_x} < 0.2$ and $\frac{M_z}{M_y} < 0.1$ for

effective magnitude of accommodation coefficients the relation of $\frac{\alpha_n + \alpha_\tau}{2} > 0.9$ holds true. It agrees with the

mechanism of effective interaction between attacked surfaces and flow of ions accelerated by the electric field of plasma and wall boundary layer as well. Quantitative estimation on a base of experimental dependencies of M_x , M_y , M_z allows to define identically the values of accommodation coefficients $\alpha_n=0.9$ and $\alpha_\tau=0.95$ for front surface of the solar battery and $\alpha_n = \alpha_\tau=1.0$ for back surface of the solar battery. Results of torque calculations coincide with experimental data keeping within the range of errors ($\Delta M \sim 1 \text{ mNm}$).

According to SSM-model density of propellant in the flow periphery is more, than it may predicted by models based on simple conical expansion. It is caused by additional expansion of the jet in the far distances under effect of the electrical field. Besides, the SSM model takes into account the fact that a boundary layer with the potential drop appears close to the surface flown by the plasma. Ions are further accelerated there¹³⁴. Both effects increase significantly the density of normal force, which influences on the far area of the solar battery. Due to the big arm this increased force makes a significant contribution to M_y and M_x values. Use in calculations of the torque of more correct mathematical model of plume allows to get a good agreement with experimental data even without artificial decrease of accommodation coefficients α_n and α_τ (that was required in earlier models, see Ref.¹³⁵ for instance).

7.4. Verification of SSM-model on measurements of D-55 plume parameters obtained on TSNIMASH test facility

One of the goal of the experimental study of D-55 plume parameters was to provide optimal conditions for a comparison of experimental data with self-similar flow describing by SSM-model. Results of the measurements were provided in cylindrical system of coordinates (x, r) , as most natural and convenient for description of axis-symmetrical plume characteristics (as it was discussed in Section 7.2.1). It is one of the most important conclusions of SSM model that the plasma plume characterized by non-vanishing electron temperature is non-conical. This property is the result of generation into focused plasma flow of noticeable radial electric field $E_r \gg E_x$, which accelerates the beam ions in radial direction.

Important difference of presented below comparison of experiment with mathematical model from many works published before is that that the consideration additionally includes:

- The initial part of a flow, which contains the zone with high temperature T_e , with big gradients ∇T_e and $\nabla \varphi$.
- The dense neutral background; an interaction with background influences on the plume characteristics.

At each operation mode of D-55 thruster the radial distributions of several parameters are measured in three cross sections, among them: the axial component of ion current density j_x , electron temperature T_e , electric potential φ . In this Section the comparison of calculated parameters with values measured at D-55 thruster operation in mode $\varphi_d=300\text{V}$, $I_d=3\text{A}$ is given.

Availability of experimental distributions of several plume parameters allows conducting comprehensive, complex verification of the SSM model. This model gives solution of complete system of equations for dynamical, electrical and thermal characteristics of the plasma flows. All plume parameters are described by this model as interrelated data. That is why the analysis of real experimental distributions of independent parameters allows not only to verify the self-similarity of description of different processes inside the plume, but also to determine some unknown initial and boundary conditions in a flow. Besides, it is possible to get the information about collective processes inside the plume, which are unknown a priori.

To calculate all plume parameters it is enough to process the distribution of anyone parameter at specified cross section $x=x_i$. In our case the most convenient experimental dependence is the spatial distribution of current density of accelerated ions $j=j_x(x_i, r)$. This dependence looks like direct lines in special coordinates:

$$f_1\left(\frac{r}{a}\right) = \left[\left(\frac{j_c}{j} \right)^{1/p} - 1 \right]^{1/2} = \frac{r}{a} \text{ , or } f_2 = \ln\left(\frac{j_c}{j}\right) = p \cdot \ln \eta; \quad \eta = 1 + \frac{r^2}{a^2}.$$

From these functions the values $a_i=a(x_i)$ and p (see Figure 137) are being determined. These operations are similar to processing of a volt-ampere characteristic of a probe.

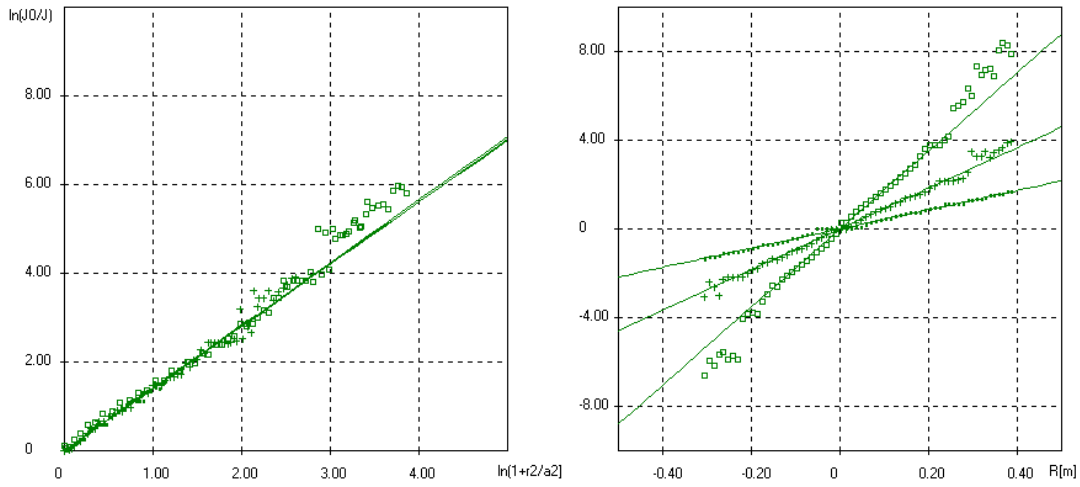


Figure 137 Comparison of self-similar and experimental distribution of current density at three cross sections: $x=0.3m$ (squares), $x=0.5m$ (crosses) and $x=1m$ (dots).

In the right window of Figure 137 three lines of $f_1(r/a)$ corresponding to three cross sections $x=0.3, 0.5, 1m$ are shown. The magnitude of transverse size of the flow, a , is being determined with regard to the line inclination in given cross section. On the left of Figure all of three sections are re-united in one dependence, at that the value of $\ln\left(1 + \frac{r^2}{a^2}\right)$ is depicted on the X-axis, and the value of $f_2 = \ln\left(\frac{j_c}{j}\right)$ is depicted on the Y-axis, where the value of j_c is the current density on the flow axis. The existence of united rectilinear dependence for experimental data received in three cross sections demonstrates directly the self-similarity of EP plume parameters.

In chosen initial cross section at $x=x_i$ it is possible to calculate the ion flow rate $\dot{N} = \frac{1}{e} \int_0^\infty j_x 2\pi r dr$.

Then, one should measure (or assign) at flow axis the magnitudes of velocity $u_c(x_i)$, temperature $T_c(x_i)$ and potential $\varphi_c(x_i)$. After that, using two systems of non-linear ordinary differential equations with independent

variables x and $\frac{r}{a}$, the distributions of all parameters are being calculated in required range of x and r . Note, the linear sizes of computational domain have not limits caused by computation troubles.

On Figure 138 the values of both the transverse size $a(x)$ and the ion flow rate $\dot{N}(x)$ measured at $x_i=1m$ are compared with results of the calculation. Decreasing of the ion flow rate \dot{N} along X-axis is caused by ion-neutral charge-exchange processes and expansion of secondary ions in radial direction.

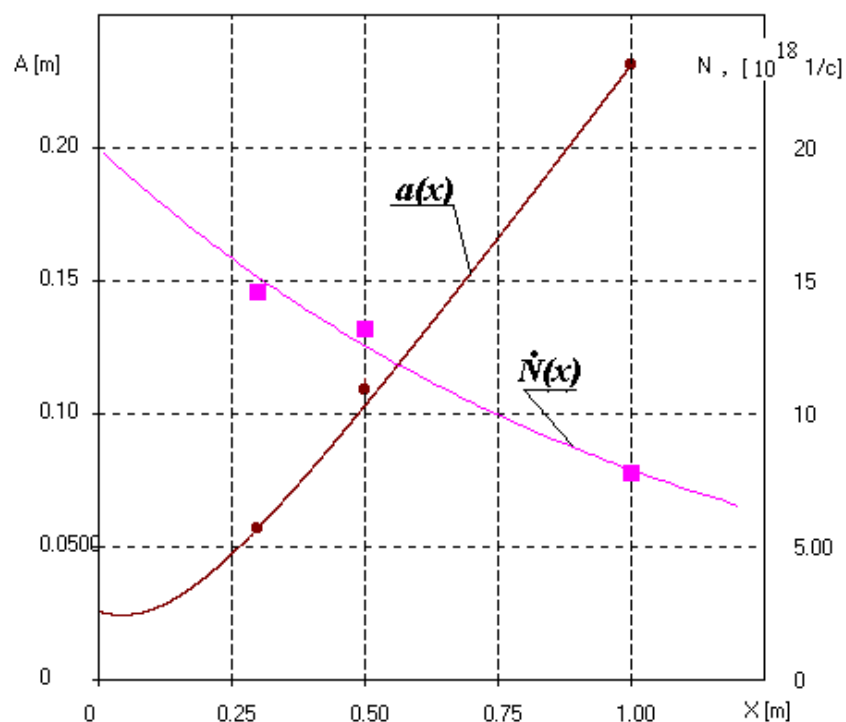


Figure 138 Longitudinal dependencies of transverse size of flow, $a(x)$, and ion flow rate, $N(x)$.

Comparison of measured and calculated radial distributions of the D-55 plume parameters are given in Figure 139- Figure 141.

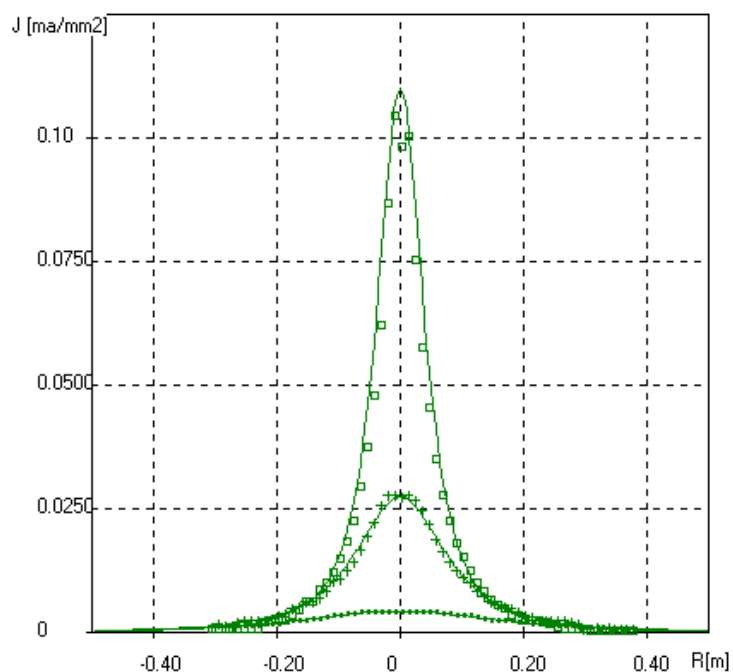


Figure 139. Calculated (solid lines) and measured (symbols) radial distribution of current density in the D-55 plume at three cross-sections $x=0.3$ m (squares), $x=0.5$ m (crosses) and $x=1$ m (dots).

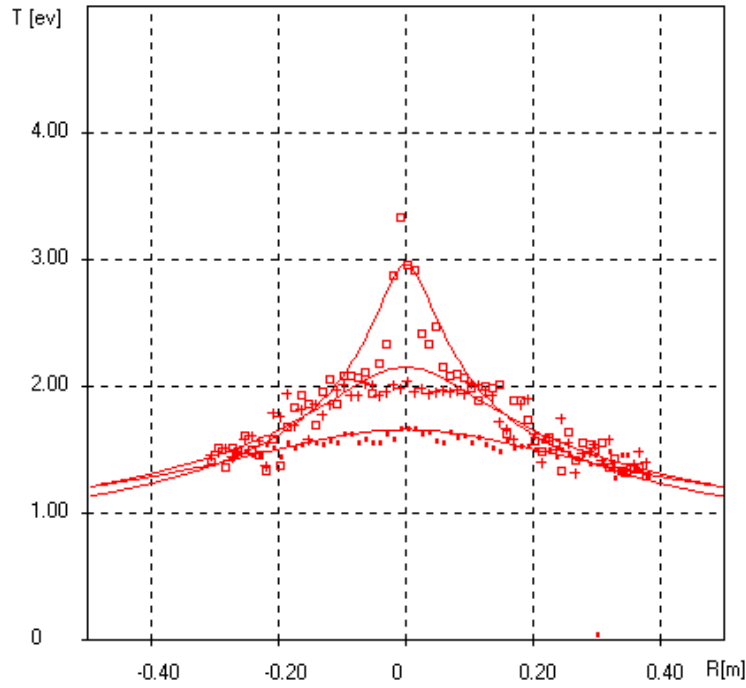


Figure 140 Calculated (solid lines) and measured (symbols) radial distribution of electron temperature in the D-55 plume at three cross-sections $x=0.3m$ (squares), $x=0.5m$ (crosses) and $x=1m$ (dots).

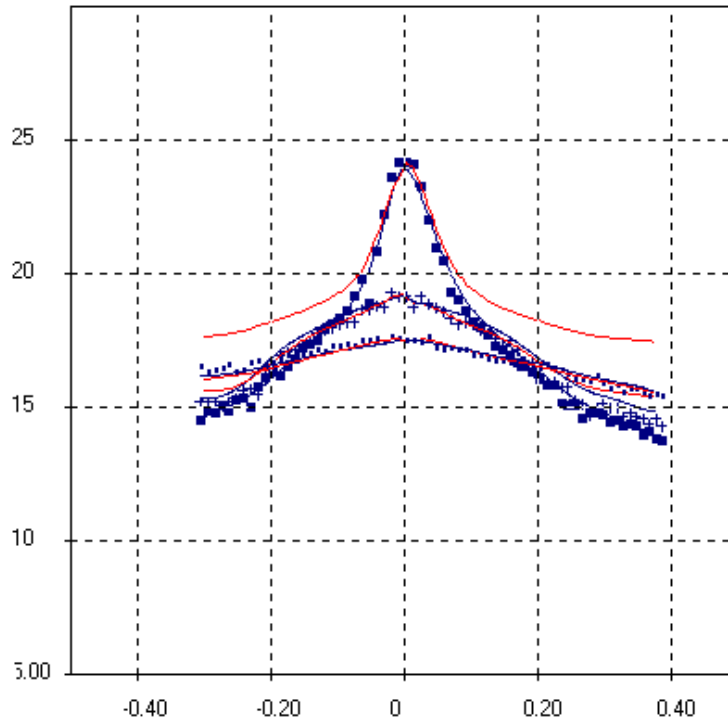


Figure 141 Calculated (solid blue lines - SSM, red - Boyd's model) and measured (symbols) radial distribution of electric potential in the D-55 plume at three cross-sections $x=0.3m$ (squares), $x=0.5m$ (crosses) and $x=1m$ (dots).

The experimental distribution of the potential is compared with two theoretical dependencies: i) SSM-model and ii) kinetic model from Ref.¹⁰⁷. One can see that in the zone characterized by relatively big magnitudes of electron temperature T_e and a gradient of potential $\nabla\phi$, which influence essentially on initial divergence of

the flow, the SSM model result agrees well with experimental data. The dependence from Ref.¹⁰⁷ proposes conservative values of a transverse drop of the potential.

In Figure 142 the calculated and measured values of $j_c(x)$, $T_c(x)$ and $\phi_c(x)$ at the D-55 plume flow axis are compared.

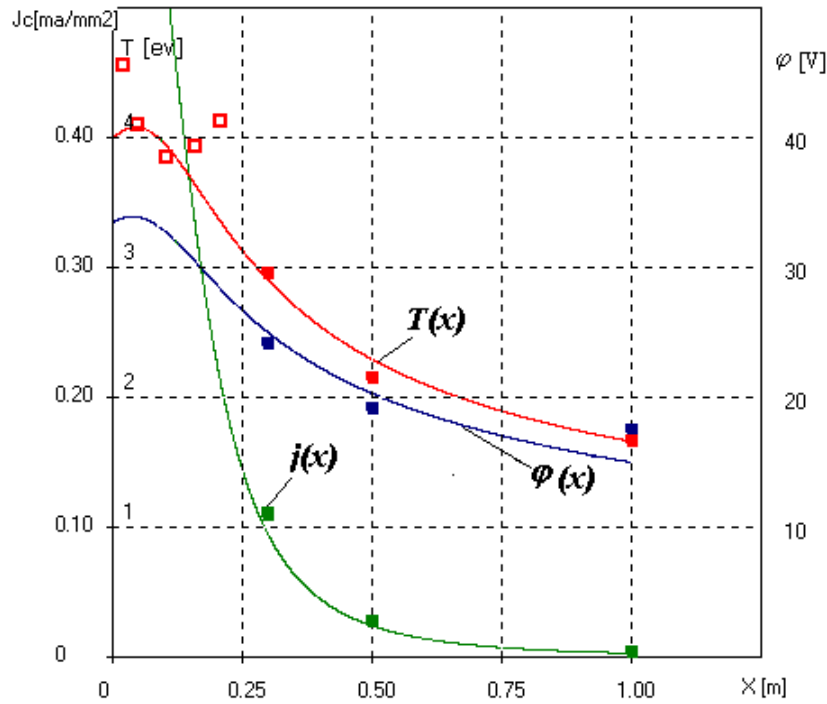


Figure 142. Comparison of calculated and measured longitudinal distributions of parameters at flow axis. Data presented at the cross sections $x=0.3, 0.5, 1.0m$ were obtained with the probes. Data at cross sections $x = 0.025, 0.05, 0.1, 0.15$ and $0.2m$ were obtained by optical diagnostic methods.

On Figure 143- Figure 146 calculated isolines of D-55 plume parameters are shown. The calculation was executed for baseline thruster operation mode, $U_d=300V$, $I_d=3A$.

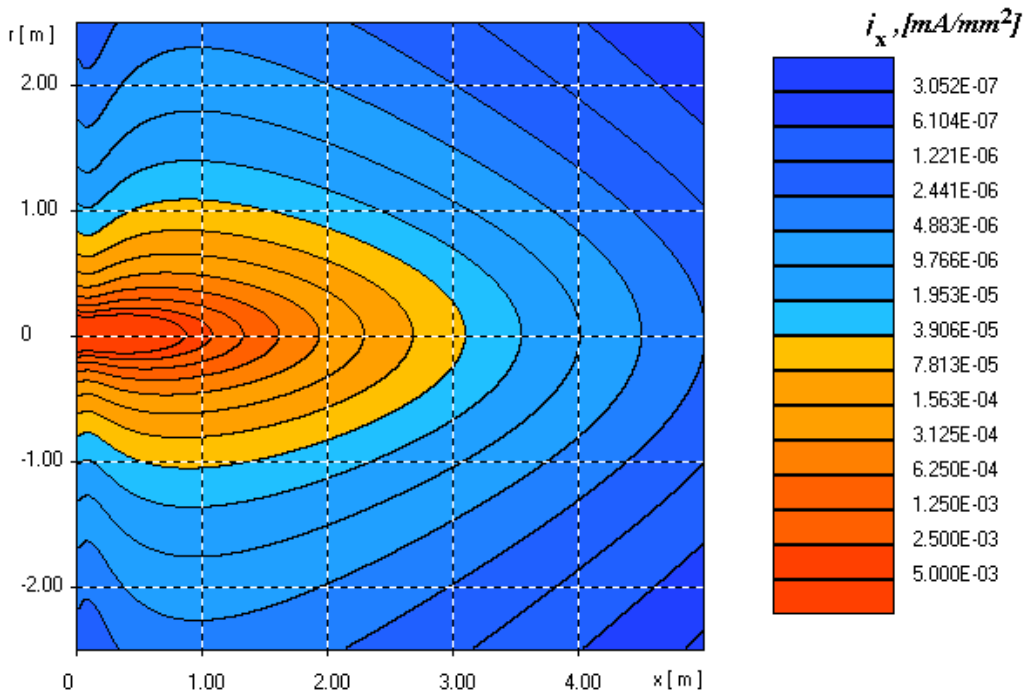


Figure 143 Calculated isolines of axial component of ion current density.

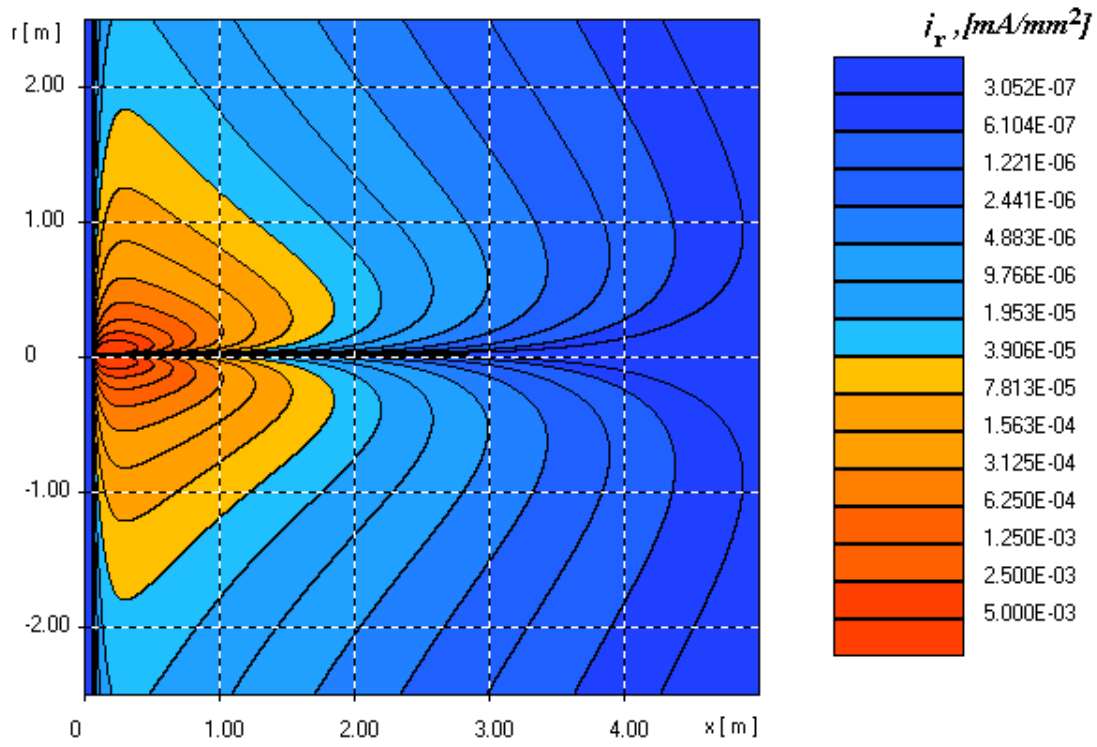


Figure 144 Calculated isolines of radial component of ion current density.

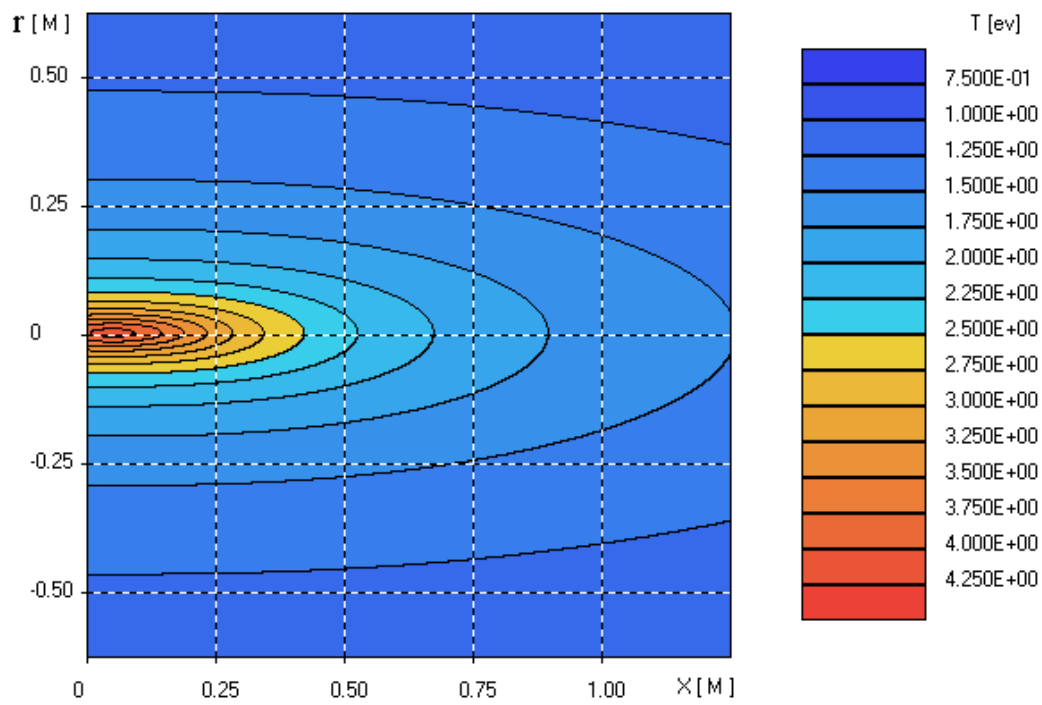


Figure 145 Calculated isolines of electron temperature.

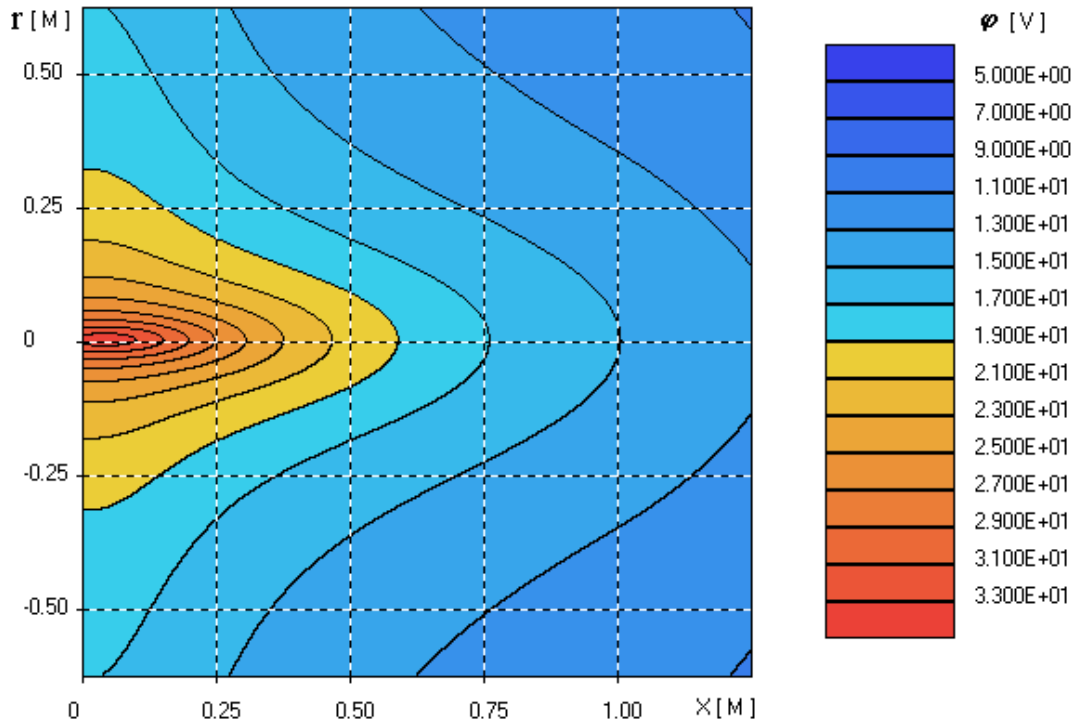


Figure 146 Calculated isolines of electric potential in the plume.

Analysis of the presented distributions discovers a cardinal property of the plasma flow accelerated in the EP thruster channel, namely: the effective mean free path of electrons is some orders of magnitude less in the flow, than the path estimated through the collision frequency, due to collective processes in the plasma. Similar collective processes take place when beam-plasma instabilities develop. So, if the 2D distribution of temperature (see Figure 140 and Figure 142) and the expression for classical heat conductivity of plasma (from Ref.¹⁰⁸) are applied, one can receive that flux of thermal energy W at $x=0.3$ m scattered by this thermal heterogeneity should be equal $W \approx 60$ kW that is physically unreasonable. Consequently, the experimentally registered existence of a heterogeneity of temperature T_e means, that a heat transfer in a plasma plume is controlled by an effective mean free path, which is some orders of magnitude less than the collisional one.

It should be noted, that local growth of temperature in the region of 0.1-0.25 meters from the thruster is most probably related to formation of the bright needle-like crossover region along the plume axis (see Figure 129). In this region the initially ring-shaped plume flow converges. Actually the SSM plume simulation doesn't reproduce this region.

7.5. Conclusions for Chapter 7.

Following conclusions may be inferred from the analysis of the SSM model and its predictions with results experimental results, in particular D-55 plume parameters distributions:

1. Use of the SSM makes possible to calculate equally well a spatial distribution of plume parameters of different engines (from arcjet to ion electrostatic engine) working with various propellant, in different modes and under different vacuum conditions. These engines generate plasma flows with density and velocity differing on orders of magnitude.
2. SSM-model describes adequately distribution of HET plasma plume parameters both for thrusters operating in a ground-based vacuum chambers and in space conditions. It allows accounting for such factors as a background pressure and conductivity of the vacuum chamber walls. It effectively works not only very far isothermal plume zone, but also the near field of the thruster plume, where considerable temperature variations of the electron temperature T_e exist.
3. An analysis of thermal processes right behind the crossover zone of HET thruster plume and distribution of the plasma parameters indicate development of intensive collective processes, which reduce the effective collision mean free path of electrons on some orders of magnitude. These processes also control electrostatic field intensity and dynamics of the flow expansion further downstream.
4. Results of space experiments prove dominating effect of both internal electrical self-consistent field and external magnetic field on the dynamics of the exhausted plume. Characteristics of the plume flow in a far field are controlled not only by initial flow parameters, but also by intrinsic electro-dynamical

processes in the plume. Mathematical description of the plume far field ($x \sim 5-10$ m), which is based only on either extrapolation (usually for conical expansion) of values obtained in a vacuum chamber or data calculated closer to the thruster ($x \sim 0.5-1$ m), can differ essentially from real values of plume parameters. It, in turn, can cause inaccuracies in evaluation of plasma plume/spacecraft interaction. To calculate correctly the plume expansion far from the thruster exit it is necessary to accurately describe the distribution of electric fields and currents and, in particular, take into account contribution of the thermal force and collective processes. Precise calculation of these parameters is specific feature of the SSM.

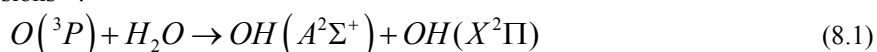
5. Developed model has all advantages of analytical solutions. Among them comparative simplicity of practical application, absence of computational constraints of calculated area, possibility to create on its basis high-speed methods including real-time analysis of experimental data and at the same time it doesn't concede to the most precise numerical solutions.
6. On the bases of the SSM-model a number of software codes have been developed and successfully applied. They are intended for evaluation of interaction between plasma plumes and on-board spacecraft systems and sensitive elements. Developed codes are characterized by very fast run-time (some seconds on standard PC), providing outcomes in the form of graphic diagrams and electron databases.

8. Modeling of the high altitude plume glow intensity and verification of the molecular collision cross-section models through comparison with space experiment data

The high altitude plume glow characteristics measured in the April 26, 2000 experiment on board of Russian space station “Mir” were discussed in Chapter 2. Modeling of the glow radiation intensity represents a big challenge. Basically the radiation characteristics are directly related to the collisions between the plume molecules and the free stream oxygen atoms. Molecular collision models are not completely elaborated so far for application in the condition of the high altitude plume flow of the space vehicle moving with orbital velocity. So, the experimental data represent significant value for verification of the glow and molecular collision models. Modeling of the glow radiation and comparison of the experimental data with the model outcomes are discussed in this Chapter.

8.1. General description of the glow model and basic assumptions

A large scale UV-glow was observed both from the US Shuttle¹ and Russian “Soyuz” and “Progress” space vehicle plumes² at altitudes 250-400 km. The glow ranged along hundreds meters and even some kilometers from the space vehicles. The plume flow at these altitudes is highly rarified. Travel path of a molecule between two subsequent collisions varies from several to twenty km depending on the altitude. This implies each molecule should leave the plume flow region after one or two collisions, having no more opportunity to generate any radiation inside the plume. So, assumption was put forward that glow radiation is a product of single step collisional reactions. The OH(A→X) 310-320 nm and NH(A→X) 336-337 nm molecular band emissions were found to be most intensive glow emissions in the UV region of spectrum. In particular, this idea was supported by spectral measurements of the glow radiation^{1,7,36}. Corresponding single step collisional processes were suggested to explain these emissions^{1,2}:



In reaction (8.2) the UDMHF stands for fragments of the unburned fuel (UDMH) molecules. This particular work is aimed on study of the first reaction only. There are two reasons for this choice. First, the UV-imager which provided most of the radiometric data of the glow intensity was more sensitive to the OH(A→X) band radiation (see Paragraph 2.5.1.4). Second, one of the main goals of the study was to validate different glow models through comparison of the modeling results with experimental data. Given a high degree of uncertainty of the unburned fuel and its fragments content in the plume flow, modeling of the NH(A→X) absolute intensities through reaction (8.2) is more discommoded in contrast to the OH(A→X) radiation modeling through reaction (8.1). The water molecule content in the plume is much better specified.

Water molecules are one of the major constituents in the LP motor plume whereas atomic oxygen content in the Earth atmosphere ranges from 80 to 95 percents at the flight altitudes. So, suggesting reaction (8.1) for explanation of the glow origin seemed making a sense. One more evidence that favors reaction (8.1) is that OH(A→X) glow was observed when the motor fired against the atmospheric wind, providing a decelerating impulse to the space vehicle (retro firing). No glow was observed during accelerating (direct) firings^{6,36}. High endothermicity of reaction (8.1) explains this fact. At the retro firing condition the plume and atmospheric flows are oppositely directed and typical collision energy of the water molecules and oxygen atoms slightly exceeds reaction (8.1) threshold. At the direct-firing condition the typical collision energy is well below the threshold and only negligibly small amount of the oxygen atoms at the tail of energy distribution meet the endothermicity requirement of reaction (8.1). So, intensity of the glow generated through reaction (8.1) should be very sensitive to the direction of firing, as it has been observed in the experiments.

A number of attempts have been made to model the high altitude plume OH(A→X) band radiation basing on reaction (8.1). General problem inherent to all these efforts was uncertainty of the elastic cross-sections for collisions between atomic oxygen and plume molecules and complete absence of the cross-section energy dependence data for reaction (8.1). Spatial distribution of the glow radiation was found to be very sensitive to the choice of the elastic scattering model^{21,23}, whereas absolute radiation intensity must have direct relation to the reaction (8.1) cross-section^{4,21}. In this regard, proposed was to use the experimental data obtained on “Mir” space station for verification of the elastic collision models and derivation of the reaction (8.1) cross-section. Further paragraphs elaborate this idea.

8.2. Comparison of different computing models of the glow

Various approaches may apparently be utilized for developing a computational model of the rarified plume glow. Choice of the computational model is a trade-off between accuracy and efficiency of the model. Exact and comprehensive models of the glow should be cumbersome and inappropriate for practical computations. More simple models loose in accuracy, indeed. Most of the computation results, which are compared in this Report with the April 26, 2000 experiment data, were obtained basing on a simple model, which ensures satisfactory accuracy, however. This section discusses on how a general glow model may be reasonably simplified. The simplified models are compared with more accurate approximation where possible. The comparison is made basing on computation of the PME plume gasdynamic parameters and radiation. Modeling of the single PME exhaust plume flow is much easier than eight-motor ACS plume flow. From the other hand, some experimental data for the PME plume glow (from February 28, 1999 experiment, in particular) are available as well³.

8.2.1. General formulation and possible simplifications

Accurate mathematical model of the rarified plume flow interacting with atmosphere should be the Boltzmann kinetic equation, which includes all physical, chemical and radiation processes. However, exact modeling of the glow radiation in this formulation is unjustifiably complex approach to the problem solution. Instead, some very reasonable simplification may be applied. One of these simplifications is based on the fact that radiative lifetime of the OH(A) molecule is very small ($\sim 10^{-6}$ sec) in comparison with all characteristic times of physical processes in the plume. So, the OH(A) molecule may be safely assumed radiating at the same place where it has been excited. Furthermore, reactive collisions should be relatively seldom events compared with the elastic collisions. So, reactive collisions can't affect the molecular species distribution in the plume flow and the radiation may be computed by so called "overlay" method. This method neglects influence of the radiating collisions onto the plume gasdynamic parameters and in our particular case disregards re-absorption and all OH(A) molecule de-excitation mechanisms other than radiative decay. This, in turn, allows abandoning the solution of radiation transfer equation and reduces the problem to modeling of the gas-dynamic properties of the hypervelocity plume flow interacting with atmosphere. Under these assumptions the number of reactive collisions per second N_{reac} and plume radiation intensity W in a point with coordinates $\vec{r}(x, y, z)$ equals to:

$$N_{\text{reac}}(\vec{x}) = \iint f_{H_2O}(\vec{x}, \vec{\xi}_{H_2O}) f_O(\vec{x}, \vec{\xi}_O) \sigma_r [E_c(\vec{\xi}_{H_2O}, \vec{\xi}_O)] \left| \vec{\xi}_{H_2O} - \vec{\xi}_O \right| d\vec{\xi}_{H_2O} d\vec{\xi}_O \quad (8.3)$$

$$W(\vec{x}) = \frac{h\nu}{4\pi} \iint f_{H_2O}(\vec{x}, \vec{\xi}_{H_2O}) f_O(\vec{x}, \vec{\xi}_O) \sigma_r [E_c(\vec{\xi}_{H_2O}, \vec{\xi}_O)] \left| \vec{\xi}_{H_2O} - \vec{\xi}_O \right| d\vec{\xi}_{H_2O} d\vec{\xi}_O \quad (8.4)$$

Here $\vec{\xi}$ - molecular velocity, $f(\vec{x}, \vec{\xi})$ - molecular distribution function, E_r - collision energy σ_r - reaction (8.1) cross-section. Subscripts H_2O and O affiliate respective parameters to water and atomic oxygen. Total radiation intensity observed along a particular instrument line of sight equals:

$$W_s = \int_{\text{los}} W(\vec{x}) ds \quad (8.5)$$

Key terms in these equations are particle distribution functions and reaction collision cross-section. In general case Boltzmann equations for the distribution functions may be formulated as follows:

$$\xi_k \frac{\partial}{\partial x_k} f_i = \sum_j J(f_i, f_j) + J(f_i, f_O) \quad (8.6)$$

$$\xi_k \frac{\partial}{\partial x_k} f_O = \sum_i J(f_i, f_O) + J(f_O, f_O) \quad (8.7)$$

where f_i - molecular velocity distribution function for i -th gas component in plume gas mixture, J - collisional term (collision integral).

Direct Simulation Monte-Carlo (DSMC) method is well known technique for solution of Boltzmann equations. Provided that initial data and molecular collision parameters are known the DSMC method can accurately simulate the particle distribution functions. However, as it has been already mentioned collisional cross-sections are not exactly known for the hypervelocity condition. So, in present work the elastic and reactive collision cross-sections were used as parameters. Meanwhile, full 3-D DSMC modeling of the high-altitude plume glow still remains a complex and time-consuming procedure. This fact hampers parametric computations, which require numerous repetitions of the computation with variation of molecular collisional parameters. Therefore, suggested were further simplifications that made computing codes faster and more flexible, providing almost the same outcomes, indeed. These simplifications come out from consideration of spatial scales of principal processes in the plume.

8.2.1.1. Spatial scales for principal processes in the plume

In the condition of orbital flight the hypervelocity PME plume flow expands into highly rarified atmosphere. So, the flow regime changes from continuous at the motor vicinity to a free-molecular one in the far field. This

circumstance suggests an idea of division of the plume flow onto several characteristic regions, where different flow models and computing methods (more simple than 3-D DSMC) may be applied. Possibility of such division becomes clear upon consideration of typical spatial scales of principal processes in the plume flow.

Distance L_1 at which the plume flow density becomes equal to atmospheric density may be evaluated given the approximate reverse square dependence of the plume flow density on the distance from the nozzle

$n_a \approx n_{p*} \left(\frac{x_*}{L_1} \right)^2$, where n_a - atmospheric number density, n_{p*} - plume species number density at some distance x_* not far from the nozzle. For the PME plume flow at altitude 380-400 km this estimate results in:

$$L_1 \propto x_* \sqrt{\frac{n_{p*}}{n_a}} \propto 10 \text{ km} \quad (8.8)$$

Knudsen number value in terms of ratio of the local mean free path in the reference frame fixed at the motor nozzle $\lambda_{p,p}$ to the distance from the motor becomes equal to unity at:

$$L_2 \propto \lambda_{p,p} \approx x_*^2 \frac{\sqrt{2}c(T_p)}{U} \sigma_{p,p} n_{p*} \approx 1 \text{ km} \quad (8.9)$$

where c – mean molecular velocity, T_p – plume temperature at large distance from the motor, $\sigma_{p,p}$ - effective elastic cross-section between different molecules in plume, U is directed velocity of the exhaust flow. This value of Knudsen number implies that starting from about 1-2 km the PME plume flow at 380-400 km altitude becomes almost collisionless. Cross-section for the collisions between plume molecules was taken $\sigma_{pp}=10^{-18} \text{ m}^2$ in this estimate.

The effluent molecule mean free path in the motor reference frame between subsequent collisions with atmospheric oxygen may be evaluated as:

$$\lambda_{p,a} \sim \frac{U}{(U+V)n_a\sigma} \approx 10\text{-}20 \text{ km} \quad (8.10)$$

Evidently, value of $\lambda_{p,a}$ depends on the choice of the effective cross-section $\sigma_{e,eff}$. The effective collision cross-section modeling at hypervelocity condition and related problems will be discussed in Section 8.3 in detail. For this particular estimate value of $\sigma_{e,eff} = 1\text{-}2 \cdot 10^{-19} \text{ m}^2$ was used. Obviously, the mean free path value defines the plume flow zone where the plume molecules most probably experience only a single collision with atmospheric oxygen. In the regions located closer to the nozzle the plume molecules may be considered as not colliding with atmospheric species.

And finally, mean free path of the oxygen atoms in the free stream in the reference frame fixed at the motor nozzle equals to:

$$\lambda_{a,nozz} \propto \frac{V}{c_a} \lambda_a \sim 170 \text{ km} \quad (8.11)$$

where c_a and λ_a - mean free path and mean molecular velocity in the reference frame bound to the atmosphere.

This means collisions between atmospheric oxygen atoms may be completely disregarded.

8.2.1.2. Simplification of the plume flow kinetic model

Given the estimates (8.8) and (8.10) collisional integral $J(f_i, f_o)$ may be omitted in the flow region of several km downstream from the PME. Similarly integral $J(f_o, f_o)$ may be neglected basing on the estimate (8.11). So, first simplification should be that flowfield parameters in this region may be simulated disregarding the atmospheric free stream.

As will be shown below translational temperature of the plume species falls down to 100°K and lower within hundred of meters downstream. Very soon the energy of the chaotic motion of the effluent molecules becomes negligibly small in comparison with the directed energy. Therefore, plume species distribution functions may be approximated by δ -functions:

$$f_i(\vec{\xi}_i) \approx n_i(\vec{x}) \delta(\vec{\xi}_i - \vec{U}) \quad (8.12)$$

here $n_i(\vec{x})$ molecular number density of i -th plume component.

Furthermore, high value of the reaction (8.1) threshold suggests that mostly those free stream oxygen atoms, which have not yet collided with the plume molecules, can initiate the reaction. Apparently any perceptible elastic collision between atmospheric oxygen and plume species is accompanied by the momentum and energy exchange. After the collision oxygen velocity vector changes its direction as well. So, that at the next collision the oxygen atom becomes unable to overcome reaction (8.1) threshold. It should be outlined, however, that such approach works only if the criterion is precisely specified which collision is “perceptible” one and which is not. This should be controlled by the effective collision cross-section (see Section 8.3). Within this approach each oxygen atom colliding with a plume flow molecule must be withdrawn from further consideration

and distribution function f_0 in equations (8.3), (8.4) and (8.7) should take into account only the atoms, which were not collided yet, that is $f_0 = f_{00}$. After these simplifications equation (8.7) is transformed to:

$$\xi_k \frac{\partial}{\partial x_k} f_{00} = -f_{00}(\vec{\xi}, \vec{x}) g_{U,\xi} \sum_i \sigma_i(g_{U,\xi}) n_i(\vec{x}) \quad (8.13)$$

and equation (8.3) to:

$$N_{\text{reac}}(\vec{x}) = n_{H_2O} \int f_{00}(\vec{\xi}_1) g_{U,\xi_1} \sigma_r(E_{U,\xi_1}) d\xi_1 \quad (8.14)$$

Evidently, equation (8.14) assumes that reactive collisions do not affect the particle distribution function. So, the distribution functions may be determined disregarding inelastic collisions and radiation is modeled over the fields of the gasdynamic parameters by the overlay method. This method was used before^{2,20,23} and demonstrated high efficiency of the computation. It substantially reduced the computation time. From the other side, the overlay method is fully justified in the high altitude plume flow, where the reacting collision frequency is much less than elastic collision frequency. This was proved through dedicated comparison of the overlay method with the full DSMC one²⁰.

Consideration of the spatial scales and general simplifications give rise to the idea of dividing the PME plume flow onto three zones.

Zone I is confined by a distance of about $L_2 \sim 1$ km downstream or even closer to the motor. In this zone the flow develops exclusively under effect of the plume intermolecular collisions. Molecular distribution functions are described by equation (8.6) with $J(f_i, f_0)$ term omitted. As it will be shown below, intermolecular collisions influence onto the plume flow very weak and the plume flow forms up already at some hundred meters from the motor. So, the boundary of Zone I may be set at this distance.

Zone II extends from some hundreds meters to about λ_{pa} . The flow in this zone has already formed up being still unaffected by the atmospheric free stream. Plume species distribution functions here may safely be approximated by the δ -functions, whereas atomic oxygen distribution function is fixed by linear equation (8.13). At the border of this zone plume species number density becomes comparable with the atmospheric one and further downstream the plume is mixed with atmosphere. In Zone II most of the reacting collisions occur. The reacting collision frequency is determined by the overlay method through equation (8.14).

Zone III is located at the distance $L_I \sim \lambda_{pa}$ and farther downstream. In this zone plume flow effectively mixes with the atmospheric stream. Collisions resulting in reaction (8.1) are rare events in this zone. However, some other physical processes may occur here, which could affect the plume glow radiation (see Chapter 9).

8.2.2. *Computation of the gasdynamic parameters of the PME plume flow in Zone I*

At the initial stage of the computation the PME nozzle and plume flow (20 meters downstream) was modeled by NARJ¹³⁶ (Numerical Analysis of Real Jets) CFD package. The nozzle flow computation started from the combustion chamber. Following input data were used:

Fuel and oxidizer – UDMH+NTO ((CH₃)₂N₂H₂+N₂O₄)

Mixture ratio (O/F) – 1.84

Combustion chamber pressure, P_0 – $9 \cdot 10^5$ Pa

Combustion chamber temperature, T_0 – 2935 K

Nozzle throat radius, R_{th} – 0.02445 m

Nozzle exit radius, R_{ex} – 0.1568 m

2D modeling of the nozzle flow has been made. The computation resulted in almost flat distribution of main molar components across the nozzle exit. Relative contents of the main exhaust components is as follows:

CO₂ = 0.524e-01

H₂O = 0.289e+00

NO = 0.107e-02

H₂ = 0.190e+00

N₂ = 0.267e+00

CO = 0.190e+00

H = 0.102e-01

Further downstream the flow was modeled both by DSMC method and NARJ code. This approach ensured crosschecking and higher reliability of the results.

Starting surface for the DSMC computation was chosen at 20.18 meters downstream from the PME. This choice was dictated by the necessity to have relatively small collisional mean free path making sure that CFD approach still works here. Particle distribution functions at this surface assumed to be Maxwellian. Pressure, temperature and the plume dimension in the perpendicular to the PME axis direction were taken from outputs of the NARJ computation. For modeling of the elastic collisions Variable Hard Sphere (VHS) model¹⁷ was applied. In the collisional processes the molecules were considered as identical species. This approximation should be accurate enough if the plume flow temperature is low and the flow shear layer is negligibly small in comparison with the main flow. According to NARJ computations number density of the plume molecules at the center point of the starting surface is $0.3313 \cdot 10^{20} \text{ m}^{-3}$ and temperature 37.5 K°. It should be noted, that in contrast

to hypervelocity condition inherent to plume-atmospheric stream counterflow, collisional processes in a low temperature media have been better studied. So, at very low temperatures intermolecular collisions may be described basing on the Maxwell molecular model, which, in particular, assumes linear dependence of the viscosity coefficient on temperature. Correctness of this assumption was checked through comparison of the air viscosity coefficient with its linear approximation. At $T < 37.5 \text{ K}^\circ$ the dependence appeared to be linear with high degree of accuracy. At $T = 50 \text{ K}^\circ$ discrepancy was found to be about 15%. So in the DSMC modeling of the plume flow the VHS model parameters were determined assuming linear dependence of the viscosity coefficient on temperature.

DSMC computation cell dimension is used to be smaller than local mean free path of the molecules. In other words the flow macroparameters have to experience just a small variations within the computation cell. Due to substantial variation of the flow species number density both in axial (X) and radial (R) directions the computation grid has to be non-uniform. For particular case of the PME plume flow modeling the flow region was subdivided onto five domains along X and two domains along R direction. Each domain included cells of different dimension ranged in X direction from 0.05 to 50 meters and in R direction from 0.015 to 25 meters. Total number of cells was 28704, whereas number of simulating molecules was about 270000. Entire dimension of the computational region extended to about 1000 meters downstream along the axis and to $R = 1.5X$ in radial direction. The plume flow appeared to be self-similar already at some hundreds meters downstream from the nozzle. So, computations further than 1000 m were not needed. It should be also noted that computation ran with different time steps specified particularly for each computation domain.

As mentioned above all molecules in the flow were considered as identical species having rotational degrees of freedom. Exchange between translational and rotational degrees of freedom was specified basing on the Larsen-Borgnakke model. Rotational relaxation parameter was chosen to be equal 3, being in compliance with the low temperature condition.

Results of modeling of the PME plume flow gasdynamic parameters are presented in Figure 147 through Figure 153. Figure 147 demonstrates how the DSMC modeled plume species number density along the axis may match a second order hyperbolic approximation. Such kind of approximation is often used in gasdynamic computations of plume flows. It should be mentioned, that due to low temperature and absence of the share layer in the computation model, same approximation turns out to be valid also for the number density distributions along the off-axis directions. This is important fact alluding to self-similarity of the flow and possibility to describe the particle number density distributions in this 2-D axially symmetric flow by an analytic approximation.

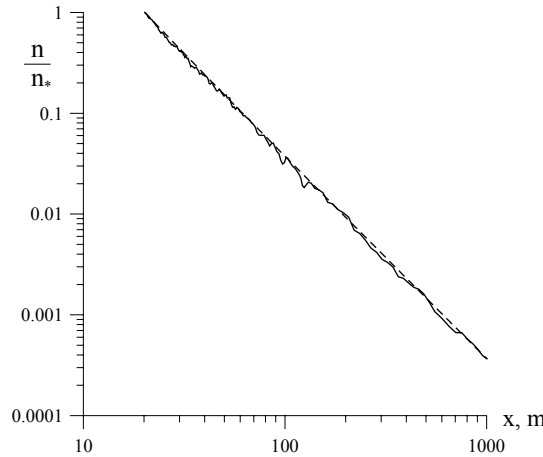


Figure 147. Normalized PME plume flow species number density along the plume axis modeled by DSMC (solid line) compared with second order hyperbolic approximation (dashed line).

Figure 148 demonstrates self-similarity of the DSMC flow modeling results. Normalized particle number density $n_l(x, r_l) = n(x, r_l)/n(x, 0)$ is presented in the figure versus normalized radial distance from the axis $r_l = r/(1.5x)$. As becomes evident from this figure the plume flow is self-similar starting from about 100-200 meters from the nozzle. Self-similarity of the CFD solution is demonstrated in Figure 149. As it's seen from the figure the NARJ (CFD) computation provides a quite self-similar solution too. Furthermore, the NARJ results of the particle number density almost coincide with the DSMC results. This is clearly seen from Figure 150. So, both DSMC and CFD solutions may be approximated by the same analytical expression. Good analytical approximation for the PME plume flow was found to be:

$$n(x, r) = f(x) \cdot f(r) \cdot n_0, \quad (8.15)$$

$$f(x) = \frac{1}{\left(1 + \frac{x - 20.18}{19.18}\right)^2}, \quad f(r) = 0.95 \exp\left(-\frac{71.707}{1 + 9.609} \frac{r^{3.5}}{r^{2.5}}\right)$$

where n_o – is the plume flow number density in the initial section $X_0=20.18$ m.

Profile computed with formula (8.15) is compared with natural DSMC profile in Figure 151.

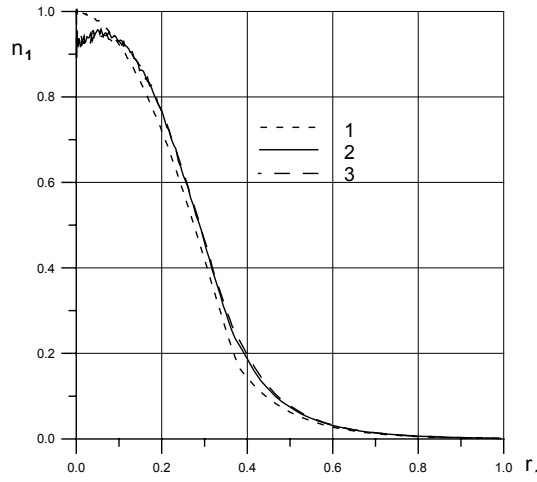


Figure 148. Dependence of normalized particle number density versus normalized radial distance as modeled by DSMC method (see text): 1 – NARJ solution at 20.2 meters plume section (input data), 2 – DSMC solution at 115 meters downstream, 3 – DSMC solution at 1003 meters downstream.

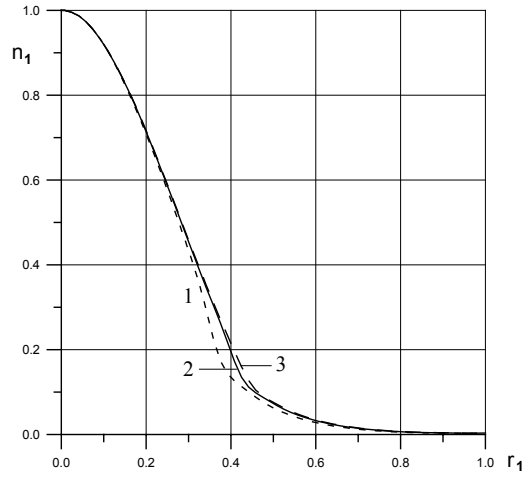


Figure 149. Dependence of normalized particle number density versus normalized radial distance as modeled by NARJ method (see text): 1 – NARJ solution at 20.2 meters plume section (input data), 2 – NARJ solution at 120 meters downstream, 3 – NARJ solution at 1153 meters downstream.

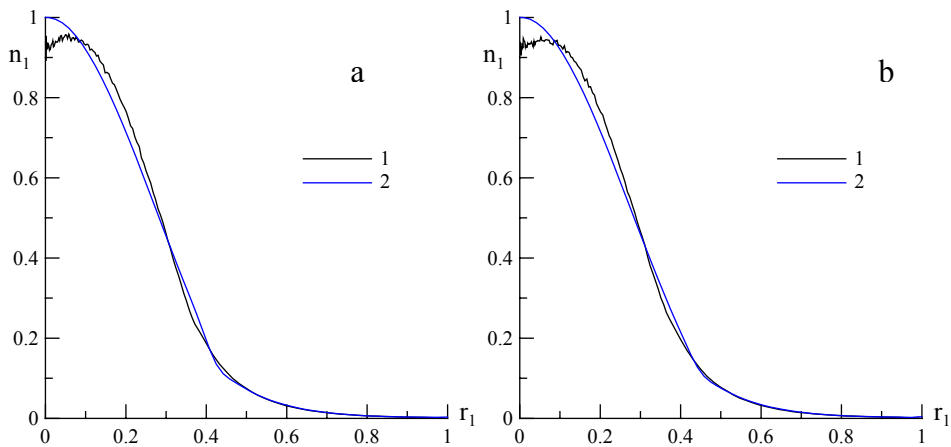


Figure 150. Comparison of the normalized number density profiles computed by DSMC and NARJ: a) 1 – DSMC result at 115 m section, 2 – NARJ result at 120 m section; b) 1 – DSMC result at 1003 m section, 2 – NARJ result at 1153 m section.

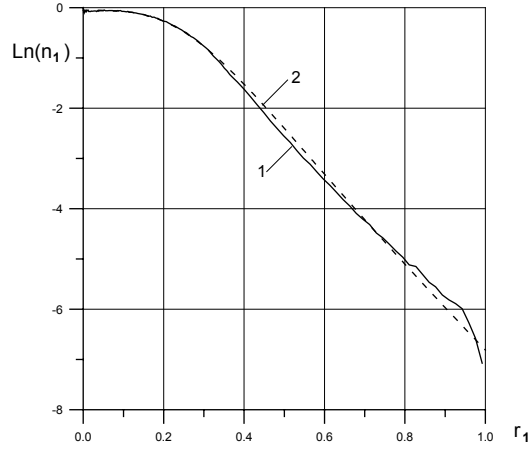


Figure 151. Approximation of the self-similar particle number density profile: 1 – DSMC computation, 2 – approximation by formula (8.15).

Profiles of the plume flow axial and radial velocity components are shown in Figure 152. Again, excellent agreement between DSMC and NARJ results is evident. The profiles of the velocity components result in the relation:

$$\frac{U_r}{U_x} \approx \frac{r}{x}, \quad U = \sqrt{U_x^2 + U_r^2} \approx 3338 \text{ m/s} \quad (8.16)$$

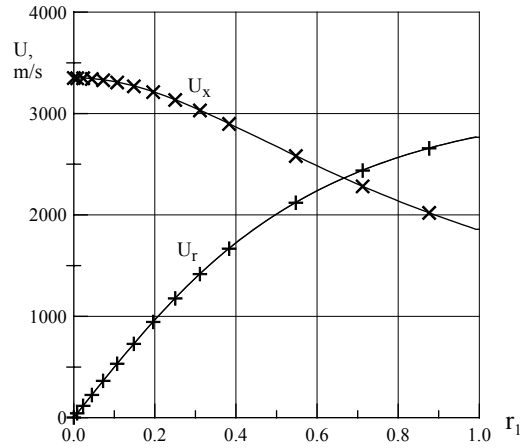


Figure 152. Velocity components profiles: solid lines – NARJ computation, crosses – DSMC computation.

And finally, Figure 153 shows temperature profiles computed by DSMC and NARJ (CFD) methods. DSMC computation resulted in higher values of temperature. However, for most practical application including the glow radiation modeling this discrepancy may be disregarded, because both methods resulted in very low plume species translational temperatures.

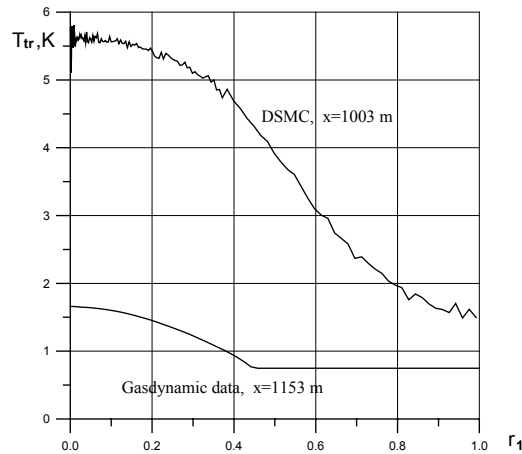


Figure 153. Translational temperature profiles modeled by DSMC and NARJ.

8.2.3. Algorithms for simulation of radiation intensity in Zone II

As it was demonstrated in previous paragraph both DSMC and CFD methods result in the same values of the particle number densities in the plume flow. Furthermore, analytical expression (8.15) may be applied for axially symmetric plume flow. Because of the plume flow similarity expressions (8.15) may be applied for modeling of the flow particle number densities in Zones II as well. So, the glow radiation was computed over the fields of the molecular number densities, which were simulated either by CFD method or analytically.

8.2.3.1. TPMC method for glow radiation modeling

A Test Particle Monte-Carlo method (TPMC) has been applied for modeling of the glow radiation in Zones I and II. The TPMC method is much simpler than DSMC one, being capable at the same time to take into account multiple collisions of the oxygen atoms in the plume flow. In this approximation number density of the oxygen atoms and number of the reactive collisions is computed over the fields of the plume species number densities, which in turn are considered as being not affected by the atmospheric stream. From this standpoint the TPMC method may be considered as an overlay approximation. Basic principles of the TPMC method, which was used in this work, are as follows.

Consider oxygen free stream entering the plume flow through some boundary surface. Scheme of an oxygen atom scattering in the plume flow is shown in Figure 154. The plume flow is axially symmetric. In general case the free stream velocity vector has an angle α to the plume axis. In case of $\alpha=0$ the problem becomes completely axially symmetric. The plume particle number densities have been modeled analytically through formulas (8.15) in all TPMC computations. Molar fractions X_i of different plume species were borrowed from the NARJ computation outputs. Energy distribution functions for the plume species are considered as δ -functions (formula (8.12)). For oxygen atoms Maxwellian energy distribution with real atmospheric temperature and number density is applied.

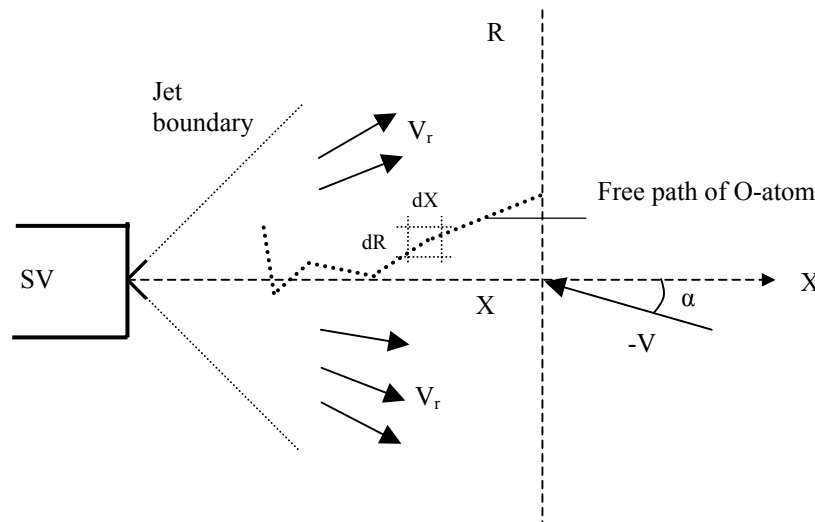


Figure 154. Scheme of scattering of the free stream oxygen atom in the plume flow.

The oxygen atoms travel across the plume flow, having some probabilities for elastic and reactive collisions. Sharp bends of the atom trajectory in Figure 154 represent collisions of the oxygen atom with the flow molecules. The trajectory terminates if the atom either experience any reaction collision or leaves the flow boundary.

For modeling of the collisional processes the oxygen atom mean free path in the plume flow is sampled. For simulation of the mean free path distribution effective cross-section weighted on individual cross-sections of each collisional partner is used. If the collision occurs within the plume boundaries a collisional partner is being chosen with probability density:

$$p_{M_i} = \frac{X_i \sigma_i}{\sum_{i=1}^K X_i \sigma_i} \quad (8.17)$$

If a water molecule has happen to be the collisional partner and total collision energy exceeds reaction (8.1) threshold, the reaction is sampled with probability:

$$p_r = \frac{\sigma_r}{\sigma_{H_2O}} \quad (8.18)$$

If the reaction hasn't occurred the oxygen atom post-collision energy and trajectory is being determined, basing on the adopted collisional model (see Section 8.3.1). Otherwise the trajectory terminates. The number of the reactive collisions in each computational cell is stored in the computer memory.

8.2.3.2. FNSAF method

Further simplification of the equation (8.13) comes from the assumption that oxygen velocity V_o yielding the relative collision velocity g is almost undistinguished from the average free stream velocity and energy distribution function of the non-scattered oxygen atoms f_{O0} stays the same all along the plume flow. This assumption leads in a simple solution of the equation (8.13):

$$f_{O0} = f_{O\infty} \exp \left[- \int \left(\frac{g_{U,V}}{V} \Sigma \sigma_i(g_{U,V}) n_i \right) dx \right] \quad (8.19)$$

where $f_{O\infty}$ - oxygen atom distribution function in undisturbed atmosphere.

Actually, expression (8.19) states that the free stream oxygen attenuation in the plume represents just a plain diminution of the free stream number density. Introduction of this expression into (8.14) provides a simplified form for the number of reacting collisions:

$$N_{\text{reac}}(\vec{x}) = n_{H_2O} n_{O\infty} \sigma_{r,\text{eff}} g_{U,V} \exp \left[- \int \left(\frac{g_{U,V}}{V} \Sigma \sigma_i(g_{U,V}) n_i \right) dx \right] \quad (8.20)$$

In this expression $\sigma_{r,\text{eff}}$ is effective cross-section for reaction (8.1) defined by:

$$\sigma_{r,\text{eff}} = \frac{1}{g_{U,V} n_{O\infty}} \int f_{O\infty}(\vec{\xi}) \sigma_r(E_{U,\xi}) g_{U,\xi} d\vec{\xi} \quad (8.21)$$

Note, that substitution of the oxygen velocity distribution function in (8.21) by δ -function from average stream velocity would not be correct. Translational energy of a colliding pair water-oxygen, which have relative velocity around 10.5 km/s is very close to the reaction (8.1) threshold. Effect of the velocity thermal dispersion is very important in this case.

When dependence of the reaction cross-section on the collision energy is explicitly defined, integral in expression (8.21) may be readily taken numerically. Similarly, having the plume species number density distribution and elastic cross-section energy dependence available the number of reactions may easily be computed through (8.20). A simple code has been developed for numerical solution of equation (8.20). Running this code on a common PC almost doesn't require any considerable time. So, the approach was conventionally named as Fast Numerical Solution of the Analytical Formulation (FNSAF) method. This approach has been widely used in this work for computation of the glow radiation. In fact, elastic and reactive cross-sections may be considered as parameters in equations (8.20) and (8.21). So, these equations are very convenient for parametric computation, doesn't matter in how wide ranges the parameters have to be varied.

Within the frames of the FNSAF approximation the flowfield molecular number densities have been computed by NARJ code. In each computational cell the effective elastic and reaction collision cross-sections have been modeled by method discussed in Section 8.3.1. Reactive collision frequency is computed through relation (8.20).

8.2.3.3. 1-D analytical solution

Expression (8.20) becomes extremely simple in a 1-D case. This case may be considered as a reasonable approximation for modeling of the glow intensity along the plume axis when this axis is co-aligned with the free stream atomic oxygen velocity vector. As mentioned above, number density of the plume molecules along the axis (formula (8.15)) may be well reproduced by a reverse square expression:

$$n_i(x) = X_i n = X_i \frac{A}{x^2} \quad (8.22)$$

where A is a constant characteristic to the motor type. Introduction of the particle number density in the form of (8.22) into expression (8.20) allows simple integration of the exponential factor resulting in a formula for specific radiation power $W(x)$ along the plume axis:

$$W(x) = \frac{h\nu}{4\pi} N_{\text{reac}}(x) \quad (8.23)$$

$$N_{\text{reac}}(x) = \frac{A \cdot X_{H_2O}}{x^2} n_{O\infty} \sigma_{r,\text{eff}} \cdot (U + V) \cdot \exp \left(- \frac{A \cdot (U + V) \cdot \sigma_{e,\text{eff}}}{x \cdot V} \right)$$

where $h\nu$ is average energy of the single photon of the OH(A \rightarrow X) radiation. Also in relation (8.23), relative velocity is explicitly expressed as the sum of free stream velocity V and plume flow velocity U , $g_{U,V}=U+V$ and effective elastic collision cross-section of oxygen atoms with the plume molecules $\sigma_{e,eff} = \sum_i X_i \sigma_i(g_{U,V})$ is introduced.

Further integration of this expression along the plume axis x will give a formula for integral radiation that should be observed along the plume flow axis in a tail viewing geometry:

$$W_{ax} = \frac{h\nu}{4\pi} \int_0^\infty N_{reac}(x) dx = \frac{h\nu}{4\pi} \frac{X_{H_2O} n_{O\infty} \sigma_{r,eff} V}{\sum_i X_i \sigma_i(g_{U,V})} = \frac{h\nu}{4\pi} \frac{X_{H_2O} n_{O\infty} \sigma_{r,eff} V}{\sigma_{e,eff}} \quad (8.24)$$

Expression (8.24) is very convenient for estimates of the glow intensity (reaction collision frequency) and analysis of influence of the collision cross-section values and plume flow parameters on the radiation intensity.

8.3. Modeling of the molecular collisions at hypervelocity condition

Above consideration of different methods for the glow radiation modeling showed that computation results strongly depend on the choice of the elastic and reaction cross-sections for collisions of atmospheric oxygen with the plume flow molecules. So, special attention has been paid to modeling of these collisions.

8.3.1. Elastic collisions

Molecular elastic collisions can be accurately treated through solution of the dynamic problem in the intermolecular potential field (see Ref.¹⁷ for example). Apparently this approach requires specification of the intermolecular potentials. Shapes of the intermolecular potentials may be retrieved from analysis of deflection angles of high-energy oxygen atoms scattered on the molecular targets. The deflection functions, in turn, are measured experimentally. This analysis was carried out in Ref.¹³⁷ and further elaborated in Ref.¹³⁸. In Ref.¹³⁷ author analyses two sets of data: i) obtained in his own experiments, where deflection functions of high-energy molecular beams were measured and ii) obtained in Ref.¹³⁹ in similar experiments. Molecular potentials were modeled in the Born-Mayer form:

$$U(r) = D e^{-\alpha r}, \quad (8.25)$$

which assumes only repulsive intermolecular forces. Disregarding of the attractive component is reasonable at high energies of the colliding partners.

Parameters of the Born-Mayer potentials, which were derived from the two sets of experimental data, are given in Table 22. These parameters were recommended by respected authors for application in the collision energy interval $E=1-10$ eV. Translational energies of the colliding partners E_{tr} are also presented in the table.

Table 22. Parameters of the Born-Mayer potentials of oxygen colliding with some molecular partners.

Collision partner	Ref.	D, eV	$\alpha, \text{\AA}^{-1}$	E_{tr}, eV	$\sigma_{tr}(E_{tr}), \text{\AA}^2$	$[X]$
N_2	137	11350	5.12	6.07	7.415	0.267
N_2	139	700	3.11	6.07	8.458	0.267
H_2	137	186	3.56	1.06	7.548	0.190
H_2	139	440	3.92	1.06	8.300	0.190
H_2O	138	17350	4.69	5.05	10.25	0.288
H_2O	139	1480	3.72	5.05	8.246	0.288
CO	137	1220	3.05	6.07	10.792	0.189
CO	139	5330	4.21	6.07	8.974	0.189
CO_2	137	10000	3.89	6.995	11.99	0.053
CO_2	139	2350	3.32	6.995	10.82	0.053

Deflection functions $\chi(b)$ (dependence of the scattering angle on the impact parameter) may be computed for each pair of the colliding partners basing on these potentials. Evidently, the deflection angle is function of the collision energy as well. Figure 155 exemplifies dependence of the O- N_2 deflection function on energy. Dependence of the deflection angle on the impact parameter and energy is similar for other colliding pairs.

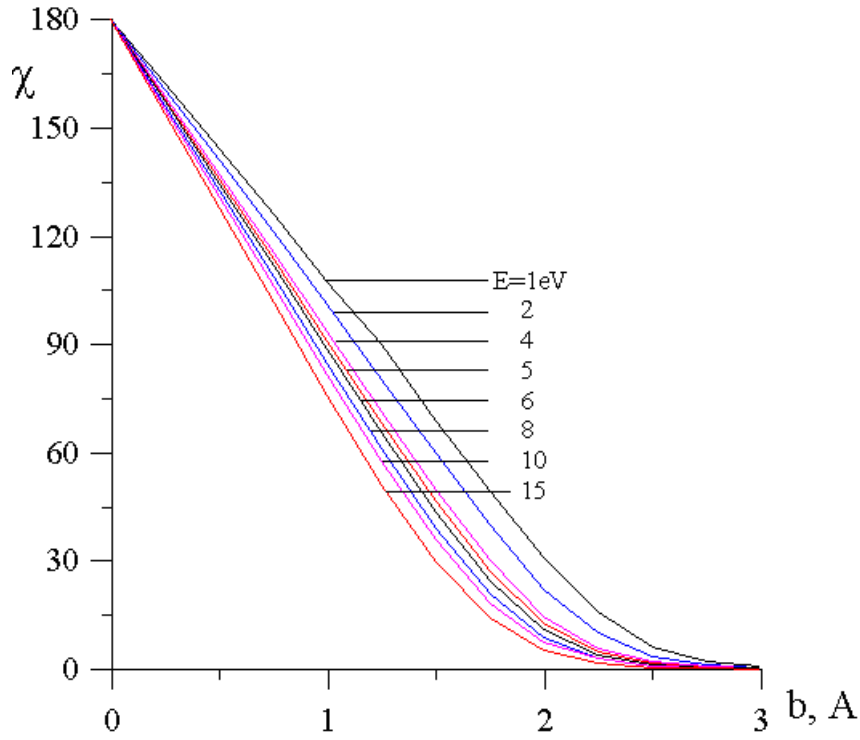


Figure 155. Deflection functions computed for O-N₂ collision at different energies. Molecular potential in the Born-Mayer form was applied with parameters $D=11350$ eV, $\alpha= 5.12$ Å.

Actually the deflection angles $\chi(b)$ do not come exactly to zero even at very large meanings of the impact parameters b , because potentials in the form (8.25) have finite values all over the physical space. From this standpoint any interaction of two particles even at long distance may be considered theoretically as a “collision” resulting in very small deflection. Obviously, modeling of the molecular collisions for the full set of the impact parameters including the big values technically is not possible in real flows. Therefore, statistical methods like DSMC and TPMC exploit the concept of total collision cross-section, which exactly defines whether the collision has happened or not¹⁷. In general, the total collision cross-section should be a function of the collision energy. Together with the total cross-section a scattering law, which defines the scattering probability at specified angle, should be introduced.

Choice of the total cross-section assumes some arbitrariness. Several kinds of the total cross-sections are discerned. General requirement is that the choice must be physically reasonable and introduction of the total cross-section into the computing model should lead in correct results. Technically, the total collision cross-sections values may be determined from either deflection functions or molecular potential curves by different ways, having different names at that. Ref.⁷¹ gives approximate formula for so called transport cross-sections derived from the Born-Mayer potential parameters:

$$\sigma_{tr}(E) = \frac{8\pi(0.124 + 0.0849\beta + 0.0567\beta^2)}{\alpha^2 \beta^2} \quad (8.26)$$

where $\beta = \frac{1}{\ln(D/E)}$.

Values of this transport cross-sections for collisions between oxygen and major plume molecules $\sigma_{tr}(E)$ are presented in Table 22 too. Despite that parameters of the intermolecular potentials borrowed from two different experimental data sets may substantially differ, difference between the transport cross-sections appears to be not that big. This fact makes choice of the potential parameters more flexible. So, at the earlier stage of the PME plume flow simulations by TPMC method parameters listed in Table 23 were used for the elastic collision modeling, whereas FNSAF method has been utilizing the parameters listed in Table 24.

Table 23. Parameters of the Born-Mayer potential used in TPMC computations.

i	Collision partner	D_i , eV	α_i , Å ⁻¹	p_i	b_i^* , Å
1	H ₂ O	131517	5.952	0.1	2.7

2	N ₂	11350	5.12	0.1217	2.7
3	H ₂	85.103	2.85	0.2	3.6
4	CO	1220	3.56	0.18	3.2
5	CO ₂	10000	3.89	0.14	3.4

Table 24. Parameters of the Born-Mayer potential used in FNSAF computations.

<i>i</i>	Collision partner	D_i , eV	α_i , Å ⁻¹
1	H ₂	186	3.56
2	CO	1220	3.56
3	CO ₂	7000	3.89
4	N ₂	11350	5.12
5	H ₂ O	17350	4.69

Last column in Table 22 represents mole fraction of the specie in the PME exhaust. The transport cross-sections averaged over the molecular composition

$$\sigma_{av,tr} = \sum_i X_i \sigma_{i,tr}(E_{i,tr}) \quad (8.27)$$

are equal to 9.11 Å² (Ref.^{137,138} parameters), 8.54 Å² (Ref.¹³⁹ parameters), 8.64 Å² (Table 23 parameters) and 8.55 Å² (Table 24 parameters). Difference between the averaged transport cross-section is less than 7%. So, utilization of each set of the parameters for solution of any problem where integral characteristics are addressed should probably lead in almost the same results. Average transport cross-section (formula (8.27)) was used in most simulations by the FNSAF method.

Another approach for elastic collision modeling has been used in the TPMC computations. In general case exact dynamic problem was solved for each pare of the colliding partners. Deflection functions associated with particular colliding partners were cut somewhat arbitrarily at the meanings of impact parameter b_i^* corresponding to the deflection angles $\chi_i^*(b)$ of about 2°. The b_i^* values are presented in Table 23 for reference. At higher values of b the deflection angles were set to zero. The b_i^* values fixed the total cross-sections $\sigma_i^* = \pi(b_i^*)^2$. Note, that both b_i^* and σ_i^* depend on energy, because the deflection function is computed at specified collision energy value. Energy dependence of the total cross-section was found from parametric computations and approximated by a power law:

$$\sigma_i(E) = \sigma_i(E_{i,tr}) \times \left(\frac{E_{i,tr}}{E} \right)^{p_i} \quad (8.28)$$

The p_i -values are presented in Table 23 as well.

Having the collision event fixed through introducing of the total cross-sections, impact parameter b for particular collision was arbitrarily sampled with probability density $p_b = \frac{2}{(b^*)^2} b$. These impact parameters

were used further for determination of the post-collision dependences of the deflection angle and energies of the colliding partners basing on the molecular potential and deflection functions.

Test computation of the plume glow radiation intensity showed that increase of the b_i^* values (that is inclusion of the slipping angles $\chi_i(b) < 2^\circ$ into consideration) didn't change output results, rising the computation time substantially. Therefore, modeling of the "Progress" plume glow by TPMC method has adopted the above-discussed way for treating of the elastic collisions between atmospheric oxygen and the plume flow molecules. Comparison between the computation results and experimental results provides indirect opportunity to judge on how accurately the intermolecular potentials were modeled.

Disadvantage of this approach (TD – "trajectory dynamics" approach hereinafter) is that the collision dynamic problem has to be resolved at each collision. This requirement inevitably leads in the growth of computation time. Eventually, the TD approach becomes unaffordable for application in a more complex simulation method, such as the DSMC one, when billions of collisions are considered. Apparently, reasonable simplifications of the TD approach should be implemented in this case. So, instead of using different potentials for each colliding pare, perhaps a single one may properly be chosen. This simplification was tested with TPMC method. O-N₂ potential curve was used for solution of the dynamic problem for each pare of the colliding partners. As before, total collision cross-sections were chosen corresponding to the deflection angle $\chi(b) \leq 2^\circ$. Despite the common potential, the cross-sections appeared to be not exactly the same, because the colliding partners still had different collision energy (see Table 22) and because the deflection function depends on this energy (see Figure 155).

And finally an effective cross-section may be introduced representing the simplest approach of treating the molecular collision problem. This approach should be reasonable for application with any simplified computation method. Both FNSAF and simplified TPMC methods are less complex than DSMC one. Accuracy of the TD approach looks too high in comparison with the accuracy of the computation method itself. In the trade-off between the accuracy and simplicity of the elastic collision model simplicity should be favored in this case.

In the meantime, introduction of the effective elastic collision cross-section in the TPMC method could bring substantial benefits as well. By definition, the oxygen atom colliding a plume flow molecule with effective cross-section $\sigma_{e,eff}$ gives part of its energy up to the molecule, being unable to enter the reaction (8.1) at the next collision. As discussed in paragraph 8.2.1.2, this approximation is justified by a high value of the reaction (8.1) threshold, which is very close to the water-oxygen total collision energy in the plume flow. Introduction of the effective cross-section offers an opportunity to confine consideration of any atomic oxygen trajectory in the plume by the first collision with a plume molecule. Collided atoms are to be withdrawn out from consideration and the free stream oxygen number density in the plume is computed through a simple attenuation law. This approach (SC – single collision approach hereinafter) for treating of the elastic collisions between atomic oxygen and plume molecules was eventually utilized in simplified TPMC method providing substantial reduction of the computation time. Also, the effective cross-section has been used in analytical formulas (8.23), (8.24) for the reaction collision frequency in 1-D case. Effect of different elastic collision models onto the results of the glow radiation computation by the TPMC method is addressed in Section 8.3.3.

There are a number of other collisional models dealing with the elastic scattering and feasible for DSMC computer simulations. One of the most frequently used is the Variable Hard Sphere (VHS) model^{17,19}. The VHS model is essentially phenomenological one. In this model colliding molecules are treated as a hard spheres with diameters depending on the relative velocity of the colliding partners in the center of mass system.

Total elastic cross-section in the VHS model is expressed as:

$$\sigma_T = \sigma_{T, ref} \left(\frac{E}{E_{ref}} \right)^{-\nu} \quad (8.29)$$

where $\sigma_{T,ref}$ - is total reference cross-section at a reference energy E_{ref} and ν is power law exponent. According to relation (8.29), the VHS cross-section has two adjustable parameters – reference molecular cross-section $\sigma_{T,ref}$ and exponent factor ν in the power law. Transport properties (viscosity and mobility coefficients in particular) of the real flows are very sensitive to the value of elastic cross-sections¹⁷. If total elastic cross-section in the form of (8.29) is utilized for modeling of a viscous gas flow, temperature dependence of the viscosity coefficient will be controlled by the VHS power law exponent¹⁷: $\mu \propto T^{0.5+\nu}$. This fact allows numerous experimental data on the viscosity coefficient temperature dependence to be used for accurate determination of the VHS power law exponent. By proper choice of this factor and the reference cross-sections it's easy to fit modeled transport properties of a gas flow to experimentally measured values. In particular, exponent factor $\nu=0.25$ is often successfully utilized for practical applications. Basing on the analysis of numerous experimental data on the viscosity coefficient measurements, values of the VHS model parameters were proposed in Ref.^{17,140} for different molecules. Typically, available experimental data were taken in the conditions when collision energy of most molecules didn't exceed 0.1-0.5 eV. From the other hand big variety of the real space flows (including a motor plume flow at LEO conditions) involve molecular velocities corresponding to energies $E \sim 1-10$ eV. The VHS model has not been tested at those high energies and application of the available VHS model parameters doesn't warrant true results. Nevertheless it has been utilized for modeling of the elastic collisions in the PME plume flow^{20,21}, because it's very convenient for DSMC computations. In the meanwhile, results of the elastic cross-section modeling by VHS model utilizing conventional parameters may noticeably differ from the values obtained above with formula (8.26). For instance, VHS parameters for collision between atomic oxygen and molecular nitrogen at temperatures 2500-3000°K may be borrowed from Ref.¹⁴⁰. The VHS cross-section modeled with these parameters at hypervelocity conditions ($E \sim 5$ eV) will be about 1.6-1.8 times higher of the values presented in Table 22.

Basically, experiments with the plume glow radiation measurements render an opportunity to indirectly validate one or another collisional model. For this validation spatial distribution of the plume glow radiation intensity has to be modeled and compared with experiment. As shown below, the distribution is very sensitive to the choice of the collisional model parameters (that is either parameters of intermolecular potentials or parameters of the VHS model or the elastic cross-sections themselves). So, comparison of the modeled distribution with measured in experiment allows making a judgment about appropriateness of the collisional model parameters. Comparison of the glow computation results with experimental data and verification of the elastic cross-section models is addressed in Section 8.5.

8.3.2. Reaction cross-section

Similarly to the elastic scattering problem inelastic collision accompanied by a chemical reaction can be most accurately described through consideration of the collision dynamics. However, in comparison with the elastic collisions the problem is much more complicated in case of the chemical reactions. Accurate solution of

the problem requires modeling of 3-D distribution of the intermolecular potential of the colliding partners and simulation of the nuclei motion in this complex potential field. Key point of this approach is detailed knowledge of the potential distribution. Uncertainty of this distribution results in inaccuracy of the prediction of the reaction parameters. Also, this approach turns out to be not relevant for practical computations due to its complexity. In this connection simplified phenomenological models for chemical reactions are often exploited in practice^{17,18,141,142,143}. Concept of the reaction cross-section is introduced in these models making easier practical simulation of chemically reacting flows. The reaction cross-section controls probability of the collisional partners to enter in chemical reaction once the collision has occurred. As always, the phenomenological models have some adjustable parameters, which are assumed to be adjusted to provide best fit to experimental data.

Reacting Hard Sphere (RHS) model suggests the simplest form of the reaction cross-section:

$$\begin{aligned}\sigma_r &= 0, & E < E_{th} \\ \sigma_r &= \sigma_0, & E \geq E_{th}\end{aligned}\quad (8.30)$$

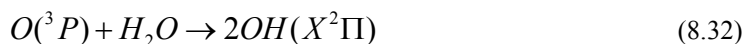
where E_{th} - the reaction threshold, σ_0 - constant. The RHS cross-section has just a single parameter σ_0 , which doesn't depend on the collision energy. Of course, this is too simplified approach, which may be applied only within limited interval of the collision energy. From the other hand, the RHS is consonant with the effective cross-section concept (8.21) and may be readily verified through experiment. The cross-section value σ_0 may be suggested basing on the direct measurements of the "Progress" plume OH(A→X) radiation intensity.

More elaborated models, such as modified line-of-centers (MLOC)¹⁴¹ model, Transition State Theory (TST)¹⁴² based models, Total Collision Energy (TCE)¹⁷ model and like consider the reaction cross-section dependent on energy. Generally, this dependence has a form of:

$$\sigma_r = \sigma_0 \frac{(E - E_{th})^n}{E^m} \quad (8.31)$$

where E_{th} - is the reaction threshold and σ_0 , p , q - constants, which may be considered as the model parameters.

This form of the reaction cross-section may be directly related to the reaction rate constant. So, the cross-section parameters may be derived from the reaction rate constant temperature dependence. Two different forms of the rate constant temperature dependence for reaction



were analyzed and analytically expressed in Ref.^{144,145} for applications in the temperature range up to 2000 K°. Reaction (8.32) differs from reaction (8.1) by that both product OH molecules are in the ground state. Because no data have been available about similar reaction producing electronically excited OH molecules, two different forms for the reaction (8.1) cross-section have been derived in Ref.¹⁴⁶ from the reaction (8.32) rate constants basing on the TST theory:

$$\sigma_r = 1.15 \cdot 10^{-16} \frac{(E - E_{th})^{0.5}}{E} \text{ cm}^2 \quad (8.33)$$

$$\sigma_r = 3.1 \cdot 10^{-16} \frac{(E - E_{th})^{1.8}}{E} \text{ cm}^2 \quad (8.34)$$

Both forms of the cross-sections were utilized earlier for modeling of the "Progress" plume glow intensity and the intensity was compared with experimental data^{4,20,21,23}. These comparisons brought forth an assumption, that cross-sections in the form (8.33), (8.34) overpredicted the radiation intensity on 1-2 orders of magnitude.

To reduce this discrepancy contribution of internal energy into reaction (8.1) was taken into account in Ref.²⁰. Amount of this contribution is accounted for differently in different models (see Ref.¹⁸ for example on how it makes in case of some dissociation models). In practice it reduces to introduction of additional parameters characterizing the internal energy contribution. In Ref.²⁰ the TCE model was utilized for the analysis of internal energy contribution effect. Actually, the TCE model suggests similar to (8.31) form for the reaction cross-section, but includes one more parameter, which controls contribution of the internal energy. Actually, variation of multiple parameters in the cross-section energy dependence to fit experimental data doesn't make a big sense in our particular case. Analysis of the experimental data from "Mir" station suggests only effective value of the reaction cross-section defined by relation (8.21). Any discrepancy between model and experiment may easily be removed by adjusting of a sole parameter. From the other side, such approach is quite appropriate. Indeed, direct extrapolation of the adiabatic reaction (8.32) onto a non-adiabatic case (8.1) has not been reasonably augmented so far. Moreover, there is a big skepticism that it can be done. Unfortunately, too little works are available where reaction (8.1) is considered at hypervelocity conditions. Some evidence that reaction (8.1) might take a place was found in Ref.¹, where the OH(A→X) emission is visible in some spectra. In more recent paper¹⁴⁷ calculations of the potential energy surfaces related to collision of atomic oxygen with water molecules were presented. Authors found conical intersection seems, which tie the potential energy surfaces of reactants and electronically excited products. This means that reaction (8.1) may potentially take a place. However, no data about energy dependence and absolute value of the reaction cross-section have been reported. So, cross-section energy

dependence in its general form (8.31) and in particular forms (8.33), (8.34) should be considered as a practical substitution for the real one, which is actually unknown. In this regard, basic parameters of the reaction cross-section such as σ_0 and power law exponent may already be considered as variable parameters, despite their direct coupling with corresponding parameters of the reaction rate temperature dependenceⁱ.

Revision of the reaction (8.1) cross-section value was suggested in Ref.⁵ and further implemented in Ref.²³, where effective cross-section value (8.21) was estimated from experiment and compared with result of prediction by formula (8.33). Under the circumstances of a complete absence of any data about cross-section of non-adiabatic single step reaction (8.1) such simplified verification of the reaction cross-section model had incontestable value. Recently this approach has been utilized in Ref.³⁶, where reaction (8.1) was studied in the Shuttle plume glow and the MLOC reaction cross-section was found to be 2 orders of magnitude overpredicting the experimental data. This Report suggests further verification of the effective reaction cross-section values against experimental data.

8.3.3. *Influence of the elastic collision cross-section choice onto results of the glow intensity computation by TPMC method*

Purpose of this analysis was to prove that even a simple molecular collision model could provide accurate results of the glow radiation modeling, if the collisional cross-sections are properly chosen. As mentioned above, spatial distribution of the “Progress” plume glow radiation was found to be very sensitive to the elastic cross-section choice^{21,23}, whereas integral over line-of-sight of absolute radiation intensity strongly depends on both elastic and reaction cross-sections. This is also clearly seen from expressions (8.23), (8.24). So, the radiation spatial distributions are modeled in this section at varying values of the elastic cross-sections. The test computation were conducted for PME plume OH(A→X) glow parameters. Reaction collision frequency was computed by TPMC method with different parameters for the elastic collisions between the atmospheric oxygen and plume molecules. For the reaction cross-section relation (8.33) was used in this set of computation.

First test was aimed to study the problem of how the intermolecular potential form for different pares of molecules influences the glow radiation intensity. Figure 156 through Figure 159 illustrate how utilization of a common potential characteristic for the O-N₂ collision instead of different potentials for each colliding pare affects the glow radiation distribution. Actually, the difference is small. So, the concept of common potential for all colliding pares has been adopted in further TPMC computations.

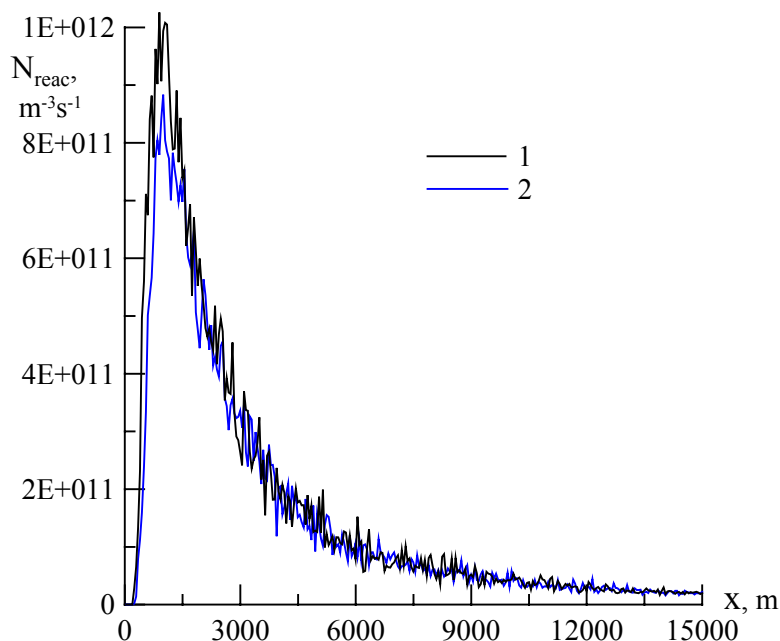


Figure 156. Reactive collision frequency along PME axis: 1 – TD-approach with common potential; 2 – TD approach with different potentials.

ⁱ Analysis in Ref.¹⁴⁷ shows that reaction (8.1) doesn't assume any activation energy other than required by the energy conservation law. So, the reaction threshold can't be considered as a variable parameter.

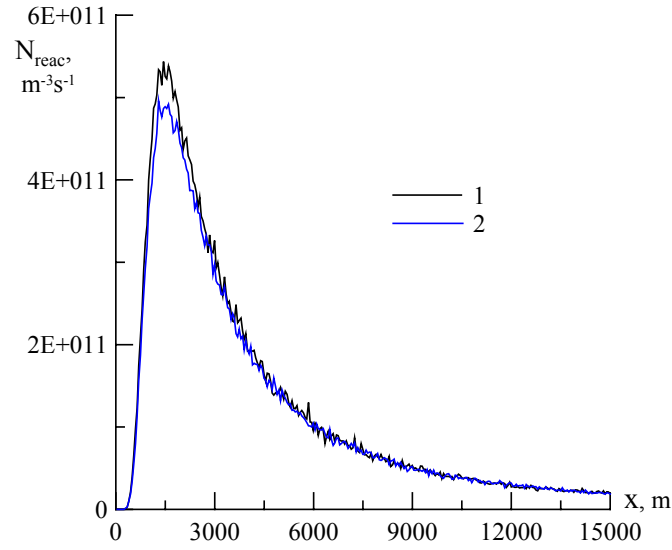


Figure 157. Reactive collision frequency along the line parallel to the PME axis 475 meters away: 1 – TD-approach with common potential; 2 – TD approach with different potentials.

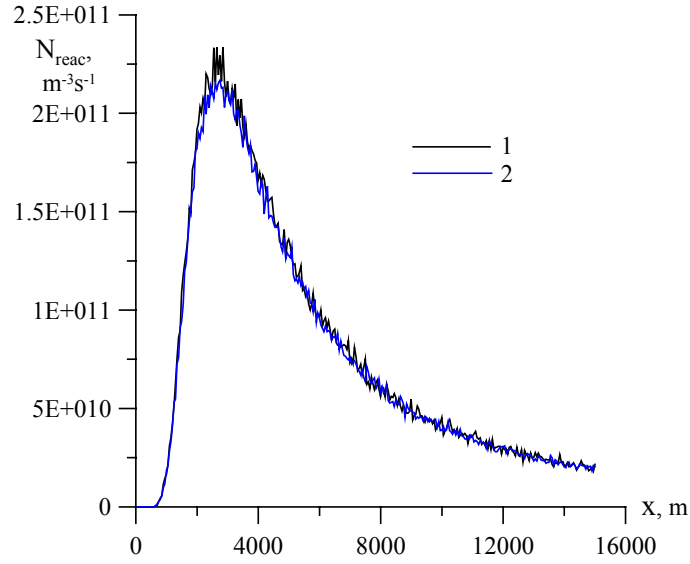


Figure 158. Reactive collision frequency along the line parallel to the PME axis 975 meters away: 1 – TD-approach with common potential; 2 – TD approach with different potentials.

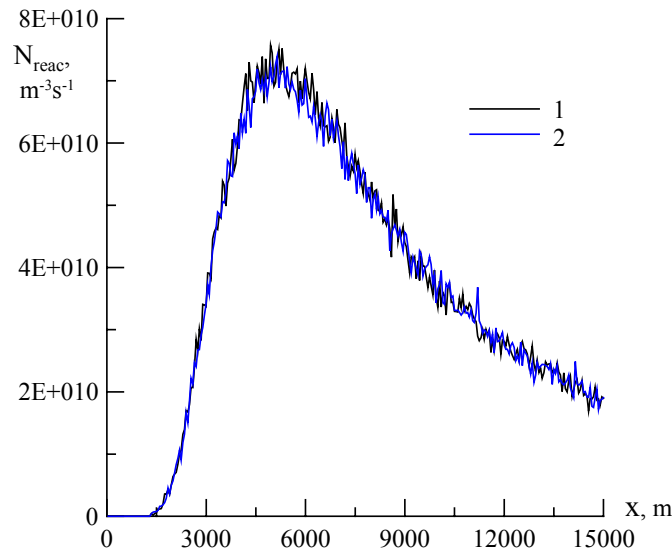


Figure 159. Reactive collision frequency along the line parallel to the PME axis 1975 meters away: 1 – TD-approach with common potential; 2 – TD approach with different potentials.

Accurate solution of the dynamic problem is compared with simpler approach of the effective elastic cross-section in Figure 160. Curves 4, 5 and 6 represent the TD approach with different condition of the termination of the atomic oxygen trajectory in the plume. The trajectory is artificially terminated after the first (curve 4), fourth (curve 5) and fifth (curve 6) collision with a plume specie. Obviously, there is no need to follow on with further collisions, because curves 5 and 6 almost coincide. As also evident from the figure, the SC approach with effective cross-section of about 10 \AA^2 should provide the same result as the accurate TD approach. The value of $\sigma_{e,eff}=10 \text{ \AA}^2$ is very close to the transport cross-sections averaged over the plume flow molecular composition (see Section 8.3.1).

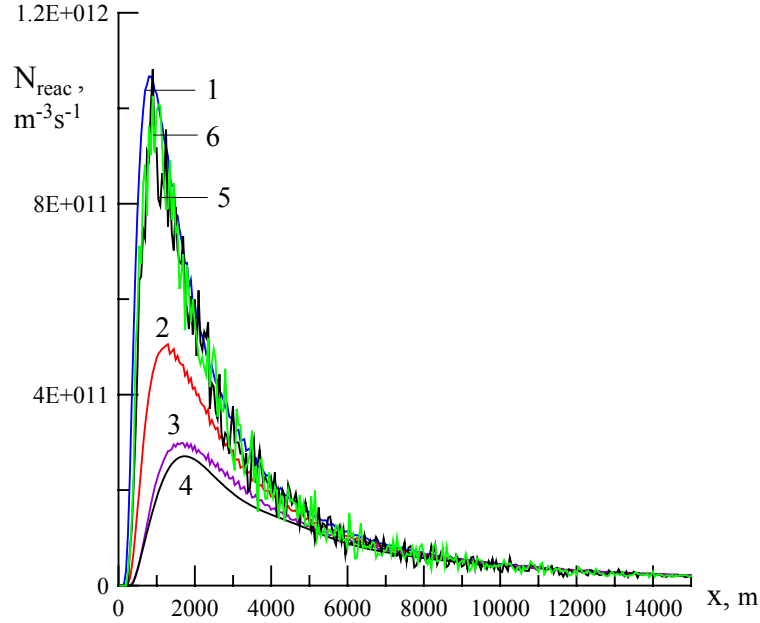


Figure 160. Number of the reactive collisions along the PME axis computed by TPMC method with different elastic collision models: 1 – SC approach, $\sigma_{e,eff}=10 \text{ \AA}^2$; 2 – SC approach, $\sigma_{e,eff}=15 \text{ \AA}^2$; 3 – SC approach, $\sigma_{e,eff}=20 \text{ \AA}^2$; 4 – TD approach Born-Mayer potential, one collision; 5 – TD approach Born-Mayer potential, four collisions; 6 – TD approach Born-Mayer potential, five collisions.

Similar results were obtained from computation of the reactive collision frequency along other lines parallel to the PME axis. These results are demonstrated in Figure 161, Figure 162 and Figure 163.

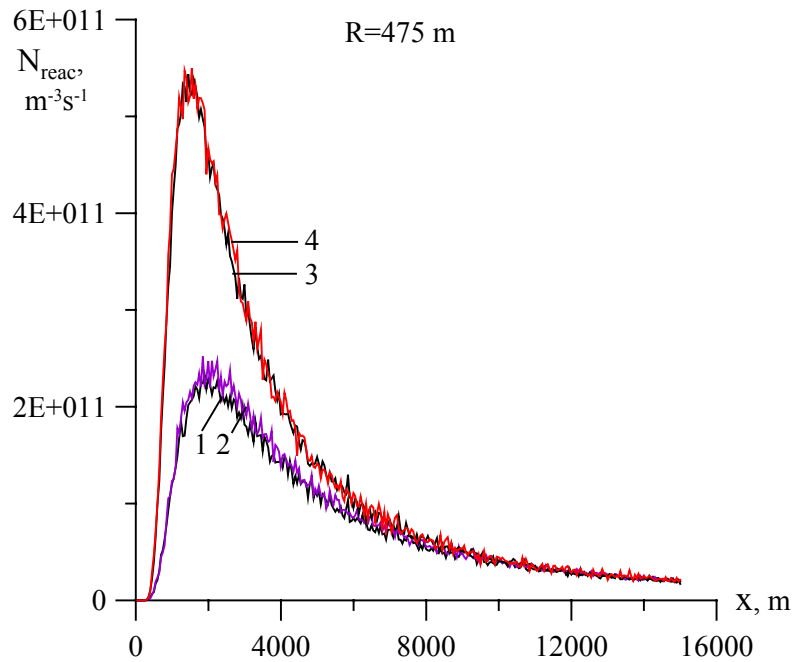


Figure 161. Number of the reactive collisions along the line 475 meters away from the PME axis computed by TPMC method with different elastic collision models: 1 – TD approach Born-Mayer potential, single collision; 2 – SC approach, $\sigma_{e,eff}=20 \text{ \AA}^2$; 3 – TD approach Born-Mayer potential, four (five) collisions; 4 – SC approach, $\sigma_{e,eff}=10 \text{ \AA}^2$.

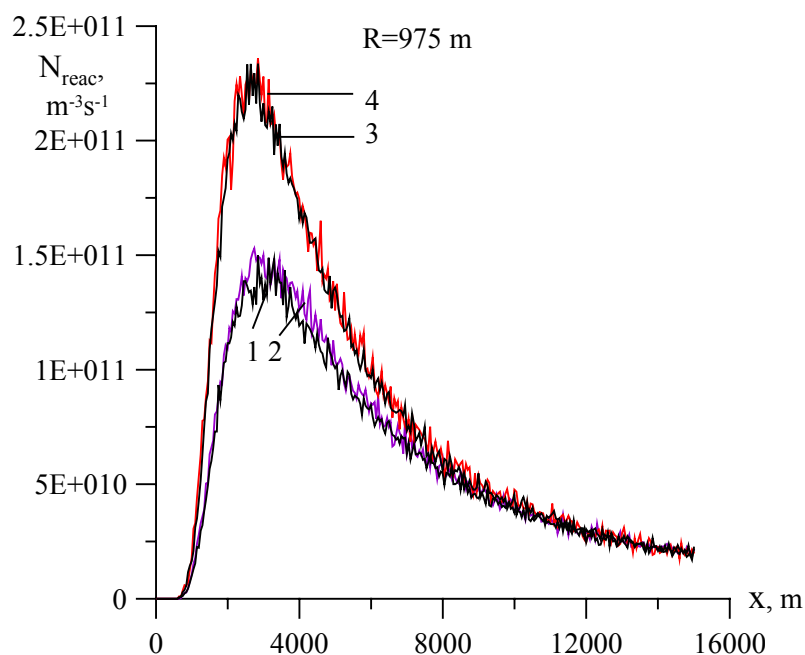


Figure 162. Number of the reactive collisions along the line 975 meters away from the PME axis computed by TPMC method with different elastic collision models: 1 – TD approach Born-Mayer potential, one collision; 2 – SC approach, $\sigma_{e,eff}=20 \text{ \AA}^2$; 3 – TD approach Born-Mayer potential, four (five) collisions; 4 – SC approach, $\sigma_{e,eff}=10 \text{ \AA}^2$.

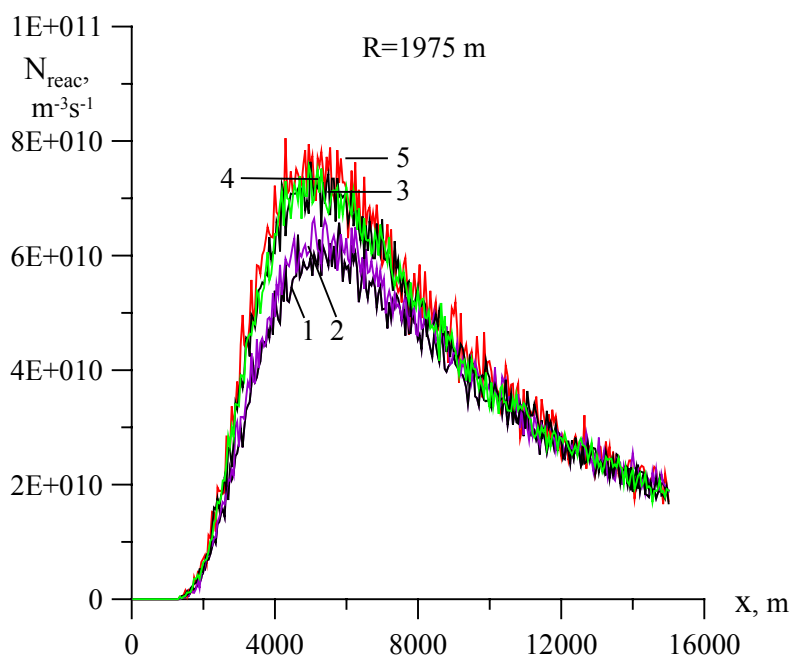


Figure 163. Number of the reactive collisions along the line 1975 meters away from the PME axis computed by TPMC method with different elastic collision models: 1 – TD approach Born-Mayer potential, one collision; 2 – SC approach, $\sigma_{e,eff}=20 \text{ \AA}^2$; 3 – TD approach Born-Mayer potential, four collisions; 4 – TD approach Born-Mayer potential, five collisions; 5 – SC approach, $\sigma_{e,eff}=10 \text{ \AA}^2$.

The elastic collision model analysis may be concluded by the statement that properly chosen effective elastic cross-section in the reactive collision computation results in outputs, which are in a good agreement with those obtained through accurate solution of the molecular collision dynamic problem. Therefore, in the next section the simplest model based on the effective cross-section concept is utilized for comparison of the TPMC method results with other methods and with experimental data.

8.4. Computation of the PME glow radiation

The PME plume glow radiation was modeled by different methods and with different parameters of collisional models. Purpose of this part of work was to compare results of computation and check the accuracy of simplified FNSAF method versus more complex TPMC and DSMC methods. This analysis allows to specify the radiation modeling technique, which is relatively simple from one side and provides satisfactory agreement with more complex and accurate computation from another side.

8.4.1. Influence of the dimensions of the computational domain

Influence of the simulation parameters such as dimensions of the computation domain and grid cell, number of particles, time step etc. onto the results of DSMC modeling of the PME radiation were analyzed in detail in Ref.²⁰. Optimal parameters were chosen then basing on this analysis. Similar analysis has been made in this work with regard to the TPMC method too.

Influence of the computational domain onto the modeled radiation intensity is caused by the assumption that at the boundary of the computational domain the free stream oxygen number density was set equal to the undisturbed atmospheric oxygen number density. As soon as the atmosphere is somehow disturbed by the plume flow even far away from the space vehicle, the free stream number density should be overestimated at any finite dimension of the computation domain. Effect of limitation of the computational domain was tested through direct modeling of the reaction collision frequency in various places of the PME plume flow. In these computations simplified model for elastic collisions (SC approach, $\sigma_{e,eff}=15 \text{ \AA}^2$) was adopted. Reactive collision cross-section was modeled through relation (8.33). Results of the reactive collision frequency computation along the PME axis are shown in Figure 164. Dimension of the computational domain in radial direction adaptively changed along the X-axis and reached 20 km at the far field.

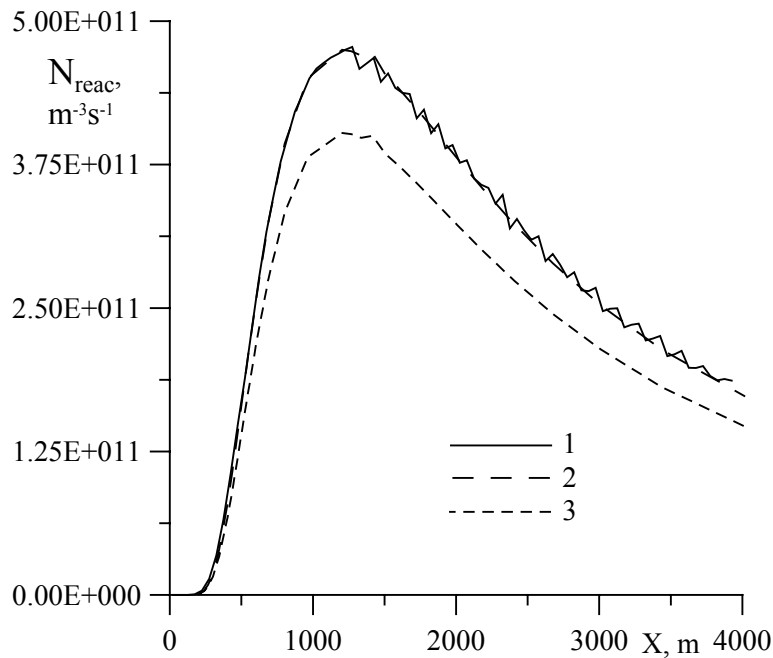


Figure 164. Influence of the computational domain dimension along the X-axis: 1 – TPMC method, 15 km domain dimension; 2 – analytical solution (formula (8.23)), 15 km domain dimension; 3 – analytical solution, infinite domain dimension.

Difference between 15 km and infinite along X-axis domains is about 18% in Figure 164. Good agreement between the TPMC result and analytical solution should also be noted.

Effect of the computational domain dimension in radial direction is demonstrated in Figure 165. Two curves are demonstrated in this figure: one corresponds to the computation domain radial dimension 5 km, another – 10-20 km. All curves between 10 and 20 km were almost identical. Despite that reactive collision frequency in Figure 165 was computed relatively far from the axis and close to the radial boundary, influence of the computation domain dimension becomes noticeable only at the dimensions $R_{max} \leq 5 \text{ km}$.

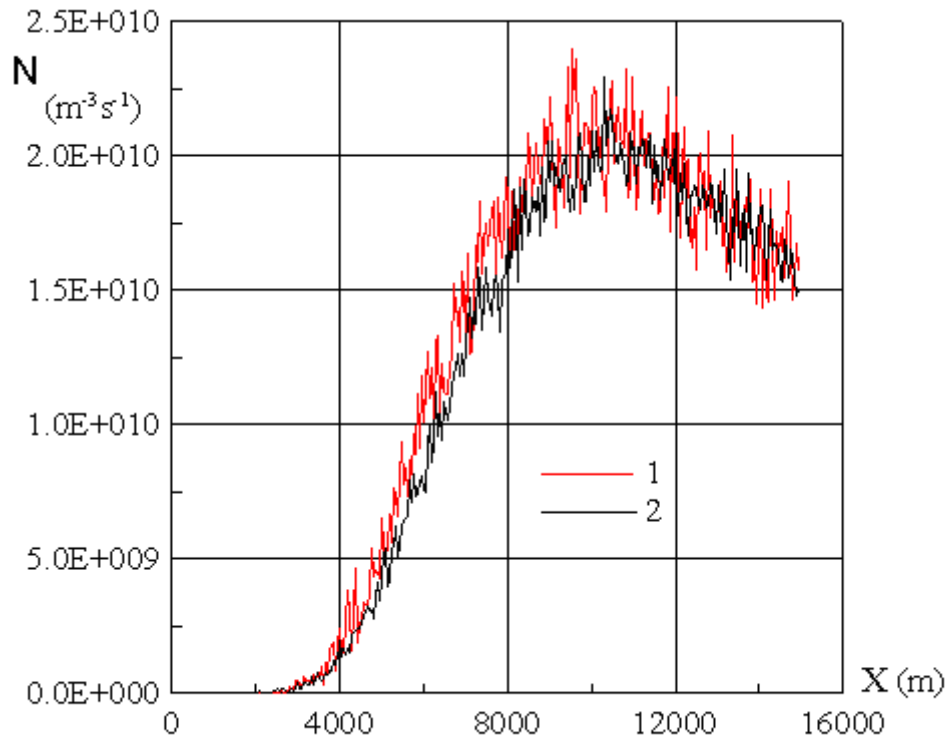


Figure 165. Reactive collision frequency along the line parallel to the PME axis 4025 meters away: 1 – TPMC method, computation domain radial dimension 10-20 km, 2 – TPMC method, computation domain radial dimension 5 km.

Further computations of the PME plume glow $\text{OH}(\text{A} \rightarrow \text{X})$ radiation intensity were confined by the computation domain dimensions $X_{\max} = 15\,035$ meters and $R_{\max} = 10\,000 - 20\,000$ meters.

8.4.2. Comparison between TPMC and full DSMC computation

Reactive collision frequency computed by the TPMC method was compared with the one computed by DSMC method. The DSMC computation results were borrowed from Ref.²⁰. Results of the comparison are presented in Figure 166.

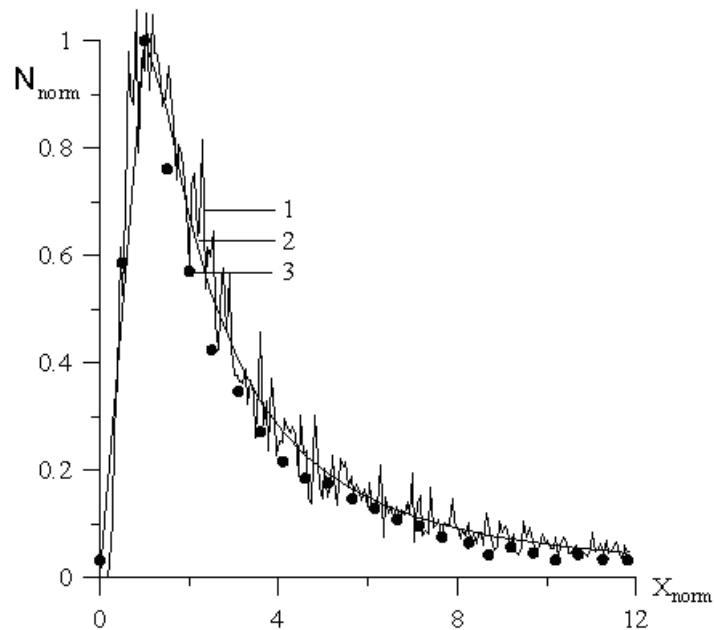


Figure 166. Distribution of the reaction collision frequency along the PME X-axis: 1 – TPMC method, 2 – analytical solution (formula (8.23)), 3 – DSMC method²⁰.

As soon as the computation results depend on the choice of the elastic and reaction collision models, that was different in the TPMC and DSMC computation, compared were the curves normalized both in intensity and spatial scale. The intensity was normalized to maximum and spatial scale was normalized to the X distance where this maximum was achieved. By this way accentuated is comparison between the computation methods rather than between different collision models. Obviously, Figure 166 demonstrates good agreement between the TPMC and DSMC methods. That means the simplifications of the glow radiation models discussed in Section 8.2.1 are justified.

8.4.3. Comparison between TPMC and FNSAF methods

The PME plume glow radiation intensities computed by TPMC and FNSAF methods have been compared. Both methods utilized the same collision models in this computation. Elastic collisions between atmospheric oxygen and plume flow molecules were treated by the SC method and effective elastic cross-section $\sigma_{e,eff}$ was used as a parameter. Reaction cross-section energy dependence was modeled by expression (8.33) in TPMC computation. Same dependence was utilized in the FNSAF computation for determination of the effective reaction cross-section value through relation (8.21).

Figure 167 represents results of computation of distribution of the glow radiation intensity along the PME X -axis (side view). This distribution was obtained by integration of the specific (per unit volume) radiation intensity along the lines perpendicular to the X -axis. In fact, the picture represents the case when observer is located at infinite distance from the plume axis. Retrofiring condition with $\alpha=0$ (Figure 154) was assumed.

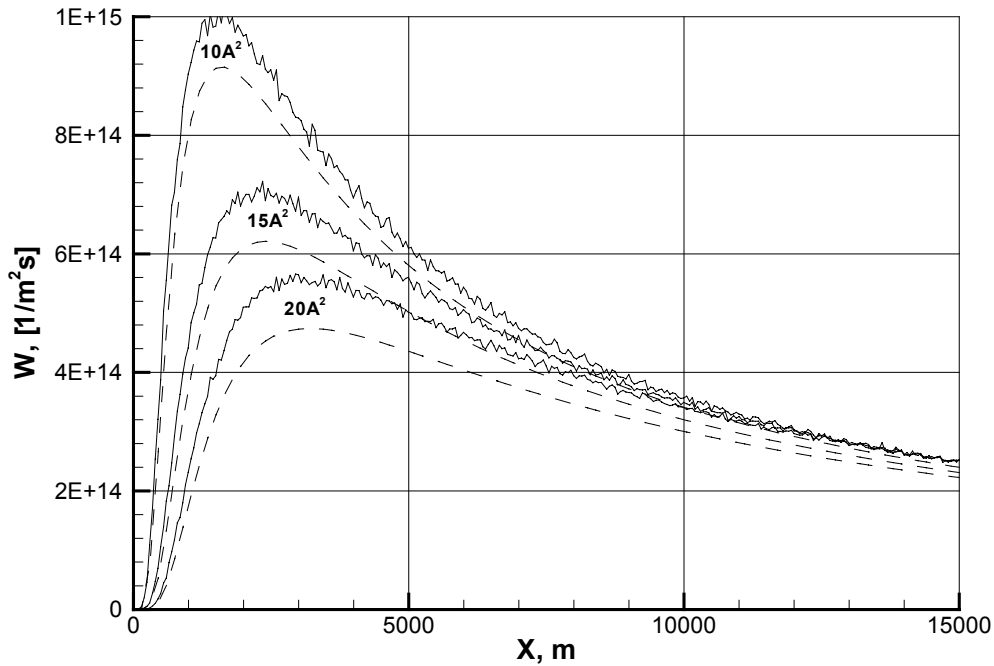


Figure 167. Comparison of the glow radiation intensity (side view) modeled by TPMC (solid lines) and FNSAF (dashed lines) methods for retrofiring condition and with different values of $\sigma_{e,eff}$.

Obviously both methods result in very close intensity profiles. Small difference in the curves behavior is explained by different boundary conditions adopted by TPMC and FNSAF methods. The first one starts computation at 15 km from the motor, whereas the latter one - from infinity.

Results of computation of the glow radiation profile perpendicular to the PME axis (tail view) are shown in Figure 168. These curves were obtained by the same way, but integration was made along parallel to the X -axis lines. In general, agreement between the results is satisfactory. Noticeable departure is observed only in Figure 168 at relatively big values of $R \geq 2.5$ km. The FNSAF method results in up to 50% higher values of the radiation intensity in comparison with TPMC method. Most probably this is result of limitation of the computation domain in the TPMC modeling by 15 km. As evident from Figure 165 reactive collision frequency in peripheral off-axis regions is still relatively high even at 15 km downstream from the nozzle.

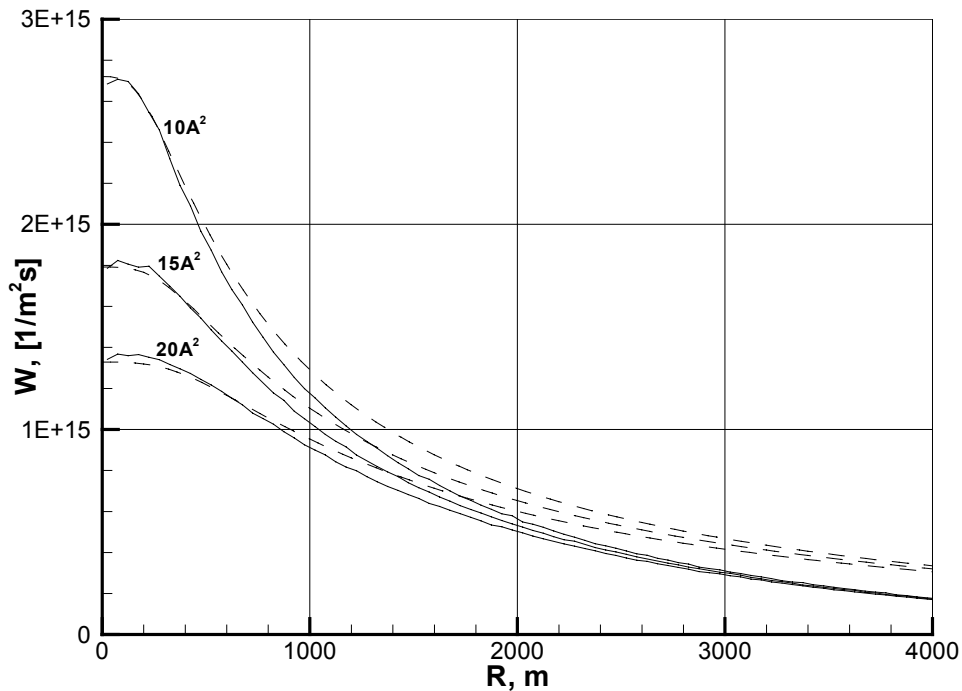


Figure 168. Comparison of the PME plume glow radiation intensity (tail view) modeled by TPMC (solid lines) and FNSAF (dashed lines) methods for retrofiring conditions and with different values of $\sigma_{e,eff}$.

8.5. Comparison of the PME glow modeling results with experiment and determination of the elastic and reaction cross-sections.

PME glow radiation modeling results are compared in this Section with experimental data obtained in February 28, 1999 experiment. Basing on this comparison effective values of both elastic and reaction (8.1) cross-sections may be suggested, which ensure best fit of the simulation results to the experimental data.

Logistics and results of the February 28, 1999 experiment were reported in Ref.⁵. Detailed processing and interpretation of the February 28, 1999 experiment data have not been a subject for consideration within the frame of this particular ISTC Project #2234p. However, for the sake of integrity of the April 26, 2000 data analysis some of the February 28, 1999 experiment results are addressed below and, therefore, experimental scheme and some experimental data are briefly discussed in this paragraph.

The PME exhaust plume glow radiation at the night condition was observed in February, 28 1999 experiment. The tail view observation scheme similar to 26 April 2000 experiment was utilized (see Figure 1 for details). The motor burn lasted more than four minutes. During the observation the narrowband filter centered at 315 nm (see Figure 17 for transparency curve) was installed for a short time. Same UV-imager was used in the experiment for radiometric measurement of the glow radiation distribution. It had the same FOV, spatial resolution, pixel angular dimension and relative spectral response as in the April 26, 2000 experiment. Absolute response in the maximum of the spectral sensitivity curve was about 10% lower than in April 26, 2000 experiment, due to the difference window transparency in those two cases (see paragraph 2.5.1.4). Earlier model of the spectrometer was used in the experiment. That model was less sensitive than the new one, so it failed to measure any glow spectra. Atmospheric parameters were modeled by MSIS-90 model^{25,26}, providing oxygen number density and temperature necessary for computation of the plume glow intensity. Compared with the FNSAF modeling results were data obtained at four particularly sampled moments of time. Observation conditions and some auxiliary parameters for these moments of time are listed in Table 25.

Table 25. Observation geometry and atmospheric parameters for particular moments of 28 February 1999 experiment.

Time after motor start, sec	H, km	L, km	β°	θ°	$[O], m^{-3}$	T, K°
15.2	374	11.6	7.7	1.0	$1.48 \cdot 10^{14}$	886
76.8	373	13.3	10.5	5.2	$1.42 \cdot 10^{14}$	878
172.2	371	18.4	10.7	11.4	$1.4 \cdot 10^{14}$	871
249.2	368	25.6	9.3	16.4	$1.44 \cdot 10^{14}$	869

Example of the glow images taken in 28 February 1999 experiment is presented in Figure 11. Interpretation of the image features is the same as in 26 April 2000 experiment (see Section 2.6.1). Spatial profiles of the glow radiation intensity measured at specified in Table 25 moments are presented in Figure 169. Both raw counts and normalized to unity at about 0.75° off-axis direction signal values are presented in this figure. The profiles are apparently very similar. It's interestingly to note, that normalization factors depend linearly upon the distance from the imager to the space vehicle, which is demonstrated by lower plot in Figure 169.

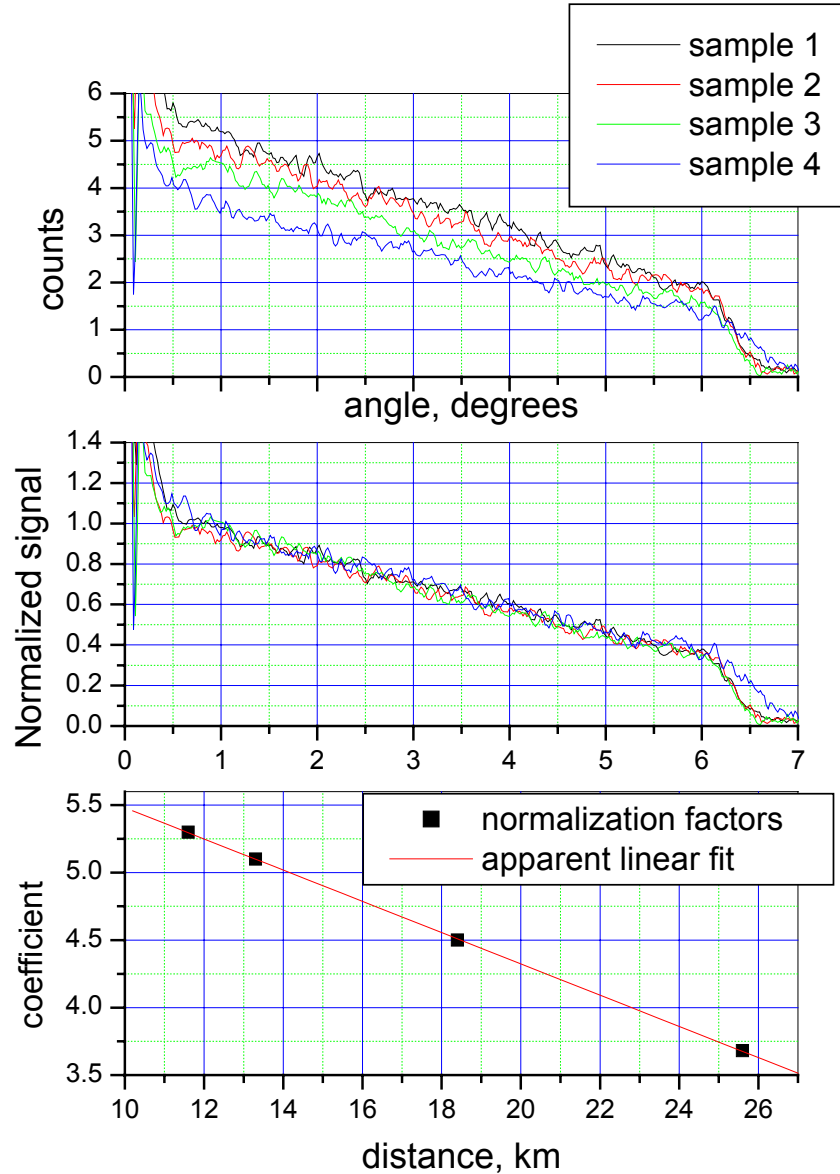


Figure 169. PME plume glow radiation intensity profiles measured at the sampled time moments: top window - raw data; middle window - normalized to unity at about 0.75° ; bottom window - dependence of the normalization factor on the distance to the space vehicle.

The PME glow radiation intensity profiles measured in February 28, 1999 were compared with FNSAF method computation result. The comparison is illustrated in Figure 170. Note, that intensity scale maximum is fixed at 7 counts per pixel in the plots and the bright spot intensity at the center of the image is not reproduced in the figure. Elastic collisions for these computations were simulated through relations (8.26), (8.27). Effective reaction cross-section (8.21) with energy dependence in the form of (8.33) has been utilized. For modeling of the radiation intensity in terms of counts per pixel computed intensity was multiplied on $R_{310}=3.58 \cdot 10^5$ cpp per W/m^2sr , that was average imager response value at 310 nm on February 28, 1999. Direct modeling of the radiation with the cross-section (8.33) resulted in substantial overprediction of the radiation intensity. Therefore, coefficient σ_0 was corrected by multiplication on factor $k_\sigma=0.1$ to provide better fit to the experimental data. Application of (8.34) cross-section energy dependence gave almost similar results when coefficient σ_0 was

corrected by multiplication on factor of $k_\sigma=0.0376$. Difference between two profiles modeled with different reaction cross-section energy dependences was maximal in peripheral regions, being, however, less than 5% at all observation distances.

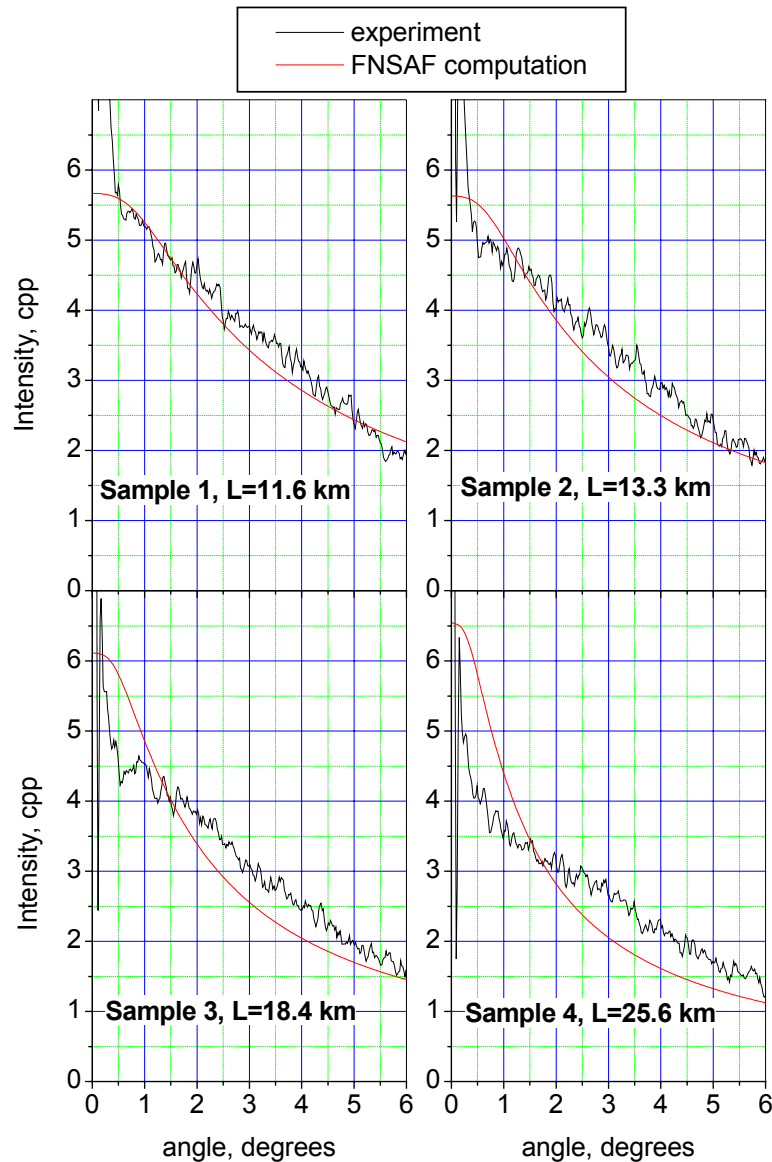


Figure 170. Comparison between results of FNSAF computation of the PME plume glow radiation profiles and experimental data obtained in February 28, 1999 experiment.

Comparison between the experimental data (sample 1) and TPMC computation has been done as well. SC approach for the elastic collisions modeling was used in the computation. Normalized glow intensity profiles are compared with the TPMC results in Figure 171. This figure also demonstrates how comparison between modeled and experimental profile may be used for verification of the effective elastic cross-section value. As evident from the figure the value $\sigma_{e,eff}=10 \text{ \AA}^2$ provides better fit than alternatively taken values $\sigma_{e,eff}=7.5$ and 15 \AA^2 . Application of the conventional VHS model would lead give the effective cross-section $\sigma_{e,eff} \geq 15 \text{ \AA}^2$, that would lead in even worse agreement. Reactive cross-section was modeled through expression (8.33). Similarly to the FNSAF computation correction factor $k_\sigma=0.092$ was introduced for σ_0 to fit modeled intensity to the experiment.

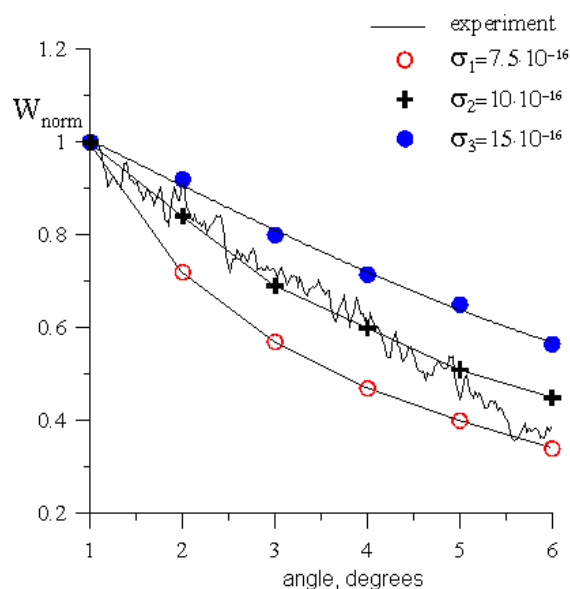


Figure 171. Comparison between TPMC radiation intensity modeling and 28 February experiment results. Values of the effective cross-sections are indicated in m^2 .

As evident from Figure 170 and Figure 171, adopted elastic and reaction cross-sections ensure satisfactory fit to the experimental data, provided that collisional cross-sections were properly chosen. Agreement with two earlier taken experimental samples may be considered even as excellent. Agreement with two later samples in Figure 170 is worse. But, it should be kept in mind, that third sample was taken from the very border of Zone II where the FNSAF method can't give accurate results. The last sample was taken from Zone III. At that location the FNSAF method may result in substantial inaccuracy. In general, agreement between the modeling and experimental results may be considered as good. Perhaps this agreement may be further improved if more accurate DSMC computational method is applied.

It should be noted, that no spectra were obtained in February 28, 1999 experiment. So, the spectral composition of the radiation registered by the imager was unknown. Some conclusion about the spectral composition may be inferred from consideration of the filtered glow image. Radiation intensity profiles of filtered and unfiltered images are compared in Figure 172.

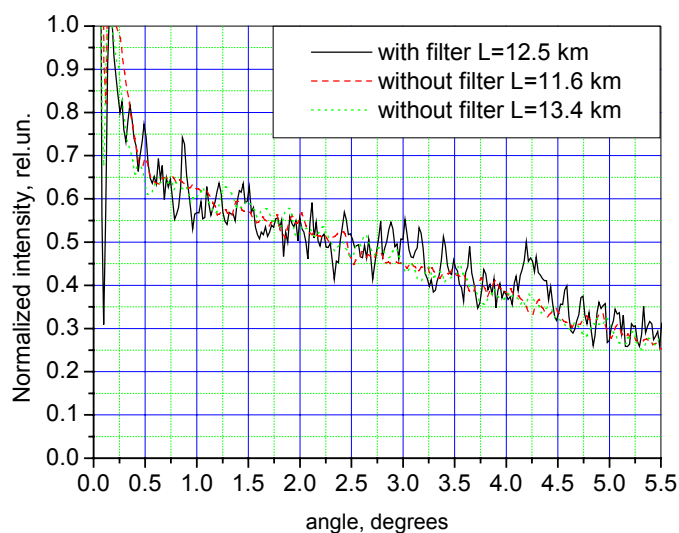


Figure 172. Comparison of filtered (filter #3, 315 nm) and unfiltered normalized glow radiation profiles.

Normalized intensity distribution is presented in this figure for convenience of the profile shape comparison. Actually, installation of the filter in the experiment reduced the signal by factor of 8. From the other hand, would the radiation be composed only from the $\text{OH}(\text{A} \rightarrow \text{X})$, $v' = v'' = 0$ band emissions the reduction factor had to be at the level of 5-6 in accord with the filter transparency curve. This implies presence of some other radiation sources in the imager's sensitivity band. Possible candidates might be the $\text{OH}(\text{A} \rightarrow \text{X})$ emissions related to other vibrational-rotational bands, $\text{NH}(\text{A} \rightarrow \text{X})$ band emissions and perhaps even others, not reported before.

Assumption that any other than OH(A→X), $v'=v''=0$ radiation source contributed in the imager's signal would necessitate reduction of the experimental curves in Figure 170 on some coefficient corresponding to the share of OH(A→X) radiation in the imager's signal. Correction coefficients k_σ for σ_0 in expressions (8.33), (8.34) must be reduced by the same factor in this case. Share of the OH(A→X) radiation in the imager's signal might be evaluated if vibrational-rotational structure of the radiation spectrum could be predicted. Recent analysis of the OH(A→X) emission spectrum from similar Shuttle PRCS motor glow³⁶ demonstrated presence of multiple vibrational-rotational bands in the OH(A→X) emission spectrum. Assuming the same spectral distribution in February 28, 1999 experiment, share of the OH(A→X) radiation in the imager's signal estimated from the filtered image intensity must be not less than 80%. Under this assumption the reaction cross-section correction factor will become $k_\sigma=0.08$. Other assumptions may lead to either smaller or bigger OH radiation shares and subsequently smaller and bigger reaction cross-sections. In subsequent sections the glow model, which utilizes correction factor $k_\sigma=0.08$ for reaction (8.1) cross-section is referred to the baseline model.

Another cause, which might influence the value of reaction cross-section, is the calibration factor R_{310} . As discussed in Paragraph 2.5.1.4, this factor might change from the moment of calibration through the end of 28 February 1999 experiment. Application of the bigger value of the R_{310} coefficient observed during the experiment will reduce the correction factor k_σ even greater. In any case, the reaction (8.1) effective cross-section derived from the February 28, 1999 measurements must be considered as an upper estimate.

In the meantime, Figure 172 clearly demonstrates that whatever the imager's spectral composition was, both OH and all non-OH components (if not minor) must have profiles similar to the total signal. Otherwise, filtering off of the non-OH(A→X) bands would change the signal profile shape, what is not observed in Figure 172. Therefore, utilization of the total imager signal profiles for verification of the elastic cross-section models in Figure 170 has been justified.

Summarizing the comparison of the PME glow modeling results with February 28, 1999 experiment data, following conclusions can be made:

- ❑ Any model, which results in the effective cross-section value for collisions between plume species and atomic oxygen $\sigma_{e,eff} = 8.5\text{-}10 \text{ \AA}^2$ should be appropriate in the condition of the high altitude plume flow interacting with atmosphere.
- ❑ Contemporary reaction cross-section models overpredict the PME glow radiation intensity on order of magnitude and more, if the model parameters derived from a ground state reaction rate temperature dependence. So, the model parameters have to be adjusted. Eventually, any reaction cross-section model must result in the effective cross-section value for reaction (8.1) $\sigma_{r,eff} \leq 0.8 \cdot 10^{-18} \text{ cm}^2$ to explain experimentally observed emissions.
- ❑ Departure of modeled curves from experimental data becomes noticeable when distance to the space vehicle grows. General tendency develops that FNSAF modeling overpredicts experiment at the axis and underpredicts it at peripheral regions. Perhaps better fit along the axis will be achieved when the plume flow scattering in atmosphere will properly be modeled by DSMC method with the same collisional model parameters. However discrepancy between wings of modeled and experimental profiles measured from longer distances can't be removed by adjusting collisional cross-sections only. More probable is that some other processes, which do not manifest themselves at smaller distances in Zone II, become playing more important role at bigger distances in Zone III. This conclusion is corroborated by the results of 26 April 2000 experiment, which were obtained from yet longer distances.

8.6. ACS motor cluster plume flowfield modeling

The model of high altitude plume glow radiation, which was initially developed for a single PME plume flow and tested on the results of February 28, 1999 experiment was further advanced for condition of the April 26, 2000 experiment, where composite 8xACS motor plume flow was studied.

8.6.1. Flow parameters at the nozzle exit

At the initial stage of the composite plume flow modeling the flow characteristics at the single ACS motor nozzle exit were computed. Input parameters for the computation are discussed in Section 2.2.1. The nozzle flow was simulated with the use of NARJ software package¹³⁶ within the frames of Euler equations. The nozzle flow computation started in the combustion chamber, where the fuel combustion product composition was determined at equilibrium temperature and pressure. Further, non-equilibrium chemical reactions including 11 components (CO_2 , H_2O , NO , H_2 , O_2 , N_2 , OH , CO , H , O , N) were taken into account in the nozzle flow. 1-D simulation resulted in the following flow parameters at the nozzle exit:

- flow velocity $u_a = 2818.2 \text{ m/s}$;
- gas density $\rho_a = 2.6907 \times 10^{-3} \text{ kg/m}^3$;
- gas pressure $p_a = 637.59 \text{ Pa}$;
- gas temperature $T_a = 591.40 \text{ K}$;
- mole fractions of the flow components X_i ;

$$\begin{array}{lll}
\text{CO}_2 = 4.946 \times 10^{-2}, & \text{H}_2\text{O} = 2.932 \times 10^{-1}, & \text{NO} = 3.392 \times 10^{-4}, \\
\text{H}_2 = 1.877 \times 10^{-1}, & \text{O}_2 = 2.744 \times 10^{-5}, & \text{N}_2 = 2.676 \times 10^{-1}, \\
\text{OH} = 2.853 \times 10^{-5}, & \text{CO} = 1.932 \times 10^{-1}, & \text{H} = 8.524 \times 10^{-3}, \\
\text{O} = 1.391 \times 10^{-5}, & \text{N} = 5.376 \times 10^{-8}.
\end{array}$$

Two-dimensional nozzle flow simulation results in substantially non-uniform spatial distribution of all flow parameters, excluding mole fractions of the main components with $X_i > 10^{-4}$. The latter are almost independent on the coordinate, being very close to the 1-D simulation results. Figure 173 illustrates the nozzle flow temperature pattern. Distribution of the flow parameters at the nozzle exit is presented in Figure 174.

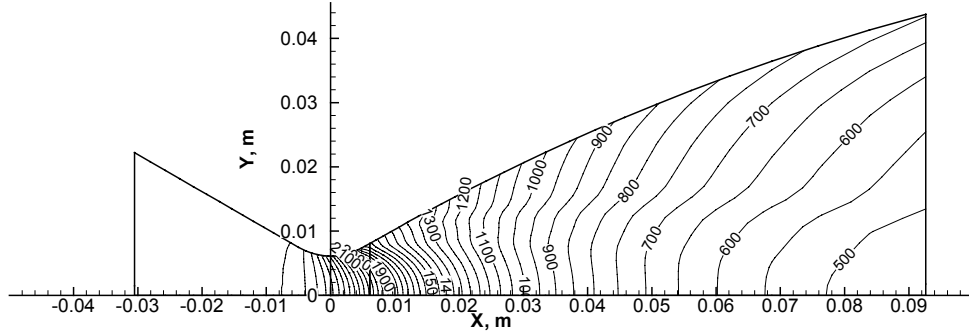


Figure 173. Lines of constant temperature in the ACS motor nozzle.

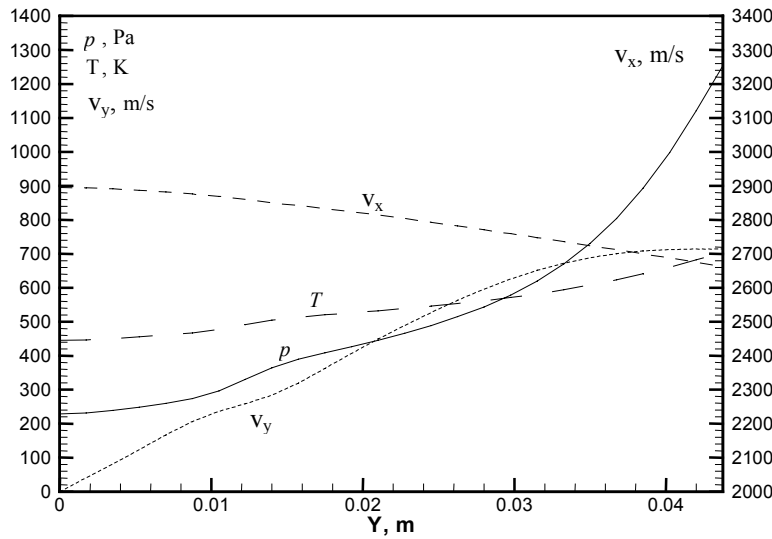


Figure 174. Spatial distribution of the flow pressure (p), temperature (T), longitudinal (v_x) and transverse (v_y) velocity vector components at the nozzle exit.

It should be noted that the nozzle flow model based on the Euler equations doesn't observe any boundary layer at the nozzle wall. The gas flow in the boundary layer has smaller velocity than in the core flow due to viscosity effects. Obviously, that relative part of the gas, which flows out from the boundary layer, should be bigger in smaller motors. Therefore, effect of the boundary layer onto the plume flow parameters may be noticeable in small motors. Mass flow rate through the boundary layer in the ACS motor was estimated and conclusion has been made that it can't exceed several percents from the total mass flow rate. So, the effect of the boundary layer onto the plume flow parameters is disregarded.

8.6.2. Modeling of a single ACS motor plume flow parameters

The single ACS flow gasdynamic characteristics were simulated by the NARJ software package¹³⁶ in the axisymmetric approximation. Input parameters for this simulation were 2-D solution of the nozzle flow at the exit. The computation was performed by marching method of solution of Euler equations. The flow composition was frozen at the nozzle exit. In fact chemical reactions between main constituents of the flow cease in the

supersonic part of the nozzle already. Meanwhile, non-equilibrium vibrational excitation of the CO_2 , N_2 , CO and H_2O molecules was taken into account. Contours of constant density and translational-rotational temperature are shown in Figure 175 and Figure 176 correspondingly. Center of the reference system in these figures is fixed at the nozzle exit, whereas X-axis coincides the motor axis. The figures illustrate how the initial non-uniformity of the flow smoothes with the flow expansion and cooling.

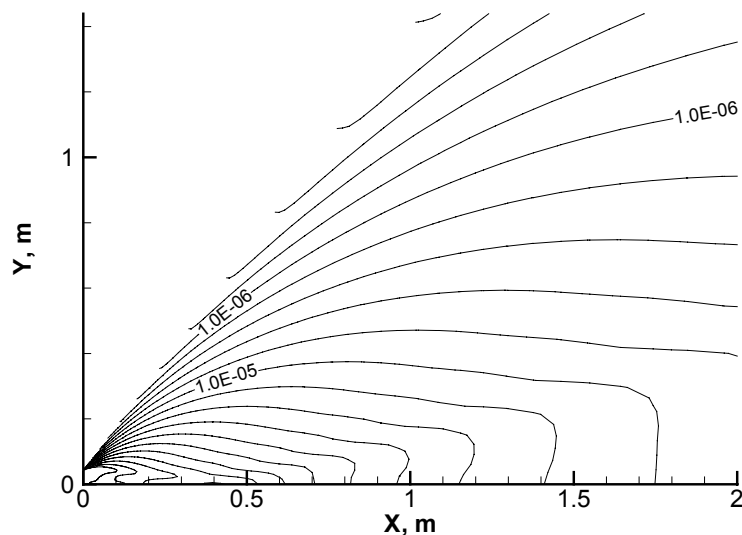


Figure 175. Lines of constant gas density (kg/m^3) in a single ACS motor plume flow.

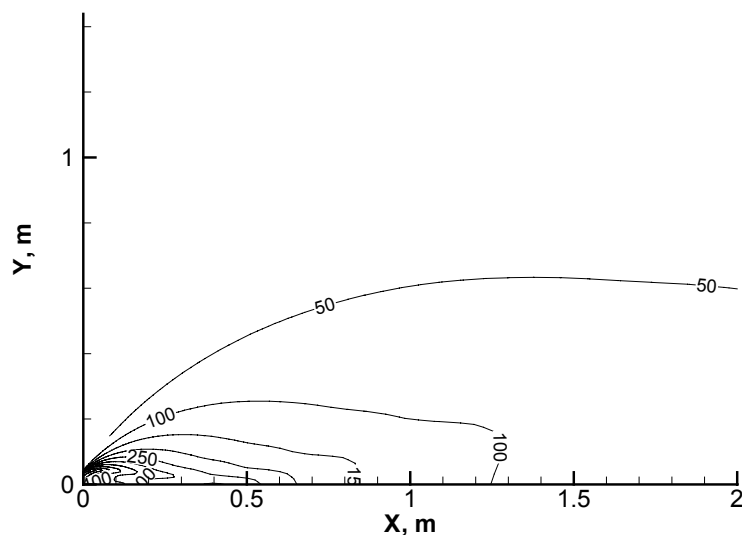


Figure 176. Contours of constant translational and rotational temperatures in a single ACS motor plume flow.

H_2O vibrational isotherms are plotted in Figure 177. Despite that vibrational temperature is substantially different from the rotation-translational temperature it still remains small in comparison with translational energy. For instance, vibrational temperature of 200 K corresponds to the 10^{-5} share of water molecules populating the first vibrational level.

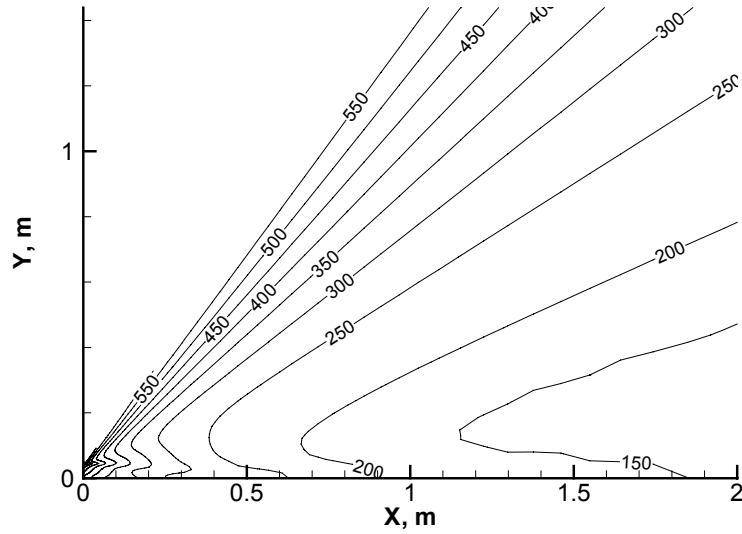


Figure 177. Contours of constant vibrational temperature of H_2O in a single ACS motor plume flow.

Water molecules may condense with the ACS motor plume flow expansion and cooling. A dedicated modeling of non-equilibrium condensation of the water in the plume flow has been carried out. Simulation of the condensation process utilized classic non-equilibrium condensation model in homogeneous approximation¹⁴⁸. The simulation resulted in very small share (not more than 2-3%) of the condensed water in the ACS motor exhaust flow. At the same time predicted dimensions of the water clusters were extremely small – order of two molecular diameters. Therefore, water condensation in the ACS motor flow has been neglected in further modeling.

8.6.3. *Modeling of the 8xACS motor cluster plume flow parameters*

The ACS motor set parameters were discussed in Section 2.2.1. Figure 178 defines the reference frame axes directions, which have been adopted for the composite plume flow consideration. As it's seen from the figure the ACS motors are grouped by pares at the close vicinity to the xy' and xz' planes, which in turn are the planes of symmetry. Two other planes of symmetry xy and xz are located between neighbor pares of the motors. As mentioned in Section 2.2.1 in each pare of the motors their axes are parallel and tilted at 20° to the X-axis.

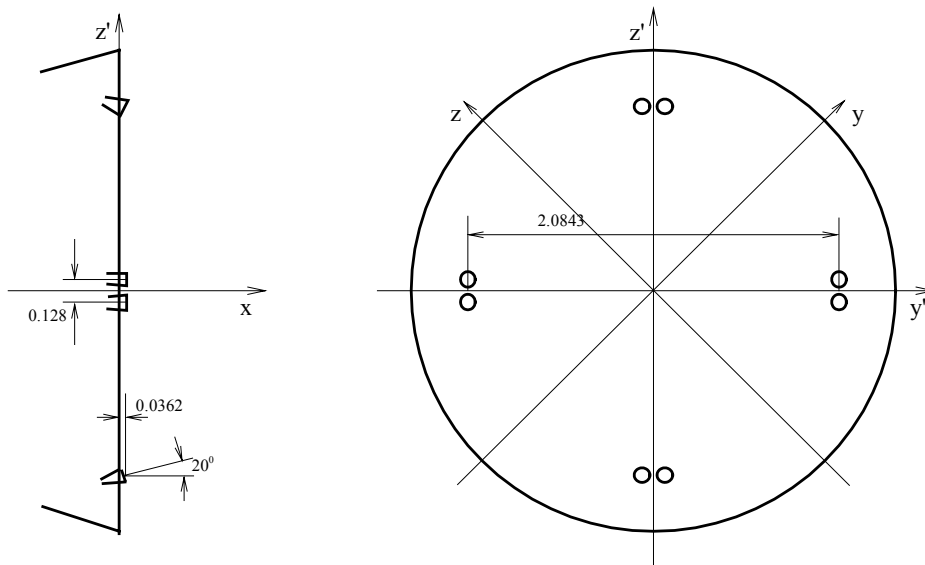


Figure 178. Sketch of the 8xACS motor set and definition of the coordinate frame.

The ACS motor set composite flow simulation included three stages.

At the initial stage of the modeling composite plume of a pair of ASC motors was simulated by time asymptotic method. This simulation was performed in the flow region confined by the planes $x=0.056$ m and $x=0.543$ m. Boundaries of this region are shown in Figure 179. Effect of other three pares of motors onto the flow in this region was neglected. The computation was made in the frames of Euler equation in approximation of perfect gas with adiabatic exponent $\gamma=1.37$. Integration of the Euler equations was made by Godunov's method of second order approximation¹⁴⁹.

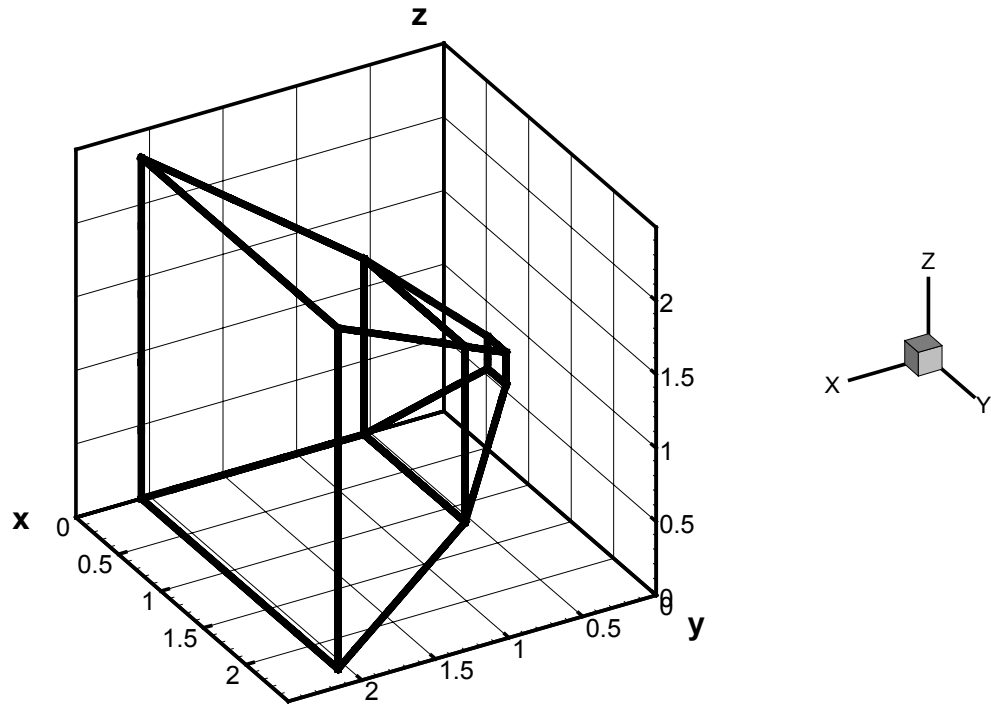


Figure 179. Computation domain boundaries at the first ($0.056 < x < 0.543$ m) and second ($0.543 < x < 2.056$ m) stages of the plume flow modeling.

At the next stage the computation was confined by the planes $x=0.543$ m and $x=2.056$ m (see Figure 179). Same computational approaches and algorithms for integration of the Euler equations were applied. Figure 180 demonstrates results of the flow simulation. 2-D density maps at some selected cross-sections of the plume flow are presented in this figure. The 2-D maps illustrate intensification of the interaction between single motor plumes with moving away from the nozzle exit. Interaction between adjacent motor flows appears first, followed by intensive interaction of all eight motor plumes. As evident from the figure this interaction is characterized by a complex shock-wave structure.

At the final stage of simulation of the plume flow gasdynamic parameters marching method for integration of the Euler equations was applied. Output results of the preceding computation served as the input data here. The computation domain stretched from $x=2.056$ through $x=14300$ m. Results of the computation are presented in Figure 181. Similar results obtained through solution of Parabolized Navier-Stokes (PNS) equations are presented in Figure 182. Comparison of PNS solution with the Euler one shows that in near field of the flow ($x < 10$ m) viscosity noticeably smoothes the flow gradients only in very rarified flow regions $\rho \leq 10^{-7}$ kg/m³. This result justifies utilization of the Euler equation at the initial stage of the computation, since the flow density is high in the plume core. Further downstream ($x > 10$ m) the viscosity smoothing effect intensifies and extends from peripheral regions toward the axis into the central part.

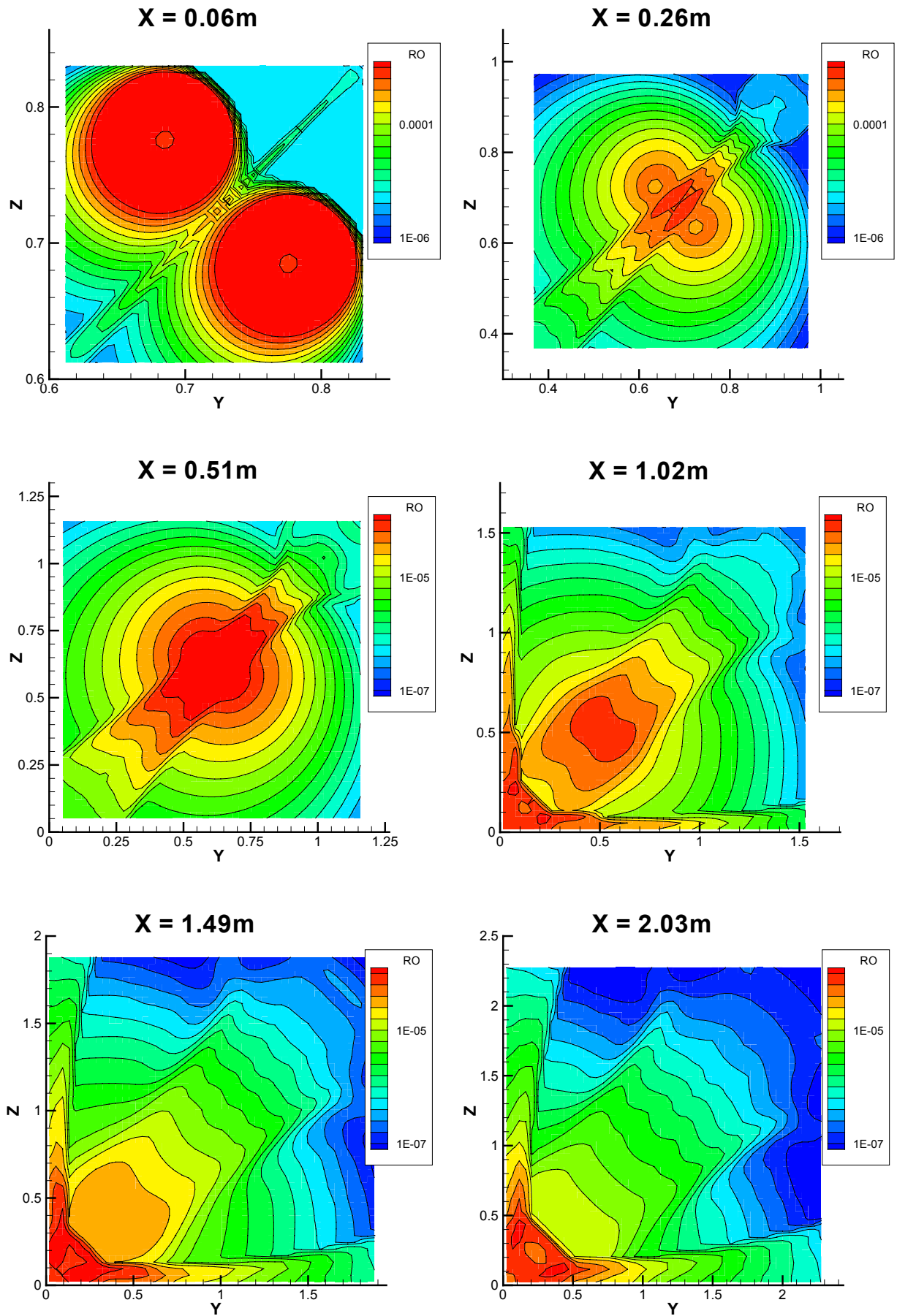


Figure 180. The plume flow density maps simulated at various cross-sections. Solution of the Euler equations.

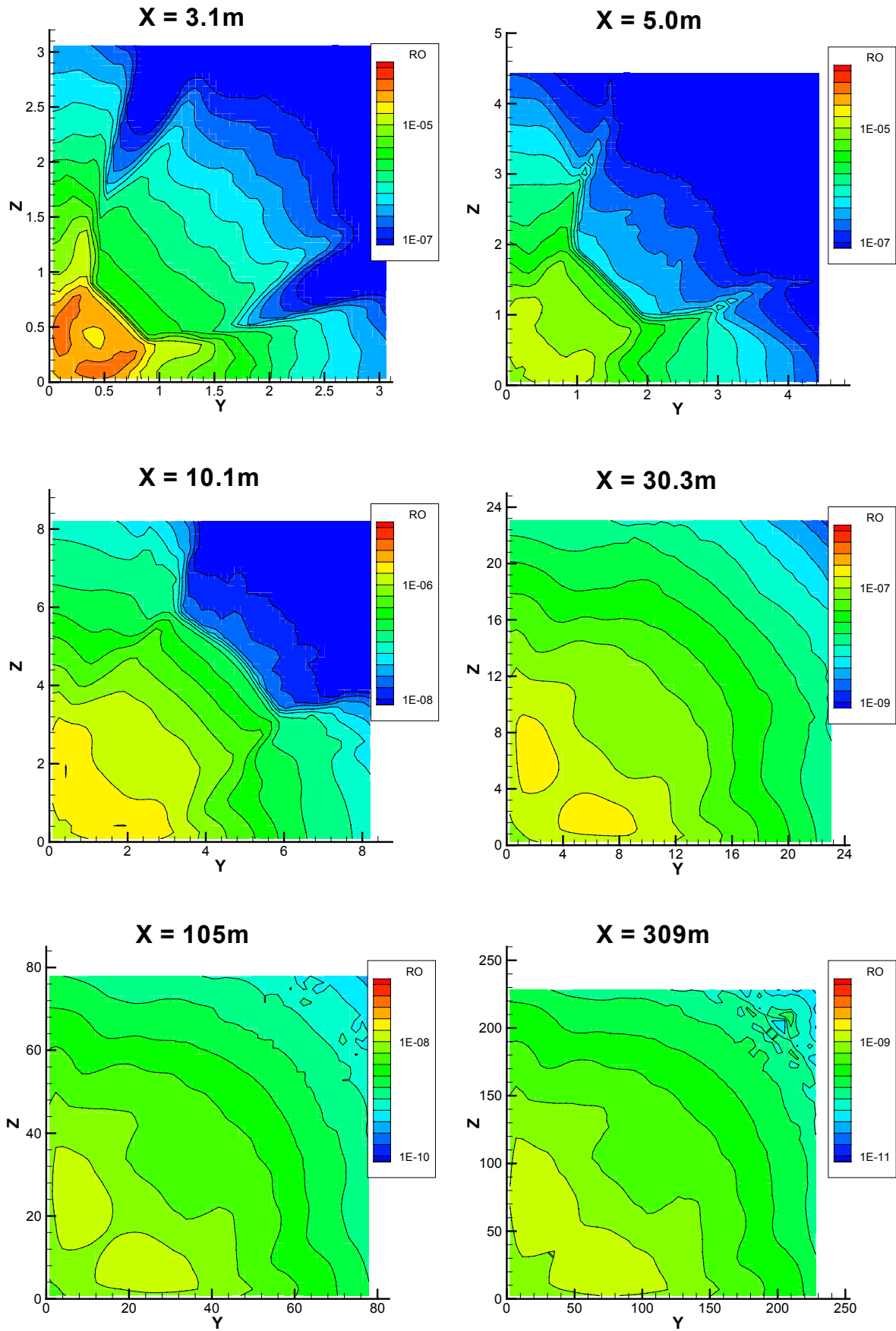


Figure 181. The plume flow color maps simulated at various cross-sections. Solution of the Euler equations.

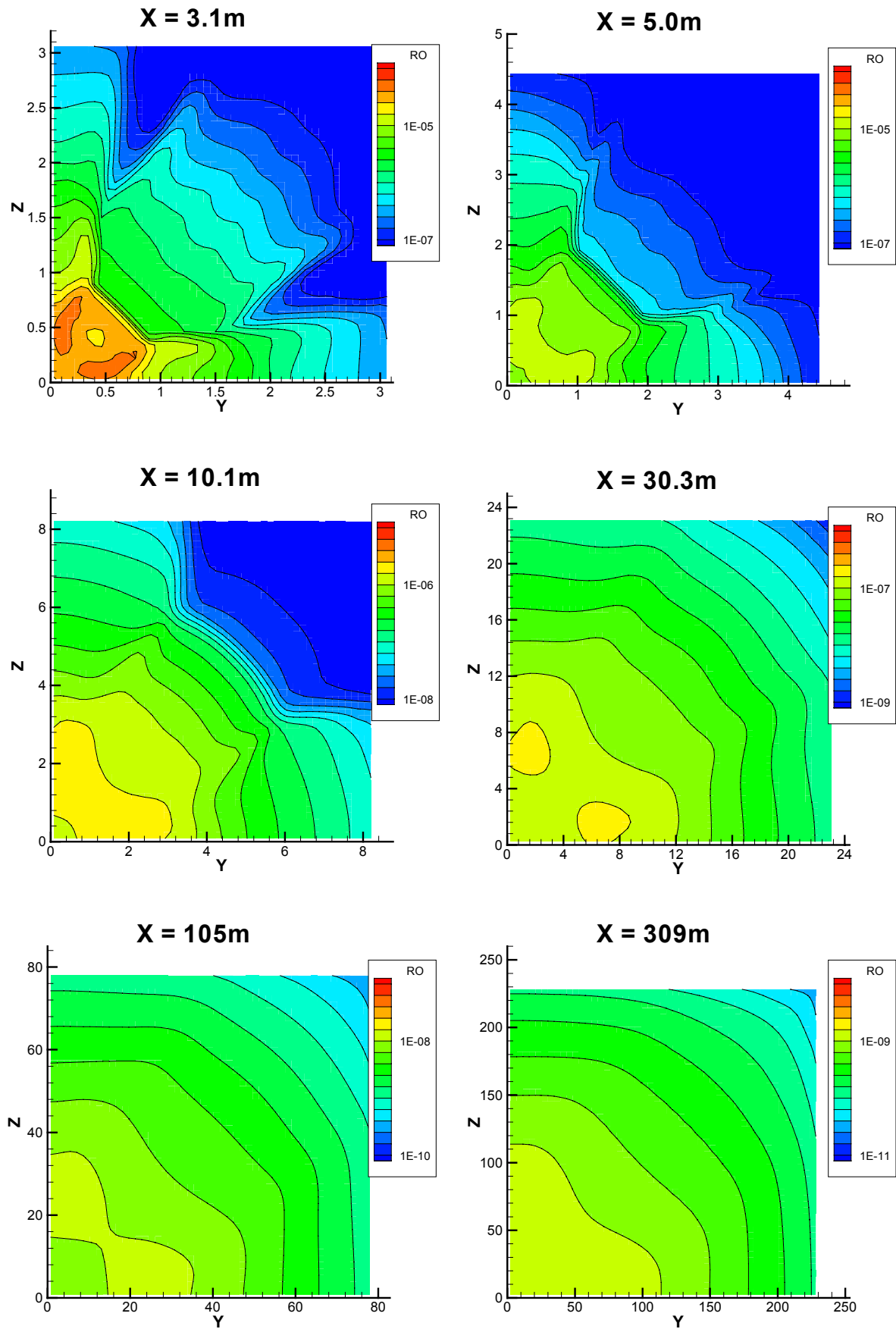


Figure 182. The plume flow color maps simulated at various cross-sections. Solution of parabolized Navier-Stokes equations.

In general, analysis of the gasdynamic parameters of the 8xASC motor set flow showed that in spite of the spatial non-uniformity in the near field the flow becomes almost axially-symmetric further downstream. Similarly to the PME exhaust flow the 8xACS plume flow may be subdivided onto three zones: Zone I where the composite plume forms up, Zone II where the plume flow is almost frozen and just slightly affected by the atmospheric flow and Zone III where the plume flow effectively scatters and mixed with the atmosphere. It's worth to evaluate spatial scales of these zones by the same way as in case of the PME (see paragraph 8.2.1.1).

Figure 183 exemplifies distribution of the water molecule number density in the plane of symmetry between two neighbor motors.

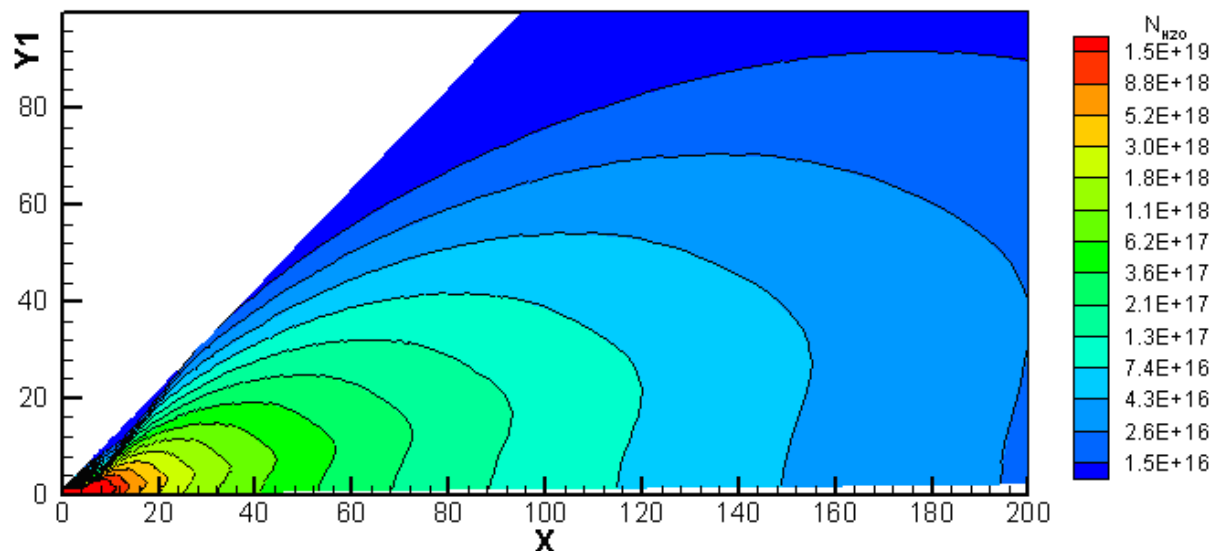


Figure 183. Distribution of the water molecule number density (m^{-3}) in the plane of symmetry between two adjacent motors.

Evidently, that the flow has a complex character starting from the near field region to about 200-300 meters downstream from the space vehicle. Actually, distance where the plume flow forms up is longer in case of the 8xACS motor set than in case of a single ACS motor. This is result of a complex interaction between the individual plumes in the cluster flowfield. So, Zone I boundary is located somewhere at 200-300 meters from the ACS motor cluster.

Mean free path of the plume molecules in the atmosphere may be evaluated with formula (8.10). In the condition of 26 April 2000 experiment the atmospheric particle number density was $n_{\infty} \approx 6.5 \times 10^{14} \text{ m}^{-3}$, space vehicle velocity $U = 7350 \text{ m/sec}$ and effluent species velocity $V = 3050 \text{ m/sec}$. Assuming the effective elastic cross-section value $\sim 10 \text{ \AA}^2$, the mean free path will be about 4.5 km. From the other side number density of the flow species becomes comparable with the number density of the atmospheric particles at about 2 km distance. So, one may assume that Zone II extends to about 2-3 km from the space vehicle. Further downstream Zone III follows, where the plume flow scatters in the atmosphere and the method discussed above is completely unable to model the flow gasdynamic parameters. From the other side, the atmospheric oxygen atoms penetrate upstream the plume flow at distances of several hundreds meters from the space vehicle. This may be easily estimated by formula (8.19) for the oxygen number density in the plume flow. For the 8xACS plume flow condition exponent factor in this formula becomes equal to unity at the distance $L_0 \approx 400 \text{ m}$. This estimate implies that most of the collisions, which result in reaction (8.1), should take place in Zone II.

8.7. Modeling of the 8xACS motor plume glow radiation

Number of the reacting collisions and intensity of the 8xACS motor set plume glow radiation have been modeled by the FNSAF method (see paragraph 8.2.3.2). Atmospheric characteristics and observation geometry inherent to 26 April 2000 experiment were used in the computation. The number of reacting collisions and radiation intensity have been computed with formula (8.20) over the field of water molecule number density. Elastic collisions have been modeled in the SC approximation through the averaged effective transport cross-section (formula (8.27)). Individual effective cross-sections were modeled by formula (8.26), which relates the transport cross-section with parameters of molecular potentials in the Born-Mayer form. The Born-Mayer potential parameters from Table 24 were utilized.

Effective cross-section for reaction (8.1) has been modeled through relation (8.21). Energy dependence of the reaction cross-section in this relation was used in the form of (8.33).

Distributions of the specific (per unit volume) radiation intensity in some selected sections ($X = \text{const}$) of the plume flow are presented in Figure 184. Apparently the radiation intensity comes over its maximum at about 200

Figure 10 consists of six contour plots arranged in a 3x2 grid, showing the distribution of the concentration of the second component (C_2) in the Y - Z plane at different X positions. The plots are labeled with their respective X values: $X = 75\text{m}$, $X = 105\text{m}$, $X = 201\text{m}$, $X = 309\text{m}$, $X = 550\text{m}$, and $X = 1050\text{m}$. The vertical axis is Z and the horizontal axis is Y . The contour lines represent different values of C_2 , with labels such as $1\text{E-}06$, $2\text{E-}07$, $4\text{E-}07$, $6\text{E-}07$, $8\text{E-}07$, $1\text{E-}06$, $1.2\text{E-}06$, $1.4\text{E-}06$, $1.6\text{E-}06$, $1.8\text{E-}06$, $2\text{E-}06$, $2.2\text{E-}06$, $2.4\text{E-}06$, $2.6\text{E-}06$, $2.8\text{E-}06$, $3\text{E-}06$, $3.2\text{E-}06$, $3.4\text{E-}06$, $3.6\text{E-}06$, $3.8\text{E-}06$, $4\text{E-}06$, $4.2\text{E-}06$, $4.4\text{E-}06$, $4.6\text{E-}06$, $4.8\text{E-}06$, $5\text{E-}06$, $5.2\text{E-}06$, $5.4\text{E-}06$, $5.6\text{E-}06$, $5.8\text{E-}06$, $6\text{E-}06$, $6.2\text{E-}06$, $6.4\text{E-}06$, $6.6\text{E-}06$, $6.8\text{E-}06$, $7\text{E-}06$, $7.2\text{E-}06$, $7.4\text{E-}06$, $7.6\text{E-}06$, $7.8\text{E-}06$, $8\text{E-}06$, $8.2\text{E-}06$, $8.4\text{E-}06$, $8.6\text{E-}06$, $8.8\text{E-}06$, $9\text{E-}06$, $9.2\text{E-}06$, $9.4\text{E-}06$, $9.6\text{E-}06$, $9.8\text{E-}06$, $1\text{E-}05$, $1.2\text{E-}05$, $1.4\text{E-}05$, $1.6\text{E-}05$, $1.8\text{E-}05$, $2\text{E-}05$, $2.2\text{E-}05$, $2.4\text{E-}05$, $2.6\text{E-}05$, $2.8\text{E-}05$, $3\text{E-}05$, $3.2\text{E-}05$, $3.4\text{E-}05$, $3.6\text{E-}05$, $3.8\text{E-}05$, $4\text{E-}05$, $4.2\text{E-}05$, $4.4\text{E-}05$, $4.6\text{E-}05$, $4.8\text{E-}05$, $5\text{E-}05$, $5.2\text{E-}05$, $5.4\text{E-}05$, $5.6\text{E-}05$, $5.8\text{E-}05$, $6\text{E-}05$, $6.2\text{E-}05$, $6.4\text{E-}05$, $6.6\text{E-}05$, $6.8\text{E-}05$, $7\text{E-}05$, $7.2\text{E-}05$, $7.4\text{E-}05$, $7.6\text{E-}05$, $7.8\text{E-}05$, $8\text{E-}05$, $8.2\text{E-}05$, $8.4\text{E-}05$, $8.6\text{E-}05$, $8.8\text{E-}05$, $9\text{E-}05$, $9.2\text{E-}05$, $9.4\text{E-}05$, $9.6\text{E-}05$, $9.8\text{E-}05$, $1\text{E-}04$, $1.2\text{E-}04$, $1.4\text{E-}04$, $1.6\text{E-}04$, $1.8\text{E-}04$, $2\text{E-}04$, $2.2\text{E-}04$, $2.4\text{E-}04$, $2.6\text{E-}04$, $2.8\text{E-}04$, $3\text{E-}04$, $3.2\text{E-}04$, $3.4\text{E-}04$, $3.6\text{E-}04$, $3.8\text{E-}04$, $4\text{E-}04$, $4.2\text{E-}04$, $4.4\text{E-}04$, $4.6\text{E-}04$, $4.8\text{E-}04$, $5\text{E-}04$, $5.2\text{E-}04$, $5.4\text{E-}04$, $5.6\text{E-}04$, $5.8\text{E-}04$, $6\text{E-}04$, $6.2\text{E-}04$, $6.4\text{E-}04$, $6.6\text{E-}04$, $6.8\text{E-}04$, $7\text{E-}04$, $7.2\text{E-}04$, $7.4\text{E-}04$, $7.6\text{E-}04$, $7.8\text{E-}04$, $8\text{E-}04$, $8.2\text{E-}04$, $8.4\text{E-}04$, $8.6\text{E-}04$, $8.8\text{E-}04$, $9\text{E-}04$, $9.2\text{E-}04$, $9.4\text{E-}04$, $9.6\text{E-}04$, $9.8\text{E-}04$, $1\text{E-}03$, $1.2\text{E-}03$, $1.4\text{E-}03$, $1.6\text{E-}03$, $1.8\text{E-}03$, $2\text{E-}03$, $2.2\text{E-}03$, $2.4\text{E-}03$, $2.6\text{E-}03$, $2.8\text{E-}03$, $3\text{E-}03$, $3.2\text{E-}03$, $3.4\text{E-}03$, $3.6\text{E-}03$, $3.8\text{E-}03$, $4\text{E-}03$, $4.2\text{E-}03$, $4.4\text{E-}03$, $4.6\text{E-}03$, $4.8\text{E-}03$, $5\text{E-}03$, $5.2\text{E-}03$, $5.4\text{E-}03$, $5.6\text{E-}03$, $5.8\text{E-}03$, $6\text{E-}03$, $6.2\text{E-}03$, $6.4\text{E-}03$, $6.6\text{E-}03$, $6.8\text{E-}03$, $7\text{E-}03$, $7.2\text{E-}03$, $7.4\text{E-}03$, $7.6\text{E-}03$, $7.8\text{E-}03$, $8\text{E-}03$, $8.2\text{E-}03$, $8.4\text{E-}03$, $8.6\text{E-}03$, $8.8\text{E-}03$, $9\text{E-}03$, $9.2\text{E-}03$, $9.4\text{E-}03$, $9.6\text{E-}03$, $9.8\text{E-}03$, $1\text{E-}02$, $1.2\text{E-}02$, $1.4\text{E-}02$, $1.6\text{E-}02$, $1.8\text{E-}02$, $2\text{E-}02$, $2.2\text{E-}02$, $2.4\text{E-}02$, $2.6\text{E-}02$, $2.8\text{E-}02$, $3\text{E-}02$, $3.2\text{E-}02$, $3.4\text{E-}02$, $3.6\text{E-}02$, $3.8\text{E-}02$, $4\text{E-}02$, $4.2\text{E-}02$, $4.4\text{E-}02$, $4.6\text{E-}02$, $4.8\text{E-}02$, $5\text{E-}02$, $5.2\text{E-}02$, $5.4\text{E-}02$, $5.6\text{E-}02$, $5.8\text{E-}02$, $6\text{E-}02$, $6.2\text{E-}02$, $6.4\text{E-}02$, $6.6\text{E-}02$, $6.8\text{E-}02$, $7\text{E-}02$, $7.2\text{E-}02$, $7.4\text{E-}02$, $7.6\text{E-}02$, $7.8\text{E-}02$, $8\text{E-}02$, $8.2\text{E-}02$, $8.4\text{E-}02$, $8.6\text{E-}02$, $8.8\text{E-}02$, $9\text{E-}02$, $9.2\text{E-}02$, $9.4\text{E$

166

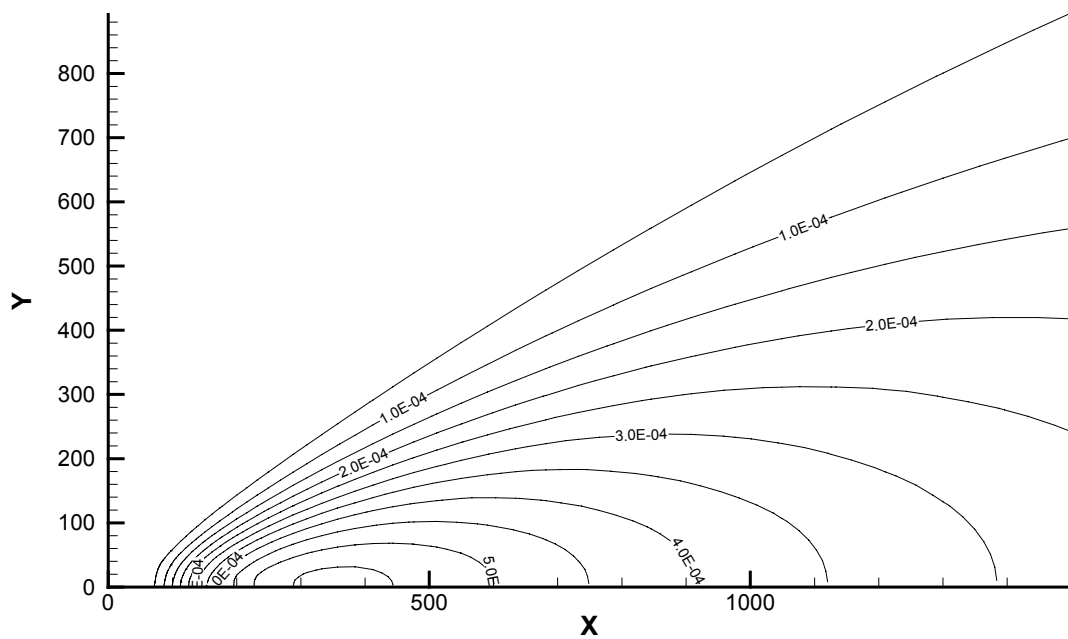


Figure 185. The motor set plume flow radiation intensity map (W/sr m^2). Side view from the infinity.

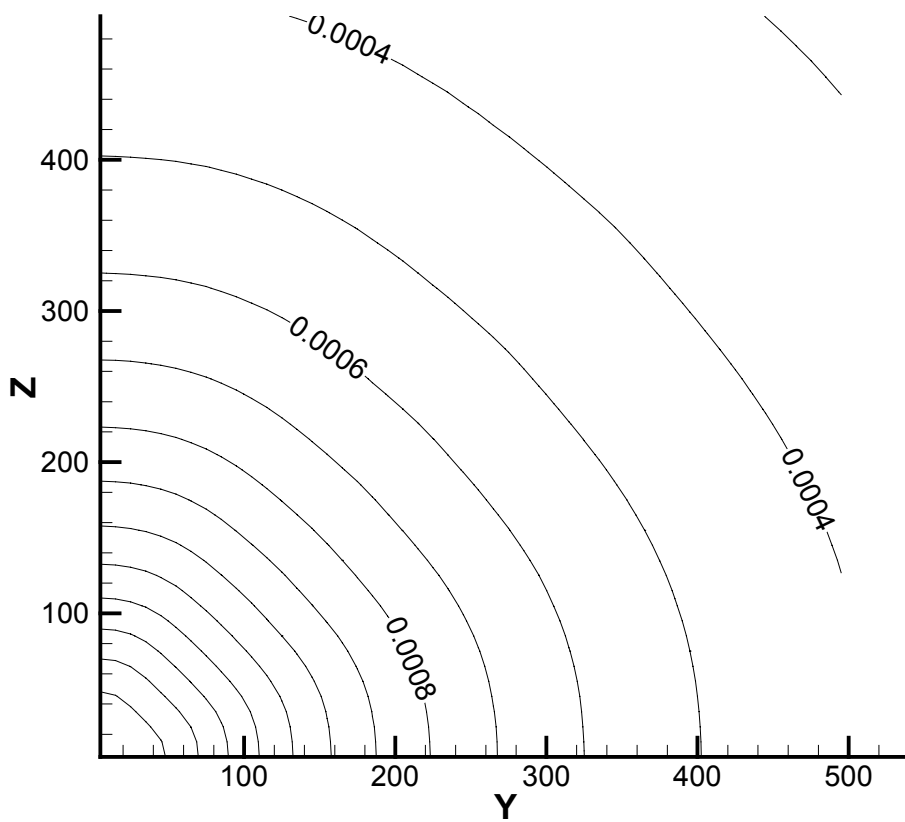


Figure 186. The motor set plume flow radiation intensity map (W/sr m^2). Tail view from the infinity.

As mentioned above, the FNSAF computation method is not valid in Zone III ($x \geq 4.5$ km), because it doesn't take into account scattering of the plume flow species on atmosphere. Despite that maximum of the reaction collision frequency is located deep inside of Zone II, disregarding of the plume flow scattering in Zone III may noticeably influence upon results of the glow radiation modeling. This is illustrated in Figure 187.

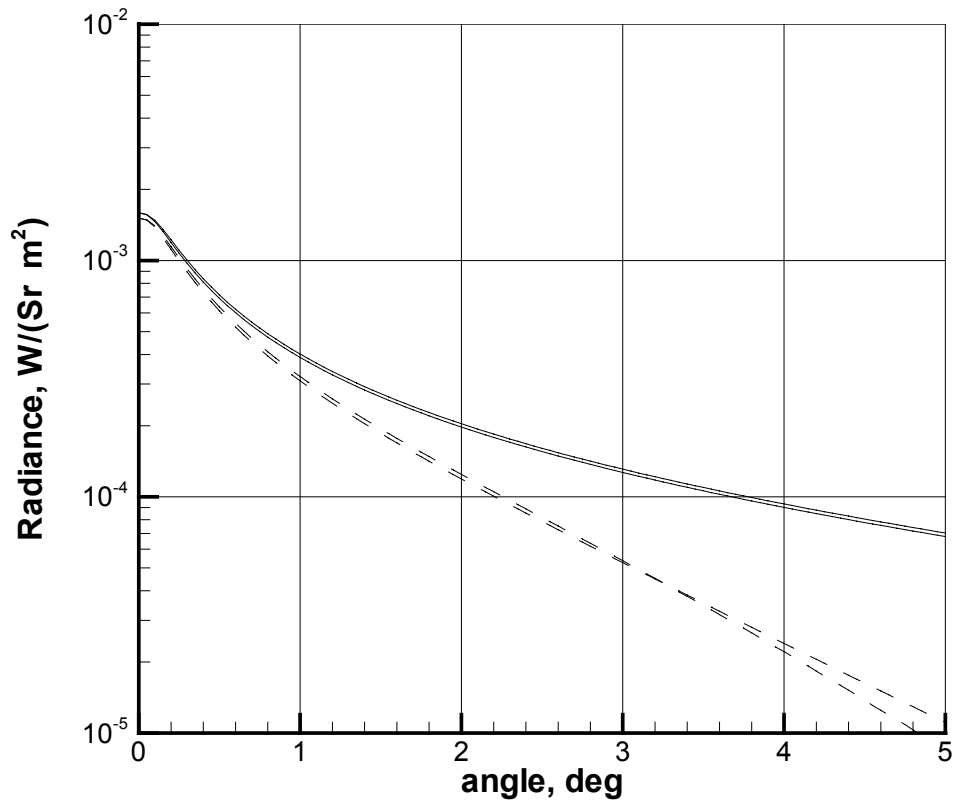


Figure 187. Distribution of the radiation intensity (tail view) computed at different approximations: solid lines – disregarding scattering in atmosphere; dashed lines – with the plume flow cut-off at the mean free path distance $x=4.5$ km. Distance to the space vehicle - 30.4 km.

Radiation intensity profiles in this figure were modeled in two extreme approximations: i) scattering of the water molecules on atmospheric species is completely neglected (baseline approximation) both in Zone II and Zone III and ii) in Zone II the baseline approximation is in effect, but no water molecules exist in Zone III. Actually, the latter approximation assumes immediate and complete scattering of the plume flow at the boundary between Zone II and III, which is set at $x=4.5$ km for this particular estimate. Obviously, the real profile should be somewhere between these extremes.

As one may conclude from Figure 187, effect of the plume flow scattering is not much important within 1-1.5° off-axis angle. At bigger angles this effect noticeably impacts the radiation intensity distribution. And finally, at the angles 2.5-3° and bigger negligence of the scattering effect may result in overprediction of the radiation intensity in several times. Note, that value of the critical angle where substantial inaccuracy may occur reduces with increase of the distance between “Progress” and “Mir” station. At the end of the observation on 26 April 2000 the distance increased almost factor of two. The critical angle should be smaller by the same factor.

Figure 187 also illustrates deviation of the integrated radiation from axial symmetry. For both extreme cases profiles in this figure are presented by pares. One curve in the pare is integral along $Y=0$ line in Figure 186, another one - along $Y=Z$ line. Due to the specifics of the motors location (see Figure 178) integrals along these lines should have the biggest difference caused by the asymmetry. In the meanwhile, the difference is fairly small, indicating that radiation intensity distribution observed in the April 26, 2000 experiment along the space vehicle axis should be almost axisymmetric.

8.8. Comparison of 8xACS motor plume flow radiation modeling results with 26 April 2000 experimental data

Direct introduction of the elastic and reaction cross-section values derived from the PME glow modeling into the 8xACS plume flow model resulted in noticeable disagreement between predicted radiation and experimental data. Figure 188 illustrates this disagreement. Left window in the figure represents direct comparison of the modeling results with 26 April 2000 (2nd sample, 155th second) observation data. Elastic and reaction (8.1) cross-sections were modeled in this computation by the same way as in the case of the PME plume glow modeling (see Section 8.5), when a good agreement with experimental data was achieved. Baseline model reaction cross-section correction coefficient $k_{\sigma}=0.08$ has been applied. 35% share of the NH(A \rightarrow X) radiation was assumed in the April 26, 2000 experiment (upper estimate in Figure 32). For modeling of the radiation intensity in terms of cpp computed intensity was multiplied on the imager response at 310 nm characteristic to particular April 26, 2000 experiment, $R_{310}=3.93\cdot10^6$ cpp per W/cm²sr. Right window represents comparison of spatial distributions of the radiation intensity. The profiles were normalized there making them equal in the maximum.

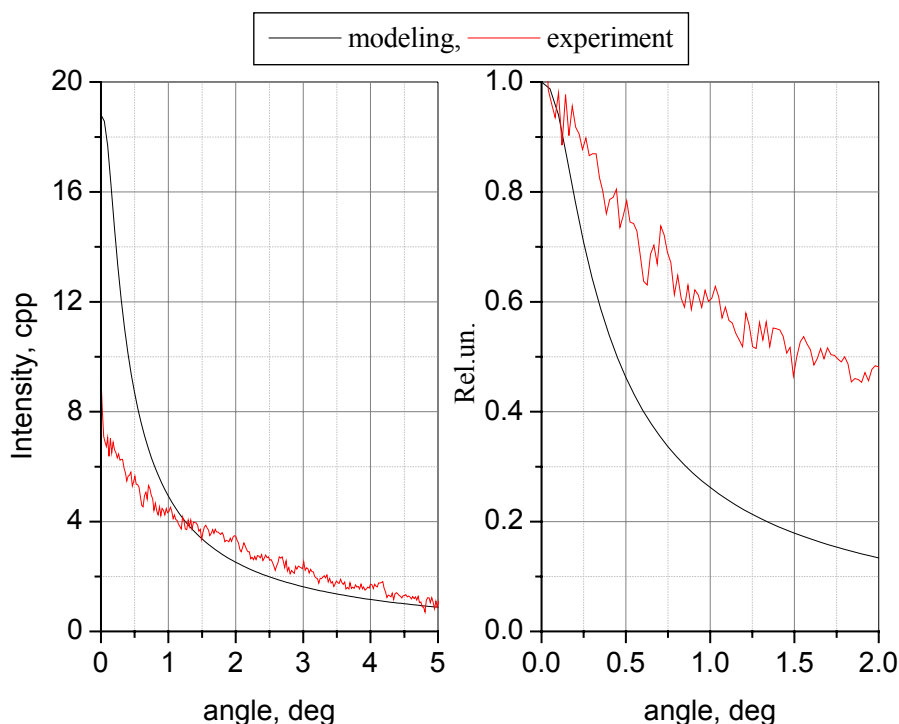


Figure 188. Radiation intensity profile computed by the FNSAF method in comparison with 26 April 2000 experiment data: 155th second after the burn start, L=30.4 km.

In contrast to Figure 170, where similar comparison was made for the PME glow, profiles in Figure 188 disagree substantially both in absolute intensity and spatial distribution. Note, that apparent agreement between modeled and experimental curves in the left window of Figure 188 in the region of angles over 1° is absolutely illusive. As mentioned above the FNSAF method is unable to predict accurately distribution of the radiation at these angles. So, compared must be only the profile parts, which are closer to the axis. In this region disagreement is evident (right window in Figure 188). Similar disagreement has been found at comparison of the FNSAF computation results with experimental data obtained in other moments of the April 26, 2000 experiment. Modeling of the 8xACS plume glow radiation distribution by DSMC method failed to come to agreement with experiment as well^{22,150}.

General tendency of the modeled profiles, which was found during comparison of the PME plume glow data (i.e. modeling overpredicts experimental results at the axis and underpredicts at peripheral regions), is evident in Figure 188 too. Numerous parametric computations with variable collisional cross-sections failed to bring satisfactory agreement for both February 28, 1999 and April 26, 2000 experiments simultaneously. Any change of the collisional parameters in the model, which gives better agreement in one experiment, immediately comes into a conflict with results of another. Principal disagreement is that model predicts much narrower radiation profiles than measured in April 26, 2000 experiment. This disagreement couldn't be overcome within

the frame of baseline glow radiation model. General revision of the model is probably required at this moment to resolve the problem developed. In this connection, it would be worth to consider additional sources of the glow radiation. Introduction of the additional radiation source would bring additional parameter into the computation, which would make easier to achieve better agreement between the computations and experimental data. Some sources of radiation other than reaction (8.1) have been discussed at the earlier stages of the PME plume glow study^{2,5}. However, that time main problem of the modeling was eliminating of the substantial discrepancy between prediction of the absolute value of the radiation intensity and experiment. Modeling overpredicted the experimental results on one-two orders of magnitude. Introduction of additional to reaction (8.1) radiation source would increase the discrepancy yet more. At the current moment, irrelevance of the reaction cross-sections applied in past for prediction of the glow radiation intensity has become evident. Instead, the experimental data are utilized now for estimate of the reaction cross-section. Therefore, consideration of the new radiation sources and radiation related processes does make a sense now.

Improvement of the plume glow physical model is addressed in the next Chapter.

9. Extension of the glow radiation model

Simplified glow radiation model, which includes only reaction (8.1) failed to explain 26 April 2000 experimental data. So, necessity has arisen to improve the glow radiation model by introduction of some other processes, which might influence the glow radiation in the UV region. In addition to already mentioned reaction (8.2) there are some other processes leading to the OH(A) single step excitation. For instance, in Ref.² mentioned were excitation of the OH molecule by solar radiation and photoluminescence of water molecules under VUV solar radiation, hydrogen Lyman alpha (L_{α}) in particular. Moreover, recent analysis of similar Shuttle glow evidenced these sources to be dominating at the daytime condition³⁶. Since the resonant scattering may occur only at daytime, we do not take this process into account during our nighttime measurements. Photodissociation of the water molecules by solar VUV radiation can also occur only at daytime. The only exclusion is photodissociation by L_{α} . This emission presents in the Earth atmosphere in the nighttime as well, in smaller amount however. Reaction of carbon oxides with atmospheric oxygen may also lead to production of the UV radiation, which may be detected by the imager. Content of the carbon oxides is relatively big both in the PME and ACS motor exhaust. So, reaction with them may occur at the first collision, similarly to the primary reactions (8.1) and (8.2).

In contrast to the primary sources (that is single step reactions) this secondary source (or sources) must be more pronounced in the peripheral plume flow regions and in Zone III, where the plume flow has already scattered and mixed with atmosphere. In these regions secondary reactions (that is reactions involving a primary reaction products) may occur¹. In the first turn, reactions involving rotationally excited water molecules should be mentioned here. These molecules may easily be produced at the first non-reactive collision between fast atmospheric atom and the water molecule. At the secondary collision these molecules may enter reaction (8.1), even with reduced translational energy.

Attention must also be paid to reactions involving metastable oxygen atoms. These atoms have considerable amount of internal energy that would help to overcome reaction (8.1) threshold at a collision with the plume molecules. Presence of the metastable oxygen atoms in the exhaust flow has been proved by spectroscopic measurements both on US Shuttle and Russian "Progress"/"Soyuz" space vehicles.

Consideration of the secondary reactions could reduce disagreement between the 26 April 2000 radiation profiles and modeling results in the off-axis regions. From the other hand, secondary processes can't seriously affect onto the February 28, 1999 experiment profiles. In that experiment Zone III of the plume flow was out of the imager's FOV, at least at the earlier moments of observation.

One more distinctive feature of the April 26, 2000 experiment was that content of the unburned propellant in the ACS motor exhaust might be substantially different from the PME one. Furthermore, in small motors substantial part of the unburned propellant components outflows in the form of droplets, especially when they work in a transient pulse mode²⁴. As mentioned in Subsection 2.2.1 some of motors in the 8xACS set permanently switched off and on in the April 26, 2000 experiment providing auspicious conditions for the droplets production. Content of the droplets in the motor exhaust must become even bigger if some part of fuel (either oxidizer) is injected along the nozzle walls for cooling. These droplets may attenuate and scatter radiation in the exhaust flow. From the other hand, one should expect the droplets effect to be much smaller in February 28, 1999 experiment, because i) the PME was substantially bigger and ii) it was cooled radiatively.

In subsequent paragraphs all the abovementioned processes and mechanisms are discussed. Their potential effect onto the experimentally measured glow radiation profiles and intensity is considered.

9.1. Improvement of the computational methods

As mentioned in Subsection 8.6.3 the 8xACS plume flow may be roughly subdivided onto three zones: Zone I (0÷0.2 km) – where the plume flow forms; Zone II (0.2÷2-3 km) – where the plume flow has already formed, but still not affected by the free stream oxygen flow and Zone III (>2-3 km) where substantial scattering of the plume flow occurs in the atmosphere. 26 April 2000 experiment has two important differences in comparison with February 28, 1999 experiment i) the glow was observed in the 26 April 2000 from longer distances and ii) experiment was conducted at lower altitude, where atmospheric density is almost five times higher and, therefore plume molecule collisional mean free path in the atmosphere is the same factor smaller. Because of these particularities Zone III and peripheral off-axis plume regions where secondary collisions take place become observable in the April 26, 2000 experiment. The TPMC and FNSAF methods, utilized for the glow radiation modeling in this study (see Subsection 8.2.3), are good for modeling of the primary radiation processes in Zone II only. So, computation scheme has been modified and two new computation methods have been suggested.

¹ Note, that division of the radiation sources as well as reactive collisions onto primary and secondary is absolutely conventional and not accentuate their importance in general.

Figure 189 illustrates the complex character of the flow in Zone III and new computation method scheme. The computation domain became bigger making sure that neither of important secondary collisions and processes is lost. In the selected reference frame the motor is located at $x_{sc}=46$ km point.

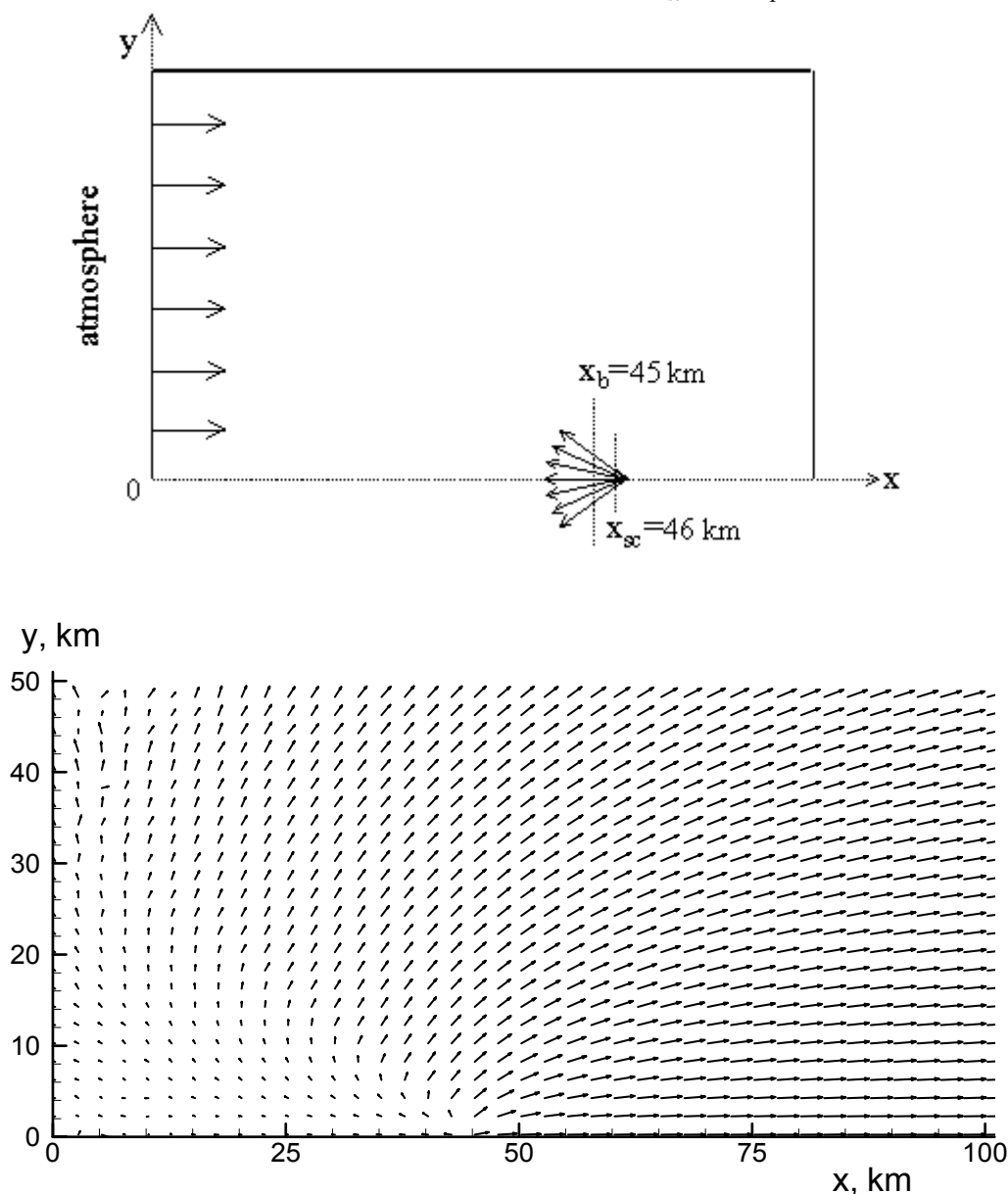


Figure 189. Scheme of the new computation method (top window) and map of the flow velocity vectors (bottom window).

The first new method is actually a modified TPMC (referred to MTPMC). In contrast to the baseline TPMC method (Paragraph 8.2.3.1) the new one takes into account attenuation of both the atmospheric oxygen flow in the plume and plume flow in the atmosphere. For this purpose the flow field was conventionally divided on two zones “near field” and “far field”. Boundary between the zones has been set at 1 km downstream from the motor and 5 km away from the axis in radial direction. Within the near field zone undisturbed plume flow discussed in Subsection 8.6.3 is considered. Scattering of atmospheric oxygen and reactive collision frequency in the near field have been modeled by baseline TPMC method. In the far field problem of the plume flow scattering in atmosphere has been solved. The atmospheric flow itself was assumed undisturbed in the far field zones. Plume specie number density and reactive collision frequency have been modeled in the far field by the TPMC method as well. However, in contrast to the baseline TPMC applied in the near field, plume molecules served as the test particles in this case.

Another method, which has been utilized for modeling of the flow parameters and glow radiation, is actually combination of the TPMC and DSMC methods. Therefore, it is referred to as Combined Monte-Carlo (CMC) method herein. Principal difference between the CMC and MTPMC methods is that CMC approach utilizes DSMC method for modeling of the flow parameters and reactive collision frequency in the far field zone.

The DSMC computation domain extended from 1 km to 15 km downstream from the motor. In radial direction the DSMC computation domain size was 5 km. Initial parameters for this computation were the undisturbed plume flow parameters at the boundary between near field and far field and free stream parameters at the utmost limit of the computational domain. In the near field the CMC approach utilized TPMC method. However, in contrast to the MTPMC, initial parameters at the near field boundary are no more assumed as in undisturbed atmospheric flow. Instead, results of the DSMC modeling in the far field were utilized as the boundary conditions.

And finally, baseline TPMC method has been applied for computation of the flow parameters and reaction collision frequency all over extended computational domain region. This has been done for illustrative comparison of the baseline TPMC method results with results of more accurate MTPMC and CMC computational methods.

Results of different computations of the plume density along the flow axis and three other lines parallel to the axis are presented in Figure 190. Apparently, MTPMC and CMC results are almost identical. Baseline TPMC agrees satisfactorily with them along the axis and not far from the motor set. However in general the baseline TPMC overpredicts the plume density, because it doesn't take into account the plume flow scattering in atmosphere.

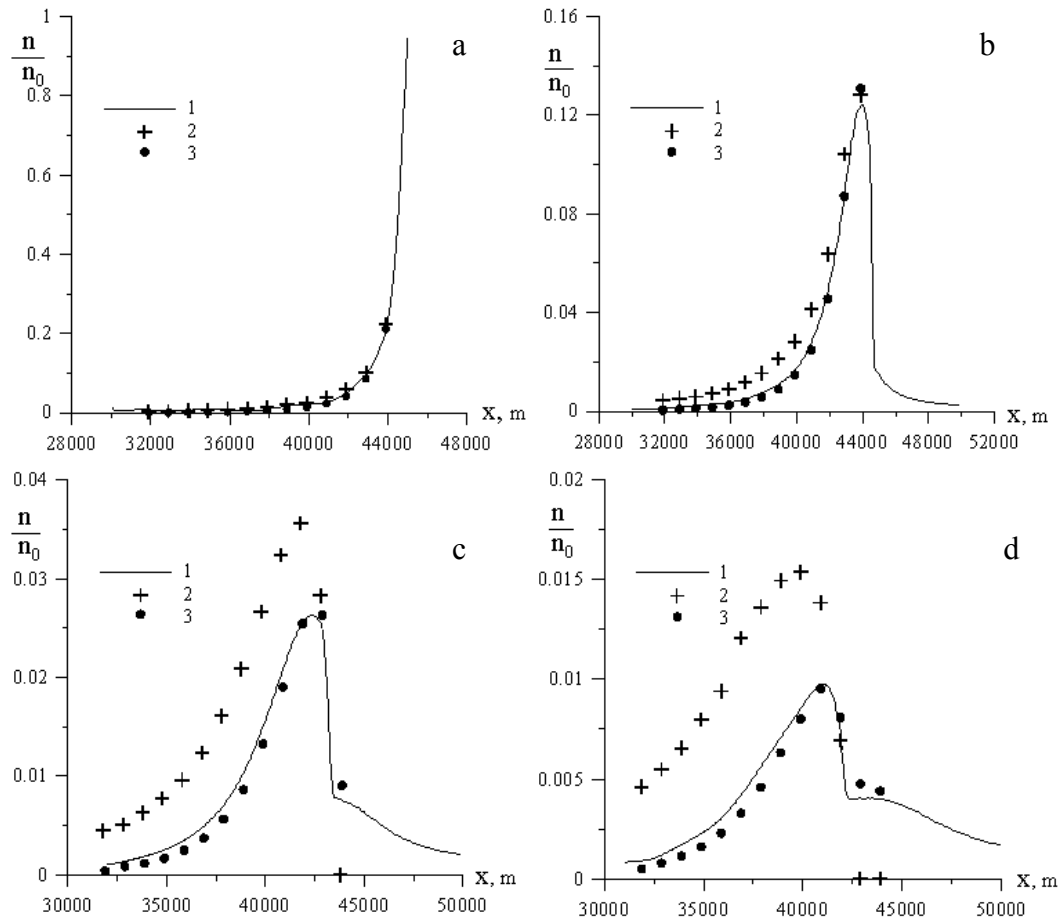


Figure 190. Normalized number density of the plume molecules: a) along the flow axis, b) parallel to the axis 1050 m away, c) parallel to the axis 2050 m away, d) parallel to the axis 3050 m away. 1 - MTPMC method, 2 -baseline TPMC, 3 - CMC method.

Results of the glow radiation modeling by different methods are presented in Figure 191. Near field and far field yields are shown separately in the figure too. Because the radiation intensity is very sensitive to the choice of the collisional models, same elastic and reaction cross-sections were applied at these computations: $\sigma_{e,eff} = 10^{-15} \text{ cm}^2$, σ_r - modeled through formula (8.33). So that difference between computational methods is compared in Figure 191, rather than difference between the collisional models.

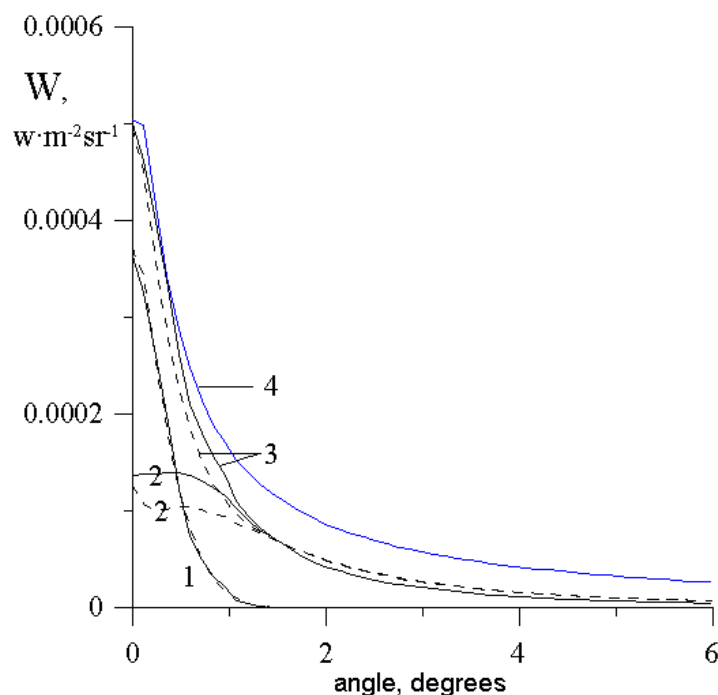


Figure 191. Radiation intensity modeled for conditions of 26 April 2000 experiment, 2nd sample (155th sec, $L=30.4$ km): 1 - near field yield, 2 - far field yield, 3 - total yield; solid lines - modified TPMC, dashed lines - CMC; 4 - baseline TPMC.

Obviously, the baseline TPMC satisfactorily agrees with more accurate computations only within the off-axis angles less than 1° . This once again emphasizes limitations of the baseline TPMC method. Agreement between the MTPMC and CMC is good over entire computational region. Some departure of the MTPMC far field yield from the CMC one (curves 2) is evident near the axis. However, in this region radiation contribution from the near field (curves 1) dominates. So that total radiation profiles are very close to each other.

Complementing Figure 188, glow radiation profile measured at 155th second (2nd sample) in 26 April 2000 experiment is compared with modeling results in Figure 192. Collisional parameters derived from February 28, 1999 experiment were utilized in this computation: effective elastic cross-section $\sigma_{e,eff}=10^{-15}$ cm² and reaction (8.1) cross-section in the form (8.33). Correction factor for σ_0 was taken 0.074 in accordance with baseline share of the OH(A \rightarrow X) radiation in February experiment - 80%. For the April 26, 2000 experiment this share was set at 65%.

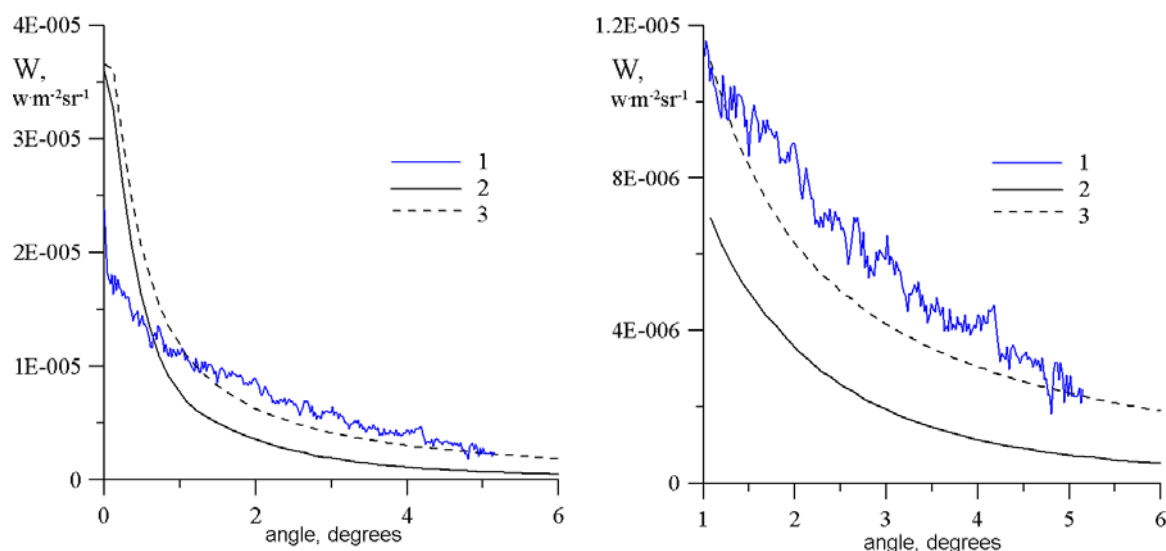


Figure 192. Comparison of the experimentally measured radiation profile (26 April 2000, 2nd sample) with modeling results: 1 - experiment, 2 - DSMC method, 3 - baseline TPMC method.

As expected, improved computational methods are unable to make satisfactory fit to the 26 April 2000 experimental data, if just a single reaction (8.1) is included into the glow radiation model.

9.2. Consideration of other reactions producing excited OH(A) molecules

9.2.1. Reaction between hydrogen and oxygen

Recombination between atomic oxygen and hydrogen is well studied reaction in the plume¹⁵¹. In presence of a third body this used to be one of the primary mechanisms of the OH(A→X) emission excitation in flames. Obviously, in the condition of extremely rarified high altitude plume flow the three body recombination has to be completely ruled out. Meanwhile, two body recombination: $O+H\rightarrow OH(A)$ may also take place. However, cross-sections for such two body recombination reactions are very small. Estimate of the cross-section made on the basis of published rate constants for the two body recombination¹⁵¹ allowed making a conclusion that this reaction couldn't provide any noticeable contribution to the OH(A→X) glow in condition of the experiments discussed in this Report. Same conclusion may be done about other multistep and three body flame reactions.

9.2.2. Water luminescence under VUV radiation

Reaction of water photoluminescence under hydrogen L_α , VUV radiation ($\lambda=121,6$ nm)



was found to be one of the major OH(A→X) emission production mechanisms in the Shuttle motor plume glow at the daytime condition³⁶. Due to resonant scattering of the L_α emission in the Earth upper atmosphere, flux of the L_α radiation doesn't come to zero at the night side. Hence, reaction (9.1) may occur here as well. To estimate contribution of this reaction into the OH(A→X) glow intensity at night condition let's suppose total flux of the L_α at nighttime equals $J_L \sim 2 \text{ kR} = 2 \cdot 10^{13} \text{ photons/m}^2\text{sec}$ ³⁵, absorption cross-section of the L_α by water $\sigma_L \sim 10^{-17} \text{ m}^2$ (Ref.¹⁵²) and OH(A) efficiency $q \sim 0.1$ (Ref.¹⁵³). With these parameters the ACS plume flow may be considered as optically thin and the photoluminescent radiation intensity may be approximated by:

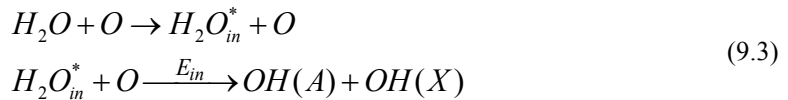
$$W = \frac{h\nu}{4\pi} J_L \sigma_L q \int_{x_0}^{\infty} X_{H_2O} \left(\frac{A_{ACS}}{x} \right)^2 dx = \frac{h\nu J_L \sigma_L q X_{H_2O} A_{ACS}}{4\pi x_0} \quad (9.2)$$

where water number density was approximated by a reverse square law ($A_{ACS}=2.8 \cdot 10^{21} \text{ m}^{-1}$), $X_{H_2O}=0.3$ the water molar content in the exhaust, $h\nu$ - OH(A→X) photon mean energy and x_0 - distance from the nozzle where the integration starts from. This distance would be reasonable to set at 50-70 meters from the space vehicle, because closer regions of the plume flow can't be resolved by the imager from 30 km distance. At these settings the photoluminescent radiation intensity will be order of $1 \cdot 10^{-9} \text{ W/m}^2\text{sr}$. This is about four orders of magnitude below the plume glow intensity level measured in 26 April 2000 experiment.

In contrast to Ref.³⁶, present analysis demonstrates negligibly small effect of the water photoluminescence onto production of the OH(A→X) radiation in the plume glow. This is most probably explained by different conditions of the experiments (daytime versus nighttime) and different observation geometries (very near field side view versus long range tail view).

9.2.3. Reaction of the vibrationally-rotationally excited water molecules with atmospheric oxygen

At the first collision in the plume flow the water molecule has some probability to become vibrationally-rotationally excited and carry the internal excitation energy E_{in} till the second collision with atmospheric oxygen atom. Despite that at the second collision translational energy of the water molecule will be most probably below the reaction (8.1) threshold, total collision energy, which includes the internal energy, may eventually exceed the threshold. In this case reaction may happen with some probability. This two step processes may be expressed as:



where $H_2O_{in}^*$ represents water molecule which possesses by internal energy E_{in} . Efficiency of process (9.3) depends on the probability of translational-rotational (TR) energy transfer at the first collision and on amount of internal energy, which may be given up for the reaction at the second collision. Kinetics of these processes is not well studied at high collision energies. So, parametric study of the process (9.3) has been undertaken. In this study supposed was that at each first collision part of the available collision energy was transferred into internal energy. This part served as a variable parameter. At the second step this internal energy was given up to the reaction. No other excitation/quenching processes were considered for simplicity. Cross-section for the first collision was set constant $\sigma_{eff}=10^{-15} \text{ cm}^2$, reaction cross-section energy dependence was utilized in a similar to (8.33) form:

$$\sigma_r = 1.15 \cdot 10^{-16} \frac{(E_c - E_{th})^{0.5}}{E_c} \text{ cm}^2, \quad E_c = E_{tr} + E_{in} \quad (9.4)$$

where E_c - represents total collision energy, E_{tr} - translational energy and $E_{th} = 4.8 \text{ eV}$ is the reaction threshold, same as in (8.33). The reaction collision frequency was modeled by the MTPMC method.

Figure 193 illustrates results of parametric modeling of the OH(A→X) radiation in process (9.3). Absolute and normalized radiation intensity profiles are presented in this figure. Also, normalized profile of the radiation produced by the primary reaction (8.1) is shown in Figure 193 for reference.

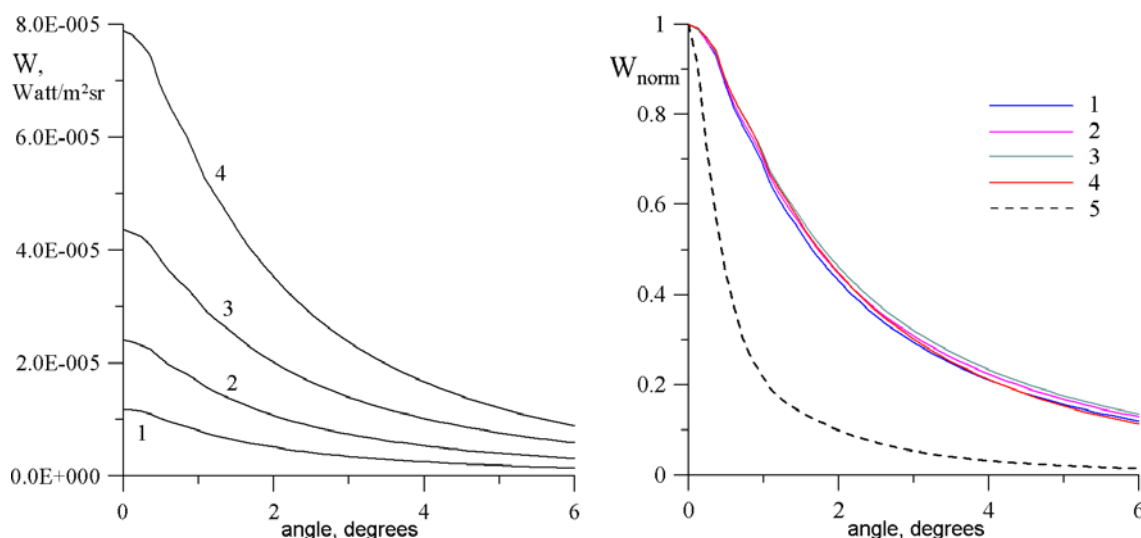
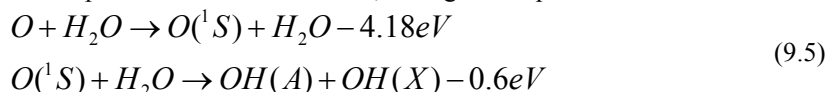


Figure 193. OH(A→X) radiation intensity profiles modeled in process (9.3) with variable amount of internal energy gained by the water molecule at the first collision: 1 - $E_{in}=1$ eV, 2 - $E_{in}=2$ eV, 3 - $E_{in}=3$ eV, 4 - $E_{in}=4$ eV, 5 - profile of the radiation from primary reaction (8.1). 1 through 4 modeled by MTPMC method, 5 - modeled by CMC method

As evident from this figure, for all values of E_{in} spatial distribution of the radiation generated in process (9.3) results in much wider profile in comparison with reaction (8.1). At the same time, absolute radiation intensity in the region of angles $\chi \geq 1.5-2$ is comparable with the experimentally measured one, dominating over the primary mechanism at reasonable meanings of $E_{in} \leq 0.5-1.5$ eV alreadyⁱ (compare with Figure 192). So, inclusion of process (9.3) into the glow radiation model may substantially improve agreement between modeled and 26 April 2000 experiment profiles in the off-axis region. In the meantime, this process should not impact the near axis radiation that much, because primary reaction (8.1) dominates here. For the same reason one could expect just a weak effect of reaction mechanism (9.3) onto February 28, 1999 radiation profiles.

9.2.4. Reaction of water with metastable oxygen

Spectral measurements of the plume glow evidenced presence of the metastable $O(^1D)$ and $O(^1S)$ oxygen atoms in the plume flow (see Subsection 2.6.2). These atoms possess by a substantial amount of internal energy and may easier enter into reaction with water molecules. As usually, no reliable data about this kind of reactions are available. Therefore, importance of this process has been estimated, basing on simplified reaction scheme:



Higher (1S) level has been taken for this estimate, because it has bigger reserve of the internal energy. At the first step in process (9.5) any other plume molecule might be introduced instead of the water. However, there are some references indicating higher probability of the $O(^1S)$ production in collisions of oxygen with water than with other plume components^{35,154}. The metastable oxygen atom produced at the first step of process (9.5) was allowed to move away in any direction with sampled velocity. Further the metastable atom either collided with water, entering into reaction with some probability or decayed through radiation with characteristic time $\tau = 0.73$ sec¹⁵⁵. It should be noted that quenching rate of the $O(^1S)$ atoms by water molecules is much bigger in comparison with other major plume species^{35,154}. Therefore, quenching of the metastable oxygen may be roughly accounted by proper choice of the elastic and reaction cross-sections.

MTPMC method has been used for evaluation of the OH(A→X) radiation output from process (9.5). The following effective cross-sections were applied:

Elastic collision of water with atmospheric oxygen - 10^{-15} cm²
Non-reactive collision of water with metastable oxygen - $1.5 \cdot 10^{-15}$ cm²

ⁱ Recall that total collision energy is more than 5 eV in average

First step reaction in process (9.5) - 10^{-17} cm^2

Second step reaction in process (9.5) - 10^{-16} cm^2

This choice of the cross-sections is rather extreme. One should expect maximal radiation output with these values of the collisional parameters. In the meanwhile, even in this case the output of process (9.5) appeared to be more than two orders of magnitude less than output from primary reaction (8.1) with cross-sections (8.33) and more than order of magnitude less than radiation intensity measured in April 26, 2000 experiment. Furthermore, spatial profile of the radiation intensity produced in process (9.5) is very similar to the primary reaction profile (see Figure 194). This is not unexpected result, because the radiation profile in both cases reflects distribution of the plume flow density. So, if the real radiation intensity in process (9.5) were even higher than this extreme estimate, it would not improve the disagreement between modeled and experimental radiation profiles. Neither it could help elucidate discrepancy of absolute radiation intensities, because the same process (9.5) should take place in the Zone II of the PME plume flow in February 28, 1999 experiment.

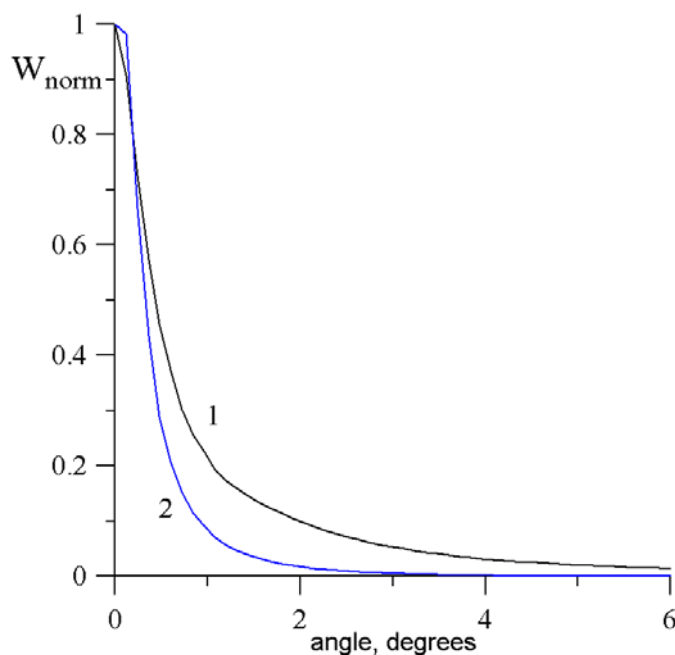


Figure 194. Normalized radiation intensity profiles modeled through primary reaction (8.1) with the ground state oxygen and secondary process (9.5) with metastable oxygen.

9.3. Consideration of other molecular band emissions

In addition to the $\text{OH}(\text{A} \rightarrow \text{X})$ emission the UV imager onboard the "Mir" space station might detect other molecular band emissions located in the region of its sensitivity. Analysis of corresponding reactions may be found in Ref.¹⁴⁶. Among different reactions between atmospheric oxygen and plume flow species only two were found so far, which may have potential capability to contribute to the imagers signal. These are i) reactions with unburned fuel fragments, producing NH excited molecules and ii) reactions with carbon dioxide, producing excited O_2 molecules. Other reactions either have very small cross-sections or produce radiation, which is located out of the imager sensitivity band.

9.3.1. Reactions producing $\text{NH}(\text{A})$ radiation

These reactions have already been mentioned in the Report. Presence of the $\text{NH}(\text{A} \rightarrow \text{X})$ component in the high altitude plume glow can't be called in question at this moment. The problem is that share of the $\text{NH}(\text{A} \rightarrow \text{X})$ radiation is not exactly known in both February 28, 1999 and April 26, 2000 experiments. Meanwhile, variation of this share within reasonable margins may somewhat influence to comparison of the experimental data with modeling results. For example, assume that share of the $\text{NH}(\text{A} \rightarrow \text{X})$ radiation in the February 28, 1999 images was 40%, whereas in April 26, 2000 images it was 10%. This will immediately result in noticeable improvement of the agreement between modeled results and experimental data near the flow axis. This is illustrated in Figure 195, where the radiation profiles are compared with computation results. As always, the same collisional models were applied, the only difference was the aforesaid difference in the $\text{NH}(\text{A} \rightarrow \text{X})$ radiation shares.

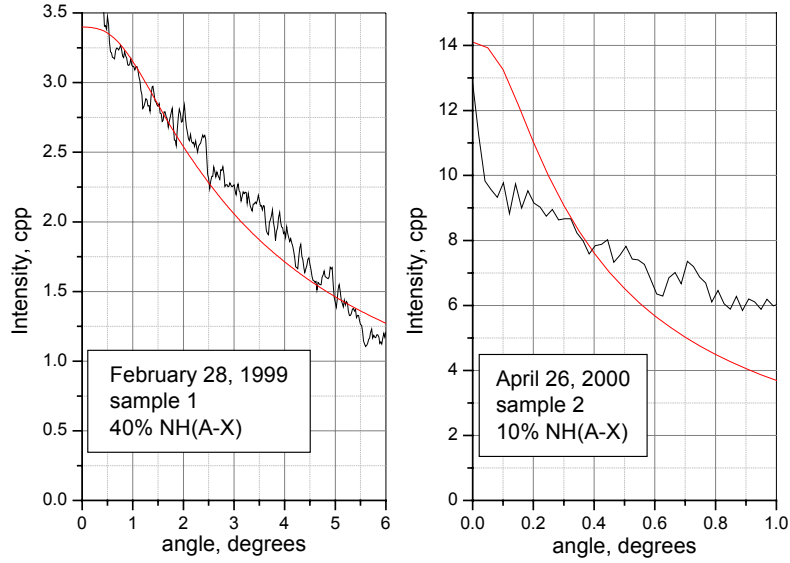
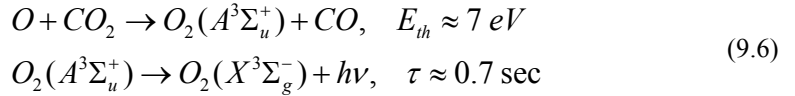


Figure 195. Comparison of modeling result with experimental data near the axis, assuming unequal shares of the NH(A→X) radiation in the two sets of experiments.

Comparison of Figure 195 with Figure 188 shows that assumption about unequal NH (A→X) radiation shares may reduce discrepancy between the modeling and experiment to about 40%.

9.3.2. *Reaction between carbon dioxide and atmospheric oxygen*

Carbon dioxide molecules are available in the PME and ACS motor exhaust flow in amount of about 5%. They can enter into a first collision reaction with atmospheric oxygen, producing excited O₂ molecules^{156,157}:



This process result in well-studied oxygen Herzberg band emission related to the forbidden transition^{158,159}. In spite of the fairly long radiative time of the upper A-state, Herzberg band radiation may be noticeable in rarified medium, where collisional quenching is not important. The radiation spectrum includes multiple bands extending from 250 to 450 nm. Some of these bands fall into the imager sensitivity region. As mentioned in Subsection 2.6.3 the Herzberg band emission is most probable source of the Earth limb nightglow often detected by the imager (see Figure 26d). Threshold energy E_{th} and spontaneous radiation lifetime τ may vary within the electronically excited A-state from one vibrational-rotational level to another. So, some typical values for upper levels of stronger emissions are chosen in (9.6).

Reaction (9.6) has higher threshold than reaction (8.1) with water. At the same time, total translational energy available for the reaction in the plume-atmosphere counterflow is also higher - about 7 eV. From this aspect reaction (9.6) is somewhat similar to the primary reaction (8.1). For instance, spatial distribution of the reactive collision frequency should be similar to the OH(A) production frequency. Its maximum should be located far from the space vehicle, where collisional mean free path for excited oxygen molecule is relatively long and part of the excited molecules have enough time to radiate before collisional quenching. From the other hand, due to the long radiative lifetime of the O₂(A) molecule, the radiation intensity spatial profile must be wider than in case of the short-living OH(A) molecule. So, that this reaction might potentially become a reason for wider radiation profile in 26 April 2000 experiment. All these arguments encouraged more thorough consideration of reaction (9.6).

Cross-section energy dependence for reaction (9.6) was recommended in Ref.¹⁴⁶ in the form of

$$\sigma_r = 0.69 \cdot 10^{-16} \frac{\sqrt{E - E_{th}}}{E} \text{ cm}^2 \quad (9.7)$$

Similarly to cross-section for reaction (8.1) this one has been derived from the reaction rate constant measured in reaction with non-excited products¹⁵⁶. As soon as no other data have been found, the cross-section (9.7) was utilized for the reaction frequency computation.

The problem of O₂(A→X) radiation intensity computation has been solved by MTPMC method. Diffusion of the metastable oxygen molecule has been also modeled within the MTPMC computation. All collisional quenching processes were neglected. Only radiative decay of the metastable oxygen molecule was taken into account, making the estimate rather overpredicting. To pick up all radiative events the computational domain has

been extended to extra two km in each direction. Radiation profile modeled for condition of April 26, 2000 experiment (sample 2, 155th sec) is presented in Figure 196. Contributions from the near field and far field zones are also shown for reference.

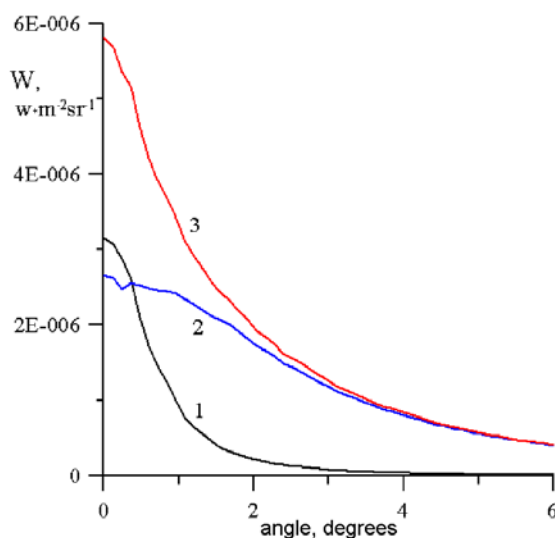


Figure 196. Herzberg band radiation intensity profiles caused by reaction (9.6): 1 - contribution from the near field, 2 - contribution from the far field, 3 - total radiation profile.

Of course, this analysis is rather qualitative. However it yields two important conclusions.

The $O_2(A \rightarrow X)$ radiation intensity profile is obviously much wider than profile of the primary $OH(A \rightarrow X)$ radiation. This is expected result, related to difference between radiative times of these two molecules

Absolute radiation intensity absolute value of the $O_2(A \rightarrow X)$ radiation intensity not exceed a few percent of the $OH(A \rightarrow X)$ radiation intensity modeled through reaction (8.1). However, it constitutes tens percents from the radiation intensity measured in April 26, 2000 experiment. One may argue that this cross-section (9.7) is overestimated like the one for primary reaction (8.1). There are no arguments now either to accept or reject this assertion. What can be definitely stated is that effect of the reaction (9.6) is substantially overestimated for April 26, 2000 experiment, because $O_2(A)$ collisional quenching has not been taken into account. Our estimate shows that quenching effect reduces the radiation to the level below 10% of the measured signal. So, this reaction may probably be ruled out in the 26 April 2000 experiment condition.

On the contrary in the condition of 28 February this process may play more important role. There are two reasons supporting this idea. First, number density of atmosphere and plume species in the region of maximal $O_2(A)$ production was about 5 times lower in the February 28, 1999 experiment. Second, velocity of effluent molecules in the ACS plume flow is slightly lower than in PME flow. In the condition when the reaction threshold almost equals to the average collision energy, this factor may become important. Simple estimate based on similarity of the plume flows shows that $O_2(A \rightarrow X)$ radiation might be at the level of 10-30% of the measured signal in 28 February experiment, if relation (9.7) is applied for the reaction cross-section.

9.4. Attenuation of the radiation in the plume flow

Plume flow species may absorb and scatter the $OH(A \rightarrow X)$ radiation on its way from the source to detector. As the result attenuation of the radiation and spatial re-distribution of its intensity may occur.

9.4.1. Resonant scattering of the $OH(A \rightarrow X)$ radiation in the plume flow

Resonant scattering of the $OH(A \rightarrow X)$ radiation in the plume flow represents absorption of the radiation on its way to the detector by a ground state $OH(X)$ molecule followed by a spontaneous re-emission of the same radiation. The radiation is re-emitted in arbitrary direction uniformly in space. Due to the short lifetime of the excited $OH(A)$ molecule, in practice this process looks like a scattering of the $OH(A \rightarrow X)$ radiation by $OH(X)$ molecule. As usually, the denser is medium and longer is path to the detector, the bigger is the scattering effect, which is characterized by product of the scattering species number density and the radiation optical path. In conditions of rarified plume flow a long optical path may compensate small number density of the plume species, so that resonant scattering effect may become noticeable. Effect of the resonant scattering of solar radiation on the $OH(X)$ molecules was reported as a primary source of the Shuttle plume $OH(A \rightarrow X)$ glow on the day part of the orbit³⁶. This fact encourages closer consideration of the $OH(X)$ scattering capabilities in the "Progress" motor plume flow.

Two different sources of the $OH(X)$ molecules may be found in the plume flow. The first source is the motor itself. Modeling of non-equilibrium nozzle flow by the NARJ gasdynamic codes¹³⁶ results in the $OH(X)$ mole fraction at the nozzle exit $X_{OH} \approx 3 \cdot 10^{-5}$ for ACS motor and $X_{OH} \approx 10^{-5}$ for PME. In the near field of the plume

flow some chemical reactions still persist. However, simple estimates show that even in the region of strong interaction between the plumes of the 8xACS motor set water dissociation is weak, so that mole fraction of the OH(X) doesn't changes. Hence, further downstream the number density of the effluent OH(X) molecules may be expressed by a reverse square law:

$$N_{OH}^{(1)} = X_{OH} N_p \approx X_{OH} \frac{A}{x^2} \quad (9.8)$$

where N_{OH} - is the OH(X) molecule number density at the point x on the axis (superscript "1" relates the OH(X) molecules to the first source), N_p - is plume species number density at this point and A is a constant featuring the motor type: $A = 2.8 \cdot 10^{21} \text{ m}^{-1}$ for the 8xACS motor set and $A = 1.23 \cdot 10^{22}$ for the PME. The first source dominates in the near field of the plume. It is important when the plume glow is observed from the space vehicle through these near field regions, because most of the OH(A→X) radiation is produced further downstream. In both experiments discussed in this Report the glow was observed from the tail, so the near field regions were out of the observation optical path.

Second source of the OH(X) molecules in the plume flow is reaction (8.32) between the atmospheric oxygen and water molecules. DSMC modeling of this process in the PME plume flow has been carried out in Ref.²⁰. Substantial excess of the reaction (8.32) products over the effluent OH(X) molecules was found in the far field of the plume flow. So, it's worth evaluating the OH(X) production rate in the 8xACS motor set plume flow as well. This evaluation has been accomplished in the frame this Project. Generally, computations of the OH(X) number density has been done by CMC method in the far field of the plume flow, where excess of the second source OH(X) molecules over the first one was expected. At the same time analytical approximation has been derived for the OH(X) number density along the axis and verified through the CMC modeling results. Utilization of the analytical expression is more convenient for subsequent estimate of the resonant scattering effect. So, its derivation is suggested below.

Consider the steady state balance equation for the OH(X) molecules produced in reaction (8.32) at any point along the motor set axis:

$$W^*(x) = \frac{N_{OH}^{(2)}}{\tau_{OH}} \quad (9.9)$$

where $W^*(x)$ - is frequency of the reactive collisions in the point x , N_{OH} - number density of the OH(X) molecules in the considered point (superscript "2" indicates to the second source of the OH molecules) and τ_{OH} - characteristic residence time of the OH(X) molecule around considered point. DSMC computations in Ref.²⁰ showed that in the region of the OH(X) maximal production number density of the atmospheric oxygen is almost as in undisturbed atmosphere. Despite that noticeable part of the atmospheric oxygen has already experienced a collision with plume specie by this region, all oxygen atoms may be considered as potential reactants due to relatively small threshold of reaction (8.32). In this approximation OH(X) molecule production rate may be expressed as:

$$W(x) = 2 \frac{A \cdot X_{H_2O}}{x^2} n_{O\infty} \sigma_{r,eff}^* \cdot (U + V) \quad (9.10)$$

where $\sigma_{r,eff}^*$ - is effective cross-section for reaction (8.32), $n_{O\infty}$ - atmospheric oxygen number density ($1.48 \cdot 10^{14} \text{ m}^{-3}$ on February 28, 1999 and $5.55 \cdot 10^{14} \text{ m}^{-3}$ on April 26, 2000), $U+V \approx 10400 \text{ m/s}$ - relative velocity of oxygen atoms and plume flow molecules. Coefficient 2 is applied to accounts for the pair of the OH(X) molecules is produced in each reaction. Note, that this approximation is not valid both in the near field of the plume, where the atmospheric oxygen can't penetrate and very far field where the plume flow scatters due to interaction with atmosphere. It may be applied only in Zone II of the plume (see Paragraphs 8.2.1.2 8.6.3), where most of the emission-absorption processes take place. Indeed, this approximation results in overestimated number density of the OH molecules.

Standard expression may be suggested for the characteristic residence time:

$$\tau_{OH} \approx \frac{L}{U_{OH}} = C \frac{x}{U_{OH}} \quad (9.11)$$

where U_{OH} - is velocity of the newly born OH(X) molecule, L - characteristic scale for the OH(X) number density gradient variation, x - current coordinate and C - constant, which should be order of unity. Introduction of (9.10) and (9.11) into (9.9) will give the OH(X) number density:

$$N_{OH}^{(2)} = 2C \frac{A X_{H_2O} \cdot n_{O\infty} \cdot \sigma_{r,eff}^*}{x} \cdot \frac{(U + V)}{U_{OH}} \quad (9.12)$$

As discussed in Subsection 8.3.2 two forms of reaction (8.32) cross-section energy dependence may be inferred from Ref.¹⁴⁶. For unambiguity of the estimate, let's consider the cross-section in the form of:

$$\sigma_r = 2.3 \cdot 10^{-16} \frac{(E - E_{th})^{0.5}}{E} \text{ cm}^2 \quad (9.13)$$

Threshold value $E_{th}=0.8$ eV was derived in Ref.¹⁴⁶ from thermodynamic consideration. Assuming average pre-collision energy $E=5.1$ eV, effective reaction cross-section $\sigma_{r,eff}^* \approx 10^{-16} \text{ cm}^2$ may be estimated from formula (9.13). And finally, OH(X) molecule velocity may be set at the maximal value $U_{OH} \approx 4880$ m/s allowed by the energy conservation law. Actually not all the reaction energy excess must be spent for translational velocity of the reaction products. Part of the energy will certainly be transferred to the internal degrees of freedom of the OH(X) molecules. In this case the U_{OH} , velocity will be smaller. However setting the OH(X) velocity to maximum will partially compensate inaccuracy caused by overestimation of the oxygen number density. In any case, relation (9.12) includes factor C , which may be adjusted to best fit with accurate computation. Having all aforesaid parameters introduced into relation (9.12) one may easily obtain the OH(X) number density dependent on the parameter C . Comparison of the analytical approximation (9.12) with CMC computation results provided best fit with $C=0.7$.

In presence of scattering the 1-D radiation transfer equation may be formulated as follows:

$$\frac{dI(x)}{dx} = J(x) - I(x)N_{OH}(x)\sigma_s \quad (9.14)$$

where $J(x)$ specific (per unit of volume) radiation power, $I(x)$ - radiation intensity at point x on the axis, N_{OH} - number density of the OH(X) molecules and σ_s - effective cross-section for absorption of the OH(A \rightarrow X) radiation by OH(X) molecule. In this formulation multiple scattering is disregarded, so that each absorbed and re-emitted photon is considered to be lost.

Modeling of the specific radiation power along the flow axis has been already discussed above (see Sections 8.4 and 8.7). Number density of the OH(X) molecules is approximated by expression (9.12). Assuming that effective cross-section σ_s doesn't depend on x , the radiation transfer equation may be integrated. Upper limit for the integral should be set at the point where observer is located. Lower limit would be reasonable to set some distance before the OH(A) maximum production place. It should be noted that lower limit uncertainty doesn't influence much onto the integration result, which depends logarithmically on the ratio of the upper to lower limit. It is convenient to analyze results of the integration in terms of parametric dependence of the plume flow transparency $T(\sigma)$ on the absorption cross-section value. The plume transparency may be defined as:

$$T(\sigma) = \frac{I_\sigma}{I_0} \quad (9.15)$$

where I_σ - is intensity at specified value of the absorption cross-section $\sigma_s=\sigma$ and I_0 - intensity at $\sigma_s=0$. When $T(\sigma)=1$ the plume flow medium is absolutely transparent for the OH(A \rightarrow X) radiation. $T \approx 0.5-0.8$ would improve comparison of the 8xACS plume flow modeling results with experimental data along the axis (see Figure 192). At smaller $T(\sigma)$ the plume flow becomes fairly opaque. Multiple scattering effect can't be neglected in this situation and radiation transfer equation in the form (9.14) becomes too rough approximation both for 8xACS and PME plume flows.

Dependence of the plume flow transparency on the effective absorption cross-section is plotted in Figure 197 both for PME and 8xACS cases.

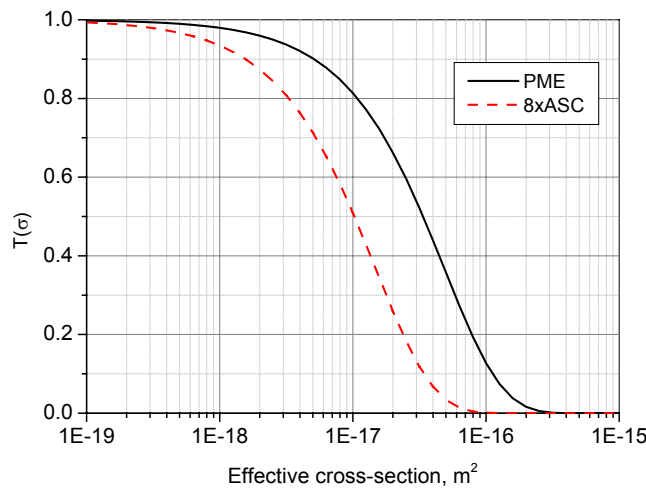


Figure 197. Transparency of the PME and 8xACS motor plume flow along the axis depending on the absorption cross-section value.

Effective absorption cross-section for the OH(X) molecules depends on population of the absorption levels, width of individual absorption lines, strength of electronic transition and Franck-Condon factors for the absorption lines. Assuming Doppler broadening, integral cross-section for individual lines with common rotational quantum number of lower state K'' in the vibrational band (0,0) may be expressed as:

$$\sigma(T_{rot}, T_{tr}, K'') = \frac{4.14 \cdot 10^{-15}}{T_{rot} \cdot T_{tr}^{1/2}} \cdot (2K'' + 1) \cdot \exp\left(-\frac{24.96 K''(K'' + 1)}{T_{rot}}\right) \quad (9.16)$$

where T_{rot} – rotational temperature of the absorbing molecules, T_{tr} – translational temperature of these molecules. To derive this cross-section, expressions for Doppler width and integral absorption coefficient of individual line were borrowed from Ref.^{159,160}. Other parameters, which are necessary for the cross-section modeling are as follows: electron transition strength¹⁵⁹ – $S_{00}=0.042$ a.u., Frank-Condon factor¹⁶¹ – $q_{00}=0.907$ and rotational constant for the lower state¹⁶² – $B_{00}=17.35$ cm⁻¹. Figure 198 illustrates dependence of the OH(X) absorption cross-section on temperature for some separate lower vibrational levels. Equal translational and rotational temperatures $T_{tr}=T_{rot}$ were assumed both for radiating and absorbing molecules.

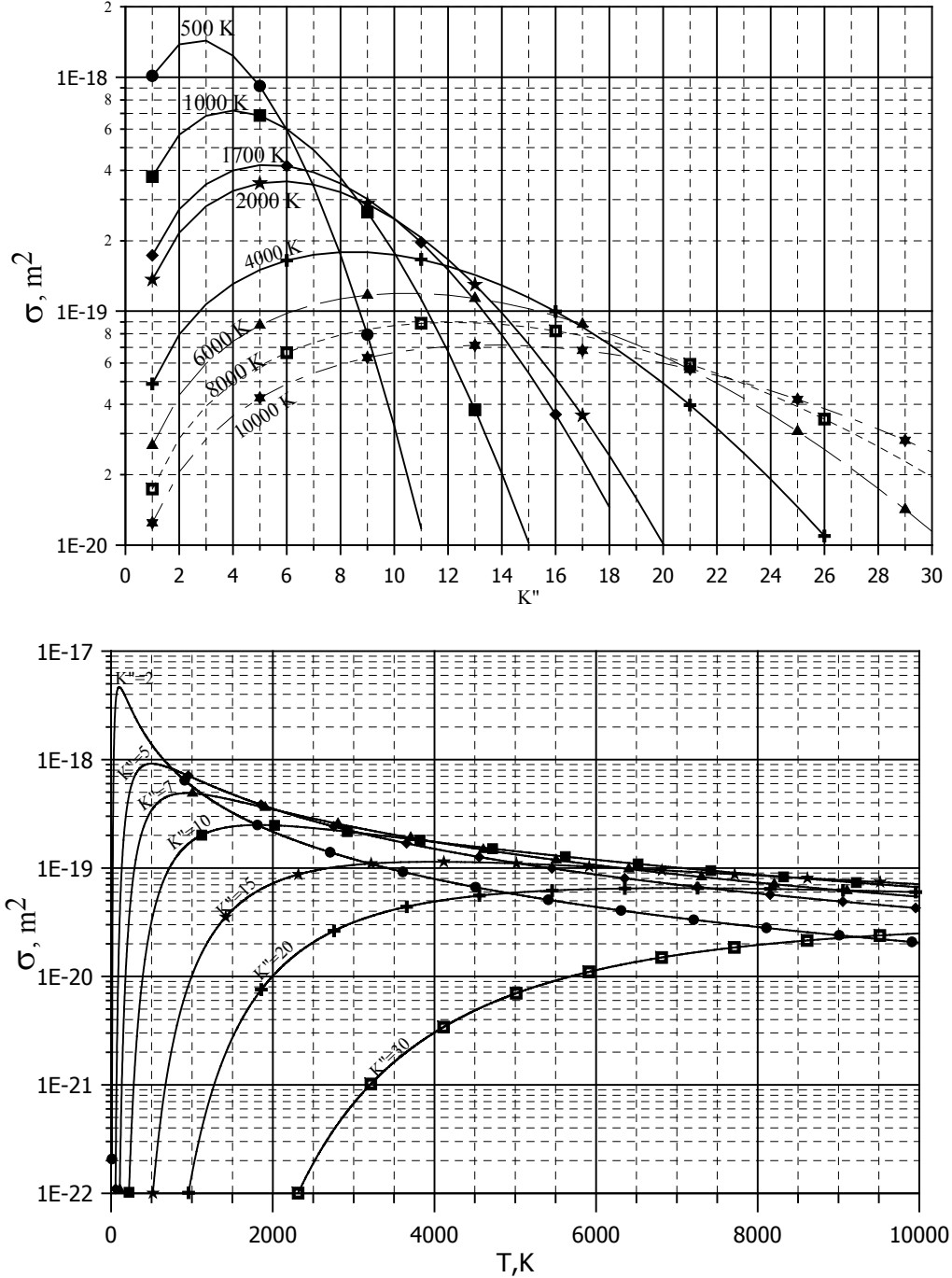


Figure 198. Absorption cross-section of the OH(X²Π) molecules in individual lines the (0,0) band for different temperatures $T_{tr}=T_{rot}$ and different rotational quantum numbers K'' .

Effective temperature of the OH(X) molecules produced in reaction (8.32) may be thousands of K and higher, due to considerable excess of the post-reaction energy. Evidently reasonable estimate for the effective cross-section would be $\sigma \approx 10^{-19} \text{ m}^2$. With this cross-section effect of the resonant scattering must be negligibly small along the axis. It will be even weaker in other plume flow regions, because maximum of the optical opacity should be expected along the axis. It should be noted, however, that Ref.¹⁴⁶ suggests to forms of the cross-section energy dependence for reaction (8.32). Alternative to the cross-section (9.13) energy dependence results in about 15 times bigger effective value of the cross-section. In compliance with expression (9.12) the OH(X) number density will be the same factor bigger if this another reactive cross-section is used. Attenuation of the radiation depends on the product of the number density and absorption cross-section. Hence, formally, increase of the number density on factor of 15 would be equivalent to increase of the cross-section in (9.14) on the same factor. This would make the resonant scattering effect a little stronger, but still not very important for the radiation modeling.

And final reason which could intensify the resonant scattering effect is higher fraction of the OH(X) molecules in the motor exhaust. Content of the OH(X) in the Shuttle PRCS motor exhaust $X_{OH} = 4.4 \cdot 10^{-3}$ has been estimated in Ref.³⁶. That big amount of effluent OH(X) might already compete with the second source production rate. There is no accurate data about amount of minor components like OH in the PME and ACS motor exhaust. However, it is known that ACS motor has an inner oxidizer-rich zone near the nozzle wall, which is not modeled by NARJ. So, it might have substantially higher content of the OH(X) in the exhaust. Figure 199 demonstrates how the 8xACS plume transparency would depend on the effective cross-section should the ACS motor exhaust have higher OH(X) content.

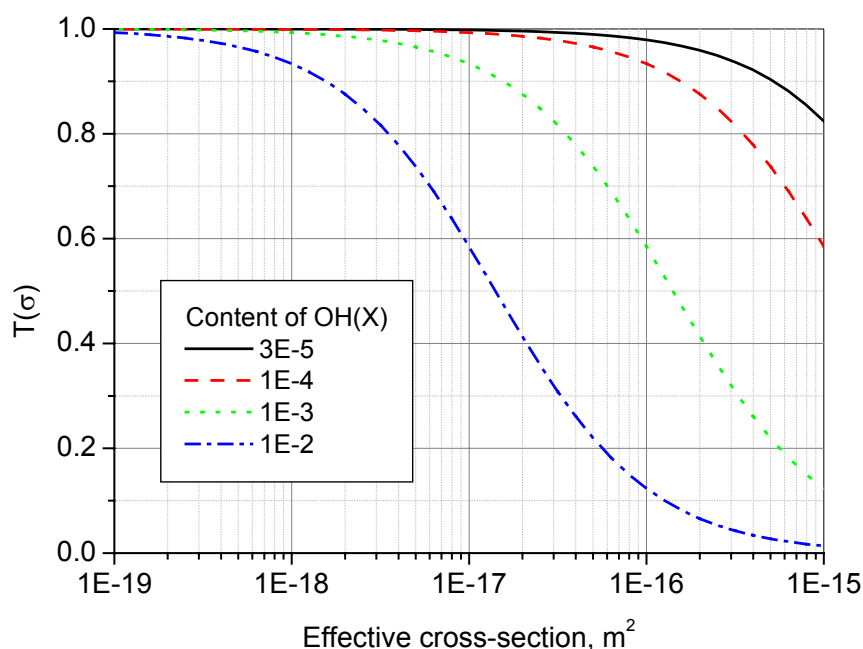


Figure 199. Transparency of the 8xACS motor plume flow along the axis depending on the absorption cross-section value at different contents of effluent OH(X).

Note, that absorption cross-section for the "cold" OH(X) molecules emanating from the motor may be substantially higher in comparison with "hot" OH(X) molecules produced in reaction (8.32). Figure 198 can't be used directly for evaluation of the cross-section, because in case of source 1 OH(X) molecules translational and rotational temperatures of emitting and absorbing molecules are very different. For rough estimates effective cross-section value $\sigma_s \sim 10^{-18} \text{ m}^2$ may be applied. With this cross-section the resonant scattering effect is still very weak even at high level of the OH(X) content in the motor exhaust. Perhaps only combination of increased OH(X) content in the plume with increased cross-section for the reaction (8.32) would raise the resonant scattering effect to noticeable level. Given approximate character of the analysis and uncertainty of the parameters involved, possibility to have the resonant scattering noticeable in the 8xACS motor plume flow can not be simply waved aside.

9.4.2. Evaluation of the effect of the unburned fuel droplets onto redistribution of the $OH(A \rightarrow X)$ radiation in the 8xACS plume flow

As discussed in the beginning of this Section, some unburned propellant may present in the motor exhaust in the form of droplets. One should expect much less amount of the droplets in the PME exhaust in comparison with the ACS motor one, because the PME was bigger and more efficient motor and because it didn't utilize any propellant injection contour for refrigerating its nozzle. Abundance of the droplets in the 8xACS motor set exhaust might influence the glow radiation measurements in 26 April 2000 experiment. There were two possible ways of the droplets effect onto the glow radiation intensity: i) the droplets might play a role of centers for heterogeneous condensation of water in the plume flow, reducing the water molecule number density and reaction (8.1) frequency and ii) the droplets might absorb and scatter the radiation causing its attenuation on the way to detector. Prior to evaluation of these two effects, let's briefly consider characteristics of the droplet flux in the plume flow.

Generally, droplet content, size distribution and optical properties in the plume flow are very specific features of a particular motor. Therefore, a parametric study of the droplet effect would make sense at the initial stage of the droplet effect study. First of all, reasonable margins for the parameters variation has to be specified. Extended material about the droplet properties in the exhausts of a number of commercial motors may be found in Ref.²⁴. Following conclusions may be inferred from analysis of this reference.

- ❑ Mass content of the droplets in motor exhaust is on the level of 1%. Perhaps for less efficient motors it may be at the level of a few percents.
- ❑ Size distribution of the droplets ranges from sub-micron to 10 micron dimensions. Typical distribution borrowed from Ref.²⁴ is shown in Figure 200. It should be noted, that content of the sub-micron droplets is not reproduced in this figure. Witness plate technique, which was utilized for determination of the particle size distribution didn't allow accurate determination of the amount of the sub-micron droplets.
- ❑ The droplet flux was found to be considerably narrower than gas effluent flux. The bigger was a droplet size the closer was the droplet trajectory to the axis. Angular distribution of the droplet trajectories in polar coordinate system appeared to be almost self-similar. Figure 200 illustrates this distribution depending on normalized angle. For big particles $\theta_0 \approx 5^\circ$, for smaller particles $\theta_0 \approx 10^\circ$. Distribution of the droplet number density along the motor axis (either along R coordinate in a polar system) was found to be well reproduced by a reverse square law.

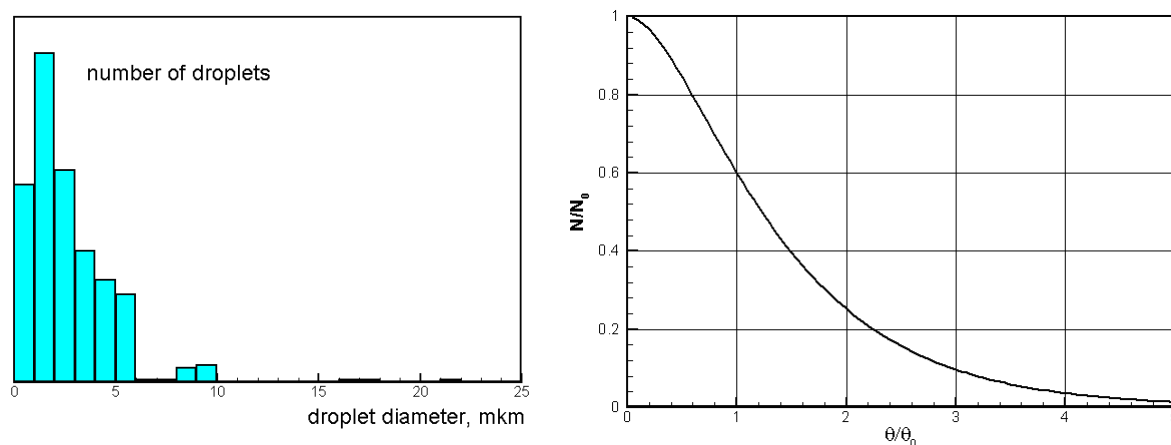


Figure 200. Typical droplet size distribution (left window) and normalized angular distribution of their trajectories.

9.4.2.1. Water condensation on unburned propellant droplets

Pressure and temperature color maps of the 8xACS plume flow near field are presented in Figure 201. The maps are given in xy' symmetry plane located between two closest motors (see Figure 178). Possible trajectories of droplets within $\pm 10^\circ$ angle are also shown in this figure.

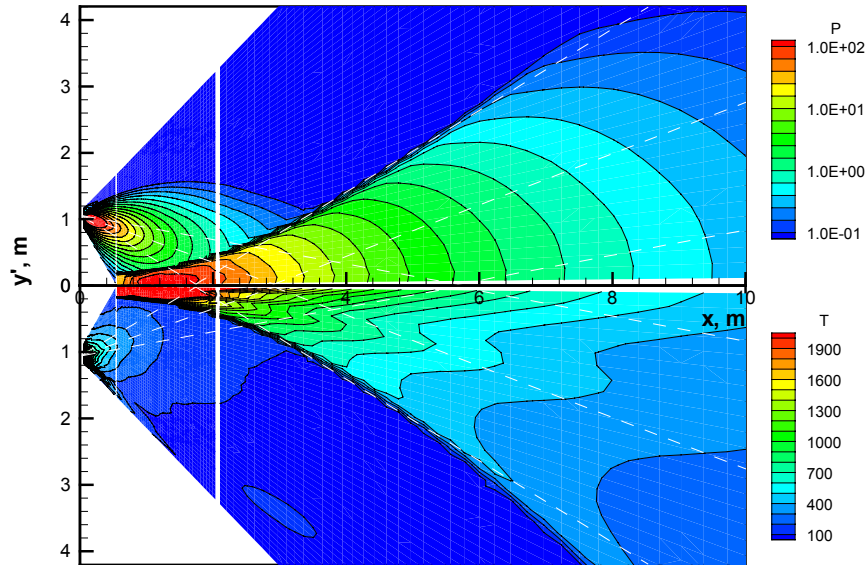


Figure 201. Maps of pressure (upper semi-plane) and temperature (lower semi-plane) in xy' (see Figure 178) symmetry plane of the 8xACS exhaust flow. Possible droplet trajectories are shown by dashed lines.

Water condensation on droplets may occur when water molecule collides the droplet surface. Frequency of these collisions is proportional to the water molecule number density and velocity component, which is normal to the droplet surface. The water molecule velocity includes two components, chaotic thermal velocity and directed gas flow velocity in the reference frame of the droplet. In these conditions, collisional frequency between the water molecules and droplets may be expressed as:

$$Z_{H_2O} = \frac{1}{4} N_{H_2O} (V_{rel} + V_{H_2O}), \quad V_{H_2O} = \sqrt{\frac{8kT}{\pi m_{H_2O}}} \quad (9.17)$$

where V_{H_2O} - is chaotic velocity V_{rel} - is directed velocity, m_{H_2O} - mass of the water molecule.

Looking at the droplet trajectories in Figure 201, one can see that central trajectories (along the axis of individual motor) cross the densest regions of the flow, where separate plumes effectively interact. Collisional frequency (9.17) is maximal here, indeed. Consideration of these trajectories for computation of the collision frequency would provide an upper estimate for the heterogeneous condensation effect. Table 26 exemplifies parameters of the plume flow in some selected points along centerline of an individual motor. Collision frequency between water molecules and unburned propellant droplets is presented in the last column in the table. Also, the collision frequency is plotted in Figure 202.

Table 26. Parameters of the flow along centerline of an individual motor and collisional frequency between water molecules and propellant droplets.

x, m	P, Pa	T, K	$u_x, m/s$	$u_{y'}, m/s$	$N_{H_2O}, 1/m^3$	$V_{H_2O}, m/s$	$V_{rel}, m/s$	$Z_{H_2O}, 1/m^2s$
2.0	54.8	1310	2390	376	8.88×10^{20}	1241	1466	6.01×10^{23}
2.5	42.6	1530	2260	103	5.91×10^{20}	1341	1260	3.84×10^{23}
3.0	23.4	1650	2180	-30	3.01×10^{20}	1393	1183	1.94×10^{23}
3.5	13.1	1050	2550	-187	2.65×10^{20}	1111	881	1.32×10^{23}
4.0	7.74	780	2690	-402	2.11×10^{20}	958	637	8.41×10^{22}
5.0	3.11	650	2720	-638	1.02×10^{20}	874	400	3.25×10^{22}
6.0	1.41	510	2760	-775	5.87×10^{19}	775	258	1.52×10^{22}
8.0	0.44	360	2800	-919	2.60×10^{19}	650	109	4.93×10^{21}
10.	0.19	280	2810	-990	1.44×10^{19}	574	37	2.20×10^{21}

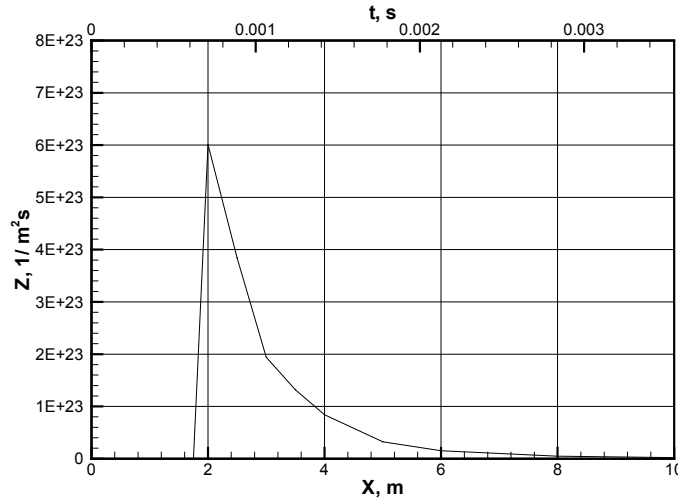


Figure 202. Collision frequency of the water molecules with propellant droplets along the axis of an individual motor. Top axis represents the time of the droplet motion.

Evidently, the collision frequency is maximal within 2-6 meters from the motor, falling down abruptly further downstream. So, there is no reason to consider the water condensation farther than in the near field.

Assume that each collision of the water molecule results in its attachment to the particle. Under this considerably overpredicted assumption increase of a particle radius r caused by the water condensation may be expressed as:

$$\Delta r = \frac{m_{H_2O}}{\rho_{H_2O}} \int_0^{\infty} Z_{H_2O} dt \quad (9.18)$$

doesn't matter whatever the droplet radius is (m_{H_2O} - mass of the water molecule, ρ_{H_2O} - water density). The only requirement is that it must be big in comparison with the surplus: $r \gg \Delta r$. Integration of the collisional frequency over the time along the droplet trajectory results in $\Delta r \approx 7.5 \cdot 10^{-3}$ micrometers. Apparently influence of the water condensation onto the motion of even small droplets of 0.1-1 μm size is almost imperceptible. From the other hand, the droplets can pick up extremely small amount of water from the plume flow. According to the afore-cited analysis mass of the condensed water should be much smaller than mass of droplets and yet more smaller than mass of non-condensed water at any point of the flow.

Note, that situation may substantially change if very small size ($r \sim 0.01 \mu m$) is assumed for the majority of the droplets. In this case the droplet radius increase will be comparable with its size and total mass of the condensed water may exceed the total mass of the droplets. However, this situation doesn't look natural. Hundred percent sticking coefficient adopted in the model above is unrealistic even for moderate temperatures, not speaking about the $T \sim 1000 K^\circ$ in the considered flow region. Moreover, the high temperature particles may heat the droplet causing its evaporation. So, summarizing this part of the study, one may conclude, that heterogeneous condensation of water on the unburned propellant droplets most probably can't effect the glow radiation.

9.4.2.2. Attenuation of the radiation by the droplets

Attenuation of the UV radiation in the plume flow may be characterized by the ratio of intensity of the radiation, which was absorbed and scattered by the plume flow, to the initial radiation intensity:

$$\frac{\Delta I}{I} = 1 - e^{-\tau_a}, \quad \tau_a = \sigma_{ext} \int_{X_0}^L n_d(x) dx \quad (9.19)$$

where n_d - number density of the droplets, σ_{ext} - the extinction cross-section, X_0 and L integration limits. Apparently, attenuation should be maximal along the flow axis, where optical thickness τ_a is maximal. As discussed in previous paragraph a reverse square law may approximate the droplet number density along the axis. Assuming conical character of the droplet flow and conservation of the total droplet flux, number density in (9.19) may readily be integrated along the axis:

$$\tau_a = \sigma_{ext} \int_{X_0}^L \frac{N_r}{tg^2 \theta \cdot x^2} dx = \frac{\sigma_{ext} N_r}{tg^2 \theta \cdot X_0} \quad (9.20)$$

where θ - is the droplet flow divergence half-angle and N_r - total flux of the droplets, which may be easily calculated if the droplet size and mass flow rate are specified. For simplicity all droplets are assumed having the same size in this analysis.

Given very long distance between the “Progress” and “Mir” station in 26 April 2000 experiment upper limit in integral (9.20) was set to infinity. For estimates $X_0=200$ m was chosen, because number of emitters decreases abruptly further upstream (see Figure 184).

Extinction cross-sections in formula (9.20) were modeled with the use of Mie theory. Complex refraction index of the droplet material $m=n+i\kappa$ had to be specified for this modeling. As soon as no data were available about optical properties of the droplets in the plume flow, the cross-section was modeled with different values of real and imaginary parts of the refraction index. Radiation wavelength was set to be 310 nm.

Attenuation of the glow radiation by the droplets in condition of 26 April 2000 experiment is plotted in Figure 203 depending on the droplet radius. Mass fraction of the droplets in the flow 1% and divergence half-angle of the droplet flow 5° were specified for this particular analysis. Two different cases have been considered: i) transparent particle, which has imaginary part of the refractive index $\kappa=1.6 \cdot 10^{-8}$ (kind of water) and ii) opaque particle, which has imaginary part of the refractive index $\kappa=1.6$ (kind of soot). Real part of the refractive index was set at $n=1.349$, like in water.

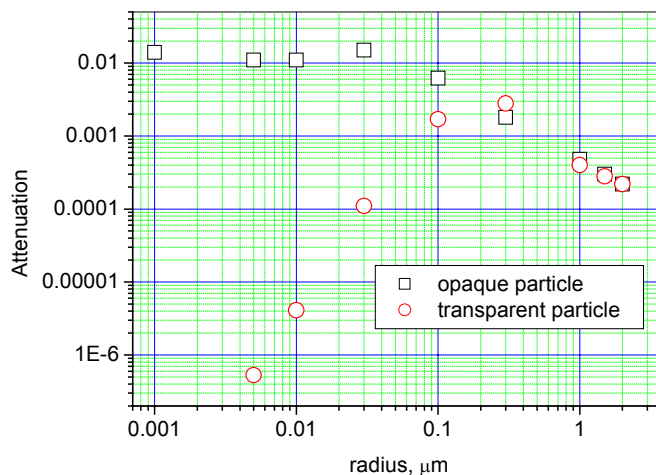


Figure 203. Attenuation of the glow radiation by droplets in condition of 26 April 2000 experiment.

One can conclude from the figure, that even at the small divergence angle clean particles can't noticeably attenuate the radiation along the flow axis. Only small opaque particles have a chance to reduce the plume flow transparency, so the clean particles were not considered further.

To make the attenuation effect more pronounced, the droplet mass flow rate was increased in subsequent analysis at the level of 10% from total mass flow rate. Figure 204 illustrates how the attenuation by the opaque particle flow depends on the real part of the refractive index. And finally, Figure 205 illustrates dependence of the attenuation on the divergency of the droplet flux. Computation results for some selected radii are presented in these figures.

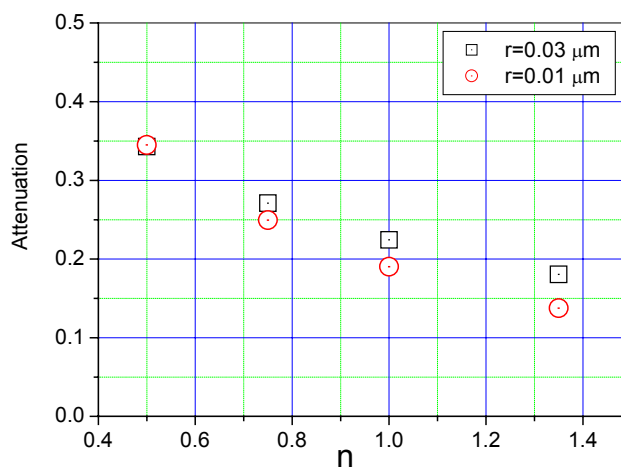


Figure 204. Dependence of the attenuation on the real part of the complex refractive index. Imaginary part was set as $k=1.6$ (opaque particles).

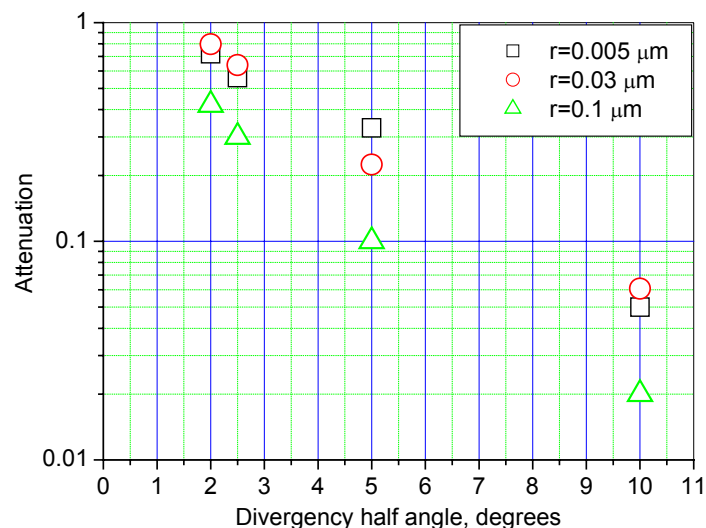


Figure 205. Dependence of the radiation attenuation by the droplet flow in dependence on the flow divergency. Complex refractive index was set as $m=1.0+1.6i$.

Summarizing the analysis one may say that noticeable attenuation of the radiation in the 8xACS plume flow might be ensured in 26 April 2000 experiment only if considerable portion of droplets (some percents of total mass flow) had very small sizes (0.01-0.03 μm), were opaque (like a soot) and flew within a very small divergence angle (less than $\pm 5^\circ$). These requirements look rather contradictory. All predictions show that small particles (if they have happened to be found in the plume!) must follow the gas flow, which has much bigger divergence angle. Also, that high absorptive index looks too extreme for the unburned propellant. Therefore, most probably the droplets couldn't attenuate the plume glow radiation in condition of 26 April 2000 experiment.

9.5. Comparison of the improved glow radiation model predictions with results of 26 April 2000 experiment.

In this section the baseline glow model modifications are considered, which allow better fit to 26 April 2000 experimental data. As mentioned above, principal problem of the baseline model was that it can't explain wide glow radiation profile observed in the 26 April 2000 experiment (see Section 8.8). As analysis in previous section shows, substantial improvement in this direction may be achieved by inclusion of the two-step reaction (9.3) into the model. Note, that two-step process (9.3) might occur in the PME flow as well. Generally, it may be modeled in the PME plume flow condition by either DSMC or CMC method. Accurate modeling of the PME flow was not assumed within the frame of this Project. However, simple estimates based on the similarity of the flows in two experiments showed that two-step process (9.3) could not seriously change shape of the radiation profile in 28 February experiment, but it could contribute about 20-30% into total OH(A \rightarrow X) radiation intensity measured by the imager. So, the radiation output from the two-step reaction may be considered as additional source to the primary single-step reaction. As discussed in Section 8.5, the primary reaction cross-section in the baseline model must be corrected to account for the presence of additional radiation sources in February 28, 1999 experiment. So, the cross-section correction factor has been reduced on 25% and become $k_\sigma=0.06$. Figure 206 illustrates how the modeled radiation profile changes with inclusion of process (9.3) into the baseline model. Share of the OH(X) radiation in 26 April 2000 experiment was assumed 65% in this modeling. Amount of energy E_{in} , which passed to water molecule at the first collision, has been chosen $E_{in}=0.86$ eV to provide the best fit to the experimental data in the off-axis regions.

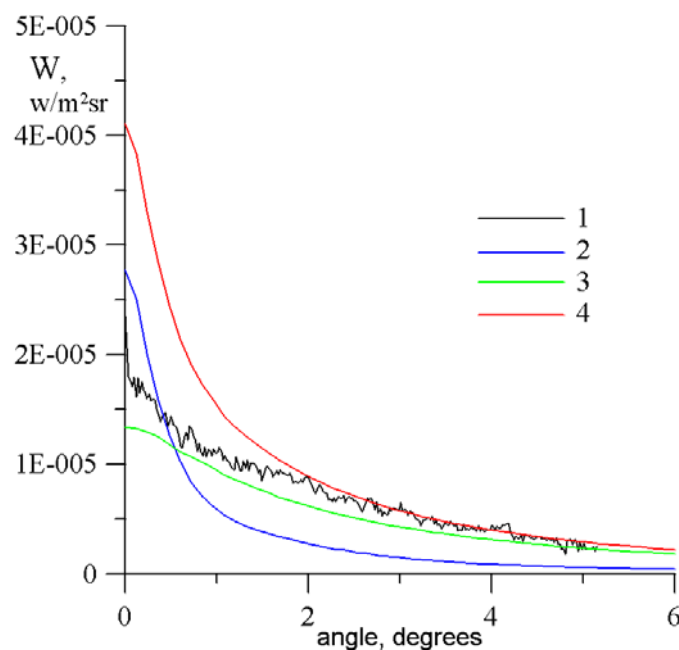


Figure 206. Spatial distribution of the radiation predicted by the baseline model complemented by two-step reaction (9.3) between water and oxygen, $E_{in}=0.86$ eV, 1 - experiment, 2 - baseline model prediction with improved coefficient $k_o=0.06$, 3 - two-step reaction prediction, 4 - sum of 2 and 3.

Apparently, agreement between modeling and experiment has become much better in the wings of the radiation profile, but not better in the center. Departure of the modeled curve from experiment at the axis may be partially reduced if bigger share of the $\text{OH}(\text{A} \rightarrow \text{X})$ radiation is assumed in the April 26, 2000 experiment. This case is illustrated in Figure 207.

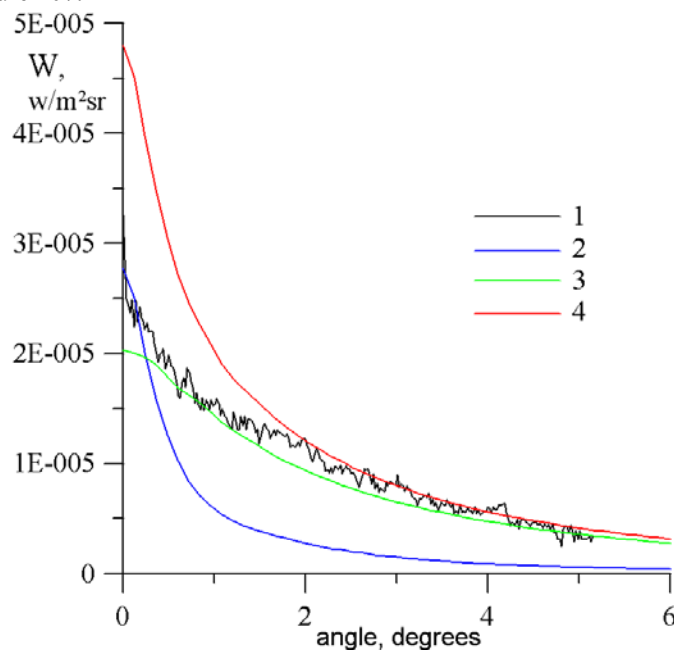


Figure 207. Spatial distribution of the radiation predicted by the baseline model complemented by two-step reaction (9.3) between water and oxygen, $E_{in}=1.3$ eV, 1 - experiment, 2 - baseline model prediction with improved coefficient $k_o=0.06$, 3 - two-step reaction prediction, 4 - sum of 2 and 3.

Agreement between the curves became just a little better, despite that $\text{OH}(\text{A} \rightarrow \text{X})$ radiation share has been set above the upper margin specified in Figure 32.

Allowing for attenuation of the radiation in the 26 April 2000 plume flow would further improve agreement at the centerline. However, as analysis in previous section shows, serious improvement should not be expected even at very extreme assumptions about the plume flow attenuation properties.

Radical improvement of the agreement between modeled and measured radiation intensity along the plume flow axis in 26 April 2000 experiment may be achieved if smaller share of the OH(A→X) radiation is assumed in February 28, 1999 experiment. This has already been illustrated above in Figure 195. Actually, uncertainty of the spectral composition of the imager signal and analysis of the O₂(A→X) potential contribution in Subsection 9.3.2 allow to hypothesize 30% shares for both NH(A→X) and O₂(A→X) emissions in February 28, 1999 experiment. With this assumption overprediction along the centerline will be about 50% from measured intensity.

And finally, accounting for the variation of the imager calibration factor in February 28, 1999 (see Section 8.5) may almost eliminate the discrepancy. The glow radiation profile modeled in the frames of the modified model, which has been complemented by all discussed corrections, is compared with experiment in Figure 208. Share of the OH(A→X) radiation in 26 April 2000 experiment was assumed 65% in this modeling.

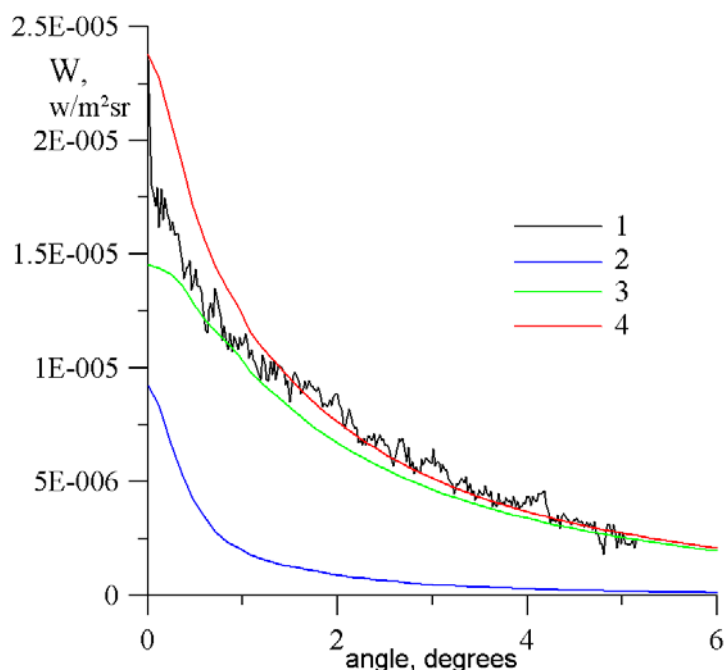


Figure 208. Spatial distribution of the radiation predicted by the baseline model complemented by two-step reaction (9.3) between water and oxygen, $E_{in}=0.93$ eV, 1 - experiment, 2 - baseline model prediction with improved coefficient $k_{\sigma}=0.04$, 3 - two-step reaction prediction, 4 - sum of 2 and 3.

Given approximate character of the modeling agreement between modeled and experimental curves in Figure 208 should be considered as very good.

9.6. Concluding remarks on the glow radiation modeling

Cross-comparison of the Progress/Soyuz plume glow modeling results with experimental data obtained in two sets of the experiments (see Sections 8.5, 8.8 and 9.5) may be concluded as follows.

Baseline model of the plume glow, which includes only sole reaction (8.1) between water and oxygen, can predict results of February 28, 1999 experiments with a good accuracy. The baseline model works well within the plume region where the flow has not yet experienced noticeable scattering in the atmosphere. This region extended to about 12-15 km downstream from the space vehicle in February 28, 1999 and to about 2-3 km in April 26, 2000 experiment. Outside this region the baseline model provides much poorer agreement with experimental data (factor of 2-3). Given substantially different types of the flow fields and observation conditions in the two complex space experiments, even this poor accuracy may be considered as satisfactory. For more accurate modeling of the glow radiation in the region where the plume flow mixes with atmosphere improvement of the baseline model is necessary.

Complementing of the baseline model by additional processes noticeably improves the model predictions. Among the new processes, two-step reaction (9.3) between water and oxygen is a principal one. This reaction should be not too important in the undisturbed plume flow region, where single collision processes dominate. However, farther from the space vehicle, where two- and multi-step processes develop, the two-step (multi-step) reaction mechanism (9.3) may compete and eventually substitute the single-step one.

Some other reactions did contribute to the imager's signal in both sets of the experiments. Primarily that were reactions producing NH(A→X) radiation and, possibly, reaction (9.6) between carbon dioxide and atmospheric oxygen, producing O₂ Herzberg band radiation. Other processes were most probably unable to

seriously affect to the measured radiation in both experiments. Attenuation of the radiation in the plume flow might have a chance to become a sole exclusion. Effect of this process depends on the content of minor plume components (unburned fuel droplets and OH molecules), which can't be predicted at this moment. However, even very brave, extreme suppositions about this content result in not more than 10% attenuation.

The modified model substantially reduces discrepancy between the model predictions and 26 April 2000 experiment data. It also, corrects margins for the effective elastic and reaction cross-sections derived from the earlier experiment. The effective elastic cross-sections $\sigma_{e,eff} = 9.0 \pm 1.5 \text{ \AA}^2$ may be suggested for verification of contemporary collisional models. From this prospective, elastic collision models based on consideration of intermolecular potentials (see Subsection 8.3.1) may be utilized in simulations of the hypervelocity collisions, since they result in the effective cross-sections comparable with those derived from discussed experiments. Utilization of conventional VHS model parameters would be not relevant for hypervelocity conditions, because in this case effective elastic cross-section value will be 1.5-2 times bigger than value derived from the experiments. New parameters (namely VHS power law exponent), which yield the true effective cross-section value, have been suggested in Ref.²². With those parameters the VHS model should also result in successful predictions of the collisional phenomena at hypervelocity conditions.

The glow observation experiments render an opportunity for verification of the reaction (8.1) cross-section value. Any reaction model must result in the effective cross-section $\sigma_{r,eff} \leq 0.6 \pm 0.2 \cdot 10^{-18} \text{ cm}^2$ in the condition of February 28, 1999 experiment and $\sigma_{r,eff} \leq 0.5 \pm 0.17 \cdot 10^{-18} \text{ cm}^2$ in the condition of April 26, 2000 experiment. Note, that different values of the effective cross-sections do not imply any inconsistency between the two experimental data sets. The difference is caused by different experimental conditions, which result in not equal effective cross-section values in accordance with relation (8.21). Inability to set up a lower limit for the reaction (8.1) cross-section is not caused by the glow model shortcomings. It results from uncertainty of the spectral composition of the glow radiation measured by the imager in February 28, 1999 experiment and uncertainty of share of the multi-step reactions like (9.3) in production of the OH(A \rightarrow X) radiation. Problem with the reaction cross-section lower limit will be overcome as soon as the aforementioned uncertainties are eliminated. At this moment suggested upper limits for the effective cross-sections may be considered as a total effective cross-sections, which include both single and multi step reactions.

Analysis of the glow intensity shows that reaction cross-sections in the form (8.33) and (8.34) must be corrected. Easiest way to make this correction is introduction of the correction factor k_σ for σ_0 . This factor should be $k_\sigma \leq 0.06 \pm 0.02$ for the cross-section (8.33) and $k_\sigma \leq 0.023 \pm 0.008$ for cross-section (8.34). However, experimental data do not prohibit variation of other parameters like the power law exponent instead of the σ_0 . Those models, which have a parameter controlling contribution of internal energy into the reaction, may adjust it as well. For instance, similarly to (8.33) and (8.34) models, the TCE model substantially overpredicts effective reaction cross-section when the model parameters are derived from the ground-state reaction rate constant and no contribution of the internal degrees of freedom is allowed. However, allowing for this contribution would reduce the TCE effective cross-section on more than one order of magnitude¹⁶³, bringing it to closer agreement with the experiments.

The question on what particular parameter has to be adjusted in one or another cross-section model can't be answered within the scope of this study. Further research is necessary to elucidate this problem. In particular, the PME and ACS plume glow spectra measured with high resolution and high signal to noise ratio would help to shrink the uncertainty margins for effective reaction cross-section, and address other reactions. Glow imagers and spectra obtained at various directions of the plume flow axis (not only retro firing) would provide an experimental material for consideration of the reaction cross-section energy dependence. For analysis of the single-step reactions like (8.1), the data acquired from the undisturbed plume flow zone are preferable. Analysis of the glow radiation from the extended zone, where the plume flow effectively mixes with atmosphere, should start from detailed consideration of the translational-internal-chemical energy exchange process at the hypervelocity conditions followed by accurate DSMC modeling of the multiple collisional processes in the mixing zone. And finally, other emitting plume glow species have to be addressed. Extension of the research beyond the OH and NH molecular band consideration would allow deeper insight into generic problems related to the hypervelocity reactive collisions.

Appendix

Intensity of a XeI emission is given by formula (3.33) in paragraph 3.2.2.1. The formula is reproduced below for convenience:

$$J_\nu = \frac{h\nu_{ij}}{4\pi} N_0 N_e \left(R_{ve0} + \frac{N_m}{N_0} R_{vem} + \alpha \cdot R_{v1} + \frac{1-\alpha}{2} R_{v2} \right) \quad (10.1)$$

where R_{ve0} - the electron/ground state atom collision excitation rate coefficient; R_{vem} - electron/ metastable atom collision excitation rate coefficient; R_{v1} - first ion/atom collision excitation rate coefficient; R_{v2} - second ion/atom collision excitation rate coefficient.

The formula includes a term with ratio of metastable atoms to the neutral xenon atoms in the ground state. In many cases of practical interest this term may bring substantial contribution to the total radiation power. So, a problem arises to evaluate the metastable to ground state atom number density in typical conditions of a HET operation.

Evaluation of the metastable atom content may be carried through the balance equation. In this equation collisions of neutral atoms in the ground state with electrons and heavy particles provide a source for the metastable states excitation. The metastable state population loss is controlled by collisions and drift of the metastable atoms out from the plasma region. Under these assumptions, the balance equation for particular metastable state takes a form:

$$N_0 \left(N_e R_{eM} + \sum_q N_q R_{qM} \right) = N_m (\nu_{dm} + \nu_{dexm}) \quad (10.2)$$

Here R_{eM} - rate coefficient for excitation of the metastable level by electron impact, R_{qM} - rate coefficient for excitation of metastable level in a collision with first ($q=1$) and second ($q=2$) ion, ν_{dm} - frequency of the metastable atoms loss due to diffusion, ν_{dexm} - frequency of the metastable atom loss due to collisions, N_0 - number density of the neutral xenon atom in the ground state and N_m - number density of the considered metastable states. Below computation is being made for XeI $5p^56s(3/2)_2$ ($1s^5$ in Paschen notation) state for the sake of unambiguity. Evaluation of the $1s^3$ state content may be done similarly.

Excitation of the metastable states in xenon goes predominantly through cascade transitions⁶⁴. This is not surprising, because many of intensive XeI emissions stemming from $5p^56p(p')$ levels end at the metastable levels. Therefore, the source term of expression (10.2) may be presented as the sum of respective emission excitation rates:

$$N_0 \left(N_e R_{eM} + \sum_q N_q R_{qM} \right) = N_0 N_e \sum_\nu \left(R_{ve0} + \alpha R_{v1} + \frac{1-\alpha}{2} R_{v2} \right) \quad (10.3),$$

where relative content of the first ion $\alpha = \frac{N_1}{N_e}$ has been introduced and charge neutrality equation $N_e = N_1 + 2N_2$

has been utilized. Summation in the right side of equation (10.3) has to be done over all emissions that end on the considered metastable state. Actually the sum may be limited only by components related with cascades from five $5p^56p[J=1,1,2,2,3]$ states. These cascades are most intensive in the HET spectrum, prevailing substantially over others. In this case the sum may be readily modeled as the function of T_e and α , basing on the excitation rates discussed in Section 3.2.2. Accuracy of the total rate coefficient evaluation will be better if the excitation rate coefficients are represented in some relative units, say in terms of function $K^{823}(T_e, \alpha)$, which represents ratio of the total excitation rate of the $1s^5$ state to the excitation rate through XeI 823.16 emission ($2p^6 \rightarrow 1s^5$ transition):

$$K^{823}(T_e, \alpha) = \frac{\sum_\nu \left(R_{ve0} + \alpha R_{v1} + \frac{1-\alpha}{2} R_{v2} \right)}{R_{e0}^{823} + \alpha R_1^{823} + \frac{1-\alpha}{2} R_2^{823}} \quad (10.4)$$

where 823 superscript indicates that total excitation rate coefficient of the metastable level is rationed to the excitation rate coefficient of XeI 823.16 nm emission line. Actually, the $2p^6 \rightarrow 1s^5$ transition has been chosen for normalization of the excitation rate quite arbitrarily. Any other allowed XeI $5p^56p \rightarrow 5p^56s(3/2)_2$ transition excitation rate coefficient may be utilized for the normalization. In practice, that transition should be employed, which intensity is going to be modeled afterwards through relation (10.1).

In general case the $K^{823}(T_e, \alpha)$ function depends on electron temperature and relative content of the first ion. This dependence is plotted in Figure 209. Evidently, variation of the $K^{823}(T_e, \alpha)$ is relatively small even in the wide range of T_e and α , that minimizes potential errors associated with uncertainty of these parameters.

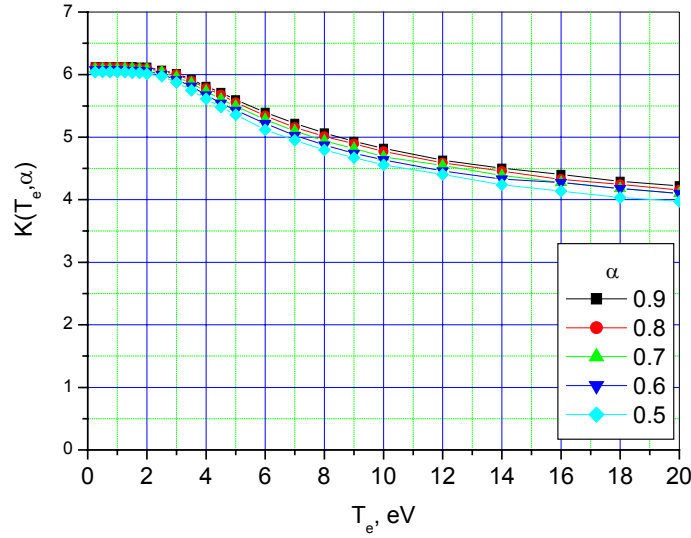


Figure 209. Temperature dependence of the total rate coefficient for excitation of xenon $5p^5 6s[J=2]$ metastable state out from the ground state at different value of α .

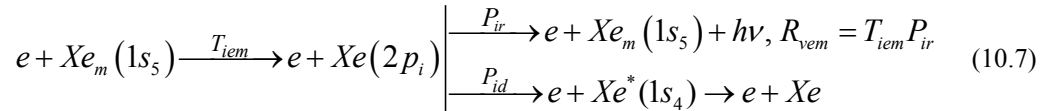
In terms of the $K^{823}(T_e, \alpha)$ function the metastable excitation rate may be expressed as:

$$N_0 \left(N_e R_{eM} + \sum_q N_q R_{qM} \right) = N_0 N_e \left(R_{e0}^{823} + \alpha R_{i1}^{823} + \frac{1-\alpha}{2} R_{i2}^{823} \right) \cdot K^{823}(T_e, \alpha) \quad (10.5)$$

Collisional de-excitation of the metastable states is enforced by electrons mainly. Atomic collision quenching rate coefficients are not sufficiently big^{68,164} to make the atomic collision quenching competitive with the electron one. In turn, among the electron collisions inelastic collisions transferring the metastable atom to an upper $5p^5 6p(p')$ levels dominate over superelastic collisions if the electron temperature is not too low⁶⁸. Given also that rate coefficients for transitions between optically coupled levels are much higher than the rate coefficients for non-coupled levels (see Figure 39), the collisional de-excitation rate ν_{dexm} in equation (10.2) may be represented as a sum of de-excitation rates corresponding to five $5p^5 6s(3/2)_2 \rightarrow 5p^5 6p[J=1,1,2,2,3]$ transitions. These de-excitation rate coefficients, in turn, may be unambiguously coupled to the respective transition rate coefficients T_{iem} (Figure 39) and the excitation rate coefficients R_{vem} , which are involved into expression (10.1):

$$\nu_{dexm} = N_e \sum_i P_{id} T_{iem} = N_e \sum_v k_v R_{vem} \quad (10.6)$$

Coefficients P_{id} and k_v in relation (10.6) reflect the fact that collisional transitions $5p^5 6s(3/2)_2 \rightarrow 5p^5 6p[J=1,1,2,2,3]$ not necessarily result in depopulation of the $1s_5$ metastable state. Within the frames of adopted in Section 3 CRM, excited xenon atom may either return back to the $5p^5 6s(3/2)_2$ metastable state (releasing respective emission of frequency ν) or relax through $5p^5 6s(3/2)_1$ resonant state down to the ground state. Evidently, the first pathway is described by the R_{vem} rate coefficient and can't be considered as a de-excitation process, whereas the latter one is real de-excitation. Following scheme may represent the branching process:



Branching coefficients for P_{ir} and P_{id} are controlled by respective transition probabilities, which are atomic constants independent on plasma characteristics. Evidently that for transitions from $2p_5$ - $2p_{10}$ levels $P_{ir} + P_{id} = 1$ and, therefore:

$$k_v R_{vem} = P_{id} T_{iem} = R_{vem} \frac{P_{id}}{P_{ir}}, \quad k_v = \frac{P_{id}}{P_{ir}} \quad (10.8)$$

In general formulation, cross-sections for transitions $5p^5 6s(3/2)_2 \rightarrow 5p^5 6p[J=1,1,2,2,3]$ must slightly differ by the excitation threshold, having almost similar energy dependence form. That implies energy

dependence curves of the emission excitation rate coefficients R_{vem} must be the similar to each other already at temperatures $T_e \geq E_{th} \approx 1.5-2$ eV. Principal difference between the cross-sections and excitation rates should be in their absolute value, which must be proportional to the degeneracy $2J+1$ of particular level (J is total angular momentum). Taking this reasoning into account, the de-excitation rate may be readily estimated. Again, accuracy of this estimate may be considerably increased if the total rate ν_{dexm} is normalized to the rate coefficient R_{em}^{823} related to the same transition as before ($1s^5 \rightarrow 2p^6$).

$$\nu_{dexm} = N_e \sum_v R_{vem} = R_{em}^{823} \sum_v k_v \frac{2J_v + 1}{2J_{823} + 1} \quad (10.9)$$

where J_v is total angular moment of the upper state of the transition responsible for emission line with frequency ν . Coefficients k_v for the five upper levels involved in the sum can be determined directly from experiment: that is luminescent spectra obtained in AFRL beam experiments^{12,13} and HET spectra available in TSNIIMASH. It is simply related with the ratio of intensities of respective emissions:

$$k_v = \frac{P_{id}}{P_{ir}} = \frac{J_{v(2p_i \rightarrow 1s_5)} \cdot \lambda_{(2p_i \rightarrow 1s_4)}}{J_{v(2p_i \rightarrow 1s_5)} \cdot \lambda_{(2p_i \rightarrow 1s_4)}}$$

Table 27 illustrates results of computation of different parameters involved in formula (10.9).

Table 27.

Upper level/Parameter	2p ₆	2p ₇	2p ₈	2p ₉	2p ₁₀
$2J_v + 1$	5	3	7	5	3
k_v	0.33	10	0	2	0.054
$k_v \frac{2J_v + 1}{2J_{823} + 1}$	0.33	6	0	2	0.032

Introduction of the data from Table 27 into equation (10.9) results in:

$$\nu_{dexm} = N_e \sum_v R_{vem} = R_{em}^{823} \sum_v k_v \frac{2J_v + 1}{2J_{823} + 1} = 8.36 R_{em}^{823} \quad (10.10)$$

And finally diffusion losses may be estimated as ratio of the metastable atom thermal velocity u_m to the characteristic scale of space occupied by the plasma L :

$$\nu_{dm} = \frac{u_m}{L} \quad (10.11)$$

Introduction of expressions (10.5), (10.10) and (10.11) into equation (10.2) results in (after trivial algebraic manipulations):

$$\frac{N_m}{N_0} = \frac{N_e \left(R_{e0}^{823} + \alpha R_1^{823} + \frac{1-\alpha}{2} R_2^{823} \right) \cdot K^{823}(T_e, \alpha)}{\frac{u_m}{L} + 8.36 N_e R_{em}^{823}} \quad (10.12)$$

It should be once again noted that choice of reference emission (XeI 823.16 nm) was quite arbitrary. By no way it may influence the estimate result, which has to be the same at any choice of the reference emission.

Ratio (10.12) is plotted in Figure 210 versus electron number density. The figure provides an impression on what is the range of the metastable atom relative content variation in HET plasma. More detailed analysis of relation (10.12) suggests two important conclusions:

- ❑ Relative content of the metastable atoms in the discharge is order of 0.1%. It grows downstream in the plume. Perhaps in some regions of the plume flow, where electron temperature is low $T_e < 1.5$ eV and number density is still not very small $N_e > 10^9$ cm⁻³, the metastable atom content may be higher, not exceeding one percent most likely. At smaller electron number densities it becomes lower again.
- ❑ In wide range of HET plasma parameters variation diffusion term in the metastable balance equation holds much smaller than collisional de-excitation one. This is seen from asymptotical behavior of the curves in Figure 210. At $N_e > 10^{11}$ cm⁻³ in the discharge and $N_e > 10^{10}$ cm⁻³ in the plume diffusion term in the denominator of the right side ratio in (10.12) may be neglected and the expression for metastable atoms relative content becomes independent on the electron number density.

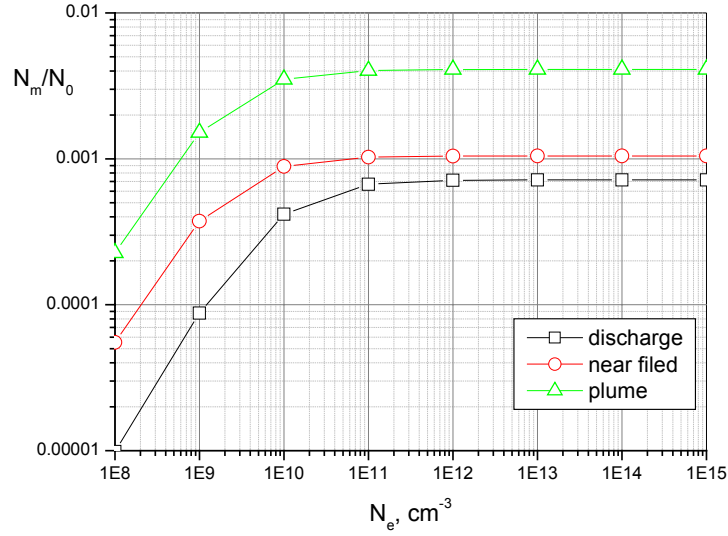


Figure 210. Dependence of relative content of the metastable atoms on the electron number density at typical conditions of a HET plasma.

In case when the second condition takes place formula for relative content of the metastable atoms becomes simpler:

$$\frac{N_m}{N_0} = \frac{\left(R_{e0}^{823} + \alpha R_1^{823} + \frac{1-\alpha}{2} R_2^{823} \right) \cdot K^{823}(T_e, \alpha)}{8.36 R_{em}^{823}} \quad (10.13)$$

Introduction of this ratio into expression (10.1) provides an easy way to reduce the emission intensity value:

$$J_v = \frac{h\nu_{ij}}{4\pi} N_0 N_e \left(R_{e0}^{823} + \alpha R_1^{823} + \frac{1-\alpha}{2} R_2^{823} \right) \left(\frac{R_{ve0} + \alpha \cdot R_{v1} + \frac{1-\alpha}{2} R_{v2}}{R_{e0}^{823} + \alpha R_1^{823} + \frac{1-\alpha}{2} R_2^{823}} + \frac{R_{vem}}{R_{em}^{823}} \cdot \frac{K^{823}(T_e, \alpha)}{8.36} \right) \quad (10.14)$$

Relation (10.14) explains the choice of reference emission in expressions (10.4) and (10.9). Indeed, in particular case of the XeI 823.16 nm line intensity modeling, relation (10.14) is reduced to the form, which is very convenient for practical applications:

$$J_{823} = \frac{h\nu_{823}}{4\pi} N_0 N_e \left(R_{e0}^{823} + \alpha R_1^{823} + \frac{1-\alpha}{2} R_2^{823} \right) \left(1 + \frac{k(T_e, \alpha)}{8.36} \right) \quad (10.15)$$

References

- ¹ Viereck, R. A., Murad, E., Knecht, D. J., Pike, C. P., Bernstein, L. S., Elgin, J. B., and Broadfoot, A. L., "The Interaction of the Atmosphere with the Space Shuttle Thruster Plume: The $\text{NH}(\text{A} \rightarrow \text{X})$ 336-nm Emission." *J. Geophys. Res.*, Vol. 101, 1996, p. 5371.
- ² Karabadzhak, G. F., Plastinin, Yu.A., Khmelinin, B.A., Teslenko, V.P., Shvets, N., Drakes, J. A., Swann, D. G., and McGregor, W. K., "Experimentation Using the Mir Station as a Space Laboratory," AIAA Paper 98-0288, 36th AIAA Aerospace Sciences Meeting & Exhibit, Reno NV, January 1998.
- ³ Karabadzhak G.F., Plastinin Yu.A., Afansiev A.V., Szhenov E.Yu., Drakes J.A., McGregor W.K., Nichols J.A., Reed R.A., Bradley D., Teslenko V.P., Shvets N.I., Volkov O.N., and Kukushin V., "Measurements of the Progress-M Main Engine Retrofiring Plume at Orbital Conditions", 37th AIAA Aerospace Sciences Meeting, AIAA Paper 99-1042, Reno, NV, January 1999.
- ⁴ J.A. Drakes, D.G. Swann, G.F. Karabadzhak, and Yu. Plastinin, "DSMC Computations of the Progress-M Retrofiring Exhaust Plume", AIAA Paper 99-0975, 37th AIAA Aerospace Sciences Meeting & Exhibit, Reno NV, January 1999.
- ⁵ Karabadzhak G.F., Plastinin Yu., Szhenov E.Yu., Afanasiev A.V., Drakes J.A., McGregor W.K., Bradley D., Teslenko V., Shvets N., Volkov O., Kukushkin V., Gimelshein S. and Levin D.A., "Mir-based Measurements of the Ultraviolet Emissions from Rocket Exhaust Plume Interactions with the Atmosphere at 380-km Altitude", AIAA Paper 2000-0105, 38th AIAA Aerospace Sciences Meeting & Exhibit, Reno NV, January 2000.
- ⁶ Karabadzhak, G. F., Plastinin Yu., et al. "Preliminary Analysis of Exhaust Plume Radiation during Soyuz-TM Retrofirings", AIAA-paper 2000-2373, 34th AIAA Thermophysics Conf., Denver, CO, 2000.
- ⁷ Karabadzhak, G. F., Khmelinin, B.A., Plastinin, Yu. A. and Rodionov A.V., "Analysis of New Spacecraft Plume Glow Data Taken Onboard of the Mir Space Station", AIAA paper 2003-0509, 41st Aerospace Sciences Meeting, Reno, NV, January 2003.
- ⁸ D.H. Manzella, "Stationary Plasma Thruster Plume Emissions", IEPC-93-097, Proc. of 23 Int'l Electric Propulsion Conference, 1993, p.913.
- ⁹ G.Karabadzhak, A. Semenkin, S.Tverdokhlebov, D.Manzella, "Investigation of TAL optical emissions", IEPC 97-131, Proc. of 25 Int'l Electric Propulsion Conference, Cleveland, OH, 1997.
- ¹⁰ G.Karabadzhak, A.Semenkin, S.Tverdokhlebov, "Evaluation of a Xenon Operating Hall Thruster Body Erosion Rate Through Analysis of its Optical Spectra", 37th Joint Propulsion Conference, paper AIAA-2001-3889, Salt Lake City, 2001.
- ¹¹ G.Karabadzhak, Y.-H.Chiu, S.Williams, R.Dressler, "Hall thruster optical emission analysis based on single collision luminescence spectra", 37th Joint Propulsion Conference, paper AIAA-2001 -3893, Salt Lake City, 2001.
- ¹² S. H. Pullins, Y. H. Chiu, D. J. Levandier et al., "Ion Dynamics in Hall Effect and Ion Thrusters: $\text{Xe}^+ + \text{Xe}$ symmetric Charge Transfer", presented at the 38th Aerospace Sciences Meeting & Exhibit, 2000, AIAA-2000-0603..
- ¹³ G. F. Karabadzhak, Y.H. Chiu, B. L. Austin, S. Williams and R. A. Dressler, "Passive optical diagnostics of Xe propelled Hall effect thrusters: Emission cross sections and collisional-radiative model", in preparation for publishing in JAP.
- ¹⁴ G. Spangers, M. Birkan, T. Lawrence, "The USAF Electric Propulsion Research Program", 36th JPC Conference, AIAA Paper 2000-3146, Huntsville, AL, 2000.
- J.Dunning, J.Sancovic, "NASA Electric Propulsion Program", AIAA Paper 2000-3145.
- ¹⁵ S.O. Tverdokhlebov et al., "Development strategy for 100kW-class Hall propulsion", IAF-00-S.4.07.
- ¹⁶ S.O. Tverdokhlebov, A.V. Semenkin et al., "Consideration of cluster design approach for high power hall propulsion", AIAA-2003-0494.
- ¹⁷ Bird G.A., "Molecular gas dynamics and the direct simulations of gas flows", Clarendon Press, Oxford, 1994.
- ¹⁸ Wysong, I. J.; Dressler, R. A.; Chiu, Y.; Boyd, I. D., "Direct simulation Monte-Carlo dissociation model evaluation: comparison to measured cross-sections", *J. Thermophys.Heat Transfer* 2002, v.16, N1, p.83.
- ¹⁹ Bird, G.A., "Monte-Carlo simulation in an engineering context, Rarefied Gas Dynamics", edited by S. Fisher, Vol. 74, Progress in Astronautics and Aeronautics, 1981, pp. 239-255.
- ²⁰ Gimelshein, S. F., Levin, D. A., Drakes, J. A., Karabadzhak, G. F. and Ivanov, M. S., "Ultraviolet Radiation Modeling from High Altitude Plumes and Comparison with Mir Data", *AIAA Journal*, Vol. 38, No. 9, 2000, pp. 2344–2352.
- ²¹ Gimelshein, S. F., Levin, D. A., Drakes, J. A., Karabadzhak, G.F., Plastinin, Yu.A., "Modeling of Ultraviolet Radiation in Steady and Transient High-Altitude Plume Flows", *Journ. Thermophys. Heat Transfer*, 2002, v.16, N1, p. 58.

- ²² S.F. Gimelshein, D.A. Levin and G.F. Karabadzha, "Modeling of Jet Interactions in a Space Environment Using the Direct Simulation Monte Carlo Method", AIAA paper 2003-1032, 41st AIAA Aerospace Sciences Meeting & Exhibit, Reno NV, January 2003.
- ²³ Erofeev A.I., Friedlander O.G., Karabadzha, G.F., Plastinin Yu.A., "Comparison of Monte-Carlo Modeling and Experimental Results of UV-emission from Engine Exhaust Plume Interacting with Upper Atmosphere", 22nd Symposium on Rarefied Gas Dynamics, paper-585-812, Sydney, 2000.
- ²⁴ "Exhaust Plume Handbook", EPDH-1 prepared of H.Trinks Technical University Hamburg, 1989.
- ²⁵ Hedin, A. E., "Extension of the MSIS Thermosphere Model into the Middle and Lower Atmosphere", J.Geophys.Res, Vol. 96, No A2, pp. 1159-1172.
- ²⁶ Hedin, A. E., "MSIS-86 Thermospheric Model", J.Geophys.Res, Vol. 92, No A5, pp. 4649-4662.
- ²⁷ Karabadzha G., "High-sensitive ultraviolet sensors for rocket exhaust plume and shock waves plasma diagnostics", Proceedings SPIE, vol.1952, p. 75, 1993.
- ²⁸ Jamar C., Macau-Hercot D., Monfils A., Thompson G.I., Houziaux L., Wilson R., "Ultraviolet Bright Stars", Spectrophotometric CATalogue, ESA SR-27 (1976)
Burnashev V.I., "Spectrophotometry of 1588 stars", Abastumanskaya Astrofiz. Obs. Bull., 59, 83, (1985).
Kharitonov A.V., Tereshchenko V.M., Knyazeva L.N., "Spectrophotometric Catalogue of Stars", Alma-Ata, Nauka, p. 484 (1988).
INES ESA INES: IUE (International Ultraviolet Explorer) Newly Extracted Spectra <http://ines.vilspa.esa.es/>
Alekseeva G.A., Arkharov A.A. , Galkin V.D. , Hagen-Thorn E.I., Nikanorova I.N., Novikov V.V., Novopashenny V.B., Pakhomov V.P., Ruban E.V., Shchegolev D.E., "The Pulkovo spectrophotometric catalog of bright stars in the range from 320 to 1080 nm", Baltic Astron. 5, 603 (1996); 6, 481 (1997)
Macau-Hercot D., Jamar C., Monfils A., Thompson L., Houziaux L., Wilson R., Supplement to the Ultraviolet Bright Star Spectrophotometric Catalogue ESA Special Report 28 (1978)
Heck A., Egret D., Jaschek M., Jaschek C., IUE Low-Dispersion Spectra Reference Atlas. I. Normal Stars, ESA SP-1052 (1984)
Astron. Astrophys. Suppl. Ser., 57, 213 (1984)
Spectrophotometry of the bright stars, edited by Glushneva I.N., Moscow, Nauka, 1982.
- ²⁹ Arhipova T.A., Debur V.G., Kuptsova G.z., Mechetin A.M., Pakhomov M.T., Smirnova M.I., "Coordinate-sensitive detector and electron-optical converters, operating in a photon counting mode", Pribori i Tekhnika Experimentov (Experimental Instruments and Technique), N2, 1993, p.146 (in Russian).
- ³⁰ C. Stein, T.R. King, W.G. Wilson and R. Robertson, "Spacecraft contamination, active cleaning and control", Proceedings of SPIE, v.3427, pp.56-64.
- ³¹ Allen C.W. "Astrophysical quantities", University of London, London, 1973.
- ³² Tousey R., "The Radiation from the Sun" in The Middle Ultraviolet: Its Science and Technology, A.E.S. Green, Editor., John Wiley & Sons, Inc. New York-London-Sydney, 1966.
- ³³ Engineering Handbook for space technologies (In Russian: Inzhenernii spravochnik po kosmicheskoi tekhnike), Edited by Solodov A.V. Voennoe izdatelstvo ministerstva oboroni. Moscow, 1977.
- ³⁴ Dobber M. R., "Moon observations with GOME", Proceedings SPIE, Vol.2831, 1996, pp.154-168.
- ³⁵ McEwan M.J., Phillips L.F., "Chemistry of the Atmosphere", Edward Arnold, 1975.
- ³⁶ L.S. Bernstein, Yu.H. Chiu, J.A. Gardner, A.L. Broadfoot, M.I. Lester, M.Tsiouris, R.A. Dressler and E. Murad, "Molecular beams in Space: Sources of OH(A→X) Emission in the Space Shuttle Environment", J.Phys.Chem. A, 2003, v.107, pp10695-10705.
- ³⁷ Bogaerts A., Gijbels R., Vlcek J., Collisional-radiative model for an argon glow discharge, Journ. Appl. Phys. vol.84, 1998, pp. 121-136.
- ³⁸ Vlcek J., "A collisional-radiative model applicable to argon discharges over a wide range of conditions", Journ. Phys. D: Appl. Phys., vol.22, 1989, pp. 623-631.
- ³⁹ Colonna G., Pietanza L.D., Capitelli M., "A collisional radiative model for Xe electrical thrusters, AIAA paper 2000-2349", 31st AIAA Plasmadynamics and Lasers Conference, Denver, CO, June 2000
- ⁴⁰ Leray Ph., Bonnet J., Pigache D., Minea T., Bretagne J., Touzeau M., "Spatially resolved emission spectroscopy along a SPT channel. Interpretation of data by a collisional-radiative model", IEPC-97-054, 25th Int. Electric Propulsion Conf., Cleveland OH, 1997.
- ⁴¹ Sobelman I.I., Vainshtein L.A., Yukov E.A., "Excitation of Atoms and Broadening of Spectral Lines", Second edition, Springer Series on Atoms+Plasmas, v.15, Springer, 1998 (in English).
Vainshtein L.A., Sobelman I.I., Yukov E.A., "Vozbuzhdenie atomov i ushirenie spectral'nih linii", Moscow, Nauka, 1979 (in Russian).
- ⁴² G.Griem, "Spektroskopia plazmi", Atomizdat, Moscow, 1969 (in Russian), supplemented edition of H.G.Griem, Plasma spectroscopy, McGraw-Hill Book Company, New-York, San-Francisco, Toronto-London, 1964.
- ⁴³ "Plasma diagnostics", edited by W. Lochte-Holtgreven, Kiel University, North-Holland Publishing Company, Amsterdam, 1968.

- ⁴⁴ Bugrova A.I., Ermolenko V.A., Niskin V.T., Sokolov A.S., "Spectral'nie harakteristiki energii izluchenija plazmi UZDP (Spectral characteristics of plasma radiation power in closed drift accelerator)", *Teplofizika visokih temperatur*, v.19, N2, 1981, p.428 (in Russian).
- ⁴⁵ N.B. Meezan, W.A. Hargus, D. P. Schmidt, M. A. Cappelli, "Optical Study of Anomalous Electron Transport in a Laboratory Hall Thruster", AIAA Paper-99-2284, 35th Joint Propulsion Conference, Los Angeles, CA, 1999
- ⁴⁶ Bugrova A.I., Volkova L.M., Ermolenko V.A., Kral'kina E.A., Devyatov A.M., Kharchevnikov V.K., "Dinamika funktsii raspredelenija elektronov po energijam v kanale UZDP" (Dynamics of the electron energy distribution function in channel of a plasma thruster with extended acceleration zone), *Teplofizika visokih temperatur*, v.19, N6, 1981, p.1149 (in Russian, translated in *High Temp.*, v.19, 882, 1982)
- ⁴⁷ Bugrova A.I., Ermolenko V.A., Sokolov A.S., "Opticheskie issledovaniya neytral'noy komponenti ksenonovoy plazmi v usloviyah neravnovesnosti" (Optical study of xenon plasma neutral component in non-equilibrium conditions), *Teplofizika visokih temperatur*, v.25, N6, 1987, p.1080 (in Russian).
- ⁴⁸ Prioul M., Roche S., Pagnon D., Magne L., Touzeau M., Bouchoule A., Lasgorceix P., "Insight on closed electron drift thrusters obtained with a discharge shutter as diagnostic tool", AIAA-2001-3358, 37th Joint Propulsion Conference, July 2001, Salt Lake City, UT.
- ⁴⁹ Meezan N.B., Hargus W.A., Capelli M.A., "Optical and electrostatic characterization of oscillatory Hall discharge behavior", AIAA-98-35, 34th Joint Propulsion Conference, July 1998, Cleveland, OH.
- ⁵⁰ Darnon F., Lyszyk M., Bouchoule A., "Optical investigation on plasma oscillations of SPT thrusters", AIAA-97-3051, 33rd Joint Propulsion Conference, July 1997, Seattle, WA.
- ⁵¹ Komurasaki K., Sakurai Y., Kusamoto D., "Optical oscillations in a Hall thruster", AIAA-98-3638, 34th Joint Propulsion Conference, July 1998, Cleveland, OH.
- ⁵² Massey H.S., Burhop E.H.S., "Electronic and ionic impact phenomena", London and New-York, 1952.
- ⁵³ F.J. de Heer, D. Jacks, A. Salop, L. Wolterbeek Muller, B.F.J. Luyken, "Excitation of Ne, Ar, Kr and Xe by He⁺ impact (0.3-35 keV)", and S. Dworetzky, R. Novick, W.W. Smith, N. Tolk, "Failure of the Adiabatic Criterion; Structure and Coherence in the Low Energy Excitation of Helium Atoms by Helium Ions", presented on V Int. Conf. on the Physics of Electronic and Atomic Collisions, Leningrad, USSR, July, 1967.
- ⁵⁴ A.V. Phelps, B.M. Jelenkovic, "Excitation and Breakdown of Ar at very high Rates of Electric Field to Gas Density", *Phys. Rev.*, A38, N6, 1988, pp.2975-2990.
- ⁵⁵ A.V. Phelps, "Cross-sections and Swarm Coefficients for Nitrogen Ions and Neutrals in N₂ and Argon Ions and Neutrals in Ar for Energies from 0.1 eV to 10 keV", *Journ. Phys. Chem. Ref. Data*, v.20, N3, 1991, p.557.
- ⁵⁶ Fons J.T., Lin C.C., "Measurements of the cross-sections for electron impact excitation into 5p⁵6p levels of xenon", *Phys. Rev. A*, v.58, N6, 1998, pp.4603-4615.
- ⁵⁷ Gulczinski F.S., Gallimore A.D., "Near-field ion energy and species measurements of a 5-kW Hall thruster, *Journal of Propulsion and Power*", v.17, N2, March-April, 2001, pp.418-427.
- ⁵⁸ King L.B., Gallimore A.D., "Ion energy diagnostics in the plume of an SPT-100 from thrust axis to backflow region, AIAA-98-3641 and Propellant ionization and mass spectral measurements in the plume of SPT-100", AIAA-98-3657, 34th AIAA/ASME/SEA/ASEE Joint Propulsion Conference, July, 1998, Cleveland, OH
- ⁵⁹ Pollard J.E., Beiting E.J., "Ion energy, ion velocity and thrust vector measurements for the SPT-140 Hall thruster", 3rd International Conference on Spacecraft Propulsion, October 2000, Cannes, France.
- ⁶⁰ Biberman L.M., Vorob'ev V.S., Jakubov I.T., "Kinetics of non-equilibrium low-temperature plasma", Nauka publishing, Moscow, 1982 (in Russian).
- ⁶¹ Rostovikova G.S., Samoylov V.P., Smirnov Yu.M., "Measurements of xenon lines excitation cross-sections by electron impact", *Optika i Spektroskopiya*, v.XXXIV, issue 1, 1973, pp.7-12 (in Russian).
- ⁶² Allen L., Jones G.C. and Schofield D.G., "Radiative lifetimes and collisional cross-sections for Xe I and II", *Jour. of the Opt. Soc. of America (JOSA)* v.59, N7, 1969, pp.842-847.
- ⁶³ Bogdanova I.P., Yurgenson S.V., "Cross-sections for direct electron collision excitation of atomic levels: measurements with pulsed electron beam and radiation time scanning. V. Xenon, 5p⁵6p-levels", *Optika i spektroskopija*, v.70, issue 2., 1991, pp.486-487.
- ⁶⁴ Mityureva A.A. and Smirnov V.V., "Excitation of heavy rare gases to metastable states by electron impact", *J. Phys. B: At. Mol. Opt. Phys.*, v.27, 1994, pp.1869-1880.
- ⁶⁵ S. Nakazaki, K.A. Berrington, W.B. Eissner and Y. Itikawa, "Excitation of xenon by electron impact", *Journ. of Phys. B: At. Mol. Opt. Phys.*, v.30, 1997, pp. 5805-5818.
- ⁶⁶ M.A. Khakoo, S. Trajmary, L. R. LeClair, I. Kanik, G. Csanak and C. J. Fontes, "Differential cross sections for electron impact excitation of Xe: I. Excitation of the five lowest levels; experiment and theory", *J. Phys. B: At. Mol. Opt. Phys.* v.29, 1996, 3455-3475.
M.A. Khakoo, S. Trajmary, S. Wangyz, I. Kanik, A. Aguirre, C. J. Fontes, R. E. H. Clark and J. Abdallah Jr., "Differential cross sections for electron impact excitation of Xe: I. Excitation of the sixth to twentieth lowest levels; experiment and theory", *J. Phys. B: At. Mol. Opt. Phys.* v.29, 1996, 3477-3486.
- ⁶⁷ G.N. Malovic', A.I. Strinik, Z.Lj. Petrovic', J.V. Bozin, and S.S. Manola, Electron excitation coefficients for 2p and 3p levels of Xe, *Eur. Phys. Journ. D*, v.10, 2000, pp. 147-151.
- ⁶⁸ "Handbook for elementary processes involving atoms, ions, electrons and photons", edited by Prof. A.G. Zhiglinski, St.Petersburg Univ. Publishing, St.Petersburg, 1994.

- ⁶⁹ Human H.A., "Electron impact excitation cross-section $(n-1)p^5ns-(n-1)p^5np$ in the rare gases", *Phys.Rev A*, v.24, N2, 1981, p.1094-1095.
- ⁷⁰ Kolokolov N.B., Kudrjavev A.A., Nikitin A.G., "Investigation of step-wise excitation in xenon", *Optica i Spektroskopia (Optics and Spectroscopy)*, v.67, N4, 1989, pp.766-772.
- ⁷¹ "Physical-Chemical Processes in Gas Dynamics. Volume I. Dynamics of Physical-Chemical Processes in Gases and Plasma", Handbook, edited by G.G. Chernii and S.A. Losev, Moscow Univ. Publishing, 1995 (in Russian, English version is available through AIAA)
- ⁷² Sabbagh J. and Sadeghi N., "Experimental transition probabilities of some Xe(I) lines", *Journ. Quant. Spectr. & Radiative Transfer*, v.17, N3, pp. 297-301 (1977).
- ⁷³ Planeuf R.A., "Experiments on Electron-Impact Excitation and Ionization of Ions", *Proc. of NATO ASI, ser.B*, v.145, 1985, pp.117-156.
- ⁷⁴ N.Sadeghi, Z.Lj.Petrovich, G.N.Malovich and A.I.Strinic, "Excitation coefficients for ionic levels of Xe", Workshop on Frontiers in Low Temperature Plasma Diagnostics IV, March 25-29, Roldic, The Netherlands, 2001.
- ⁷⁵ Domonkos M.T., Gallimore A.D., Marrese C.M. and Haas J.M., "Very-Near-Field Plume Investigation of the Anode Layer Thruster", *Journal of Propulsion and Power*, v.16, N1, January-February 2000, pp.91-98.
- ⁷⁶ Boyd I.D., "Computation of the plume of anode-layer Hall thruster", *Journal of Propulsion and Power*, v.16, N5, September-October 2000, pp.902-909.
- ⁷⁷ Allen L., Jones D.G.C. and Schofield, "Radiative Lifetimes and Collisional Cross Sections for Xe I and II", *J. Opt. Soc. Am.* Vol. 59, No 7, pp. 842-847(1969)
- ⁷⁸ Miller M.H., Roig R.A. and Bengtson R.D., "Transition Probabilities of Xe I and Xe II", *Phys. Rev. A*, Vol.8, No. 1, pp. 480 – 486 (1973).
- ⁷⁹ Wiese W.L. and Martin G.A., "Wavelength and Transition Probabilities for Atoms and Atomic Ions, Part II: Transition Probabilities", US NBS NSRDS – NBS 68, 1980.
- ⁸⁰ Martin I., Hernando C., Lavin C. and Velasco A.M., "Transition probabilities for singly ionized xenon", *J. Quant. Spec. & Rad. Transfer*, v.62, pp.71-83, 1999.
- ⁸¹ Lazovskaya V.R., Tumakaev G.K., "Determination of the oscillator strengths and Stark constants for s-p atomic xenon transitions in a shock tube", *Zhurnal Tech. Fiziki (Journal of Technical Physics)*, v.49, issue 3, 573-580, 1979 (in Russian).
- ⁸² Hirata R., Horaguchi T., "Atomic Spectral Line List, in Atomic and Molecular Optical Database System (AMODS)", <http://amods.kaeri.re.kr/spect/xs.html>, 1994.
- ⁸³ L.E. Zakharenkov, A.V. Seminkin. et al., "Study of multi thruster assembly operation", IEPC-2003-0311.
- ⁸⁴ A.V. Rusakov et al., "Multiple thruster propulsion system integration study", IEPC-97-130.
- ⁸⁵ A.V. Seminkin et al., "RHETT/EPDM Flight anode layer thruster development", IEPC-97-106.
- ⁸⁶ B. Beal, A. Gallimore et al., "Preliminary plume characterization of a low-power Hall Thruster Cluster", AIAA 2002-4251.
- ⁸⁷ D. Keefer et al., "Multiplexed LIF and Langmuir probe diagnostic measurements in the TAL D-55 thruster", AIAA 99-2425.
- ⁸⁸ Y. Azziz, M. Martinez-Sanchez, "Plasma measurement on a 200-watt Hall thruster plume", IEPC-2003.
- ⁸⁹ A.I. Morozov, "Basic physics of space electric propulsions", Vol.1 ,Moscow: Atomizdat, 1978 (in Russian).
- ⁹⁰ B.S. Borisov, "Experimental study of exhaust beam of anode layer thruster", IEPC-95-51.
- ⁹¹ V.I. Garkusha et al., "Ion energy measurement of a D-55 Hall thruster", 3rd International conference on spacecraft propulsion, 2000.
- ⁹² S.A. Khartov et al., "Some remarks about published data concerning the SPT-100 jet parameters distribution", IEPC-97-152.
- ⁹³ Questions of Plasma Theory , v.1, #8, M.: Atomizdat, 1973.
- ⁹⁴ D.Rose, M.Clark, J., "Plasmas and Controlled Fusion", New-York-London, 1961.
- ⁹⁵ L.A.Arzhimovich, "Controlled thermonuclear reactions", Moscow, Fizmatgiz, 1963 (in Russian).
- ⁹⁶ A.I.Morozov. "Physical basics of space electric propulsion. V.1. Elements of flows dynamics in Electric Propulsion", M.: Atomizdat, 1978.
- ⁹⁷ K.D.Sinelnikov, Yu.S.Azovskiy, B.G.Safronov. Proc. Plasma physic and problems of controlled thermonuclear fusion. V.1, Kiev, AN USSR, 1962.
- ⁹⁸ R.M.Myers, D.H.Manzilla. "Stationary Plasma Thruster Plume Characteristics", 23rd Int.Electric Propulsion Conf. Seattle, 1993, IEPC-93-096
- ⁹⁹ I.Boyd. "A review of Hall thruster plume modeling", 38th AIAA Aerospace Sci. Meeting, Reno 2000, AIAA-00-0466.
- ¹⁰⁰ A.G.Korsun. "Temperature layer in magnetized plasma", *J. of Plasma physic*, v.7, N1, is.14 , 1981, p.145-158. (in Russian)
- ¹⁰¹ A.B.Michailovskiy. "Theory of plasma non-stability", V.1, M.: Atomizdat, 1971.
- ¹⁰² K.P. Kirdjashev at.al. "Measurements of electromagnetic emissions at long-term tests of T-100", IEPC-95-073. 24th IEPC, Moscow, 1995

- ¹⁰³ Garner C.E. and et.ab. "Performance evaluation and life testing of the SPT-100", IEPC-93-091. 23rd IEPC, Seattle, 1993.
- ¹⁰⁴ Sankovik J. and et.ab. "Performance evaluation of the Russian SPT-100 thruster at NASA LeRC", IEPC-93-094. 23rd IEPC, Seattle, 1993
- ¹⁰⁵ Questions of Plasma Theory, v.2, M.: Atomizdat, 1973.
- ¹⁰⁶ A.M.Bishaev, V.K.Kalashnikov, V.Kim, A.V.Shavikina. Numerical modeling of SPT plasma plume expanding into the low pressure environment.// J. Plasma Physics, v.24, #11, 1998, pp.923-928
- ¹⁰⁷ I.Boyd, "Hall thruster far field plume modeling and comparison to Express flight data", 40th ASME, Reno 2002, AIAA 2002-0487.
- ¹⁰⁸ Braginskiy S.I." The transfer phenomena in plasma", Proc.: Questions of plasma theory. M.: Gosatomizdat, 1963, N1. (in Russian).
- ¹⁰⁹ L.I.Sedov. "The methods of similarity and dimension in mechanics", M: Nauka, 1967 (in Russian).
- ¹¹⁰ A.G.Korsun, E.M.Tverdokhlebova. "The Characteristics of the EP Exhaust Plume in Space", 33rd Joint Prop.Conf. Seattle, 1997, AIAA-97-3065
- ¹¹¹ A.G.Korsun, E.M.Tverdokhlebova, F.F.Gabdullin. The Earth's Magnetic Field Effect upon Plasma Plume Expansion./ 25th Int. El. Prop. Conf., Cleveland, 1997, IEPC-97-178
- ¹¹² R.M.Myers, D.H.Manzella. Stationary Plasma Thruster Plume Characteristics./23rd Int.Electric Propulsion Conf. Seattle, 1993, IEPC-93-096
- ¹¹³ A.V.Semenkin et.al., "Experimental study of exhaust beam of anode layer thruster", IEPC-95-51.
- ¹¹⁴ V.Garkusha, A.Kochergin, A.Rusakov, A.Semenkin, E.Evlanov, S.Podkolzin, Yu.Lebedev. Ion energy measurement of a D-55 Hall thruster//3rd Int.conf. "Spacecraft Propulsion", Cannes, France, 2000.
- ¹¹⁵ Sankovik J. and et.ab. Performance evaluation of the russian SPT-100 thruster at NASA LeRC. IEPC-93-094. 23rd IEPC, Seattle, 1993
- ¹¹⁶ Hasted J., "Physics of Atomic Collisions", Moscow, Mir, 1965. (Russian translation)
- ¹¹⁷ Tables of physical values, Handbook, Editor I.K.Kikoin, Moscow. Atomizdat, 1976. (in Russian)
- ¹¹⁸ A.G.Korsun, B.S.Borisov, E.M.Tverdokhlebova, F.F.Gabdullin, "Comparison between plasma exhaust theoretical models and experimental data", 26th IEPC, 1999, paper IEPC-99-221.
- ¹¹⁹ Absalamov S.K. and et.ab., "Measurement of Plasma Parameters in the Stationary Plasma Thruster (SPT-100) Plume and its Effect on Spacecraft Components", 28th Joint Propulsion Conference and Exhibit. July 6-8, 1992. Nashville, TN, Paper AIAA-92-3156.
- ¹²⁰ A.Korsun, F.Gabdullin, E.Tvedokhlebova, "Performance evaluation of the secondary plasma of Hall type thruster", 37th Joint Prop.Conf., Salt Lake City, 2001, AIAA 2001-3508.
- ¹²¹ R.R. Hofer, A.D. Gallimore, "Recent Results from Internal and Very-Near-Field Plasma Diagnostics of a High Specific Impulse Hall Thruster", 28th IEPC, Toulouse, France, 2003. IEPC-2003-037.
- ¹²² L.M.Carney, "Evaluation of the Communications Impact of a Low Power Arcjet Thruster", 24th Joint Propulsion Conference, Boston, July 1988.AIAA-88-3105.
- ¹²³ Roberts L., South I.C. Jr., "Comments on Exhaust Flow Field and Surface Impingement", AIAA Journal, No 5, 1964, p. 238.
- ¹²⁴ Narasimha A., "Collisionless expansion of gases into vacuum", Journal of Fluid Mechanics Vol 12, No 12, 1962, pp. 294-308.
- ¹²⁵ S.G.Ohler, A.B.Ruffin, B.E.Gilchrist, A.D.Gallimore, "RF Signal Impact Study of an SPT", 32nd Joint Propulsion Conference, Lake Buena Vista, July 1996.AIAA-96-2706.
- ¹²⁶ A.M.Bishaev, V.K.Kalashnikov, V.Kim, A.V.Shavikina. "Numerical modeling of SPT plasma plume expanding into the low pressure environment", J. Plasma Physics, v.24, #11, 1998, pp.923-928.
- ¹²⁷ D.Oh,D.Hastings, "Experimental Verification of a PIC-DSMC Model for Hall Thruster Plumes", 32nd Joint Propulsion Conference, Lake Buena Vista, July 1996, AIAA-96-3196.
- ¹²⁸ L.B.King, "Transport- property and mass spectral measurements in the plasma exhaust plume of a Hall – effect space propulsion system", Doctoral thesis, The University of Michigan, 1998.
- ¹²⁹ D.Keefer, N.Wright, J.Hornkohl, J.Bangasser. "Multiplexed LIF and Langmuir Probe Diagnostic Measurements in the TAL D-55 Thruster", 35th JPC. LA, 1999, AIAA-99-2425.
- ¹³⁰ A.G.Korsun, F.F.Gabdullin, E.M.Tverdokhlebova, V.I.Garkusha, V.P.Khodnenko, "Comparison of mathematical model of a plasma plume with outcomes of space experiments", IEPC-2003-0206
- ¹³¹ A.G.Korsun, E.M.Tverdokhlebova, F.F.Gabdullin, "The Earth's Magnetic Field Effect upon Plasma Plume Expansion", 25th Int. El. Prop. Conf., Cleveland, 1997, IEPC-97-178.
- ¹³² D.Manzella, "Hall Thruster Plume Measurements Onboard the Russian Express Satellite", 27th IEPC, Pasadena 2001, IEPC-01-044.
- ¹³³ I.Boyd, "Hall thruster far field plume modeling and comparison to Express flight data", 40th ASME, Reno 2002, AIAA 2002-0487.
- ¹³⁴ A.G.Korsun, E.M. Tverdokhlebova, F.F. Gabdullin, "The estimation of the torque and forces arising due to interaction of the exhaust plume with SC body", Proc. 3rd Int. Conf. on Spacecraft Propulsion, Cannes, October 2000, ESA SP-465, December 2000.

- ¹³⁵ P.Cheoux-damas, J.M.Stefan, S.Castejon, A.Romashko, V.Petrusevith, D.Volkov, "Validation of an ion thruster plume impingement software by in-flight measurements", Proc. 2nd Europ. Spacecraft Prop.Conf., 1997, ESA SP-398, Aug.,1997.
- ¹³⁶ A.V. Rodionov, Yu.A. Plastinin, J.A. Drakes, M.A. Simmons and R.S. Hiers III, "Modeling of Multiphase Alumina-Loaded Jet Flow Fields", 34th AIAA Joint Propulsion Conference, July, 1998, Cleveland, OH, AIAA 98-3462.
- ¹³⁷ Leonas V.B., "Intermolecular interactions and collisions between atoms and molecules", VINITI, Summary on Science and Technology, Atomic and Molecular Physics series, Optics, Magnetic resonance, v.1, Moscow, 1980.
- ¹³⁸ Gordeev O.A., Kalinin A.P., Komov A.L., Lusternik V.E., Samuilov E.V., Sokolova I.A., Fokin L.V., "Interaction potentials, elastic cross-sections, collisional integrals for air components at temperatures up to 2000 K", Review of Thermophysical Properties of Matter, IVTAN, N5(55), M. 1985.
- ¹³⁹ P.B.Foreman et al., Chem.Phys., 1976, N12, 213 (as cited in Ref.¹³⁷).
- ¹⁴⁰ J.N.Moss, G.A.Bird, "Monte-Carlo Simulation in Support of the Shuttle Upper Atmospheric Mass Spectrometer Experiment", AIAA 20th Thermophysics Conference, 1985, Williamsburg, Virginia, AIAA-85-0968.
- ¹⁴¹ Levine, R. D.; Bernstein, R. B., J. Chem. Phys. 1972, 56, 2281
- ¹⁴² Morokuma K., Eu B.C., Karplus M., "Collisional Dynamics and Statistical Theories of Chemical Reactions. I. Average Cross-Section from Transition-State Theory", Journ.Chem.Phys., v.51, N12, 1970, 5193.
- ¹⁴³ Kondratiev V.N., Nikitin E.E., Reznikov A.I., Umanskii S.Ya., "Thermal bimolecular reactions in gases", Nauka, Moscow, 1976 (in Russian).
- ¹⁴⁴ Baulch D.L., Drysdale D.D., Horn E.G. and Lloyd A.C., "Evaluated kinetic data for high temperature reactions, v.I: Homogeneous gas phase reactions of the H₂-O₂ system", Butterworths, London, 1972.
- ¹⁴⁵ Cohen, N. and Westberg, K. R., "Chemical kinetic data sheets for high temperature chemical reactions", J. Phys. Chem. Ref. Data, Vol. 12, 1983, p. 531-558.
- ¹⁴⁶ Kofsky, I. I., Barrett, J. L., Brownrigg, T. E., McNicholl, P. N., Tran, N. H., and Trowbridge, C.A., "Excitation and Diagnostics of Optical Contamination in the Spacecraft Environment," AFGL-TR-88-0193, July 1988.
- ¹⁴⁷ Matsika, S., Yarkony, D. R., "Conical interceptions and non-adiabatic reactions H₂O + O(³P) → OH(A²Σ⁺) + OH(X²Π)", J. Chem. Phys., 2002, 117, 3733.
- ¹⁴⁸ Sternin L.E., "Gasdynamic fundamentals of two-phase flows in nozzles", M., Mashinostroenie. 1974.
- ¹⁴⁹ Rodionov A.V. "Methods of Increasing the Accuracy in Godunov's Scheme", USSR Comput. Maths. Math. Phys., 1987, Vol.27, No.6, pp.164-169.
- ¹⁵⁰ S.Gimelshein, Private communication. A mistake was found in computation results reported in Ref.²². After correction the modeled radiation profile became yet more narrower than experimental one.
- ¹⁵¹ Plastinin Yu., Karabadzha G., Khmelin B., Baula G., Rodionov A., "Ultraviolet visible and Infrared Spectra modeling for Solid and Liquid Fuel Rocket Exhausts", 39th AIAA Aerospace Sciences Meeting, Reno, 2000, AIAA Paper 2001-0660.
- ¹⁵² L.C. Lee, L. Orent, E. Phillips, D.L. Junge, Journ.Phys. B: Atom.Molec.Phys., v.11, 1978, p.47. L.C. Lee, Journ.Chem.Phys., v.72, 1980 p.4334.
- ¹⁵³ S.A. Harrieh, H.D.W. Hwang, X. Yang, J.J. Lin, R.N. Dixon, Journ.Chem.Phys., v.113, 2000, p.1073.
- ¹⁵⁴ Vierek R.A, Murad E., Pike C.P., Mende S.B., Swenson G.A., Elgin J.B., Bernstein L.S. and Lucid S., "O(¹S) 557.7 nm and O(¹D) 630 nm emissions in shuttle thruster plumes", Journ.Geoph.Res., v.100, N.A4, 1995, pp.5819-5825.
- ¹⁵⁵ W.L. Wiese, M.W. Smith, B.M. Glennon, "Atomic Transition Probabilities", v.1, Hydrogen through Neon, NBS, 1966.
- ¹⁵⁶ Baulch, D.L., Drysdale, D.D., Duxbury, J., Grant, S.J., "Evaluated Kinetic Data for High Temperature Reactions. V. III: Homogeneous Gas Phase Reactions at the O₂-O₃ System, CO-O₂-H₂ System and Sulfur-Containing Compounds", Butterworth,London,1976.
- ¹⁵⁷ Sulzman,K.G.P., Myers,B.F., Bartle,E.R. J. Chem. Phys. 1965, V.42, p.3969.
- ¹⁵⁸ Begen, V., "Vibrational Populations of O₂(A³Σ_u⁺) and Synthetic Spectra of Herzberg Bands in the Night Airglow", J. Geophys. Res., 1969, V.74, N.21, pp. 5145-5154.
- ¹⁵⁹ Kuznetsova,L.A., Kuzmenko, N., E., Kuzyakov, Yu.Ya., Plastinin, Yu. A., "Optical Transition Probabilities for Diatomic Molecules", Moscow, Nauka, 1980 (in Russian).
- ¹⁶⁰ Kamenshikov V.A., Plastinin Yu.A., Nikolaev V.M., Novitskii L.A., "Radiative Properties of gases at High Temperatures", Moscow, Mashinostroenie, 1971 (in Russian)
- ¹⁶¹ Kuzmenko N.E., Kuznetsova L.A., Kuzyakov Yu.Ya., "Frank-Condon factors for diatomic molecules", Moscow, MGU Publishing, 1984 (in Russian).
- ¹⁶² Huber K.P., Herzberg G., "Molecular spectra and molecular structure. IV. Constants of diatomic molecules", 1979.
- ¹⁶³ I.J. Wysong, Private communication

¹⁶⁴ N. Sadeghi and J. Sabbagh, "Collisional transfer between the $6s'[1/2]_{0,1}$ and $6p[1/2]_1$ xenon levels", Phys.Rev. A, v.16, N6, 1977, pp.2336-2345.